

Dartmouth College

## Dartmouth Digital Commons

---

Dartmouth College Ph.D Dissertations

Theses and Dissertations

---

Fall 9-15-2023

# Development of Single-Crystalline and 3D-Printable Porous Organic Materials

Mingshi Zhang

mingshi.zhang.gr@dartmouth.edu

Follow this and additional works at: <https://digitalcommons.dartmouth.edu/dissertations>

 Part of the [Materials Chemistry Commons](#)

---

### Recommended Citation

Zhang, Mingshi, "Development of Single-Crystalline and 3D-Printable Porous Organic Materials" (2023).  
*Dartmouth College Ph.D Dissertations*. 217.  
<https://digitalcommons.dartmouth.edu/dissertations/217>

This Thesis (Ph.D.) is brought to you for free and open access by the Theses and Dissertations at Dartmouth Digital Commons. It has been accepted for inclusion in Dartmouth College Ph.D Dissertations by an authorized administrator of Dartmouth Digital Commons. For more information, please contact [dartmouthdigitalcommons@groups.dartmouth.edu](mailto:dartmouthdigitalcommons@groups.dartmouth.edu).

# Development of Single-Crystalline and 3D-Printable Porous Organic Materials

A Thesis

Submitted to the Faculty

in partial fulfillment of the requirements for the

degree of

Doctor of Philosophy

in

Chemistry

by Mingshi Zhang

Guarini School of Graduate and Advanced Studies

Dartmouth College

Hanover, New Hampshire

Sep 15<sup>th</sup>, 2023

Examining Committee:

---

(Chair) *Chenfeng Ke, Ph.D.*

---

*Mahima Sneha, Ph.D.*

---

*Katherine Mirica, Ph.D.*

---

*Michael Mastalerz, Ph.D.*

---

F. Jon Kull, Ph.D.

Dean of the Guarini School of Graduate and Advanced Studies



## Abstract

Porous organic materials with designable structures, large surface areas, low densities, and unique electronic and optical properties have found widespread applications in adsorption, separation, energy storage, and catalysis. However, the majority of organic porous materials are synthesized as fluffy powders, which poses two fundamental challenges for them. Firstly, they lack a single-crystal structure at the microscopic scale, making it difficult to study the specific pore size, shape, and potential substrate binding sites at the atomic level and further establish the structure-property relationship. Secondly, they lack the general processing method and macroscopic shape design, making it difficult to manufacture suitable components for specific applications in real-world settings. Such deficiencies can also potentially impact the material's mass transfer efficiency and other performance aspects. In this thesis, based on my research on porous organic materials, I propose my thoughts and design to help solve the two challenges mentioned.

Firstly, I discussed why we need single crystals and how to synthesize a single-crystalline covalently connected framework. (1) I present examples of the fundamental study of host-guest and guest-guest interactions of multiple guest molecules within a hydrogen-bonded organic framework (HOF) through single-crystal structure analysis. (2) Using our group's unique method for designing hydrogen-bonded cross-linked organic frameworks (HcOFs), I demonstrate the synthesis of single-crystal ionic HcOF-7 with halogen bonding and anion exchanging active sites, which is utilized for both  $I_2$  and  $I^-$  at high temperatures.

Second, I introduce 3D-printing technology to fabricate porous organic materials with macroscopic structures. (1) For the first time, I describe a general method for large-scale synthesis of 3D-printable imine-based covalent organic frameworks (COFs) using the hierarchical self-assembly enabled template synthesis. (2) I discovered that the template synthesis-based 3D printing technique could also be employed for the fabrication of covalently cross-linked amorphous porous polymers with nano-tubular cavities, which could be used for highly efficient natural product separation.

Overall, by integrating knowledge from different fields, I aim to help connect the micro to the macro and establish bridges between the molecular design, materials properties, and real-life application of porous organic materials.

## Acknowledgements

First and foremost, I would like to take this opportunity to extend a special thank you to my advisor, Prof. Chenfeng Ke. I am deeply grateful for his unwavering support, guidance, and nurturing, which have set me on the path to becoming an independent researcher. I am also thankful for his assistance in both my research and personal life, as well as his strong support for my career development. The knowledge he has imparted to me is an invaluable treasure that will benefit me throughout my life. Under his instruction, I have focused on addressing fundamental challenges in materials development. Through countless hours spent studying porous materials and reviewing numerous articles, I gradually realized the urgency of the research problem investigated in this topic, sparking a profound interest within me. I would also like to express my gratitude to my undergraduate advisor, Prof. Xianhe Bu, who introduced me to the field of porous materials and provided continuous assistance even after graduation.

I extend my heartfelt thanks to my committee members, Profs. Mahima Sneha, Katherine Mirica, Michael Mastalerz for their guidance and invaluable feedback on my thesis. I would like to also thank Profs. Robert Cantor and Glenn Micalizio for serving as the examiners for my PhD qualify exam. In addition, I am also grateful to my instructors of courses, Profs. Ivan Aprahamian, Jane Lipson, and Gordon Gribble, for their teachings and the knowledge they have shared with me.

I would like to acknowledge the department staff, including Jean Carlen and Paul Defino, for their support in equipment maintenance, training, and assistance. I am grateful for the collaborative work provided by Anita Prasad, Catherine O. Welder, and others during my time as a teaching assistant. I extend my thanks to Andrew G. Coombs, Hillerie R. Stone, Rebecca Talmadge, and other administrative staff for their support.

I would like to express my appreciation to my research collaborators, including Dr. Longyu Li, Dr. Qianming Lin, Dr. Wenxing Liu, Dr. Miao Tang, Dr. Jayanta Samanta, Dr. Richard Staples, Dr. Aaron J. Rossini, Benjamin A. Atterberry, and Yuyang Wu. It's an honor to work with you. I would also like to thank other colleagues in my lab, including Haoyi Wang, Xunzhe Cui, Dr. Xuanfeng Jiang, Dr. Krishanu Samanta, Dr. Dan Zheng, Dr. Errui Li, Dr. Andrew Duncan, Yunjia Zhang, Zhuoran Zhong, Fangzhou Li, Albert Chen, Yingzi Ma, Deng Zhou, and others. Their kindness, responsibility, and insightful discussions have greatly influenced my work. I consider myself fortunate to have had the

opportunity to work alongside them, and I am proud of their expertise and competitiveness. I extend my best wishes to each and every one of them.

Furthermore, I would like to extend special thanks to the pioneers in the field, including Omar Yaghi, James Wuest, William Dichtel, and Banglin Chen, whose outstanding contributions have provided theoretical support and important references for my research.

I want to acknowledge funding support from the American Chemical Society Petroleum Research Fund (58377-DNI10), the National Science Foundation EPSCoR New Hampshire BioMade Center (1757371), National Science Foundation CAREER award (DMR 1844920), Arnold & Mabel Beckman Foundation Beckman Young Investigator program, Department of Energy the Basic Energy Sciences (grant Nos. DE-SC0022267 and NSF EPSCoR-1757371), and the startup fund of Dartmouth College.

I would like to express my heartfelt appreciation to my parents for their unwavering support and encouragement. I am also grateful to my friends and relatives for their support. Lastly, I would like to thank my partner, Xuting Zhu, for being a part of my life.

## Table of Contents

Chapter 1 Introduction .....	1
1.1 Introduction.....	3
1.2 Single-crystalline hydrogen-bonded crosslinked organic frameworks and their dynamic guest sorption .....	5
1.2.1 Molecularly engineering porous hydrogen-bonded networks .....	8
1.2.2 Accessing Single-Crystalline Frameworks and Polymers .....	11
1.2.3 Design and synthesis of H <sub>c</sub> OF.....	16
1.2.4 SCXRD analysis of H <sub>c</sub> OFs.....	22
1.2.5 Dynamic sorption of H <sub>c</sub> OFs .....	25
1.3 3D printing porous organic materials using direct ink writing.....	27
1.3.1 3D printing methods .....	30
1.3.2 Tools and design considerations for 3D printing porous materials using DIW.....	32
1.3.3 3D printing inorganic porous materials .....	36
1.3.4 3D printing organic porous materials .....	41
1.3.5 The applications of 3D-printing porous materials .....	47
1.4 Conclusion and Outlook .....	57
1.5 References.....	59
Chapter 2 Assembling Guests as Cyclic Tetramers in a Porous Hydrogen-Bonded Organic Framework .....	68
2.1 Introduction.....	70

2.2 Experimental Section .....	71
2.3 Results and Discussions .....	72
2.4 Summary .....	78
2.5 Appendices.....	79
2.5.1 General Methods .....	79
2.5.2 Synthetic Procedures.....	79
2.5.3 Single-crystal X-ray data .....	82
2.5.4 <sup>1</sup> H NMR spectra.....	93
2.5.5 Vapor sorption analysis.....	105
2.6 References.....	105
Chapter 3 A Crosslinked Ionic Organic Framework for Efficient Iodine/Iodide Remediation in Water .....	
	109
3.1 Introduction.....	111
3.2 Results and Discussion .....	113
3.3 Summary .....	124
3.4 Appendices.....	124
3.4.1 General Information.....	124
3.4.2 Synthesis and characterization of H <sub>C</sub> OF-7 .....	125
3.4.3 Single-crystal X-ray data .....	137
3.4.4 Porosity Analysis .....	147



3.4.5 Residual Iodine and iodide sorption investigations. ....	148
3.4.6 Static iodine adsorption investigations. ....	151
3.4.7 Iodine solution breakthrough experiment .....	160
3.4.8 <sup>1</sup> H NMR, <sup>13</sup> C NMR, and HR-MS spectra .....	163
3.5 References.....	170
Chapter 4 Hierarchical Co-assembly-enabled 3D-Printing of Homogeneous and Heterogeneous Covalent Organic Frameworks .....	
	173
4.1 Introduction.....	175
4.2 Results and Discussions.....	177
4.3 Summary .....	183
4.4 Appendices.....	184
4.4.1 General Information.....	184
4.4.2 Synthetic Methods .....	185
4.4.3 Structural modeling and Powder X-ray diffraction analysis.....	195
4.4.4 FT-IR Spectroscopies.....	208
4.4.5 Rheological Studies and 3D Printing.....	211
4.4.6 Morphology Analysis.....	217
4.4.7 Porosity Analysis .....	222
4.4.8 Solid-state NMR Spectra .....	228
4.5 References.....	230

Chapter 5 Hierarchically templated synthesis of 3D-printed crosslinked cyclodextrins for lycopene harvesting .....	232
5.1 Introduction.....	234
5.2 Results and Discussions.....	235
5.3 Summary.....	244
5.4 Appendices.....	245
5.4.1 General Information.....	245
5.4.2 Formation of kinetically trapped 3D-printable PRHs.....	258
5.4.3 Post-printing synthesis.....	274
5.4.4 Materials characterizations .....	280
5.4.6 Lycopene harvesting .....	287
5.5 References.....	308
Chapter 8 Conclusion.....	311

## List of Figures

- Figure 1.1.** Schematic illustration of structure-property-application relationship in covalently connected porous organic materials. ....5
- Figure 1.2.** The design of H<sub>c</sub>OFs through crystallization and subsequent SCSC transformation. Upon guest adsorption, the framework will dynamically change its 3D architecture based on substrate-framework interactions. Copyright 2017 American Chemical Society. ....7
- Figure 1.3.** (a) Homo- hydrogen bonding synthons and their corresponding hydrogen bonding patterns in HOFs' design. (b) Hetero-hydrogen bonding synthons and their corresponding hydrogen bonding patterns in HOFs' design. (c) Core struts used for HOFs. Copyright 2022 American Chemical Society. ....10
- Figure 1.4.** (Struts that have been used in isoreticularly expanding the pore of HOFs. Copyright 2022 American Chemical Society. ....11
- Figure 1.5.** (a) Synthesis of COF-5 and a TEM image of COF-5 crystal. Copyright 2018 Science. (b) Synthesis of Nitroso-COFs via nitroso dimerization. Right: single-crystal structures of Nitroso-COF-2.<sup>11</sup> (c) Synthesis of single crystalline imine-based COF-303 through transamination. Right: the single-crystal structure of COF-303.<sup>10</sup> (d) Solid-state structure of COF-320 with nine-fold interpenetration and their RED pattern. Copyright 2013 American Chemical Society. (e) Solid-state structures of active COF-300, COF-300•H<sub>2</sub>O, and COF-300•polymethylmethacrylate (COF-300•PMMA). Copyright 2019 American Chemical Society. ....13
- Figure 1.6.** (a) Topochemical [2 + 2] cycloaddition and the synthesis of a single-crystalline 2D polymer sheet obtained from **M<sub>T</sub>-1**. (31) Solid-state (b) 1,3-diyne polymerization and (c) [3 + 2] azide-alkyne cycloaddition. (d) Topochemical [4 + 2] anthracene-alkyne cycloaddition and the monomer **M<sub>T</sub>-2** used for 2D polymer synthesis. (28) (e) [4 + 4] anthracene dimerization and the monomer **M<sub>T</sub>-3** used for 2D polymer synthesis. (33) Unreacted **M<sub>T</sub>-3** units removed for clarity. Packing distances between two diacetylenes  $d_s$ , the distance between reactive carbons  $d_{CC}$ , and tilt angles  $\theta$  are highlighted. Copyright 2022 American Chemical Society. ....15
- Figure 1.7.** Connections between H<sub>c</sub>OFs and other organic materials, including COFs, HOFs, single-crystalline 2D polymers, and conventional polymer networks. The solid-state structures of COF-300, HOF-1, a single-crystalline 2D polymer, and H<sub>c</sub>OF-101 are shown here. Copyright 2022 American Chemical Society. ....17

<b>Figure 1.8.</b> Hydrogen-bonding patterns and topologies of precursor crystals of (a) H <sub>c</sub> OF-1 and H <sub>c</sub> OFs-2-4, (b) H <sub>c</sub> OF-6, and (c) H <sub>c</sub> OF-101. Copyright 2022 American Chemical Society. ....	19
<b>Figure 1.9.</b> (a) Topochemical crosslinking taking place in a precursor crystal using dithiols of different lengths. (b) Optimization and characterization of H <sub>c</sub> OFs. Copyright 2022 American Chemical Society. ....	21
<b>Figure 1.10.</b> (a) Single crystal structures of H <sub>c</sub> OF-2 and <b>P2</b> , H <sub>c</sub> OF-3 and <b>P3</b> viewed along different axes. Reproduced with permission from ref 14. Copyright 2019 American Chemical Society. (b) Overlaid single crystal structures of [M <sub>6</sub> •3H] <sup>3+</sup> •3HSO <sub>4</sub> <sup>-</sup> and H <sub>c</sub> OF-6. The anion cluster joint and voids of H <sub>c</sub> OF-6 are highlighted on the right. Reproduced with permission from ref 16. Copyright 2022 Elsevier B.V. (c) Single crystal structure of H <sub>c</sub> OF-101 with detailed dithioether linkages connecting between different layers. Copyright 2022 American Chemical Society. ....	24
<b>Figure 1.11.</b> (a) Graphical illustration of the dynamic sorption of H <sub>c</sub> OFs upon disrupting and reforming hydrogen-bonded networks. (b) Crystal size expansion of H <sub>c</sub> OFs-2-3 upon DMSO or I <sub>2</sub> guest uptake. Copyright 2022 American Chemical Society. ....	26
<b>Figure 1.12.</b> 3D printing porous materials, including MOFs, COFs, porous polymer, porous alloy, porous carbon, and zeolite. ....	29
<b>Figure 1.13.</b> (a) A direct-ink-write 3D printing system equipped with two extrusion nozzles. (b) Desired rheological properties of a typical DIW ink. (c) Graphical illustration of the design of a 3D-printable polymer. Copyright 2019 John Wiley & Sons, Inc. ....	33
<b>Figure 1.14.</b> (a) Graphical illustration of creating porosity by pre-synthesized adsorbents. (b) Graphical illustration of creating porosity by secondary growth. (c) Graphical illustration of creating porosity by phase separation. ....	35
<b>Figure 1.15.</b> 3D-printing pre-synthesized zeolite 13X and images of the printed monolith.108 Copyright 2016 American Chemical Society. ....	37
<b>Figure 1.16.</b> Schematic illustration of the synthesized procedures of 3D-printed binder-free zeolite monoliths and images of as printed zeolite monolith, zeolite monolith with binders, and binder-free zeolite monolith. Copyright 2019 John Wiley & Sons, Inc. ....	38
<b>Figure 1.17.</b> Photographs of 3D-printed objects from MFC/LS/CP hydrogel after air drying; and after pyrolysis at 1000 °C. Copyright 2018 Elsevier B.V. ....	39

<b>Figure 1.18.</b> Preparation of TEOS/F127 co-assembled supramolecular hydrogel inks, and images of printed monolith prepared at room temperature and after calcined at 200 °C, 700 °C, and 1000 °C, respectively. Copyright 2018 John Wiley & Sons, Inc. ....	40
<b>Figure 1.19.</b> (a) 3D printing MOFs monolith by physically mixing pre-synthesized MOF-74 powder, PVA, and bentonite clay. Copyright 2017 American Chemical Society. (b) An extrudable gel formed by self-assembled additives and precursors of MOFs, followed by the secondary MOF growth. Copyright 2020 American Chemical Society. (c) An additive-free 3D-printable gel developed by self-assembled precursors of MOFs, followed by the secondary MOF growth. Copyright 2020 American Chemical Society. ....	42
<b>Figure 1.20.</b> Schematic representation of the synthesis and 3D printing of COF-GO foams. The mixture of COF precursors, water, and graphene oxide forms a hydrogel, which is used for 3D-printing. Copyright 2020 American Chemical Society. ....	45
<b>Figure 1.21.</b> (a) Schematic illustration of 3D printing porous polymer. The printable ink is prepared by mixing PLGA polymer and CuSO <sub>4</sub> salt. After slat leaching, the 3D-printed polymer monolith shows highly porous. Copyright 2018 Elsevier B.V. (b) Schematic illustration of 3D printing porous polymer using DIW. The ink is composed of paraffin wax beads and photopolymerizable resin Copyright 2021 American Chemical Society. ....	46
<b>Figure 1.22.</b> Schematic illustration of the pellets packed bed adsorbers, extrudates packed bed adsorbers, and 3D-printed zeolites and their CO <sub>2</sub> separation performance. Copyright 2019 John Wiley & Sons, Inc. (b) The H <sub>2</sub> adsorption performance of 3D-printed ABS and ABS-MOF composites. Copyright 2017 John Wiley & Sons, Inc. (c) The CH <sub>4</sub> adsorption performance of powdery and 3D-printed HKUST-1. Copyright 2020 American Chemical Society. ....	48
<b>Figure 1.23.</b> (a) Schematic illustration of Cu <sup>2+</sup> and Pb <sup>2+</sup> removal using 3D-printed zeolite-Y. Copyright 2021 Elsevier B.V. (b) Scheme of dyes removal performance using 3D-printed COF foams. Copyright 2020 American Chemical Society. ....	49
<b>Figure 1.24.</b> Schematical illustration of 3D-printed MIL-100 (Fe) catalytic filter and impeller for dye degradation. Copyright 2020 Elsevier B.V. ....	51
<b>Figure 1.25.</b> (a) Scheme of 3D-printed ZSM-5 for light olefin reaction. Copyright 2022 Elsevier B.V. (b) Scheme of 3D-Printed Cu-SSZ-13 zeolite for NH <sub>3</sub> -SCR. Copyright 2021 Chinese Chemical Society. ....	52
<b>Figure 1.26.</b> Preparation of Co nanoparticles assembled in nitrogen-doped mesoporous carbon (3DP-NC-CO) flakes and their electrochemical performances. Copyright 2018 John Wiley & Sons, Inc. ....	53

<b>Figure 1.27.</b> (a) Photographs of MOF-based ionogel and the acidic and auxetic sensitivity. Copyright 2019 Elsevier B.V. (b) Printed lines of COF-5 and their thermo-sensitivity. Copyright 2023 John Wiley & Sons, Inc.....	54
<b>Figure 1.28.</b> (a) A 3D-printed porous polylactide-co-glycolide improving cell viability and proliferation. Copyright 2018 Acta Materialia Inc. (b) A via 3D-printed porous scaffolds for doxorubicin delivery. Copyright 2020 John Wiley & Sons, Inc.....	56
<b>Figure 2.1.</b> (a) Chemical structures of <b>H1</b> and substrates used in this investigation. (b) Solid-state structure of HOF-1 viewed along the <i>c</i> -axis. Vacant amino groups are highlighted in red color. Disordered solvent molecules are omitted for clarity. (c) The hydrogen-bonding arrays formed between 2,4-diamino-1,3,5-triazine (DAT) arms. ....	71
<b>Figure 2.2.</b> (a) Solid-state structure of HOF-1·PhNH <sub>2</sub> viewed along the <i>c</i> -axis. (b) Hydrogen-bonding and (c) N-H••• $\pi$ interaction between HOF-1 and aniline. The N-H••• $\pi$ distance is measured as the distance between the N atom and the center of the phenyl ring. (d) The cyclic aniline tetramer in HOF-1·PhNH <sub>2</sub> with C-H••• $\pi$ interactions highlighted. (e) The layered packing of cyclic aniline tetramers in HOF-1·PhNH <sub>2</sub> . The aniline molecules are highlighted in red. (f) Solid-state structure of aniline. ....	73
<b>Figure 2.3.</b> (a) Solid-state structure of HOF-1·Tol viewed along the <i>c</i> -axis. (b) N-H••• $\pi$ interaction between HOF-1 and toluene. (c) The cyclic toluene tetramer in HOF-1·Tol with C-H••• $\pi$ interactions highlighted. ....	74
<b>Figure 2.4.</b> (a) Solid-state structure of HOF-1· <i>o</i> -Tld, HOF-1· <i>m</i> -Tld, and HOF-1· <i>p</i> -Tld viewed along the <i>c</i> -axis. (b) Hydrogen-bonding interactions and (c) N-H••• $\pi$ interaction between HOF-1 and <i>o</i> -Tld, <i>m</i> -Tld, and <i>p</i> -Tld, respectively. (d) The C-H••• $\pi$ interactions in the cyclic tetramers of <i>o</i> -Tld, <i>m</i> -Tld, and <i>p</i> -Tld, respectively. (e) The layered packing structures of cyclic tetramers of <i>o</i> -Tld, <i>m</i> -Tld, and <i>p</i> -Tld from the top to bottom. The <i>o</i> -Tld, <i>m</i> -Tld, and <i>p</i> -Tld molecules are highlighted in yellow, green and blue, respectively. ....	76
<b>Figure 2.5.</b> (a) Solid-state structure of HOF-1·VP complex viewed along the <i>c</i> -axis. (b) Hydrogen-bonding interactions between HOF-1 and VP (c) C-H•••O interactions between VP molecules in the channels of HOF-1. (d) The process by which aniline and VP meet and react with each other in the channels of HOF-1. Aniline and VP are first co-adsorbed into HOF-1, and they are catalyzed by the residual formic acid within HOF-1 to afford 1-(1-anilinoethyl)-2-pyrrolidinone (AEP). The amino and alkenyl reactive functional groups are highlighted in yellow and green respectively. ....	77
<b>Figure 3.1.</b> Schematic representation of a synergistic I <sub>2</sub> /I <sup>-</sup> removal in water using an ionic H <sub>c</sub> OF-7. ....	113

**Figure 3.2.** (a) The chemical structure of **1**, (b) solid-state structure of **1**. ..... 114

**Figure 3.3.** (a) The chemical structure of **1•4H<sup>+</sup>•4NO<sub>3</sub><sup>-</sup>**, (b) its solid-state structure, and (c) super-structure. (d) The nitrate dimer-directed hydrogen-bonding joint formed between two repulsive nitrate anions and four melaminium arms. (e) The *flu* topology of **1•4H<sup>+</sup>•4NO<sub>3</sub><sup>-</sup><sub>crystal</sub>**. (f) Highlighted void space of **1•4H<sup>+</sup>•4NO<sub>3</sub><sup>-</sup><sub>crystal</sub>**. ..... 115

**Figure 3.4.** (a) Synthesis of H<sub>C</sub>OF-7 via an SCSC thiol-ene crosslinking. (b) Stacked FT-IR spectra of **1**, **1•4H<sup>+</sup>•4NO<sub>3</sub><sup>-</sup><sub>crystal</sub>**, and H<sub>C</sub>OF-7. (c) Stacked Raman spectra of **1•4H<sup>+</sup>•4NO<sub>3</sub><sup>-</sup><sub>crystal</sub>** and H<sub>C</sub>OF-7. (d) Stacked <sup>13</sup>C solution NMR spectrum of **1•4H<sup>+</sup>•4NO<sub>3</sub><sup>-</sup>** in DMSO-*d*<sub>6</sub> (bottom, 150 MHz, 298 K) and solid-state <sup>13</sup>C cross-polarization magic angle spinning NMR spectrum of H<sub>C</sub>OF-7. (e) Simulated and experimental PXRD profiles of **1•4H<sup>+</sup>•4NO<sub>3</sub><sup>-</sup><sub>crystal</sub>** and H<sub>C</sub>OF-7, respectively. .... 117

**Figure 3.5.** (a) Crystal structure of H<sub>C</sub>OF-7 with dithioether crosslinkages and nitrate dimer highlighted in ball-stick model. (b) Overlaid structures of **1•4H<sup>+</sup>•4NO<sub>3</sub><sup>-</sup><sub>crystal</sub>** (red color) and H<sub>C</sub>OF-7 (blue color). Hydrogen atoms are omitted for clarity. (c) Covalent connections in H<sub>C</sub>OF-7. Nitrate anions and hydrogens are omitted for clarity. (d) Highlighted void spaces of H<sub>C</sub>OF-7. .... 118

**Figure 3.6.** (a) Time-dependent total iodine adsorption of H<sub>C</sub>OF-7 measured at different temperatures (23, 40, 50, 90 °C) using UV-Vis spectroscopy by monitoring the absorption band at 292 nm. Inset: fitted reaction rate versus the inverse temperature. (b) The increased weight of H<sub>C</sub>OF-7, CHOP-7 and activated carbon after I<sub>2</sub> and I<sup>-</sup> uptake measured at different temperatures. (c) The I<sup>-</sup> exchange efficiency measured using H<sub>C</sub>OF-7 and I<sub>2</sub>•H<sub>C</sub>OF-7 samples (0.1-0.3 g/g of I<sub>2</sub> per H<sub>C</sub>OF-7). The confidence coefficient *p* was obtained using Tukey's honest significance test. (d) Measured concentrations of total residual iodine (input: 5 ppm of I<sub>2</sub> + I<sup>-</sup>) before and after adsorption using H<sub>C</sub>OF-7 (6 mg) in deionized (DI) water in the presence of NO<sub>3</sub><sup>-</sup> (5 ppm), H<sub>2</sub>PO<sub>4</sub><sup>-</sup> (5 ppm), SO<sub>4</sub><sup>2-</sup> (20 ppm), Cl<sup>-</sup> (80 ppm), HCO<sub>3</sub><sup>-</sup> (60 ppm), and their mixture. .... 120

**Figure 3.7.** (a) Experimental setup of the temperature-controlled iodine/iodide breakthrough analysis. Iodinated deionized (DI) or tap water (I<sub>2</sub> + KI, 3.5 + 1.5 ppm) was pumped into a customized steel precolumn (d: 50 × l: 220 mm) and heated to the desired temperatures under continuous flow (5 mL/min). After passing through the H<sub>C</sub>OF-7 column (d: 4.5 × l: 27 mm), the deiodinated water was collected by a fraction collector. (b) The total residual iodine (I<sub>2</sub> + I<sup>-</sup>) concentrations measured in the breakthrough experiments. Each column was packed with 240 mg of H<sub>C</sub>OF-7, activated carbon, or mixed-bed activated carbon/anion exchange resin, respectively. .... 123

<b>Figure 4.1.</b> Design and synthesis of 3D-printed hierarchically porous imine and $\beta$ -ketoenamine-linked COFs through a supramolecularly templated co-assembly process followed by a two-stage post-printing imine network transformation. ....	176
<b>Figure 4.2.</b> Synthesis of <b>3D-TpPa-1</b> through Pluronic F127 templated co-assembly followed by post-printing framework re-organization. Inset: a robust <b>3D-TpPa-1</b> cubic lattice (32 mg) loaded with a 100 g weight. ....	178
<b>Figure 4.3.</b> Stress-strain ( <i>left</i> ) and step-strain ( <i>right</i> ) rheological measurements of hydrogel <b>G1</b> . ....	179
<b>Figure 4.4.</b> (a) FT-IR spectra of <i>s</i> - <b>TpPa-1</b> , F127 and <b>3D-TpPa-1</b> , respectively. (b) PXRD profiles of <i>s</i> - <b>TpPa-1</b> , as synthesized <b>3D-TpPa-1</b> after F127 removal and annealed <b>3D-TpPa-1</b> , respectively. (c) SEM images of a <b>3D-TpPa-1</b> and its focused ion beam sliced cross-section. Nano-crystalline fibers were observed in the cross-section. ....	180
<b>Figure 4.5.</b> Synthesis of 3D-printed monoliths of <b>3D-TpBD-Me<sub>2</sub></b> (a) and <b>3D-TPE-COF</b> (b). (c) PXRD profiles of <i>s</i> - <b>TpBD-Me<sub>2</sub></b> , as synthesized and annealed <b>3D-TpBD-Me<sub>2</sub></b> , respectively. (d) PXRD profiles of <i>s</i> - <b>TPE-COF</b> , as synthesized and annealed <b>3D-TPE-COF</b> , respectively. ....	182
<b>Figure 4.6.</b> (a) Dual-material 3D printing of heterogeneous COF monoliths and the obtained lattice of <b>3D-TpPa-1/TpBD-Me<sub>2</sub></b> and <b>3D-TpPa-1/TPE-COF</b> . No mechanical fracture was observed after placing 100 g weight on the <b>3D-TpPa-1/TpBD-Me<sub>2</sub></b> monolith (221 mg). (b) SEM image of an exposed interface formed between <b>3D-TpPa-1</b> and <b>3D-TpBD-Me<sub>2</sub></b> in the printed heterogeneous monolith. (c) PXRD profiles of <i>s</i> - <b>TpPa-1</b> , <i>s</i> - <b>TpBD-Me<sub>2</sub></b> , and a 3D-printed heterogeneous monolith <b>3D-TpPa-1/TpBD-Me<sub>2</sub></b> , respectively. ....	183
<b>Figure 5.1.</b> (a) Previous method of templated synthesis of $\alpha$ -CD tubes. (b) Previous method of templated synthesis of 3D-printable polyrotaxanes. ....	235
<b>Figure 5.2.</b> Templated synthesis of 3D-printed crosslinked urethane- $\alpha$ -CD monoliths. PEG-2Si(OEt) <sub>3</sub> and $\alpha$ -CD were employed to form 3D-printable hydrogels, which were crosslinked to form polyrotaxane monolith after base-catalyzed polycondensation. After diisocyanate crosslinking of the threaded $\alpha$ -CDs followed by PEG axles removal, 3D-printed urethane- $\alpha$ -CD monoliths were obtained. ....	236
<b>Figure 5.3.</b> (a) Time-dependent transmittance (550 nm) of the polypseudorotaxanes upon mixing the PEG axle and $\alpha$ -CD. Black dots: PEG <sub>4k</sub> -2OH (2.5 mM) and $\alpha$ -CD (102.8 mM), red and blue dots: PEG <sub>4k</sub> -2Si(OEt) <sub>3</sub> (2.5 mM) and $\alpha$ -CD (102.8 mM) at 24 °C and 60 °C, respectively. (b) Stress-strain and alternative step-strain rheological sweeps of a polypseudorotaxane hydrogel PRH[6, 27]. (c) Images of two 3D-printed lattices of PRH[6, 27]. ....	237



**Figure 5.4.** (a) Images (top and side views) of the 3D-printed PM, TDU-PM, and TDU-CD lattices from left to right, respectively. (b) <sup>1</sup>H NMR (600 MHz, 298 K) of the completely hydrolyzed PM, TDU-PM, and TDU-CD in NaOD/D<sub>2</sub>O (5%) from the bottom to the top, respectively. ....239

**Figure 5.5.** (a) SEM images of a TDU-CD lattice (b) SEM image of TDU-CD<sub>ref</sub>. ....241

**Figure 5.6.** (a) Chemical structures of the major phytochemicals in tomato juice. (b) Normalized UV-Vis spectra of lycopene and β-/γ-carotenes in acetone. (c) Selective extraction of lycopene from tomato juice using TDU-CD. ....243

**Figure 5.7.** (a) HPLC-MS diagrams of phytochemicals extracted from tomato juice using CH<sub>2</sub>Cl<sub>2</sub> (top), purified after silica gel chromatography (middle), and adsorbed in TDU-CD. (b) Recovered lycopene after UV-irradiation and thermos-treatments, measured using the UV/Vis-spectrometer. ....244

## List of Tables

<b>Table 1.1.</b> Comparison of extrusion-based and vat-polymerization-based 3D printing methods. ....	31
<b>Table 1.2.</b> Comparison of 3D printing MOF materials using DIW. ....	44
<b>Table 2.1.</b> Summary of crystallographic data of HOF-1 and HOF-1·guest complexes. All crystals are tetragonal in the I4 space group with $\alpha = \beta = \gamma = 90^\circ$ . ....	75
<b>Table 5.1.</b> Summary of the elastic moduli and PEG/CD ratios of the PRHs and PM hydrogels. ....	238
<b>Table 5.2.</b> Adsorption of PEGs of different molecular weights using TDU-CD and TDU-CD <sub>ref</sub> . ....	242

## **Chapter 1 Introduction**

PREFACE for “Single-Crystalline Hydrogen-Bonded Crosslinked Organic Frameworks and Their Dynamic Guest Sorption” in section 1.2 published in *Accounts of Materials Research*. Reproduced from The American Association for the Advancement of Science.

Samanta, J.; Zhang, Y.; Zhang, M.; Chen, A.; Ke, C. Single-Crystalline Hydrogen-Bonded Crosslinked Organic Frameworks and Their Dynamic Guest Sorption. *Accounts Mater. Res.* **2022**, 3, 1186–1200.

The feature article in this chapter was recently published in collaboration with several other researchers in our lab. Dr. Jayanta Samanta, Yunjia Zhang, Mingshi Zhang, Albert Chen worked the organization, gathering of articles, and composing of figures. The corresponding author, Professor Chenfeng Ke provided guidance on idea and focus of the manuscript, lead the organization of the topics to include and discuss, and significantly contributed to the writing and editing of the manuscript.

## 1.1 Introduction

In recent decades, porous organic materials, including Metal-Organic Frameworks (MOFs),<sup>1-2</sup> Covalent Organic Frameworks (COFs),<sup>3</sup> Hydrogen-Bonded Organic Frameworks (HOFs),<sup>4-5</sup> and Porous Organic Polymers (POPs),<sup>6</sup> have rapidly advanced in the field of scientific research due to their tunable pore sizes, designable structural units, and versatile applications. Among these materials, covalently connected porous materials like COFs and POPs have garnered extra attention due to their stable chemical structures,<sup>7</sup> making them widely applicable in energy storage,<sup>8-9</sup> heterogeneous catalysis,<sup>10-11</sup> and pollutant remediation,<sup>7</sup> among other fields. However, fundamental challenges faced by many covalently connected porous materials as they are typically synthesized in the form of loose powders (Figure 1.1).

Firstly, at the microscopic scale, the condensation reactions of covalently connected porous materials are often limited in reversibility, resulting in the lack of single-crystal structures.<sup>12</sup> While it is possible to create covalent organic frameworks in a crystalline powder and utilize computational simulation with PXRD data to establish crystal models,<sup>13</sup> this falls shortcomings in obtaining reliable information about pore size, shapes, and potential substrate-binding sites at the atomic level, as well as establishing clear structure-property relationships for the developed materials.

Secondly, at the macroscopic scale, these materials lack effective methods to be processed into usable and designable devices on a large scale.<sup>14</sup> The rigid network of covalently connected organic frameworks hinder traditional processing methods like melting and recasting, dissolution doping, and molding. Incorporating large amounts of additives during processing may lead to partial or complete blocking of COF pores, compromising the mechanical performance of the obtained devices.<sup>15</sup> As a result, they are challenging to be standardized and utilized in real-world industrial applications.

To address the issue of crystallinity, drawing from successful experiences in synthesizing single-crystal COFs and 2D polymers, our group proposes the design of Hydrogen-bonded Crosslinked Organic Frameworks (H<sub>c</sub>OFs).<sup>16</sup> We first design and synthesize monomers that simultaneously contain hydrogen-bonding units and cross-linkable functional groups. By pre-assembling the monomers into a porous framework through hydrogen-bonding interactions, followed by diffusion of the cross-linkers into the pores. Through a single-crystal to single-crystal transformation for cross-linking, we can obtain covalently connected organic porous frameworks in a single-crystal form.<sup>17-18</sup>

Moreover, H<sub>c</sub>OFs exhibit unique flexibility, enabling them to undergo expansion and contraction upon stimulation by guest molecules.<sup>19</sup> In this thesis, we first report a series of single-crystal complexes of HOF-1 with different guest molecules.<sup>20</sup> These examples demonstrate the use of single-crystal structures to study host-guest and guest-guest interactions. Additionally, the selective adsorption of different guests and their chemical reaction characteristics inside the HOF-1 pores can also be explained using single-crystal data. This example underscores the importance of obtaining single crystals to study porous materials at an atomic level. Furthermore, following the design strategy of our group's H<sub>c</sub>OF materials, I successfully developed a novel ionic framework H<sub>c</sub>OF-7.<sup>21</sup> I obtained single-crystal data after covalent cross-linking, which revealed that halogen-bonding functional groups and ion-exchange active sites are exposed to the pores. With high stability and multifunctional guest-binding sites, H<sub>c</sub>OF-7 can efficiently remove iodine and iodide ions simultaneously at elevated temperatures (23-90°C), resulting in a total iodine residual concentration as low as 0.22 ppm. The H<sub>c</sub>OF-7 packed column exhibited a breakthrough volume of up to 18.3 L/g during I<sub>2</sub> and I<sup>-</sup> removal at high temperatures (90°C).

To address the processability challenge of porous organic materials, we proposed using 3D printing technology. 3D printing offers strong designability, material diversity, and flexibility, allowing for the manufacture of more complex structures. In this thesis, we first report a general method to integrate imine-based COFs into three-dimensional (3D) printed materials.<sup>22</sup> By introducing 3D printing templates of Pluronic F127 and imine oligomers in an aqueous environment, a co-assembly hydrogel with appropriate shear thinning and rapid self-healing properties was achieved. After 3D printing, the imine compounds further polymerize and the template F127 is removed, resulting in three different 3D printed imine-based COFs. The obtained 3D printed COFs exhibit high crystallinity, high surface areas with hierarchical pores, excellent structural integrity, and robust mechanical stability. Additionally, when multiple COF precursors were used as inks for 3D printing, heterogeneous multi-component COFs connected by covalent bonds were achieved in one monolith. In addition to 3D-printed COFs, this thesis also reports 3D-printed amorphous polymers with nanotubular cavities. By precisely controlling the co-assembly PEG derivatives and  $\alpha$ -cyclodextrins ( $\alpha$ -CDs),  $\alpha$ -CDs were arranged in a tubular arrangement.<sup>21</sup> The obtained polyrotaxane hydrogel exhibited excellent 3D printability. After printing, multi-step cross-linking and the removal of the PEG axle resulted in a 3D printed polymeric monoliths with hierarchical pore sizes and nanotubular cavities. Due to

the specific pore size of  $\alpha$ -CD, the obtained material can be used for the efficient and selective extraction of lycopene in tomato juice.

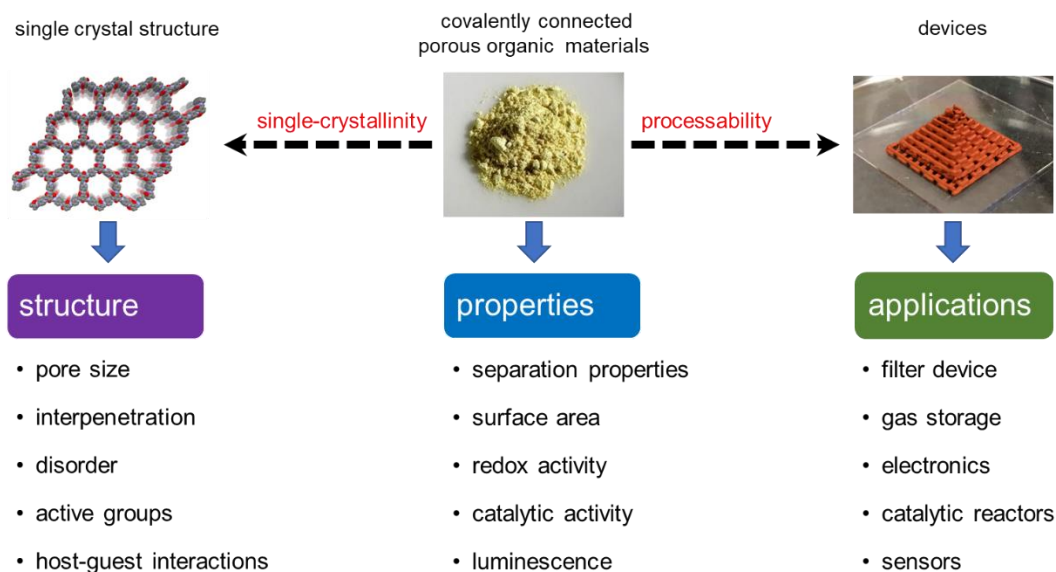


**Figure 1.1.** Schematic illustration of structure-properties-applications relationship in covalently connected porous organic materials.

In conclusion, in this thesis, I focus on porous organic materials and their crystallinity and processability issues, based on the research of this thesis, we aim to provide some insights to help establish the link between microscopic and macroscopic aspects of porous organic materials (Figure 1.1).

## 1.2 Single-crystalline hydrogen-bonded crosslinked organic frameworks and their dynamic guest sorption

For decades, researchers have been studying crystalline porous materials with periodic nanoscale pores.<sup>23</sup> Leveraging these nanoscale voids, crystalline porous materials were widely used in applications such as gas adsorption,<sup>24</sup> catalysis,<sup>25</sup> water remediation,<sup>26</sup> and energy storage.<sup>27</sup> Zeolites are widely found in natural mineral deposits. In the 1950s, Linus Pauling *et al.* analyzed the structure of zeolites in detail using techniques like X-ray diffraction.<sup>28</sup> They discovered that zeolites are intricate inorganic materials composed of silica and alumina, forming a unique network structure with distinctive pore channels. Zeolites are a kind of cheap material which can be produced on a large scale in industry.<sup>29</sup> Currently, over 200 types of zeolites have been identified. However, compared to organic

materials, zeolites have relatively limited design flexibility. Metal-Organic Frameworks (MOFs) are a class of crystalline porous materials composed of metal ions (or metal clusters) coordinated to organic ligands. Since their discovery in the 1990s, they have experienced explosive development and have become one of the focal points in chemical research. MOFs exhibit diverse topological structures and can be designed with specific organic ligands, allowing for highly controllable surface area, pore size, and functional group structure.<sup>30</sup> Numerous new types of MOFs have been developed. The crystal structures of different single-crystalline MOFs have been elucidated using X-ray single-crystal diffraction techniques.<sup>31</sup> Currently, MOFs can achieve maximum void space exceeding 90%<sup>32</sup> and specific surface areas exceeding 6000 m<sup>2</sup>/g.<sup>33</sup> Similar to MOFs, Covalent Organic Frameworks (COFs) are a class of crystalline materials constructed from connected by covalent bonds.<sup>3</sup> They were first proposed by Omar Yaghi *et al.* in 2005. Compared to MOFs, COFs linked by covalent bonds generally exhibit higher stability. They possess tunable designability in topology, pore size, and functional groups. In recent years, scientists have used a variety of chemical reactions, including previously considered irreversible organic reactions, to construct numerous novel COFs.<sup>34</sup> The initial attempt of constructing porous organic framework materials using hydrogen bonds interactions started from 1990s.<sup>35</sup> In 2011, hydrogen-bonded frameworks were successfully activated and demonstrated permanent porosity,<sup>36</sup> and since then, the name Hydrogen Organic Frameworks (HOFs) has gradually become well-known.

Single-crystal data is crucial for an atomic-level understanding of the organic framework structure and detailed local chemical environment, including interpenetration, active sites, and guest molecules. The obtained information aids in further elucidating the structure-performance relationship. Therefore, it is necessary to first obtain large single crystals suitable for the material and analyze them using single-crystal X-ray diffraction (SCXRD)<sup>37-38</sup> or rotation electron diffraction (RED).<sup>39</sup> Among the previously mentioned porous crystalline materials, both COFs and HOFs offer excellent designability due to their periodic organic structural units, and they do not contain any metal elements. However, most COFs are polycrystalline powders, making them unsuitable for SCXRD analysis. Powder X-ray diffraction (PXRD) has become the most useful characterization tool for COFs. Typically, the structure of COFs is validated by matching simulated PXRD patterns with experimental patterns, which limits the revealing of information such as interpenetration and guest molecules.<sup>37</sup> Therefore, achieving a comprehensive understanding of the structure-performance relationship of COFs with atomic precision



remains challenging. On the other hand, HOFs are much easier to synthesize as single crystals as they are constructed with weaker interactions with better. The stability of HOFs is much lower than that of COFs since HOFs are connected by weak hydrogen bonds. This limits the chemical post-modification and applications of HOF materials under extreme conditions. Consequently, developing single-crystalline covalently connected organic frameworks remains a significant challenge in the field of porous organic framework materials development.

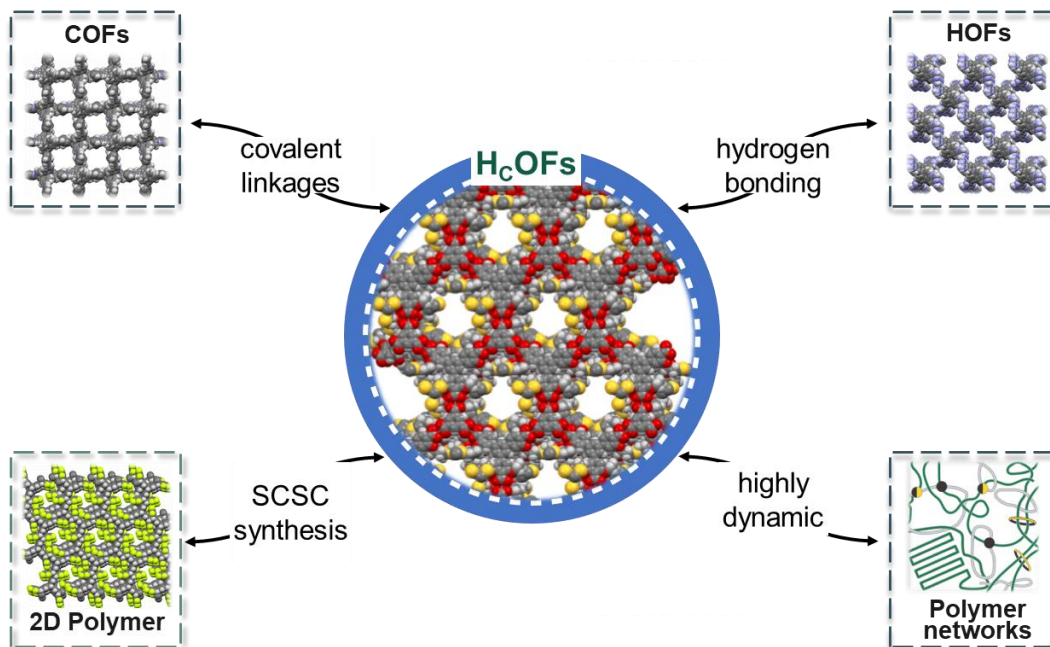


**Figure 1.2.** Connections between  $H_cOFs$  and other organic materials, including COFs, HOFs, single-crystalline 2D polymers, and conventional polymer networks. The solid-state structures of COF-300,<sup>10</sup> HOF-1,<sup>41</sup> a single-crystalline 2D polymer,<sup>33</sup> and  $H_cOF$ -101<sup>15</sup> are shown here. Copyright 2022 American Chemical Society.

To achieve a balance between the single-crystallinity and chemical stability of porous organic materials. Building on insights from HOFs, single-crystal COFs, and single-crystal polymers<sup>40</sup>, our group has reported a new class of porous organic frameworks known as Hydrogen Bonded Cross-Linked Organic Frameworks ( $H_cOFs$ ) (Figure 1.2).<sup>17-19, 41-42</sup> The synthesis of  $H_cOFs$  involves a two-step process: firstly, the self-assembly of monomers with hydrogen-bonding functional groups and cross-linking active sites into a single-crystalline network; secondly, the diffusion of cross-linking agents into the crystal pores

and the covalent cross-linking of monomers through a single-crystal-to-single-crystal transformation. H<sub>c</sub>OFs not only possess single-crystal structures suitable for precise structure-property analysis but also exhibit high chemical stability. Additionally, they demonstrate remarkable flexibility. Upon adsorbing certain guest molecules that can disrupt hydrogen bonds, the framework undergoes significant expansion. This is attributed to its dual cross-linking network of hydrogen bonds and covalent bonds. The removal of guest molecules allows H<sub>c</sub>OFs to reorganize their hydrogen-bonding network, partially restoring their original highly crystalline state. The guest-induced expansion and contraction of H<sub>c</sub>OFs resemble the behavior of traditional polymer networks (Figure 1.2), where interpenetrating polymer chains recover their shape after mechanical stress is relieved, as the chains tend to maximize their randomness for entropy gain.

In this section, we first provide a brief overview of traditional crystalline porous materials, including zeolites, MOFs, and conventional COFs. Next, we explore methods for directing the assembly of HOFs using hydrogen-bonding motifs and different core building blocks. Then we summarize various approaches to obtain single-crystal COFs and polymers, including their synthesis strategies, characterization method single-crystal structure analysis, and corresponding structure-performance relationships. We emphasize the knowledge revealed through solid-state structures, including three-dimensional stacking of building blocks, network topology, pore distribution, and network interpenetration. Overall, these efforts contribute valuable information for the design, synthesis, and characterization of H<sub>c</sub>OFs. The report provides a step-by-step guide to the synthesis and characterization of single-crystal H<sub>c</sub>OFs, as well as a detailed exploration of network topology related to the framework flexibility and dynamic guest adsorption properties. We hope that the understanding of H<sub>c</sub>OFs will inspire future designs of HOFs and COFs and encourage more researchers to investigate H<sub>c</sub>OFs for a better understanding of the structure-performance relationships in the development of porous organic materials.

### **1.2.1 Molecularly engineering porous hydrogen-bonded networks**

Hydrogen-bonded organic frameworks (HOFs) are framework materials composed of monomers connected through hydrogen bonds, exhibiting permanent porosity (Figure 1.3).<sup>5, 43-45</sup> An early example of a hydrogen bonding network was reported in 1969, where terephthalic acid (TA) was linked by carboxylic acid dimers (S1).<sup>46</sup> Since the 1990s, Wuest *et al.* have focused on designing porous hydrogen bonding networks, introducing S1 (Figure 1.3a) as a complementary donor-acceptor (DA) hydrogen-bonding motif to form the

hydrogen bonding network.<sup>47</sup> They also reported a diamond-like network formed by C6/S2 monomers, with 42% of the void space occupied by solvent molecules.<sup>48</sup> In 2011, Chen *et al.* successfully activated the framework and demonstrated permanent porosity in HOF-1 (C6/S2 monomer).<sup>36</sup> By removing solvents without disrupting the hydrogen bonding network, HOF-1 showed excellent separation of C<sub>2</sub>H<sub>4</sub> and C<sub>2</sub>H<sub>2</sub>. Indeed, this has opened a new frontier in HOF research. Currently, HOFs have emerged as a promising class of crystalline porous materials, captivating an increasing number of researchers. Unlike Metal-Organic Frameworks (MOFs) and Covalent Organic Frameworks (COFs), hydrogen bonding in HOFs exhibits lower orientational preference. Additionally, due to the weaker strength of hydrogen bonds compared to coordinate and covalent bonds, hydrogen bonding in HOFs is more susceptible to influences such as van der Waals forces and  $\pi$ - $\pi$  stacking, making their construction more challenging to predict. In current HOF development, motifs with multivalent hydrogen bonding capacity are commonly used to enhance the strength and orientational preference of the hydrogen bonding network. Various hydrogen-bonding motifs are connected to different cores to form permanent porous frameworks.

Compared to **S2**, which has a donor-acceptor-donor (DAD) hydrogen-bonding array, self-complimentary carboxylic acids **S3** with a DA array (Figure 1.3a) are widely used to construct HOFs. Attaching phenyl carboxylic acid groups to **C1** and **C3-4** affords a variety of HOFs with different network topologies and pore sizes.<sup>45</sup> In these HOFs, the carboxylic acid dimers are highly directional due to the R<sub>2</sub><sup>2</sup>(8) hydrogen bonding connection. The topologies of these networks (without considering the network interpenetration) are much more predictable compared to those formed by **S2**-based monomers. However, carboxylic acid-based HOFs are generally not stable under basic conditions. Other self-complimentary hydrogen bonding synthons such as **S4-S6**, pyrazole **S8**,<sup>49-50</sup> maleimide **S9**,<sup>51</sup> and **S10** have also been used in the synthesis of HOFs.<sup>43</sup> Recently, very weak C-N...H<sub>Ar</sub> hydrogen bonding interacting moiety **S7** has also been introduced in HOFs.<sup>52</sup> Hetero-synthons such as pyridine-carboxylic acid **S11** (Figure 1.3) have also been used<sup>53</sup> to construct HOFs. Furthermore, charged hydrogen bonding pairs such as guanidium cation and di-, tri-, or tetra-sulfonate anion **S12** have been successfully introduced by Ward *et al.* and others to HOF synthesis.<sup>54-56</sup> The ionic interaction and the hydrogen bonding (e.g. **S11-14**) enhance the stability of HOFs. The highly directional and strong hydrogen bonding in this charged pair allows for precise crystal engineering.<sup>54</sup> These hydrogen-bonding synthons

are also used for the design and synthesis of H<sub>c</sub>OFs, and their similarities and differences are discussed later.

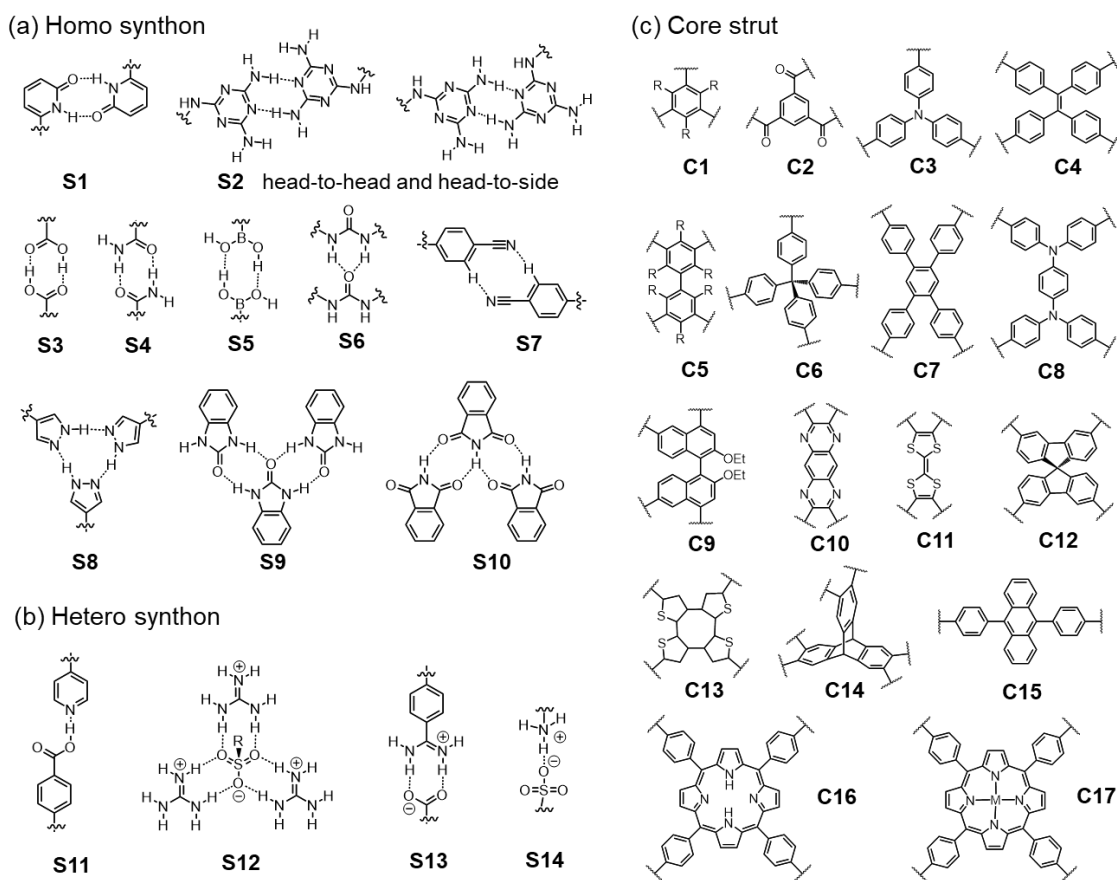


**Figure 1.3.** (a) Homo- hydrogen bonding synthons and their corresponding hydrogen bonding patterns in HOFs' design. (b) Hetero-hydrogen bonding synthons and their corresponding hydrogen bonding patterns in HOFs' design. (c) Core struts used for HOFs. Copyright 2022 American Chemical Society.

While microporous HOFs have been demonstrated efficient for gas separations,<sup>46</sup> expanding the pore size of HOFs is important to absorb larger substrates for separation and catalysis. Isorecticular expansion has been widely used to construct large pore COFs (diameters up to 10nm).<sup>57</sup> However, this approach faces many problems in HOF construction (similar to H<sub>c</sub>OFs later discussed). The molecular building blocks tend to pack denser in the solid state as different polymorphs. For example, Hisaki *et al.* synthesized a series of planar  $\pi$ -conjugated molecules with **C18-C21** cores and carboxylic acid arms (Figure 1.4a).<sup>58</sup> Despite the similar geometry and hydrogen bonding, these monomers

stacked differently in the solid state. To date, limited success has been made in isoreticularly expanding the pores of HOFs. A  $C_3$ -symmetric hexaazatriphenylene<sup>59</sup> **C24** was isoreticularly expanded to **C25** and **C26**,<sup>60</sup> and topologically identical HOFs were obtained with pore sizes increasing from 6 Å to 20 Å (Figure 1.4c). Another successful example includes the use of rigid pyrene core **C27** and its derivatives **C28/C29**,<sup>61</sup> and the pore sizes of HOFs were expanded from  $8 \times 12$  Å to  $25 \times 30$  Å. **S8** and **C22-23** have also been demonstrated for isoreticular expansion of HOFs.<sup>49-50</sup> We share our insights on isoreticular expansion in the later sections. The design of H<sub>c</sub>OFs require larger pores because the pore aperture should allow the diffusion of external crosslinker, and the void space of H<sub>c</sub>OFs synthesized after crosslinking is reduced compared to their precursor crystals.

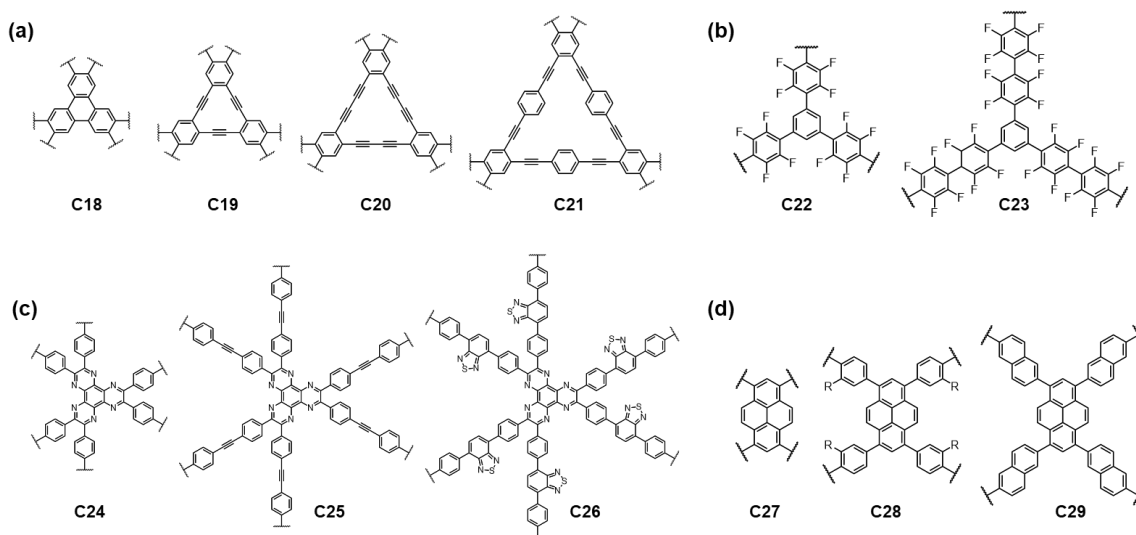


**Figure 1.4.** Struts that have been used in isoreticularly expanding the pore of HOFs. Copyright 2022 American Chemical Society.

### 1.2.2 Accessing Single-Crystalline Frameworks and Polymers

Rational synthesis of single crystalline polymers, networks, and frameworks is not trivial. There have been two general approaches demonstrated successful– (1) utilization of highly reversible reactions, and (2) solid-state topochemical synthesis through single-crystal to single-crystal (SCSC) transformations. In this section, we will discuss these two approaches and their connections to H<sub>c</sub>OF synthesis.

COFs (COF-1 and COF-5) were first synthesized by Yaghi *et al.*<sup>62</sup> through reversible boronic acid/ester condensation reactions (Figure 1.5a). These boronic acid/ester-based

COF materials are polycrystalline, and their structures were elucidated through PXRD. Dichtel *et al.* attributed the formation of polycrystalline boronate ester-linked COFs to the irreversible stacking of the nano-crystallites.<sup>63</sup> Later, they reported single-crystalline boronic ester-based COFs through a seed growth method.<sup>64</sup> The crystallinity was confirmed through high-resolution TEM investigations, but the crystals were not big enough for SCXRD analysis.

Optimizing the reversibility of the reactions could improve the crystallinity of COFs. In 2013, Wuest *et al.* introduced the highly reversible nitroso dimerization reactions for COF synthesis.<sup>38</sup> The low bond energy of dinitroso enables room temperature covalent bond breakage and reformation. Therefore, they successfully obtained a series of tetrakis(4-nitrosophenyl) methane/silane/adamantane-based single-crystalline COFs (Figure 1.5), which are diamond networks with four- or six-fold interpenetration confirmed by SCXRD. Although these single crystals showed guest accessible void spaces of 35-39%, they did not exhibit permanent porosity, likely due to weak linkages.

The synthesis of COFs has expanded rapidly in the last decade, with examples such as the well-established imine (Figure 1.5c) and ketoenamine<sup>65</sup> condensations to other reversible reactions.<sup>66</sup> For imine COFs, Dichtel *et al.* suggested a model that includes nano-crystallite formation,<sup>67</sup> followed by polymerization to amorphous polymers, and then crystalline transformations for COFs. However, most COFs are polycrystalline powders, and their solid-state structures are largely proposed based on their PXRD profiles. The key challenge preventing easy access to single-crystalline COFs is the mismatch of (de)polycondensation reaction rates ( $k_{\text{bond-formation}}$  and  $k_{\text{bond-rearrangement}}$ ) and the crystallization rates (nucleation and phase separation) during COF synthesis.<sup>37</sup>

In 2018, Wang and Yaghi *et al.* reported the first sets of single-crystalline imine COFs' solid-state structures (Figure 1.5c).<sup>37</sup> In this work, a large amount of aniline was added as a reaction rate modulator to match polycondensation and nucleation rates. As a result, large single crystals of imine-based COF-300, COF-303, LZU-79, and LZU-111 were obtained. It was also found by SCXRD analysis that the water molecules are arranged into infinite chains within the channel of COF-300. In the SCXRD structure, a 7-fold interpenetrated network of the COF-300 synthesized by the aniline modulator method was determined with atomic-level precision.

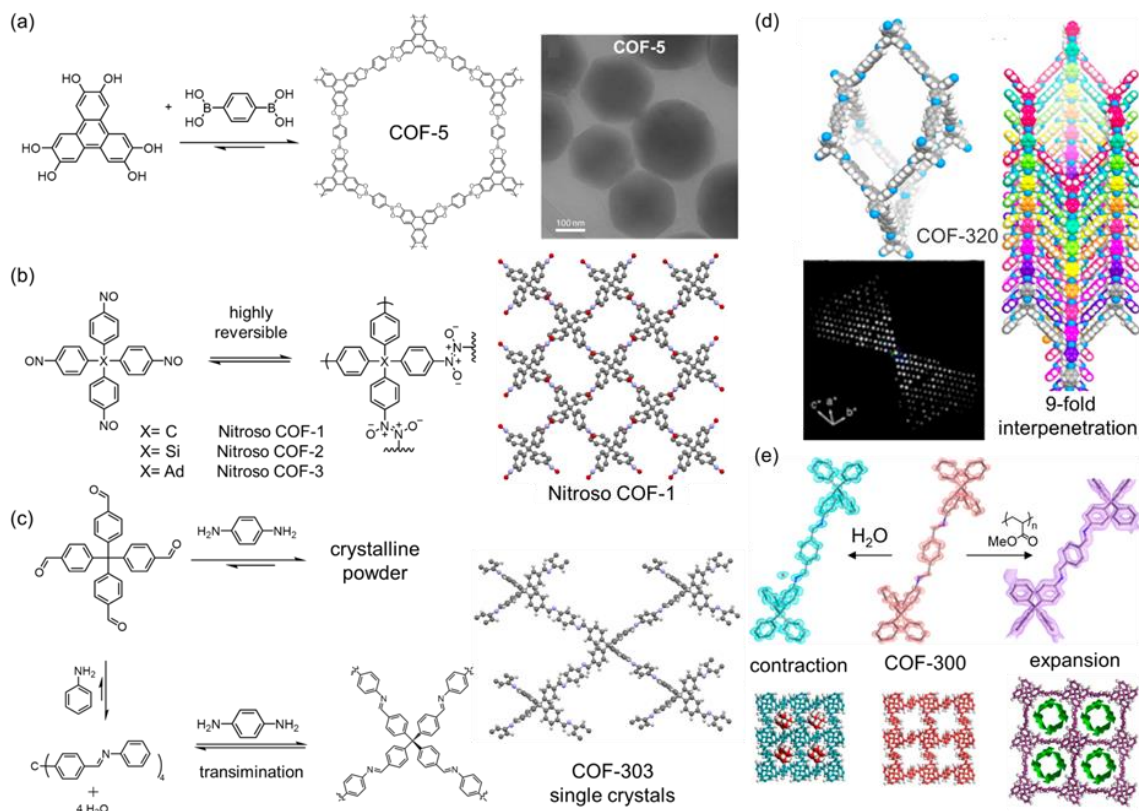


**Figure 1.5.** (a) Synthesis of COF-5 and a TEM image of COF-5 crystal. Copyright 2018 Science. (b) Synthesis of Nitroso-COFs via nitroso dimerization. Right: single-crystal structures of Nitroso-COF-2.<sup>11</sup> (c) Synthesis of single crystalline imine-based COF-303 through transamination. Right: the single-crystal structure of COF-303.<sup>10</sup> (d) Solid-state structure of COF-320 with nine-fold interpenetration and their RED pattern. Copyright 2013 American Chemical Society. (e) Solid-state structures of active COF-300, COF-300•H<sub>2</sub>O, and COF-300•polymethylmethacrylate (COF-300•PMMA). Copyright 2019 American Chemical Society.

Aside from SCXRD, RED has recently been introduced for structure determination of single crystalline framework materials.<sup>39</sup> Crystals viable for RED can be as small as 50 nm in diameter, while SCXRD analysis generally requires crystals larger than 5 μm. The structure of COF-320,<sup>68</sup> which was synthesized via imine condensation between dialdehyde and (tetra-aminophenyl)-methane, was characterized using RED as a 9-fold interpenetrated diamond network (Figure 1.5d). Using RED, Wang *et al.* discovered that single-crystals of COF-300 with 5-fold interpenetration were transformed into a 7-fold interpenetrated diamond network upon aging.<sup>69</sup> Zhang *et al.* reported the framework dynamics of COF-300

upon guest adsorption. The structures of the activated phase of COF-300, its hydrated COF-300•H<sub>2</sub>O, and expanded COF-300•PMMA revealed atomic-level dynamics of the COFs (Figure 1.5e).<sup>70</sup> When the diffraction with RED is poor, it can partially refine the structure to construct the solid-state structures of COFs by computational modeling and refinement with the help of PXRD data.<sup>71</sup>

Unlike MOFs and COFs, frameworks assembled by weaker interactions are difficult to post-modify without disrupting their crystallinity. Solid-state topochemical reactions provide another path to construct single-crystalline covalent polymers or networks.<sup>40, 72</sup> In this approach, the organic building blocks are first organized by crystallization so that the reactive motifs are in close proximity for reaction under thermal or photochemical conditions. This transformation is often referred to as SCSC transformation<sup>40</sup> if the single crystallinity is retained. Early studies of [2+2] cyclobutane formation (Figure 1.6a) in crystals demonstrated the feasibility of topochemical reactions.<sup>73</sup> Today, besides [2+2] additions, other topochemical reactions, including [3+2] azide-alkyne cycloaddition, [4+2] anthracene-alkyne cycloaddition, [4+4] anthracene-anthracene dimerization, 1,4-dialkene addition, diacetylene polymerization, have also been introduced into polymer or network synthesis (Figure 1.6).<sup>72</sup>

In a successful topochemical synthesis, reactive sites should be aligned in the suggested conformation and distance in the solid state (Figure 1.6). For example, in a [2+2] reaction, two olefins should be arranged in parallel within a distance of 3.5–4.2 Å.<sup>73</sup> 2D polymerization has been demonstrated using a pyrylium-based triolefinic monomer **L1**,<sup>74</sup> in which **L1** were  $\pi$ - $\pi$  stacked, and the olefin groups were parallel to each other with a distance of 3.9 Å. Other parameters such as tilt angle  $\theta$ , carbon atom distance  $d_{CC}$ , and packing distance  $d_S$  should also be taken into consideration (Figure 1.6).<sup>72</sup> Schlüter *et al.* prepared a crystal of **L2** packed so that the alkyne and anthracene distances ( $d_{CC}$  4.4 and 3.6 Å, Figure 1.6) and their orientations are suitable for [4+2] cycloaddition.<sup>75</sup> After photo-irradiation, the crystals were successfully polymerized as 2D networks. Later, they reported 2D polymerization of a triazene-based double-decker monomer **L3** (Figure 1.6).<sup>76</sup> The anthracene blades packed in the face-to-face (FTF, blue colored) and edge-to-face (ETF, green colored) manner, and the crystals underwent FTF dimerization upon photoirradiation. King *et al.* reported a similar 2D polymer synthesis using a triptycene-based molecular crystal.<sup>77</sup> The internal stress generated during the SCSC process can shatter the crystal into



smaller fragments. Moieties with rotatable bonds, such as C-C and C-O single bonds, have been introduced to compensate for the internal stress.<sup>78</sup>

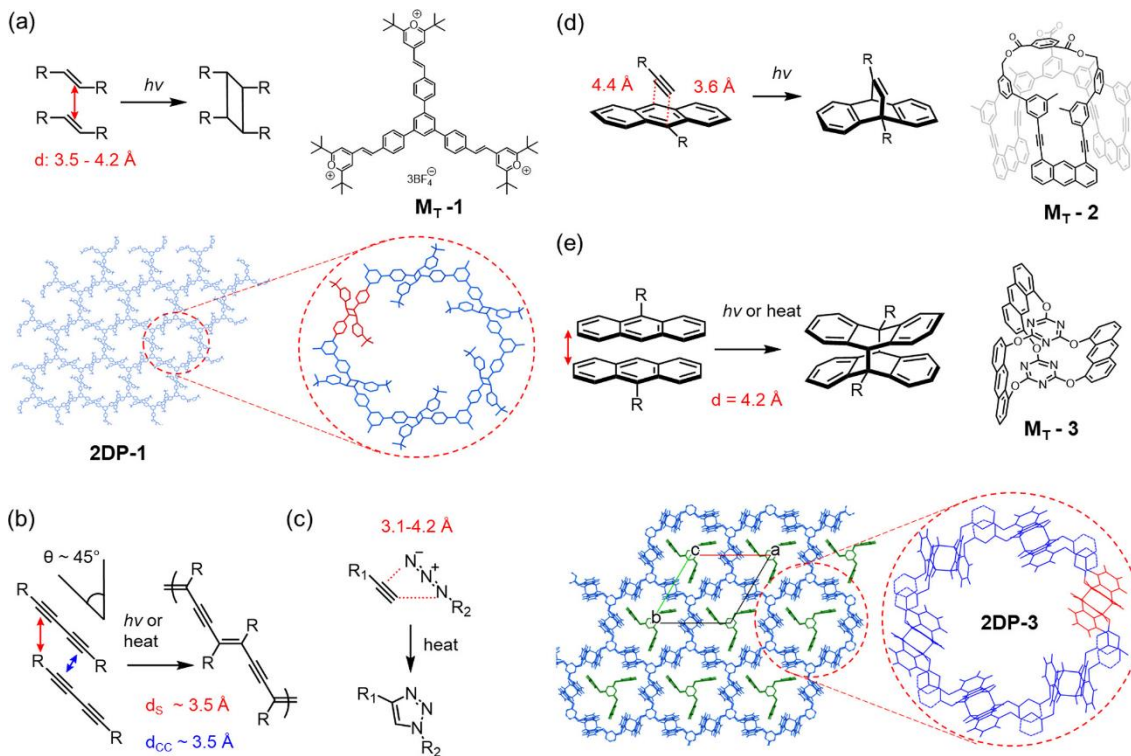


**Figure 1.6.** (a) Topochemical [2 + 2] cycloaddition and the synthesis of a single-crystalline 2D polymer sheet obtained from  $M_T-1$ . (31) Solid-state (b) 1,3-diyne polymerization and (c) [3 + 2] azide–alkyne cycloaddition. (d) Topochemical [4 + 2] anthracene–alkyne cycloaddition and the monomer  $M_T-2$  used for 2D polymer synthesis. (28) (e) [4 + 4] anthracene dimerization and the monomer  $M_T-3$  used for 2D polymer synthesis. (33) Unreacted  $M_T-3$  units removed for clarity. Packing distances between two diacetylenes  $d_s$ , the distance between reactive carbons  $d_{cc}$ , and tilt angles  $\theta$  are highlighted. Copyright 2022 American Chemical Society.

It is worth noting that the utilization of photo-based SCSC is particularly favored for single crystals containing large solve-filled voids, e.g. in the case of  $H_cOF$  synthesis, because photo-reactions usually occur at ambient or low temperatures and therefore mitigate disruption to crystallinity during the SCSC transformation. Although no addition of an external cross-linker is required in the homo-photodimerization-based SCSC transformation (Figure 1.6a and 1.6e), reaction-induced geometry changes in the molecular arrangement may be detrimental to the crystallinity of the final product. In comparison, the hetero-

crosslinking strategy appears to be a more adaptive approach for H<sub>C</sub>OF development, provided that the crystalline molecular precursors form interconnected pores in the solid state large enough for the crosslinkers to diffuse in.

### 1.2.3 Design and synthesis of H<sub>C</sub>OF

H<sub>C</sub>OFs, featuring a 3D porous network with single-crystalline nature and chemical stability, are obtained through covalent cross-linking by pre-organizing molecular crystals with hydrogen bonds. The design of H<sub>C</sub>OFs draws inspiration from HOFs, COFs, and single-crystal polymers (Figure 1.7). H<sub>C</sub>OFs possess hydrogen-bonding and covalent-bonding dual cross-linking networks, making them potentially advantageous in both HOFs and COFs. The synthesis involves the preparation and crystallization of monomers comprising rigid cores, hydrogen-bonding functional groups, and crosslinking active-site to form precursor crystals. The cross-linkers diffuse into the precursor crystals and undergo photochemical cross-linking, leading to the desired H<sub>C</sub>OF structure.

Most porous framework materials classify guest species based on their defined pore structures in terms of size and shape. However, some flexible MOFs,<sup>79</sup> COFs<sup>70</sup>, and HOFs<sup>80</sup> have been reported to exhibit dynamic behaviors for achieving highly selective adsorption and separation. Nevertheless, the degree of flexibility in MOFs, COFs, and HOFs is often limited due to their rigid coordination, covalent, or hydrogen-bonded structures. H<sub>C</sub>OFs, on the other hand, possess a unique responsive dynamic guests' adsorption, owing to their rigid hydrogen-bonded network and flexible covalent crosslinking network. When strongly binding guests are absorbed by H<sub>C</sub>OFs, the hydrogen-bonded network may be disrupted, and the network can expand to the extent allowed by the expansion of crosslinkers.

In 2003, Wuest *et al.* demonstrated the first example<sup>41</sup> of crosslinking a hydrogen-bonded network through the diffusion of ethanedithiol (EDT) followed by photo-irradiation. The monomer consists of a tetraphenylmethane **C6** core and diallyl-melamine arms, which crystallize into a hydrogen-bonded network with interconnected helical channels. When EDT was employed as the crosslinker, a stable, covalently crosslinked 3D network was obtained, which retained its crystallinity upon heating to 200 °C; although this new material was not further investigated until the following decade, it demonstrated the feasibility of achieving long-range order and chemical stability in organic frameworks by covalently crosslinking pre-organized molecular crystals.

An ideal H<sub>c</sub>OF precursor crystal should have large voids for crosslinker diffusion and subsequent adsorption of the guest molecules, as well as the accessible crosslinking active sites exposed to the void. While adding crosslinking active moieties to reported HOFs might be a starting point, it is important to consider that the introduction of reactive groups may alter the packing of the hydrogen-bonded network.<sup>42</sup> Moreover, the precursor crystal of H<sub>c</sub>OFs doesn't necessarily need to possess permanent porosity like HOFs; the crosslinker can diffuse into the framework through solvent exchange. Covalent crosslinking will then stabilize the framework and demonstrate the adsorption of gases such as solvent vapors. Thus, HOFs that may not survive after solvent removal can also be utilized in H<sub>c</sub>OF design. The greater diversity of potential hydrogen-bonded networks marks one of the most significant distinctions between precursor crystals of HOFs and H<sub>c</sub>OFs.

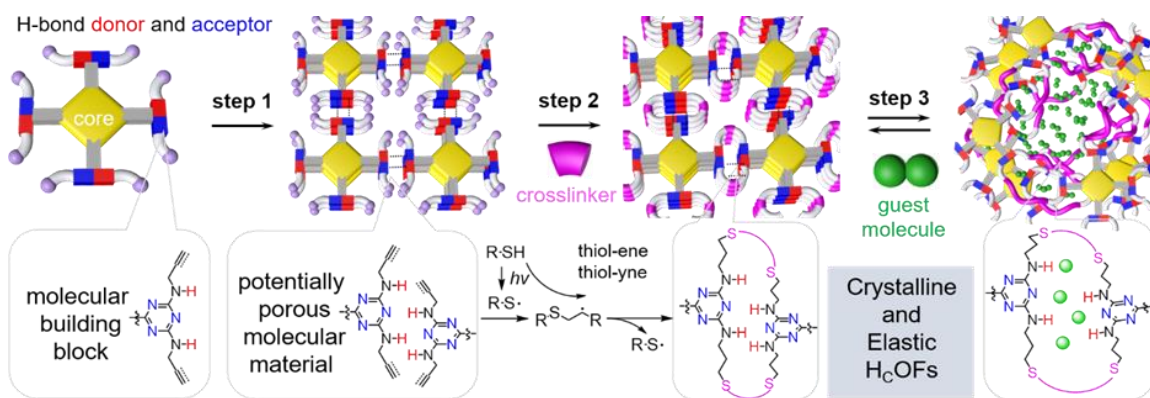


**Figure 1.7.** The design of H<sub>c</sub>OFs through crystallization and subsequent SCSC transformation. Upon guest adsorption, the framework will dynamically change its 3D architecture based on substrate-framework interactions. Copyright 2017 American Chemical Society.

In 2017, we synthesized a propargyl-melamine-based molecule **M1** (Figure 1.8a) by attaching four dipropargyl-melamines onto a tetraphenylethylene (TPE) core.<sup>17</sup> As a result of the –NH– connection between TPE and propargyl-melamine and the non-complementary hydrogen bonding array of propargyl-melamine, **M1** crystallized into a 3D hydrogen-bonded network of *pcu* topology. Later, an allyl-melamine-based monomer **M2** was synthesized and crystallized.<sup>18</sup> Despite nearly identical chemical structures shared by **M1** and **M2**, a hydrogen-bonded network of *snw* topology was formed by **M2** with the alternative and tilted packing (Figure 1.8a). In **M1**<sub>crystal</sub> and **M2**<sub>crystal</sub>, interconnected voids of 51% and 21% filled with solvent molecules were discovered through SCXRD analysis. The reactive propargyl

and allyl groups decorated the pore surfaces, and the neighboring propargyl and allyl groups were 3.3-11.9 Å apart,<sup>17-18</sup> suitable for the subsequent thiol-yne and thiol-ene SCSC transformation. Though propargyl/allyl-melamine was effective for constructing large void H<sub>c</sub>OF precursor crystals, the DAD hydrogen bonding array, multiple potential directions for hydrogen bonding, and rotatable –NH– connections complicate crystal engineering. Network topologies formed by melamine-based monomers are hard to predict.

To increase the directionality and the predictability of the hydrogen-bonded network and reduce the complexity of the crystal engineering, we protonated allyl-melamine to allyl-melaminium with a DDD hydrogen bonding array.<sup>19</sup> When allyl-melaminiums were hydrogen-bonded to a nitrate dimer (NO<sub>3</sub><sup>-</sup>)<sub>2</sub> or a bisulfate dimer (HSO<sub>4</sub><sup>-</sup>)<sub>2</sub>, they formed directional, linear hydrogen bonding joints, in which the (NO<sub>3</sub><sup>-</sup>)<sub>2</sub> or (HSO<sub>4</sub><sup>-</sup>)<sub>2</sub> acted as dual AAA arrays connecting two melaminium units. The connection is further reinforced by electrostatic interactions between the cationic melaminium and anion dimers. For example, protonated [M6•3H]<sup>3+</sup> formed solvent-filled hydrogen-bonded networks with nitrate and bisulfate anion clusters (Figure 1.8b).<sup>19</sup> We discovered that the nitrate anion cluster consists of three nitrate anions and three DMSO, making the joint unstable. [M6•3H]<sup>3+</sup> formed an *hxl* network with tri-bisulfate anion clusters (HSO<sub>4</sub><sup>-</sup>)<sub>3</sub> with large 1D voids (51%) along the *c*-axis with a pore size of 15.3 × 13.8 Å (Figure 1.8b). Allyl groups pointed toward the pore surface with distances between 2.5-11.7 Å, suitable for crosslinking. It is worth noting that the *hxl* network was formed at higher temperatures (~80 °C), and we also obtained a different hydrogen-bonded network formed between [M6•4H]<sup>4+</sup> and (HSO<sub>4</sub><sup>-</sup>)<sub>4</sub> at room temperature.

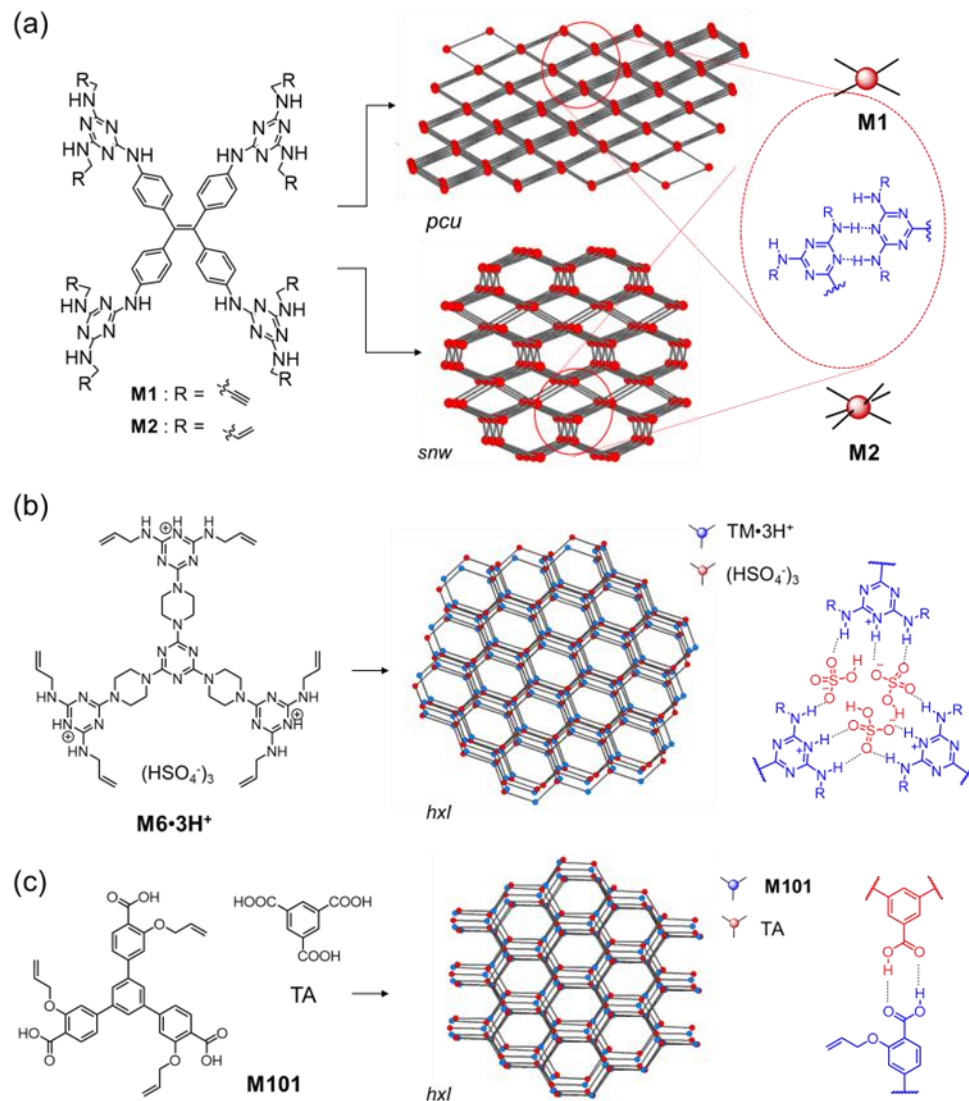


**Figure 1.8.** Hydrogen-bonding patterns and topologies of precursor crystals of (a) H<sub>c</sub>OF-1 and H<sub>c</sub>OFs-2-4, (b) H<sub>c</sub>OF-6, and (c) H<sub>c</sub>OF-101. Copyright 2022 American Chemical Society.

We also introduced carboxylic acid-based monomers for H<sub>c</sub>OF synthesis<sup>42</sup> since they are highly directional. R<sub>2</sub><sup>2</sup>(8) joints formed by carboxylic acid dimers would direct the assembly of monomers. **M101** was synthesized with three allyl ether groups attached to the *ortho* position of the carboxylic acid moiety (Figure 1.8c). Not surprisingly, the substitution of the *ortho* position of the monomer disrupted the carboxylic acid dimerization in the solid state, common in crystal engineering of carboxylic acid-based monomers. To overcome this problem, we introduced trimesic acid (TA) as a co-crystallization joint. **M101** and TA

possess different  $pK_a$  values and electron densities at the phenyl moieties, promoting heteromeric carboxylic acid dimerization between **M101** and TA and inhibiting the homodimerization of **M101**. **M101**/TA co-crystallized to form a hexagonal non-interpenetrated large pore network ( $d = 16 \text{ \AA}$ ), with allyl groups exposed to pore surfaces for crosslinking. We emphasize that, in the **M101** and TA co-crystal, **M101** and TA have similar symmetries, but different sizes. Hence, **M101** and TA are packed in an alternating pattern along the  $c$ -axis, effectively inhibiting the interpenetration of the network. In principle, this approach of employing size-mismatched monomers to form co-crystallized hydrogen-bonded networks provides solutions to address the isorecticular expansion of HOFs and H<sub>C</sub>OF precursor crystals. Of note is that the alternating stacking of **M101** and TA is not perfectly eclipsed. Such information may be helpful for researchers working in 2D COF structural modeling because most 2D COFs are modeled as perfectly eclipsed or staggered conformations.

After successful crystallization of the precursor crystals, the next step is to crosslink the reactive sites of the precursor crystals, converting these hydrogen-bonded networks into covalently connected frameworks. Heterogeneously introducing flexible crosslinkers into the voids of the precursor crystal allows for bypassing the strict geometric constraints in topochemical synthesis. This method also allows us to employ a variety of flexible building blocks and linking motifs and a plethora of irreversible reactions that are largely avoided in the current design of COFs. SCXRD analysis of the precursor crystal provides distances between nearby reactive alkenes/alkynes in the crystal lattice, which guides dithiol crosslinker selection. From our experience, EDT is suitable to crosslink the reactive sites between distances of 3.9 to 7  $\text{\AA}$ , whereas the longer linkers, such as propanedithiol (PDT) and butanedithiol (BDT), are suitable for linking proparyl/allyl that is under 8.5  $\text{\AA}$  and 10  $\text{\AA}$  apart, respectively.

Unlike solution phase synthesis, when the distances between two reactive sites match the length of the crosslinker, the crosslinking reaction can occur between non-neighboring reactive sites in the solid state (Figure 1.9a). Hence, topologically different H<sub>C</sub>OFs can be obtained from the same molecular precursor crystals. The divergent H<sub>C</sub>OF synthesis was illustrated when EDT and PDT were employed to crosslink **M2**<sub>crystal</sub>.<sup>18</sup> The olefine motifs in the allyl melamine were distributed along the wide and narrow pore openings in **M2**<sub>crystal</sub>, with olefin-olefin distances ranging between 3.5-11  $\text{\AA}$ . When EDT was used as the crosslinker, it stoichiometrically reacted with most nearby allyl groups,

converting them to the dithioethers in H<sub>C</sub>OF-2. When PDT was employed, six of eight allyl groups reacted, leaving two olefines located in the more congested area unreacted.

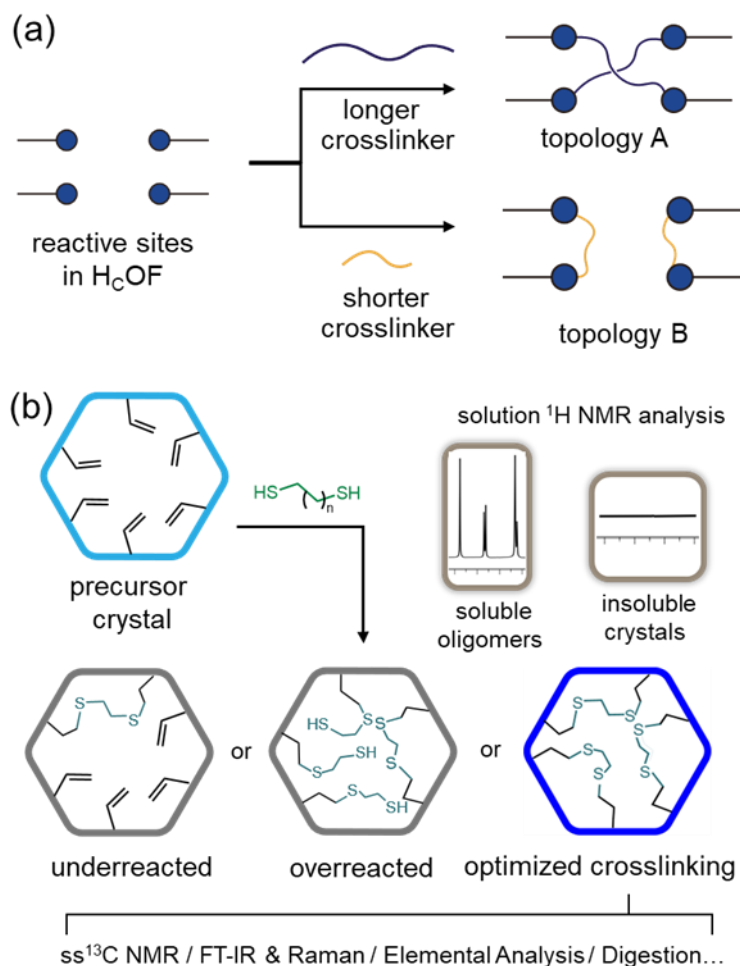


**Figure 1.9.** (a) Topochemical crosslinking taking place in a precursor crystal using dithiols of different lengths. (b) Optimization and characterization of H<sub>C</sub>OFs. Copyright 2022 American Chemical Society.

When the pore aperture of the precursor crystal is expanded, the use of higher crosslinker concentrations may result in overreaction (with unreacted thiols) and significantly reduce the crosslinking degree of H<sub>C</sub>OFs (Figure 1.9b). This overreaction was observed during the synthesis of H<sub>C</sub>OF-6 (pore diameter ~15 Å)<sup>19</sup> and H<sub>C</sub>OF-101 (pore diameter ~16 Å),<sup>42</sup> when overreaction afforded products soluble in hot DMF and DMSO that can be monitored using <sup>1</sup>H NMR spectroscopy. On the other hand, underreacted products obtained from dilute dithiol solutions are also soluble for <sup>1</sup>H NMR analysis (Figure

1.9b). Therefore, reducing the soluble species to a minimum by adjusting crosslinker concentrations is the first step in the optimization of the H<sub>C</sub>OF synthesis. The chemical compositions of the synthesized crystals need to be thoroughly characterized before SCXRD analysis. After photo-crosslinking, FT-IR and Raman spectroscopy analyses reveal whether free thiols exist. Solid-state <sup>13</sup>C NMR spectroscopy is used to confirm the consumption of allyl/propargyl groups and the formation of thioethers. Elemental analysis is important for the composition analysis of H<sub>C</sub>OFs. The experimentally measured weight percentages of C/H/N/S elements of a synthetically well-optimized H<sub>C</sub>OF are found within 0.5 wt% of the theoretical values, similar to the accuracy of small molecule elemental analysis. We also introduced a digestion method to confirm the composition of H<sub>C</sub>OF-101 by hydrolyzing the framework into soluble species for <sup>1</sup>H NMR analysis. After confirming the chemical composition of the synthesized H<sub>C</sub>OFs, high-quality single crystal samples are prepared for SCXRD analysis.

#### 1.2.4 SCXRD analysis of H<sub>C</sub>OFs

In general, single crystals of H<sub>C</sub>OFs obtained can be analyzed using Single-Crystal X-ray Diffraction (SCXRD) to determine their crystal structure, which is crucial for establishing the structure-property relationships. The pre-crosslinked H<sub>C</sub>OF precursors can typically yield high-quality single-crystal data on a general X-ray diffractometer. However, after crosslinking, an increase in disorder can lead to a certain degree of reduction in crystal quality. Crosslinked H<sub>C</sub>OFs often require high-energy synchrotron radiation for data refinement. During the data refinement process, the hydrogen-bonded network of H<sub>C</sub>OFs would be similar to the precursors and is usually modeled unambiguously. On the other hand, the flexible disulfide crosslinkers in H<sub>C</sub>OFs may exhibit a more pronounced disorder. In cases where the crystal structure of H<sub>C</sub>OF cannot be directly determined through SCXRD analysis, we have developed several methods to overcome these challenges, which are described in the following cases. We emphasize that the standard used for small molecule crystallography (e.g., R<sub>1</sub> < 10%) is not suitable for evaluating the crystal data quality of H<sub>C</sub>OFs, as these networks are large and possess significant disorder due to the flexible crosslinkers. Instead, standards similar to those used in macromolecular crystallography analysis should be considered (e.g., R ~20-30%).<sup>81</sup>

H<sub>C</sub>OF-1.<sup>17</sup> Due to the high numbers of disordered flexible dithioether linkages as well as the randomly generated stereogenic centers after crosslinking, the quality of the X-ray diffraction data was too poor for SCXRD analysis. Only the unit cell parameters were



reported, and the crosslinked structure was obtained through simulation using unit cell parameters and PXRD data.

H<sub>C</sub>OFs-2-3.<sup>18</sup> The hydrogen-bonded networks of H<sub>C</sub>OFs-2-3 were found to be very similar to the structure of the precursor crystal **M2**<sub>crystal</sub>. The assignment of four out of eight dithioether linkages was straightforward, with disordered atoms modeled over several positions. Due to the weak and smeared electron density, atomic placements of the other four dithioether linkages were ambiguous based on the SCXRD data of H<sub>C</sub>OFs-2-3 alone. Therefore, we synthesized two analogous polymers **P2** and **P3**, by reducing the number of dithioether linkages on each DAT moiety from two to one. The resolved SCXRD structures of **P2** and **P3** (Figure 1.10a) not only confirmed the correct atomic placements of the four modeled-in linkages but also provided important structural guidance for the modeling of the other four linkages. Furthermore, we performed a two-step reaction on the precursor crystal of H<sub>C</sub>OFs-2-3 using ethanethiol first to consume four allyl groups in each **M2** and then crosslinking the remaining four allyl groups using EDT. Combining the SCXRD analysis of H<sub>C</sub>OFs-2-3, **P2-3**, and two-step reaction outcomes, the network structures of H<sub>C</sub>OF-2 and H<sub>C</sub>OF-3 were determined unambiguously (Figure 1.10a). H<sub>C</sub>OF-2 was found as a new, 3-nodal 3,3,4-connected self-entangled 3D network (*cdc*, named after Chemistry Dartmouth College), whereas H<sub>C</sub>OF-3 was found as a 2D 3,4-connected bilayer network.

H<sub>C</sub>OF-6.<sup>19</sup> The precursor crystal [**M6•3H**]<sup>3+</sup>•**3HSO<sub>4</sub><sup>-</sup>** diffracted weakly, and the quality of the diffraction was further reduced in H<sub>C</sub>OF-6 after crosslinking. Surprisingly, data of reasonable quality were collected using a Mo-radiation source with an extended exposure time. The backbone of H<sub>C</sub>OF-6 and (HSO<sub>4</sub><sup>-</sup>)<sub>3</sub> anion clusters were resolved in a straightforward manner (Figure 1.10b). Smeared electron densities attributed to dithioether linkages were distributed near the backbone, making the atomic placement ambiguous. To assist the SCXRD analysis, we experimentally swelled H<sub>C</sub>OF-6 in phenol and found that this crystal expanded more than 2.5 times along the *c*-axis and shrunk slightly along the *a/b* plane. We also set up hypothetical models of H<sub>C</sub>OF-6 within molecular dynamics (MD) simulations with varying proportions of crosslinking assigned as inter- vs intralayer. Only models with over 67% crosslinking assigned as intralayer could match experimental observations. Thus, a representative crystal structure of H<sub>C</sub>OF-6 possessing 100% intralayer linkages was modeled (Figure 1.10b), while we acknowledge the existence of a small percentage of interlayer crosslinks as defects.

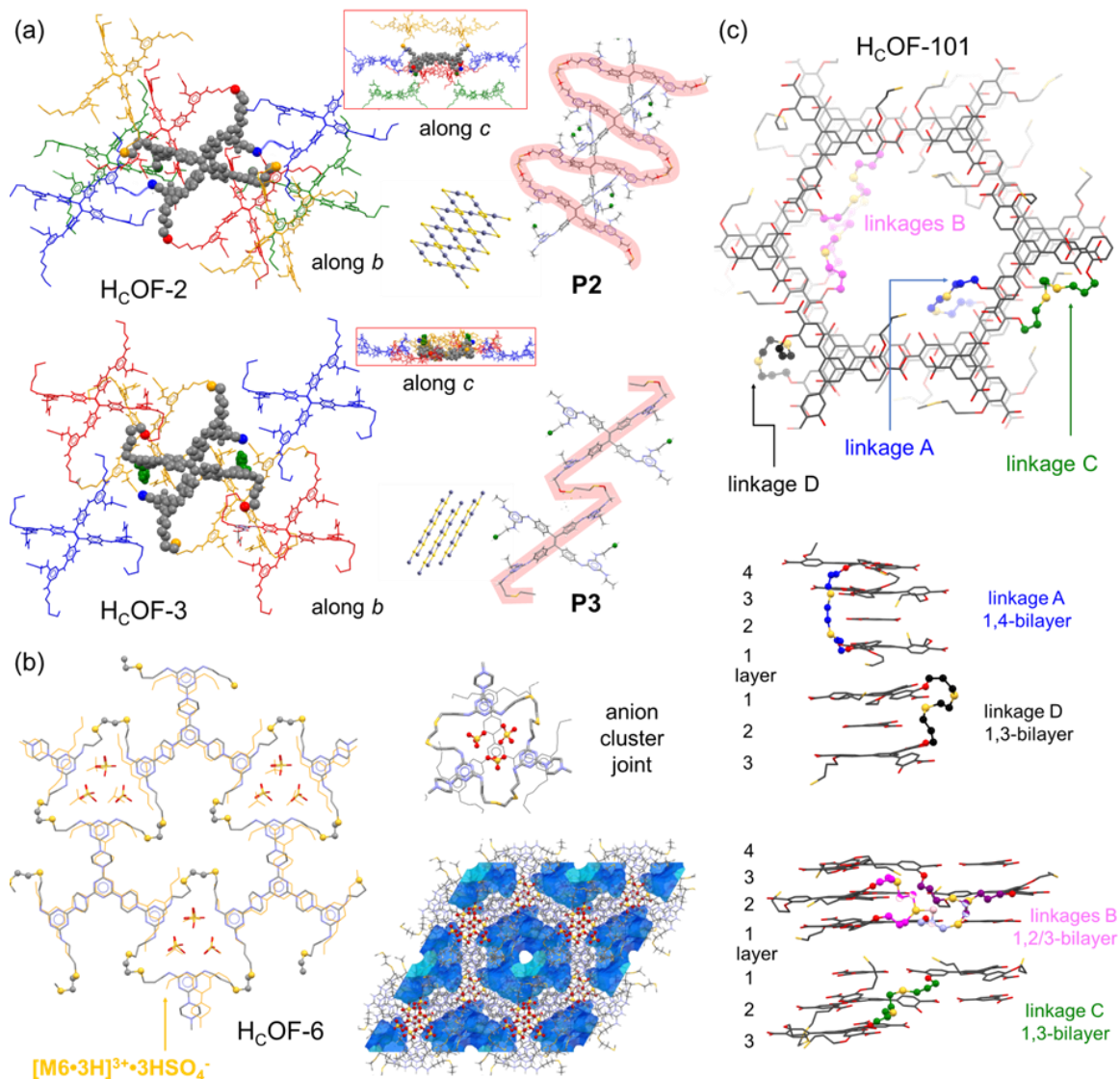


**Figure 1.10.** (a) Single crystal structures of H<sub>c</sub>OF-2 and P2, H<sub>c</sub>OF-3 and P3 viewed along different axes. Reproduced with permission from ref 14. Copyright 2019 American Chemical Society. (b) Overlaid single crystal structures of [M6·3H]<sup>3+</sup>·3HSO<sub>4</sub><sup>-</sup> and H<sub>c</sub>OF-6. The anion cluster joint and voids of H<sub>c</sub>OF-6 are highlighted on the right. Reproduced with permission from ref 16. Copyright 2022 Elsevier B.V. (c) Single crystal structure of H<sub>c</sub>OF-101 with detailed dithioether linkages connecting between different layers. Copyright 2022 American Chemical Society.

H<sub>c</sub>OF-101.<sup>42</sup> The allyl groups in the M101/TAc<sub>crystal</sub> co-crystal were disordered over two positions with equal probability on both sides of the phenyl rings of M101. After crosslinking, the formed dithioether linkages in H<sub>c</sub>OF-101 reduced the symmetry of the

crystal and changed its unit cell compared to that of the co-crystal. The rigid hydrogen-bonded network of H<sub>C</sub>OF-101 was found to be nearly identical to the precursor co-crystal. Luckily, synchrotron data provided sufficient electron densities to model dithioether linkages, some of which were overlapped. Refinement of the H<sub>C</sub>OF-101 revealed the formation of a 3D crosslinked network featuring a pore diameter of 14 Å and 27% void, with crosslinking between 1,2-, 1,3-, and 1,4- layers (Figure 1.10c).

### 1.2.5 Dynamic sorption of H<sub>C</sub>OFs

The unique flexibility and dynamic guest adsorption properties of H<sub>C</sub>OFs are imparted by the dual crosslinking network of flexible covalent linkages and rigid hydrogen-bonded network (Figure 1.11a). H<sub>C</sub>OFs can exhibit permanent porosity like other framework materials through appropriate activation and removal of distributed voids in solvents. When H<sub>C</sub>OFs adsorb common organic solvent or water vapor, they show moderate adsorption capacity, and their crystallinity remains unaffected. However, when guests with the ability to disrupt hydrogen bonding enter the voids of H<sub>C</sub>OFs, the hydrogen-bonded network would be broken, leading to the expansion and loss of crystallinity of H<sub>C</sub>OFs material. The flexible crosslinkers are stretched during the expansion (entropy loss), and the extent of expansion depends on the length and density of the crosslinkers. These stretched crosslinkers retain a certain degree of alignment in the expanded H<sub>C</sub>OFs. The size expansion caused by guest adsorption in H<sub>C</sub>OFs resembles the swelling of crosslinked polymers. When guests are released from the framework, the hydrogen bonds are reconstructed, allowing the framework to recover a certain degree of crystallinity.

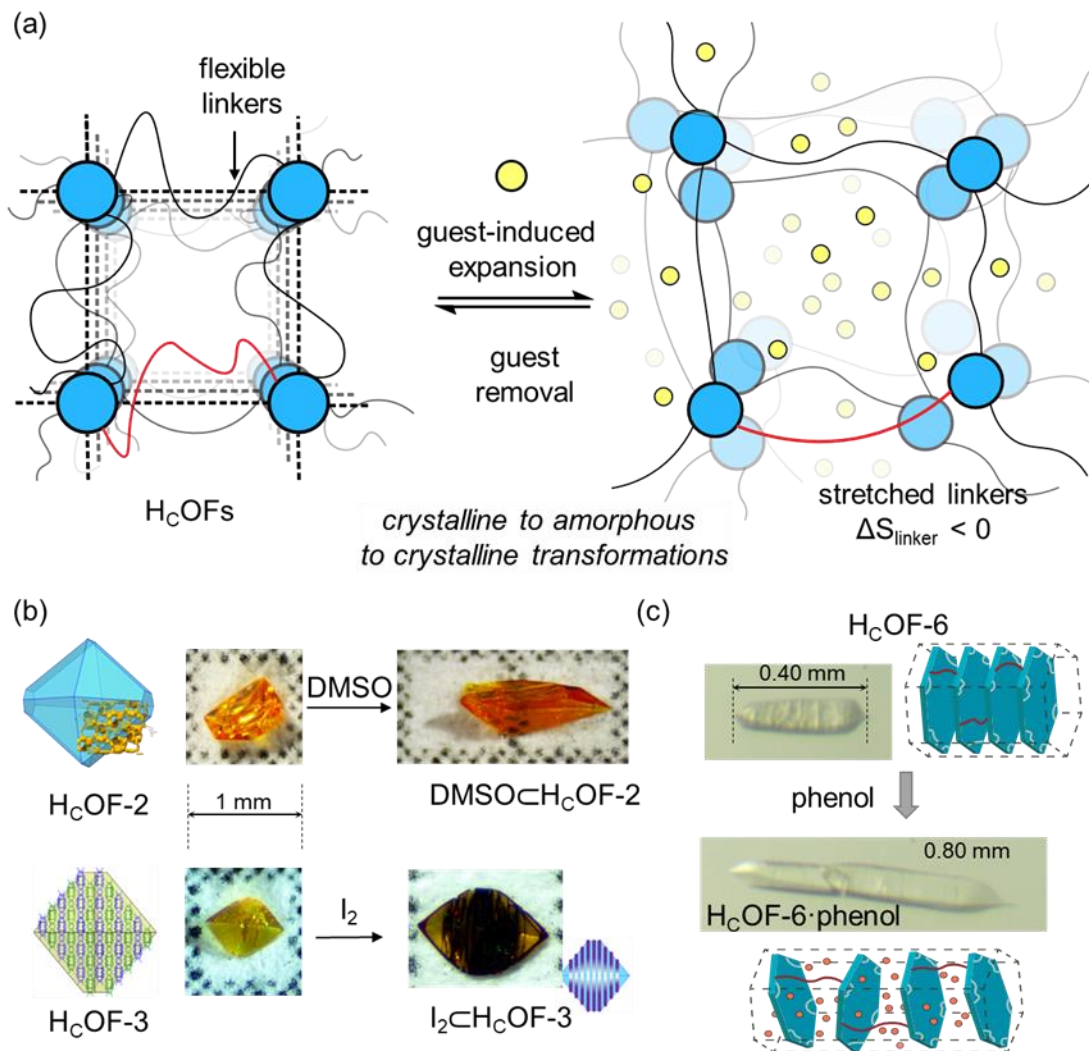


**Figure 1.11.** (a) Graphical illustration of the dynamic sorption of H<sub>c</sub>OFs upon disrupting and reforming hydrogen-bonded networks. (b) Crystal size expansion of H<sub>c</sub>OFs-2-3 upon DMSO or I<sub>2</sub> guest uptake. Copyright 2022 American Chemical Society.

Iodine (I<sub>2</sub>) forms halogen bonding interactions with the triazine moieties in H<sub>c</sub>OFs, disrupting the original hydrogen-bonded network and activating the dormant voids in H<sub>c</sub>OFs. H<sub>c</sub>OFs-1-4 exhibit significant I<sub>2</sub> adsorption capacity in aqueous environments, ranging from 2.1 to 3.6 g/g. The crystals of H<sub>c</sub>OFs-2 show visible size expansion to more than twice their original size (Figure 1.11b), and the framework loses its crystallinity and becomes completely amorphous after iodine adsorption. The size expansion caused by iodine adsorption is anisotropic, with the maximum extension direction indicating the lowest crosslinking density. For instance, the crystals of H<sub>c</sub>OF-3 exhibit a double-layered

delamination-like expansion upon I<sub>2</sub> absorption. Therefore, the macroscopic size expansion provides indirect information about the network architecture in H<sub>C</sub>OFs. Due to the elastic expansion of the framework during the adsorption process, the calculated I<sub>2</sub> adsorption van der Waals volume exceeds the available void spaces in H<sub>C</sub>OF-2 and H<sub>C</sub>OF-3 by 473% and 668%, respectively. The high-capacity adsorption of iodine by H<sub>C</sub>OF in water environments, along with their good chemical stability, makes these materials potentially useful for the removal of radioactive iodine or water treatment. We also found that DMSO can effectively activate the dormant voids in H<sub>C</sub>OF, transforming them into isotropically poor amorphous materials (Figure 1.11b). After washing out guest molecules such as I<sub>2</sub> or DMSO with solvents, the crystals can usually recover their original arrangement to a large extent.

Due to the multivalent hydrogen bonding network, only strongly binding guests can activate the dormant voids of melamine-based H<sub>C</sub>OFs. This feature, on one hand, significantly enhanced the substrate selectivity but, on the other hand, limited the substrate scope. To this end, the anion-cluster-based H<sub>C</sub>OF-6 was synthesized. The electrostatic repulsion between bisulfate anions in H<sub>C</sub>OF-6 requires a smaller energy penalty for the disruption of the hydrogen-bonded network to trigger the expansion of H<sub>C</sub>OFs. Phenol and its analogs demonstrated their capabilities of expanding the size of H<sub>C</sub>OF-6 crystal (Figure 1.11c) during adsorption, disrupting the anion clusters. Multi-cycle crystal size expansions and contractions were found when H<sub>C</sub>OF-6 absorbs and desorb phenols. In H<sub>C</sub>OF-101, the disruption of the hydrogen-bonded network of H<sub>C</sub>OF-101 resulted in the loss of TA in hot DMSO, since TA was not covalently crosslinked to the framework.

### **1.3 3D printing porous organic materials using direct ink writing.**

Porous materials, possessing high surface area and low density, have found widespread applications in adsorption, separation, energy storage, and catalysis. Inorganic porous materials such as zeolites,<sup>82</sup> porous carbons,<sup>83 84</sup> and porous metal-based materials<sup>85-86</sup> offer advantages such as high thermal and chemical stability. These inorganic materials are suitable for large-scale production with low cost. The development of organic porous materials, including Metal-Organic Frameworks (MOFs),<sup>87</sup> Covalent Organic Frameworks (COFs),<sup>88</sup> and Porous Organic Polymers (POPs),<sup>6</sup> has brought new opportunities to the field. Organic materials offer the advantage of design flexibility, as they can be tailored with a variety of organic building blocks to achieve desired interactions with target molecules and to tune their optical, electrical, and other properties. MOFs and COFs, as crystalline porous

frameworks, have nowadays become hot research areas. They allow precise control over pore size through reticular chemistry. Their atomic-level structures enable the understanding of topology, interpenetration, structural flexibility, and host-guest interactions, elucidating the relationships between structure and properties.<sup>89</sup>

Porous materials hold enormous potential in industrial production, biochemistry, environmental remediation, and many other fields. However, one of the existing challenges is that these materials are often synthesized as powders rather than macroscopic 3D devices. The networks of porous materials are typically rigid and stable, making it difficult to process. Various manufacturing methods have been employed, including extrusion,<sup>90</sup> granulation,<sup>91</sup> pelletization,<sup>92</sup> coating,<sup>93</sup> and molding.<sup>94</sup> However, compared to these conventional methods, 3D printing offers unique advantages, including material versatility and the ability to fabricate highly customized and structurally complex designs, enabling superior mechanical performance, higher surface area, and better mass-transfer efficiency.<sup>95</sup> This has opened up new possibilities for the development of advanced functional materials with tailored properties and enhanced performance.

Although various 3D printing methods exist, direct ink writing (DIW) is one of the most widely used techniques for 3D printing porous materials due to its simple operation and flexibility. However, porous materials typically cannot be directly extruded; instead, ink with specific rheological properties needs to be prepared beforehand. Supramolecular interactions, such as van der Waals forces, hydrogen bonding, coordination bonding, and self-assembly between different components in the ink, are crucial for its printability and can be characterized through techniques like NMR, spectroscopies, and electron microscopy. Furthermore, maintaining the porosity of the printed material while ensuring 3D printability remains a challenge. The direct method involves mixing pre-synthesized porous materials with templates to introduce porosity. Alternatively, the precursors of porous materials can be 3D printed first, followed by secondary growth to generate pores. By carefully removing different phases, such as 3D printing templates and solvents, mesoporosity can be introduced. These methods enable the production of porous materials with different mass-loadings, surface area and mechanical strengths.

DIW demonstrates strong material compatibility. With proper design, inorganic materials such as zeolites, porous carbons, porous silicon-based materials, metal derivatives, as well as organic materials like metal-organic frameworks (MOFs), covalent organic frameworks (COFs), macrocycles, and polymers, can all be 3D printed using DIW (Figure

1.12). However, each material has its unique chemical bonding, solubility, thermal stability, and synthesis method, necessitating a flexible application of the principles mentioned above to fabricate high-performance 3D-printed porous materials. 3D printing endows porous materials with macroscopic shapes, and by using methods like phase separation, it is possible to achieve hierarchical pore sizes, thereby increasing the diffusion rate of guest molecules. Consequently, 3D printing extends the application performance of porous materials beyond powdery materials, especially in gas adsorption and separation, water remediation, catalysis, and various biomedical fields.

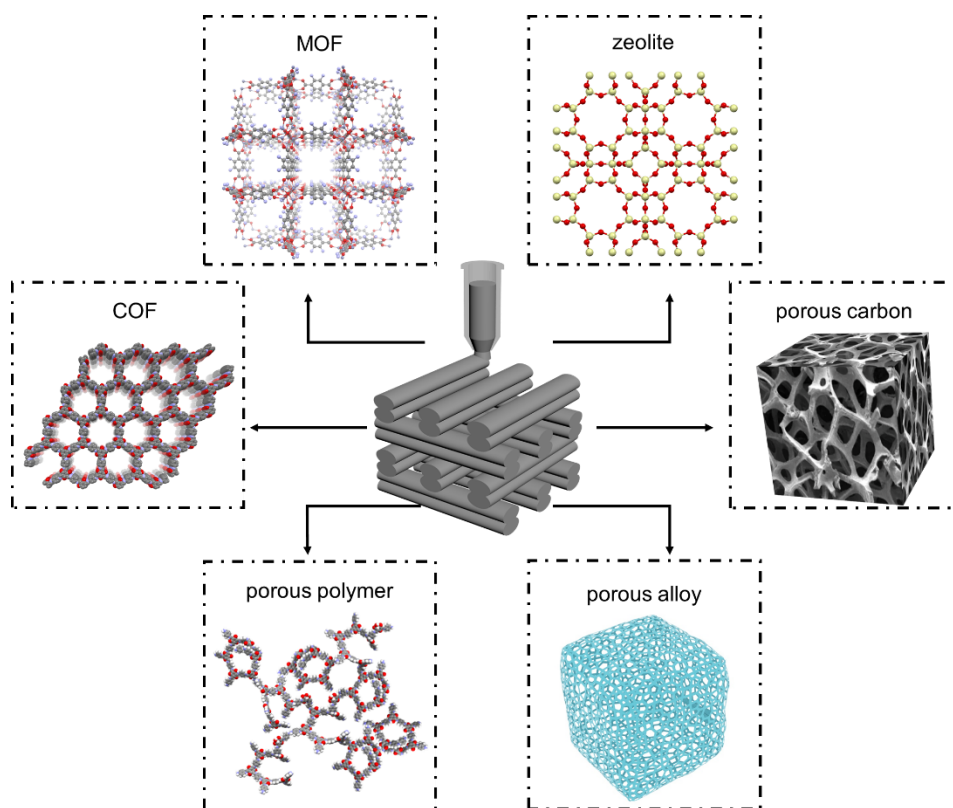


**Figure 1.12.** 3D printing porous materials, including MOFs, COFs, porous polymer, porous alloy, porous carbon, and zeolite.

In this section, we start with introducing general 3D-printing methods, and we mainly focus on direct ink writing (DIW). Then, the design considerations and general characterization methods for 3D printing porous materials using DIW are discussed. In addition, significant emphasis has been placed on the methods used to achieve 3D printing and the strategies employed to create porosity in printed materials. The diverse range of porous materials that can be fabricated using 3D printing techniques, including MOFs, COFs, porous polymers, zeolites, activated carbons, and composite materials, were

examined. The resulting materials' mass loading, surface area, and mechanical properties have also been documented. We also delve into the applications of 3D-printed porous materials in adsorption separation, water remediation, catalysis, and various biomedical fields.

### **1.3.1 3D printing methods**

Currently, there have been many types of 3D printing technologies developed. Followed by the invention of stereolithography (SLA) in 1986,<sup>96</sup> various AM methods were developed, including Fused Deposition Modeling (FDM),<sup>97</sup> Binder Printing, Inkjet Printing,<sup>98</sup> Selective Laser Sintering (SLS),<sup>99</sup> and Laminated Object Manufacturing (LOM),<sup>100</sup> with different characteristics, resolutions, and material compatibility. Among these, extrusion-based printers,<sup>101</sup> including FDM and direct ink writing (DIW),<sup>102-103</sup> and vat-polymerization-based printers, including SLA and digital light processing (DLP),<sup>104</sup> were commercialized and remained the most widely used in 3D printing materials. Both FDM and DIW printers work by extruding loaded materials through a nozzle as it moves across the xy-plane, leaving a single printed layer on the substrate. Then the extrusion head raises in the z-direction relative to the print bed and proceeds with the next layer printing. The printing resolution is therefore determined by the nozzle diameter. The difference between the two, however, lies between the printing condition and material selection. FDM employs continuous filament of thermoplastics such as acrylonitrile butadiene styrene (ABS) and poly(lactic acid) (PLA) as feedstock material. These materials have to have relatively low melting temperature and appropriately high glass transition temperature so that the filament can be melted at the heated print head and flows out of the nozzle and solidifies quickly at room temperature. DIW, on the other hand, operates under ambient temperature and extrusion is achieved through viscoelastic soft materials. DIW inks need to possess reversible shear-thinning and self-healing properties during and after extrusion to allow smooth deposition and good structural integrity of printed objects. Therefore, supramolecular interactions are often employed to design DIW ink. While extrusion-based printings are low-cost, user friendly, and offer multi-material integration, they suffer from relatively low resolution, slow printing speed, and between-layer anisotropy.



**Table 1.1.** Comparison of extrusion-based and vat-polymerization-based 3D printing methods.

<b>AM methods</b>	<b>Extrusion-Based</b>		<b>Vat-Polymerization-Based</b>	
<b>Subtypes</b>	<b>FDM</b>	<b>DIW</b>	<b>SLA</b>	<b>DLP</b>
<b>Condition</b>	Heated nozzle	Ambient	UV irradiation	UV irradiation
<b>Feedstock material property</b>	Thermoplastics	Sheer-thinning and self-healing fluid	Newtonian liquid	
<b>Crosslinking</b>	Van der Waals	Multiple crosslinking methods	Mostly photo-crosslinking	
<b>Material</b>	Thermoplastics	Hydrogels, organogels, elastomers, bio-inks	Thermosets, elastomers, hydrogels	
<b>XY-resolution</b>	Nozzle 0.1mm to cm-width scale	Nozzle 0.1mm to 1mm	Laser spot <100 micron	Screen Pixel <100 microns
<b>Speed</b>	slow	slow	slow	fast
<b>Strength</b>	Strong and durable prints, inexpensive	Biocompatible, Stimuli-responsive material	Scalable volume independent of resolution	Fast printing with high resolution and throughput
	Multimaterial integration		High resolution and smooth surface, isotropic layers	

In comparison, Vat-polymerization-based printing offers relatively faster printing speed and higher resolution. Both SLA and DLP work by selectively exposing liquid resin to a light source and a thin layer of solid is formed on the build platform via photopolymerization. The platform then lifts up to allow uncured resin to flow in to print the next layer. The resin material not only needs to be photocurable but also with low viscosity. The only difference between the two methods is the light source: SLA uses a UV laser while DLP uses a projector screen. Therefore, SLA resolution (xy-plane) is determined by the minimum laser spot size while DLP resolution depends on the minimum pixel size of the screen. The z-resolution for both can range between 25-300 microns, the finest of all 3D printing methods, yielding a smoother surface finish. While the SLA printer's build volume is more scalable without sacrificing printing resolution, DLP can print faster with high throughput.

### **1.3.2 Tools and design considerations for 3D printing porous materials using DIW**

As a highly flexible and versatile 3D printing method, Direct Ink Writing (DIW) possesses unique advantages in material design and device manufacturing compared to other 3D printing methods (Figure 1.13a). In a typical DIW process, the ink needs to undergo shear thinning during the extrusion process and self-healing after deposition (Figure 1.13b). During the 3D-printing extrusion process, the viscosity of inks decreases due to the disruption of the supramolecular interactions. When the shear force is removed after printing, these dynamic crosslinks quickly re-establish, and the printed material regains its elastic modulus (Figure 1.13c). Various supramolecular gels or pastes, which form a supramolecular network, have been successfully employed as DIW inks. Examples of supramolecular interactions include hydrogen-bonds,<sup>42-44</sup> host-guest interactions, coordination bonds,<sup>39-41</sup> electrostatic interactions,<sup>45-47</sup> van der Waals interaction<sup>48,49</sup> and mechanical bonds. These ink systems have been extensively discussed in previous reviews. Additionally, the addition of colloidal particles has been proven effective in adjusting the rheological properties of DIW inks. Classic systems such as poly(vinyl alcohol) (PVA), Pluronic F127, and polypseudorotaxane systems based on  $\alpha$ -cyclodextrin and PEG have been developed for DIW printing of porous materials. During DIW printing of porous materials, a typical method is that these 3D printing templates physically mix or co-assemble with a certain proportion of porous materials or their precursors to form printable gels.

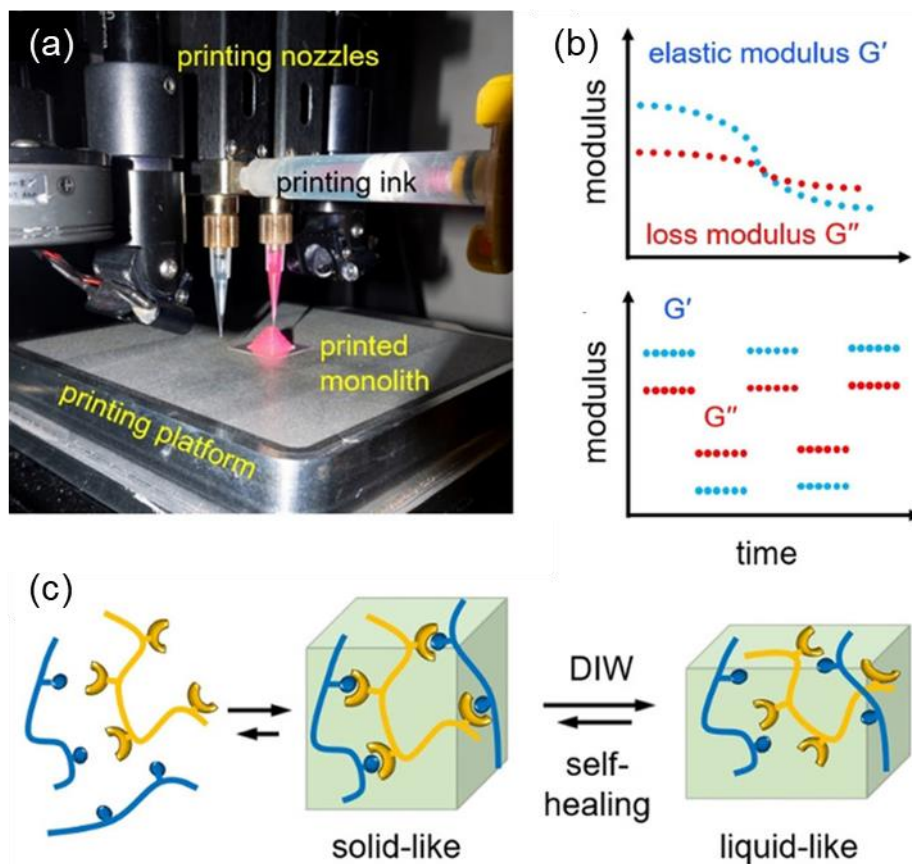


**Figure 1.13.** (a) A direct-ink-write 3D printing system equipped with two extrusion nozzles. (b) Desired rheological properties of a typical DIW ink. (c) Graphical illustration of the design of a 3D-printable polymer.<sup>105</sup> Copyright 2019 John Wiley & Sons, Inc.

Currently, maintaining the porosity of materials while 3D printing remains a challenge. There are several methods to create porous structures in 3D-printed materials. One approach is to pre-synthesize materials that inherently possess pores, such as MOFs,<sup>106</sup> macrocycles,<sup>107</sup> porous carbon,<sup>108</sup> and zeolites.<sup>109</sup> The microcrystals of the materials with intrinsic porosity can be synthesized beforehand or by grinding the material and then mixed with a 3D printing template, along with a binder or crosslinking agent. Then the mixture can be 3D-printed into the desired shapes (Figure 1.14a). Although this printing method is relatively straightforward, it comes with several challenges. For instance, the small particles of self-porous materials are difficult to homogeneously assemble with the template, often leading to nozzle clogging and limiting printing resolution. Moreover, to ensure the integrity of the 3D-printed monolith, a significant amount of 3D printing template or binder needs to

be added, which is challenging to remove completely and often reduces or blocks the inherent pores of the material.

Another approach involves mixing the precursor of porous materials with a 3D printing template. The reaction between precursors is preferably slowed down before printing. After printing, the secondary growth of precursors into porous materials would perform through suitable treatments without compromising the overall integrity of the monolith (Figure 1.14b).<sup>110-112</sup> The macroscopic shape does not collapse even after the complete removal of the template in this method. The resulting porous monoliths are expected to exhibit higher printing resolution and mechanical strength compared to the pre-synthesizing method.<sup>22</sup> In addition, the obtained 3D-printed materials could achieve comparable or even higher porosity and surface area than those prepared through the solvothermal method. However, the self-assembly process is often sensitive to reaction conditions. Compared to conventional methods, self-assembly in the gel state is generally more complex and difficult to control.

Additionally, there is another method that avoids the introduction of inherently porous materials. It involves mixing non-porous materials with a 3D printing template in a solvent to form a colloidal system with different phases. After printing, the solvent and template are removed, leaving behind the base material, which generally forms a porous structure with pore sizes ranging from several micrometers to tens of micrometers (Figure 1.14c).<sup>113-114</sup> This method is commonly used for the 3D printing of porous metal-based materials or other inorganic materials. Although this method is convenient and easy to operate, it is not easy to precisely control the size of pores. In addition, this approach could be combined with the first two methods to develop a 3D-printed monolith with hierarchical pores.

Moreover, many studies have reported an alternative approach, where a 3D scaffold is first printed, and then porous materials are deposited to the surface of the printed framework or allowed to grow in situ.<sup>115-116</sup> This method enables the incorporation of porous materials into devices with a 3D-printed macroscopic shape. However, the focus of this approach is not on the 3D printing itself. The resulting devices only have limited mass loading of porous materials, so they are not extensively discussed in this section.

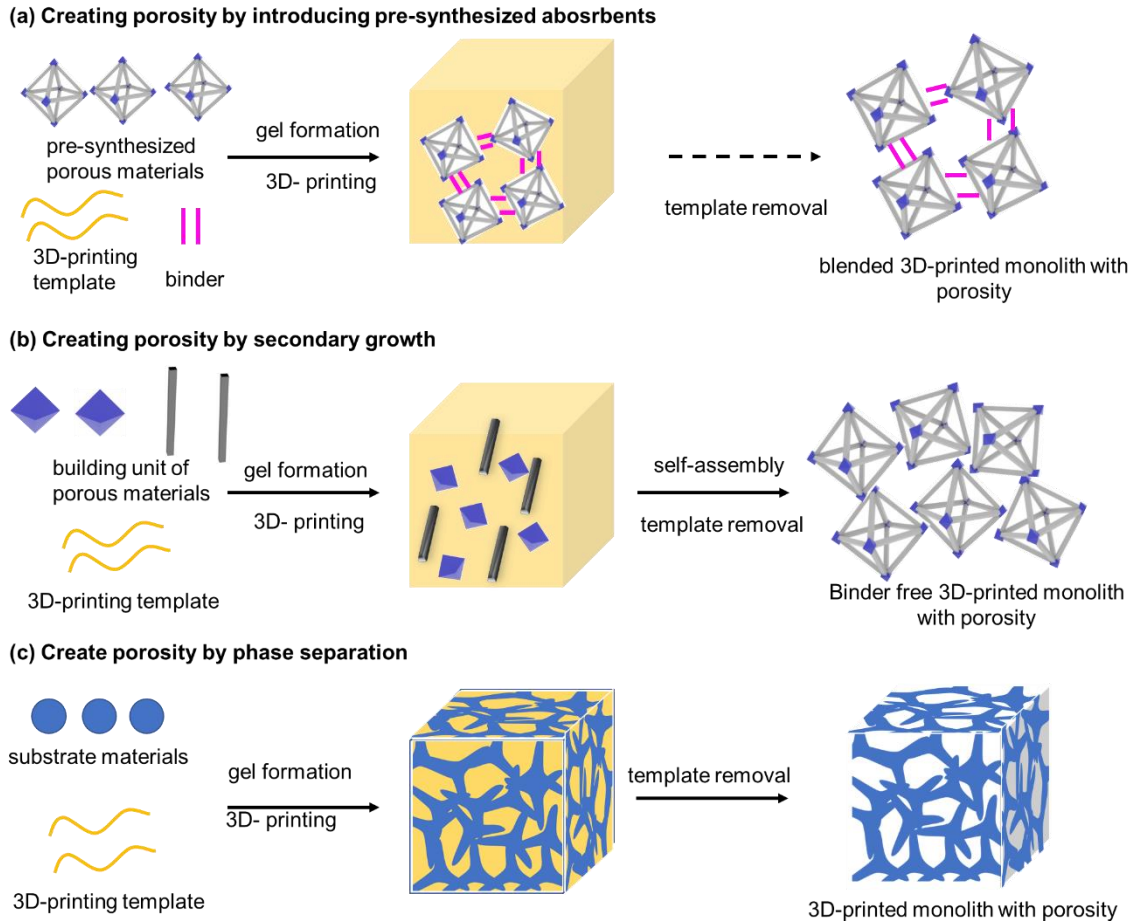


**Figure 1.14.** (a) Graphical illustration of creating porosity by pre-synthesized adsorbents. (b) Graphical illustration of creating porosity by secondary growth. (c) Graphical illustration of creating porosity by phase separation.

The porosity formulation of 3D-printed materials can be achieved through various methods with their advantages and challenges. It is necessary to have a comprehensive understanding of the 3D printing method and the properties of the printed materials in order to choose the appropriate approach for creating pore sizes and optimizing printing resolution, mechanical strength, surface area, and other performance factors. The development of innovative strategies and optimization of printing parameters will further drive the advancement of 3D printing in the field of porous materials, unlocking its vast potential for applications.

**Tools for of ink characterization:** In the direct ink writing (DIW) method, it is common to characterize the rheological properties of the gel to ensure its printability. A

suitable 3D-printable material typically exhibits appropriate strength and modulus, good shear-thinning behavior, and self-healing properties. Rheological characterization typically includes oscillation strain sweep, angular frequency sweep, shear rate sweep, and step-strain sweep. In a previous review, we provided a detailed introduction to rheological studies and explanations at the supramolecular level. The relevant supramolecular interactions can be characterized using techniques such as NMR,<sup>117</sup> ITC,<sup>118</sup> infrared and Raman spectroscopy.<sup>119</sup> In addition, the morphology of 3D-printed gels can be characterized using SEM,<sup>120</sup> TEM,<sup>121</sup> and AFM,<sup>122</sup> providing information about particle size and distribution within the gel. Occasionally, the ordered self-assembly of molecules in the gel can be studied using X-ray diffraction techniques.<sup>123</sup>

**Tools for 3D-printed porous material characterization:** FTIR spectroscopy, Raman spectroscopy, solid-state <sup>13</sup>C NMR, digested <sup>1</sup>H NMR, and elemental analysis could characterize the chemical composition of the obtained 3D-printed materials. For 3D-printed crystalline materials, such as MOFs, COFs, and zeolites, although single crystals cannot typically be obtained after 3D printing, the framework structure can be characterized using techniques such as PXRD. By combining this information with previously published single-crystal data, pore size information can be obtained for the 3D-printed MOFs and COFs. As for porous materials, the pore size of the printed structure can be investigated using standard BET or Langmuir gas adsorption models. SEM and other electron microscopy techniques can also provide information about pore size on a larger scale.<sup>124</sup> Techniques such as 3D X-ray tomography<sup>125</sup> and micro-CT<sup>126</sup> can also be employed to investigate pore size information. We will discuss specific characterization in the examples in the following sections.

### 1.3.3 3D printing inorganic porous materials

There is significant interest in using 3D printing methods to produce porous inorganic materials as inorganic materials prohibit the advantages of low price and high stability. One example is the 3D printing of zeolites, which are highly crystalline materials with inherent pore structures. The majority of zeolites are printed using the direct ink writing (DIW) method. A typical approach involves crushing pre-synthesized zeolites and mixing them with a 3D printing template and a binder to create a gel with suitable rheological properties. This gel is then 3D-printed into the desired shapes. The use of a template and

binder helps maintain the integrity of the printed structure and allows for control over the shape and porosity of the resulting zeolite.

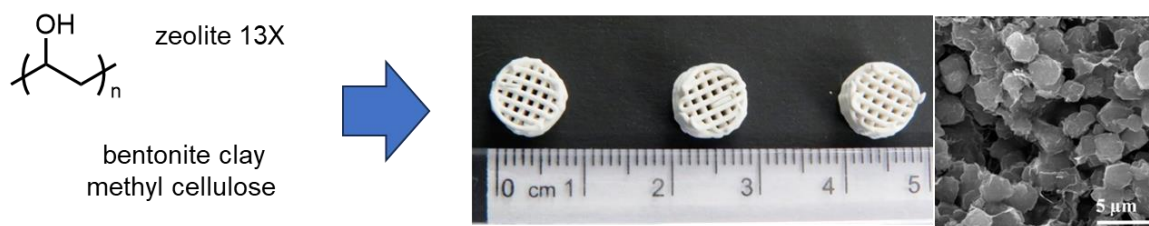


**Figure 1.15.** 3D-printing pre-synthesized zeolite 13X and images of the printed monolith.<sup>109</sup> Copyright 2016 American Chemical Society.

In 2016, Rezaei *et al.* developed a printable gel by mixing zeolite 13X and 5A powders with bentonite clay as a binder, methylcellulose as a plasticizing organic binder, and poly(vinyl) alcohol (PVA) as a co-binder (Figure 1.15).<sup>109</sup> After DIW, the printed structures were subjected to high-temperature calcination, resulting in 3D monoliths with zeolite mass loading as high as 90%. Although slightly lower than the zeolite powder, the 3D-printed zeolite exhibited a specific surface area of up to 571 m<sup>2</sup>/g. One notable advantage of 3D-printed zeolite is the enhanced adsorption kinetics. The resulting 3D-printed monoliths also exhibited excellent mechanical properties, with a maximum compressive strength of 0.69 MPa. In 2018, 2021, and 2022, similar approaches were adopted by Rownaghi,<sup>127</sup> Yu,<sup>128</sup> Hilal,<sup>129</sup> and Fu,<sup>110</sup> respectively, to pre-synthesize zeolites with binders to create printable gels.

In addition to the use of pre-synthesized zeolites, printable gels can be created by incorporating zeolite precursors, allowing for the production of binder-free 3D-printed monoliths that can be transformed into zeolite structures through calcination. In 2019, Yu *et al.* developed a printable gel by mixing NaX zeolite with colloidal silica and hydroxypropyl methylcellulose (HPMC) as a plasticizing agent (Figure 1.16).<sup>110</sup> Halloysite nanotubes (HNTs) were also introduced as additives to enhance the mechanical strength of the zeolite monoliths. After calcination, HPMC was removed. During subsequent hydrothermal crystallization, the interface "HNT bridges" transformed into zeolite, ensuring that the binder-free zeolite monoliths exhibited higher mechanical strength, larger surface area, and faster diffusion kinetics. The binder-free monolith shows excellent mechanical

properties with a compressive strength of 5.24 MPa. The surface areas of binder-free zeolite monolith and zeolite monolith with binders are measured as 571 and 470 m<sup>2</sup>/g.

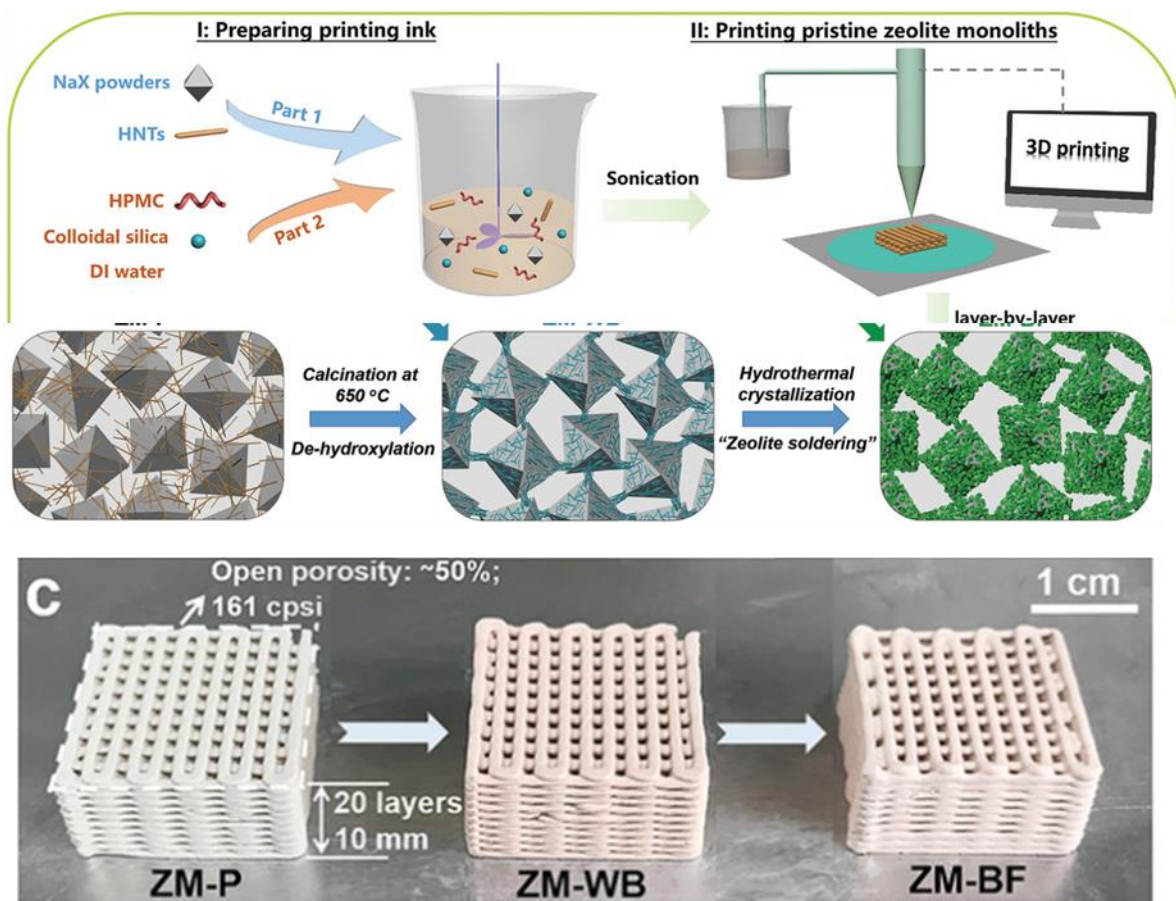


**Figure 1.16.** Schematic illustration of the synthesized procedures of 3D-printed binder-free zeolite monoliths and images of as printed zeolite monolith, zeolite monolith with binders, and binder-free zeolite monolith. <sup>110</sup> Copyright 2019 John Wiley & Sons, Inc.

Porous carbon has attracted significant interest from researchers due to its excellent chemical stability, porous nature, and unique mechanical, thermal, and electrical properties. With the advancements in 3D printing technology, researchers have started utilizing additive manufacturing to fabricate highly complex systems and explore more applications, particularly in the field of energy.<sup>130</sup>

Currently, researchers have dedicated considerable effort to developing various forms of carbon-based materials using 3D printing techniques, including carbon fiber, carbon black, carbon nanotubes, graphene, and graphene oxide. One printing method



involves the use of composite printable inks consisting of 3D printing templates, binders, and porous carbon fillers. This manufacturing approach offers great flexibility, as the carbon fillers can vary from carbon fibers, carbon nanotubes, and carbon black to graphene. Various 3D printing technologies can be employed, such as DIW (Direct Ink Writing), FDM (Fused Deposition Modeling), SLA (Stereolithography), and DLP (Digital Light Processing), among others. The performance of the printed material depends on factors such as the type and content of the carbon filler, as well as the preparation method.<sup>105</sup>

After 3D printing the composite materials, sacrificial templates can be removed through processes like calcination, resulting in pure carbon materials with 3D macroscopic structures. Additionally, many printable polymers can serve as carbon sources, which can be directly converted or grown in situ into 3D carbon materials through proper pyrolysis (Figure 1.17).<sup>131</sup> It has also been demonstrated that carbon materials can be directly printed. Graphene suspensions, for example, can be used in DIW printing, and the printed structures are often freeze-dried to remove solvents, yielding carbon materials with high surface area.<sup>132</sup>

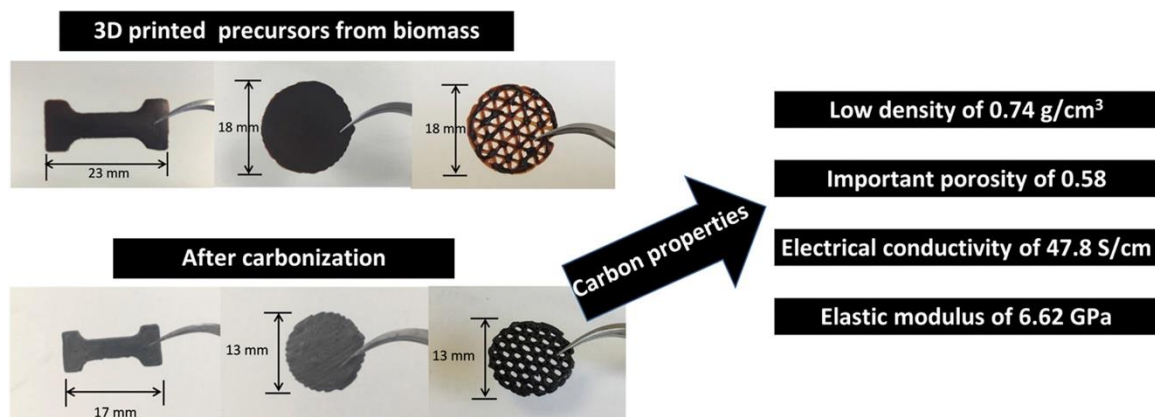


**Figure 1.17.** Photographs of 3D-printed objects from MFC/LS/CP hydrogel after air drying; and after pyrolysis at 1000 °C.<sup>131</sup> Copyright 2018 Elsevier B.V.

In addition to carbon materials, many porous silicon-based materials, such as silica and ceramics, can also be 3D printed. Porous silica, ceramics, and similar materials are characterized by their low cost and structural stability, making them widely used in applications such as catalyst supports and energy storage. Currently, various 3D printing technologies have been employed for silicon-based materials, including DIW, FDM, SLA, SLS, and others. The imparting of porosity to silica and ceramic materials is crucial, and

therefore, 3D printing technology is often combined with processes such as direct foaming, sacrificial templating, and freeze casting. A typical approach involves the preparation of printable inks by mixing 3D additives and silicon-containing fillers in solvents. Once printed into the desired shape, sacrificial templates, and solvents are removed through methods like solvent-washing and freeze-drying, followed by further calcination to obtain 3D silica or ceramics.<sup>133</sup>

In 2018, Ke's group developed 3D-printed porous silica by DIW (Figure 1.18).<sup>134</sup> The 3D printing template Pluronic F127 is co-assembled with tetraethyl orthosilicate (TEOS) in a mixture of water and ethanol to form an extrudable gel. After DIW, calcination of the 3D-printed monoliths at different temperatures would cause further polycondensation of TEOS and the removal of the F127 template. After calcination at 1000 °C, the ten times shrink of linewidth and 97–99 % reduction of volume of the monoliths were achieved. Finally, silica monoliths with good macroscopic and mesoscopic structural integrity were obtained (Figure 1.18).

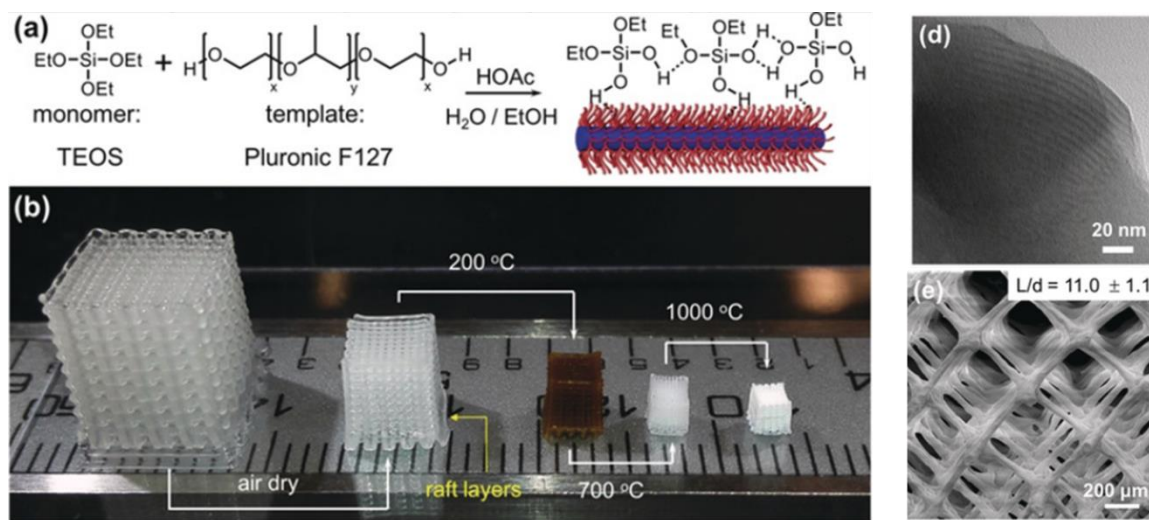


**Figure 1.18.** Preparation of TEOS/F127 co-assembled supramolecular hydrogel inks and images of printed monolith prepared at room temperature and after calcined at 200 °C, 700 °C, and 1000 °C, respectively.<sup>134</sup> Copyright 2018 John Wiley & Sons, Inc.

Many metals, alloys, or metal/polymer composites can also be 3D printed using techniques such as selective laser melting (SLM), electron beam melting (EBM), selective laser sintering (SLS), laser engineering net shaping (LENS), and others.<sup>135</sup> Porous metal scaffolds are widely used in human implants, where porosity is of critical importance to provide sufficient space for cell attachment and proliferation for bone ingrowth. 3D printing

technology facilitates the introduction of porosity and offers advantages due to its controllability, precision, and customization based on individual patient needs.<sup>136</sup> Currently, the 3D printing of porous metals has been extensively researched, allowing for precise control over the pore size and mechanical properties of the resulting 3D structures. The surface of 3D-printed porous metals can also undergo post-processing modifications, such as heat treatment, acid-alkali etching, and coating additives, to alter the surface roughness and enhance biocompatibility. However, it should be noted that the pore sizes of 3D-printed porous metals are typically in the range of hundreds of micrometers, which will not be the main focus of this study.

In addition, many porous metal compounds can also be 3D printed, such as LTO ( $\text{Li}_4\text{Ti}_5\text{O}_{12}$ ), LFP ( $\text{LiFePO}_4$ ), LMO ( $\text{LiMn}_2\text{O}_4$ ), LCO ( $\text{LiCoO}_2$ ), which are widely used in electrode development. Various 3D printing methods are employed for these purposes, including DIW, FDM, SLA, inkjet printing, and more.<sup>137</sup> Typically, the preparation of printable inks involves the incorporation of templates such as polyvinylidene fluoride (PVDF), polyvinylpyrrolidone (PVP), and conductive materials like graphene, CNTs, etc. For FDM and SLA printing, thermoplastics or photosensitive materials are also added.<sup>138</sup> 3D printing not only enhances the electrode performance through macroscopic shape optimization but also enables the hierarchical porosity of 3D-printed metal compounds by removing the templates and solvents, which would further improve electrolyte penetration, ion diffusion, and ion transport.

#### **1.3.4 3D printing organic porous materials**

Most 3D-printed MOFs are achieved using direct ink writing (DIW). A typical approach involves physically mixing pre-synthesized MOFs with a 3D printing template and binders in a solvent. Once a homogeneous printable gel is obtained, it can be 3D-printed into the desired shape. Depending on the design, the template can be further removed by solvent washing or calcination in some cases. In 2017, Rezaei *et al.* mixed MOF-74(Ni) or UTSA-16(Co) with bentonite clay and poly(vinyl alcohol) (PVA) in ethanol to get an extrudable paste (Figure 1.19a).<sup>139</sup> The gel could be 3D-printed to the desired structure from a 0.85 mm diameter nozzle. The mass-loading of MOF-74(Ni) or UTSA-16(Co) could get to 80 and 85%, respectively. Moreover, the surface area of MOF-74(Ni) and UTSA-16(Co) monoliths reached 737 and 568  $\text{m}^2/\text{g}$ , respectively, which is slightly lower than powdery MOF-74(Ni) (1180  $\text{m}^2/\text{g}$ ) and UTSA-16(Co) (727  $\text{m}^2/\text{g}$ ). Soon after, using a similar method, different 3D printing templates such as Pluronic F-127, trimethylolpropane

propoxylate triacrylate (TMPPTA), sodium alginate, and gelatin are applied to 3D printing different MOFs such as UIO-66 and Cu-BTC.

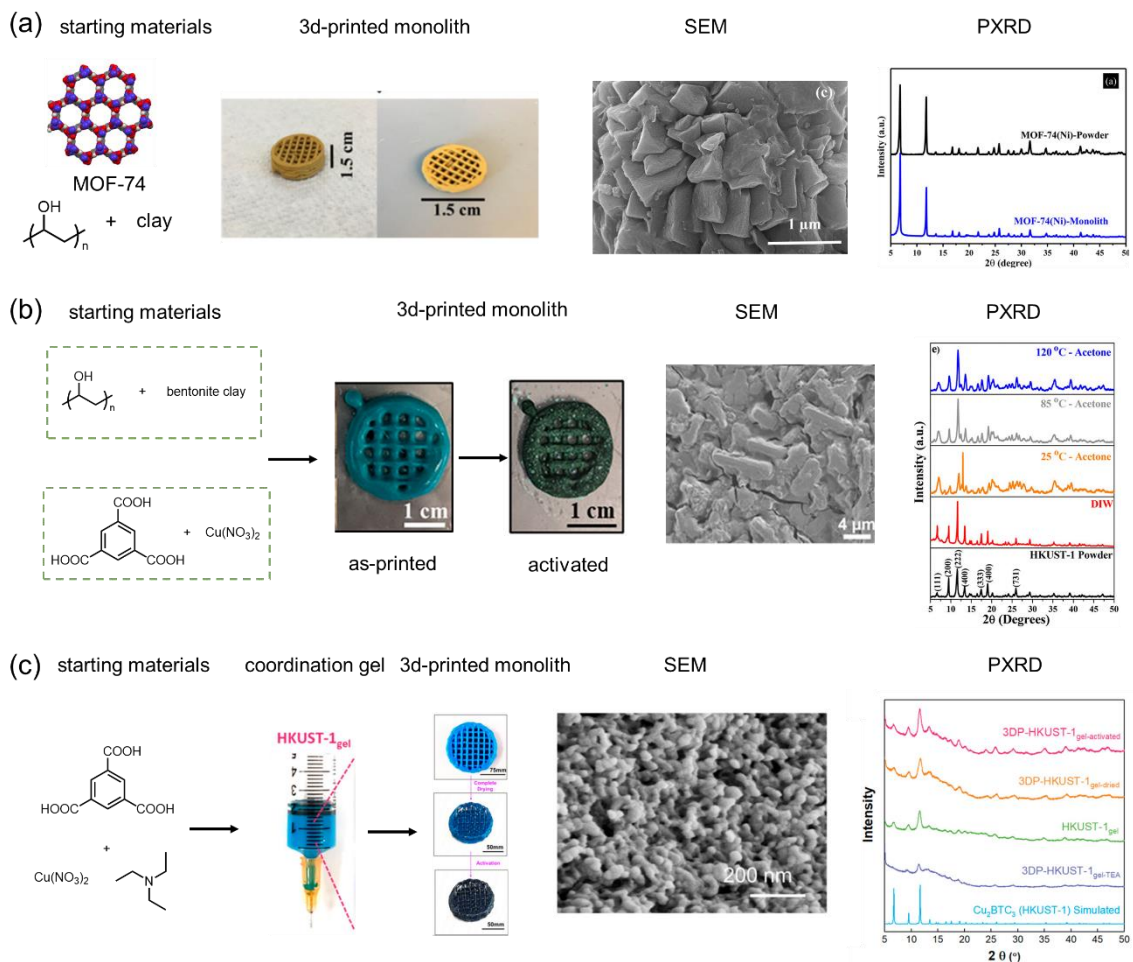


**Figure 1.19.** (a) 3D printing MOFs monolith by physically mixing pre-synthesized MOF-74 powder, PVA, and bentonite clay.<sup>139</sup> Copyright 2017 American Chemical Society. (b) An extrudable gel formed by self-assembled additives and precursors of MOFs, followed by the secondary MOF growth.<sup>111</sup> Copyright 2020 American Chemical Society. (c) An additive-free 3D-printable gel developed by self-assembled precursors of MOFs, followed by the secondary MOF growth.<sup>112</sup> Copyright 2020 American Chemical Society.

Another method involves mixing the metal salts and ligands required for the MOF directly with the 3D printing template instead of pre-synthesizing the MOF. This approach often yields more uniform gels. After 3D printing, the metal nodes and ligands self-assemble into MOF structures through appropriate methods. In 2020, Fateme Rezaei *et al.* reported a "gel-print-grow"

method for 3D-print MOFs (Figure 1.19b). They used poly(vinyl) alcohol (PVA) as a gelation template and bentonite clay as a binder. Trimesic acid and copper nitrate are also included as the precursors of HKUST-1 to form the 3D-printable sol-gel. After printing, the monoliths were heated to 120 °C, allowing the HKUST-1 crystals to grow. The macroscopic 3D-printed structures will be retained after acetone washing and activation. The maximal mass loading of HKUST-1 in the monolith could reach ~71% with high crystallinity. The surface area of 3D-printed HKUST-1 is measured as 500 m<sup>2</sup>/g, which is slightly lower than HKUST-1 powder (830 m<sup>2</sup>/g). Compared to 3D printing pre-synthesized HKUST-1 powder, the MOF monolith fabricated by the "gel-print-growth" method shows an enhanced mass-transfer efficiency.<sup>111</sup>

Generally, the DIW method requires the addition of a certain number of 3D printing additives to adjust the rheological properties and achieve desirable printability, which limits the mass-loading of MOF materials. However, there have also been reports of DIW examples without the need for added templates. In 2019, Wang and Ding *et al.* synthesized an additives-free hydrogel by mixing 1,3,5-Benzenetricarboxylic acid, triethylamine (TEA), and copper(II) acetate in ethanol (Figure 1.19c). The obtained coordinated colloidal sol-gel shows suitable rheology properties, which could be extruded from a 300 µm nozzle for 3D printing. The HKUST-1 crystals would gradually form at room temperature. After ethanol washing, the binder-free 3D-printed HKUST-1 shows a high BET surface area of up to 1134 m<sup>2</sup>/g, which is slightly lower than powdery HKUST-1 (1850 m<sup>2</sup>/g).<sup>112</sup>

**Table 1.2.** Comparison of 3D printing MOF materials using DIW.

Method of MOF Synthesis	Printed MOFs	Additives	Print resolution	Mass-loading of MOFs	Surface area of 3D-printed monolith (m <sup>2</sup> / g)	BET surface area of powdery MOFs (m <sup>2</sup> / g)
Pre-synthesis MOFs	MOF-74(Ni) <sup>139</sup>	PVA, bentonite clay	0.85 mm	80%	737	1180
	UTSA-16(Co) <sup>139</sup>	PVA, bentonite clay	0.85 mm	85%	568	727
	Ni(bdc)(ted) <sub>0.5</sub> <sup>140</sup>	PVA	0.85 mm	80%	1325	1802
	ZIF-7 <sup>140</sup>	silica	0.85 mm	85%	40	16
	Co-MOF <sup>140</sup>	F127	200 μm	~44%	--	--
	Zn-MOF <sup>141</sup>	F127	300 μm	~40%	--	--
	UIO-66 <sup>142</sup>	TMPPTA, EBECRYLS 8413	1.6 mm	74%	633	--
	Cu-BTC <sup>143</sup>	sodium alginate-gelatin	0.21 mm	13%	83	1562
	HKUST-1 <sup>143</sup>	PVA, bentonite clay	--	83.5%	470	830
Secondary growth	HKUST-1 <sup>111</sup>	PVA, bentonite clay	--	70%	500	830
	HKUST-1 <sup>112</sup>	none	300 μm	100%	1134	1850

Compared to MOFs, COFs are more challenging to form single crystals. The majority of COFs are crystalline polymers that contain a certain ratio of amorphous domains. This characteristic allows for the formation of self-supporting structures with interconnectivity at a larger scale in 3D-printed COFs, whereas 3D-printed MOFs tend to consist of stacked crystalline particles. The substrate content in 3D-printed COFs is generally higher than that in 3D-printed MOFs. 3D-printed COFs may be composed of pure COFs with self-supporting structures, meaning that they do not require additional additives or binders to maintain their shape.

The first example of 3D-printed COF was reported by our group in 2019, which will be introduced in detail in the later section. In 2020, Banerjee *et al.* mixed COF precursors and graphene oxides in water in the presence of *p*-toluenesulfonic acid to form a 3D-printable hydrogel (Figure 1.20).<sup>144</sup> Then the COF-GO mixture was 3D-printed into foams with abundant interconnected macroporous volume (55%), which significantly improved the mass-transfer efficiency and guest adsorption. The mass loading of COFs is around 85%. The BET surface area of 3D-printed TpBD, TpDq, and TpAzo foams show surface areas of 971, 500, and 624 m<sup>2</sup>/g, respectively. The slight drop in the surface area compared to the powdery COFs may be caused by the lower crystallinity and the graphene oxide additives in the COF-GO foams. In 2021, Wang *et al.* reported a binder-free 3D-printable paste by adding the precursors of COFs in organic solvents.<sup>145</sup> Through controlling the evaporation of the solvent, 3D-printed crack-free COF monoliths were obtained.

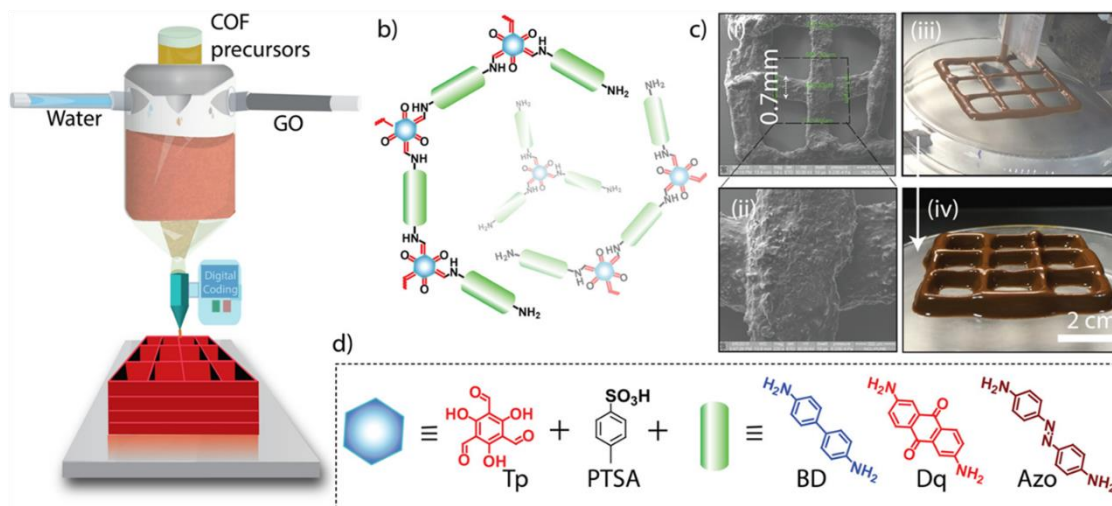


**Figure 1.20.** Schematic representation of the synthesis and 3D printing of COF-GO foams. The mixture of COF precursors, water, and graphene oxide forms a hydrogel, which is used for 3D-printing.<sup>144</sup> Copyright 2020 American Chemical Society.

In addition to crystalline porous organic materials such as MOFs and COFs, other types of amorphous porous organic material, such as crosslinked polymers, can also be 3D-printed. One approach is to incorporate molecules with intrinsic porosity, such as porous organic molecular cages or macrocyclic molecules, into the 3D printing ink and then crosslink them after printing. Porous organic molecular cages or macrocyclic molecules possess well-defined pore sizes, which could realize the strong binding capabilities towards specific guest molecules. In addition, they generally exhibit good solubility in solvents, facilitating the production of more homogeneous gels.

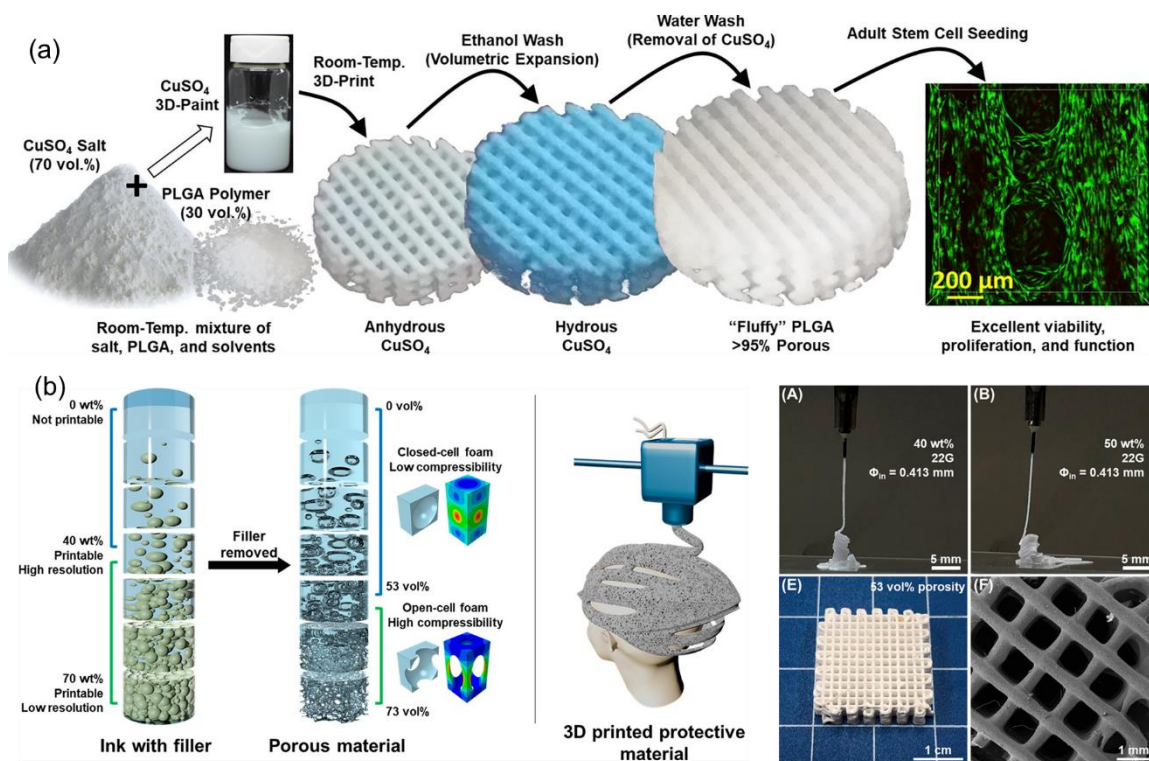


**Figure 1.21.** (a) Schematic illustration of 3D printing porous polymer. The printable ink is prepared by mixing PLGA polymer and  $\text{CuSO}_4$  salt. After salt leaching, the 3D-printed polymer monolith shows highly porous.<sup>113</sup> Copyright 2018 Elsevier B.V. (b) Schematic illustration of 3D printing porous polymer using DIW. The ink is composed of paraffin wax beads and photopolymerizable resin.<sup>114</sup> Copyright 2021 American Chemical Society.

The porosity of some 3D-printed organic polymers is achieved through phase separation. A typical approach involves mixing the 3D-printed polymer precursor with a solvent. After printing and crosslinking, the solvent and inorganic salt are removed to obtain the desired pore size (Figure 1.21a).<sup>113-114</sup> In 2018, Shah and coauthors prepared 3D-



printable inks comprised of varying volume ratios of CuSO<sub>4</sub> salt (25- 70 vol%) and polylactide-co-glycolide (PLGA). After DIW and slat leaching, the 3D-printed polymer monolith shows highly porous, highly absorbent, high flexibility, and mechanically robust (Figure 1.21b). In 2021, Pentzer, Wei, and coauthors used a similar strategy to prepare printable inks by mixing photocurable resins with paraffin beads (40- 70 wt %) as fillers. After DIW and UV irradiation, paraffin beads were removed by solvent washing to form a 3D-printed porous polymer.

Polymers have various polymerization and cross-linking methods, making the 3D printing techniques of polymers more diverse compared to other materials. In addition to DIW, porous polymers could be 3D-printed by different methods, including stereolithographic apparatus (SLA),<sup>146</sup> digital light processing (DLP),<sup>147-148</sup> and photon microprinting.<sup>149</sup> This chapter will not go into detailed elaboration on them.

### **1.3.5 The applications of 3D-printing porous materials**

#### **(a) Gas Storage and Separation**

One of the key applications of porous materials is gas adsorption and separation due to their high surface area, designable structure, and controllable size. In this regard, 3D-printed porous materials offer several advantages that contribute to improved gas adsorption and separation efficiency, as well as the ability to design devices with specific macroscopic structures.

Among the various gases, carbon dioxide (CO<sub>2</sub>) adsorption and separation have gained significant attention due to its role as a greenhouse gas, its wide industrial applications, and its potential as a carbon source for renewable green energy. A series of 3D-printed zeolites,<sup>109</sup> MOFs,<sup>111, 139, 150</sup> and COFs<sup>145</sup> are reported to be used for the selective uptake of CO<sub>2</sub> from N<sub>2</sub>. In 2019, Yu *et al.* reported a 3D-printed binder-free zeolite. The CO<sub>2</sub> uptake of ZM-BF reached 5.58 mmol g<sup>-1</sup> (298 K, 1 bar). In the breakthrough experiment, CO<sub>2</sub> could be selectively adsorbed by ZM-BF in the CO<sub>2</sub>/N<sub>2</sub> (Figure 1.22a) and CO<sub>2</sub>/CH<sub>4</sub> mixture with a higher uptake amount. Compared to conventional zeolite adsorbents (or catalysts), the authors illustrated that the 3D-printed zeolite with hierarchical pores shows faster mass transfer and heat transfer, lower pressure drops, and good attrition resistance (Figure 1.22a).<sup>151</sup>

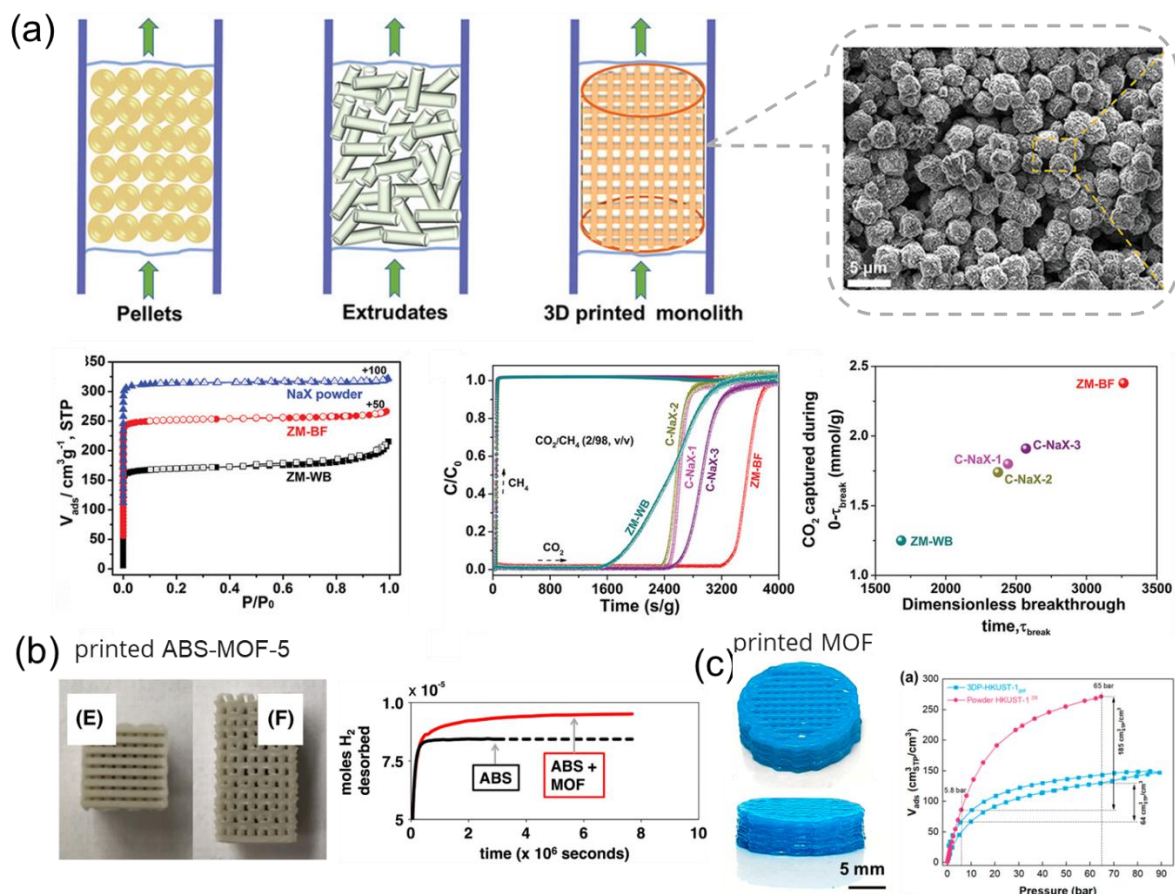


**Figure 1.22.** Schematic illustration of the pellets packed bed adsorbents, extrudates packed bed adsorbents, and 3D-printed zeolites and their  $CO_2$  separation performance.<sup>151</sup> Copyright 2019 John Wiley & Sons, Inc. (b) The  $H_2$  adsorption performance of 3D-printed ABS and ABS-MOF composites.<sup>152</sup> Copyright 2017 John Wiley & Sons, Inc. (c) The  $CH_4$  adsorption performance of powdery and 3D-printed HKUST-1.<sup>112</sup> Copyright 2020 American Chemical Society.

Other gases, including  $H_2$  and hydrocarbons, such as  $CH_4$  and  $C_2H_6$ , are important green energy and industrial raw materials. Therefore, their adsorption and separation have become a hot research area. In 2017, Hartings *et al.* reported 3D-printed MOF/ABS composites for  $H_2$  storage (Figure 1.22b).<sup>152</sup> In 2019, Cheetham, Wang, Ding, and coauthors developed a 3D-printed binder-free HKUST-1, which could be used for methane storage (Figure 1.22c).<sup>112</sup> The absolute methane uptake capacities of 3DP-HKUST-1<sub>gel</sub> and HKUST-1 were measured as 131 and 271  $cm^3$  (STP)/ $cm^3$  (Figure 11c). In 2020, Furukawa 3D-printed a series of MOFs with a comparable surface area of MOF powders.<sup>153</sup> The 3D-

printed HKUST-1, ZIF-8, and UiO-66-NH<sub>2</sub> could be used for methane storage. Moreover, 3D-printed CPL-1 shows good performance in ethane/ethylene separation. Moreover, the 3D-printed porous materials could also be used as filters for toxic gas removal. In 2020, Gandía *et al.* fabricated a ZIF-8 coated 3D-printed ABS to effectively remove dimethyl methylphosphonate (DMMP).<sup>154</sup>

### (b) Water remediation.

Porous materials have been extensively applied in water pollution treatment due to their ability to adsorb guest molecules in solvents. With the advent of 3D printing, porous materials can now possess designed macroscopic structures, enabling their application in a wide range of scenarios. The 3D-printed porous materials offer additional advantages, particularly in terms of their hierarchical macro- and mesoporosity, which greatly enhance mass transfer efficiency and enable rapid adsorption.

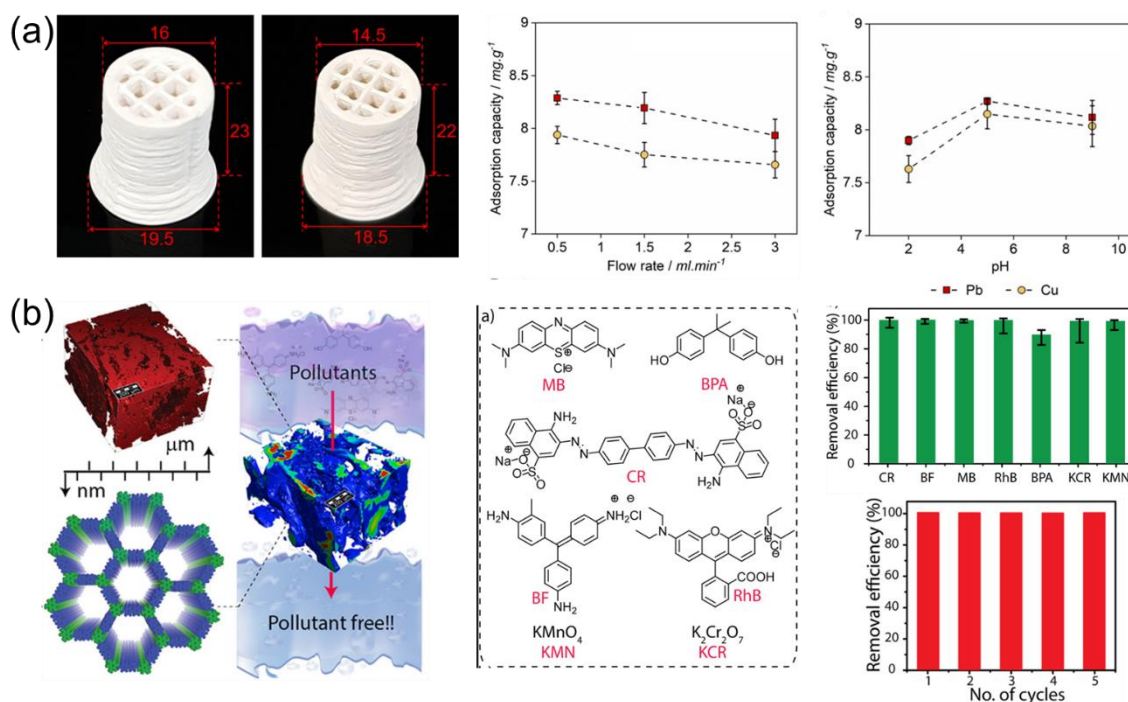


**Figure 1.23.** (a) Schematic illustration of Cu<sup>2+</sup> and Pb<sup>2+</sup> removal using 3D-printed zeolite-Y.<sup>129</sup> Copyright 2021 Elsevier B.V. (b) Scheme of dyes removal performance using 3D-printed COF foams.<sup>144</sup> Copyright 2020 American Chemical Society.

One of the common pollutants in water is toxic ions. In 2021, Cabello and coauthors 3D-printed silver-functionalized UiO-66 monoliths to remove radioiodine.<sup>155</sup> Hilal *et al.* 3D-printed zeolite-Y for removing heavy metals (Pb and Cu) from water (Figure 1.23a).<sup>129</sup>

In addition to inorganic pollutants, dyes are one of the most common types of organic pollutants. Liu,<sup>156</sup> Zhang,<sup>115</sup> Zhan,<sup>143</sup> *et al.* developed a series of 3D-printed MOFs to remove organic dyes such as methylene blue, malachite green, methyl violet, rhodamine B, and auramine O. Some 3D-printed porous materials could be used for both organic and inorganic pollutants treatment. In 2019 Banerjee *et al.* developed 3D-Printed COF-GO foams with hierarchical pores. By removing the water by freeze drying, meso and macropores (50 nm to 200  $\mu\text{m}$ ) were formed, creating interconnected macroporous volume (55%) in the 3D-printed COF-GO foam (Figure 1.23b). The hierarchical pores could significantly enhance efficient mass transport and adsorption. The flow of water could reach  $1.13 \times 10^{-3}$  m/s. And the 3D-printed COF-GO foam shows ultra-fast adsorption (>95% removal within 30 s) of organic pollutants such as methylene blue (MB), basic fuschin (BF), and congo red (CR) and inorganic pollutants such as  $\text{KMnO}_4$  and  $\text{K}_2\text{Cr}_2\text{O}_7$  from water. In addition, the 3D-printed COF-GO foam shows good reusability (Figure 1.23b). The pollutants can be desorbed back in suitable organic solvents.<sup>144</sup>

### (c) Heterogeneous catalysis

Porous materials possess a high surface area and tunable pore sizes, making them widely utilized in selective heterogeneous catalysis. The advent of 3D printing technology has opened up new possibilities for the fabrication of porous materials, which can enhance catalytic efficiency through improved mass transfer. The ability to design the macroscopic structure and control the hierarchical porosity of 3D-printed porous materials offers advantages for catalytic applications.

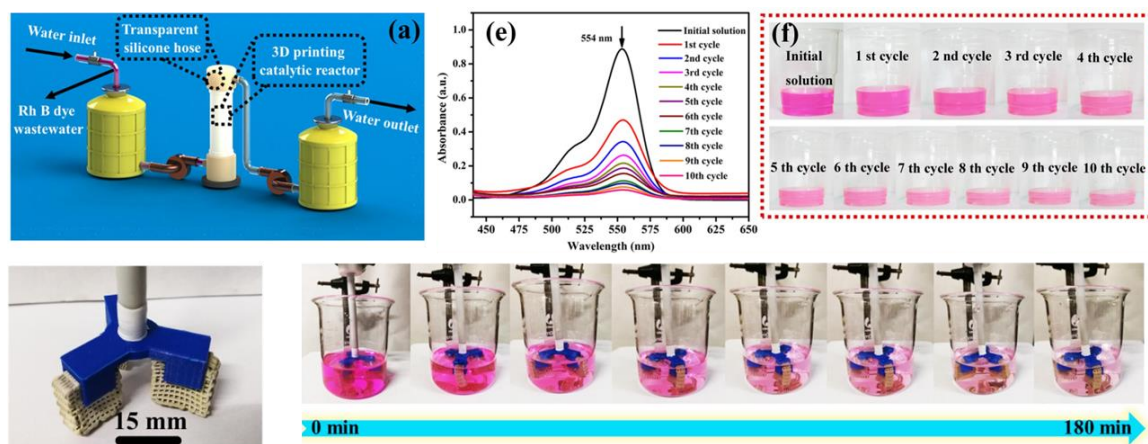


**Figure 1.24.** Schematical illustration of 3D-printed MIL-100 (Fe) catalytic filter and impeller for dye degradation. Copyright 2020 Elsevier B.V.

MOFs exhibit excellent design flexibility, allowing for the incorporation of functional groups to confer unique catalytic properties. Lewis acid or base sites, redox-active centers, and chiral pockets can be introduced through functionalization, enabling precise control over catalytic reactions. The large surface area and porosity of MOFs provide abundant active sites for reactant adsorption, promoting efficient catalytic transformations. In 2019, Reithofer, Chin, and coauthors 3D-printed UIO-66 by mixing the pre-synthesized MOF particles with templates by DIW. Some 3D printing templates could be removed by calcinating under 280 °C without sacrificing the crystallinity of UIO-66.<sup>142</sup> The content UIO-66 could reach 76%. The obtained 3D monolith could be used for the catalytic breakdown of methyl-paraoxon. In addition, MOFs could, in situ, grow on the surface of a 3D-printed matrix for catalytic applications.<sup>157</sup> In 2020, Zhou *et al.* reported the in-situ growth of MIL-100(Fe) and HKUST-1 MOFs on 3D-printed structures.<sup>158</sup> The resultant 3D-MOF with hierarchical porosity could be used for the high efficiency (up to 99.7%, 0.2915 min<sup>-1</sup>) catalytic decomposition of organic dyes based on Fenton reactions (Figure 1.24), which is much higher than other reported Fe-/Cu-based powdery MOFs. In addition, the 3D-printed MOFs show high recyclability, whose degradation efficiency could reach > 75% over 50 cycles. Moreover, the 3D-printed catalytic filter and impeller agitator were successfully manufactured by the present strategy (Figure 1.24).

Another noteworthy porous material is zeolites, which are characterized by their low cost and structural stability. Zeolites have been extensively investigated for catalytic applications due to their well-defined pore structures and unique framework compositions.

In 2018, Rownaghi *et al.* reported the 3D-printed ZSM-5 monoliths and SAPO-34 crystals could form on the as-synthesized monoliths via a secondary growth.<sup>159</sup> The resultant monolith shows hierarchical porosity for catalyzing selective methanol to light olefin reaction (Figure 1.25a). In 2022, Fu and coauthors reported the 3D-printed zeolite for xylene isomerization.<sup>110</sup> In 2022, Yu *et al.* developed a Cu-SSZ-13 zeolite-coated cordierite monolith.<sup>128</sup> In addition, Mn could be in-situ introduced into the Cu-SSZ-13 zeolite monoliths during the 3D printing process. The 3D-printed self-supporting monolith shows excellent catalytic activity for NH<sub>3</sub>-SCR with NO<sub>x</sub> conversion of above 80% (Figure 1.25b).

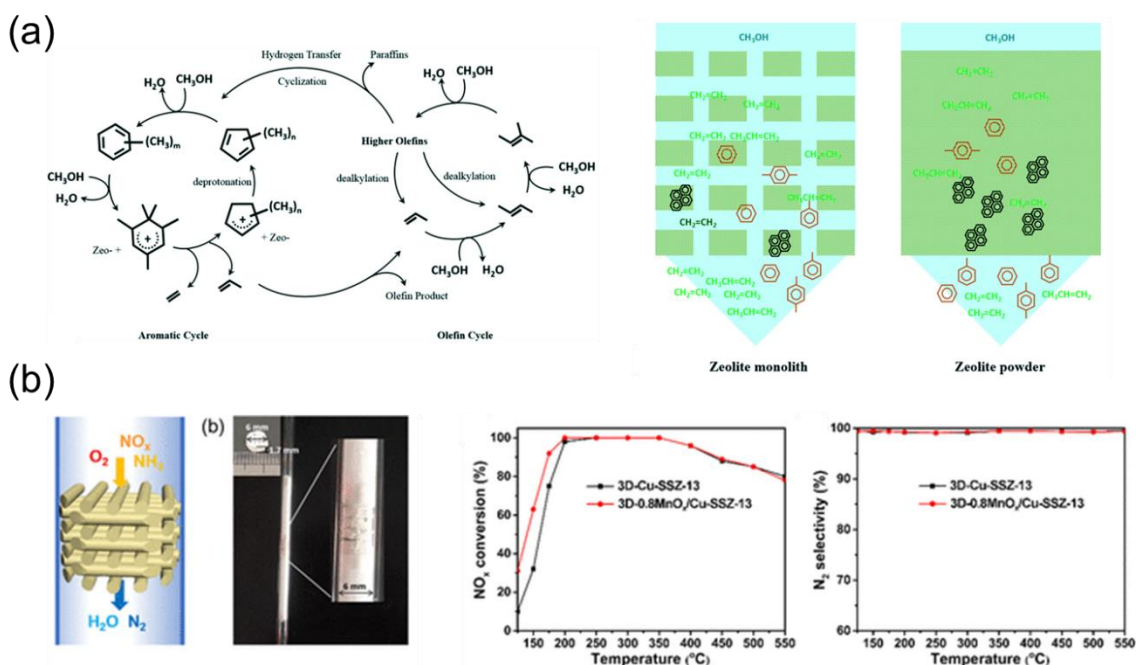


**Figure 1.25.** (a) Scheme of 3D-printed ZSM-5 for light olefin reaction.<sup>159</sup> Copyright 2022 Elsevier B.V. (b) Scheme of 3D-Printed Cu-SSZ-13 zeolite for NH<sub>3</sub>-SCR.<sup>128</sup> Copyright 2021 Chinese Chemical Society.

#### (d) Electronics

Compared to traditional manufacturing methods, 3D-printed porous materials offer unique advantages in geometric design and rapid prototyping. In addition to these benefits, they exhibit hierarchical pore structures and high surface areas, making them widely applicable to electronic devices. Specifically, 3D-printed porous carbons, including graphene, carbon nanotubes, and their composites, are frequently used as electrodes in supercapacitors or cathodes in batteries. These materials provide a large surface area for

electrochemical reactions, facilitating high-energy storage and efficient charge/discharge processes. The 3D printing approach allows for precise control over the structure and composition of these electrodes, optimizing their electrochemical performance. Metal-based porous materials, such as lithium titanium oxide (LTO), lithium iron phosphate (LFP), lithium manganese oxide (LMO), and lithium nickel manganese cobalt oxide (LMFP), are commonly printed as electrodes for batteries. The porous structure enhances the ion diffusion kinetics, increasing the battery's capacity, stability, and overall performance. With 3D printing, intricate electrode designs can be realized, leading to improved energy storage and electrochemical efficiency.

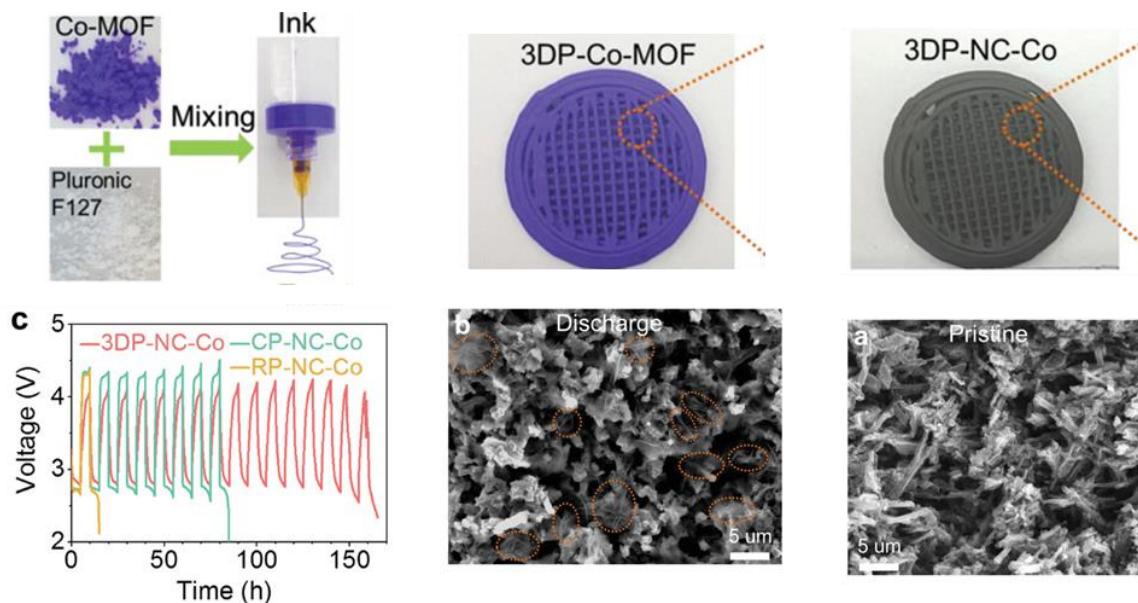


**Figure 1.26.** Preparation of Co nanoparticles assembled in nitrogen-doped mesoporous carbon (3DP-NC-CO) flakes and their electrochemical performances.<sup>160</sup> Copyright 2018 John Wiley & Sons, Inc.

In addition to carbon and metal-based materials, 3D printing is also employed in fabricating electronic components using coordination polymers, such as covalent organic frameworks (COFs), metal-organic frameworks (MOFs), and their derivatives. These materials offer designable functional groups, high surface areas, and abundant doping sites, making them attractive for 3D-printed electronic devices. In 2018, Ding, Chen, Wang, *et al.* reported a 3D-printed MOF-derived porous carbon framework as a cathode of Li-battery.<sup>160</sup> The cobalt-based MOFs were first 3D-printed by the DIW method and then calcinated to a porous carbon framework (Figure 1.26). The hierarchical pores of 3D-printed Co-MOF-

derived carbon could realize a more efficient  $\text{Li}_2\text{O}_2$  particle deposition (Figure 1.26) and electrolyte diffusion and prevent passivation of the cathode surface by the insulating  $\text{Li}_2\text{O}_2$  product (Figure 1.26). Overall, the 3D-printed self-standing porous architecture significantly enhances the energy density value to 798 Wh/ kg. Then in 2020, they used a similar method to 3D-print a Zn-MOF-derived N-doped carbon framework as an anode for lithium metal batteries with high areal capacity and high-rate capability.<sup>141</sup> In 2023, Li and coauthors reported a 3D-printed Zn-MOF(ZIF-8) and annealed it to an N-doped carbon framework. For the zinc-ion hybrid capacitor, we achieved an aerial capacitance of 16.9 F  $\text{cm}^{-2}$  and an energy density of 7.23  $\text{mWh cm}^{-2}$ .<sup>161</sup>

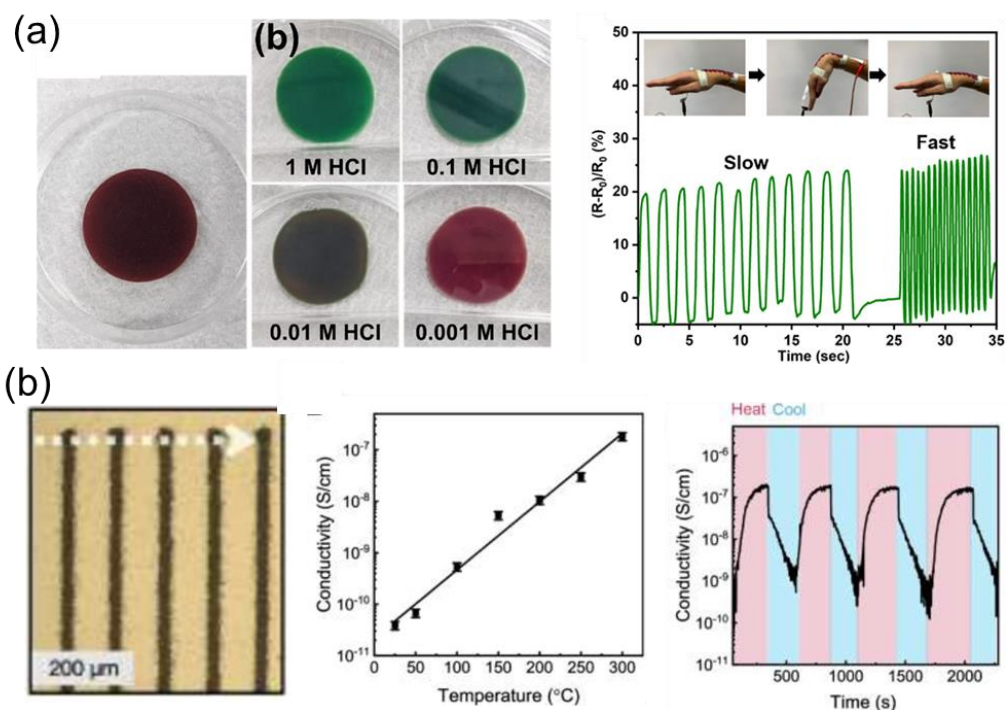


**Figure 1.27.** (a) Photographs of MOF-based iongel and the acidic and auxetic sensitivity.<sup>162</sup> Copyright 2019 Elsevier B.V. (b) Printed lines of COF-5 and their thermo-sensitivity.<sup>163</sup> Copyright 2023 John Wiley & Sons, Inc.

In addition to energy storage, 3D-printed porous materials could be used for electronic sensors. In 2022, Kung and Yu et al. developed a porphyrinic Zr-MOF-based wearable iongel.<sup>162</sup> The obtained materials show significant color changes when exposed to acid (Figure 1.27a). Moreover, the resistance of the iongel is sensitive to mechanical deformation, which could be used for monitoring various human body movements (Figure



1.27a). In 2023, Dichtel and Hersam *et al.* reported an AJP 3D-printed boronate-ester COFs and carbon nanotubes (CNTs) composites, showing four orders of electrical conductivity variation between room temperature and 300 °C (Figure 1.27b).<sup>163</sup>

#### **(e) Biomedical applications**

3D-printed porous materials find applications in the field of biology. The use of 3D printing technology allows for precise design and control of the structure of porous materials, enabling the creation of various biomimetic structures. Shape memory<sup>147</sup> can also be achieved through 3D printing. The large surface area of 3D-printed porous materials facilitates interactions with biological entities, such as the adsorption and sensing of biomolecules<sup>164</sup> and cell attachment. These materials can also be utilized for drug delivery<sup>165-166</sup> and release. Furthermore, by designing the materials appropriately, it is possible to 3D print devices with excellent biocompatibility.<sup>148</sup>

In 2018, Shah *et al.* reported a 3D-printed porous polylactide-co-glycolide (PLGA).<sup>114</sup> The elevated porosity could improve cell adhesion, viability, and proliferation of adult human mesenchymal stem cells (hMSCs) (Figure 1.28a). In 2020, Tran and coauthors developed a 3D-printed porous poly( $\epsilon$ -caprolactone) by salt leaching (Figure 1.28b). The chemotherapeutic drug doxorubicin (DOX) could be loaded onto the porous scaffolds with efficacy as high as 90%.<sup>167</sup> The DOX-loaded porous polymer shows a b monotonic drug release up to 28 d to cure MDA-MB-231 breast cancer cells. Compared to one-time injection, the implantation of DOX-loaded porous polymer prohibits lower cardiotoxicity and reduces local cancer recurrence. (Figure 1.28b)

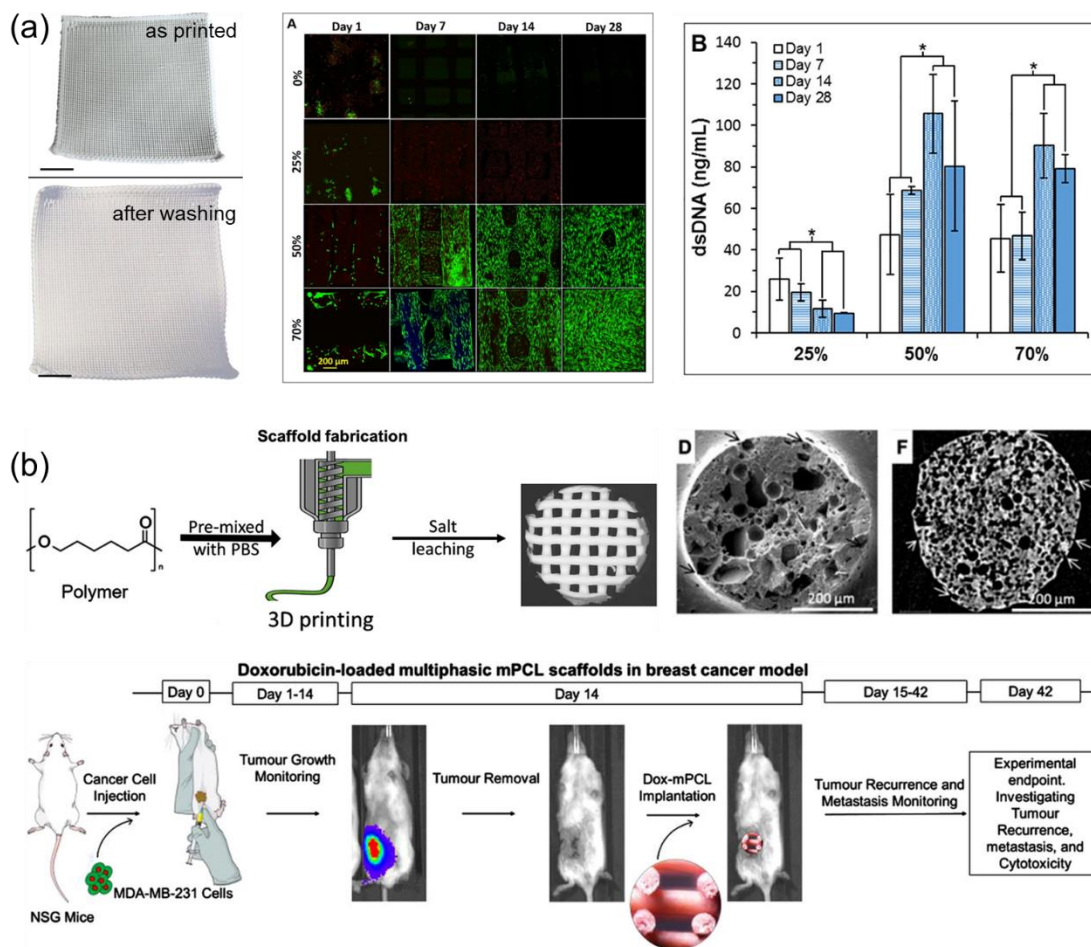


**Figure 1.28.** (a) A 3D-printed porous poly(lactide-co-glycolide) improving cell viability and proliferation.<sup>114</sup> Copyright 2018 Acta Materialia Inc. (b) A via 3D-printed porous scaffolds for doxorubicin delivery.<sup>167</sup> Copyright 2020 John Wiley & Sons, Inc.

### (f) Other applications

3D-printed porous materials offer tailorable mechanical properties and additional porosity, further improving the versatility and controllability of material functions. Jakus *et al.* fabricated a 3D-printable salt ink composed of  $\text{CuSO}_4$  salt and poly(lactide-co-glycolide) (PLGA).<sup>114</sup> Volumetric expansion in ethanol followed by salt removal in water yields an F-PLGA elastomer with high porosity (66.6–94.4%), high absorbance (195.7–742.2%), excellent mechanical robustness, and biocompatibility. The porosities and absorbance are proportional to the  $\text{CuSO}_4$  content, whereas mechanical properties such as tensile strength and modulus are higher with lower salt content. For hydrated F-PLGA with varied salt content, ultimate strengths ranging from 0.8 to 9.5 MPa, elastic moduli from 2.7 to

112.6 MPa, and strain to failure of 46.8–95.2%, demonstrating flexible tunability. Similarly, Cipriani *et al.* performed DIW printing using photopolymer/sacrificial paraffin filler composite inks.<sup>113</sup> The porosity of the printed structures varied from 43 to 73 vol% depending on the paraffin particle content, and higher porosity corresponds to increased compressibility, increased extensibility, and decreased tensile modulus. It was also found that below 53 vol% of porosity, the material mainly exhibited closed-cell pores, in which pores were enclosed with polymer and isolated from one another, whereas open-cell pores were found above 53%. Precise control over porosities, pore structures, and mechanical properties of the material allows greater flexibility with a wide range of applications.

Furthermore, 3D-printed porous materials are also a powerful tool for molecule separation. For example, Lv *et al.* 3D printed superhydrophobic membranes with a hydrophobic nano silica-filled polydimethylsiloxane (PDMS) ink to achieve water-oil separation.<sup>168</sup> The printed membrane contains an ordered porous structure and high mechanical stability, unlike traditional "coating on a mesh structure." The membrane pore size is also easily tunable, and with an optimal 0.37mm pore size, maximum oil–water separation efficiency (~99.6%) could be achieved.

#### **1.4 Conclusion and Outlook**

This introduction is divided into two parts. The first part discusses the development history of crystalline porous organic materials. It focuses on the design and synthesis methods of single-crystalline hydrogen-bonded crosslinked frameworks (H<sub>c</sub>OFs) and related framework materials, including HOFs and COFs, and 2D polymers.

Looking ahead, from a crystal design perspective, studying the hydrogen-bonded networks of HOFs and strategies for iso-reticular expansion can provide inspiration for the development of H<sub>c</sub>OF precursor crystal materials. In addition, the use of Lewis acid-base structural units can construct stable hydrogen-bonded supramolecular interactions, providing reliable models for controlling crystal structures. Exploring methods such as co-crystallization with strong acids like sulfuric acid, nitric acid, and hydrochloric acid can facilitate the construction of ionic frameworks, which is an interesting direction. Furthermore, exciting progress has been made in the prediction of crystal stacking through machine learning, which can be extended to predict the stacking of porous molecular crystals in the foreseeable future. Regarding crosslinking methods, the experiences gained from constructing single-crystal COFs or 2D polymers can be further applied to H<sub>c</sub>OFs. For

example, strategies such as [2+2] and [4+2] cycloaddition, free-radical polymerization, olefin metathesis, and cationic/anionic ring-opening polymerization hold promise for integration into H<sub>c</sub>OF designs. In terms of characterization techniques, 3D electron diffraction and high-resolution transmission electron microscopy (TEM) can complement X-ray single-crystal diffraction. In terms of applications, H<sub>c</sub>OFs exhibit unique flexibility and can expand or contract under the influence of guest molecules, thereby increasing the adsorption capacity of guest molecules. This has the potential to extend traditional adsorption mechanisms based on size sieving and find applications in molecular recognition and separation.

The second part introduces the methods and applications of 3D-printed porous materials. It focuses on the design and synthesis of crystalline and amorphous organic porous materials using the direct ink writing (DIW) method. From the perspective of 3D printing molecular design, the introduction of different functional groups and the expansion of photo-crosslinking or chemical crosslinking methods are important for increasing the diversity of 3D printable materials. Furthermore, maintaining the crystallinity of the porous material during 3D printing is crucial. At the mesoscopic level, understanding the supramolecular interactions between components at the molecular level is essential for 3D printing porous materials. Although there have been important publications on supramolecular interactions, these interactions have not received sufficient attention in the field of 3D printing porous materials. In terms of porosity, increasing the mass loading of the porous material and preventing pore blockage are crucial. Thus, the production of binder-free 3D-printed objects using methods such as second-growth has gained attention. Additionally, the combination of intrinsic pore sizes with mesopores created through phase separation can improve mass transfer efficiency. Furthermore, the impact of macroscopic shape on performance has been poorly studied and is an area that can be further explored. In terms of printing technologies, the DIW method, as introduced in this introduction, is the most commonly used. However, other methods, such as fused deposition modeling (FDM) and digital light processing (DLP), have also been widely applied, and exploring new 3D printing techniques is an interesting direction. In terms of applications, 3D-printed porous materials have demonstrated effective use in water treatment, gas adsorption and separation, and heterogeneous catalysis. However, in the fields of biotechnology and wearable devices, the application of 3D-printed porous materials is still in the early stages of development, but they hold tremendous potential. Overcoming challenges related to biocompatibility and other aspects is crucial.

This section aims to provide a comprehensive overview of the progress made in the field of single-crystalline porous organic frameworks and 3D printing of porous materials and their applications. In addition, in microscopic scale, we hope to expand the synthetic methods for predictable hydrogen bonding solid-state structures, to expand the approaches to realize SCSC crosslinking. In addition, we want to design porous organic framework materials with dynamic sorption capabilities to enhance their performance for applications in molecular adsorption, separation, and sensing. On a macroscopic scale, we want to inspire the researchers to expand and improve the printable ink preparation, enhance the porosity and mechanical strength and other properties of 3D-printed porous materials, and explore potential 3D-printing-enabled applications.

### 1.5 References

- 1 H. C. Zhou, S. Kitagawa, *Chem. Soc. Rev.* **2014**, *43*, 5415-5418.
- 2 H. Furukawa, K. E. Cordova, M. O'Keeffe, O. M. Yaghi, *Science* **2013**, *341*, 974.
- 3 C. S. Diercks, O. M. Yaghi, *Science* **2017**, 355.
- 4 X. Y. Song, Y. Wang, C. Wang, D. Wang, G. W. Zhuang, K. O. Kirlikovali, P. Li, O. K. Farha, *J. Am. Chem. Soc.* **2022**, *144*, 10663-10687.
- 5 R. Lin, B. Chen, *Chem* **2022**, *8*, 1-22.
- 6 S. Das, P. Heasman, T. Ben, S. L. Qiu, *Chem. Rev.* **2017**, *117*, 1515-1563.
- 7 X. L. Li, S. L. Cai, B. Sun, C. Q. Yang, J. Zhang, Y. Liu, *Matter* **2020**, *3*, 1507-1540.
- 8 S. B. Alahakoon, C. M. Thompson, G. Occhialini, R. A. Smaldone, *ChemSuschem* **2017**, *10*, 2116-2129.
- 9 M. S. Lohse, T. Bein, *Adv. Funct. Mater.* **2018**, *28*, 1705553.
- 10 Y. G. Zhang, S. N. Riduan, *Chem. Soc. Rev.* **2012**, *41*, 2083-2094.
- 11 J. Guo, D. L. Jiang, *ACS Cent. Sci.* **2020**, *6*, 869-879.
- 12 J. Yang, F. Y. Kang, X. Wang, Q. C. Zhang, *Mater. Horiz.* **2022**, *9*, 121-146.
- 13 L. P. Guo, J. Zhang, Q. Huang, W. Zhou, S. B. Jin, *Chinese Chem. Lett.* **2022**, *33*, 2856-2866.
- 14 S. Kandambeth, K. Dey, R. Banerjee, *J. Am. Chem. Soc.* **2019**, *141*, 1807-1822.
- 15 D. Rodriguez-San-Miguel, F. Zamora, *Chem. Soc. Rev.* **2019**, *48*, 4375-4386.
- 16 J. Samanta, Y. J. Zhang, M. S. Zhang, A. D. Chen, C. F. Ke, *Accounts Mater. Res.* **2022**, *3*, 1186-1200.
- 17 Y. X. Lin, X. F. Jiang, S. T. Kim, S. B. Alahakoon, X. S. Hou, Z. Y. Zhang, C. M. Thompson, R. A. Smaldone, C. F. Ke, *J. Am. Chem. Soc.* **2017**, *139*, 7172-7175.

- 18 X. F. Jiang, X. Z. Cui, A. J. E. Duncan, L. Li, R. P. Hughes, R. J. Staples, E. V. Alexandrov, D. M. Proserpio, Y. Y. Wu, C. F. Ke, *J. Am. Chem. Soc.* **2019**, *141*, 10915-10923.
- 19 J. Samanta, R. W. Dorn, W. L. Zhang, X. F. Jiang, M. S. Zhang, R. J. Staples, A. J. Rossini, C. F. Ke, *Chem* **2022**, *8*, 253-267.
- 20 M. S. Zhang, J. Samanta, C. F. Ke, *Cryst. Growth Des.* **2022**, *22*, 3421-3427.
- 21 M. S. Zhang, J. Samanta, B. A. Atterberry, R. Staples, A. J. Rossini, C. F. Ke, *Angew. Chem. Int. Edit.* **2022**, *61*, e202214189.
- 22 M. S. Zhang, L. Y. Li, Q. M. Lin, M. Tang, Y. Y. Wu, C. F. Ke, *J. Am. Chem. Soc.* **2019**, *141*, 5154-5158.
- 23 A. G. Slater, A. I. Cooper, *Science* **2015**, *348*.
- 24 J. A. Mason, M. Veenstra, J. R. Long, *Chem. Sci.* **2014**, *5*, 32-51.
- 25 R. J. Kuppler, D. J. Timmons, Q. R. Fang, J. R. Li, T. A. Makal, M. D. Young, D. Yuan, D. Zhao, W. Zhuang, H. C. Zhou, *Coordin. Chem. Rev.* **2009**, *253*, 3042-3066.
- 26 T. Islamoglu, Z. J. Chen, M. C. Wasson, C. T. Buru, K. O. Kirlikovali, U. Afrin, M. R. Mian, O. K. Farha, *Chem. Rev.* **2020**, *120*, 8130-8160.
- 27 W. Li, J. Liu, D. Y. Zhao, *Nat. Rev. Mater.* **2016**, *1*.
- 28 W. H. Baur, R. X. Fischer, *Micropor. Mesopor. Mat.* **2008**, *116*, 1-3.
- 29 E. Perez-Botella, S. Valencia, F. Rey, *Chem. Rev.* **2022**, *122*, 17647-17695.
- 30 O. M. Yaghi, M. O'Keeffe, N. W. Ockwig, H. K. Chae, M. Eddaoudi, J. Kim, *Nature* **2003**, *423*, 705-714.
- 31 S. Oien-Odegaard, G. C. Shearer, D. S. Wragg, K. P. Lillerud, *Chem. Soc. Rev.* **2017**, *46*, 4867-4876.
- 32 O. K. Farha, A. O. Yazaydin, I. Eryazici, C. D. Malliakas, B. G. Hauser, M. G. Kanatzidis, S. T. Nguyen, R. Q. Snurr, J. T. Hupp, *Nat. Chem.* **2010**, *2*, 944-948.
- 33 H. Furukawa, N. Ko, Y. B. Go, N. Aratani, S. B. Choi, E. Choi, A. O. Yazaydin, R. Q. Snurr, M. O'Keeffe, J. Kim, O. M. Yaghi, *Science* **2010**, *329*, 424-428.
- 34 P. J. Waller, F. Gandara, O. M. Yaghi, *Accounts Chem. Res.* **2015**, *48*, 3053-3063.
- 35 S. V. Kolotuchin, E. E. Fenlon, S. R. Wilson, C. J. Loweth, S. C. Zimmerman, *Angew. Chem. Int. Edit.* **1995**, *34*, 2654-2657.
- 36 Y. He, S. Xiang, B. Chen, *J. Am. Chem. Soc.* **2011**, *133*, 14570-14573.
- 37 T. Q. Ma, E. A. Kapustin, S. X. Yin, L. Liang, Z. Y. Zhou, J. Niu, L. H. Li, Y. Y. Wang, J. Su, J. Li, X. G. Wang, W. D. Wang, W. Wang, J. L. Sun, O. M. Yaghi, *Science* **2018**, *361*, 48-52.

- 38 D. Beaudoin, T. Maris, J. D. Wuest, *Nat. Chem.* **2013**, *5*, 830-834.
- 39 Z. H. Huang, E. S. Grape, J. Li, A. K. Inge, X. D. Zou, *Coordin. Chem. Rev.* **2021**, *427*.
- 40 A. D. Schluter, T. Weber, G. Hofer, *Chem. Soc. Rev.* **2020**, *49*, 5140-5158.
- 41 P. Brunet, E. Demers, T. Maris, G. D. Enright, J. D. Wuest, *Angew. Chem. Int. Edit.* **2003**, *42*, 5303-5306.
- 42 R. Liang, J. Samanta, B. Shao, M. Zhang, R. J. Staples, A. D. Chen, M. Tang, Y. Wu, I. Aprahamian, C. Ke, *Angew. Chem. Int. Edit.* **2021**, *60*, 23176-23181.
- 43 R. B. Lin, Y. He, P. Li, H. Wang, W. Zhou, B. Chen, *Chem. Soc. Rev.* **2019**, *48*, 1362-1389.
- 44 X. Song, Y. Wang, C. Wang, D. Wang, G. Zhuang, K. O. Kirlikovali, P. Li, O. K. Farha, *J. Am. Chem. Soc.* **2022**, *144*, 10663-10687.
- 45 P. Li, M. R. Ryder, J. F. Stoddart, *Acc. Mater. Res.* **2020**, *1*, 77-87.
- 46 D. J. Duchamp, R. E. Marsh, *Acta Crystallogr. B: Struct. Sci. Cryst.* **1969**, *25*, 5-19.
- 47 M. Simard, D. Su, J. D. Wuest, *J. Am. Chem. Soc.* **1991**, *113*, 4696-4698.
- 48 P. Brunet, M. Simard, J. D. Wuest, *J. Am. Chem. Soc.* **1997**, *119*, 2737-2738.
- 49 T. H. Chen, I. Popov, W. Kaveevivitchai, Y. C. Chuang, Y. S. Chen, O. Daugulis, A. J. Jacobson, O. S. Miljanic, *Nat. Commun.* **2014**, *5*, 5131.
- 50 M. I. Hashim, H. T. M. Le, T. H. Chen, Y. S. Chen, O. Daugulis, C. W. Hsu, A. J. Jacobson, W. Kaveevivitchai, X. Liang, T. Makarenko, O. S. Miljanic, I. Popovs, H. V. Tran, X. Wang, C. H. Wu, J. I. Wu, *J. Am. Chem. Soc.* **2018**, *140*, 6014-6026.
- 51 M. Mastalerz, I. M. Oppel, *Angew. Chem. Int. Edit.* **2012**, *51*, 5252-5255.
- 52 Y. Yang, L. Li, R. B. Lin, Y. Ye, Z. Yao, L. Yang, F. Xiang, S. Chen, Z. Zhang, S. Xiang, B. Chen, *Nat. Chem.* **2021**, *13*, 933-939.
- 53 J. Lu, C. Perez-Krap, M. Suyetin, N. H. Alsmail, Y. Yan, S. Yang, W. Lewis, E. Bichoutskaia, C. C. Tang, A. J. Blake, R. Cao, M. Schroder, *J. Am. Chem. Soc.* **2014**, *136*, 12828-12831.
- 54 K. T. Holman, A. M. Pivovar, J. A. Swift, M. D. Ward, *Accounts Chem. Res.* **2001**, *34*, 107-118.
- 55 S. A. Boer, M. Morshedi, A. Tarzia, C. J. Doonan, N. G. White, *Chemistry* **2019**, *25*, 10006-10012.
- 56 I. Brekalo, D. E. Deliz, L. J. Barbour, M. D. Ward, T. Friščić, K. T. Holman, *Angew. Chem. Int. Edit.* **2020**, *59*, 1997-2002.
- 57 Z. Mu, Y. Zhu, B. Li, A. Dong, B. Wang, X. Feng, *J. Am. Chem. Soc.* **2022**, *144*, 5145-5154.

- 58 I. Hisaki, S. Nakagawa, N. Ikenaka, Y. Imamura, M. Katouda, M. Tashiro, H. Tsuchida, T. Ogoshi, H. Sato, N. Tohnai, M. Miyata, *J. Am. Chem. Soc.* **2016**, *138*, 6617-6628.
- 59 I. Hisaki, N. Ikenaka, E. Gomez, B. Cohen, N. Tohnai, A. Douhal, *Chemistry* **2017**, *23*, 11611-11619.
- 60 Y. Suzuki, M. Gutierrez, S. Tanaka, E. Gomez, N. Tohnai, N. Yasuda, N. Matubayasi, A. Douhal, I. Hisaki, *Chem. Sci.* **2021**, *12*, 9607-9618.
- 61 K. Ma, P. Li, J. H. Xin, Y. Chen, Z. Chen, S. Goswami, X. Liu, S. Kato, H. Chen, X. Zhang, J. Bai, M. C. Wasson, R. R. Maldonado, R. Q. Snurr, O. K. Farha, *Cell Rep.* **2020**, *1*, 100024.
- 62 A. P. Cote, A. I. Benin, N. W. Ockwig, M. O'Keeffe, A. J. Matzger, O. M. Yaghi, *Science* **2005**, *310*, 1166-1170.
- 63 B. J. Smith, W. R. Dichtel, *J. Am. Chem. Soc.* **2014**, *136*, 8783-8789.
- 64 A. M. Evans, L. R. Parent, N. C. Flanders, R. P. Bisbey, E. Vitaku, M. S. Kirschner, R. D. Schaller, L. X. Chen, N. C. Gianneschi, W. R. Dichtel, *Science* **2018**, *361*, 53.
- 65 S. Kandambeth, A. Mallick, B. Lukose, M. V. Mane, T. Heine, R. Banerjee, *J. Am. Chem. Soc.* **2012**, *134*, 19524-19527.
- 66 S. Dalapati, S. B. Jin, J. Gao, Y. H. Xu, A. Nagai, D. L. Jiang, *J. Am. Chem. Soc.* **2013**, *135*, 17310-17313.
- 67 C. Feriante, A. M. Evans, S. Jhulki, I. Castano, M. J. Strauss, S. Barlow, W. R. Dichtel, S. R. Marder, *J. Am. Chem. Soc.* **2020**, *142*, 18637-18644.
- 68 Y. B. Zhang, J. Su, H. Furukawa, Y. F. Yun, F. Gandara, A. Duong, X. D. Zou, O. M. Yaghi, *J. Am. Chem. Soc.* **2013**, *135*, 16336-16339.
- 69 T. Q. Ma, J. Li, J. Niu, L. Zhang, A. S. Etman, C. Lin, D. E. Shi, P. H. Chen, L. H. Li, X. Du, J. L. Sun, W. Wang, *J. Am. Chem. Soc.* **2018**, *140*, 6763-6766.
- 70 T. Sun, L. Wei, Y. C. Chen, Y. H. Ma, Y. B. Zhang, *J. Am. Chem. Soc.* **2019**, *141*, 10962-10966.
- 71 T. Sun, C. E. Hughes, L. S. Guo, L. Wei, K. D. M. Harris, Y. B. Zhang, Y. H. Ma, *Angew Chem. Int. Edit.* **2020**, *59*, 22638-22644.
- 72 K. Hema, A. Ravi, C. Raju, J. R. Pathan, R. Rai, K. M. Sureshan, *Chem. Soc. Rev.* **2021**, *50*, 4062-4099.
- 73 G. Schmidt, *Pure Appl. Chem.* **1971**, *27*, 647-678.
- 74 R. Z. Lange, G. Hofer, T. Weber, A. D. Schlüter, *J. Am. Chem. Soc.* **2017**, *139*, 2053-2059.



- 75 P. Kissel, R. Erni, W. B. Schweizer, M. D. Rossell, B. T. King, T. Bauer, S. Gotzinger, A. D. Schluter, J. Sakamoto, *Nat. Chem.* **2012**, *4*, 287-291.
- 76 M. J. Kory, M. Worle, T. Weber, P. Payamyar, S. W. van de Poll, J. Dshemuchadse, N. Trapp, A. D. Schluter, *Nat. Chem.* **2014**, *6*, 779-784.
- 77 P. Kissel, D. J. Murray, W. J. Wulfstange, V. J. Catalano, B. T. King, *Nat. Chem.* **2014**, *6*, 774-778.
- 78 S. P. Yelgaonkar, G. Campillo-Alvarado, L. R. MacGillivray, *J. Am. Chem. Soc.* **2020**, *142*, 20772-20777.
- 79 A. Schneemann, V. Bon, I. Schwedler, I. Senkovska, S. Kaskel, R. A. Fischer, *Chem. Soc. Rev.* **2014**, *43*, 6062-6096.
- 80 P. Cui, E. Svensson Grape, P. R. Spackman, Y. Wu, R. Clowes, G. M. Day, A. K. Inge, M. A. Little, A. I. Cooper, *J. Am. Chem. Soc.* **2020**, *142*, 12743-12750.
- 81 P. D. Adams, P. V. Afonine, R. W. Grosse-Kunstleve, R. J. Read, J. S. Richardson, D. C. Richardson, T. C. Terwilliger, *Curr. Opin. Struct. Biol.* **2009**, *19*, 566-572.
- 82 T. Derbe, S. Temesgen, M. Bitew, *Adv. Mater. Sci. Eng.* **2021**, *2021*, 1-17.
- 83 A. Jain, R. Balasubramanian, M. P. Srinivasan, *Chem. Eng. J.* **2016**, *283*, 789-805.
- 84 M. F. Hassan, M. A. Sabri, H. Fazal, A. Hafeez, N. Shezad, M. Hussain, *J. Anal. Appl. Pyrol.* **2020**, *145*, 104715.
- 85 A. Q. Huang, Y. Z. He, Y. Z. Zhou, Y. Y. Zhou, Y. Yang, J. C. Zhang, L. Luo, Q. M. Mao, D. M. Hou, J. Yang, *J. Mater. Sci.* **2019**, *54*, 949-973.
- 86 X. J. Wang, S. Q. Xu, S. W. Zhou, W. Xu, M. Leary, P. Choong, M. Qian, M. Brandt, Y. M. Xie, *Biomaterials* **2016**, *83*, 127-141.
- 87 O. M. Yaghi, M. J. Kalmutzki, C. S. Diercks, *Introduction to reticular chemistry: metal-organic frameworks and covalent organic frameworks*, John Wiley & Sons, **2019**.
- 88 K. Y. Geng, T. He, R. Y. Liu, S. Dalapati, K. T. Tan, Z. P. Li, S. S. Tao, Y. F. Gong, Q. H. Jiang, D. L. Jiang, *Chem. Rev.* **2020**, *120*, 8814-8933.
- 89 O. M. Yaghi, *J. Am. Chem. Soc.* **2016**, *138*, 15507-15509.
- 90 J. Y. Lee, T. Yim, H. J. Kim, S. Hong, D. W. Seo, H. S. Kim, *Energies* **2019**, *12*, 1262.
- 91 J. Y. Zheng, X. L. Cui, Q. W. Yang, Q. L. Ren, Y. W. Yang, H. B. Xing, *Chem. Eng. J.* **2018**, *354*, 1075-1082.
- 92 R. Girimonte, B. Formisani, F. Testa, *Powder Technol.* **2017**, *311*, 9-17.
- 93 J. S. Meng, X. Liu, C. J. Niu, Q. Pang, J. T. Li, F. Liu, Z. Liu, L. Q. Mai, *Chem. Soc. Rev.* **2020**, *49*, 3142-3186.

- 94 S. Karak, S. Kandambeth, B. P. Biswal, H. S. Sasmal, S. Kumar, P. Pachfule, R. Banerjee, *J. Am. Chem. Soc.* **2017**, *139*, 1856-1862.
- 95 S. Lawson, X. Li, H. Thakkar, A. A. Rownaghi, F. Rezaei, *Chem. Rev.* **2021**, *121*, 6246-6291.
- 96 E. M. Maines, M. K. Porwal, C. J. Ellison, T. M. Reineke, *Green Chem.* **2022**, *24*, 958-959.
- 97 R. B. Kristiawan, F. Imaduddin, D. Ariawan, Ubaidillah, Z. Arifin, *Open Eng.* **2021**, *11*, 639-649.
- 98 T. J. Li, J. Aspler, A. Kingsland, L. M. Cormier, X. J. Zou, *J-For* **2015**, *5*, 60-67.
- 99 S. F. S. Shirazi, S. Gharekhani, M. Mehrali, H. Yarmand, H. S. C. Metselaar, N. A. Kadri, N. A. Abu Osman, *Sci. Technol. Adv. Mat.* **2015**, *16*, 033502.
- 100 A. Jadhav, V. S. Jadhav, *Mater. Today* **2022**, *62*, 2094-2099.
- 101 D. Pranzo, P. Larizza, D. Filippini, G. Percoco, *Micromachines* **2018**, *9*, 374.
- 102 M. Tang, Z. Zhong, C. Ke, *Chem. Soc. Rev.* **2023**, 1614-1649.
- 103 L. Y. Li, Q. M. Lin, M. Tang, A. J. E. Duncan, C. F. Ke, *Chem. Eur. J.* **2019**, *25*, 10768-10781.
- 104 L. Shahzadi, F. Maya, M. C. Breadmore, S. C. Thickett, *ACS Appl. Polym. Mater.* **2022**, *4*, 3896-3907.
- 105 P. Blyweert, V. Nicolas, V. Fierro, A. Celzard, *Carbon* **2021**, *183*, 449-485.
- 106 D. Pianca, M. Carboni, D. Meyer, *Mater. Lett.-X* **2022**, *13*, 100121.
- 107 M. S. Zhang, W. X. Liu, Q. M. Lin, C. F. Ke, *Small* **2023**, 2300323.
- 108 X. H. Chen, Y. E. Wang, S. Zhang, J. S. Cui, X. Y. Ma, L. D. Tian, M. Y. Li, C. W. Bao, Q. H. Wei, B. Du, *Polym. Test* **2023**, 119.
- 109 H. Thakkar, S. Eastman, A. Hajari, A. A. Rownaghi, J. C. Knox, F. Rezaei, *ACS Appl. Mater. Inter.* **2016**, *8*, 27753-27761.
- 110 Y. F. Yang, Z. H. Zhou, X. Y. Chu, X. J. Tang, M. Zhou, W. Zhou, T. Fu, *Mater. Design* **2022**, *219*, 110744.
- 111 S. Lawson, A. A. Alwakwak, A. A. Rownaghi, F. Rezaei, *ACS Appl. Mater. Inter.* **2020**, *12*, 56108-56117.
- 112 G. J. H. Lim, Y. Wu, B. B. Shah, J. J. Koh, C. K. Liu, D. Zhao, A. K. Cheetham, J. Wang, J. Ding, *ACS Mater. Lett.* **2019**, *1*, 147-153.
- 113 C. E. Cipriani, T. Ha, O. M. Defillo, M. Myneni, Y. F. Wang, C. C. Benjamin, J. Y. Wang, E. B. Pentzer, P. R. Wei, *ACS Mater. Au* **2021**, *1*, 69-80.

- 114 A. E. Jakus, N. R. Geisendorfer, P. L. Lewis, R. N. Shah, *Acta. Biomater.* **2018**, 72, 94-109.
- 115 Z. N. Shi, C. Xu, F. Chen, Y. X. Wang, L. Li, Q. T. Meng, R. Zhang, *RSC Adv.* **2017**, 7, 49947-49952.
- 116 W. Q. Liu, O. Erol, D. H. Gracias, *ACS Appl. Mater. Inter.* **2020**, 12, 33267-33275.
- 117 P. Thordarson, *Chem. Soc. Rev.* **2011**, 40, 5922-5923.
- 118 M. V. Rekharsky, Y. Inoue, *Chem. Rev.* **1998**, 98, 1875-1917.
- 119 M. E. Belowich, C. Valente, R. A. Smaldone, D. C. Friedman, J. Thiel, L. Cronin, J. F. Stoddart, *J. Am. Chem. Soc.* **2012**, 134, 5243-5261.
- 120 K. Joseph, S. Kushida, E. Smarsly, D. Ihiawakrim, A. Thomas, G. L. Paravicini-Bagliani, K. Nagarajan, R. Vergauwe, E. Devaux, O. Ersen, U. H. F. Bunz, T. W. Ebbesen, *Angew. Chem. Int. Edit.* **2021**, 60, 19665-19670.
- 121 A. P. Haring, A. U. Khan, G. L. Liu, B. N. Johnson, *Adv. Opt. Mater.* **2017**, 5, 1700367.
- 122 V. A. Bobrin, K. Lee, J. Zhang, N. Corrigan, C. Boyer, *Adv. Mater.* **2022**, 34, 2107643.
- 123 Q. Lin, L. Li, M. Tang, S. Uenuma, J. Samanta, S. Li, X. Jiang, L. Zou, K. Ito, C. Ke, *Chem* **2021**, 7, 2442-2459.
- 124 C. Gropp, S. Canossa, S. Wuttke, F. Gandara, Q. W. Li, L. Gagliardi, O. M. Yaghi, *ACS Centr. Sci* **2020**, 6, 1255-1273.
- 125 Y. C. Liu, D. Y. Xie, R. F. Zhou, Y. X. Zhang, *Micron* **2021**, 142, 102994.
- 126 R. Song, Y. Wang, S. Y. Sun, J. J. Liu, *J. Petrol. Sci. Eng.* **2021**, 205, 108827.
- 127 X. Li, F. Rezaei, A. A. Rownaghi, *React. Chem. Eng.* **2018**, 3, 733-746.
- 128 Y. Z. Wei, M. Y. Chen, X. Y. Ren, Q. F. Wang, J. F. Han, W. Z. Wu, X. G. Yang, S. Wang, J. H. Yu, *CCS Chem.* **2022**, 4, 1708-1719.
- 129 A. Khalil, R. Hashaikh, N. Hilal, *J. Water Process Eng.* **2021**, 42, 102187.
- 130 S. Khan, M. Ul-Islam, M. W. Ahmad, M. S. Khan, M. Imran, S. H. Siyal, M. S. Javed, *Energ. Fuel* **2022**, 36, 3420-3442.
- 131 Y. Shao, C. Guizani, P. Grosseau, D. Chaussy, D. Beneventi, *Compos. Part B-Eng.* **2018**, 149, 206-215.
- 132 H. Ding, S. Barg, B. Derby, *Nanoscale* **2020**, 12, 11440-11447.
- 133 F. Zhang, Z. A. Li, M. J. Xu, S. Y. Wang, N. Li, J. Q. Yang, *J. Eur. Ceram. Soc.* **2022**, 42, 3351-3373.
- 134 L. Li, P. Zhang, Z. Zhang, Q. Lin, Y. Wu, A. Cheng, Y. Lin, C. M. Thompson, R. A. Smaldone, C. Ke, *Angew. Chem. Int. Ed.* **2018**, 57, 5105-5109.

- 135 Z. H. Wang, C. Y. Wang, C. Li, Y. G. Qin, L. Zhong, B. P. Chen, Z. Y. Li, H. Liu, F. Chang, J. C. Wang, *J. Alloy Compd.* **2017**, *717*, 271-285.
- 136 Z. L. Li, Q. H. Wang, G. D. Liu, *Micromachines*, **2022**, *13*, 528.
- 137 P. Chang, H. Mei, S. X. Zhou, K. G. Dassios, L. F. Cheng, *J. Mater. Chem. A* **2019**, *7*, 4230-4258.
- 138 J. E. Huddy, M. S. Rahman, A. B. Hamlin, Y. X. Ye, W. J. Scheideler, *Cell Rep. Phys. Sci.* **2022**, *3*, 100786.
- 139 H. Thakkar, S. Eastman, Q. Al-Naddaf, A. A. Rownaghi, F. Rezaei, *ACS Appl. Mater. Inter.* **2017**, *9*, 35908-35916.
- 140 H. Thakkar, Q. Al-Naddaf, N. Legion, M. Hovis, A. Krishnamurthy, A. A. Rownaghi, F. Rezaei, *ACS Sustain Chem. Eng.* **2018**, *6*, 15228-15237.
- 141 Z. Y. Lyu, G. J. H. Lim, R. Guo, Z. H. Pan, X. Zhang, H. Zhang, Z. M. He, S. Adams, W. Chen, J. Ding, J. Wang, *Energy Storage Mater.* **2020**, *24*, 336-342.
- 142 A. J. Young, R. Guillet-Nicolas, E. S. Marshall, F. Kleitz, A. J. Goodhand, L. B. L. Glanville, M. R. Reithofer, J. M. Chin, *Chem. Commun.* **2019**, *55*, 2190-2193.
- 143 R. Pei, L. L. Fan, F. G. Zhao, J. R. Xiao, Y. C. Yang, A. N. Lai, S. F. Zhou, G. W. Zhan, *J. Hazard Mater.* **2020**, *384*, 121418.
- 144 A. K. Mohammed, S. Usgaonkar, F. Kanheerampockil, S. Karak, A. Halder, M. Tharkar, M. Addicoat, T. G. Ajithkumar, R. Banerjee, *J. Am. Chem. Soc.* **2020**, *142*, 8252-8261.
- 145 X. M. Liu, G. J. H. Lim, Y. X. Wang, L. Zhang, D. Mullangi, Y. Wu, D. Zhao, J. Ding, A. K. Cheetham, J. Wang, *Chem. Eng. J.* **2021**, *403*, 126333.
- 146 N. A. Sears, P. S. Dhavalikar, E. M. Cosgriff-Hernandez, *Macromol Rapid Comm.* **2016**, *37*, 1369-1374.
- 147 X. Mu, T. Bertron, C. Dunn, H. Qiao, J. Wu, Z. Zhao, C. Saldana, H. J. Qi, *Mater. Horiz.* **2017**, *4*, 442-449.
- 148 N. T. H. Men, T. H. Jeong, S. Y. Kim, K. B. Kim, T. H. Ha, S. J. Ahn, Y. H. Kim, *J. Manuf. Process.* **2021**, *67*, 46-51.
- 149 F. Mayer, D. Ryklin, I. Wacker, R. Curticean, M. Calkovsky, A. Niemeyer, Z. Q. Dong, P. A. Levkin, D. Gerthsen, R. R. Schroder, M. Wegener, *Adv. Mater.* **2020**, *32*, 2002044.
- 150 S. Lawson, M. Snarzyk, D. Hanify, A. A. Rownaghi, F. Rezaei, *Ind. Eng. Chem. Res.* **2020**, *59*, 7151-7160.
- 151 S. Wang, P. Bai, M. Z. Sun, W. Liu, D. D. Li, W. Z. Wu, W. F. Yan, J. Shang, J. H. Yu, *Adv. Sci.* **2019**, *6*, 1901317.

- 152 M. C. Kreider, M. Sefa, J. A. Fedchak, J. Scherschligt, M. Bible, B. Natarajan, N. N. Klimov, A. E. Miller, Z. Ahmed, M. R. Hartings, *Polym. Advan. Technol.* **2018**, *29*, 867-873.
- 153 J. Dhainaut, M. Bonneau, R. Ueoka, K. Kanamori, S. Furukawa, *ACS Appl. Mater. Inter.* **2020**, *12*, 10983-10992.
- 154 I. Pellejero, F. Almazan, M. Lafuente, M. A. Urbiztondo, M. Drobek, M. Bechelany, A. Julbe, L. M. Gandia, *J. Ind. Eng. Chem.* **2020**, *89*, 194-203.
- 155 M. del Rio, M. Villar, S. Quesada, G. T. Palomino, L. Ferrer, C. P. Cabello, *Appl. Mater. Today* **2021**, *24*, 101130.
- 156 Z. Y. Wang, J. J. Wang, M. Y. Li, K. H. Sun, C. J. Liu, *Sci. Rep.* **2014**, *4*, 5939.
- 157 A. Figuerola, D. A. V. Medina, A. J. Santos-Neto, C. P. Cabello, V. Cerda, G. T. Palomino, F. Maya, *Appl. Mater. Today* **2019**, *16*, 21-27.
- 158 D. S. Liu, P. Jiang, X. C. Li, J. X. Liu, L. C. Zhou, X. L. Wang, F. Zhou, *Chem. Eng. J.* **2020**, *397*, 334-339.
- 159 F. Magzoub, X. Li, S. Lawson, F. Rezaei, A. A. Rownaghi, *Fuel* **2020**, *280*, 118628.
- 160 Z. Lyu, G. J. H. Lim, R. Guo, Z. Kou, T. Wang, C. Guan, J. Ding, W. Chen, J. Wang, *Adv. Funct. Mater.* **2019**, *29*, 1806658.
- 161 Y. C. Chang, C. H. Huang, W. R. Liu, *Polymers*, **2022**, *14*, 3085.
- 162 S. Pal, Y. Z. Su, Y. W. Chen, C. H. Yu, C. W. Kung, S. S. Yu, *ACS Appl. Mater. Inter.* **2022**, *14*, 28247-28257.
- 163 N. P. Bradshaw, Z. Hirani, L. Kuo, S. Li, N. X. Williams, V. K. Sangwan, L. E. Chaney, A. M. Evans, W. R. Dichtel, M. C. Hersam, *Adv. Mater.* **2023**, e2303673.
- 164 L. J. Wang, W. L. Gao, S. Ng, M. Pumera, *Anal. Chem.* **2021**, *93*, 5277-5283.
- 165 T. Limongi, F. Susa, M. Allione, E. di Fabrizio, *Pharmaceutics* **2020**, *12*, 851.
- 166 Y. Zhang, J. L. Xu, Z. Y. Fei, H. X. Dai, Q. Fan, Q. Y. Yang, Y. T. Chen, B. L. Wang, C. Wang, *Adv. Mater.* **2021**, *33*, 2106768.
- 167 H. P. Dang, A. Shafiee, C. A. Lahr, T. R. Dargaville, P. A. Tran, *Adv. Ther.* **2020**, *3*, 2000056.
- 168 J. Lv, Z. J. Gong, Z. K. He, J. Yang, Y. Q. Chen, C. Y. Tang, Y. Liu, M. K. Fan, W. M. Lau, *J. Mater. Chem. A* **2017**, *5*, 12435-12444.

## **Chapter 2 Assembling Guests as Cyclic Tetramers in a Porous Hydrogen-Bonded Organic Framework**

PREFACE for “Assembling Guests as Cyclic Tetramers in a Porous Hydrogen-Bonded Organic Framework” published in *crystal growth & design*. Reproduced from The American Association for the Advancement of Science.

Zhang, M.; Samanta, J.; Ke, C. Assembling Guests as Cyclic Tetramers in a Porous Hydrogen-Bonded Organic Framework. *Cryst. Growth. Des.* **2022**, 22, 3421-3427. The first author, Mingshi Zhang, performed most of the experimental work, data analysis and plotting. The corresponding author, Professor Chenfeng Ke provided guidance on ideas and focus of the research and significantly contributed to the writing. Jayanta Samanta provided a lot of sights and helped solve the single-crystal structures.

## 2.1 Introduction

Host-guest interactions are widely found in supramolecular systems<sup>169-170</sup> in solution<sup>171</sup> and the solid-state.<sup>172</sup> Depending on the cavity size of the host molecule, one or multiple guests could be encapsulated via hydrogen bonding,<sup>173-175</sup> hydrophobic effects,<sup>176-177</sup> and electrostatic interactions.<sup>178-179</sup> Macrocycles including  $\beta$ -cyclodextrin,<sup>180-181</sup> cucurbit[8]uril,<sup>182-183</sup> and cyclobisparaquats<sup>184-185</sup> have been reported to form ternary complexes in solution, respectively. These ternary complexes are further stabilized through guest-guest interactions. In the solid-state, organic cages<sup>186-187</sup> and porous crystals<sup>188-190</sup> have also been reported to include multiple guests. Sometimes, these guests are arranged in unique geometries through multivalent host-guest and guest-guest interactions. For example, Kim *et al.* reported a fullerene tetramer and a porphyrin cage assembly in the solid-state,<sup>191</sup> and Kubik *et al.* stabilized a dihydrogenphosphate tetramer using a cyclic pseudopeptide.<sup>192</sup>

In porous framework materials, such as metal-organic frameworks (MOFs),<sup>193-196</sup> covalent organic frameworks (COFs),<sup>197-198</sup> and hydrogen-bonded organic frameworks (HOFs),<sup>199-201</sup> the large and interconnected voids allow for the adsorption of multiple guests. In HOFs, discrete guest molecules including organic solvents<sup>202-203</sup> and aromatic compounds<sup>204-207</sup> have been identified to bind the functional groups decorated on the pore surfaces. This phenomenon is well illustrated in HOF-1 (Figure 2.1),<sup>48, 208</sup> which binds acetylene selectively through framework-substrate hydrogen bonding for ethylene/acetylene separation.<sup>208</sup> Apart from gaseous substrates, the large one-dimensional (1D) porous channels of HOF-1 also allow for the uptake of multiple guest molecules either in the liquid or solid form. Therefore, the investigation of non-gaseous substrates and HOF-1 complexes in the solid-state will provide important structural insights into the understanding of multivalent host-guest and guest-guest interactions in porous organic materials.

In this work, we chose HOF-1 as the crystalline framework host and aniline and its analogs toluidine and toluene as guests for the investigation. Different from the reported aniline or toluidines complexes formed in MOFs<sup>209</sup> or HOFs,<sup>205, 210</sup> the single-crystal X-ray structure of HOF-1·PhNH<sub>2</sub> revealed that anilines are assembled in the voids of HOF-1 as cyclic tetramers. Furthermore, cyclic guest tetramers are found in five other HOF-1·guest complexes, including toluidine isomers (*o*-, *m*-, *p*-Tld), toluene (Tol), and *N*-vinyl-2-pyrrolidone<sup>211</sup> (VP) (Figure 2.1a), respectively. We have discovered that the strong HOF-1/substrate interactions, including hydrogen bonding and N-H••• $\pi$  interactions, direct the



assembly of guests as cyclic tetramers. They are further stabilized via C-H... $\pi$  interactions. We noticed that the strong HOF-1/substrate interaction dominates the arrangement of guests in the voids of HOF-1. This feature allows for the co-adsorption of different guests in the same porous channel, as evident in the alkylation<sup>212</sup> of the co-adsorbed aniline and VP in HOF-1.

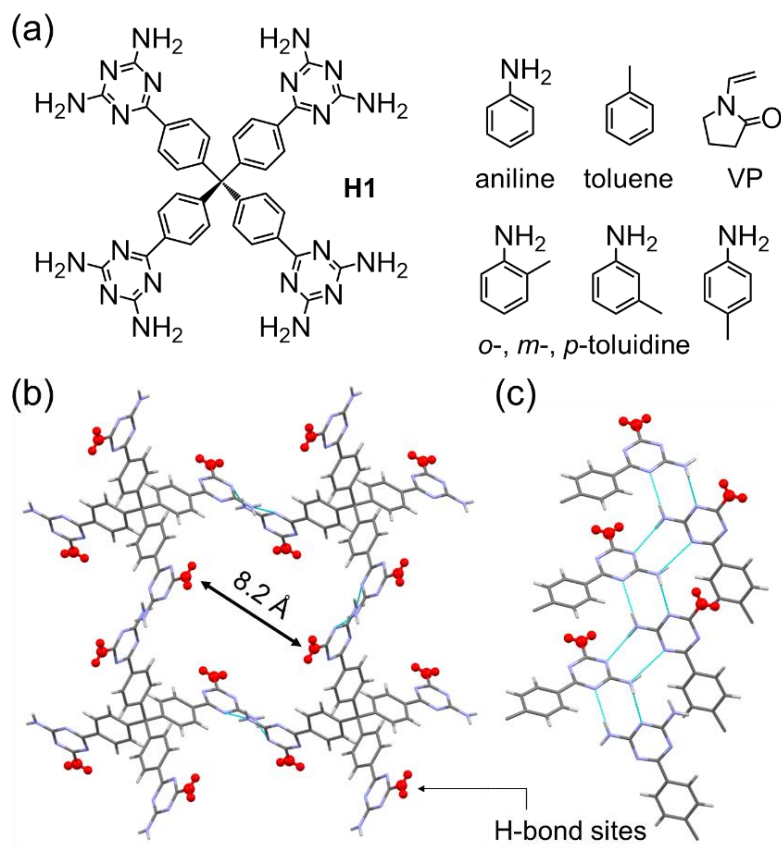


**Figure 2.1.** (a) Chemical structures of **H1** and substrates used in this investigation. (b) Solid-state structure of HOF-1 viewed along the *c*-axis. Vacant amino groups are highlighted in red color. Disordered solvent molecules are omitted for clarity. (c) The hydrogen-bonding arrays formed between 2,4-diamino-1,3,5-triazine (DAT) arms.

## 2.2 Experimental Section

**HOF-1 and HOF-1·guest complexes.** A solution of **H1** (100.0 mg, 0.132 mmol, in 0.75 mL 1,4-dioxane and 1 mL formic acid) in a 4 mL vial was placed in a 20 mL vial with 8 mL 1,4-dioxane for solvent diffusion. After 10 d at room temperature, transparent needle-like HOF-1 crystals were obtained (~ 60 mg). HOF-1 single crystals (~ 5 mg) are picked

and transferred to a vial with 2 mL of neat guest liquid (aniline, toluene, *o*-toluidine, *m*-toluidine, *p*-toluidine, *N*-vinyl-2-pyrrolidone). The samples were kept at 25°C or 50 °C for 24 h. Crystals of HOF-1·guest complexes were selected for single-crystal X-ray diffraction (SCXRD) analysis.

**Co-adsorption of guest mixtures.** HOF-1 single crystals (~ 5 mg) were selected, transferred to a mixture of guests, and kept at room temperature for 48 h. The crystals were washed with water, and dried under reduced pressure. The crystals were dissolved in DMSO-*d*<sub>6</sub> for <sup>1</sup>H NMR analysis. Fed PhNH<sub>2</sub>/Tol mixture: PhNH<sub>2</sub> (1.112 g, 1.09 mL, 12 mmol) and Tol (1.104 g, 1.27 mL, 12 mmol); found **H1**:PhNH<sub>2</sub>: Tol = 1:3.4:0.7. Fed PhNH<sub>2</sub>/toluidine isomer mixtures: PhNH<sub>2</sub> (0.556 g, 0.51 mL, 6 mmol), *o*-Tld (0.642 g, 0.64 mL, 6 mmol), *m*- Tld (0.642 g, 0.66 mL, 6 mmol), and *p*- Tld (0.556 g, 0.61 mL, 6 mmol); found **H1**:PhNH<sub>2</sub>:*o*-Tld:*m*-Tld:*p*-Tld = 1:1.1 ± 0.1:1.0 ± 0.0:1.0 ± 0.0:1.2 ± 0.1.

**Alkylation of aniline and *N*-vinyl-2-pyrrolidone in HOF-1.** HOF-1 single crystals (~ 5 mg) were selected, washed with water, and transferred to a mixture of PhNH<sub>2</sub> (1.112 g, 1.09 mL, 12 mmol) and VP (1.332 g, 1.28 mL, 12 mmol). After 48 h at room temperature, the mixture of PhNH<sub>2</sub> and VP was carefully removed for <sup>1</sup>H NMR analysis. The crystals were washed with water and dried under reduced pressure. These crystals were dissolved in DMSO-*d*<sub>6</sub> for <sup>1</sup>H NMR analysis. 1-(1-Anilinoethyl)-2-pyrrolidinone (AEP) was not detected in the mother liquid. Found **H1**:PhNH<sub>2</sub>:VP:AEP = 1:3.1 ± 0.1:0.8±0.1:0.3 ± 0.0 .

## 2.3 Results and Discussions

The compound **H1**, which is the molecular building block of HOF-1, was synthesized according to previous reports.<sup>48, 213</sup> **H1** consists of a tetraphenyl methane (TPM) core and four DAT arms (Figure 2.1a). Diffusing 1,4-dioxane into the mixed solution of formic acid/dioxane of **H1** afforded HOF-1 crystals that are suitable for SCXRD analysis. In HOF-1, each DAT arm is hydrogen-bonded with two adjacent **H1** molecules. One vacant amino group of DAT (red, Figure 2.1b) points towards the pore surface. There are square-shaped 1D porous channels<sup>208</sup> with an aperture of 8.2 Å in HOF-1, which allows for the uptake of multiple guest molecules.

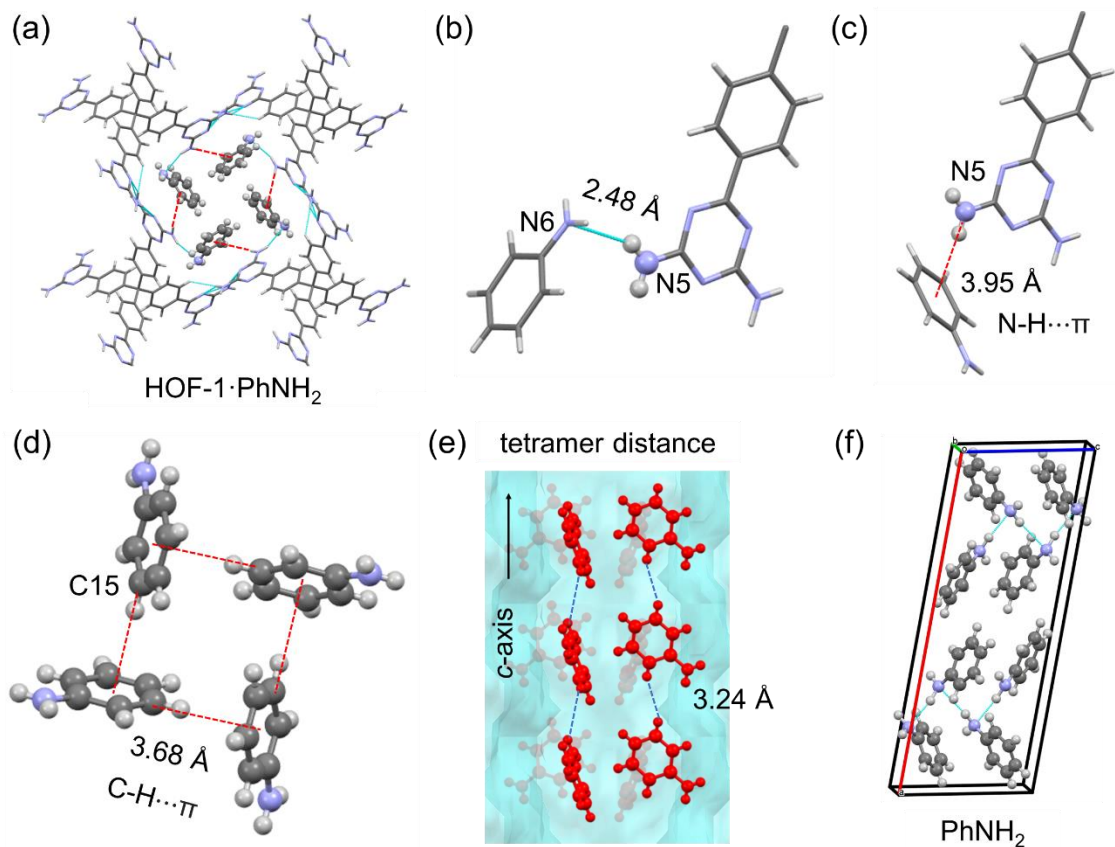


**Figure 2.2.** (a) Solid-state structure of HOF-1·PhNH<sub>2</sub> viewed along the *c*-axis. (b) Hydrogen-bonding and (c) N-H••• $\pi$  interaction between HOF-1 and aniline. The N-H••• $\pi$  distance is measured as the distance between the N atom and the center of the phenyl ring. (d) The cyclic aniline tetramer in HOF-1·PhNH<sub>2</sub> with C-H••• $\pi$  interactions highlighted. (e) The layered packing of cyclic aniline tetramers in HOF-1·PhNH<sub>2</sub>. The aniline molecules are highlighted in red. (f) Solid-state structure of aniline.<sup>214</sup>

The HOF-1·PhNH<sub>2</sub> complex was prepared by immersing solvent-filled HOF-1 crystals in neat aniline at 25 °C. After 24 h diffusion, the obtained crystal sample was subjected to SCXRD analysis. In HOF-1·PhNH<sub>2</sub>, four aniline molecules are packed in an edge-to-face manner (Figure 2.2a) as a cyclic tetramer at the cross-section of the 1D channel. SCXRD and <sup>1</sup>H NMR analyses showed that the molar ratio between **H1** and aniline is 1:4 (Table 2.1). Compared to HOF-1, the unit cell volume of HOF-1·PhNH<sub>2</sub> contracted by 2.1%, indicating that the uptake of aniline does not significantly impact the hydrogen-bonded network of HOF-1. The vacant amino groups of **H1** form hydrogen bonds (Figure 2.2b) with anilines via an N(5)-H•••N(6)-Ph interaction (2.48 Å, Table 2.1). Additional N-

H••• $\pi$  interactions (Figure 2.2c) are also noticeable between the amino groups and aniline (3.68 Å, Table 2.1). Within the pore voids, four anilines are bonded to each other as a cyclic tetramer (Figure 2.2d) via C-H••• $\pi$  interactions (3.68 Å, Table 2.1). The cyclic tetramers are repeated along the *c*-axis of HOF-1 (Figure 2.2e). Compared to the solid-state structure of aniline (Figure 2.2f),<sup>214</sup> the spatial arrangement of anilines in HOF-1 is very different, suggesting that the strong HOF-1-to-aniline interaction competes against the aniline-aniline hydrogen-bonding. To understand the framework-substrate interactions, we replaced aniline with toluene and prepared a toluene-filled HOF-1 crystal (HOF-1·Tol) for SCXRD analysis. Surprisingly, cyclic toluene tetramers were also formed within the voids of HOF-1 (Figure 2.3a), similar to HOF-1·PhNH<sub>2</sub>. Only N-H••• $\pi$  interactions (4.29 Å, Table 2.1) are established between the vacant amino groups of HOF-1 and toluene (Figure 2.3b). The Ph-H••• $\pi$  distance (3.95 Å, Table 2.1) between toluene molecules (Figure 2.3c) is larger than those of the aniline molecules (3.68 Å). These analyses suggest much weaker framework-substrate and substrate-substrate interactions in HOF-1·Tol compared to that of HOF-1·PhNH<sub>2</sub>. When HOF-1 single crystals were immersed in a 1:1 mixture of aniline/toluene at 25 °C for 24 h, the adsorbed aniline/toluene ratio was measured as 4.9:1 by <sup>1</sup>H NMR spectroscopy (Figure S20).<sup>215</sup> In vapor sorption experiments (Figure S25, S26), the adsorption of toluene in HOF-1 is relatively low at the lower pressure range, but the adsorption amount rapidly increased at higher pressure. This phenomenon is also observed in MOFs,<sup>216-217</sup> suggesting the guest-guest interaction prompts the guest uptake in HOF-1 voids.

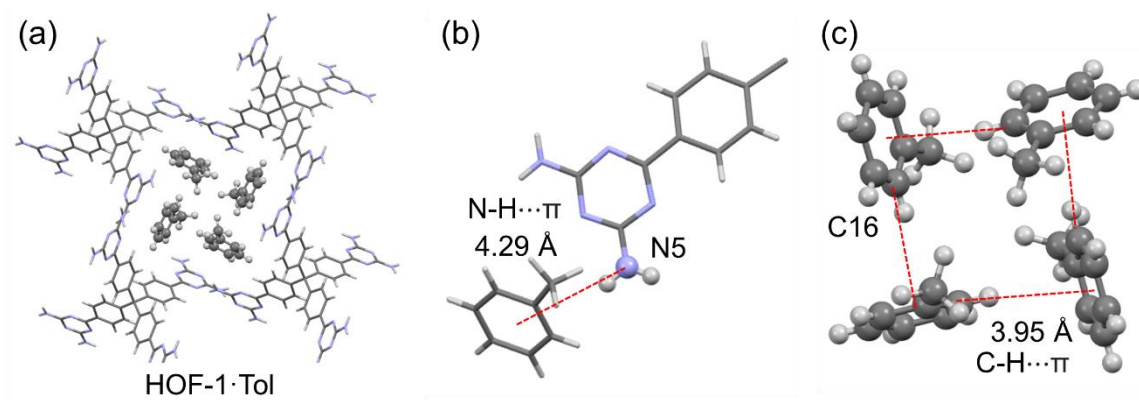


**Figure 2.3.** (a) Solid-state structure of HOF-1·Tol viewed along the *c*-axis. (b) N-H••• $\pi$  interaction between HOF-1 and toluene. (c) The cyclic toluene tetramer in HOF-1·Tol with C-H••• $\pi$  interactions highlighted.

**Table 2.1** Summary of crystallographic data of HOF-1 and HOF-1·guest complexes. All crystals are tetragonal in the I4 space group with  $\alpha = \beta = \gamma = 90^\circ$ .

	HOF-1	HOF-1·PhNH <sub>2</sub>	HOF-1·Tol	HOF-1· <i>o</i> -Tld	HOF-1· <i>m</i> -Tld	HOF-1· <i>p</i> -Tld	HOF-1·VP
formula	<b>H1</b> ·4dioxane·HCO <sub>2</sub> H	<b>H1</b> ·4PhNH <sub>2</sub>	<b>H1</b> ·4Tol	<b>H1</b> ·4 <i>o</i> -Tld	<b>H1</b> ·4 <i>m</i> -Tld	<b>H1</b> ·4 <i>p</i> -Tld	<b>H1</b> ·4VP
unit cell (Å)							
a	20.466(8)	20.3468(10)	20.1754(6)	20.2713(4)	20.1198(3)	20.2017(4)	20.3140(7)
b	20.466(8)	20.3468(10)	20.1754(6)	20.2713(4)	20.1198(3)	20.2017(4)	20.3140(7)
c	7.185(2)	7.1118(6)	7.2479(4)	7.1255(2)	7.20870(1)	7.1518(2)	7.3565(4)
cell volume change	–	–2.1 %	–2.0 %	–2.7 %	–3.0 %	–3.0 %	0.9 %
H1:guest	–	1:4.0	1:4.0	1:4.0	1:4.0	1:4.0	1:4.0
SCXRD <sup>a</sup>	–	1:3.9	1:3.2 <sup>c</sup>	1:4.0	1:4.2	1:4.1	1:3.9
<sup>1</sup> H NMR <sup>b</sup>	–	2.48	–	2.45	2.44	2.43	2.13 (N-H•••O) <sup>d</sup>
N-H•••N distance (Å)	–	3.95	4.29	4.01	3.92	3.96	–
N-H••• $\pi$ distance <sup>e</sup> (Å)	–	3.68	3.95	3.79 <sup>g</sup> 4.01 <sup>g</sup>	3.65	3.79 <sup>g</sup> 4.15 <sup>g</sup>	–
C-H••• $\pi$ distance <sup>f</sup> (Å)	–	3.24	2.60	2.23	2.30	2.22	2.92
distance of tetramers <sup>h</sup> (Å)	–						

[a] **H1**:guest ratios determined by X-ray crystallography. <sup>b</sup> **H1**:guest ratios determined by <sup>1</sup>H NMR experiment. <sup>c</sup> Fewer toluene molecules per **H1** measured in <sup>1</sup>H NMR analysis, attributed to the high volatility of toluene. <sup>d</sup> The N-H•••N hydrogen bond distance between the vacant amino group of **H1** and nitrogen atoms of substrate. <sup>e</sup> The N-H••• $\pi$  distance is measured as the distance between the N(5) atom and the center of the phenyl ring. <sup>f</sup> The C-H••• $\pi$  distance is measured as the distance between the carbon atom and the center of the phenyl ring. <sup>g</sup> Measured Ph-H••• $\pi$  and CH<sub>3</sub>••• $\pi$  distances respectively. <sup>h</sup> The measured distance between the nearest atoms of two cyclic tetramers.

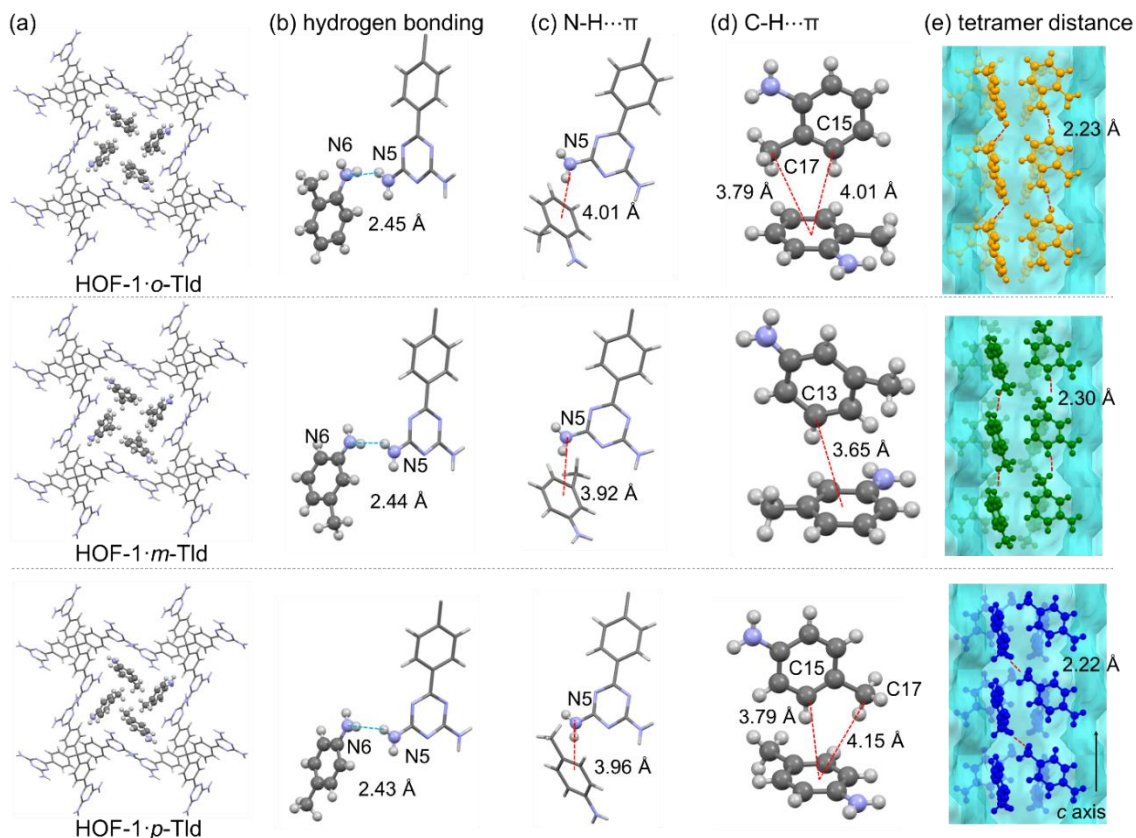


**Figure 2.4.** (a) Solid-state structure of HOF-1·*o*-Tld, HOF-1·*m*-Tld, and HOF-1·*p*-Tld viewed along the *c*-axis. (b) Hydrogen-bonding interactions and (c) N-H... $\pi$  interaction between HOF-1 and *o*-Tld, *m*-Tld, and *p*-Tld, respectively. (d) The C-H... $\pi$  interactions in the cyclic tetramers of *o*-Tld, *m*-Tld, and *p*-Tld, respectively. (e) The layered packing structures of cyclic tetramers of *o*-Tld, *m*-Tld, and *p*-Tld from the top to bottom. The *o*-Tld, *m*-Tld, and *p*-Tld molecules are highlighted in yellow, green, and blue, respectively.

Expanding the substrate scope from aniline to *o*-Tld, *m*-Tld, and *p*-Tld, we sought to investigate the co-conformations of toluidine regioisomer assemblies in HOF-1. Three HOF-1·toluidine complexes were prepared by immersing solvent-filled HOF-1 crystals in neat *o*-Tld, *m*-Tld at 25 °C, and *p*-Tld melt at 50 °C, respectively. Despite different shapes of toluidine isomers, cyclic toluidine tetramers were found in HOF-1·*o*-Tld, HOF-1·*m*-Tld, and HOF-1·*p*-Tld (Figure 2.4a). The amino groups of *o*-Tld, *m*-Tld, and *p*-Tld are hydrogen-bonded to the vacant amino group of DAT in HOF-1 (Figure 2.4b), and the N(5)-H...N(6) distances are measured as 2.45 Å, 2.44 Å, and 2.43 Å, respectively (Table 1). The N(5)-H... $\pi$  interactions were also found in HOF-1·*o*-Tld (4.01 Å), HOF-1·*m*-Tld (3.92 Å), and

HOF-1·*p*-Tld (3.96 Å) (Figure 2.4c). Both Ph-H••• $\pi$  and CH<sub>3</sub>••• $\pi$  interactions were found between the neighboring toluidine molecules in HOF-1·*o*-Tld and HOF-1·*p*-Tld (Figure 3d), while only a Ph-H••• $\pi$  interaction was found in HOF-1·*m*-Tld. The short hydrogen bonds and N-H••• $\pi$  interactions between the *p*-toluidine tetramer and HOF-1, and the two-fold C-H••• $\pi$  interactions within the cyclic tetramer suggest that HOF-1·*p*-Tld possesses slightly stronger host-guest and guest-guest interactions among the HOF-1·Tld complexes. Experimentally, when HOF-1 crystals were immersed in an equal amount of PhNH<sub>2</sub>, *o*-Tld, *m*-Tld, and *p*-Tld mixture, the uptake ratio of PhNH<sub>2</sub>, *o*-Tld, *m*-Tld, and *p*-Tld was measured as 1: 1.1±0.1: 1.0±0.0: 1.0±0.0: 1.2±0.1 using <sup>1</sup>H NMR spectroscopy (Figure S21).<sup>215</sup> The greater uptake amount of *p*-Tld in the adsorption experiment is consistent with SCXRD analyses.

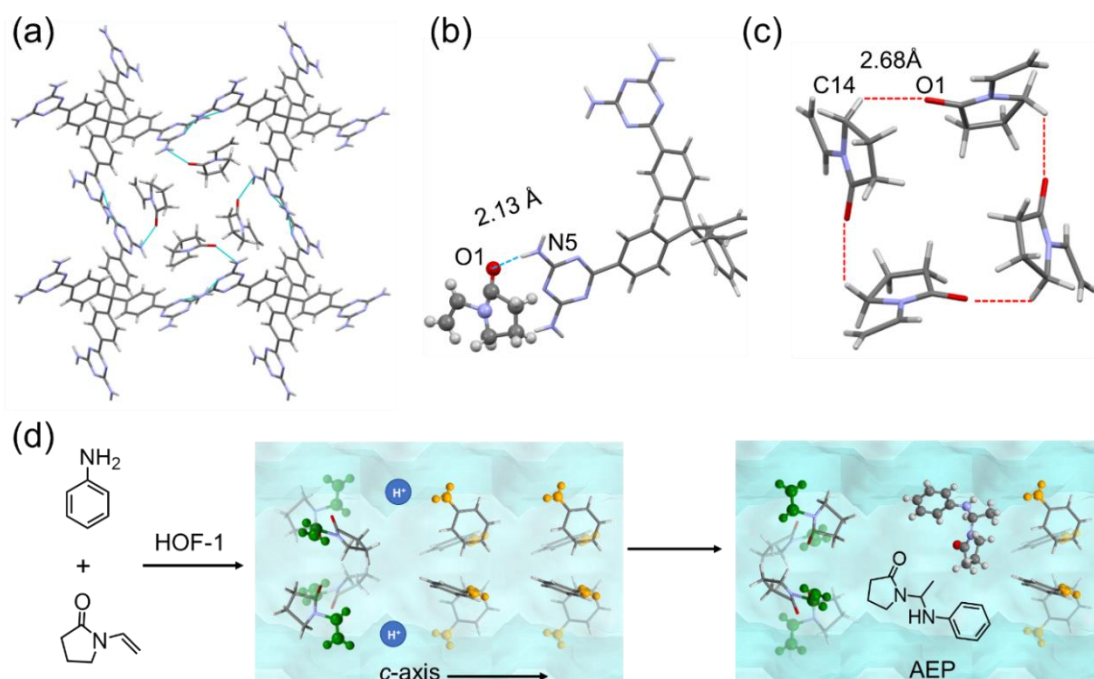


**Figure 2.5.** (a) Solid-state structure of HOF-1·VP complex viewed along the c-axis. (b) Hydrogen-bonding interactions between HOF-1 and VP (c) C-H•••O interactions between VP molecules in the channels of HOF-1. (d) The process by which aniline and VP meet and react with each other in the channels of HOF-1. Aniline and VP are first co-adsorbed into HOF-1, and they are catalyzed by the residual formic acid within HOF-1 to afford 1-(1-anilinoethyl)-2-pyrrolidinone (AEP). The amino and alkenyl reactive functional groups are highlighted in yellow and green, respectively.

When the substrate was changed from toluidine isomers (both hydrogen bonding donors and acceptors) to *N*-vinyl-2-pyrrolidone (a hydrogen bonding acceptor), tetrameric cyclic assemblies of VP were also found in the solid-state (Figure 2.5a). In the HOF-1·VP crystal, the carbonyl groups of VP tetramers form hydrogen bonds via a N(5)-H···O(1) interaction (2.13 Å, Figure 2.5b), directing the vinyl groups to point toward the pore surface of HOF-1. The closest vinyl-to-vinyl distance is measured as 6.37 Å. In the VP tetramer, only weak C(14)-H···O(1) dipole interactions (2.68 Å, Figure 2.5c) were discovered, suggesting the assembly of VP molecules in HOF-1 is primarily driven by the framework-substrate interaction.

The strong framework-guest and weak guest-guest interactions within HOF-1·PhNH<sub>2</sub>, HOF-1·Tol, HOF-1·*o*-Tld, HOF-1·*m*-Tld, HOF-1·*p*-Tld, and HOF-1·VP complexes directed the formation of guest cyclic tetramers. These cyclic tetramers were weakly packed along the 1D voids of HOF-1. Therefore, we speculated that the voids of HOF-1 could accommodate two different guests simultaneously as a mixture of cyclic tetramers.<sup>218</sup> To confirm this, we immersed HOF-1 crystals in the mixture of two reactive substrates (PhNH<sub>2</sub> and VP). PhNH<sub>2</sub> and VP could undergo an alkylation<sup>212</sup> to form 1-(1-anilinoethyl)-2-pyrrolidinone (AEP, Figure 2.5d) in the presence of an acid. In the solvent-filled HOF-1 crystals, formic acid residuals are present in the 1D voids, which could catalyze the formation of AEP when PhNH<sub>2</sub> and VP are adsorbed in the same channel. Experimentally, we immersed HOF-1 crystals in a 1:1 mixture of PhNH<sub>2</sub> and VP at room temperature. After 48 h, the crystals and mother liquid were subjected to <sup>1</sup>H NMR analysis (Figures S22-23). No AEP was detected in the mother liquid mixture, and <sup>1</sup>H NMR analysis shows the **H1**:PhNH<sub>2</sub>:VP:AEP ratio in the dissolved crystal sample as 1: 3.1±0.1: 0.8±0.1: 0.3±0.0 (Figure S24). The formation of AEP in HOF-1 confirmed that PhNH<sub>2</sub> and VP molecules were co-adsorbed within the same 1D channel of HOF-1. The found **H1**:PhNH<sub>2</sub>:VP ratio revealed that HOF-1 binds PhNH<sub>2</sub> stronger than VP, and VP was not consumed completely. This incomplete alkylation in HOF-1 indicates that PhNH<sub>2</sub> and VP are co-adsorbed as cyclic tetramer aggregates, and the alkylation only occurred at the interface of PhNH<sub>2</sub> and VP aggregates (Figure 2.5d).

## 2.4 Summary

In summary, a series of HOF-1·guest complexes with aniline, *o*-, *m*-, *p*-toluidine, toluene, and *N*-vinyl-2-pyrrolidone were prepared, and their corresponding single-crystal X-ray structures are reported here. Despite the different sizes of guests, the strong HOF-1-



substrate interactions, including hydrogen bonding and N-H... $\pi$  interactions, direct the assembly of guests as cyclic tetramers within the 1D voids of HOF-1. These cyclic tetramers are further stabilized through the guest-guest interactions, which include C-H... $\pi$  and van der Waals interactions. By comparing the packing structures of *o*-, *m*-, and *p*-toluidines in HOF-1, we discovered that the methyl groups of toluidine regioisomers only resulted in very small changes in the HOF-1•toluidine interactions. These cyclic tetramers are packed along with the 1D voids of HOF-1. No specific interactions are noticed between neighboring cyclic tetramers, which allowed for the co-adsorption of different guests inside the same 1D voids of HOF-1. This co-adsorption of different guest molecules in HOF-1 was confirmed by the alkylation between aniline and VP inside HOF-1. Our work suggests that strong framework-substrate interactions could effectively arrange multiple guests in desired co-conformations, while guest-guest interactions differ depending on the size and functional groups of the guests. These results provide important structural insights into multiple-guest inclusion and methods for conducting chemical reactions in confined environments.<sup>219-220</sup>

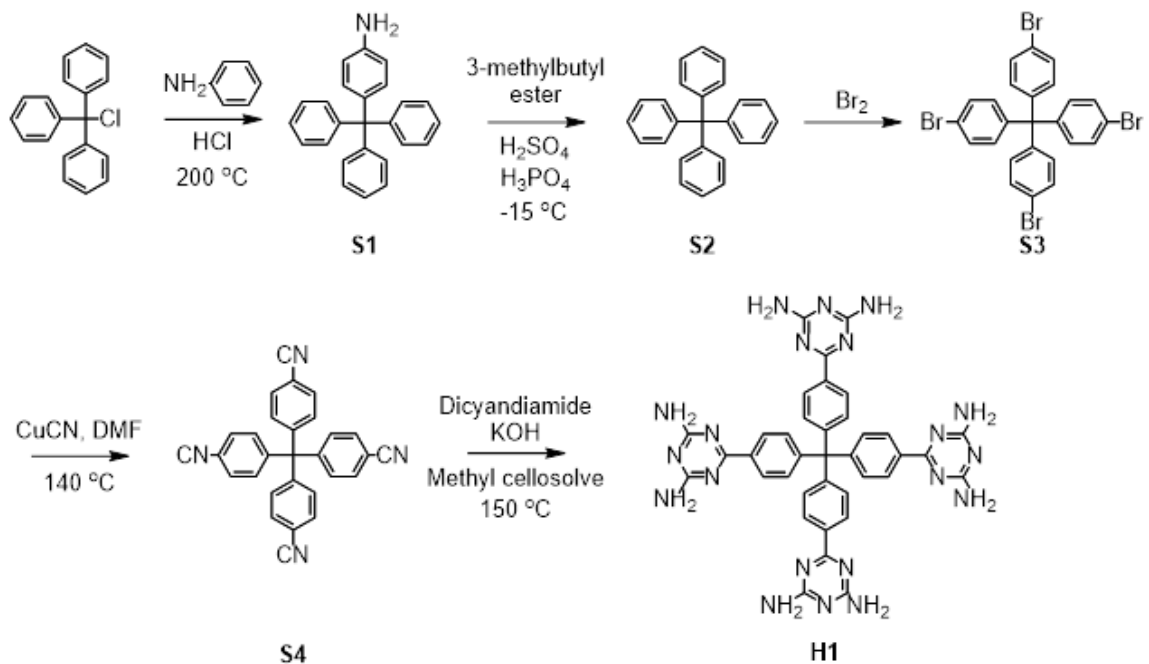
## 2.5 Appendices

### 2.5.1 General Methods

All chemical reagents and solvents were purchased from commercial suppliers, including Fisher Scientific, Sigma Aldrich, VWR, and were used as received. <sup>1</sup>H NMR spectra were recorded on either a Bruker AVIII 500 MHz spectrometer or a Bruker AVIII 600 MHz Spectrometer and referenced to residual solvent peaks. Single crystal diffraction data were collected on a Rigaku Xtalab mini II or a XtaLAB Synergy four-circle diffractometer (Dualflex HyPix detector). Vapor sorption measurements were performed on a Micromeritics FLEX 3.0 surface area analyzer at 297 K.

### 2.5.2 Synthetic Procedures

HOF-1 monomer is synthesized and crystallized based on the reported method.<sup>S208,</sup>



**Scheme S1.** Synthesis of telechelic polymer F127-MA<sub>2</sub>

**Synthesis of S1 (4-tritylaniline).**<sup>S1</sup> A mixture of trityl chloride (2.0 g, 7.2 mmol) and aniline (800 mg, 8.6 mmol) was heated to 200 °C for 20 min. Then, the mixture was cooled down to the room temperature (25 °C) with vigorous stirring. A solution of HCl (10 mL, 2.0M) and MeOH (10 mL) was added to the mixture. The mixture was allowed to reflux for another 10 min and cooled down to room temperature. The precipitate was filtered and washed with ethanol (200 mL) and dried to yield the product **S1** as a white powder (2.0 g, yield: 83%). <sup>1</sup>H NMR (500 MHz, DMSO-*d*<sub>6</sub>, 298 K): δ (ppm): 8.36 (s, 3H), 1.33 (s, 36H), 6.74 (d, *J* = 8.5 Hz, 2H), 6.45 (d, *J* = 9.0 Hz, 2H).

**Synthesis of S2 (tetraphenylmethane).**<sup>S1</sup> **S1** (2.0 g, 6.0 mmol) was dissolved in DMF (200 mL) and cooled down to -15 °C. Then sulfuric acid (4.1 g, 42.0 mmol) and 3-methylbutyl nitrite (1.4 g, 12.0 mmol) were added to the solution. The mixture was stirred for 1 h at -15 °C, followed by adding phosphonic acid (2.3 g, 34.7 mmol). The mixture was then heated at 50 °C for 5 h. The solid was filtered off and washed with DMF (200 mL), water, and ethanol to yield the product (1.8 g, yield: 94%) as a slightly yellow solid. <sup>1</sup>H NMR (DMSO-*d*<sub>6</sub>, 500 MHz, 298K) δ (ppm): 7.30 (t, 3H), 7.20 (t, 3H), 7.14 (d, *J* = 8.0 Hz, 6H).

**Synthesis of S3 (Tetrakis(4-bromophenyl)methane).**<sup>S2</sup> Liquid bromine (5.0 g, 97.4 mmol) was added dropwise to **S2** (2.0 g, 6.3 mmol) and stirred vigorously at room temperature for 6 h. Then, the mixture was poured into cold EtOH (200 mL, -78 °C). The resulting precipitate was filtered and washed with saturated aqueous NaHSO<sub>3</sub> solution (100 mL) 3 times and dried under vacuum to obtain the product as a white solid. (3.1 g, yield: 77%). <sup>1</sup>H NMR (DMSO-*d*<sub>6</sub>, 500 MHz, 298 K) δ (ppm): 7.53 (d, *J* = 7.5 Hz, 8H), 7.06 (d, *J* = 7.0 Hz, 8H).

**Synthesis of S4 (4 4' 4'' 4''' -tetracyanotetraphenylmethane).**<sup>S2</sup> **S3** (2.0 g, 3.1 mmol) and CuCN (1.4 g, 16.0 mmol) were dissolved in DMF (80 mL) and heated to 140 °C for 48 h under nitrogen atmosphere. Then, the solvent was removed under reduced pressure. The residue was extracted with CH<sub>2</sub>Cl<sub>2</sub> (150 mL × 3) and further washed with aqueous EDTA-4Na solution (100 mL × 3) and saturated NaCl solution (100 mL × 2). The organic layer was dried over anhydrous MgSO<sub>4</sub>. The solvent was removed under reduced pressure. The resulting crude product was further purified by silica gel column chromatography (CHCl<sub>3</sub>) to obtain the product as a white solid (0.38 g, yield: 29%). <sup>1</sup>H NMR (DMSO-*d*<sub>6</sub>, 500 MHz, 298 K) δ (ppm): 7.84 (d, *J* = 8.5 Hz, 8H), 7.43 (d, *J* = 8.0 Hz, 8H).

**Synthesis of H1 (4 4' 4'' 4''' -tetra(4,6-diamino-s-triazin-2-yl)tetraphenylmethane).**<sup>S2</sup> **S4** (1.0 g, 2.4 mmol), dicyandiamide (1.0 g, 12.0 mmol), and KOH (85%, 2.0 mmol) were added to a 100 round bottom flask with 30 mL 2-methoxyethanol and heated to 150 °C for 24 h under N<sub>2</sub> atmosphere. The mixture was cooled to room temperature and poured into MeOH (125 mL). The precipitate was filtered and washed with hot water (~95 °C, 100 mL) and MeOH (~50 °C, 100 mL), respectively. The residue was dried under vacuum to yield the product as a white solid (1.2 g, yield: 66%). <sup>1</sup>H NMR (DMSO-*d*<sub>6</sub>, 500 MHz, 298 K) δ (ppm): 8.17 (d, *J* = 8.5 Hz, 8H), 7.36 (d, *J* = 8.5 Hz, 8H), 6.72 (s, 16H).

**Crystallization of HOF-1.**<sup>S2</sup> The HOF-1 monomer (100.0 mg, 0.13 mmol) was dissolved in the mixture of 1,4-dioxane (0.75 mL) and formic acid (1 mL). The solution was filtered and put into a 4mL-vial. The vial was placed into a 20 mL-vial with 1,4-dioxane and kept at room temperature. Transparent, needle-like crystals of HOF-1 were obtained after 10 d.

**Synthesize of 1-(1-anilinoethyl)-2-pyrrolidinone (AEP).**<sup>S212</sup> Aniline (465.0 mg, 5.0 mmol), N-vinyl-2-pyrrolidone (555.0 mg, 5.0 mmol), and formic acid (5.0 mg, 0.11

mmol) were added to a round bottom flask with 100 mL n-hexane. The mixture is stirred 25 °C for 12 h. Then, all of the solvent was removed under reduced pressure. Needle-like white crystals (958.9 mg, 4.7 mmol) were obtained in 94% yield. <sup>1</sup>H NMR (DMSO-*d*<sub>6</sub>, 500 MHz, 298 K) δ (ppm): 7.07 (s, 2H), 6.19 (m, 1H), 5.41 (s, 1H), 3.26 (s, 1H), 3.30 (s, 1H), 2.21 (m, 2H), 1.79 (m, 2H), 1.33 (s, 3H).

### 2.5.3 Single-crystal X-ray data

Single-crystal X-ray diffraction data of HOF-1·PhNH<sub>2</sub>, HOF-1·Tol, HOF-1·VP, and AEP were collected on a Rigaku Xtalab mini II at 293 K with Mo *K* $\alpha$  radiation ( $\lambda$  = 0.71073 Å). X-ray diffraction data of HOF-1·*o*-Tld, HOF-1·*m*-Tld, and HOF-1·*p*-Tld were collected on a Rigaku XtaLAB Synergy Dualflex single crystal X-ray diffractometer at 100 K with Cu *K* $\alpha$  radiation ( $\lambda$  = 1.54184 Å). Multi-scan absorption corrections were applied in each case. The structures were solved by SHELXT and refined with SHELXL using the program Olex2. All non-hydrogen atoms of the monomers were refined anisotropically. The hydrogen atoms were modeled at geometrically constrained positions and refined using the riding model. Details of each crystal structure will be discussed in the section below. CCDC contains the supplementary crystallographic data, which can be accessed through the Cambridge Crystallographic Data Centre at <https://www.ccdc.cam.ac.uk/>.

**Table S1.** Single-crystal X-ray diffraction data of HOF-1·PhNH<sub>2</sub>, HOF-1·Tol, HOF-1·VP, and AEP

Identification code	HOF-1·PhNH <sub>2</sub>	HOF-1·Tol	HOF-1·VP	AEP
Empirical formula	C <sub>61</sub> H <sub>60</sub> N <sub>24</sub>	C <sub>65</sub> H <sub>64</sub> N <sub>20</sub>	C <sub>73</sub> H <sub>80</sub> N <sub>12</sub> O <sub>4</sub>	C <sub>12</sub> H <sub>16</sub> N <sub>2</sub> O
Formula weight	1129.33	1125.36	1189.49	204.27
Temperature/K	293(2)	293(2)	293(2)	293(2)
Crystal system	tetragonal	tetragonal	tetragonal	tetragonal
Space group	I-4	I-4	I-4	P42/n
<i>a</i> /Å	20.3468(10)	20.1754(6)	20.3140(7)	18.7881(12)
<i>b</i> /Å	20.3468(10)	20.1754(6)	20.3140(7)	18.7881(12)
<i>c</i> /Å	7.1118(6)	7.2479(4)	7.3565(4)	6.5508(7)
$\alpha$ /°	90	90	90	90
$\beta$ /°	90	90	90	90

$\gamma/^\circ$	90	90	90	90
Volume/ $\text{\AA}^3$	2944.2(4)	2950.2(2)	3035.7(3)	2312.4(4)
<i>Z</i>	2	2	2	8
$\rho_{\text{calc}}/\text{cm}^3$	1.274	1.267	1.301	1.173
$\mu/\text{mm}^{-1}$	0.082	0.08	0.083	0.076
<i>F</i> (000)	1188	1188	1268	880
Crystal size/ $\text{mm}^3$	$0.5 \times 0.1 \times 0.1$	$0.6 \times 0.4 \times 0.4$	$0.5 \times 0.15 \times 0.15$	$0.5 \times 0.4 \times 0.4$
Radiation	MoK $\alpha$ ( $\lambda = 0.71073$ )	MoK $\alpha$ ( $\lambda = 0.71073$ )	MoK $\alpha$ ( $\lambda = 0.71073$ )	MoK $\alpha$ ( $\lambda = 0.71073$ )
$2\theta$ range for data collection/ $^\circ$	5.664 to 61.142	5.712 to 56.538	5.89 to 52.738	4.336 to 52.72
Index ranges	$-13 \leq h \leq 28, -28 \leq k \leq 28, -9 \leq l \leq 9$	$-26 \leq h \leq 26, -25 \leq k \leq 25, -8 \leq l \leq 9$	$-25 \leq h \leq 20, -25 \leq k \leq 24, -9 \leq l \leq 8$	$-22 \leq h \leq 23, -15 \leq k \leq 22, -7 \leq l \leq 8$
Reflections collected	9294	9484	9434	8638
Independent reflections	3894 [ $R_{\text{int}} = 0.0362, R_{\text{sigma}} = 0.0677$ ]	3381 [ $R_{\text{int}} = 0.0349, R_{\text{sigma}} = 0.0651$ ]	3058 [ $R_{\text{int}} = 0.0557, R_{\text{sigma}} = 0.0702$ ]	2336 [ $R_{\text{int}} = 0.0597, R_{\text{sigma}} = 0.0692$ ]
Data/restraints/parameters	3894/93/180	3381/241/180	3058/217/201	2336/0/137
Goodness-of-fit on $F^2$	1.061	1.02	1.007	0.962
Final <i>R</i> indexes [ $I \geq 2\sigma(I)$ ]	$R_1 = 0.0798, wR_2 = 0.1633$	$R_1 = 0.0648, wR_2 = 0.1672$	$R_1 = 0.0800, wR_2 = 0.2041$	$R_1 = 0.0798, wR_2 = 0.1879$
Final <i>R</i> indexes [all data]	$R_1 = 0.1222, wR_2 = 0.1856$	$R_1 = 0.1127, wR_2 = 0.1926$	$R_1 = 0.1288, wR_2 = 0.2363$	$R_1 = 0.1851, wR_2 = 0.2327$
Largest diff. peak/hole / $e \text{\AA}^{-3}$	0.28/-0.24	0.22/-0.26	0.27/-0.31	0.42/-0.16

**Table S2.** Single crystal X-ray diffraction data of HOF-1·*o*-Tld, HOF-1·*m*-Tld, and HOF-1·*p*-Tld

Identification code	HOF-1· <i>o</i> -Tld	HOF-1· <i>m</i> -Tld	HOF-1· <i>p</i> -Tld
Empirical formula	C <sub>65</sub> H <sub>68</sub> N <sub>24</sub>	C <sub>65</sub> H <sub>68</sub> N <sub>24</sub>	C <sub>65</sub> H <sub>68</sub> N <sub>24</sub>
Formula weight	1185.43	1185.43	1185.43
Temperature/K	100.00(10)	99.99(10)	100.15
Crystal system	tetragonal	tetragonal	tetragonal
Space group	I-4	I-4	I-4
<i>a</i> /Å	20.2713(4)	20.1198(3)	20.2017(4)
<i>b</i> /Å	20.2713(4)	20.1198(3)	20.2017(4)
<i>c</i> /Å	7.1255(2)	7.20870(10)	7.1518(2)
<i>α</i> /°	90	90	90
<i>β</i> /°	90	90	90
<i>γ</i> /°	90	90	90
Volume/Å <sup>3</sup>	2928.05(14)	2918.13(10)	2918.71(14)
<i>Z</i>	2	2	2
$\rho_{\text{calc}}$ /cm <sup>3</sup>	1.345	1.349	1.349
$\mu$ /mm <sup>-1</sup>	0.686	0.688	0.688
<i>F</i> (000)	1252	1252	1252
Crystal size/mm <sup>3</sup>	0.7 × 0.2 × 0.2	0.4 × 0.05 × 0.04	0.39 × 0.07 × 0.05
Radiation	Cu K $\alpha$ ( $\lambda$ = 1.54184)	Cu K $\alpha$ ( $\lambda$ = 1.54184)	Cu K $\alpha$ ( $\lambda$ = 1.54184)
2 $\theta$ range for data collection/°	6.166 to 159.048	6.212 to 154.018	6.188 to 159.97
Index ranges	-25 ≤ <i>h</i> ≤ 24, -19 ≤ <i>k</i> ≤ 25, -9 ≤ <i>l</i> ≤ 9	-25 ≤ <i>h</i> ≤ 23, -25 ≤ <i>k</i> ≤ 25, -8 ≤ <i>l</i> ≤ 9	-24 ≤ <i>h</i> ≤ 25, -25 ≤ <i>k</i> ≤ 22, -8 ≤ <i>l</i> ≤ 8
Reflections collected	18085	30422	18275
Independent reflections	3151 [ <i>R</i> <sub>int</sub> = 0.0660, <i>R</i> <sub>sigma</sub> = 0.0399]	3002 [ <i>R</i> <sub>int</sub> = 0.0886, <i>R</i> <sub>sigma</sub> = 0.0368]	3126 [ <i>R</i> <sub>int</sub> = 0.0727, <i>R</i> <sub>sigma</sub> = 0.0468]

Data/restraints/parameters	3151/120/251	3002/85/189	3126/0/202
Goodness-of-fit on $F^2$	1.057	1.066	1.064
Final $R$ indexes [ $I \geq 2\sigma$ (I)]	$R_1 = 0.0695$ , $wR_2 = 0.1750$	$R_1 = 0.0754$ , $wR_2 = 0.2173$	$R_1 = 0.0578$ , $wR_2 = 0.1650$
Final $R$ indexes [all data]	$R_1 = 0.0921$ , $wR_2 = 0.1974$	$R_1 = 0.0831$ , $wR_2 = 0.2288$	$R_1 = 0.0639$ , $wR_2 = 0.1716$
Largest diff. peak/hole / e $\text{\AA}^{-3}$	0.24/-0.31	0.56/-0.45	0.37/-0.37

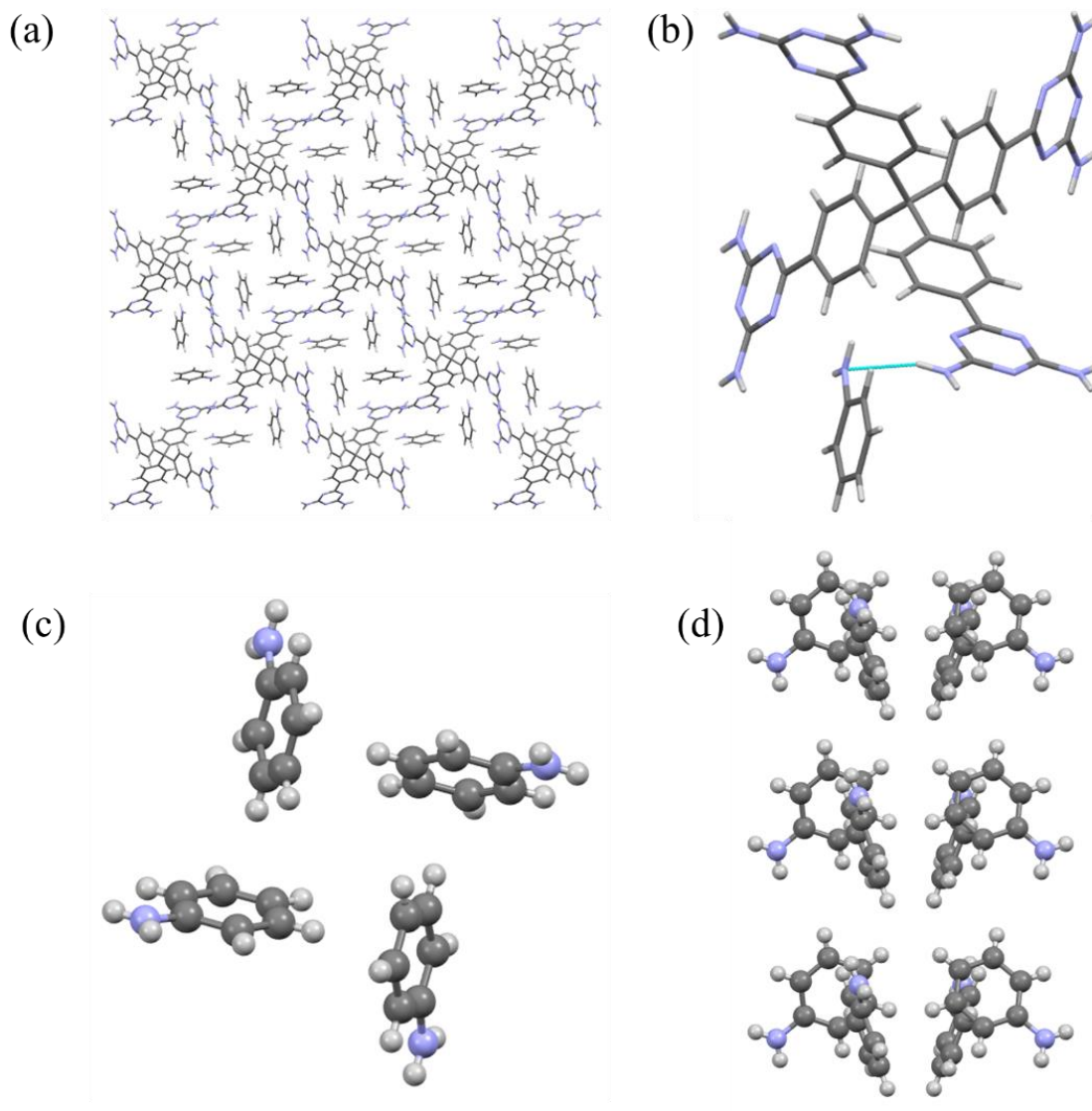


**Figure S1.** (a) The  $2 \times 2 \times 2$  packing of HOF-1-PhNH<sub>2</sub> viewed along the c-axis. (b) The hydrogen bond between HOF-1 and aniline. (c) The tetramer assembly of PhNH<sub>2</sub> in the channel of HOF-1 viewed along the c-axis. (d) The interlayer stacking of tetramer assembly of PhNH<sub>2</sub> in the channel of HOF-1 viewed along the a-axis.



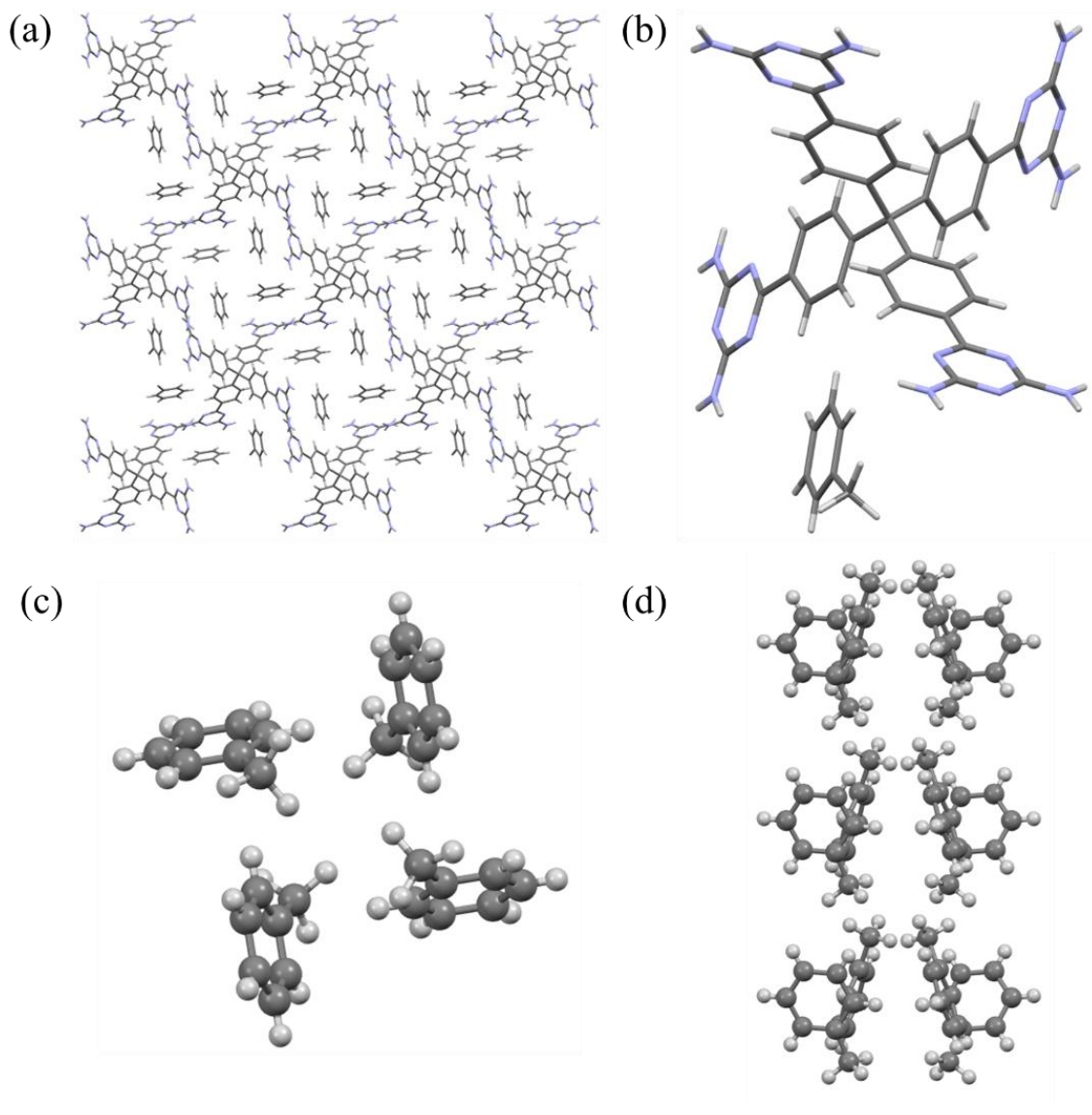


**Figure S2.** (a) The  $2 \times 2 \times 2$  packing of HOF-1·Tol viewed along the c-axis. (b) The hydrogen bond between HOF-1 and toluene. (c) The tetramer assembly of toluene in the channel of HOF-1 viewed along the c-axis. (d) The interlayer stacking of tetramer assembly of toluene in the channel of HOF-1 viewed along the a-axis.

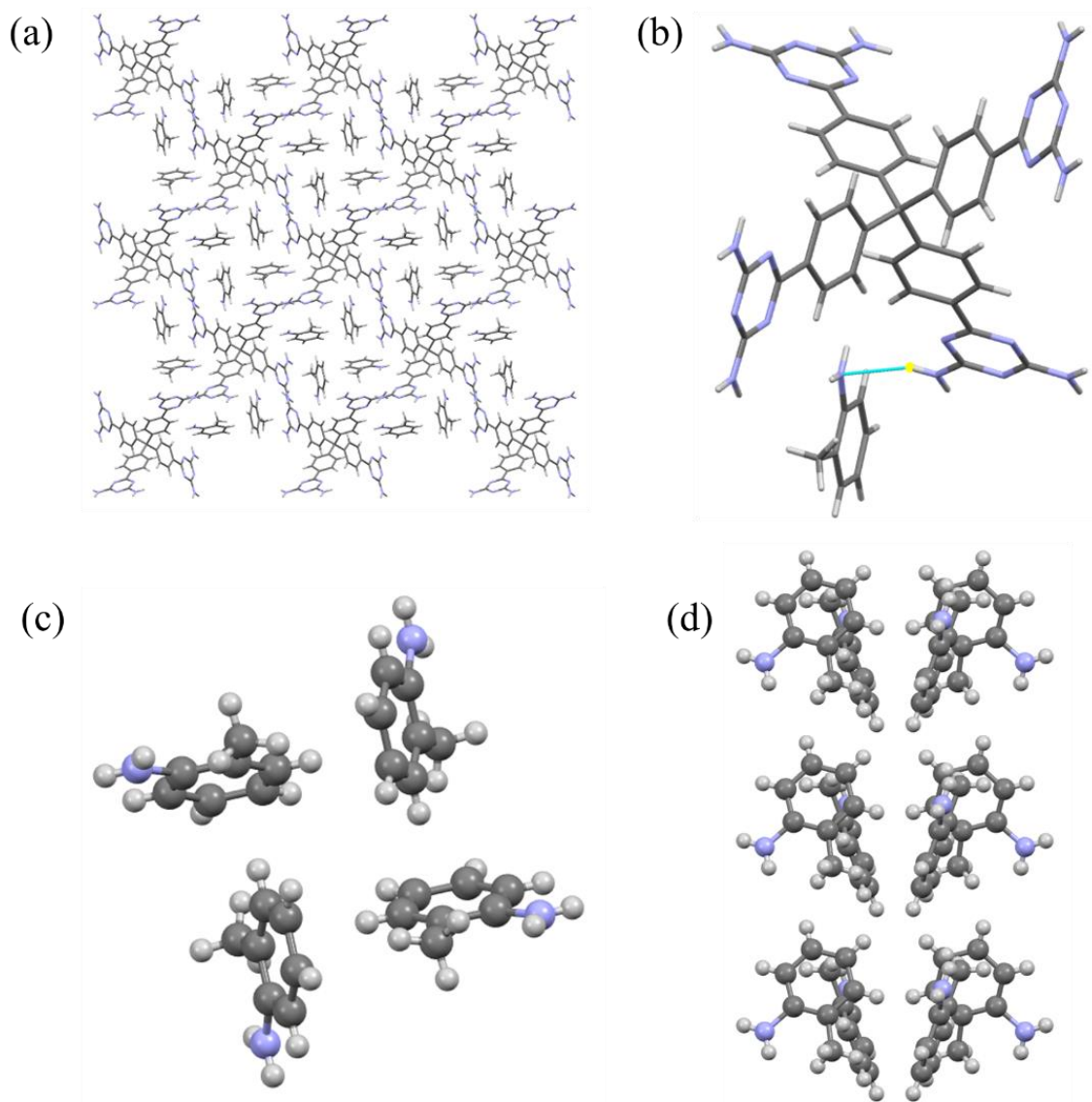


**Figure S3.** (a) The  $2 \times 2 \times 2$  packing of HOF-1·*o*-Tld part 1 viewing along the *c*-axis. (b) The hydrogen bond between HOF-1 and *o*-Tld. (c) The tetramer assembly of *o*-Tld in the channel HOF-1 view along the *c*-axis. (d) The interlayer stacking of tetramer assembly of *o*-Tld in the channel HOF-1 view along the *a*-axis of HOF-1·*o*-Tld part 1.

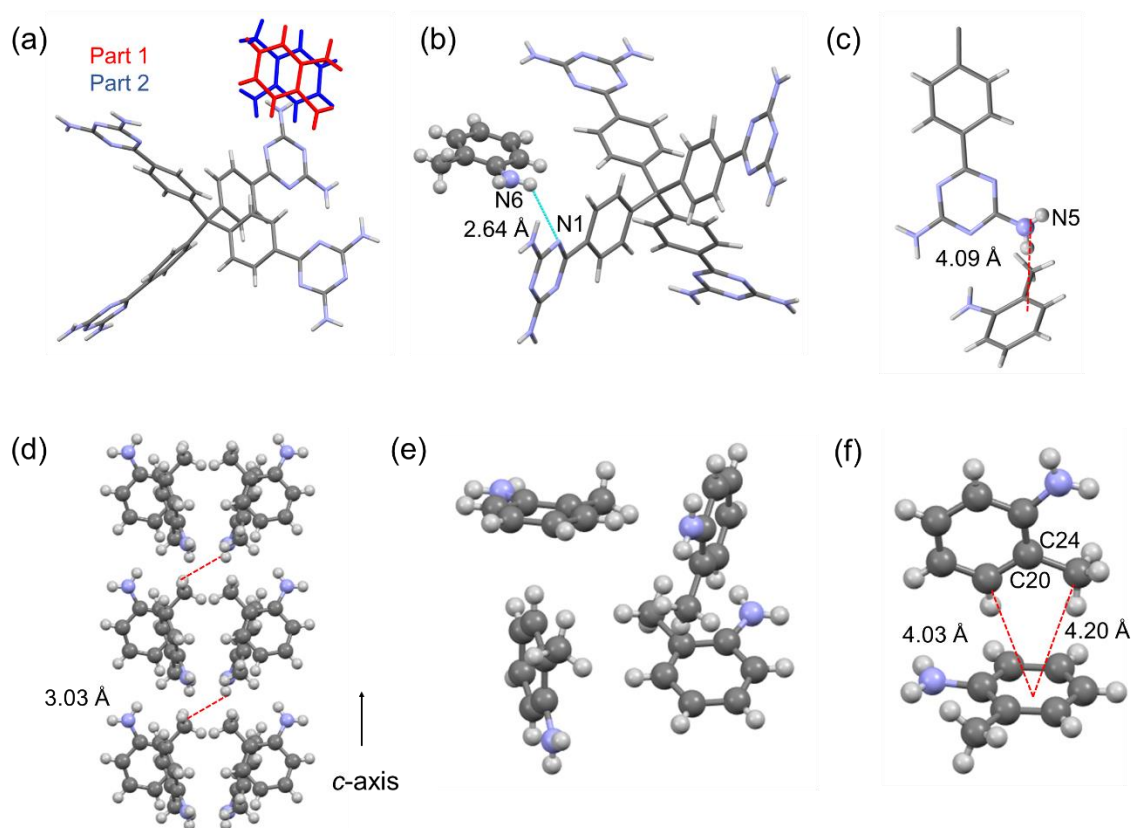


**Figure S4.** (a) The overlapped structure of part 1 and part 2 of HOF-1·*o*-Tld. (b) The hydrogen bond and (c) The N-H••• $\pi$  interaction between HOF-1 and *o*-Tld of HOF-1·*o*-Tld part 2. (d) The interlayer stacking of tetramer assembly of *o*-Tld in the channel of HOF-1 viewed along the *a*-axis of HOF-1·*o*-Tld part 2. (e) The tetramer assembly of *o*-Tld in the channel of HOF-1 viewed along the *c*-axis. (f) The double C-H••• $\pi$  interactions between *o*-Tld molecules in tetrameric assembly of HOF-1·*o*-Tld part 2.

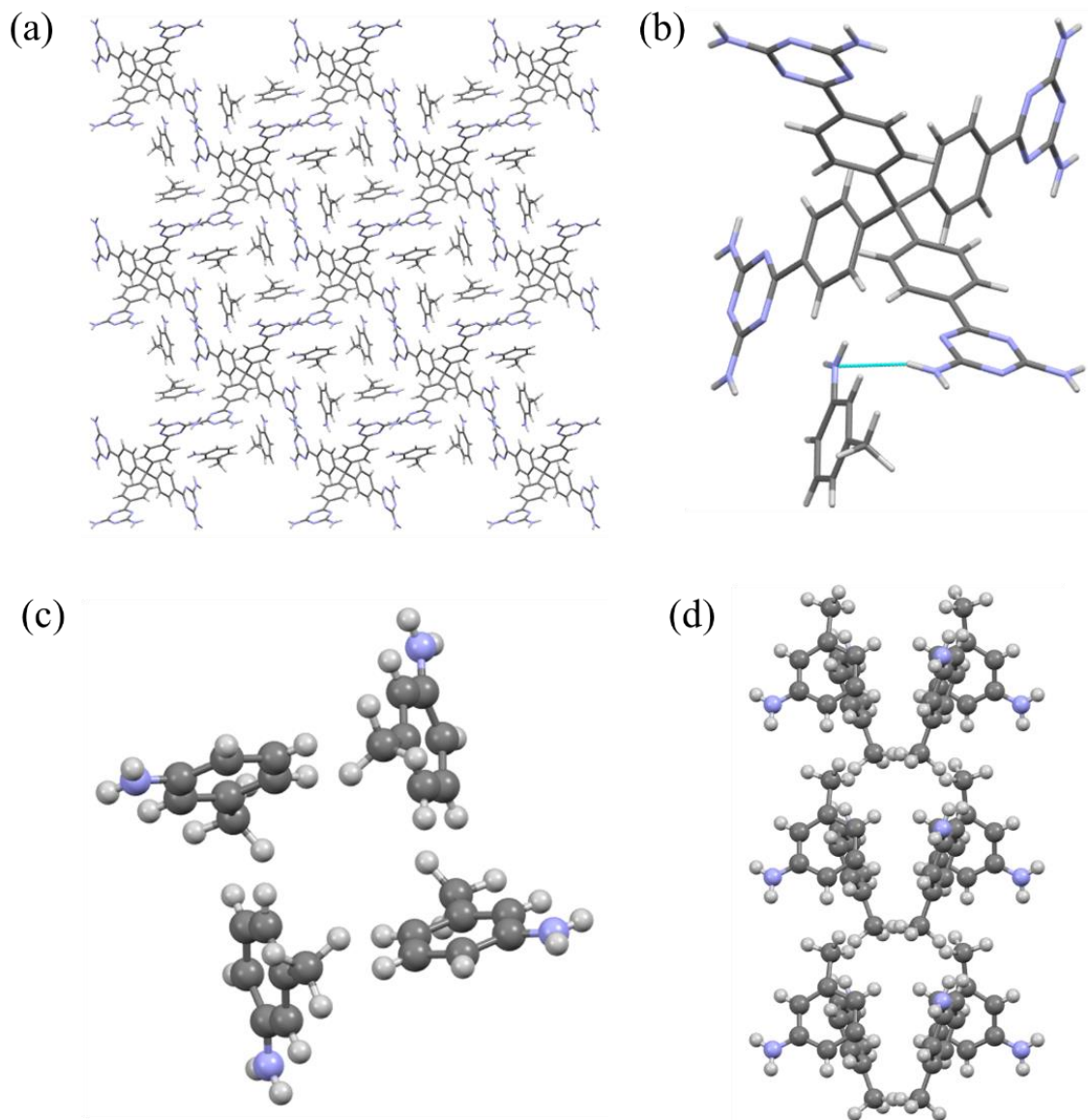


**Figure S5.** (a) The  $2\times 2\times 2$  packing of HOF-1·*m*-Tld viewed along the *c*-axis. (b) The hydrogen bond between HOF-1 and *m*-Tld. (c) The tetramer assembly of *m*-Tld in the channel HOF-1 view along the *c*-axis. (d) The interlayer stacking of tetramer assembly of *m*-Tld in the channel HOF-1 view along the *a*-axis.

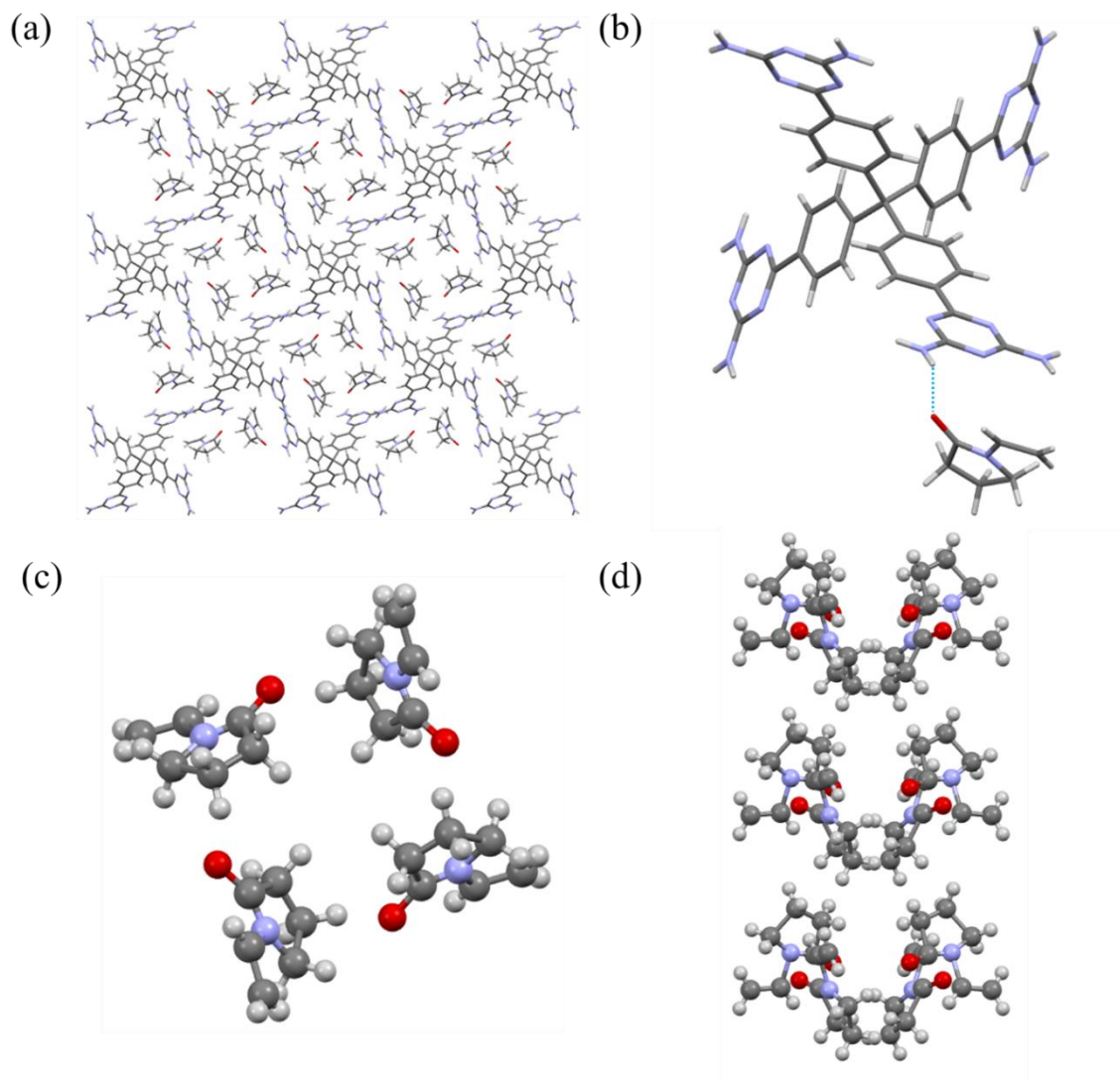


**Figure S6.** (a) The  $2 \times 2 \times 2$  packing of HOF-1·*p*-Tld viewed along the *c*-axis. (b) The hydrogen bond between HOF-1 and *p*-Tld. (c) The tetramer assembly of *p*-Tld in the channel HOF-1 view along *c*-axis. (d) The interlayer stacking of tetramer assembly of *p*-Tld in the channel HOF-1 view along *a*-axis.

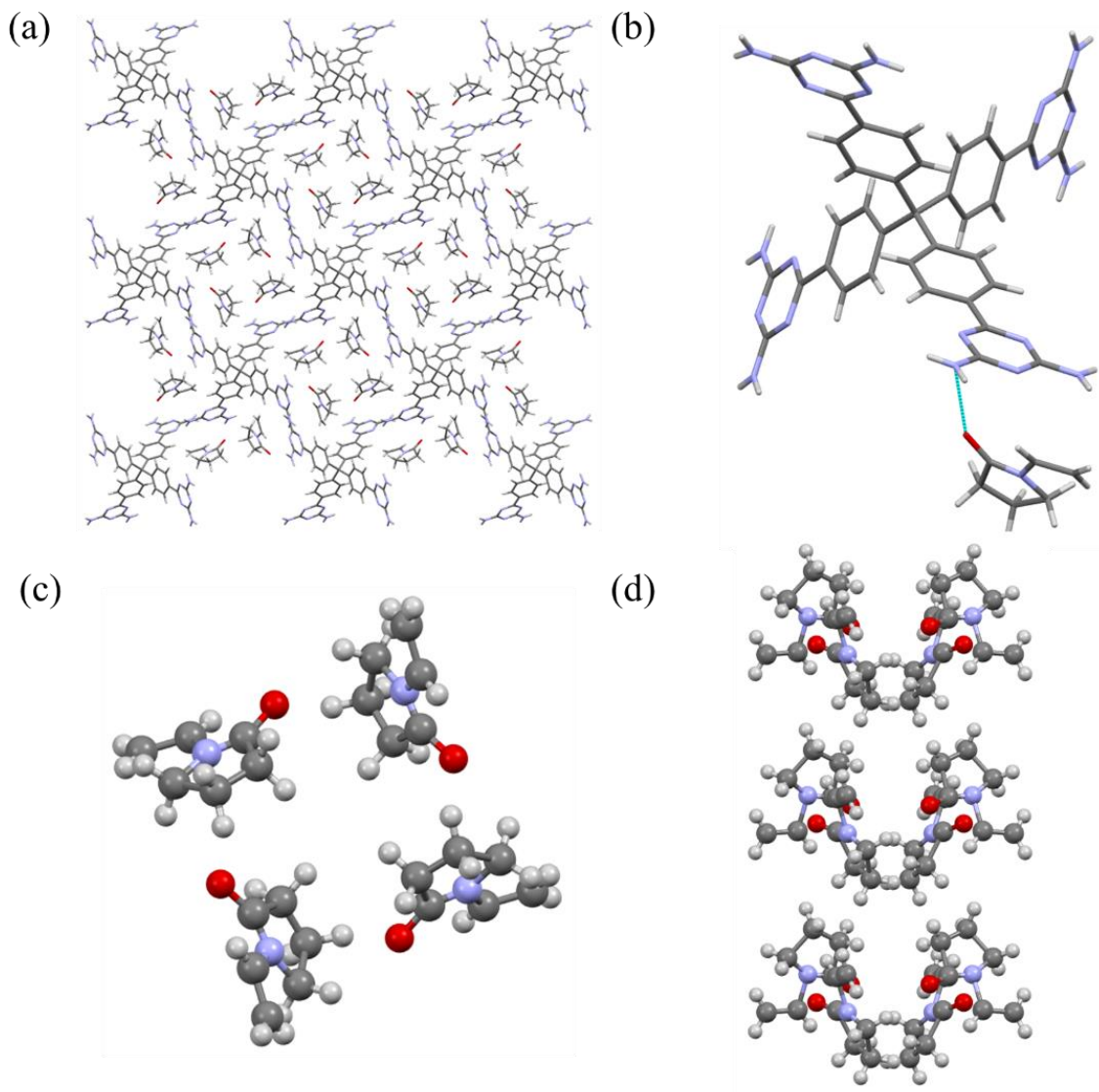


**Figure S7.** (a) The  $2 \times 2 \times 2$  packing of HOF-1·VP viewed along the  $c$ -axis. (b) The hydrogen bond between HOF-1 and VP. (c) The tetramer assembly of VP in the channel HOF-1 view along the  $c$ -axis. (d) The interlayer stacking of tetramer assembly of VP in the channel HOF-1 view along  $a$ -axis.

## 2.5.4 $^1\text{H}$ NMR spectra

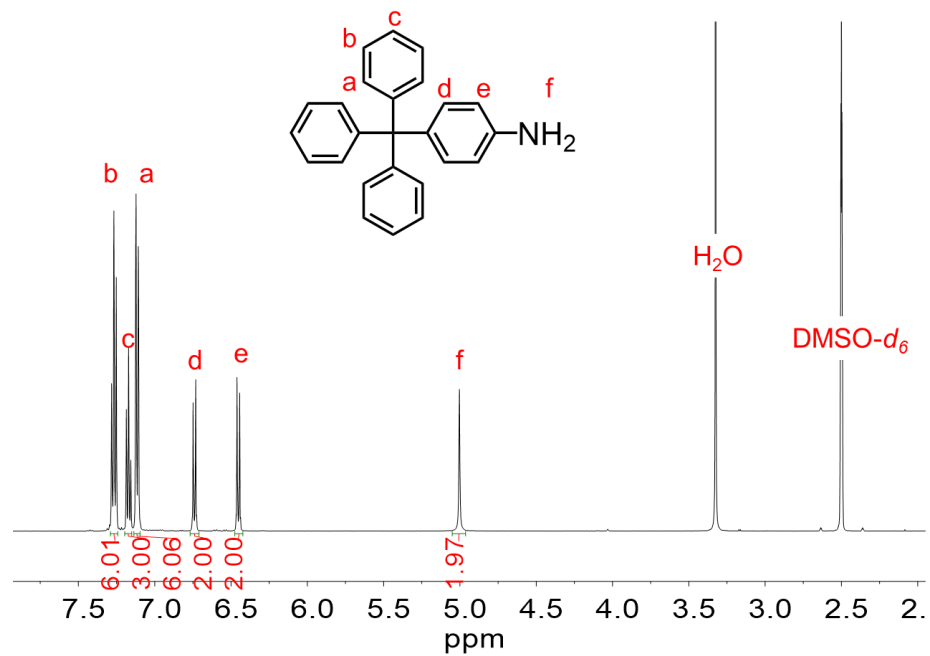


**Figure S8.**  $^1\text{H}$  NMR spectrum of **S1** in  $\text{DMSO-}d_6$  (500 MHz) recorded at 298 K.

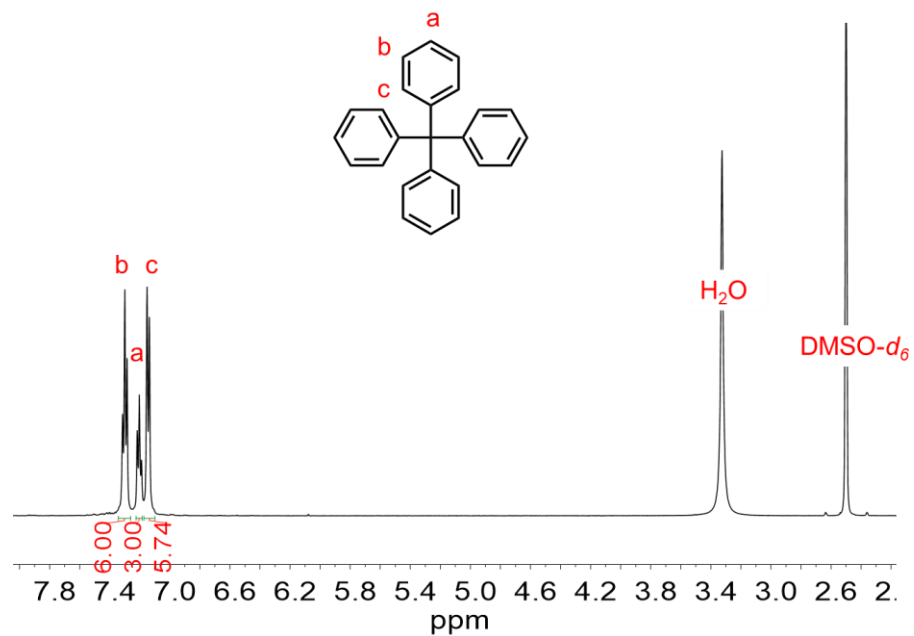


**Figure S9.**  $^1\text{H}$  NMR spectrum of **S2** in  $\text{DMSO-}d_6$  (500 MHz) recorded at 298 K.

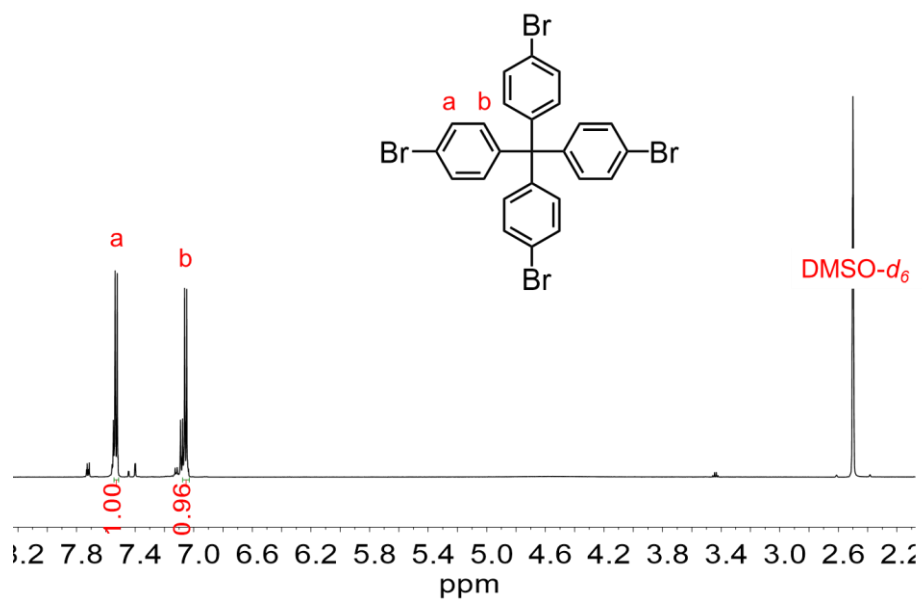


**Figure S10.** <sup>1</sup>H NMR spectrum of **S3** in DMSO-*d*<sub>6</sub> (500 MHz) recorded at 298 K.

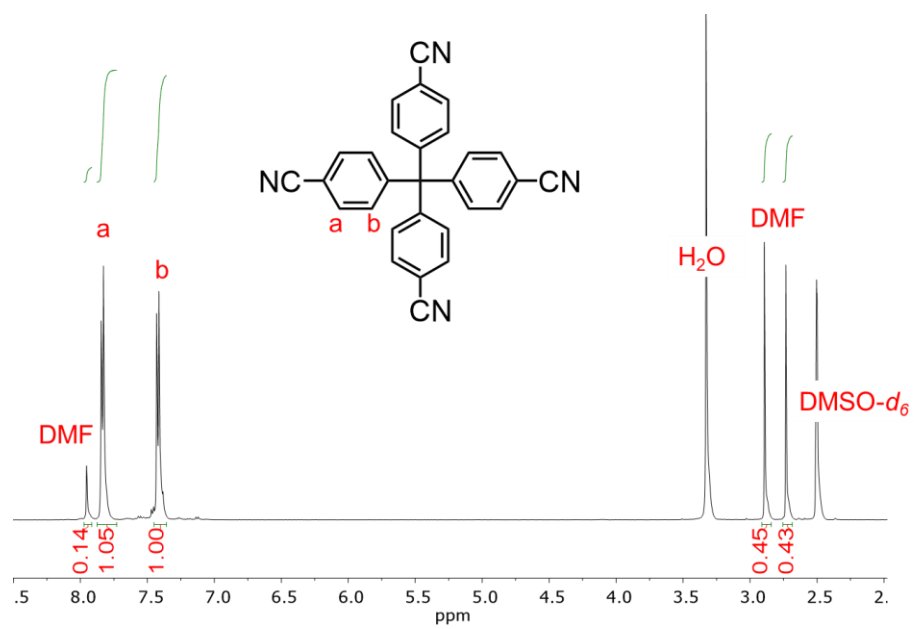


**Figure S11.** <sup>1</sup>H NMR spectrum of **S4** in DMSO-*d*<sub>6</sub> (500 MHz) recorded at 298 K.



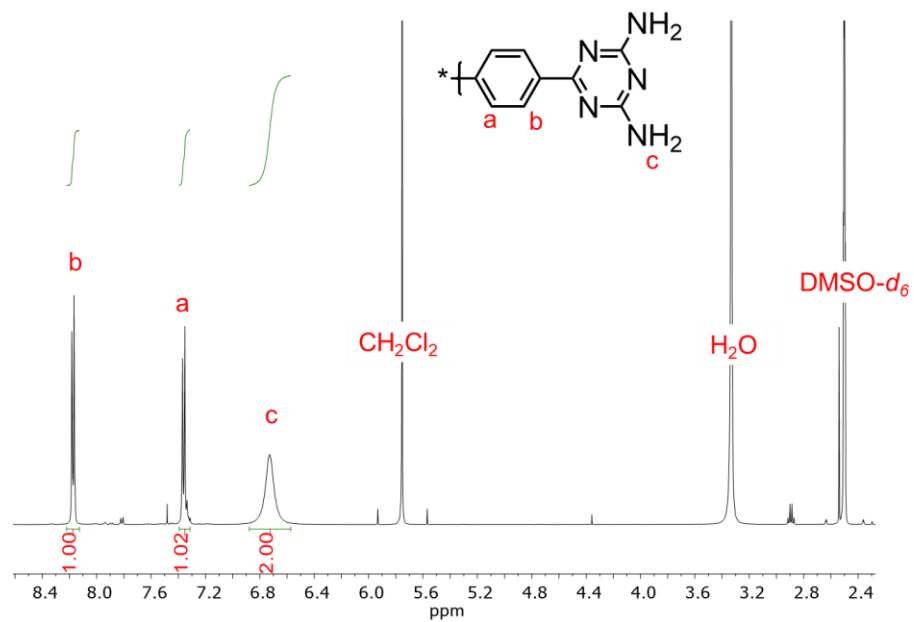


**Figure S12.**  $^1\text{H}$  NMR spectrum of **H1** in  $\text{DMSO-}d_6$  (500 MHz) recorded at 298 K.

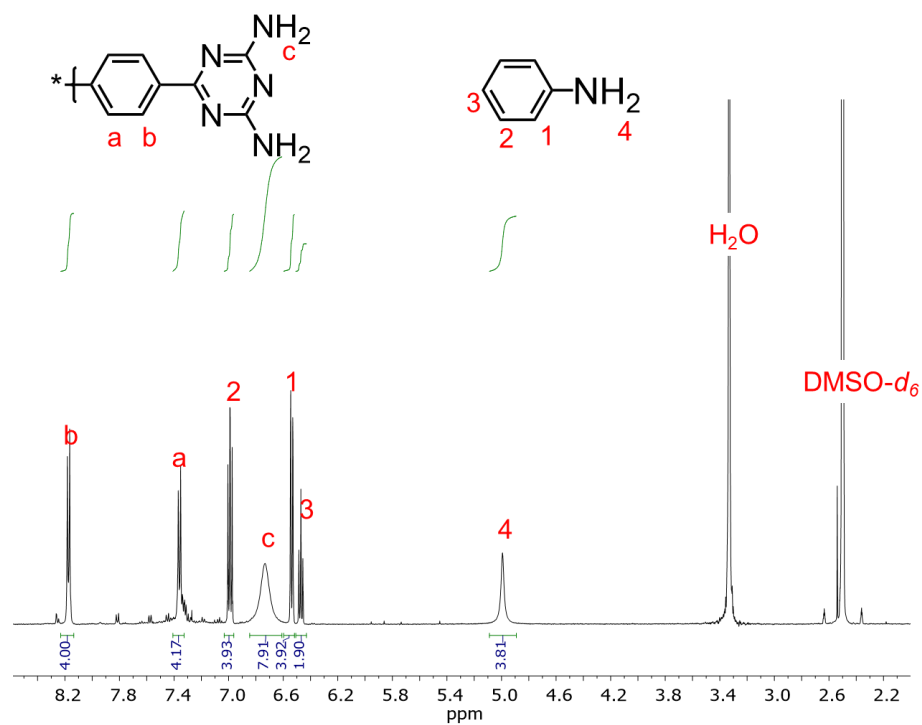


**Figure S13.**  $^1\text{H}$  NMR spectrum of  $\text{HOF-1} \cdot \text{PhNH}_2$  in  $\text{DMSO-}d_6$  (500 MHz) recorded at 298 K. **H1**:  $\text{PhNH}_2$  was measured as 1:3.9.

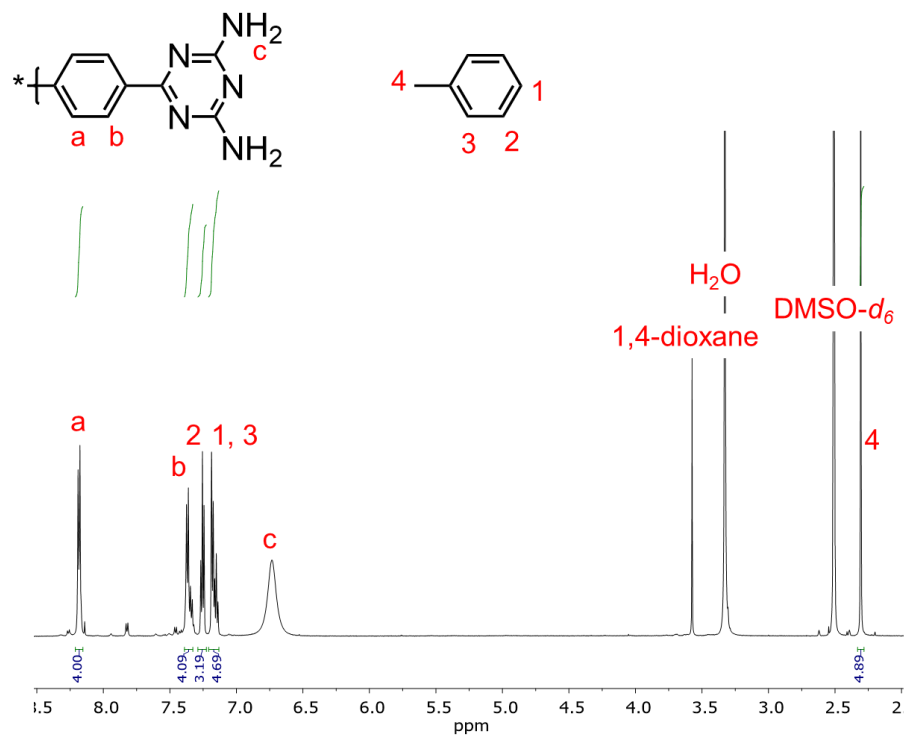


**Figure S14.**  $^1\text{H}$  NMR spectrum of HOF-1·Tol in  $\text{DMSO-}d_6$  (500 MHz) recorded at 298 K.

**H1:** toluene was measured as 1:3.2.

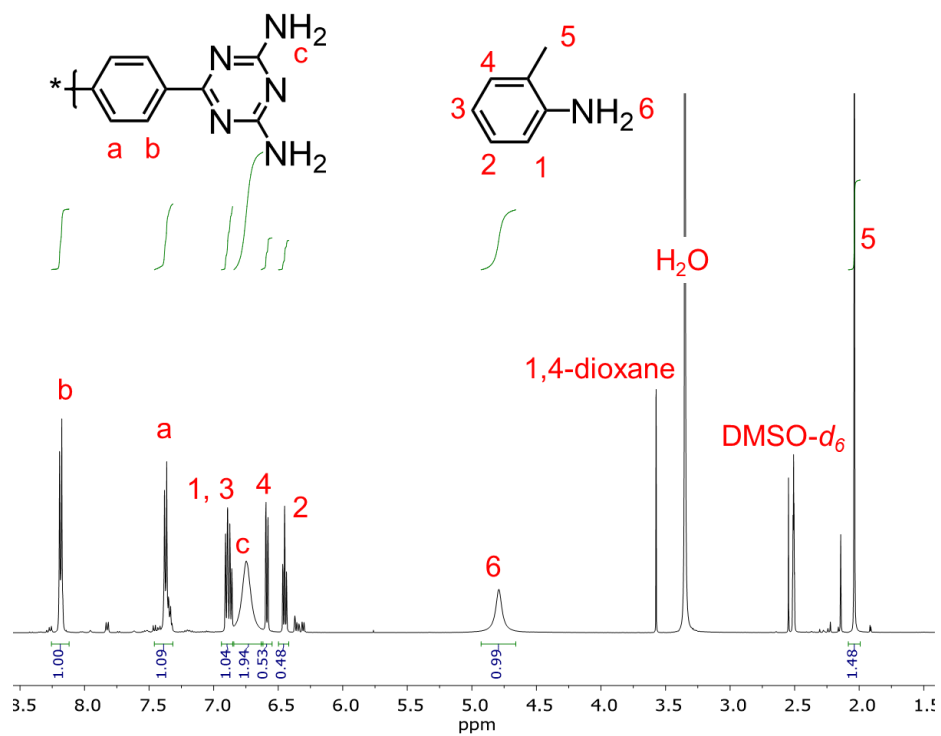


**Figure S15.**  $^1\text{H}$  NMR spectrum of HOF-1·*o*-Tld in  $\text{DMSO-}d_6$  (500 MHz) recorded at 298 K. **H1:** *o*-Tld was measured as 1:4.0.

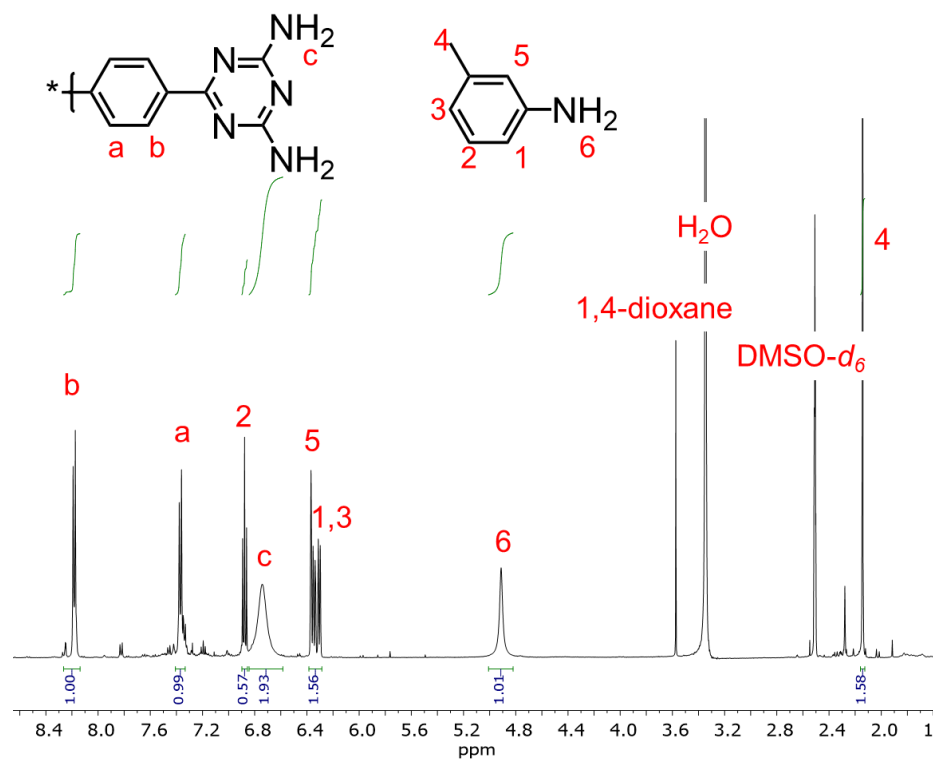


**Figure S16.** <sup>1</sup>H NMR spectrum of HOF-1·*m*-Tld in DMSO-*d*<sub>6</sub> (500 MHz) recorded at 298 K. **H1:** *m*-Tld was measured as 1: 4.2.

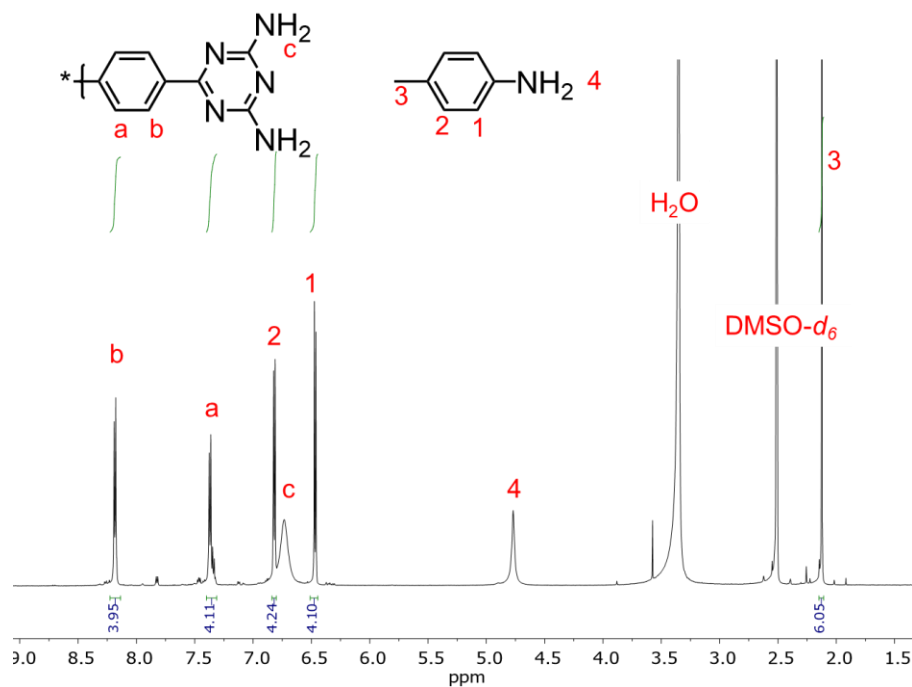


**Figure S17.** <sup>1</sup>H NMR spectrum of HOF-1-*p*-Tld in DMSO-*d*<sub>6</sub> (500 MHz) recorded at 298 K. **H1:** *p*-Tld was measured as 1: 4.1.

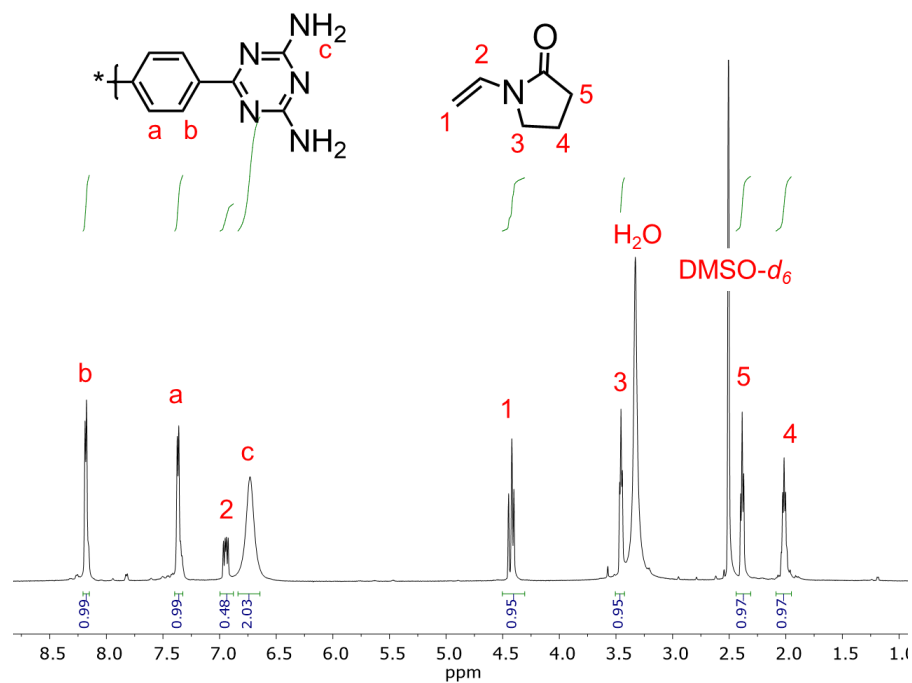


**Figure S18.** <sup>1</sup>H NMR spectrum of HOF-1-VP in DMSO-*d*<sub>6</sub> (500 MHz) recorded at 298 K. **H1:** VP was measured as 1: 4.0.

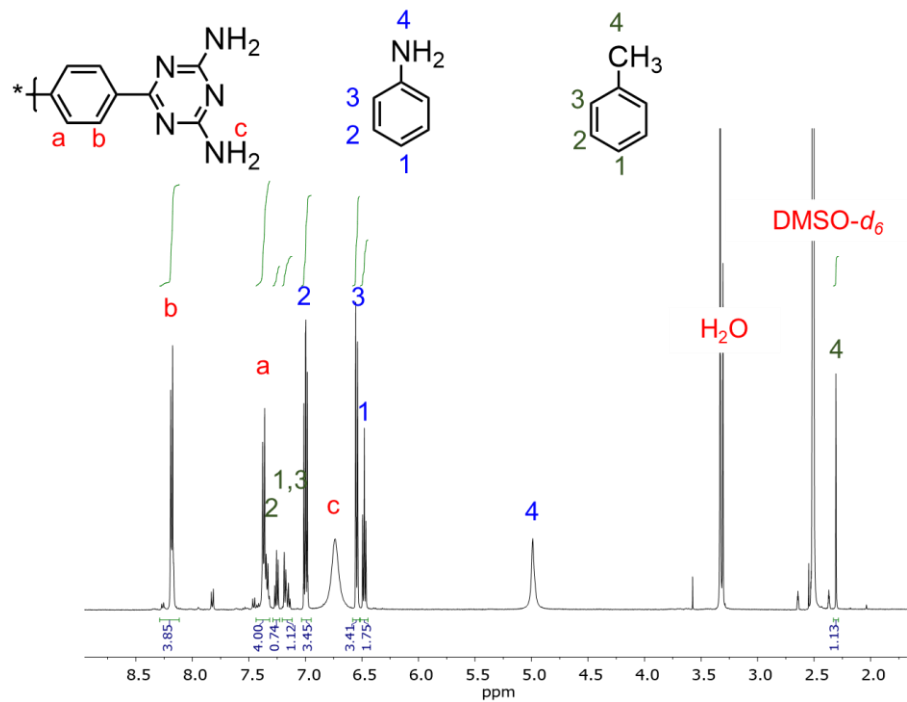


**Figure S19.**  $^1\text{H}$  NMR spectrum of HOF-1 after co-adsorption of aniline and toluene in  $\text{DMSO-}d_6$  (500 MHz) recorded at 298 K. **H1**:aniline:toluene measured as 1:0.7:3.4.

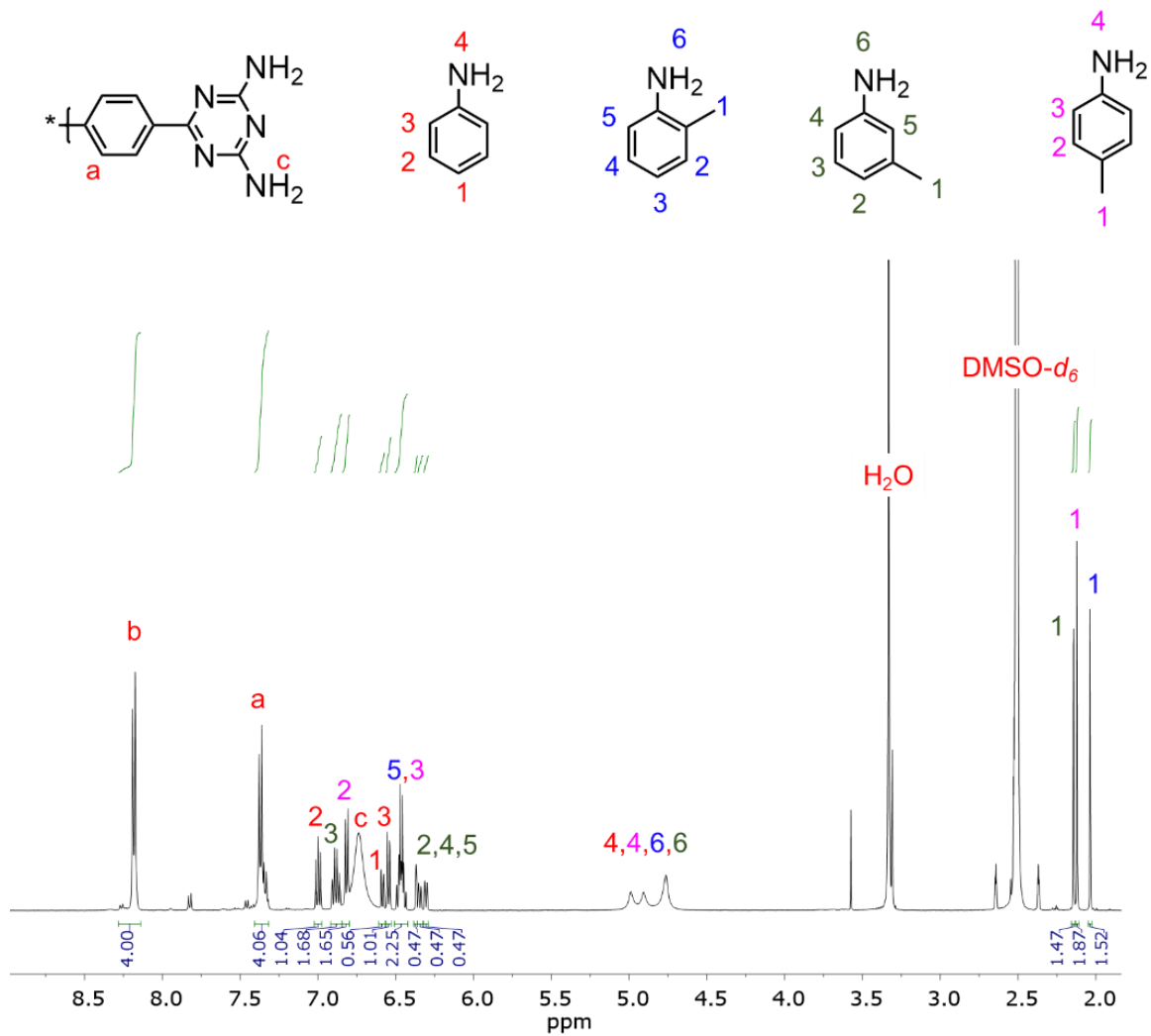


**Figure S20.** <sup>1</sup>H NMR spectrum of HOF-1 after co-adsorption of aniline and *o*-,*m*-,*p*-toluidine isomers in DMSO-*d*<sub>6</sub> (500 MHz) recorded at 298 K. **H1**:aniline:*o*-toluidine:*m*-toluidine:*p*-toluidine = 1.0:1.0:1.0:1.0:1.2.

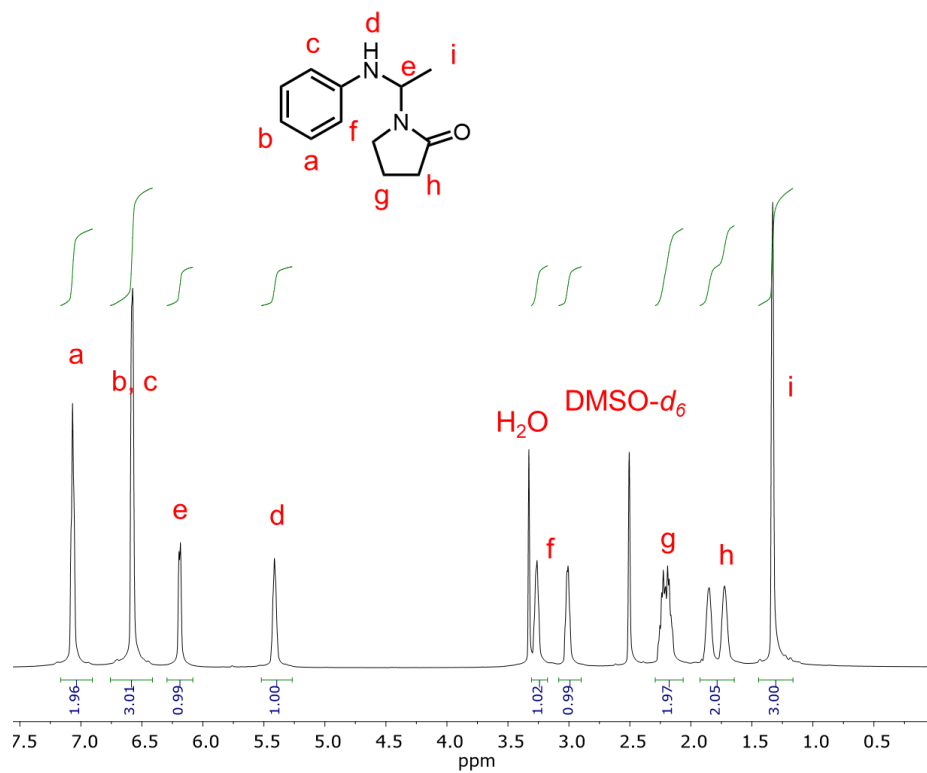


**Figure S21.** <sup>1</sup>H NMR spectrum of 1-(1-(phenylamino)ethyl)pyrrolidine-2-one (AEP) in DMSO-*d*<sub>6</sub> (500 MHz) recorded at 298 K.



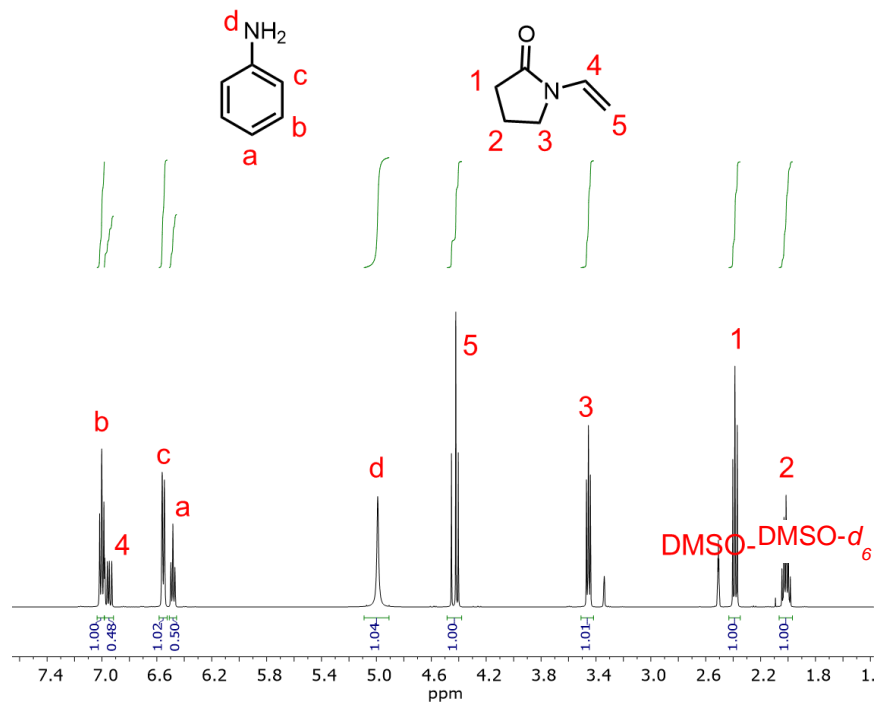


**Figure S22.**  $^1\text{H}$  NMR spectrum of aniline and VP 1:1 mixture after adsorption in  $\text{DMSO-}d_6$  (500 MHz) recorded at 298 K. No AEP was detected without the acid catalyst.

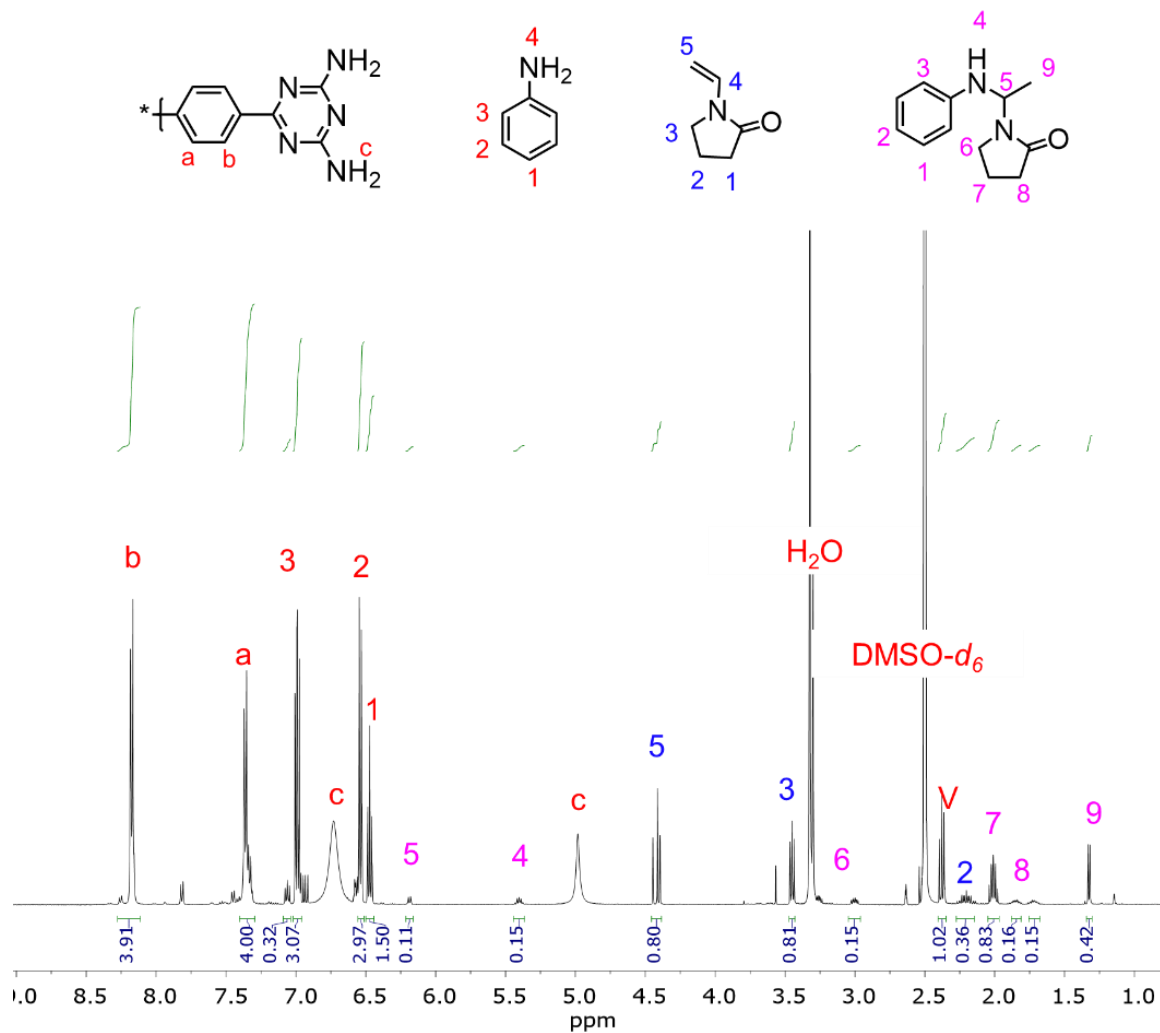


**Figure S23.**  $^1\text{H}$  NMR spectrum of HOF-1 after co-adsorption of aniline and VP in  $\text{DMSO-}d_6$  (500 MHz) recorded at 298 K. **H1**:aniline:VP:AEP measured as 1:3.0:0.8:0.3.

### 2.5.5 Vapor sorption analysis

HOF-1 (40 mg) was immersed in a 20-mL sealed container with 15 mL acetone. Acetone was removed and refilled every 8 h for 5 times. After solvents exchanging, the HOF-1 crystals were activated under vacuum at 90 °C for 24 h. Vapor sorption measurement was performed on a Micrometric FLEX 3.0 surface area analyzer at 297 K.

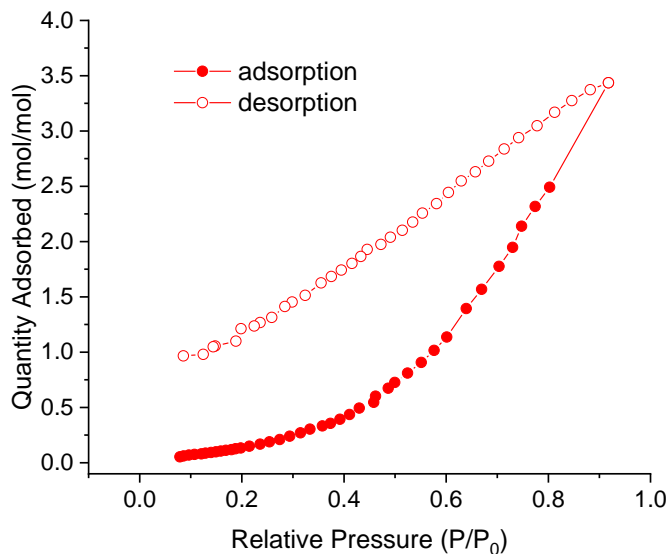


**Figure S24.** Vapor of toluene sorption isotherms of HOF-1 recorded at 297 K.

### 2.6 References

- 169 E. P. Kyba, R. C. Helgeson, K. Madan, G. W. Gokel, T. L. Tarnowski, S. S. Moore, D. J. Cram, *J. Am. Chem. Soc.* **1977**, *99*, 2564-2571.
- 170 J. W. Steed, J. L. Atwood, *Supramolecular chemistry*, John Wiley & Sons, **2022**.
- 171 G. V. Oshovsky, D. N. Reinhoudt, W. Verboom, *Angew Chem. Int. Edit.* **2007**, *46*, 2366-2393.
- 172 V. Ramamurthy, D. F. Eaton, *Chem. Mater.* **1994**, *6*, 1128-1136.
- 173 E. Weber, S. Franken, H. Puff, J. Ahrendt, *J. Chem. Soc. Chem. Comm.* **1986**, 467-469.
- 174 P. R. Ashton, R. Ballardini, V. Balzani, M. GomezLopez, S. E. Lawrence, M. V. MartinezDiaz, M. Montalti, A. Piersanti, L. Prodi, J. F. Stoddart, D. J. Williams, *J. Am. Chem. Soc.* **1997**, *119*, 10641-10651.
- 175 A. Nangia, G. R. Desiraju, *Chem. Commun.* **1999**, 605-606.

- 176 N. T. Southall, K. A. Dill, A. D. J. Haymet, *J. Phys. Chem. B* **2002**, *106*, 521-533.
- 177 C. L. D. Gibb, B. C. Gibb, *J. Am. Chem. Soc.* **2004**, *126*, 11408-11409.
- 178 P. G. Plieger, P. A. Tasker, S. G. Galbraith, *Dalton T.* **2004**, 313-318.
- 179 J. M. Mahoney, A. M. Beatty, B. D. Smith, *J. Am. Chem. Soc.* **2001**, *123*, 5847-5848.
- 180 S. Hashimoto, J. K. Thomas, *J. Am. Chem. Soc.* **1985**, *107*, 4655-4662.
- 181 A. Nakamura, Y. Inoue, *J. Am. Chem. Soc.* **2005**, *127*, 5338-5339.
- 182 H. J. Kim, J. Heo, W. S. Jeon, E. Lee, J. Kim, S. Sakamoto, K. Yamaguchi, K. Kim, *Angew. Chem. Int. Edit.* **2001**, *40*, 1526-1529.
- 183 F. Biedermann, O. A. Scherman, *J. Phys. Chem. B* **2012**, *116*, 2842-2849.
- 184 B. Odell, M. V. Reddington, A. M. Z. Slawin, N. Spencer, J. F. Stoddart, D. J. Williams, *Angew. Chem. Int. Edit.* **1988**, *27*, 1547-1550.
- 185 J. Cao, J. B. Guo, P. F. Li, C. F. Chen, *J. Org. Chem.* **2011**, *76*, 1644-1652.
- 186 G. H. Ning, P. Cui, I. V. Sazanovich, J. T. Pegg, Q. Zhu, Z. F. Pang, R. J. Wei, M. Towrie, K. E. Jelfs, M. A. Little, A. I. Cooper, *Chem* **2021**, *7*, 3157-3170.
- 187 M. A. Little, S. Y. Chong, M. Schmidtman, T. Hasell, A. I. Cooper, *Chem. Commun.* **2014**, *50*, 9465-9468.
- 188 F. J. Rizzuto, L. K. S. von Krbek, J. R. Nitschke, *Nat. Rev. Chem.* **2019**, *3*, 204-222.
- 189 C. G. P. Taylor, J. S. Train, M. D. Ward, *Chemistry*, **2020**, *2*, 510-524.
- 190 K. K. Yan, R. Dubey, T. Arai, Y. Inokuma, M. Fujita, *J. Am. Chem. Soc.* **2017**, *139*, 11341-11344.
- 191 X. Yu, B. Z. Wang, Y. Kim, J. Park, S. Ghosh, B. Dhara, R. D. Mukhopadhyay, J. Koo, I. Kim, S. Kim, I. C. Hwang, S. Seki, D. M. Guldi, M. H. Baik, K. Kim, *J. Am. Chem. Soc.* **2020**, *142*, 12596-12601.
- 192 D. Mungalpara, A. Valkonen, K. Rissanen, S. Kubik, *Chem. Sci.* **2017**, *8*, 6005-6013.
- 193 P. Deria, W. Bury, J. T. Hupp, O. K. Farha, *Chem. Commun.* **2014**, *50*, 1965-1968.
- 194 J. S. Qin, S. Yuan, A. Alsalme, H. C. Zhou, *ACS Appl. Mater. Inter.* **2017**, *9*, 33408-33412.
- 195 X. K. Pei, H. B. Burgi, E. A. Kapustin, Y. Z. Liu, O. M. Yaghi, *J. Am. Chem. Soc.* **2019**, *141*, 18862-18869.
- 196 S. Kato, K. Otake, H. Y. Chen, I. Akpınar, C. T. Buru, T. Islamoglu, R. Q. Snurr, O. K. Farha, *J. Am. Chem. Soc.* **2019**, *141*, 2568-2576.
- 197 Q. Sun, C. W. Fu, B. Aguila, J. Perman, S. Wang, H. Y. Huang, F. S. Xiao, S. Q. Ma, *J. Am. Chem. Soc.* **2018**, *140*, 984-992.

- 198 Y. C. Chen, Z. L. Shi, L. Wei, B. B. Zhou, J. Tan, H. L. Zhou, Y. B. Zhang, *J. Am. Chem. Soc.* **2019**, *141*, 3298-3303.
- 199 B. Wang, R. B. Lin, Z. J. Zhang, S. C. Xiang, B. L. Chen, *J. Am. Chem. Soc.* **2020**, *142*, 14399-14416.
- 200 P. H. Li, M. R. Ryder, J. F. Stoddart, *Accounts Mater. Res.* **2020**, *1*, 77-87.
- 201 Y. S. Yang, L. B. Li, R. B. Lin, Y. X. Ye, Z. Z. Yao, L. Yang, F. H. Xiang, S. M. Chen, Z. J. Zhang, S. C. Xiang, B. L. Chen, *Nat. Chem.* **2021**, *13*, 933- 939.
- 202 W. C. Xiao, C. H. Hu, M. D. Ward, *J. Am. Chem. Soc.* **2014**, *136*, 14200-14206.
- 203 H. Wahl, D. A. Haynes, T. le Roex, *Cryst. Growth. Des.* **2017**, *17*, 4377-4383.
- 204 Q. Y. Huang, W. L. Li, Z. Mao, L. J. Qu, Y. Li, H. Zhang, T. Yu, Z. Y. Yang, J. Zhao, Y. Zhang, M. P. Aldred, Z. G. Chi, *Nat. Commun.* **2019**, *10*, 3074.
- 205 B. Wang, R. He, L. H. Xie, Z. J. Lin, X. Zhang, J. Wang, H. L. Huang, Z. J. Zhang, K. S. Schanze, J. Zhang, S. C. Xiang, B. L. Chen, *J. Am. Chem. Soc.* **2020**, *142*, 12478-12485.
- 206 T. Liu, B. Wang, R. He, H. Arman, K. S. Schanze, S. C. Xiang, D. Li, B. L. Chen, *Can. J. Chem.* **2020**, *98*, 352-357.
- 207 L. Ma, Y. Xie, R. S. H. Khoo, H. Arman, B. Wang, W. Zhou, J. Zhang, R. B. Lin, B. L. Chen, *Chem-Eur J.* **2022**.
- 208 Y. B. He, S. C. Xiang, B. L. Chen, *J. Am. Chem. Soc.* **2011**, *133*, 14570-14573.
- 209 Q. K. Liu, J. P. Ma, Y. B. Dong, *J. Am. Chem. Soc.* **2010**, *132*, 7005-7017.
- 210 Z. J. Ke, K. X. Chen, Z. Z. Li, J. Huang, Z. Z. Yao, W. Dai, X. F. Wang, C. L. Liu, S. C. Xiang, Z. J. Zhang, *Chinese Chem. Lett.* **2021**, *32*, 3109-3112.
- 211 A. Perrin, M. J. Goodwin, O. M. Musa, D. J. Berry, P. Corner, K. Edkins, D. S. Yufit, J. W. Steed, *Cryst. Growth Des.* **2017**, *17*, 3236-3249.
- 212 A. Z. Halimehjani, M. Goudarzi, Y. L. Nosood, *Synthetic Commun.* **2017**, *47*, 2022-2029.
- 213 P. Li, Y. B. He, J. Guang, L. H. Weng, J. C. G. Zhao, S. C. Xiang, B. L. Chen, *J. Am. Chem. Soc.* **2014**, *136*, 547-549.
- 214 N. P. Funnell, A. Dawson, W. G. Marshall, S. Parsons, *Crystengcomm.* **2013**, *15*, 1047-1060.
- 215 B. Van de Voorde, A. S. Munn, N. Guillou, F. Millange, D. E. De Vos, R. I. Walton, *Phys. Chem. Chem. Phys.* **2013**, *15*, 8606-8615.
- 216 F. X. Coudert, M. Jeffroy, A. H. Fuchs, A. Boutin, C. Mellot-Draznieks, *J. Am. Chem. Soc.* **2008**, *130*, 14294-14302.
- 217 S. Aguado, G. Bergeret, M. P. Titus, V. Moizan, C. Nieto-Draghi, N. Bats, D. Farrusseng, *New J. Chem.* **2011**, *35*, 546-550.

- 218 R. Natarajan, G. Magro, L. N. Bridgland, A. Sirikulkajorn, S. Narayanan, L. E. Ryan, M. F. Haddow, A. G. Orpen, J. P. H. Charmant, A. J. Hudson, A. P. Davis, *Angew. Chem. Int. Edit.* **2011**, *50*, 11386-11390.
- 219 Y. Kobayashi, Y. Horie, K. Honjo, T. Uemura, S. Kitagawa, *Chem. Commun.* **2016**, *52*, 5156-5159.
- 220 S. Begum, Z. Hassan, S. Bräse, M. Tsotsalas, *Langmuir* **2020**, *36*, 10657-10673.
- 221 M. A. Rivero-Crespo, G. Toupalas, B. Morandi, *J. Am. Chem. Soc.* **2021**, *143*, 21331-21339.

**Chapter 3 A Crosslinked Ionic Organic Framework for  
Efficient Iodine/Iodide Remediation in Water**

PREFACE for “A Crosslinked Ionic Organic Framework for Efficient Iodine/Iodide Remediation in Water” published in *Angewandte Chemie International Edition*. Reproduced from John Wiley & Sons, Inc.

Zhang, M.; Samanta, J.; Atterberry, B.; Staples, R.; Rossini, A. J.; Ke, C. A Crosslinked Ionic Organic Framework for Efficient Iodine and Iodide Remediation in Water. *Angew. Chem. Int. Ed.* **2022**, *61*, e202214189. The first author, Mingshi Zhang, performed most of the experimental work, data analysis and plotting. Dr. Jayanta Samanta helped solve the single-crystal structure. Benjamin Atterberry and Prof. Aaron J. Rossini did the solid-state  $^{13}\text{C}$  NMR for the H<sub>C</sub>OF-7 samples, Dr. Richard Staples helped collect single-crystal data of H<sub>C</sub>OF-7. Professor Chenfeng Ke provided guidance on ideas and focus of the research, lead the organization and planning of experiments, and significantly contributed to the writing and editing of the manuscript.



### 3.1 Introduction

Access to clean water has been a continuous demand for public health for thousands of years in human society, and civil engineered water treatment plants have been constructed worldwide for water purification.<sup>222-223</sup> However, the need for disinfected water is still critical in areas such as remote places,<sup>224</sup> extreme environments,<sup>225</sup> locations with severe poverty,<sup>226</sup> and space stations in outer space.<sup>227</sup> In these places, iodine ( $I_2$ ) is an effective broad-spectrum antimicrobial reagent used for water disinfection.<sup>228</sup> For example, the United States Environmental Protection Agency recommends<sup>229</sup> iodine as an emergency biocide for drinking water. The International Space Station employs iodine (in the form of  $I_2/KI$ ) in the portable water dispenser (PWD) system for disinfection.<sup>227, 230</sup>

However, due to its negative metabolic effects<sup>226, 231</sup> and its astringent taste,<sup>232</sup> the residual iodine in water (5-16 mg/L or ppm) needs to be removed after disinfection. Currently, these iodine residues ( $I_2$  and  $I^-$ ) are removed by a composite column packed with active charcoal and ion-exchange resins.<sup>230</sup> However, the narrow working temperature of these columns (e.g., below 50 °C for the resin used for  $I^-$  exchange<sup>233-235</sup>) and the limited iodine/iodide breakthrough capacity<sup>236</sup> demonstrate the need to develop porous materials with wider working temperatures (up to 90 °C), good iodine removal efficiency at low concentrations (~5 ppm), as well as high breakthrough capacities.

To fast remove iodine ( $I_2$ ) and iodide ( $I^-$ ) species collectively in water at low residual concentrations, the porous adsorbent needs to process high affinity to iodine and iodide, and large voids for high capacitive adsorption. Recently, a series of porous materials such as metal-organic frameworks<sup>237-241</sup> (MOFs), covalent organic frameworks<sup>242-245</sup> (COFs), porous organic polymers<sup>246-249</sup> (POPs), and hydrogen-bonded organic frameworks<sup>5, 199, 250</sup> (HOFs) have been developed for iodine removal. However, in most cases, these porous materials only demonstrated high capacitive iodine ( $I_2$ ) adsorptions at high iodine concentrations in the vapor phase, and only limited progress has been achieved for low iodine residues.<sup>251-252</sup> We and others have previously reported high capacitive iodine removal in aqueous environments using hydrogen-bonded crosslinked organic frameworks (HCOFs),<sup>17-18</sup> MOFs,<sup>241</sup> COFs,<sup>253</sup> and POPs<sup>254</sup> under ambient conditions. In these investigations,  $I^-$  is introduced to stabilize  $I_2$  in water via the  $I_2 + I^- \rightleftharpoons I_3^-$  equilibrium, but these porous organic materials only remove neutral iodine ( $I_2$ ) at high concentrations ( $\gg$  100 ppm) from water. These iodine adsorption concentrations are much higher than the residual iodine levels (5-16 ppm) in treated drinking water. Yet, simultaneous remediation

of iodine and iodide at low residual concentrations has not been demonstrated using a single porous framework material.

Herein, we considered introducing melaminium moieties for the H<sub>C</sub>OF design to simultaneously adsorb iodine through halogen bonding interactions and iodide via anion exchange. In this design, a molecular precursor **1** possessing four allyl-melamine arms was synthesized and co-crystallized with nitric acids to form **1**•4H<sup>+</sup>•4NO<sub>3</sub><sup>-</sup>. These melaminium-based single crystals were converted to an ionic single-crystalline hydrogen-bonded crosslinked organic framework (H<sub>C</sub>OF-7, Figure 3.1) through a photo-irradiated thiol-ene single-crystal to single-crystal (SCSC) transformation.<sup>255-257</sup> The crystal structures of H<sub>C</sub>OF-7 revealed that it is the first porous network connected through nitrate dimers, which are hydrogen-bonded with melaminium moieties. The porous architecture was stabilized after thiol-ene crosslinking. We discovered that H<sub>C</sub>OF-7 effectively removes I<sub>2</sub> and I<sup>-</sup> in the water independently, and the NO<sub>3</sub><sup>-</sup>/I<sup>-</sup> anion exchange is more effective in H<sub>C</sub>OF-7 when I<sub>2</sub> is co-adsorbed (Figure 3.1). At low I<sub>2</sub>/I<sup>-</sup> concentrations (~5 ppm), H<sub>C</sub>OF-7 demonstrated excellent iodine/iodide removal efficiency with the overall I<sub>2</sub>/I<sup>-</sup> residue of 0.22 ppm at the 23 °C and 0.45 ppm at 90 °C. When iodinated water (3.5 mg/ L I<sub>2</sub>, 1.5 mg/L I<sup>-</sup>) was passed through, the H<sub>C</sub>OF-7-filled columns showed high breakthrough volumes of 20.0 L/g at 23 °C and 18.3 L/g at 90 °C, respectively. These benchmarks are significantly higher than any reported porous framework materials or porous polymers, demonstrating H<sub>C</sub>OF-7's promising potential for practical considerations.

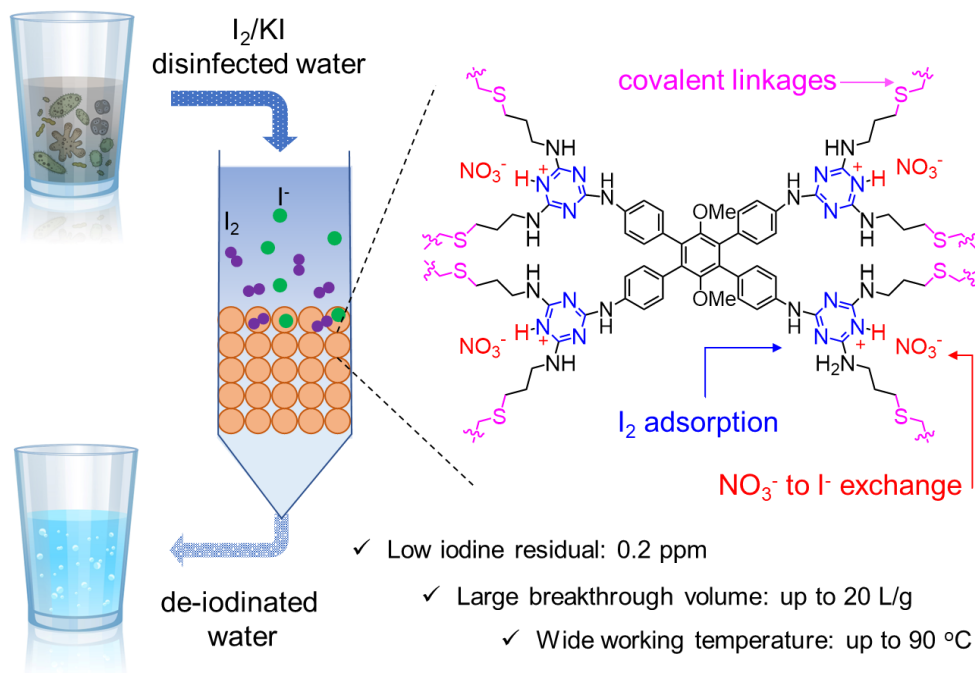


**Figure 3.1.** Schematic representation of a synergistic  $I_2/I^-$  removal in water using an ionic HcOF-7.

### 3.2 Results and Discussion

Monomer **1** was designed with a 1,2,4,5-tetraphenylbenzene core to increase the steric barrier for the four surrounding phenyl groups, forcing them to rotate perpendicularly to the center dimethoxy-benzene moiety to prevent  $\pi$ - $\pi$  stacking in the solid-state. **1** was synthesized in four steps with high yields (Figure 3.2a) without column chromatography purification (See details in the Supporting Information). Single crystals of **1** were obtained by diffusing methanol into the DMSO solution of **1** at room temperature for 5 d. Single-crystal X-ray diffraction (SCXRD) analysis (Figure 3.2b) showed that **1** crystallized in monoclinic  $P2_1/n$  space group ( $a = 15.0148$ ,  $b = 14.7706$ ,  $c = 16.4854$  Å,  $\alpha = \gamma = 90^\circ$ ,  $\beta = 103.120^\circ$ ). The dihedral angles between the four phenyl rings and the center dimethoxy-benzene moiety are measured between  $53^\circ$  and  $63^\circ$  (Figure 3.2b), which are larger than those in the tetraphenylethylene core of prior HcOFs.<sup>17-18</sup> In the solid state, each monomer forms 16 intermolecular hydrogen bonds ( $N\cdots NH$  distances between 2.99-3.09 Å) with the neighboring monomers, affording a hydrogen-bonded network (Figure 3.2b) of *pcu* topology (Figure S1). **1**<sub>crystal</sub> possesses 11% isolated voids (Figure S2) occupied by disordered solvents.

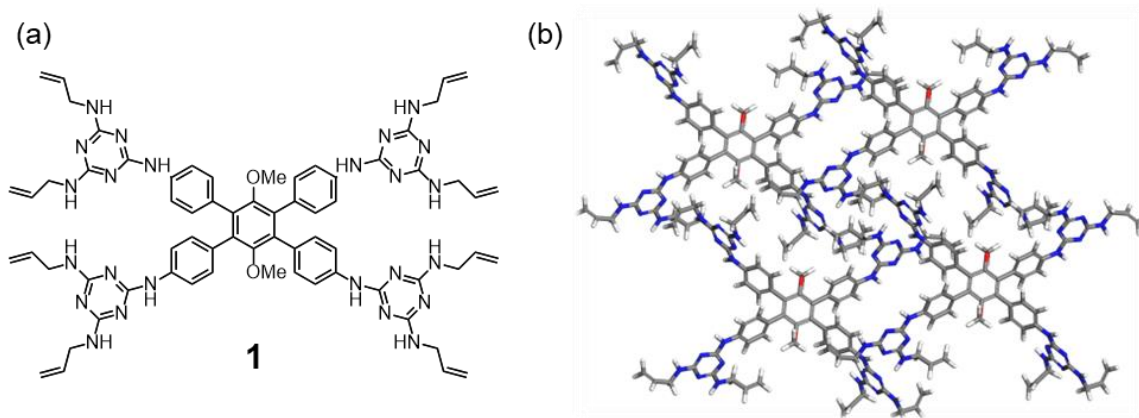


**Figure 3.2.** (a) The chemical structure of **1**, (b) solid-state structure of **1**.

Protonation of the melamine groups of **1** using nitric acid afforded  $\mathbf{1}\cdot\mathbf{4H}^+\cdot\mathbf{4NO}_3^-$ , and the proton resonance of the melaminium NH was found at 10.20 ppm in the  $^1\text{H}$  NMR spectrum (Figure S3). Thermogravimetric analysis (TGA) showed a mass loss of 17 % around 160 °C, attributed to the loss of nitrate in  $\mathbf{1}\cdot\mathbf{4H}^+\cdot\mathbf{4NO}_3^-$  (Figure S4). Single crystals of  $\mathbf{1}\cdot\mathbf{4H}^+\cdot\mathbf{4NO}_3^-$  were obtained by crystallizing **1** in the presence of nitric acid (Figure 3.3a).  $\mathbf{1}\cdot\mathbf{4H}^+\cdot\mathbf{4NO}_3^-$  crystallized in triclinic  $P\bar{1}$  space group (Figure 3.3b-f,  $a = 10.3457$ ,  $b = 15.3155$ ,  $c = 16.9364$  Å,  $\alpha = 77.121^\circ$ ,  $\beta = 77.174^\circ$ ,  $\gamma = 81.156^\circ$ ). Each melaminium moiety of  $\mathbf{1}\cdot\mathbf{4H}^+\cdot\mathbf{4NO}_3^-$  acts as a hydrogen-bonding donor, which binds two anionic nitrates with  $O\cdots\text{HN}$  hydrogen bonds ranging between 2.78 to 2.94 Å. The nitrate anion dimer is only 3.27 Å apart ( $N\cdots N$  distance, Figure 3.3d), which measures the shortest nitrate-to-nitrate distance in solid-state assemblies<sup>19, 258-261</sup> thus a large Coulombic repulsion. The donor-donor-donor (DDD) and acceptor-acceptor-acceptor (AAA) arrays formed between melaminiums and nitrate dimer are non-planar with an angle of 111.3°. One nitrate is further stabilized by two additional side-on Ph–NH–melaminium and NH–allyl hydrogen bonds (Figure 3.3d, yellow and green colored moieties), forming a third DD-AA array. This observation, in conjunction with other reported nitrate dimer assemblies,<sup>19</sup> suggests that the nitrate-melamine assembly is sensitive to the molecular geometry of the melamine-containing molecule and its packed structure. Compared to  $\text{HCO}_3^-$ ,<sup>262-263</sup>  $\text{H}_2\text{PO}_4^-$ <sup>264-265</sup> or  $\text{HSO}_4^-$ <sup>266-267</sup> anion dimers/clusters,<sup>19, 268</sup> the lack of inter-anion hydrogen bonds between two nitrates makes them less stable and directional in organizing the hydrogen-bonded networks. Consequently, the nitrate dimers should be more active in anion exchange to reduce Coulombic repulsion.

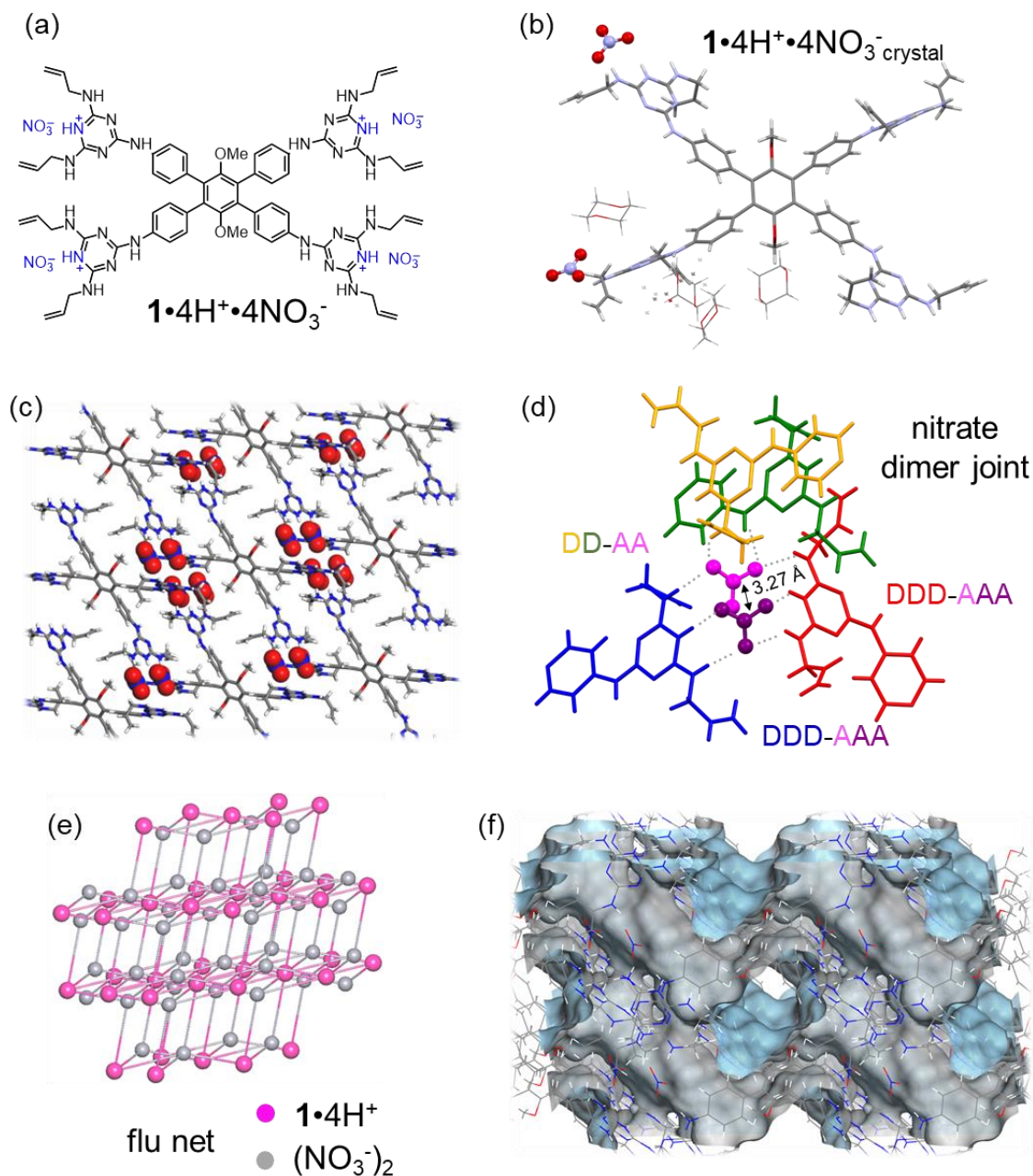


**Figure 3.3.** (a) The chemical structure of  $1 \cdot 4H^+ \cdot 4NO_3^-$ , (b) its solid-state structure, and (c) superstructure. (d) The nitrate dimer-directed hydrogen-bonding joint formed between two repulsive nitrate anions and four melaminium arms. (e) The *flu* topology of  $1 \cdot 4H^+ \cdot 4NO_3^-$  crystal. (f) Highlighted void space of  $1 \cdot 4H^+ \cdot 4NO_3^-$  crystal.

$\mathbf{1}\cdot\mathbf{4H}^+\cdot\mathbf{4NO}_3^-$  crystal dissolves in dichloromethane, acetone, acetonitrile, and methanol.  $\mathbf{1}\cdot\mathbf{4H}^+\cdot\mathbf{4NO}_3^-$  crystal lost crystallinity when it was exposed to diethylether, ethylacetate, or open-air (Figure S5). We consider the nitrate dimer as a four-connected linker and  $\mathbf{1}\cdot\mathbf{4H}^+$  as a six-connected node for the construction of the hydrogen-bonded network, the topology of  $\mathbf{1}\cdot\mathbf{4H}^+\cdot\mathbf{4NO}_3^-$  crystal is assigned as a 3D network  $[4^{12}.6^{12}.8^4]_2$  of *flu* topology (Figure 3.3e). The void space of  $\mathbf{1}\cdot\mathbf{4H}^+\cdot\mathbf{4NO}_3^-$  crystal is calculated as 35%, which is filled by 1,4-dioxanes. There are interconnected 1D channels along the *a*-, *b*-, and *c*-axis, and their aperture sizes are measured as  $3.9 \times 19.4$ ,  $6.8 \times 7.6$ , and  $4.6 \times 5.9$  Å, respectively (Figure 3.3f). The olefin groups of the diallyl-melaminium moieties are decorated on the accessible pore surface with various distances between 5 to 9 Å (Figure S7, and Table S2), which is suitable for crosslinking using 1,2-ethanedithiol (EDT).

We discovered that EDT could not replace dioxane in the voids of  $\mathbf{1}\cdot\mathbf{4H}^+\cdot\mathbf{4NO}_3^-$  crystal. Hence, dioxane in  $\mathbf{1}\cdot\mathbf{4H}^+\cdot\mathbf{4NO}_3^-$  crystal was first replaced by THF (Figure S10) without disrupting the single-crystallinity. The THF-filled single crystals of  $\mathbf{1}\cdot\mathbf{4H}^+\cdot\mathbf{4NO}_3^-$  were immersed in the cyclohexane solution of EDT (133.2 μL/mL) for 3 d in the dark (Figure S11) before UV irradiation. The crosslinked samples were subjected to  $^1\text{H}$  NMR and elemental analyses (Figure S12 and Table S3). Gradually increasing the concentration of EDT from 33.3 to 133.2 μL/mL, a close-to-stoichiometrically crosslinked H<sub>C</sub>OF-7 was obtained ( $\mathbf{1}\cdot\mathbf{4H}^+\cdot[\text{NO}_3^-]_{4.0}\cdot[\text{EDT}]_{3.95}$ , Table S3). In the FT-IR spectra (Figure 3.4b), the olefin bending peak at 915 cm<sup>-1</sup> disappeared after crosslinking. Only a trace thiol stretching band was found at 2600 cm<sup>-1</sup> in the Raman spectrum (Figure 3.4c). In the solid-state  $^{13}\text{C}$  NMR spectrum (Figure 3.4d), new carbon resonances at 30.1 ppm attributed to the dithioether were observed, and resonances attributed to the olefins (115 and 131 ppm) disappeared after crosslinking, indicating the complete allyl-to-thioether conversion. H<sub>C</sub>OF-7 showed a nearly identical PXRD profile compared to that of  $\mathbf{1}\cdot\mathbf{4H}^+\cdot\mathbf{4NO}_3^-$  crystal (Figure 3.4e). In contrast to the low stability of  $\mathbf{1}\cdot\mathbf{4H}^+\cdot\mathbf{4NO}_3^-$  crystal, H<sub>C</sub>OF-7 remained highly crystalline in water, dichloromethane, acetonitrile, and acetone, as well as in the open-air or after vacuum (Figure S13). The significantly improved stability of H<sub>C</sub>OF-7 is attributed to the covalent thioether.

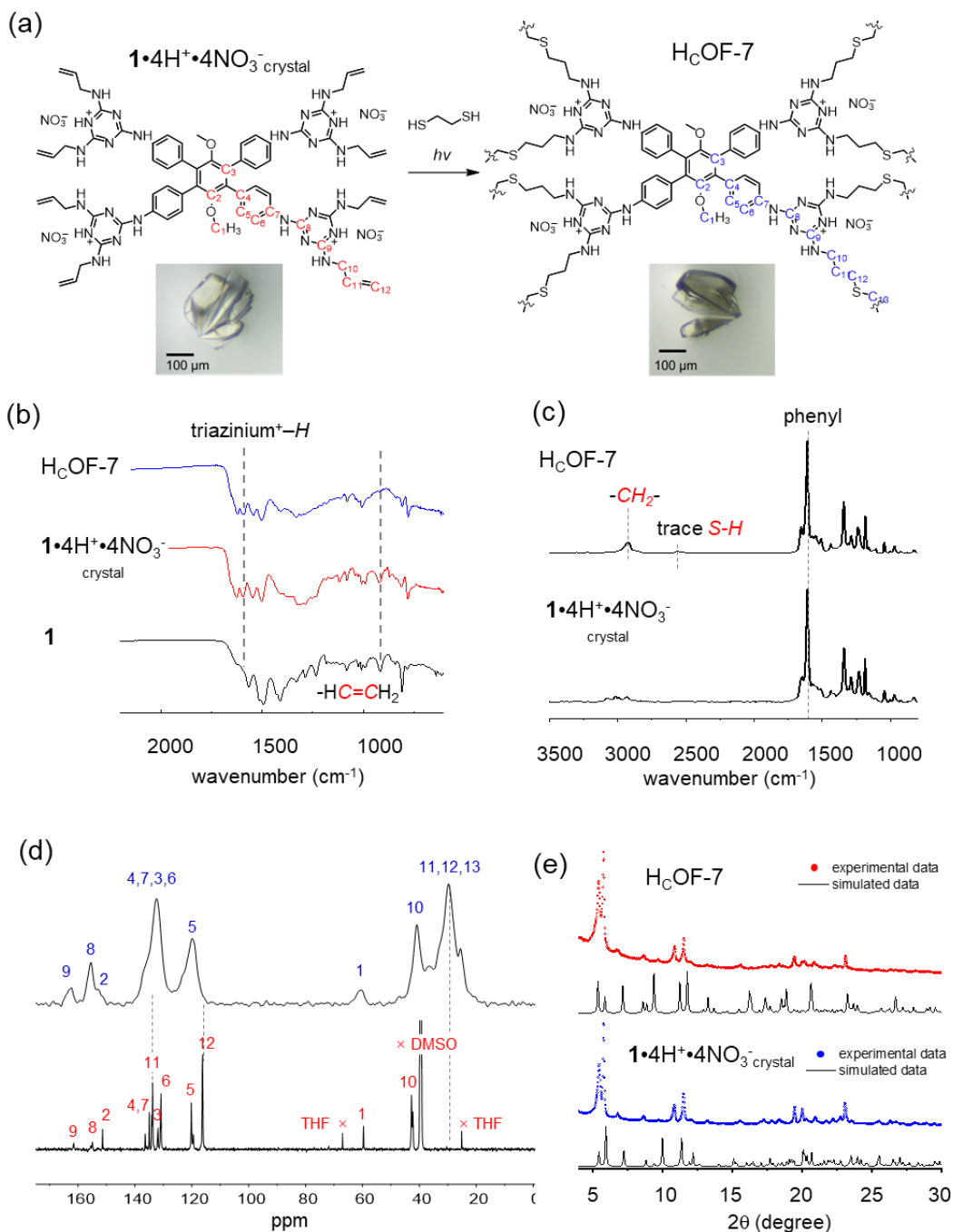


**Figure 3.4.** (a) Synthesis of H<sub>C</sub>OF-7 via an SCSC thiol-ene crosslinking. (b) Stacked FT-IR spectra of 1, 1·4H<sup>+</sup>·4NO<sub>3</sub><sup>-</sup> crystal, and H<sub>C</sub>OF-7. (c) Stacked Raman spectra of 1·4H<sup>+</sup>·4NO<sub>3</sub><sup>-</sup> crystal and H<sub>C</sub>OF-7. (d) Stacked <sup>13</sup>C solution NMR spectrum of 1·4H<sup>+</sup>·4NO<sub>3</sub><sup>-</sup> in DMSO-*d*<sub>6</sub> (bottom, 150 MHz, 298 K) and solid-state <sup>13</sup>C cross-polarization magic angle spinning NMR spectrum of H<sub>C</sub>OF-7. (e) Simulated and experimental PXRD profiles of 1·4H<sup>+</sup>·4NO<sub>3</sub><sup>-</sup> crystal and H<sub>C</sub>OF-7, respectively.

H<sub>C</sub>OF-7 is suitable for SCXRD analysis (Figure 3.5a), and its cell volume expanded 7.3 % compared to that of **1**•4H<sup>+</sup>•4NO<sub>3</sub><sup>-</sup><sub>crystal</sub>. The hydrogen-bonded network of H<sub>C</sub>OF-7 remained largely identical to **1**•4H<sup>+</sup>•4NO<sub>3</sub><sup>-</sup><sub>crystal</sub>. Analysis of the overlaid structure (Figure 3.5b) of **1**•4H<sup>+</sup>•4NO<sub>3</sub><sup>-</sup><sub>crystal</sub> and H<sub>C</sub>OF-7 showed that the O•••NH hydrogen bonding distances between melaminium and nitrate dimers increased from 2.78 to 2.88 Å after crosslinking. The distance between nitrates in the anion dimer increased from 3.27 Å to 3.48 Å. The larger hydrogen bond distances suggest weaker hydrogen bonding interactions between the melaminiums and nitrate dimers in H<sub>C</sub>OF-7, thus more favorable for anion exchange. Electron densities attributed to the dithioether crosslinkages indicate the co-existence of several crosslinking paths (Figure S15).

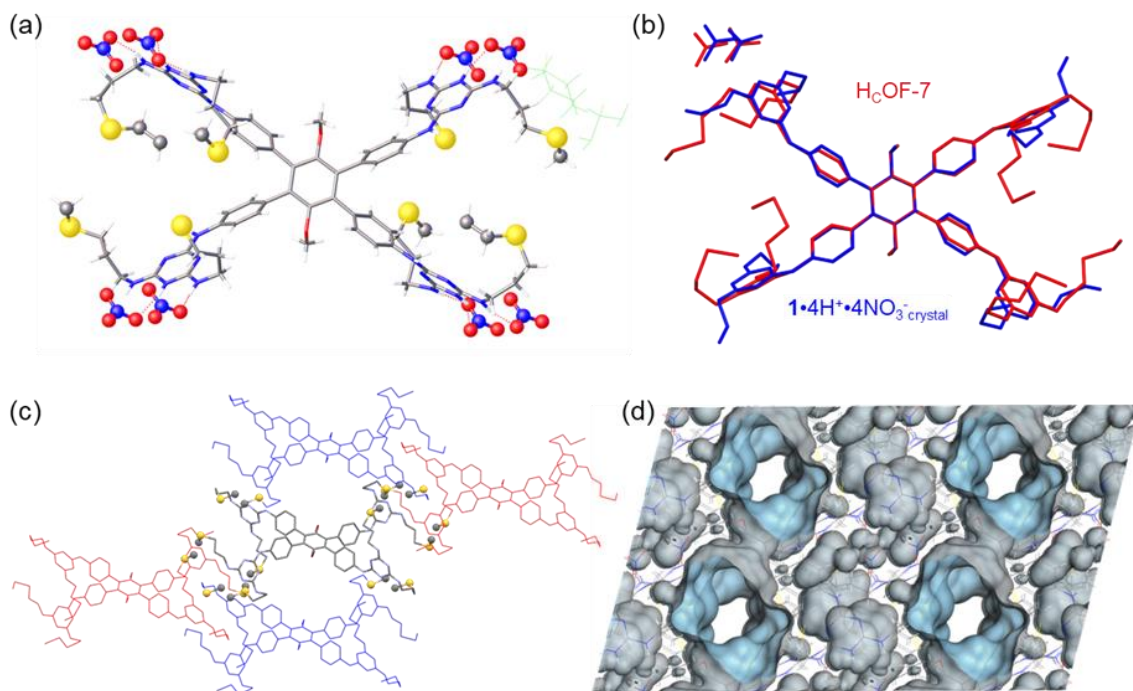


**Figure 3.5.** (a) Crystal structure of H<sub>C</sub>OF-7 with dithioether crosslinkages and nitrate dimer highlighted in ball-stick model. (b) Overlaid structures of **1**•4H<sup>+</sup>•4NO<sub>3</sub><sup>-</sup><sub>crystal</sub> (red color) and H<sub>C</sub>OF-7 (blue color). Hydrogen atoms are omitted for clarity. (c) Covalent connections in H<sub>C</sub>OF-7. Nitrate anions and hydrogens are omitted for clarity. (d) Highlighted void spaces of H<sub>C</sub>OF-7.

In the refined solid-state structure of H<sub>C</sub>OF-7 (Figure 3.5c), each **1**•4H<sup>+</sup> moiety is connected to four neighboring moieties via dithioether crosslinks. We consider the dithioether as a two-connected linker and **1**•4H<sup>+</sup> moiety as an eight-connected node of the



covalently crosslinked network, the topology of H<sub>C</sub>OF-7 is assigned as a 2-nodal 2D network with a point symbol of (4<sup>4</sup>.8<sup>16</sup>.12<sup>8</sup>)(4)<sub>4</sub> (Figure S15-16). H<sub>C</sub>OF-7 exhibit 1D channels along the *b*-axis with a pore aperture of 5.9 × 7.2 Å and void space of 20% (Figure 3.5), which are large enough for the adsorption of guest molecules such as I<sub>2</sub> (r~ 2.0 Å)<sup>269</sup> and I<sup>-</sup> (r~ 2.1 Å).<sup>270</sup>

In the aqueous environment, I<sub>2</sub> is stabilized by an excess of KI via the triiodide equilibrium (I<sub>2</sub> + I<sup>-</sup> ⇌ I<sub>3</sub><sup>-</sup>) with an equilibrium constant of 723 M<sup>-1</sup>.<sup>271</sup> We also performed a UV/Vis titration in H<sub>2</sub>O/MeOH = 99:1 solution and measured the equilibrium constant  $K_a = 792 \text{ M}^{-1}$  at 23 °C (Figure S23-24). When H<sub>C</sub>OF-7 (10 mg) was added to an I<sub>2</sub>/KI solution (0.12 mM I<sub>2</sub> + 0.5 mM KI, 15 mL), the absorption bands attributed to I<sub>2</sub> and I<sub>3</sub><sup>-</sup> diminished completely, and the adsorption band of I<sup>-</sup> decreased moderately in the UV-Vis spectra (Figure S26-29). The adsorption of total iodine (I<sub>2</sub>/I<sub>3</sub><sup>-</sup>/I<sup>-</sup>) is accelerated (Figure 3.6a) at higher temperatures. Compared to the removal of >99 % of total iodine in 6 h at 23 °C, this process only takes 15 min at 90 °C. The accelerated total iodine adsorption at higher temperatures is attributed to the faster mass transport within the porous material. The adsorption of total iodine fits with the pseudo-first-order kinetics, and the activation energy barrier of total iodine adsorption is calculated as 35.3 ± 6.0 kJ/mol (Figure 3.6a, inset). When H<sub>C</sub>OF-7 was immersed in a concentrated I<sub>2</sub>/KI solution (2.6 mM I<sub>2</sub> + 3.1 mM KI), after iodine uptake, the weight-increased amount<sup>272</sup> was measured as 1.39 ± 0.07 g/g at 23 °C by gravimetric analysis (Figure 3.6b). At higher temperatures, the weight-increased amounts of H<sub>C</sub>OF-7 gradually decreased to 1.20 ± 0.06 g/g, and 0.97 ± 0.11 g/g, at 50 and 90 °C, respectively. In comparison, the total iodine adsorptions of active charcoal measured under the same conditions are much lower, from 0.29 ± 0.02 g/g at 23 °C to 0.16 ± 0.02 g/g at 90 °C, respectively (Figure 3.6b). To reveal the contribution of the crystalline framework of H<sub>C</sub>OF-7 for total iodine removal, we also synthesized an amorphous analog of H<sub>C</sub>OF-7, namely crosslinked hydrogen-bonded organic polymer (CHOP-7), by crosslinking **1** with EDT followed by HNO<sub>3</sub> protonation. Despite the nearly identical chemical composition to H<sub>C</sub>OF-7, the total iodine uptakes of CHOP-7 at different temperatures were lower. The weight-increased amounts of CHOP-7 after the uptake of iodine species were measured as 0.93 ± 0.08 g/g at 23 °C and 0.67 ± 0.03 at 90 °C (Figure 3.6b). These results highlight the nitrate dimer containing crystalline framework in promoting total iodine removal.

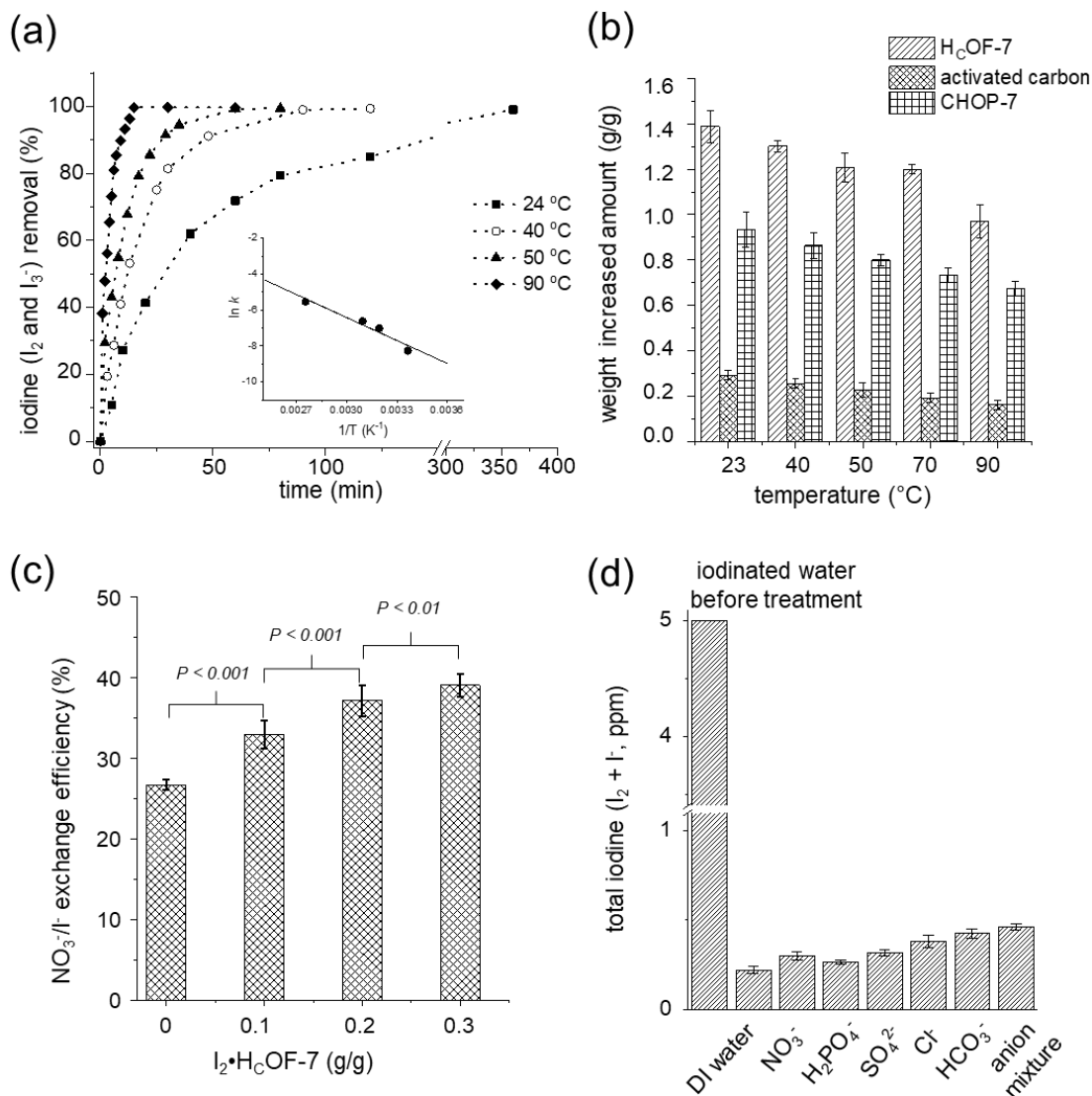


**Figure 3.6.** (a) Time-dependent total iodine adsorption of H<sub>c</sub>OF-7 measured at different temperatures (23, 40, 50, 90 °C) using UV-Vis spectroscopy by monitoring the absorption band at 292 nm. Inset: fitted reaction rate versus the inverse temperature. (b) The increased weight of H<sub>c</sub>OF-7, CHOP-7 and activated carbon after I<sub>2</sub> and I<sup>-</sup> uptake measured at different temperatures. (c) The I<sup>-</sup> exchange efficiency measured using H<sub>c</sub>OF-7 and I<sub>2</sub>•H<sub>c</sub>OF-7 samples (0.1-0.3 g/g of I<sub>2</sub> per H<sub>c</sub>OF-7). The confidence coefficient *p* was obtained using Tukey's honest significance test. (d) Measured concentrations of total residual iodine (input: 5 ppm of I<sub>2</sub> + I<sup>-</sup>) before and after adsorption using H<sub>c</sub>OF-7 (6 mg) in deionized (DI) water in the presence of NO<sub>3</sub><sup>-</sup> (5 ppm), H<sub>2</sub>PO<sub>4</sub><sup>-</sup> (5 ppm), SO<sub>4</sub><sup>2-</sup> (20 ppm), Cl<sup>-</sup> (80 ppm), HCO<sub>3</sub><sup>-</sup> (60 ppm), and their mixture.

In principle, H<sub>C</sub>OF-7 may remove the iodine species through the direct adsorption of I<sub>3</sub><sup>-</sup>, or the co-adsorption of I<sub>2</sub> and I<sup>-</sup>. To understand the adsorption process, the rates of iodine removal were measured in the H<sub>2</sub>O/MeOH = 99:1 solution in the presence of various equivalents of KI (Table S6, Figure S31-34). In the absence of KI, the rate of I<sub>2</sub> removal was measured as  $6.65 \pm 0.30 \times 10^{-4} \text{ s}^{-1}$  at 23 °C. In comparison, when I<sub>2</sub> was mixed with 12 equiv. of KI to raise the population of I<sub>3</sub><sup>-</sup> to 84% at the initial equilibrium, the total iodine removal rate (account for I<sub>2</sub> and I<sub>3</sub><sup>-</sup>) decreased to  $(2.97 \pm 0.06) \times 10^{-4} \text{ s}^{-1}$ . Furthermore, the total iodine removal efficiency (Table S7, Figure S35) of H<sub>C</sub>OF-7 reduced from 83% in the absence of KI to 48% in the presence of 12 equiv. of KI. The reduced total iodine adsorption rate and efficiency indicated that the co-adsorption of I<sub>2</sub> and I<sup>-</sup> is the major adsorption path, where H<sub>C</sub>OF-7 rapidly adsorbs I<sub>2</sub> in solution via halogen bonding interactions<sup>17, 273</sup> between the I<sub>2</sub> and melaminium moieties, shifting the equilibrium toward I<sub>2</sub> + I<sup>-</sup>.

H<sub>C</sub>OF-7 removes I<sup>-</sup> through a nitrate-to-iodide (NO<sub>3</sub><sup>-</sup>/I<sup>-</sup>) exchange. When H<sub>C</sub>OF-7 (5 mg) was immersed in a KI aqueous solution (3.5 mM, NO<sub>3</sub><sup>-</sup>: I<sup>-</sup> ratio= 1:1), 27 ± 1% of NO<sub>3</sub><sup>-</sup> in H<sub>C</sub>OF-7 was exchanged to I<sup>-</sup> at 23 °C (70.7 ± 1.8 mg/g). After the anion exchange, the N–O stretching band at 1322 cm<sup>-1</sup> attributed to the NO<sub>3</sub><sup>-</sup> decreased significantly in the FT-IR spectra (Figure S38). Despite a moderate I<sup>-</sup>/NO<sub>3</sub><sup>-</sup> exchange efficiency at equal molar ratios of NO<sub>3</sub><sup>-</sup>/I<sup>-</sup>, we noticed that the adsorbed I<sub>2</sub> in H<sub>C</sub>OF-7 promotes anion exchange efficiency (Figure 3.6c). I<sub>2</sub>•H<sub>C</sub>OF-7 samples were prepared by immersing H<sub>C</sub>OF-7 in the methanolic solutions of I<sub>2</sub> (See details in the Supporting Information). When I<sub>2</sub>•H<sub>C</sub>OF-7 (0 to 0.3 g/g) was employed for the I<sup>-</sup>/NO<sub>3</sub><sup>-</sup> exchange, the anion exchange efficiency at 23 °C increased from 27 ± 1 % to 37 ± 2% at the increased adsorbed I<sub>2</sub> amounts (Figure 3.6c). These results indicate that, despite iodine adsorption and I<sup>-</sup>/NO<sub>3</sub><sup>-</sup> exchange taking place separately, the formation of polyiodide (I<sub>3</sub><sup>-</sup> and I<sub>5</sub><sup>-</sup>, Figure S42) inside H<sub>C</sub>OF-7 promotes the anion exchange efficiency.<sup>274-275</sup> After I<sub>2</sub> adsorption and NO<sub>3</sub><sup>-</sup>/I<sup>-</sup> exchange, H<sub>C</sub>OF-7 lost crystallinity due to the disruption of the hydrogen-bonded network (Figure S39).

To mimic the iodine/iodide removal used in water treatment,<sup>236</sup> we set an I<sub>2</sub>/KI solution at 5 ppm (I<sub>2</sub>: 3.5 ppm, I<sup>-</sup>: 1.5 ppm)<sup>276</sup> and a KI solution at 1.5 ppm before iodine/iodide removal. The total iodine (I<sub>2</sub> + I<sup>-</sup>) residue is measured using the Leuco-crystal violet method.<sup>277</sup> H<sub>C</sub>OF-7 showed excellent total iodine removal capabilities for I<sub>2</sub>/KI solutions, and the total residual iodine concentrations are measured as 0.22 ± 0.02 (23 °C), 0.25 ± 0.02 (40 °C), 0.32 ± 0.01 (50 °C), 0.40 ± 0.01 (70 °C), and 0.45 ± 0.03 ppm (90 °C) (Figure S44). In contrast, the total iodine residue for KI solution is measured as 0.38 ± 0.02

(23 °C),  $0.48 \pm 0.03$  (40 °C),  $0.53 \pm 0.03$  (50 °C),  $0.64 \pm 0.01$  (70 °C), and  $0.88 \pm 0.02$  ppm (90 °C) (Figure S44). These results further support a cooperative iodine/iodide adsorption in H<sub>C</sub>OF-7. The total iodine/iodide residues after CHOP-7's adsorption were measured as  $1.06 \pm 0.02$  ppm (23 °C) to  $2.03 \pm 0.03$  ppm (90 °C), which are much higher than those of H<sub>C</sub>OF-7 (Figure S44), demonstrating the benefit of introducing crystalline framework architectures for iodine/iodide removal.

In natural water, the co-existing anions such as NO<sub>3</sub><sup>-</sup>, H<sub>2</sub>PO<sub>4</sub><sup>-</sup>, SO<sub>4</sub><sup>-</sup>, Cl<sup>-</sup>, and HCO<sub>3</sub><sup>-</sup> may impact the total iodine removal efficiency of H<sub>C</sub>OF-7. Therefore, to simulate anions in natural water,<sup>278</sup> NO<sub>3</sub><sup>-</sup> (5 ppm), H<sub>2</sub>PO<sub>4</sub><sup>-</sup> (5 ppm), SO<sub>4</sub><sup>-</sup> (20 ppm), Cl<sup>-</sup> (80 ppm), HCO<sub>3</sub><sup>-</sup> (60 ppm) were added to I<sub>2</sub>/I<sup>-</sup> solution (I<sub>2</sub>: 3.5 ppm, I<sup>-</sup>: 1.5 ppm) individually and as a mixture. H<sub>C</sub>OF-7 crystals (6 mg) were added to these solutions (3 mL). After 72 h, the total residual iodine concentrations (Figure 3.6d) were measured as  $0.30 \pm 0.02$ ,  $0.27 \pm 0.01$ ,  $0.32 \pm 0.02$ ,  $0.38 \pm 0.03$ ,  $0.43 \pm 0.03$ ,  $0.46 \pm 0.02$  ppm, respectively, confirming that the total iodine removal efficiency remained good in the presence of various competing anions.

To quantitatively analyze the dynamic iodine removal capability for H<sub>C</sub>OF-7 at different temperatures, we prepared H<sub>C</sub>OF-7 columns for chromatographic breakthrough investigations (Figure 3.7a). Ball-milled H<sub>C</sub>OF-7 crystals (240 mg) were packed in a polypropylene plastic column and loaded onto an automatic column chromatography instrument (Figure S49-50). The intake I<sub>2</sub>/KI solution (5 ppm) is pre-heated to the desired temperatures before passing through the H<sub>C</sub>OF-7 column. Iodinated water was injected into the H<sub>C</sub>OF-7 column continuously with a flow rate of 5 mL/min, and the iodine residuals were measured at different volume intervals. At 23 °C, the total iodine residues gradually increased from 0.30 ppm to 0.40 ppm in the first 1.2 L and remained constant for the subsequent 4.8 L until the breakthrough. When the temperatures were increased to 50 °C, the total iodine residues increased from 0.58 ppm to 0.8 ppm for 4.8 L of iodinated water purification until the breakthrough. At 90 °C, the column quickly reached equilibrium in the first 0.72 L of intake iodinated water, and the total iodine residues were measured at 0.8 ppm for 4.4 L before the breakthrough. The faster establishment of dynamic adsorption at higher temperatures is consistent with the accelerated iodine adsorption rates measured in the temperature-dependent rate experiments (Figure 3.7a). The decreased breakthrough volumes at higher temperatures are also consistent with the decreased binding in the static adsorption experiments. The breakthrough volumes of H<sub>C</sub>OF-7 columns are much larger than the activated carbon and activated carbon/anion exchange resin mixed-bed columns

(Figure 3.7b). The high-temperature breakthrough experiments are vital for the design of the next-generation iodine filter used in outer space, as the current design in the International Space Station requires pre-chilling of the hot water generated in the reactor before passing through the PWD and reheating water for hot beverages.<sup>227</sup>

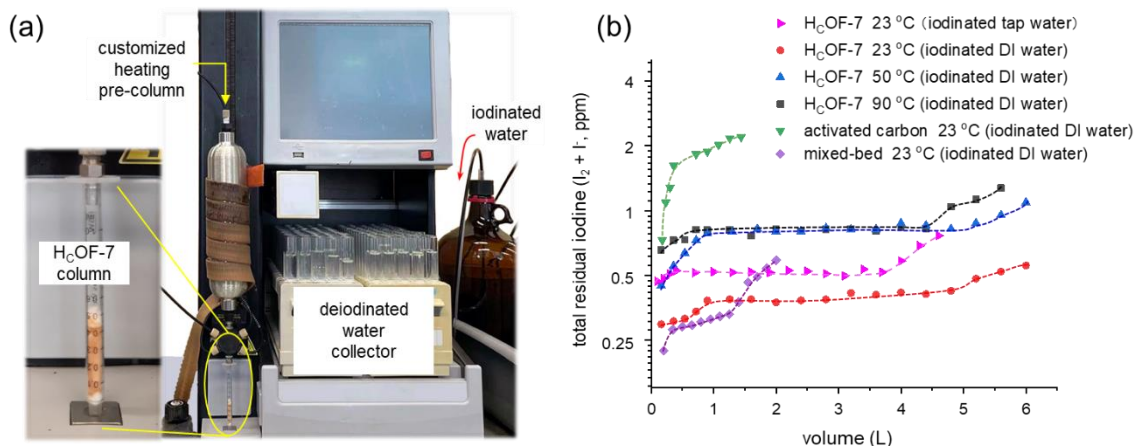


**Figure 3.7.** (a) Experimental setup of the temperature-controlled iodine/iodide breakthrough analysis. Iodinated deionized (DI) or tap water (I<sub>2</sub> + KI, 3.5 + 1.5 ppm) was pumped into a customized steel pre-column (d: 50 × l: 220 mm) and heated to the desired temperatures under continuous flow (5 mL/min). After passing through the H<sub>C</sub>OF-7 column (d: 4.5 × l: 27 mm), the deiodinated water was collected by a fraction collector. (b) The total residual iodine (I<sub>2</sub> + I<sup>-</sup>) concentrations measured in the breakthrough experiments. Each column was packed with 240 mg of H<sub>C</sub>OF-7, activated carbon, or mixed-bed activated carbon/anion exchange resin, respectively.

We also performed the breakthrough experiment in iodinated tap water (I<sub>2</sub>: 3.5 ppm, I<sup>-</sup>: 1.5 ppm) at 23 °C (Figure 3.7f), where the total residual iodine increased from 0.47 to 0.51 ppm for 3.7 L before the breakthrough. Compared to that in the deionized water, the total iodine removal efficiency maintained at ~90% (from 5 ppm of total iodine), and the breakthrough volume decreased moderately by 23%. The adsorbed iodine and iodide species were well-retained in H<sub>C</sub>OF-7 after the breakthrough experiment. Leaching was tested by passing 1L tap water through the iodine-containing H<sub>C</sub>OF-7 column, where no significant iodine residue ( $\leq 0.1$  ppm, Figure S51) was detected, suggesting that after iodine adsorption, the used amorphous H<sub>C</sub>OF-7 could be considered for long-term storage of iodine/iodide.

### 3.3 Summary

In this work, we reported the development of an ionic hydrogen-bonded crosslinked organic framework H<sub>C</sub>OF-7 through anion dimer-directed porous molecular crystal formation followed by a thiol-ene single-crystal to single-crystal transformation. H<sub>C</sub>OF-7 demonstrated significantly enhanced stability compared to its molecular crystal precursor, which could be attributed to the ethandithioether crosslinks. This ionic H<sub>C</sub>OF-7 showed collective iodine/iodide uptake in the aqueous environment between room temperature to 90 °C. H<sub>C</sub>OF-7 demonstrates excellent total iodine residue removal capability, and the residual iodine was measured as low as 0.22 ppm from an intake iodine solution of 5 ppm. The adsorption breakthrough experiments showed large breakthrough volumes (18.3 to 20.3 g/L) using packed H<sub>C</sub>OF-7 columns at different temperatures. Our investigation set up benchmarks for iodine removal using porous organic framework materials at different temperatures, which is particularly important for their potential uses in extreme environments like the wild field or outer space stations.

### 3.4 Appendices

#### 3.4.1 General Information

All chemical reagents and solvents were purchased from commercial suppliers, including Fisher Scientific, Sigma Aldrich, VWR, and were used as received. <sup>1</sup>H NMR spectra were recorded on either a Bruker AVIII 500 MHz spectrometer or a Bruker AVIII 600 MHz Spectrometer and referenced to residual solvent peaks. Single crystal diffraction data were collected on an XtaLAB Synergy four-circle diffractometer (Dualflex HyPix detector). Elemental analysis was performed by Intertek Pharmaceutical Services (Whitehouse, NJ). UV-vis spectroscopy was carried out on a Shimadzu UV-1800 UV-vis spectrometer. Fourier transform infrared (FT-IR) spectra were recorded on a Jasco 6200 spectrometer. Powder X-ray Diffraction (PXRD) data were collected on the Rigaku MiniFlex powder X-ray diffractometer. Thermogravimetric analysis (TGA) was performed on a TA instrument discovery 55 with samples held in a platinum pan under a nitrogen atmosphere. Data were collected between room temperature and 1000 °C with a ramp rate of 10 °C/min under a nitrogen atmosphere. Supercritical CO<sub>2</sub> activation was performed with a Samdri 795 Critical Point Dryer. Vapor sorption measurements were performed on a Micromeritics FLEX 3.0 surface area analyzer at 297 K.

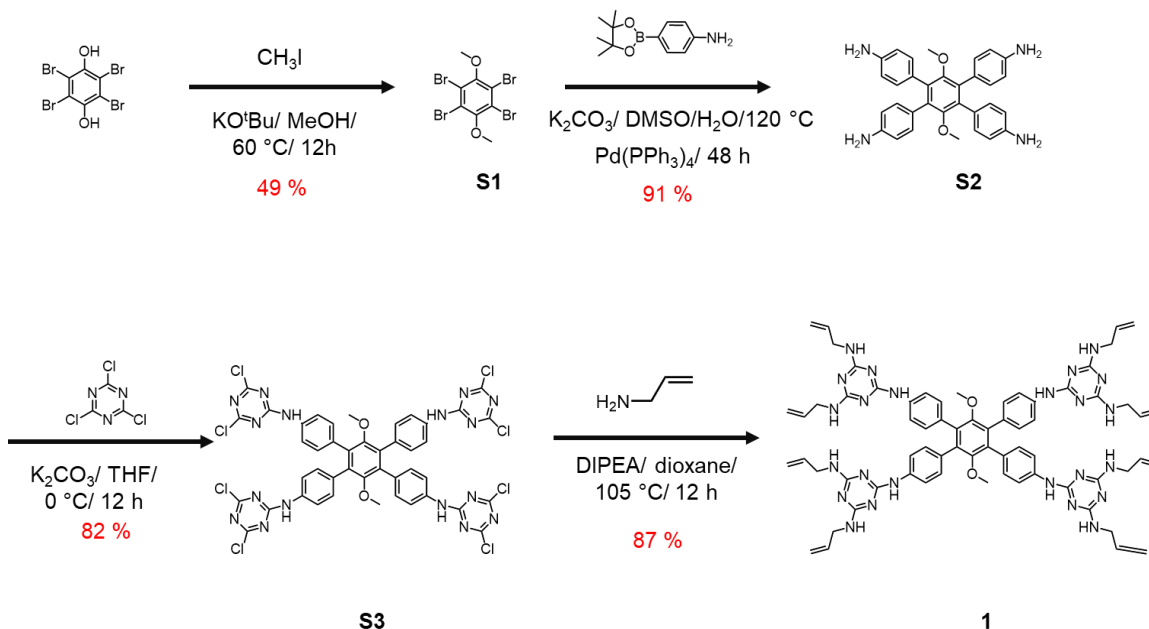
### 3.4.2 Synthesis and characterization of H<sub>c</sub>OF-7

**Synthesis of S1.**<sup>S279</sup> 2,3,5,6-Tetrabromobenzene-1,4-diol (0.85g, 2.0 mmol) was dissolved in MeOH (15 mL) in a 50 mL round bottom flask. Potassium *tert*-butoxide (0.45 g, 4.0 mmol) and iodomethane (1.2 g, 8.5 mmol) were added to the reaction. The mixture was heated to 50 °C under an N<sub>2</sub> atmosphere. After 12 h, the formed white crystalline solid was collected by filtration and washed with distilled water (50 mL) to yield the product (0.44 g, yield: 49 %). <sup>1</sup>H NMR (DMSO-*d*<sub>6</sub>, 500 MHz, 298K) δ (ppm): 3.80 (s, 6H). <sup>13</sup>C NMR (DMSO-*d*<sub>6</sub>, 150 MHz, 298K) δ (ppm): 153.34, 121.89, 61.36.

**Synthesis of S2.** Compound **S1** (0.91 g, 2.0 mmol), 4-(4,4,5,5-tetramethyl-1,3,2-dioxaborolan-2-yl)aniline (1.86 g, 8.5 mmol) and potassium carbonate (1.2 g, 8.7 mmol) were added to a mixture of DMSO (80 mL) and distilled water (20 mL) in a 250 mL round bottom flask at room temperature. The mixture was degassed for 15 min before palladium tetrakis(triphenylphosphine) (35 mg, 0.03 mmol) was added. The reaction was degassed again through three cycles of freeze-pump-thaw before heating to 120 °C under an N<sub>2</sub> atmosphere. After 48 h, the reaction was cooled down to room temperature the solid residues were filtered off. Distilled water (200 mL) was added to the filtrate and the crude product precipitated. This crude product was collected through filtration, washed with Et<sub>2</sub>O (50 mL), and dried under vacuum to yield the product as a grey-colored solid (0.91g, yield: 91 %). <sup>1</sup>H NMR (DMSO-*d*<sub>6</sub>, 500 MHz, 298K) δ (ppm): 6.74 (d, *J* = 6.5 Hz, 8H), 6.36 (d, *J* = 6.5 Hz, 8H), 4.84 (s, 8H), 2.79 (s, 6H). <sup>13</sup>C NMR (DMSO-*d*<sub>6</sub>, 150 MHz, 298K) δ (ppm): 152.46, 147.19, 135.78, 132.10, 125.59, 113.93, 59.77. HR-ESI-MS: calculated for [M + H]<sup>+</sup> *m/z* = 503.2402, found *m/z* = 503.2448.

**Synthesis of S3.** Cyanuric chloride (0.83 g, 4.5 mmol) and potassium carbonate (2.4 g, 17 mmol) were added to anhydrous THF (40 mL) in a 250 mL round bottom flask at 0 °C. Compound **S2** (1.0 g, 2.0 mmol) dissolved in THF (60 mL) was added to the reaction using a dropping funnel slowly over 15 min. The reaction was stirred for 12 h and the temperature was allowed to warm to room temperature. After then, the solid residue was filtered off. The filtrate was collected, and the organic solvent was removed under reduced pressure. The solid residue was washed thoroughly with distilled water (250 mL) to afford the product as yellow solid (1.8 g, yield: 82%). <sup>1</sup>H NMR (DMSO-*d*<sub>6</sub>, 500 MHz, 298 K) δ (ppm): 11.11 (s, 4H), 7.52 (d, *J* = 7.0 Hz, 8H), 7.22 (d, *J* = 7.0 Hz, 8H), 2.87 (s, 6H). <sup>13</sup>C NMR (DMSO-*d*<sub>6</sub>, 150 MHz, 298K) δ (ppm): 154.35, 151.82, 135.94, 135.45, 132.62, 131.53, 120.10, 60.24. HR-ESI-MS: calculated for [M + H]<sup>+</sup> *m/z* = 1094.9947, found *m/z* = 1094.9928.

**Synthesis of 1.** Compound **S3** (1.1 g, 1.0 mmol), allylamine (0.91g, 16.0 mmol), and *N,N*-diisopropylethylamine (1.0 g, 8 mmol) were dissolved in dioxane (100 mL) in a 250 mL round bottom flask. The reaction was heated to 105 °C under a N<sub>2</sub> atmosphere. The reaction was cooled down to the room temperature after 12 h, and distilled water (200 mL) was added to the reaction mixture to generate light-yellow precipitate. The product was collected through filtration, washed with Et<sub>2</sub>O (30 mL), and dried in the open air (1.1 g, yield: 87%). <sup>1</sup>H NMR (DMSO-*d*<sub>6</sub>, 500 MHz, 298 K) δ (ppm): 8.83 (m, 4H), 7.65 (s, 8H), 6.98 (d, *J* = 8.0 Hz, 8H), 6.89 (m, 8H), 5.87 (m, 8H), 5.12 (d, *J* = 17.0 Hz, 8H), 5.02 (d, *J* = 10.5 Hz, 8H), 3.87 (t, *J* = 5.5 Hz, 16H), 2.83 (s, 6H). <sup>13</sup>C NMR (DMSO-*d*<sub>6</sub>, 150 MHz, 298K) δ (ppm): 165.96, 164.44, 151.99, 139.37, 136.77, 135.44, 131.01, 129.78, 118.40, 115.05, 59.80, 42.92. HR-ESI-MS: calculated for [M + H]<sup>+</sup> *m/z* = 1259.6500, found *m/z* = 1259.6460.



**Scheme S1.** Synthesis of compound **1**.

**Crystallization of 1<sub>crystal</sub>.** Compound **1** (50.0 mg, 0.04 mmol) was dissolved in the DMSO (5 mL) in a 20 mL vial. The vial was placed in a 100 mL vial with MeOH for solvent diffusion at room temperature. Transparent block crystals of **1<sub>crystal</sub>** were obtained after 5 d.

**Crystallization of 1·4H<sup>+</sup>·4NO<sub>3</sub><sup>-</sup><sub>crystal</sub>.** Monomer **1** (50.0 mg, 0.13 mmol) was dissolved in the mixture of 1,4-dioxane (5 mL) and fuming nitric acid (0.1 mL). The solution was filtered to remove any insoluble residues and then added to a 20 mL vial. This vial was placed in a 100 mL



vial with Et<sub>2</sub>O for solvent diffusion at room temperature. Yellow block crystals of  $1 \cdot 4\text{H}^+ \cdot 4\text{NO}_3^-$  crystal were obtained after 3 d.

**Stability of  $1 \cdot 4\text{H}^+ \cdot 4\text{NO}_3^-$  crystal.** The single crystals of  $1 \cdot 4\text{H}^+ \cdot 4\text{NO}_3^-$  (5 mg) were added to 3 mL 1,4-dioxane, cyclohexane, THF, Et<sub>2</sub>O, and EtOAc for 24 hours. PXRD profiles of each sample were collected. The crystallinity of  $1 \cdot 4\text{H}^+ \cdot 4\text{NO}_3^-$  crystal decreased significantly in Et<sub>2</sub>O and EtOAc (Figure S2). In addition, the crystallinity of  $1 \cdot 4\text{H}^+ \cdot 4\text{NO}_3^-$  crystal decreased significantly in the open air (Figure S2).

**Solvent exchange of  $1 \cdot 4\text{H}^+ \cdot 4\text{NO}_3^-$  crystal.** In order to remove the dioxanes, single crystals of  $1 \cdot 4\text{H}^+ \cdot 4\text{NO}_3^-$  (10 mg) were immersed in THF and cyclohexane (10 mL×3), separately. After 12 h, the crystals were filtered off and dried in the open air for 2 h. The obtained crystals were dissolved in DMSO-*d*<sub>6</sub> for <sup>1</sup>H NMR analysis. The result shows dioxane could be effectively replaced by THF, while cyclohexane couldn't replace it. After THF exchange,  $1 \cdot 4\text{H}^+ \cdot 4\text{NO}_3^-$  crystal was immersed in cyclohexane (10 mL×3) for 12 h. <sup>1</sup>H NMR shows THF remained (Figure S3).

**Crosslinker diffusion.** Single crystals of  $1 \cdot 4\text{H}^+ \cdot 4\text{NO}_3^-$  crystal were washed with THF (10 mL × 3) for 12h to allow an extensive solvent exchange. A cyclohexane solution (3 mL) of 1,2-ethanedithiol (EDT, 300 μL) was added to the samples in a vial (~40 mg). After 72h, the crystals were filtered off and dried in the open air for 6 h. The crystals were dissolved in DMSO-*d*<sub>6</sub> and characterized by <sup>1</sup>H NMR.

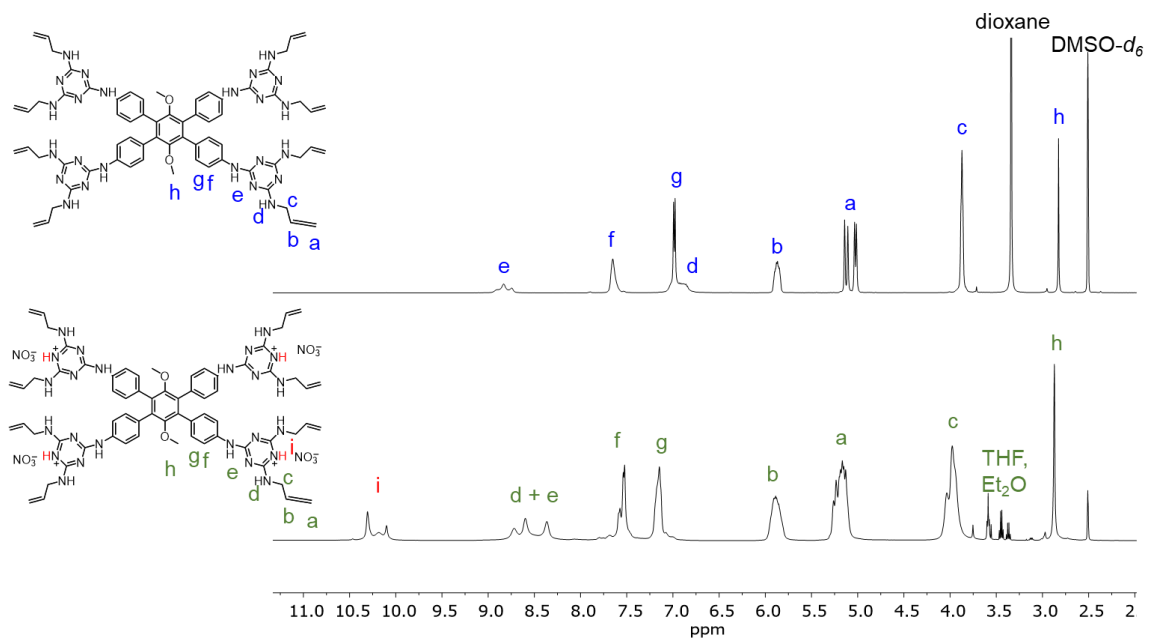


**Figure S1.** <sup>1</sup>H NMR spectra (500 MHz, DMSO-*d*<sub>6</sub>, 298 K) of **1** and **1**·4H<sup>+</sup>·4NO<sub>3</sub><sup>-</sup> crystal.

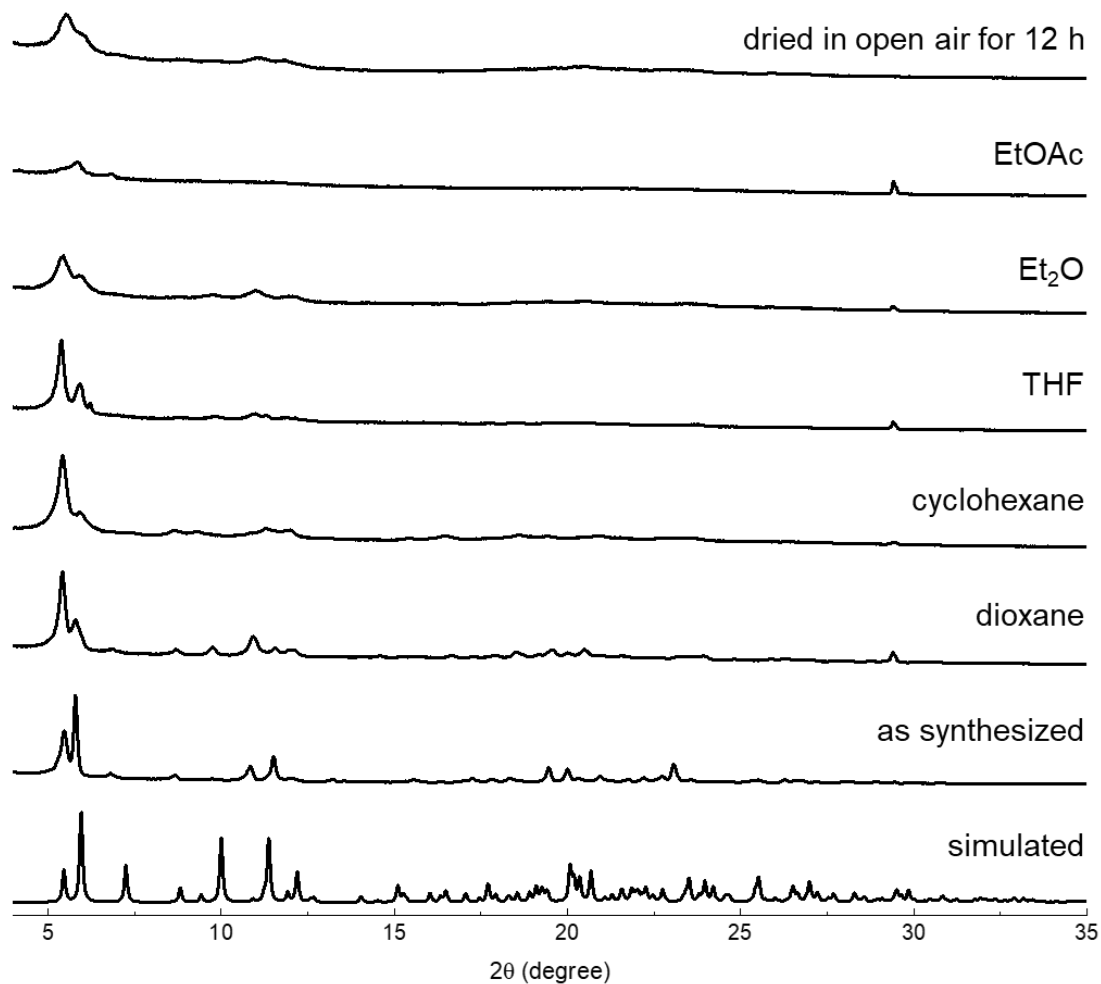


**Figure S2.** PXRD profiles of the simulated  $1 \cdot 4\text{H}^+ \cdot 4\text{NO}_3^-$  crystal and the experimental data of  $1 \cdot 4\text{H}^+ \cdot 4\text{NO}_3^-$  crystal after being immersed in different solvents for 24 h and dried in the open air for 12 h.

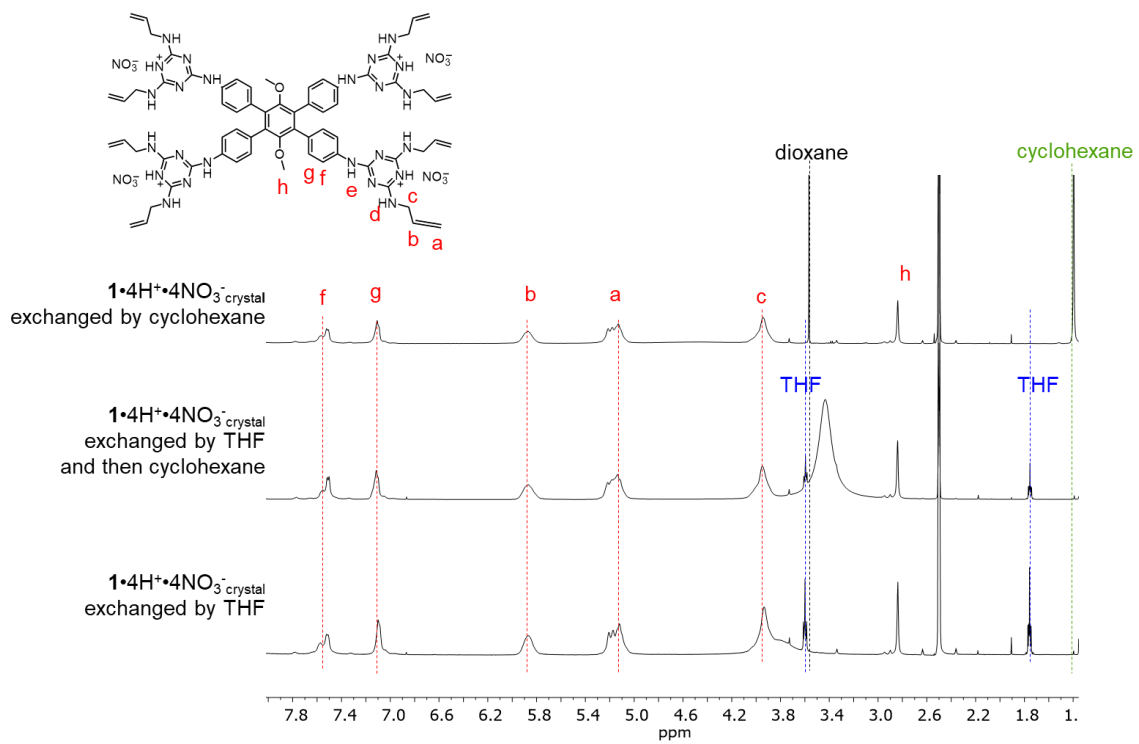


**Figure S3.**  $^1H$  NMR spectra (500 MHz,  $DMSO-d_6$ , 298 K) of  $1 \cdot 4H^+ \cdot 4NO_3^-$  crystal after solvent exchange by THF and cyclohexane.

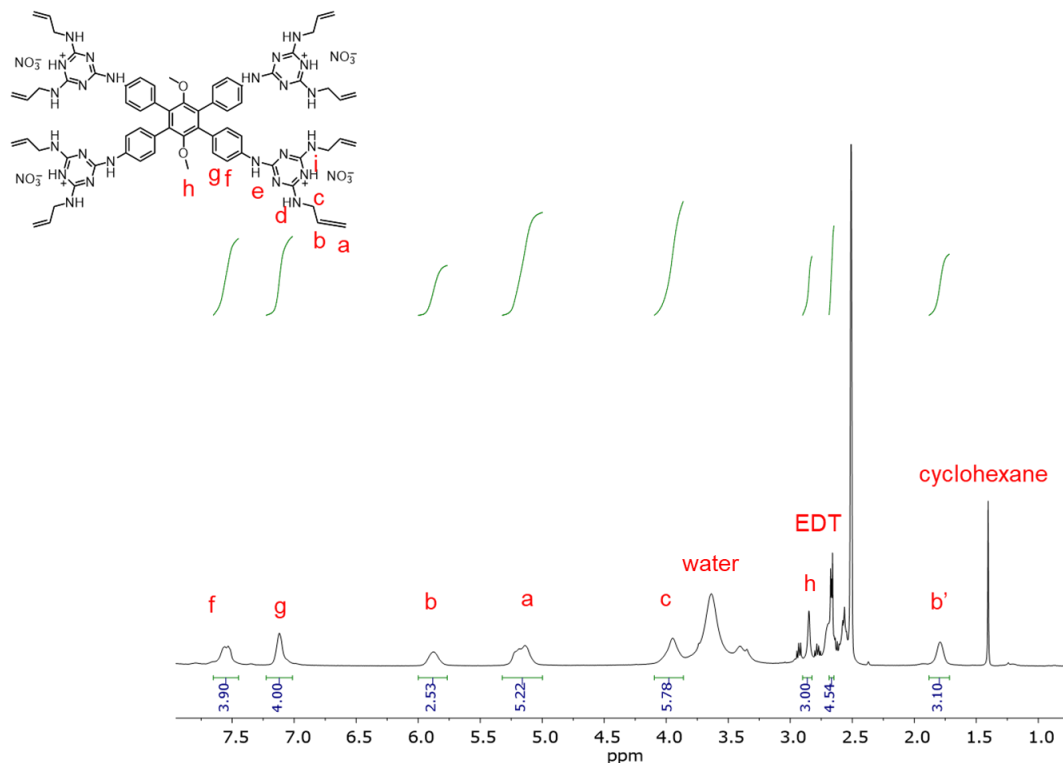


**Figure S4.**  $^1\text{H}$  NMR spectra (500 MHz,  $\text{DMSO-}d_6$ , 298 K) of  $1\cdot 4\text{H}^+\cdot 4\text{NO}_3^-$  crystal after EDT diffusion. The ratio of  $[1\cdot 4\text{H}^+]:[\text{EDT}]:[\text{consumed allyl}]:[\text{unreacted allyl}]$  is measured as 1:2.2:3:5.

**Optimization of the synthesis of single-crystalline  $\text{H}_\text{C}\text{OF-7}$ .** In order to remove the dioxanes in  $1\cdot 4\text{H}^+\cdot 4\text{NO}_3^-$  crystal, single crystals were washed with THF three times ( $10\text{ mL} \times 3$ ) to allow an extensive solvent exchange. A cyclohexane solution (3 mL) of 1,2-ethanedithiol (EDT) was added to the samples in a vial ( $\sim 40\text{ mg}$ ). To optimize the concentrations of EDT for extensive crosslinking, the synthesis of  $\text{H}_\text{C}\text{OF-7}$  was performed at various concentrations of EDT in cyclohexane solutions (33.3, 50, 58.3, 100, and 133.3  $\mu\text{L}/\text{mL}$ ). The EDT-diffused crystal samples were kept in the dark for 72 h to allow for extensive EDT diffusion. Next, the vials were irradiated under UV light (medium-pressure 175-watt Hg lamp) for 48 h with forced air cooling. The crystal samples were collected and washed with an excess of THF and hexanes to remove the unreacted EDT. The  $\text{H}_\text{C}\text{OF-7}$  crystals were further characterized by PXRD, IR spectrum, Raman spectrum, TGA, and solid-state  $^{13}\text{C}$  NMR,  $\delta$  (ppm): 162.10, 155.40, 181.86, 132.59, 121.19, 119.12, 110.69, 60.19, 40.57, 30.07.

**Table S1.** Summary of the elemental analyses of H<sub>c</sub>OF-7 synthesized at various EDT concentrations.

Concentration of EDT in solution	Composition	Cal. (%)	Found (%)	Degree of cross-linking <sup>a</sup>
33.3 μL/ mL	<b>1</b> ·4H <sup>+</sup> · [NO <sub>3</sub> <sup>-</sup> ] <sub>4</sub> · [EDT] <sub>3.05</sub> · [CO <sub>2</sub> ] <sub>3.1</sub>	C 47.59, H 5.35, N 19.97, S 9.82	C 47.01, H 5.02, N 20.27, S 10.11	76 %
50.0 μL/ mL	<b>1</b> ·4H <sup>+</sup> · [NO <sub>3</sub> <sup>-</sup> ] <sub>4</sub> · [EDT] <sub>3.1</sub> · [CO <sub>2</sub> ] <sub>2.2</sub>	C 48.02, H 5.44, N 20.42, S 10.15	C 48.29, H 5.12, N 20.64, S 10.46	78 %
58.3 μL/ mL	<b>1</b> ·4H <sup>+</sup> · [NO <sub>3</sub> <sup>-</sup> ] <sub>4</sub> · [EDT] <sub>3.3</sub> · [CO <sub>2</sub> ] <sub>2.95</sub>	C 47.43, H 5.34, N 20.06, S 10.61	C 47.71, H 5.05, N 20.09, S 10.84	83 %
100.0 μL/ mL	<b>1</b> ·4H <sup>+</sup> · [NO <sub>3</sub> <sup>-</sup> ] <sub>4</sub> · [EDT] <sub>3.8</sub> · [CO <sub>2</sub> ] <sub>2.3</sub>	C 47.26, H 5.43, N 19.65, S 12.09	C 47.78, H 5.16, N 19.9, S 12.36	95 %
133.2 μL/ mL	<b>1</b> ·4H <sup>+</sup> · [NO <sub>3</sub> <sup>-</sup> ] <sub>4</sub> · [EDT] <sub>3.95</sub> · [CO <sub>2</sub> ] <sub>2.25</sub>	C 47.13, H 5.43, N 19.6, S 12.52	C 47.34, H 5.17, N 19.78, S 12.77	99 %

[a] Degree of cross-linking= n[EDT]/ 4 × 100%

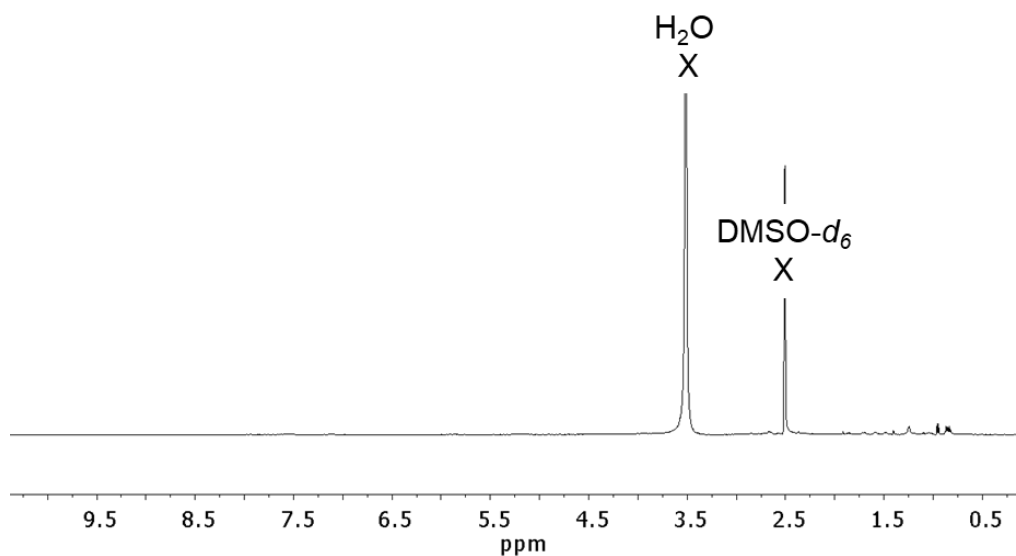


**Figure S5.**  $^1\text{H}$  NMR spectrum of  $\text{H}_c\text{OF-7}$  soluble residue after crosslinking. Single crystals of  $\text{H}_c\text{OF-7}$  (~5 mg) were added to 0.5 mL boiling  $\text{DMSO-}d_6$  to extract any unreacted species. Only trace organic residues were noticed in the  $^1\text{H}$  NMR spectrum.

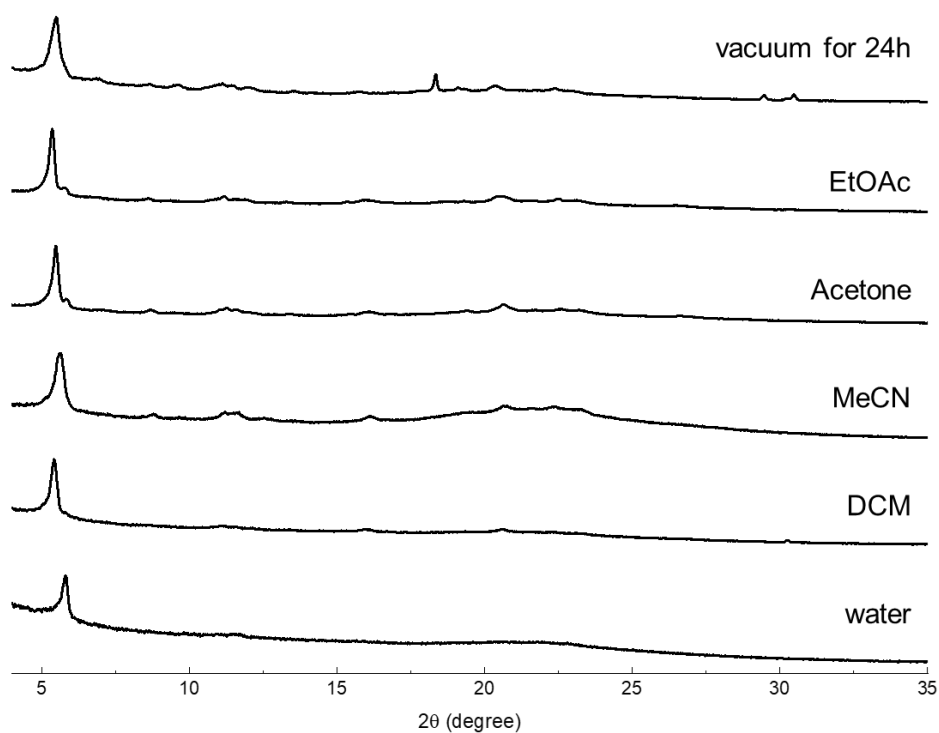


**Figure S6.** Stability of  $\text{H}_c\text{OF-7}$ . PXRD profiles of  $\text{H}_c\text{OF-7}$  after being immersed in various solvents for 24 h, and under vacuum (0.06 torr) for 24 h.

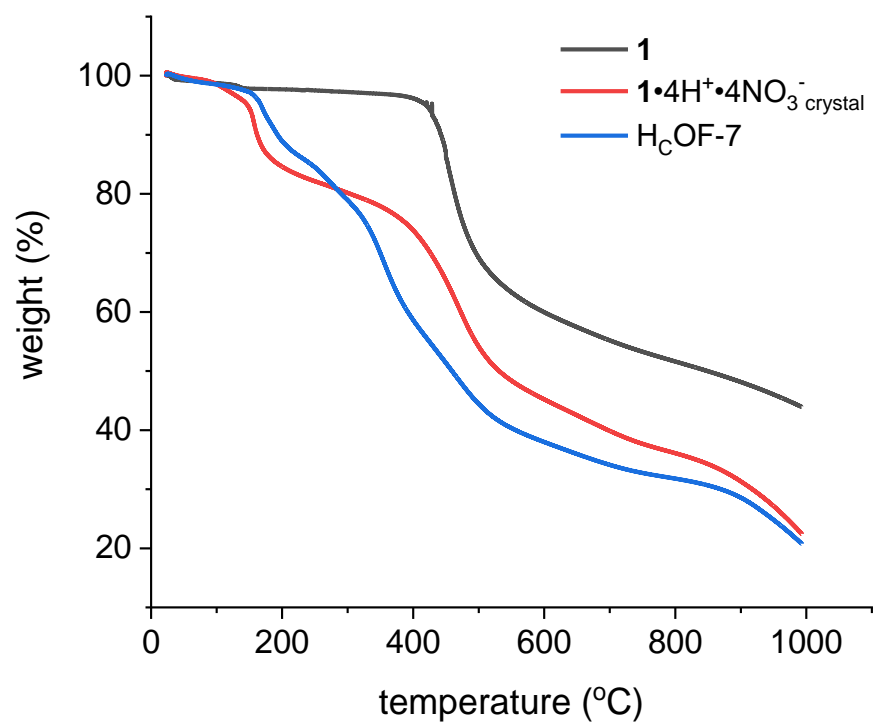
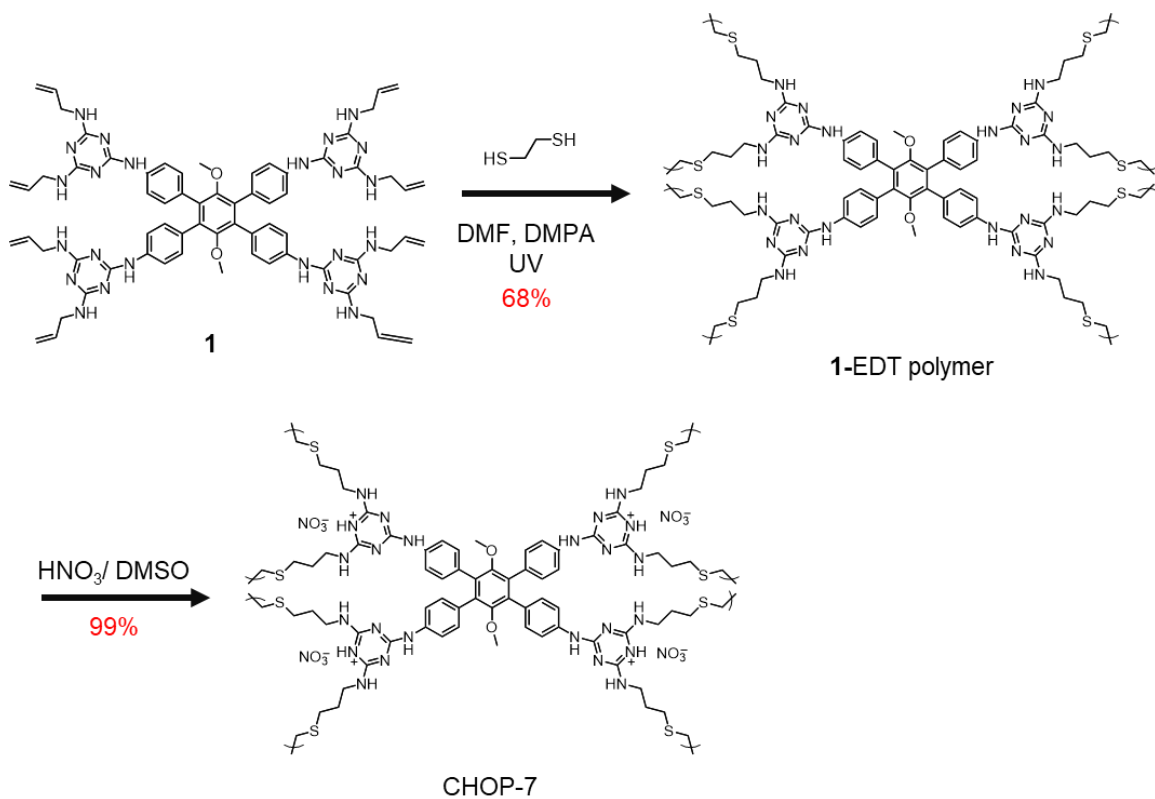


**Figure S7.** TGA profiles of **1**, **1·4H<sup>+</sup>·4NO<sub>3</sub><sup>-</sup> crystal**, and **H<sub>c</sub>OF-7** (heating rate: 10 °C /min) under a N<sub>2</sub> atmosphere.





**Scheme S2.** Synthesis of CHOP-7

**Synthesis of CHOP-7.** Compound **1** (300.0 mg, 0.24 mmol) was dissolved in the DMF (10 mL) in a 20 mL vial. EDT (112.8 mg, 1.20 mmol) and 2,2-dimethoxy-2-phenyl acetophenone (DMPA, 5.1 mg, 0.02 mmol) were added to the solution. The mixture was degassed for 30 min and irradiated under the UV light for 48 h. After that, the formed precipitate was collected by filtration and washed with DMSO (10 mL  $\times$  3) and THF (10 mL  $\times$  3). The product **1**-EDT polymer was obtained as a light yellow solid (261.5 mg, 68%) after air drying. The obtained polymer and fuming  $\text{HNO}_3$  (90%, 1.5 g, 21.4 mmol) were mixed in DMSO (10 mL). After 12 h, the solid was collected by filtration and washed with THF (10 mL  $\times$  3) to yield the CHOP-7 as yellow solid (301.0 mg, 99%).

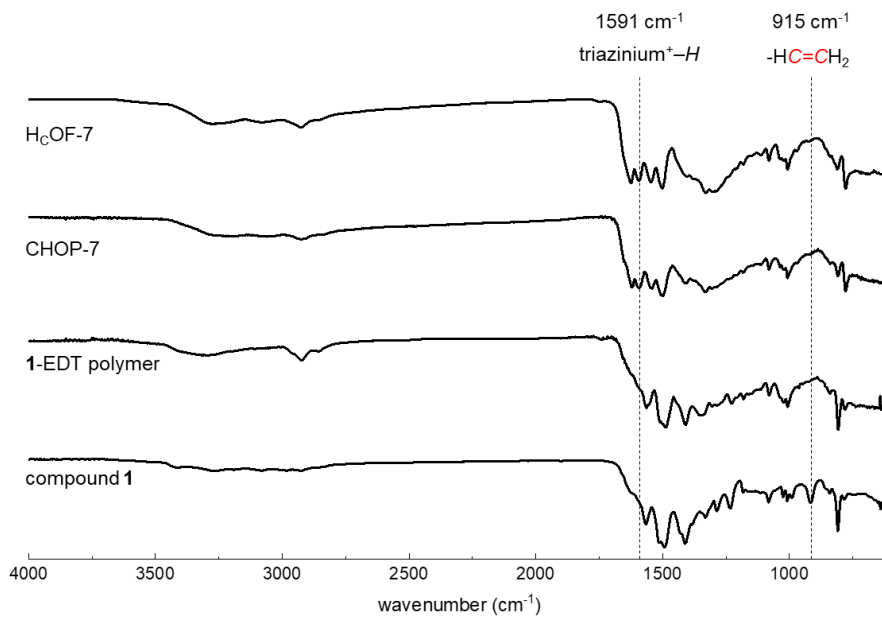


**Figure S8.** FT-IR spectra of compound **1**, 1-EDT polymer, CHOP-7, and H<sub>c</sub>OF-7.

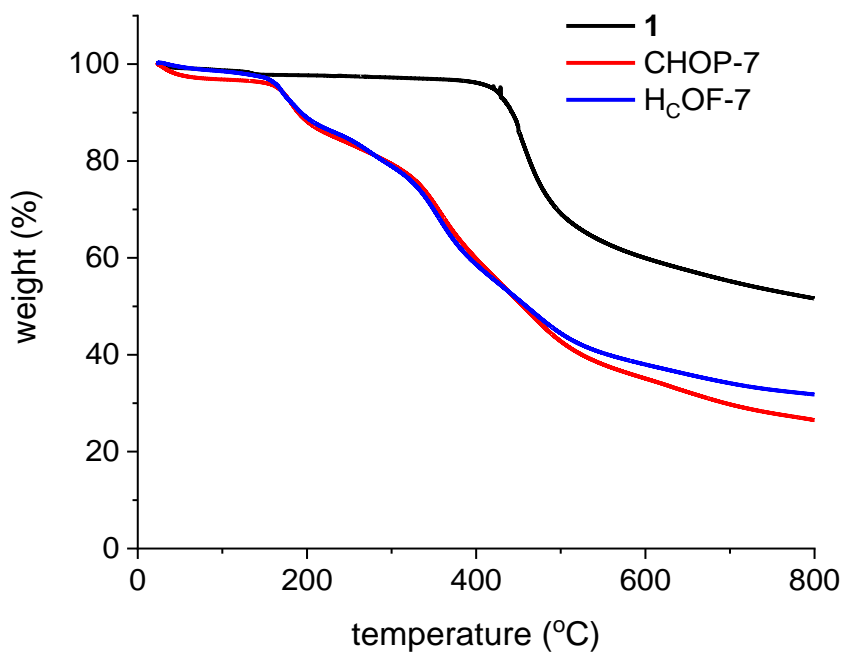


**Figure S9.** TGA profiles of **1**, CHOP-7, and H<sub>c</sub>OF-7 (heating rate: 10 °C /min) under an N<sub>2</sub> atmosphere.

### 3.4.3 Single-crystal X-ray data

**Table S2.** Single-crystal X-ray diffraction data of  $\mathbf{1}_{\text{crystal}}$ ,  $\mathbf{1} \cdot 4\text{H}^+ \cdot 4\text{NO}_3^-_{\text{crystal}}$ , and  $\text{H}_c\text{OF-7}$

Identification code	$\mathbf{1}_{\text{crystal}}$	$\mathbf{1} \cdot 4\text{H}^+ \cdot 4\text{NO}_3^-_{\text{crystal}}$	$\text{H}_c\text{OF-7}$
CCDC number	2176150	2176149	2175909
Empirical formula	$\text{C}_{68}\text{H}_{74}\text{N}_{24}\text{O}_2$	$\text{C}_{92}\text{H}_{124}\text{N}_{28}\text{O}_{26}$	$\text{C}_{94}\text{H}_{137}\text{N}_{28}\text{O}_{14}\text{S}_7$
Formula weight	1259.51	2038.18	2107.73
Temperature/K	100.00(10)	293(2)	100.00(10)
Crystal system	monoclinic	triclinic	triclinic
Space group	$\text{P2}_1/\text{n}$	P-1	P-1
$a/\text{\AA}$	15.0148(13)	10.3457(4)	10.8379(2)
$b/\text{\AA}$	14.7706(8)	15.3155(6)	15.5881(3)
$c/\text{\AA}$	16.4854(11)	16.9364(8)	17.4865(3)
$\alpha/^\circ$	90	77.121(4)	76.293(2)
$\beta/^\circ$	103.120(8)	77.174(4)	72.832(2)
$\gamma/^\circ$	90	81.156(3)	79.225(2)
Volume/ $\text{\AA}^3$	3560.7(4)	2535.39(19)	2720.32(10)
$Z$	2	1	1
$\rho_{\text{calc}}/\text{g/cm}^3$	1.175	1.335	1.287
$\mu/\text{mm}^{-1}$	0.613	0.832	1.927
$F(000)$	1332.0	1080	1121
Crystal size/ $\text{mm}^3$	$0.1 \times 0.1 \times 0.05$	$0.3 \times 0.2 \times 0.2$	$0.1 \times 0.08 \times 0.05$
Radiation	$\text{CuK}\alpha$ ( $\lambda = 1.54184$ )	$\text{CuK}\alpha$ ( $\lambda = 1.54184$ )	$\text{CuK}\alpha$ ( $\lambda = 1.54184$ )
$2\theta$ range for data collection/ $^\circ$	7.194 to 119.994	5.458 to 154.93	5.392 to 154.364

Index ranges	$-16 \leq h \leq 16, -16 \leq k \leq 12, -18 \leq l \leq 18$	$-13 \leq h \leq 10, -18 \leq k \leq 19, -20 \leq l \leq 21$	$-12 \leq h \leq 13, -19 \leq k \leq 18, -22 \leq l \leq 21$
Reflections collected	17854	27102	35759
Independent reflections	5270 [ $R_{\text{int}} = 0.1305$ , $R_{\text{sigma}} = 0.1462$ ]	10137 [ $R_{\text{int}} = 0.0455$ , $R_{\text{sigma}} = 0.0550$ ]	10787 [ $R_{\text{int}} = 0.0313$ , $R_{\text{sigma}} = 0.0306$ ]
Data/restraints/parameters	5270/0/425	10137/80/705	10787/571/657
Goodness-of-fit on $F^2$	0.924	1.457	1.909
Final $R$ indexes [ $I \geq 2\sigma(I)$ ]	$R_1 = 0.0960$ , $wR_2 = 0.2196$	$R_1 = 0.1155$ , $wR_2 = 0.3319$	$R_1 = 0.1739$ , $wR_2 = 0.4527$
Final $R$ indexes [all data]	$R_1 = 0.2426$ , $wR_2 = 0.3023$	$R_1 = 0.1282$ , $wR_2 = 0.3486$	$R_1 = 0.1955$ , $wR_2 = 0.4737$
Largest diff. peak/hole / e $\text{\AA}^{-3}$	0.20/-0.20	0.70/-0.56	1.32/-0.75

X-ray diffraction data of crystals were collected from XtaLAB Synergy Dualflex single-crystal X-ray diffractometer at 100 K with Cu  $K\alpha$  radiation ( $\lambda = 1.54184 \text{\AA}$ ). Multi-scan absorption corrections were applied in each case. The structures were solved by SHELXT and refined with SHELXL using the program Olex2. All non-hydrogen atoms of the monomers were refined anisotropically. The hydrogen atoms were modeled at geometrically constrained positions and refined using the riding model. Details of each crystal structure will be discussed in the section below. CCDC contains the supplementary crystallographic data, which can be accessed through the Cambridge Crystallographic Data Centre at <https://www.ccdc.cam.ac.uk/>. The topology of  $\mathbf{1} \cdot 4\text{H}^+ \cdot 4\text{NO}_3^-$  crystal is solved by *Topospro* software. The nitrate dimer was simplified as one node to connect different  $\mathbf{1} \cdot 4\text{H}^+$  monomers. The  $\mathbf{1} \cdot 4\text{H}^+ \cdot 4\text{NO}_3^-$  crystal is crystallized in *flu* (fluorite) topology. Each  $\mathbf{1} \cdot 4\text{H}^+$  is connected with eight nitrate dimers, while each nitrate dimer is connected with four  $\mathbf{1} \cdot 4\text{H}^+$ .

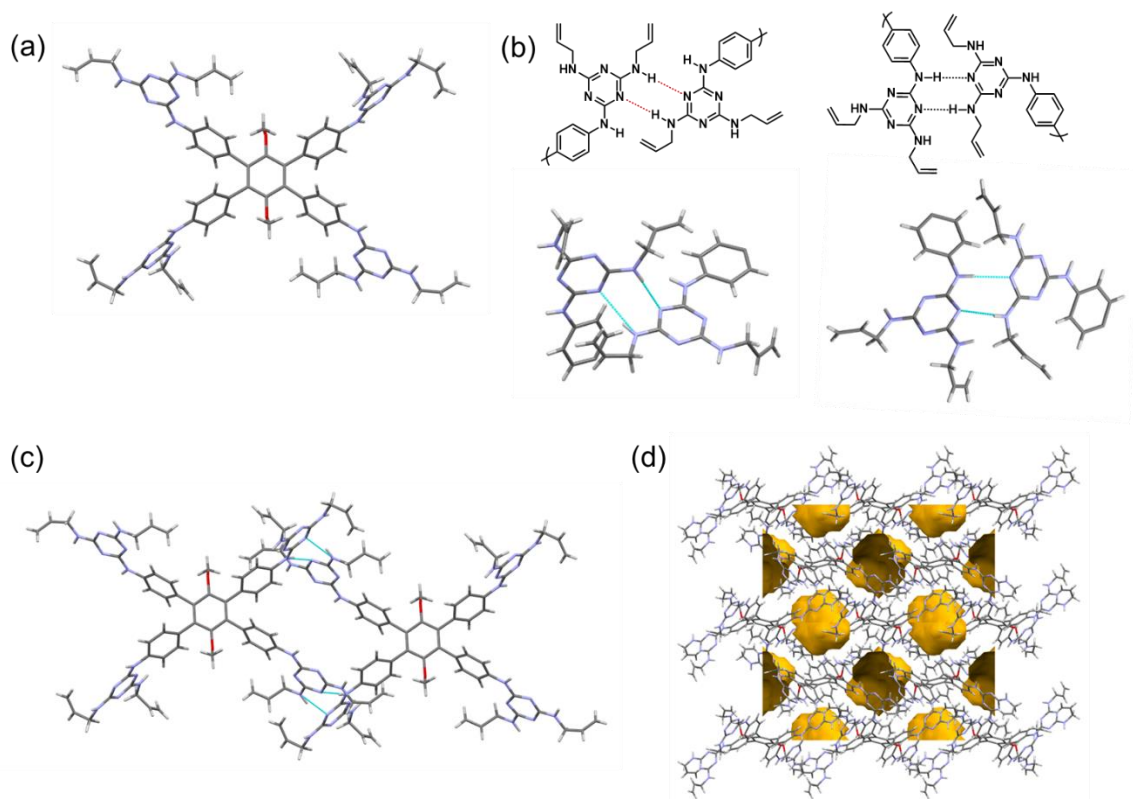


**Figure S10.** (a) Molecular structure of  $\mathbf{1}_{\text{crystal}}$  (b) The head-to-head and side-to-side hydrogen-bonding interactions of DAT functional groups with chemical formula diagram. (c) The hydrogen-bonding connection between  $\mathbf{1}$  (d) The  $2 \times 2 \times 2$  packing of  $\mathbf{1}_{\text{crystal}}$  viewed along the  $a$ -axis (void space: 10.8 %).

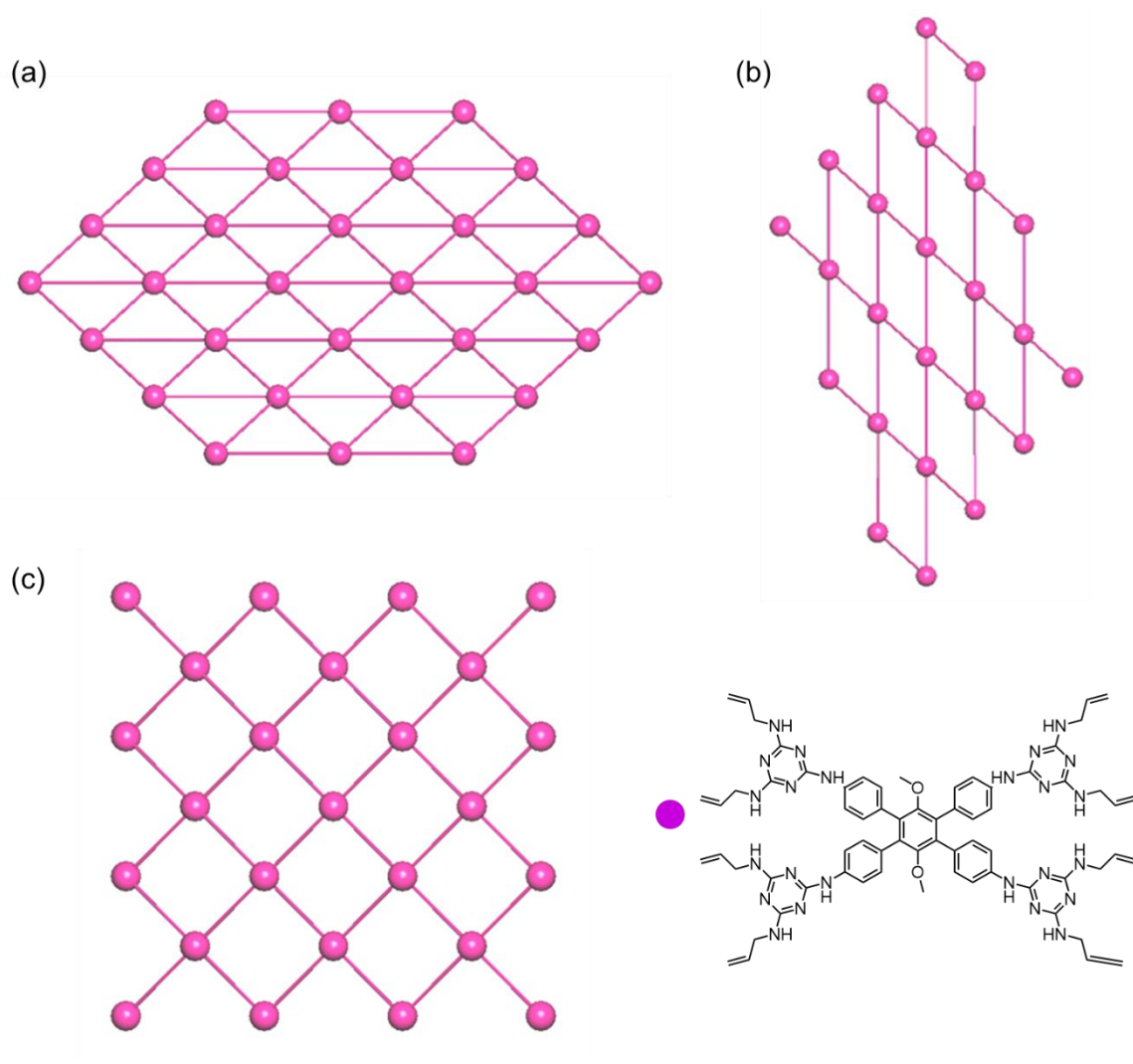


**Figure S11.** (a-c) The *pcu* topology of **1**<sub>crystal</sub> crystal along *a*-, *b*- and *c*- axis, respectively.

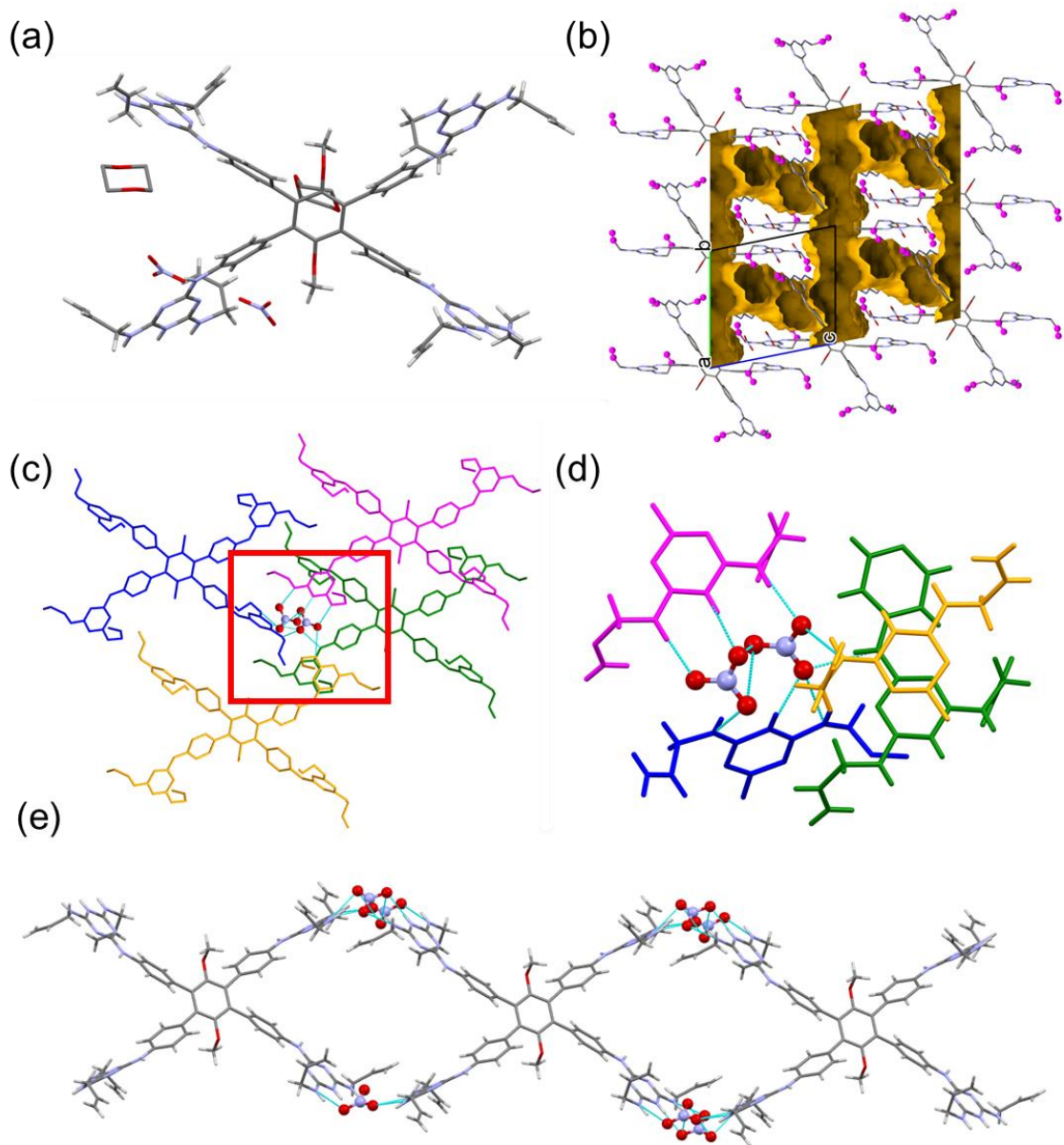


**Figure S12.** (a) Molecular structure of  $1 \cdot 4H^+ \cdot 4NO_3^-$  crystal (b) The  $2 \times 2 \times 2$  packing of  $1 \cdot 4H^+ \cdot 4NO_3^-$  crystal viewed along the  $a$ -axis with crosslinking active sites highlighted as red balls. (Void space: 35.6%) (c) The nitrate dimer connecting four  $1 \cdot 4H^+$  monomers with nitrate dimer highlighted. (d) The mode of interactions between nitrate dimer with melaminium functional groups. (e) The nitrate dimer connecting 2D chain in  $1 \cdot 4H^+ \cdot 4NO_3^-$  crystal.

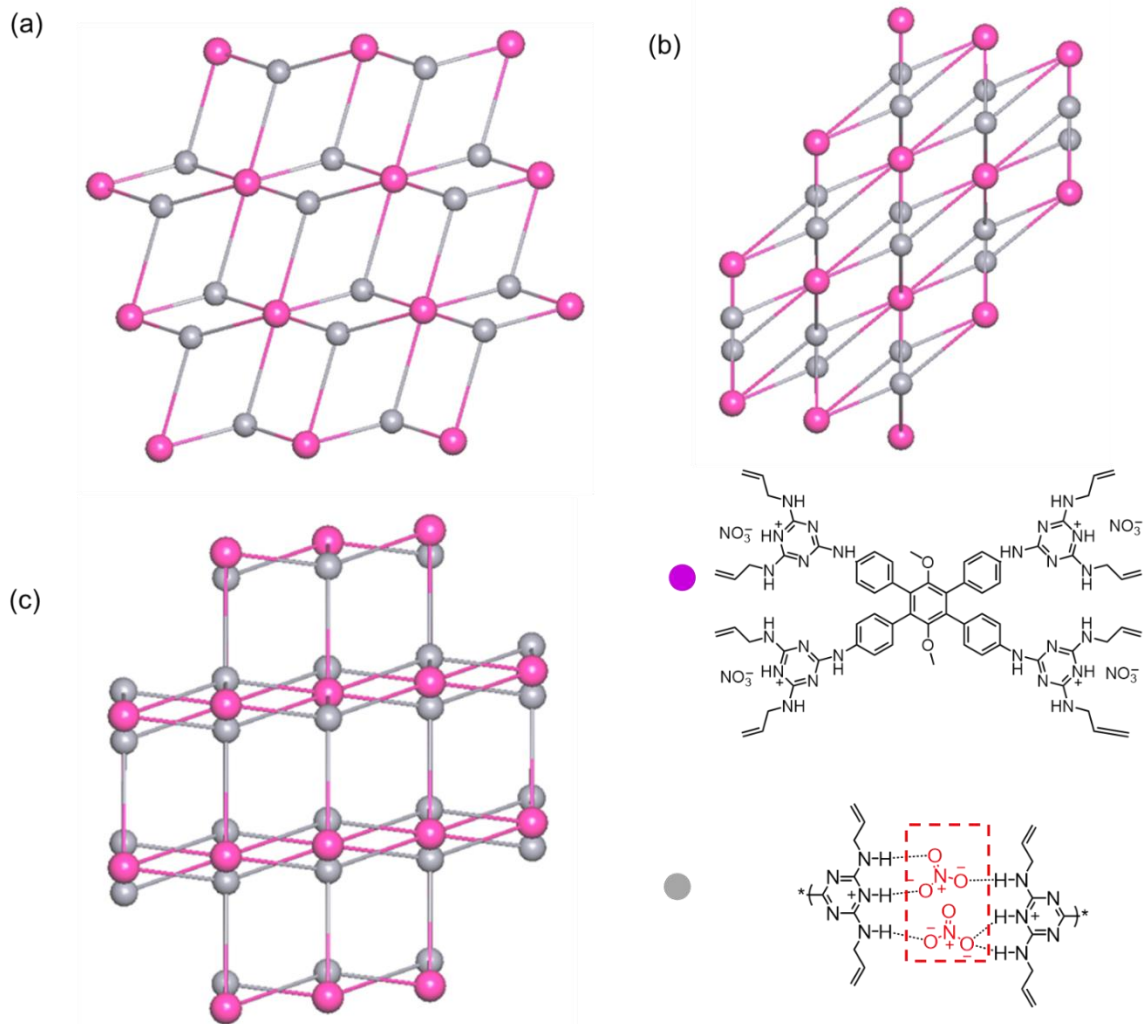


**Figure S13.** (a-c) The *flu* topology of  $1 \cdot 4\text{H}^+ \cdot 4\text{NO}_3^-$  crystal along *a*-, *b*- and *c*- axis, respectively.



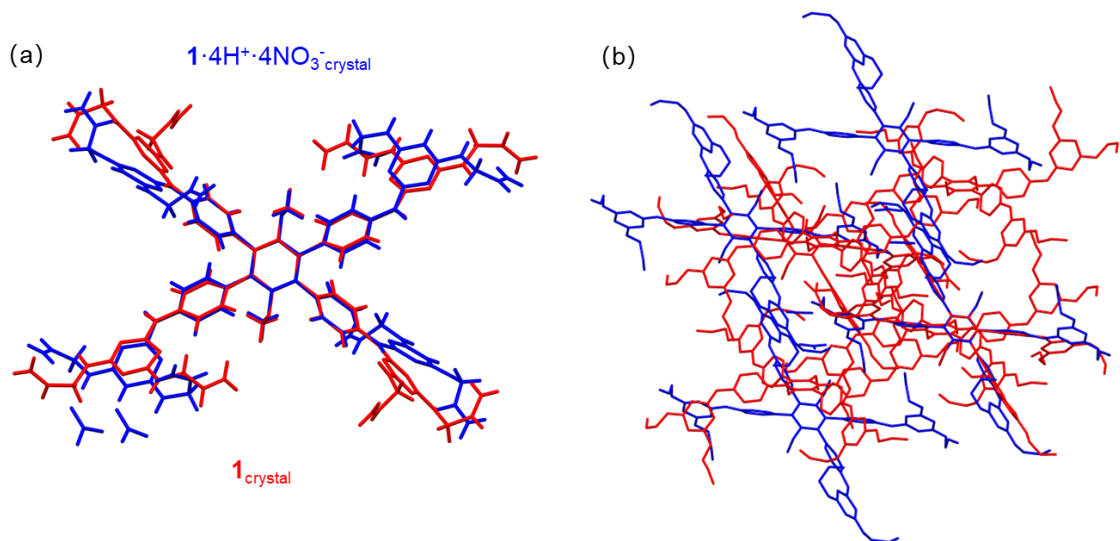


**Figure S14.** (a) Overlaid molecular structures and (b) the  $1 \times 1 \times 1$  packing of  $1_{\text{crystal}}$  and  $1 \cdot 4H^+ \cdot 4NO_3^-$ .

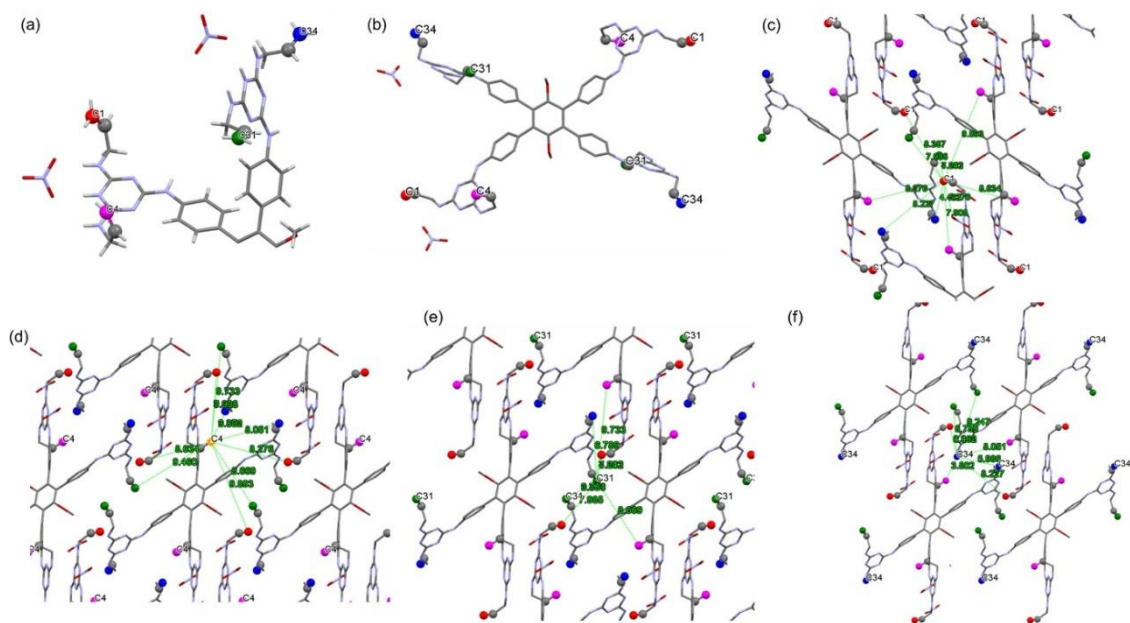


**Figure S15.** (a) Asymmetric unit and (b) the molecular structure of  $1 \cdot 4H^+ \cdot 4NO_3^-$  crystal (c-f) The alkyl groups with the distance between 4 to 10 Å in  $1 \cdot 4H^+ \cdot 4NO_3^-$  crystal, which could possibly be crosslinked by EDT.

**Table S3.** Distances of the nearby alkene carbon atoms in the lattice of  $1 \cdot 4\text{H}^+ \cdot 4\text{NO}_3^-$  crystal

alkene carbon atom		symmetry operation	distance (Å)
C4	C1	$x, y, z$	7.908
C4	C34	$-1+x, y, z$	8.0512
C4	C1	$-x, 1-y, 1-z$	8.2764
C4	C1	$-x, 2-y, 1-z$	8.6343
C4	C31	$-x, 1-y, -z$	8.6689
C4	C4	$-1-x, 2-y, 1-z$	8.8349
C4	C34	$-x, 1-y, 1-z$	9.3736
C4	C31	$-1+x, 1+y, z$	9.4597
C4	C34	$-2+x, 1+y, z$	9.4672
C4	C31	$-x, 1-y, 1-z$	9.7334
C4	C34	$1-2+x, y, z$	9.8049
C4	C1	$-1+x, y, z$	9.8179
C4	C1	$-1-x, 2-y, 1-z$	9.8337
C4	C1	$x, y, -1+z$	9.8929
C1	C34	$1-x, 1-y, 1-z$	4.4617
C1	C31	$-x, 1-y, 1-z$	4.4919
C1	C31	$1-x, 1-y, 1-z$	7.2433
C1	C31	$-1+x, y, 1+z$	7.4341
C1	C4	$x, y, z$	7.908
C1	C31	$x, y, 1+z$	7.9848
C1	C34	$-1+x, y, z$	8.2268

C1	C4	-x, 1-y, 1-z	8.2764
C1	C1	-x, 1-y, 2-z	8.3866
C1	C4	-x, 2-y, 1-z	8.6343
C1	C34	2-x, 1-y, 1-z	9.3479
C1	C4	1+x, y, z	9.8179
C1	C4	-1-x, 2-y, 1-z	9.8337
C1	C4	x, y, 1+z	9.8929
C31	C1	-x, 1-y, 1-z	4.4919
C31	C34	-1+x, y, z	6.7889
C31	C1	1-x, 1-y, 1-z	7.2433
C31	C1	1+x, y, -1+z	7.4341
C31	C1	x, y, -1+z	7.9848
C31	C4	-x, 1-y, -z	8.6689
C31	C34	2-x, 1-y, -z	9.2472
C31	C4	1+x, -1+y, z	9.4597
C31	C4	-x, 1-y, 1-z	9.7334
C31	C31	-x, 1-y, -z	9.8758
C34	C1	1-x, 1-y, 1-z	4.4617
C34	C34	2-x, 1-y, 1-z	5.9856
C34	C31	1+x, y, z	6.7889
C34	C4	1+x, y, z	8.0512
C34	C1	1+x, y, z	8.2268
C34	C31	2-x, 1-y, -z	9.2472

C34	C1	$2-x, 1-y, 1-z$	9.3479
C34	C4	$-x, 1-y, 1-z$	9.3736
C34	C4	$2+x, -1+y, z$	9.4672
C34	C4	$2+x, y, z$	9.8049

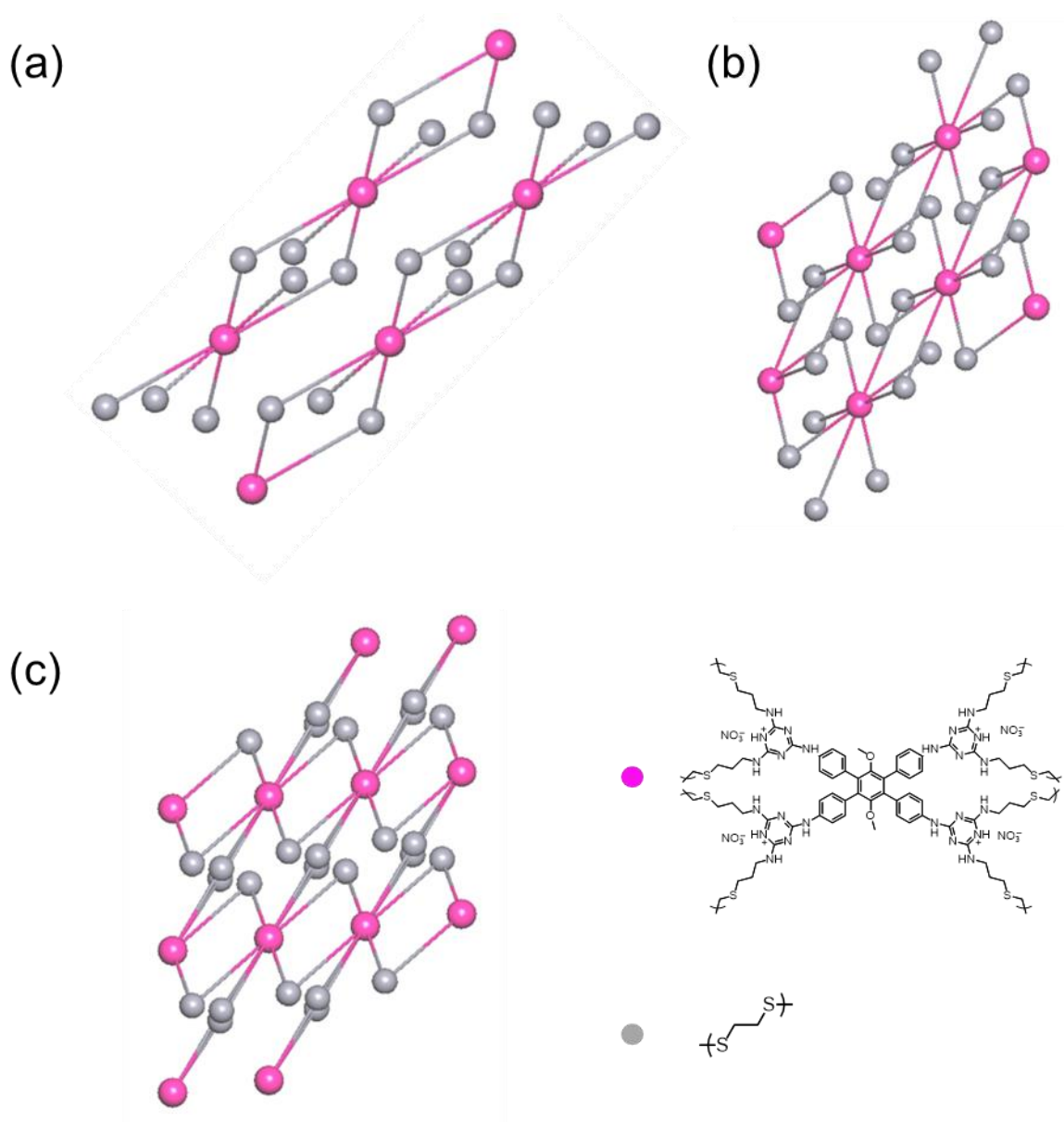


**Figure S16.** (a-c) The  $(4^4 \cdot 8^{16} \cdot 12^8)(4)_4$  topology of HcOF-7 along the *a*-, *b*-, and *c*- axis, respectively.

### 3.4.4 Porosity Analysis

H<sub>c</sub>OF-7 crystals (~45 mg) were immersed in a 20 mL vial with THF (15 mL). Then THF was piped out and refilled every 8 hours three times. After solvents exchanging, the H<sub>c</sub>OF-7 crystals were activated under vacuum at 90 °C for 24 h. Gas/vapor sorption measurements were performed on a Micromeritics FLEX 3.0 surface area analyzer. The CO<sub>2</sub> sorption and other vapor sorption isotherms were measured at room temperature.

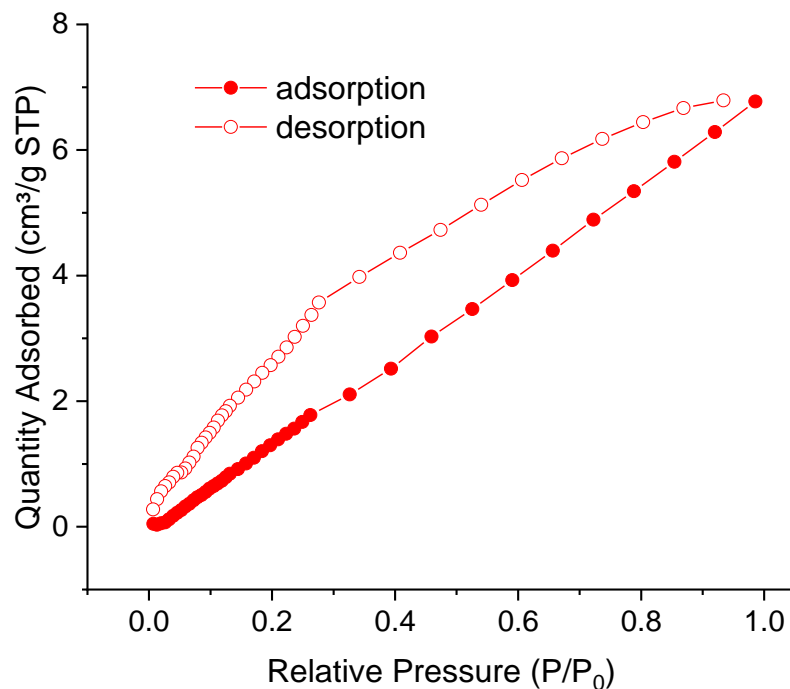


**Figure S17.** CO<sub>2</sub> sorption isotherm of H<sub>c</sub>OF-7 recorded at 298 K

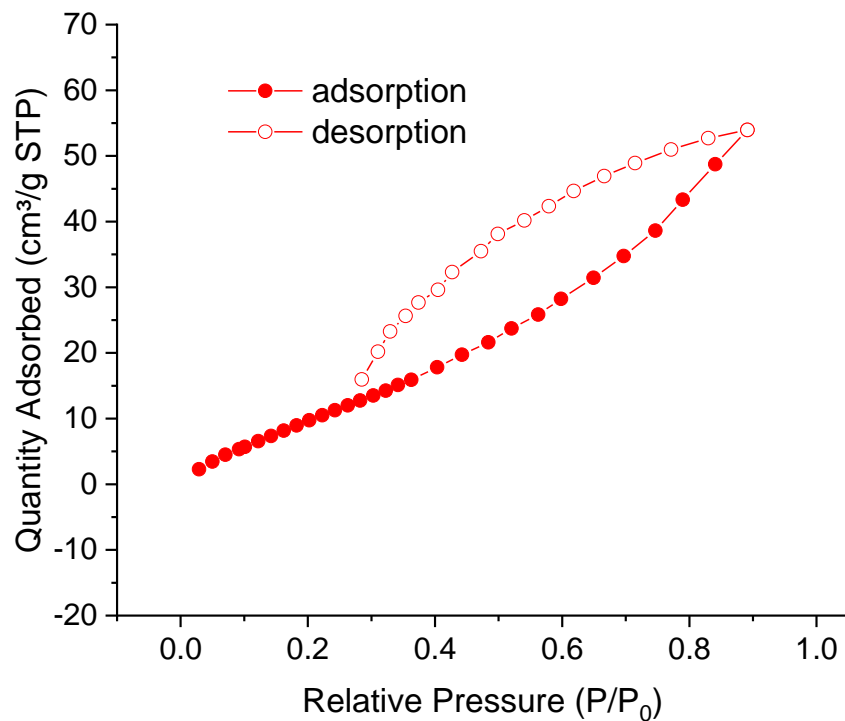
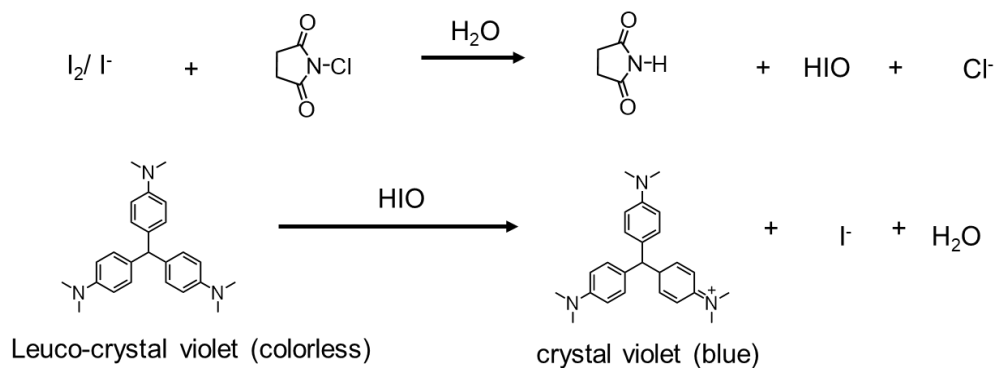


**Figure S18.** MeOH sorption isotherm of HcOF-7 recorded at 298 K

### 3.4.5 Residual Iodine and iodide sorption investigations.



**Scheme S3.** Mechanism of Leuco-crystal violet method for I<sub>2</sub>/I<sup>-</sup> residue determination

The residue of iodine and iodide is determined by the Leuco-crystal violet method.<sup>S277</sup> The solution preparation and measurement procedures are described below.

**Preparation of the standard iodide solution.** A 15 ppm I<sup>-</sup> stock solution was prepared by dissolving 19.6 mg of potassium iodide (dried at 105 °C for 1 h) in 1 L of deionized water. Then the solution was diluted to 0.1 to 0.5 ppm for the standard curve calibration.

**Preparation of the buffer solution.** A pH 4.0 buffer solution was prepared in a 50 mL volumetric flask by dissolving 1.70 grams of potassium dihydrogen phosphate (KH<sub>2</sub>PO<sub>4</sub>) in distilled water (30 mL). Phosphoric acid (85 %, 1 mL) was added to the solution. Then the solution was diluted to exactly 50 mL.

**Preparation of the Leuco-crystal violet solution.** Phosphoric acid (85%, 0.25 mL), Leuco-crystal violet, 4,4',4''-methylidynetris (25 mg, 0.067 mmol) were added to a 100 mL volumetric flask with distilled water (30 mL) and shaken until the solid completely dissolved. The solution was then diluted to exact 100 mL.

**Preparation of the N-Chlorosuccinimide-Succinimide solution.** N-chlorosuccinimide (100 mg, 0.75 mmol) and succinimide (1.0 g, 10.1 mmol) were dissolved in 75 mL distilled water in a 100 mL volumetric flask. Then the solution was diluted to 100 mL with distilled water.

**Residual concentration of [I<sub>2</sub> + I<sup>-</sup>] measurement.** Distill water (2 mL) and iodinated water (1 mL) were mixed in a 4 mL vial. Then the phosphate buffer solution (0.1 mL) and N-chlorosuccinimide-succinimide reagent solution (0.1 mL) were added to the vial. The solution was shaken after the Leuco-crystal violet solution (0.1 mL) was added. The UV-Vis absorbance was measured at 592 nm at 25 °C exactly 10 min after Leuco-crystal violet was added. The residue of [I<sub>2</sub> + I<sup>-</sup>] could be calculated based on the calibration curve.

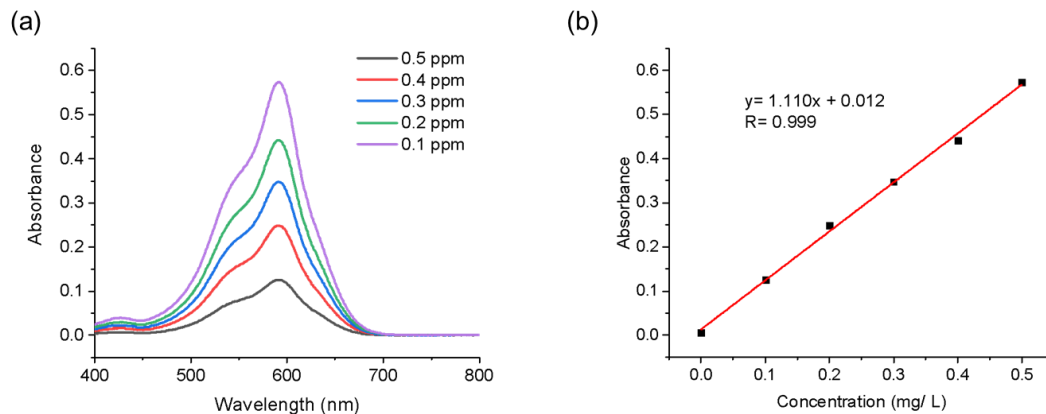


**Figure S19.** (a) UV-vis spectra of the standard iodide solution after 10 min of reaction time with Leuco-crystal violet and N-Chlorosuccinimide. (b) The linear fit of absorbance at 592 nm of standard iodide solution after 10 min of reaction time with Leuco-crystal violet and N-Chlorosuccinimide.

Dual-wavelength UV-Vis spectrometry is a simpler method to measure  $I^-$  concentration in the presence of  $NO_3^-$  interference.<sup>S<sup>280</sup></sup> When  $I^-$  or  $NO_3^-$  is directly determined by UV-Vis spectrometry, the two anions interfere due to the absorption band overlap. Therefore, a dual-wavelength method with primary wavelength (220 nm) and secondary wavelength (231 nm) was used for the determination of  $NO_3^-$  and  $I^-$  in solution. Based on the UV-vis spectra of standard KI (0.07 mmol/L) solution, standard  $KNO_3$  (0.07 mmol/L) solution and KI (0.07 mmol/L) +  $KNO_3$ (0.07 mmol/L) mixture (Figure S22), the linear equations were calculated as  $A_{220nm} - A_{231nm} = 2.960 c(NO_3^-)$ ,  $A_{220nm}(NO_3^-) = 3.667 c(NO_3^-)$ , and  $A_{220nm}(I^-) = A_{220nm} - A_{220nm}(NO_3^-) = 10.666 c(I^-)$ . The result is in good agreement with the previously reported data. <sup>S<sup>280</sup></sup>



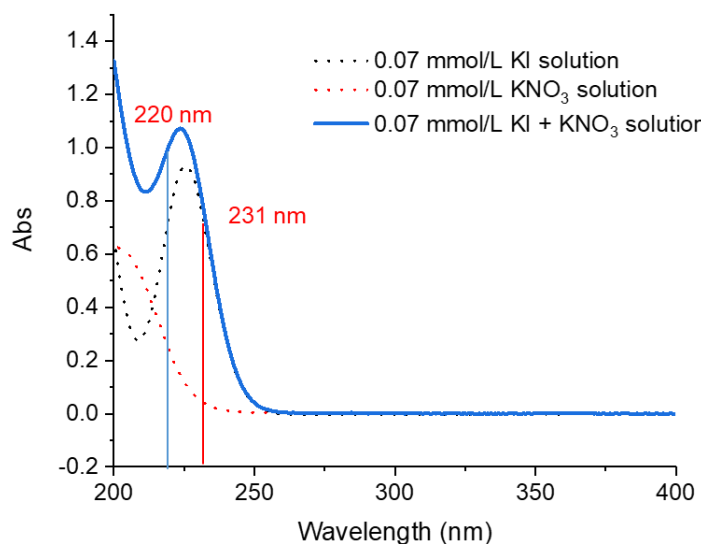
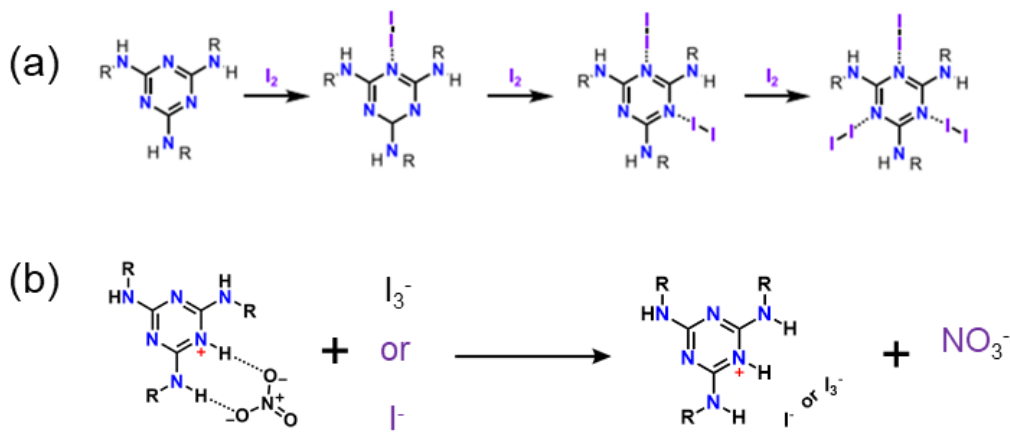


**Figure S20.** (a) UV-vis spectra of the 0.07 mM KI solution, 0.07 mM KNO<sub>3</sub> solution, and the mixture of (0.07 mM KI + 0.07 mM KNO<sub>3</sub>)

### 3.4.6 Static iodine adsorption investigations.



**Scheme S4.** (a) The halogen bond interaction between I<sub>2</sub> and the triazine rings of H<sub>c</sub>OF-7. (b) I<sub>3</sub><sup>-</sup> or I<sup>-</sup> exchange process with H<sub>c</sub>OF-7

**Iodine uptake amount measurements.** To study the I<sub>2</sub> uptake capacity of different absorbents at different temperatures in an aqueous environment, H<sub>c</sub>OF crystals-7 (10 mg), activated carbon (15mg), and CHOP-7 (10 mg) powder were soaked in a 3 mL I<sub>2</sub>/KI<sub>3</sub> concentrated

aqueous solution (0.51 g KI and 0.66 g I<sub>2</sub>) in a 4 mL vial at 23, 40, 50, 70 and 90 °C for 48 h. The solid was collected by filtration, washed with excess water until the filtrate became colorless, and dried in the open air before weighing. The experiment was repeated three times. (Figure S21)

**Kinetic study of I<sub>2</sub> adsorption.** I<sub>2</sub>/KI solution (1.2 mM I<sub>2</sub> + 5.0 mM KI, 15 mL) was prepared and added to a 20 mL sealed vial with string. The sealed vials were heated to 23, 40, 50, 70 and 90 °C on the oil bath, respectively. When the temperature stabilized, 10 mg H<sub>c</sub>OF-7 was added into the vials and the timer was started. Periodically, 3 mL of the solution was piped out for concentration measurement by UV-Vis spectroscopy (Figure S22). The solution was poured back into the vial after the measurement. We use a pseudo-first-order equation to fit the adsorption results at different temperatures (Figure S23- S26).

$$r = -\frac{d[c]}{dt} = k[c]$$

$$\ln \frac{c_0}{[c]} = kt$$

*k*: rate constant; [c]: concentration; *c*<sub>0</sub>: initial concentration.

The obtained rate constant was further fitted by Arrhenius equation (Figure S27):

$$\ln k = \frac{-E_a}{RT} + \ln A$$

*E*<sub>a</sub>: activation energy; *k*: rate constant; *A*: pre-exponential factor. The activated energy is calculated as 34.5 kJ/ mol.

**Langmuir adsorption study.** H<sub>c</sub>OF-7 crystals (10 mg) were added to 326, 489, 652, 815 mg/L I<sub>2</sub> aqueous solution (15 mL) at 23 °C. After 48 h, the uptake amount of I<sub>2</sub> was measured by UV-vis spectroscopy. We used Langmuir adsorption equation to fit the adsorption results.

$$q_e = q_{max} \times \frac{Kc}{1 + Kc}$$

*q*<sub>e</sub>: the adsorption amount at the concentration; *q*<sub>max</sub>: the theoretical maximum adsorption amount; *c*: the initial concentration before adsorption. *K*: Langmuir equilibrium constant.

The maximum adsorption amount is calculated as 722.2 mg/g. The Langmuir equilibrium constant is calculated as 4.19 × 10<sup>-3</sup> L/mg (Figure S31- S32).

**I<sub>2</sub>/I<sup>-</sup> residue investigation.** H<sub>C</sub>OF-7 crystals were exchanged by THF (10 mL × 5) for 24 h and activated under vacuum. Then 6 mg H<sub>C</sub>OF-7 was added into 3 mL iodine solution (I<sub>2</sub>: 3.5 mg/L + 1.5 mg/L I<sup>-</sup>, and I<sup>-</sup>: 1.5 mg/L) in a 4 mL vial. The mixtures were heated to different temperatures under the oil bath. After 72 h, the iodine concentration of the solution was determined by Leuco-crystal violet method (Figure S28). For reference, the 10 mg CHOP-7 was added into 3 mL iodine solution (I<sub>2</sub>: 3.5 mg/L + 1.5 mg/L I<sup>-</sup>) under different temperatures. After 72 h, the iodine concentration of the solution was determined by Leuco-crystal violet method and compared with the result of H<sub>C</sub>OF-7 (Figure S29).

**I<sup>-</sup> exchange investigation.** H<sub>C</sub>OF-7 crystals were exchanged by THF (10 mL × 5) for 24 h and activated under vacuum. Then 5 mg H<sub>C</sub>OF-7 was added into 3 mL 3.5 mM KI solution (1·4H<sup>+</sup>: NO<sub>3</sub><sup>-</sup>: I<sup>-</sup> = 1: 4: 4) in a 4 mL vial. The mixtures were heated to different temperatures under an oil bath. After 72 h, the iodine concentration of the solution and the amount of I<sup>-</sup> uptake was determined by the dual-wavelength UV-vis spectroscopy method (Figure S30).

**Investigation of I<sub>2</sub>/I<sup>-</sup> cooperative adoption.** Different amount of I<sub>2</sub> (5 mg, 10mg, 15 mg) was dissolved in MeOH (3 mL) at the room temperature, followed by adding 5 mg H<sub>C</sub>OF-7. After 48h, the I<sub>2</sub> uptake amount was calculated based on the UV-vis spectroscopy of I<sub>2</sub> solution. Then the I<sub>2</sub> MeOH solution was carefully piped out. KI solution (3 mL, 3.5 mM) was added into the vial (1·4H<sup>+</sup>: NO<sub>3</sub><sup>-</sup>: I<sup>-</sup> = 1: 4: 4). After 48 h, the I<sup>-</sup> exchange amount was measured by the dual-wavelength UV-Vis spectroscopy method. The result showed that the I<sup>-</sup> exchange amount enhanced along with the I<sub>2</sub> dosing amount increasing, which indicates that uptake of I<sub>2</sub> promotes the absorption of I<sup>-</sup>. (Figure 5c)

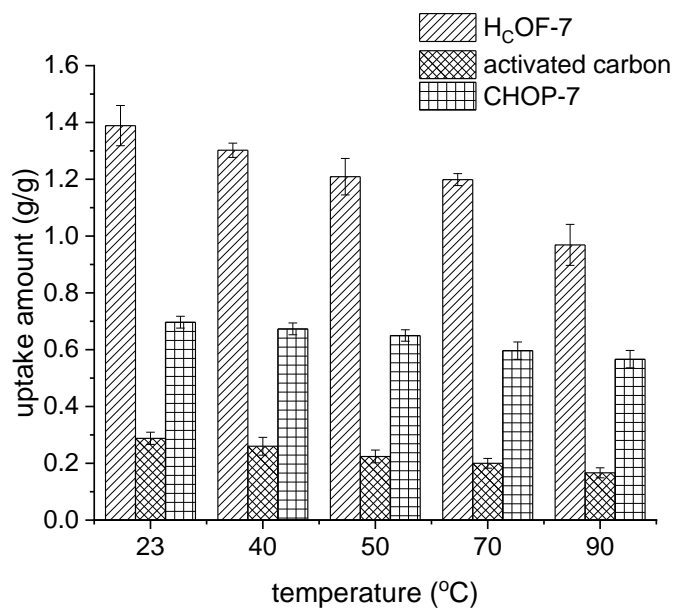


**Figure S21.** Iodine uptake amount for H<sub>c</sub>OF-7, activated carbon and CHOP-7 at different temperatures

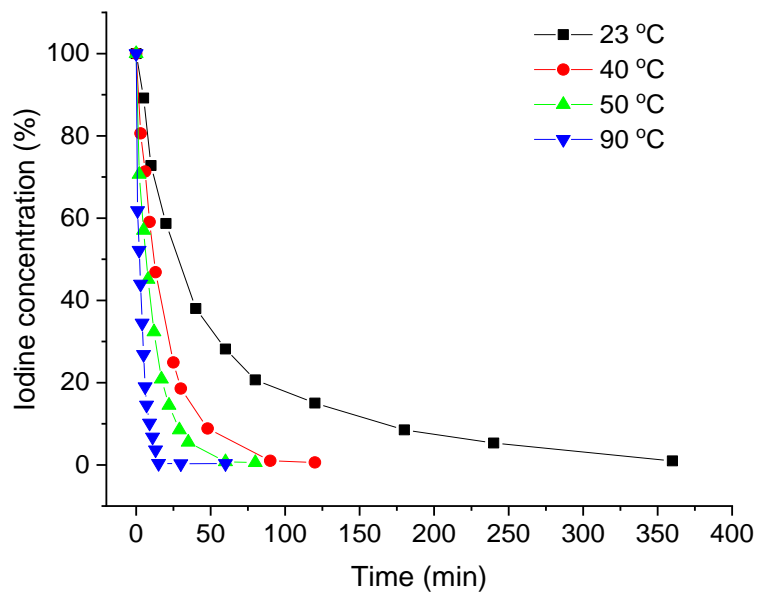


**Figure S22.** Time-dependent UV-vis absorbance intensity at 292 nm for H<sub>c</sub>OF-7 iodine uptake (I<sub>2</sub>: 1.2 mM) under different temperatures.

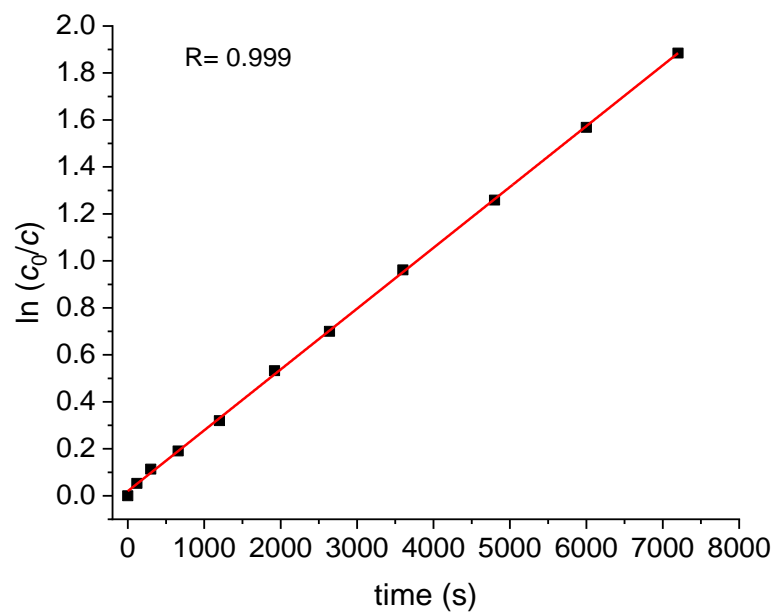


**Figure S23.** Pseudo-first-order fitting of iodine adsorption at 23 °C ( $k= 2.59 \times 10^{-4} \text{ s}^{-1}$ ).

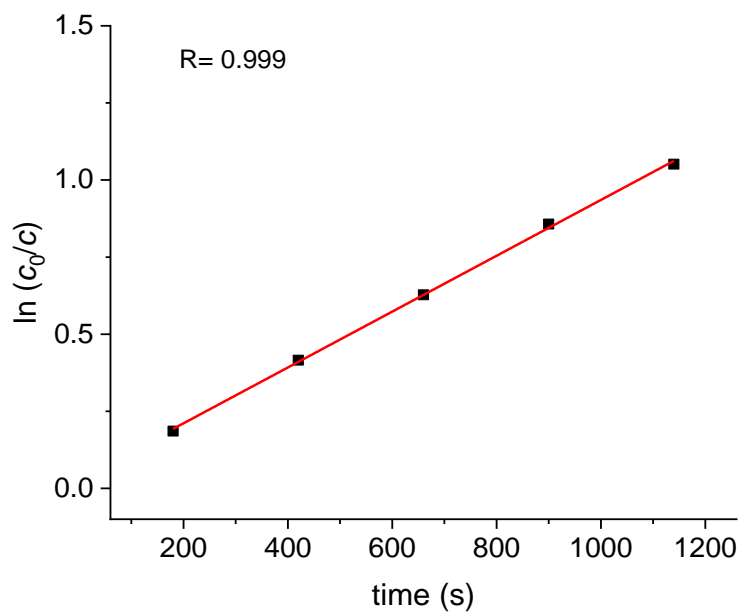


**Figure S24.** Pseudo first order fitting of iodine adsorption at 40 °C ( $k= 9.06 \times 10^{-4} \text{ s}^{-1}$ ).

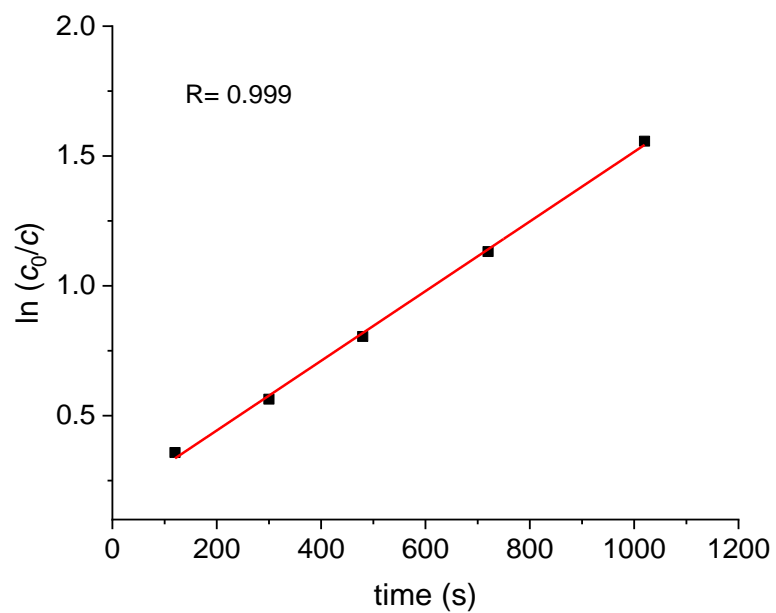


**Figure S25.** Pseudo first order fitting of iodine adsorption at 50 °C ( $k= 1.34 \times 10^{-3} \text{ s}^{-1}$ ).

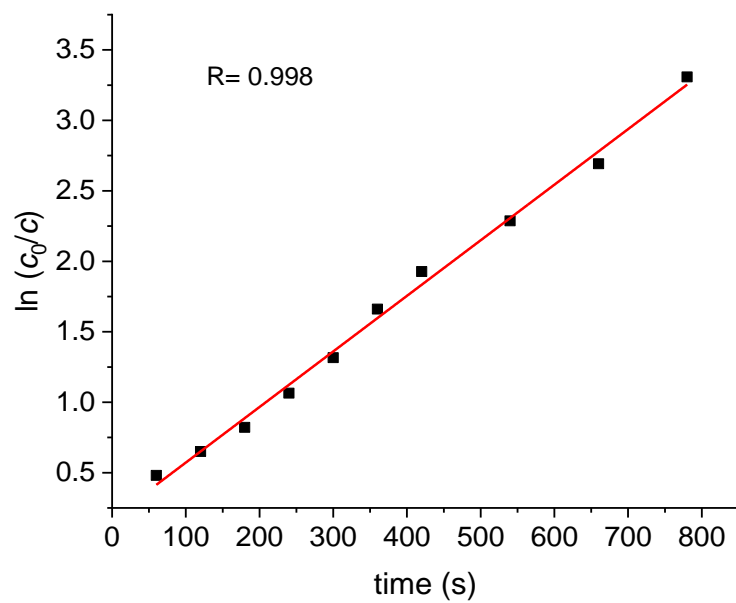


**Figure S26.** Pseudo first order fitting of iodine adsorption at 90 °C ( $k= 3.94 \times 10^{-3} \text{ s}^{-1}$ ).

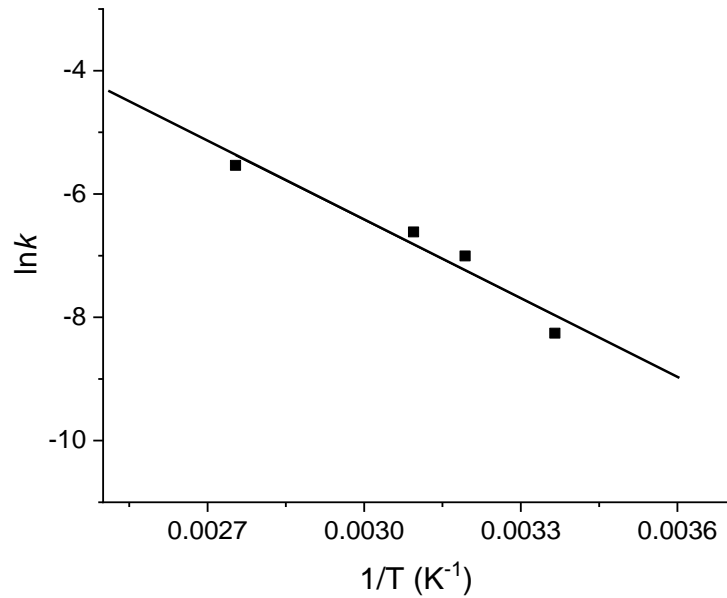


**Figure S27.** Arrhenius equation fitting of iodine adsorption ( $E_a = 34.4$  kJ/mol).

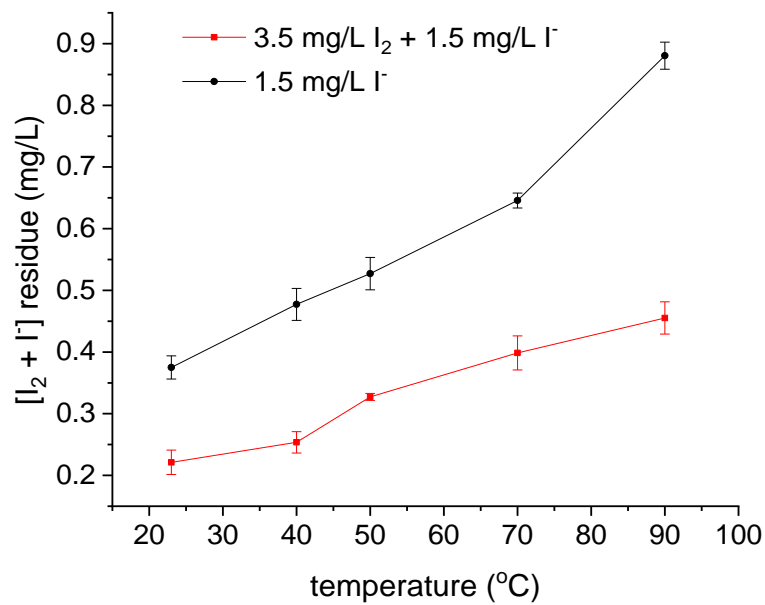


**Figure S28.** The residual concentration of  $[I_2 + I^-]$  after H<sub>c</sub>OF-7 adsorption from a mixture of (3.5 mg/L I<sub>2</sub> + 1.5 mg/L I<sup>-</sup>) solution and 1.5 mg/L I<sup>-</sup> aqueous solution at different temperatures.

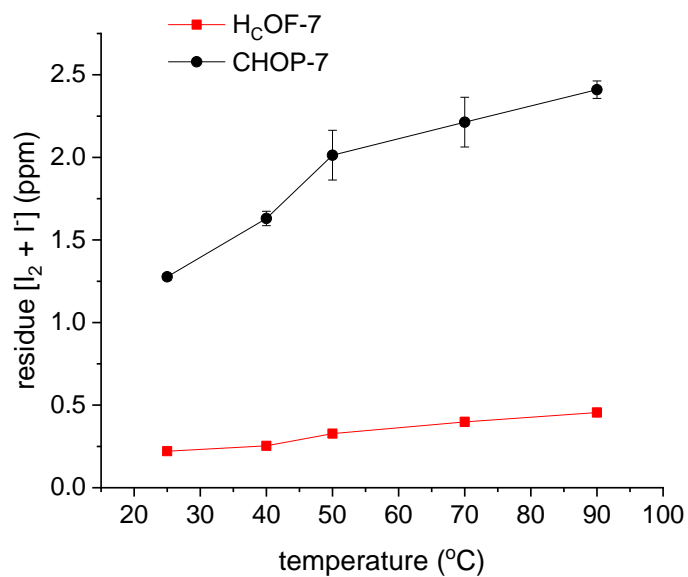


**Figure S29.** The residual concentration of [I<sub>2</sub> + I<sup>-</sup>] after H<sub>c</sub>OF-7 and CHOP-7 adsorption from a mixture of (3.5 mg/L I<sub>2</sub> + 1.5 mg/L I<sup>-</sup>) solution at different temperatures.

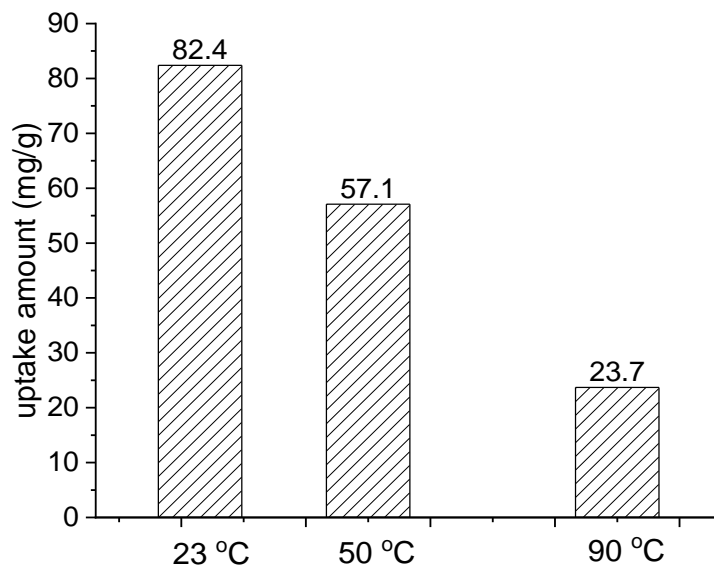


**Figure S30.** I<sup>-</sup> uptake amount for H<sub>c</sub>OF-7 at different temperatures.



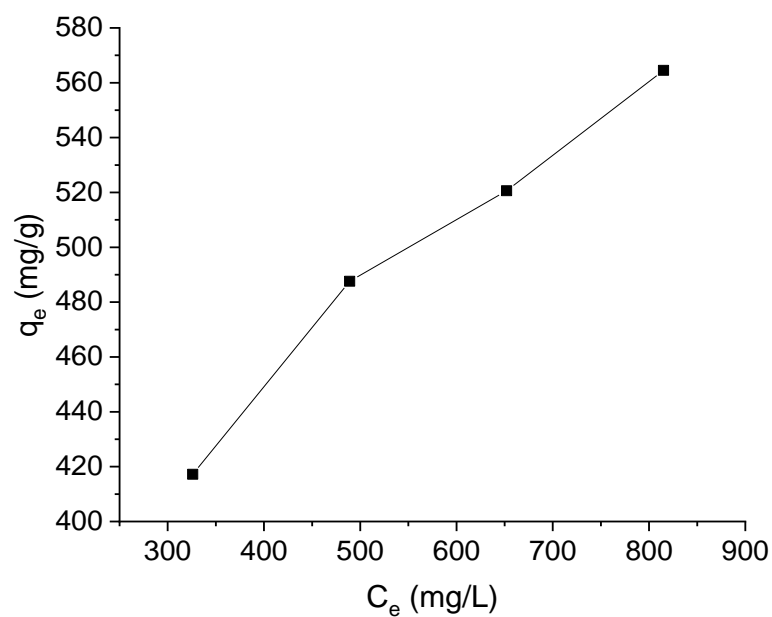


**Figure S31.** Iodine adsorption for H<sub>c</sub>OF-7 at different initial concentration.

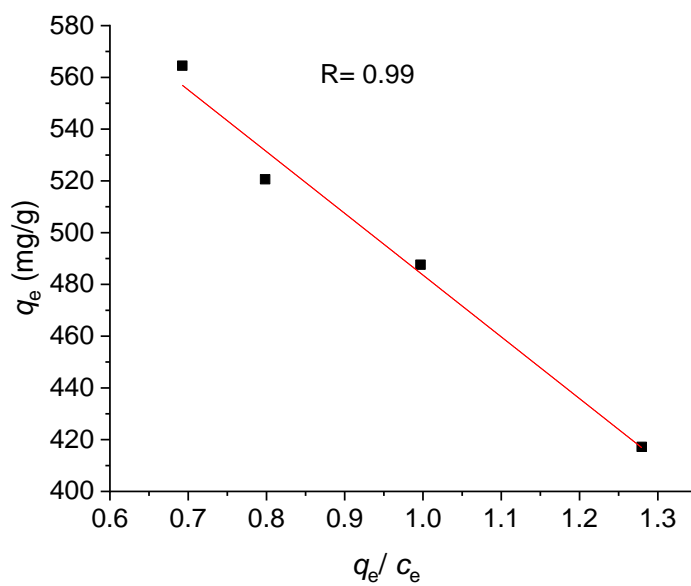


**Figure S32.** Langmuir model fitting of iodine adsorption for H<sub>c</sub>OF-7 ( $q_{\max} = 722.2$  mg/g,  $K = 4.19 \times 10^{-3}$  L/mg)

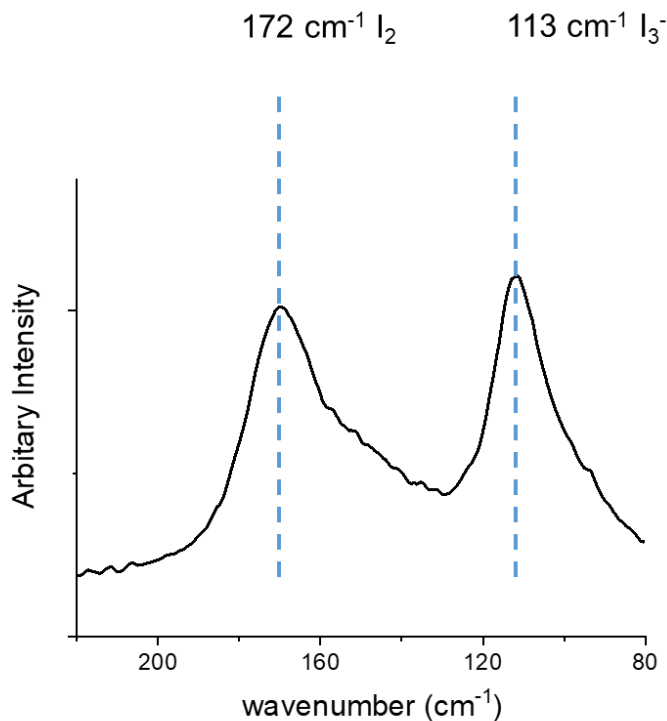


**Figure S33.** Raman spectrum of H<sub>c</sub>OF-7 after I<sub>2</sub> and I<sup>-</sup> uptake.

### 3.4.7 Iodine solution breakthrough experiment

**H<sub>c</sub>OF-7 column preparation.** H<sub>c</sub>OF-7 crystals (240 mg) were exchanged by THF (5 × 30 mL) and hexanes (5 × 30 mL) for 24 h respectively. Then H<sub>c</sub>OF-7 crystals and hexanes (10 mL) distributed evenly into a ball-milling steel container with 3 ZrO<sub>2</sub> balls. After grinding by ball-milling at 50 Hz for 3 minutes, the crystals were filled into a plastic syringe (length: 27 mm, inner diameter: 4.5 mm). Both ends of the syringe are blocked with cotton. Before iodine adsorption experiment, THF (30 mL) was passed through into the column to make the adsorbents close-packed.

**Activated carbon and [activated carbon + resin] mixed-bed column preparation.** Activated carbon (240 mg, Millipore Sigma) was ball-milled and activated at 120 °C for 24 h before using. Then, it was filled into a column (d: 4.5 × l: 26 mm), with both ends capped by cotton. Before the breakthrough experiment, distilled water (50 mL) was passed through the column.

The anion exchange resin (130 mg, Dowex 1X2, 50-100 mesh) is immersed in the distilled water for 6 h before using. Then, the resin and activated carbon (130 mg) were packed into a column (d: 4.5 × l: 30 mm), with both ends capped by cotton. Before the breakthrough experiment, distilled water (50 mL) was passed through the column.

**Temperature controlled breakthrough experiment.** Iodine solution breakthrough experiment setup is shown in Figure 3d. Iodine solution ( $I_2$ : 3.5 mg/L and  $I^-$ : 1.5 mg/L) was prepared in a plastic bottle (4 L). A steel cartridge (300 mL) with the heating tape covered was connected to the entrance of the column. The flow rate was controlled at 5 mL/min. The temperature was adjusted by controlling the voltage of the heating tape. After the temperature is stabilized, H<sub>c</sub>OF-7 column was installed. The iodine solution passed through H<sub>c</sub>OF-7 column and collected into the test tubes. The residual concentration of [ $I_2 + I^-$ ] of the collected solution after the column was determined by Leuco-crystal violet method. (Figure S35)



**Figure S34.** Image of iodine solution (35 mg/L  $I_2$  + 15 mg/L  $I^-$ ) before and after through H<sub>c</sub>OF-7 column.

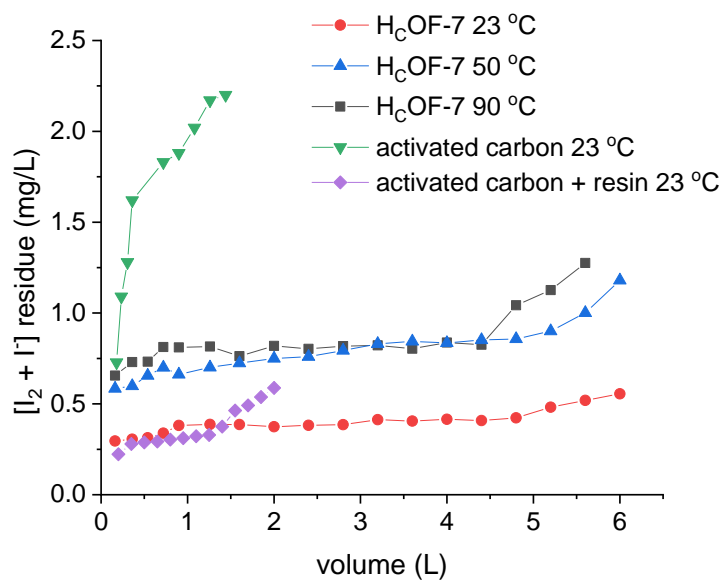


**Figure S35.** The residual concentrations of total iodine ( $I_2 + I^-$ ) in water after passing through the H<sub>C</sub>OF-7, activated carbon, and the mixture-bed columns measured using the Leuco-crystal violet method. Iodinated water ( $I_2 + KI$ , 3.5 + 1.5 ppm) was pumped into a customized steel precolumn (d: 50 × l: 220 mm) and heated to the desired temperatures under continuous flow (5 mL/min).

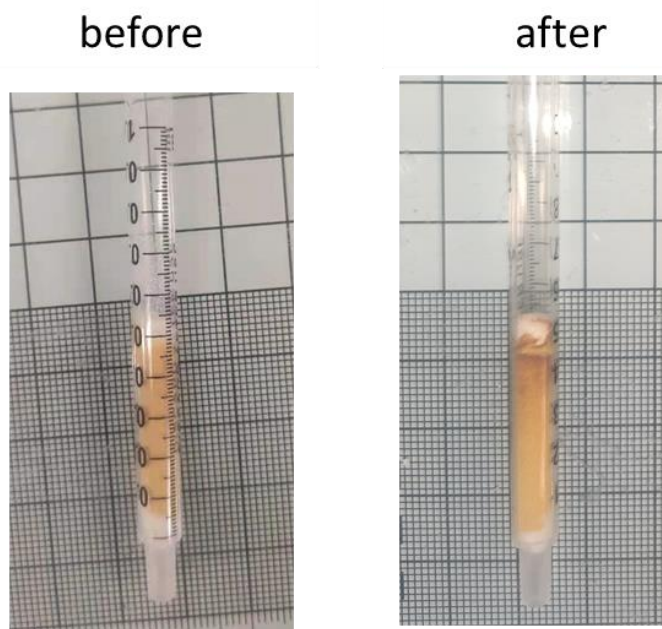


**Figure S36.** Images of H<sub>C</sub>OF-7 column before and after the iodine residue removal breakthrough experiment.

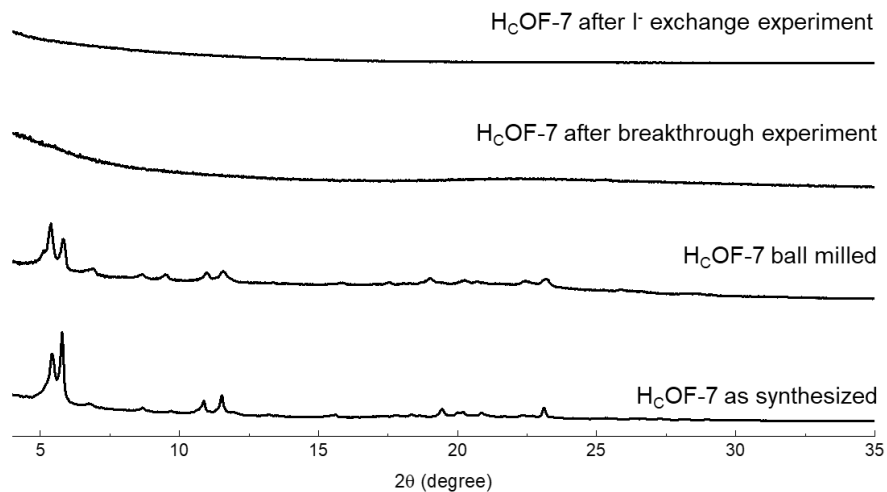


**Figure S37.** PXRD profiles of as synthesized H<sub>c</sub>OF, H<sub>c</sub>OF-7 after ball milling and H<sub>c</sub>OF-7 after the (3.5 ppm I<sub>2</sub> + 1.5 ppm I<sup>-</sup>) breakthrough experiment at the 23 °C, and after I<sup>-</sup> (3.5 mM) exchange at the room temperature.

### 3.4.8 <sup>1</sup>H NMR, <sup>13</sup>C NMR, and HR-MS spectra

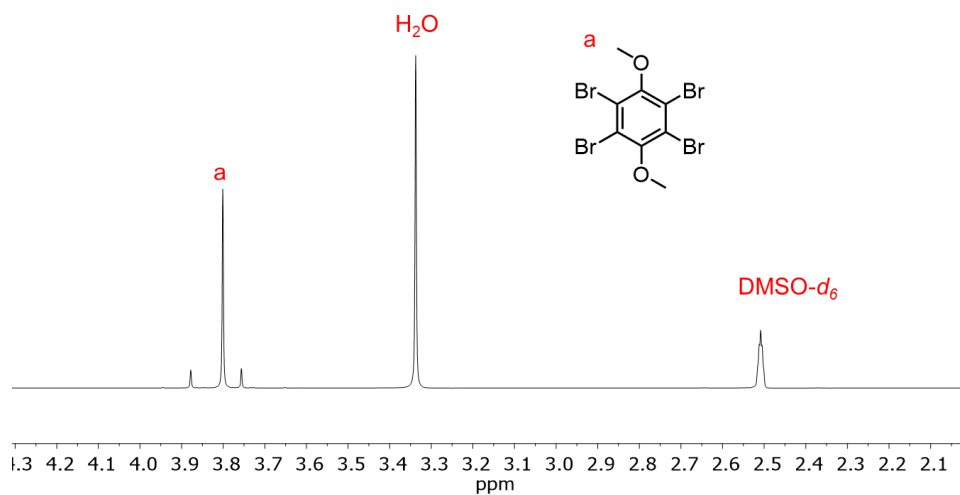


**Figure S38.** <sup>1</sup>H NMR spectrum of S1 in DMSO-*d*<sub>6</sub> (500 MHz) recorded at 298 K.

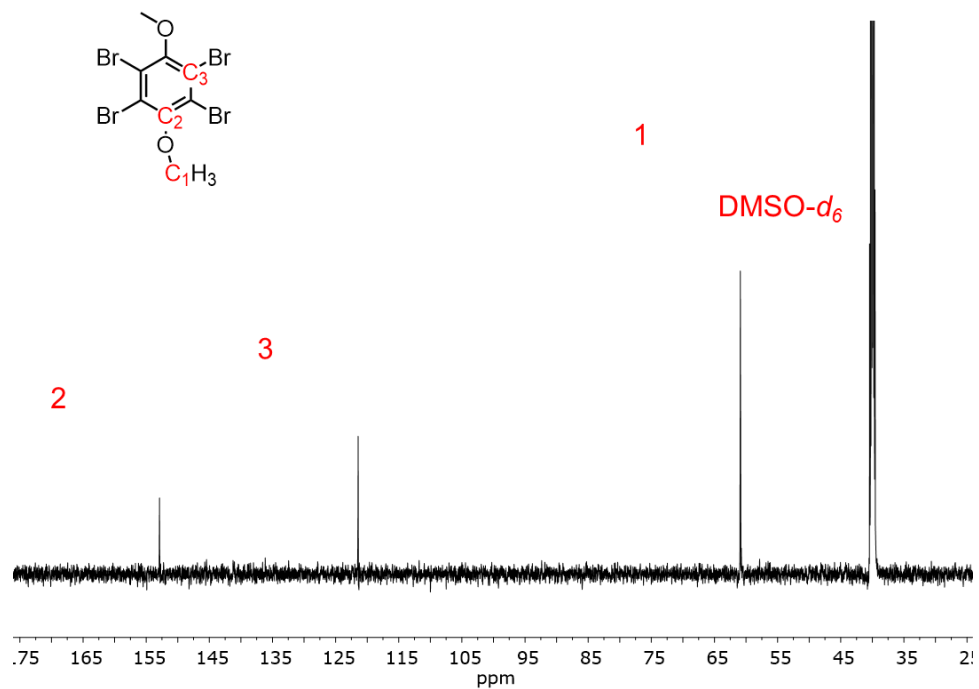


**Figure S39.**  $^{13}\text{C}$  NMR spectrum of **S1** in  $\text{DMSO-}d_6$  (150 MHz) recorded at 298 K.

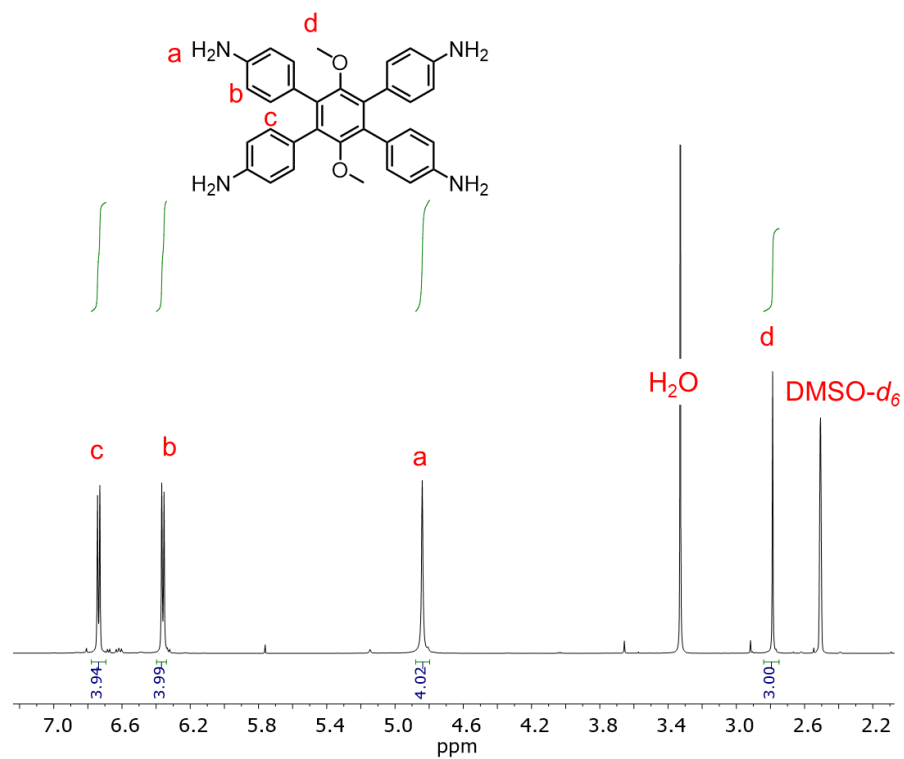


**Figure S40.**  $^1\text{H}$  NMR spectrum of **S2** in  $\text{DMSO-}d_6$  (500 MHz) recorded at 298 K.

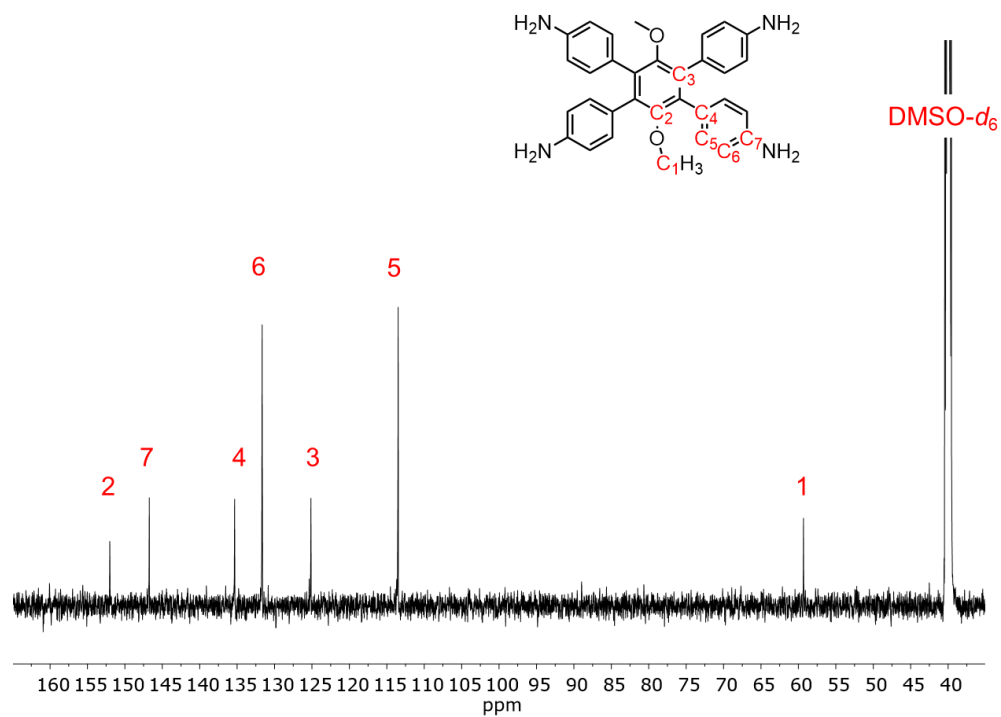


**Figure S41.**  $^{13}\text{C}$  NMR spectrum of S2 in DMSO- $d_6$  (150 MHz) recorded at 298 K.

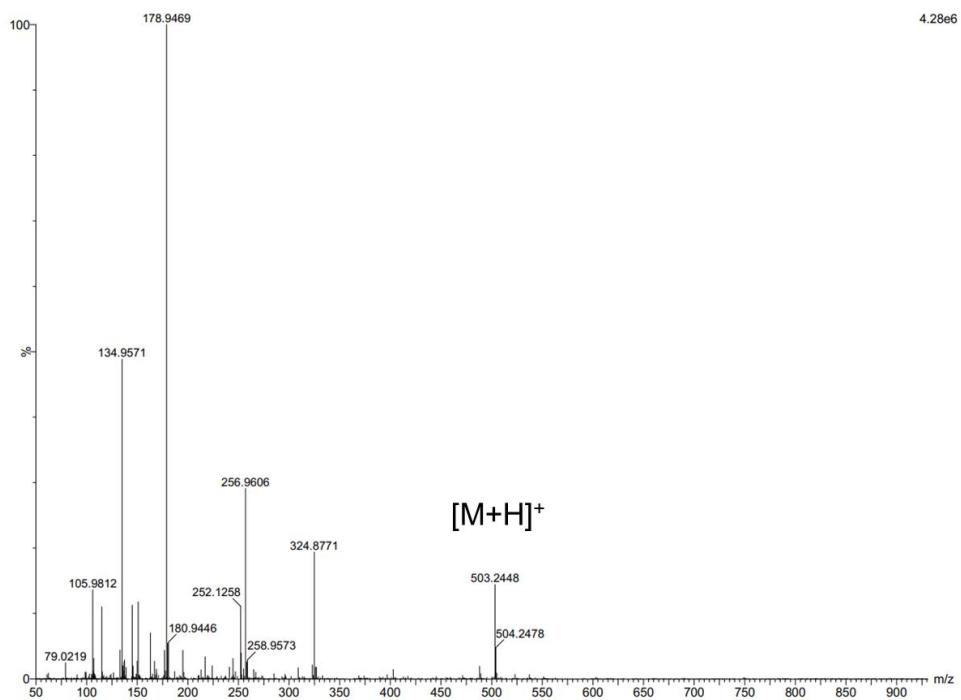


**Figure S42.** ESI-HRMS spectrum of S2

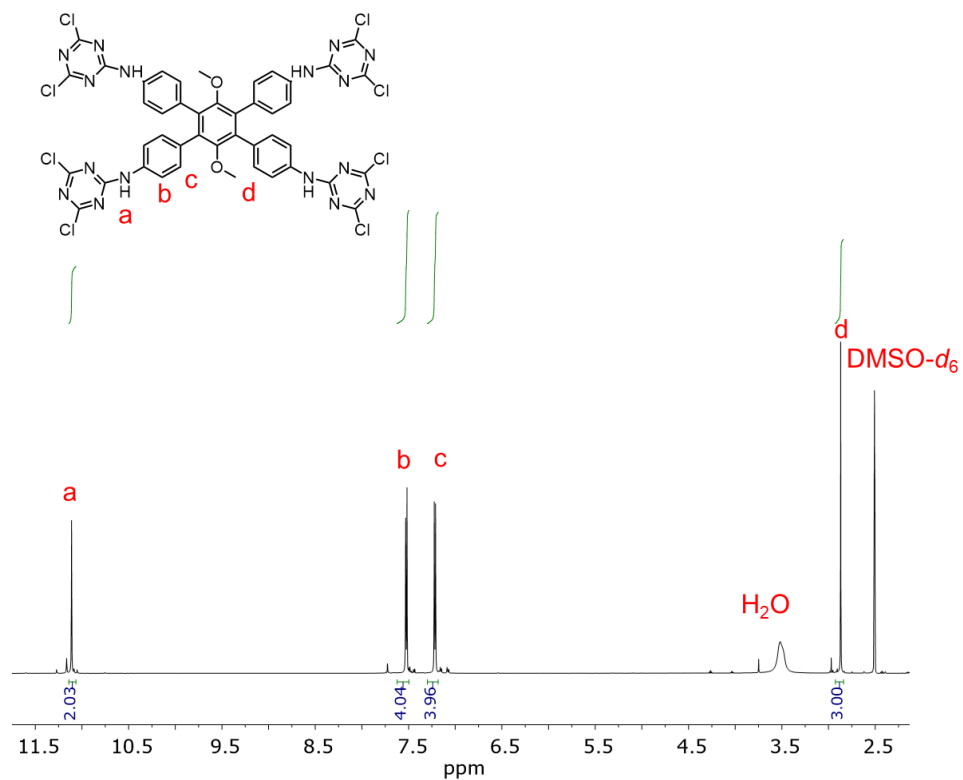


**Figure S43.** <sup>1</sup>H NMR spectrum of **S3** in DMSO-*d*<sub>6</sub> (500 MHz) recorded at 298 K

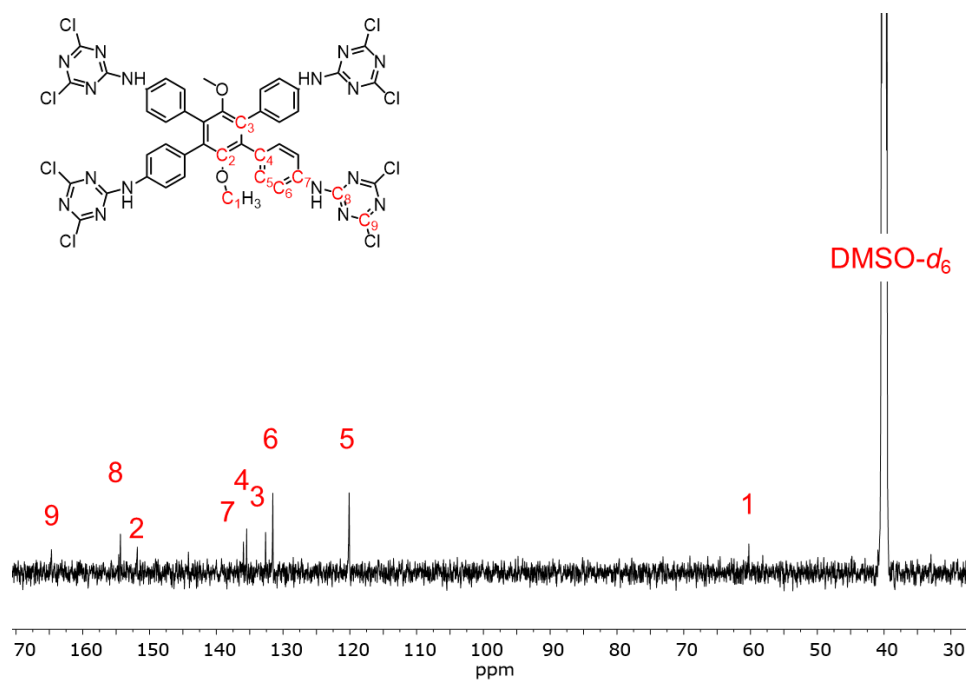


**Figure S44.** <sup>13</sup>C NMR spectrum of **S3** in DMSO-*d*<sub>6</sub> (150 MHz) recorded at 298 K



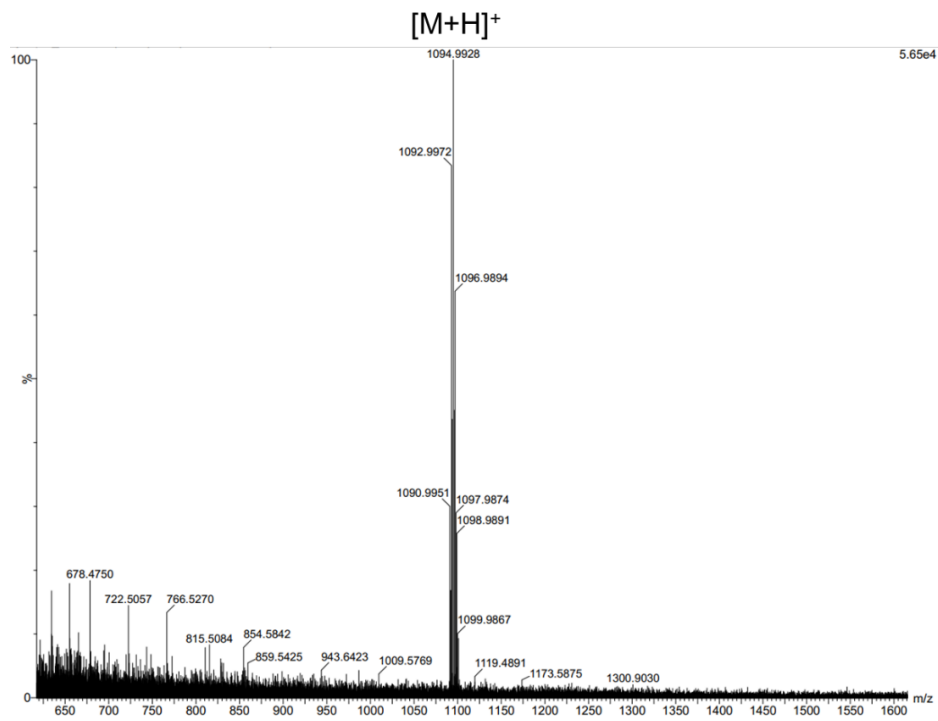


Figure S45. ESI-HRMS spectrum of S3

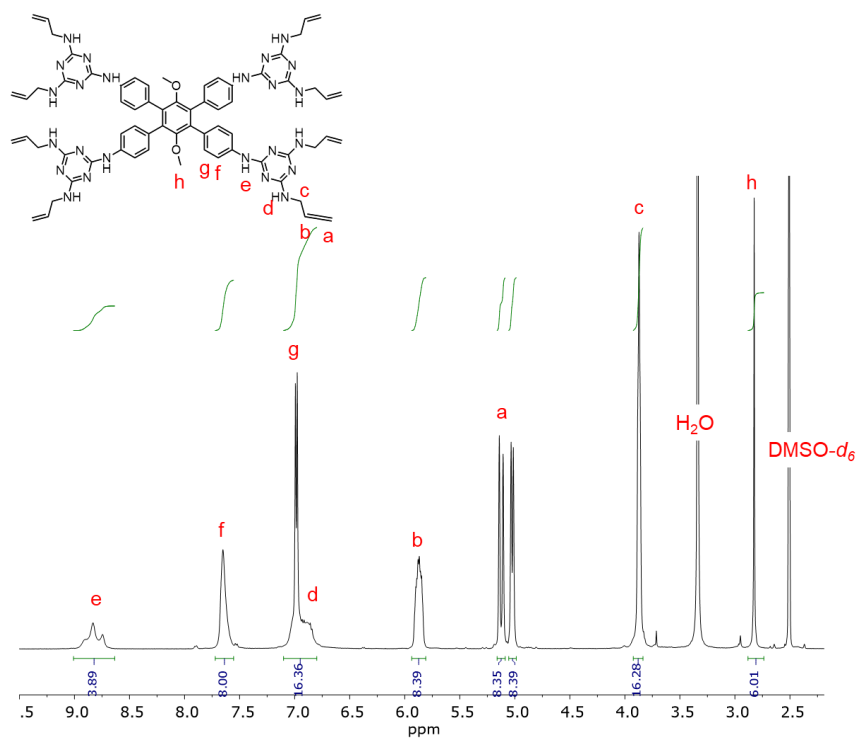
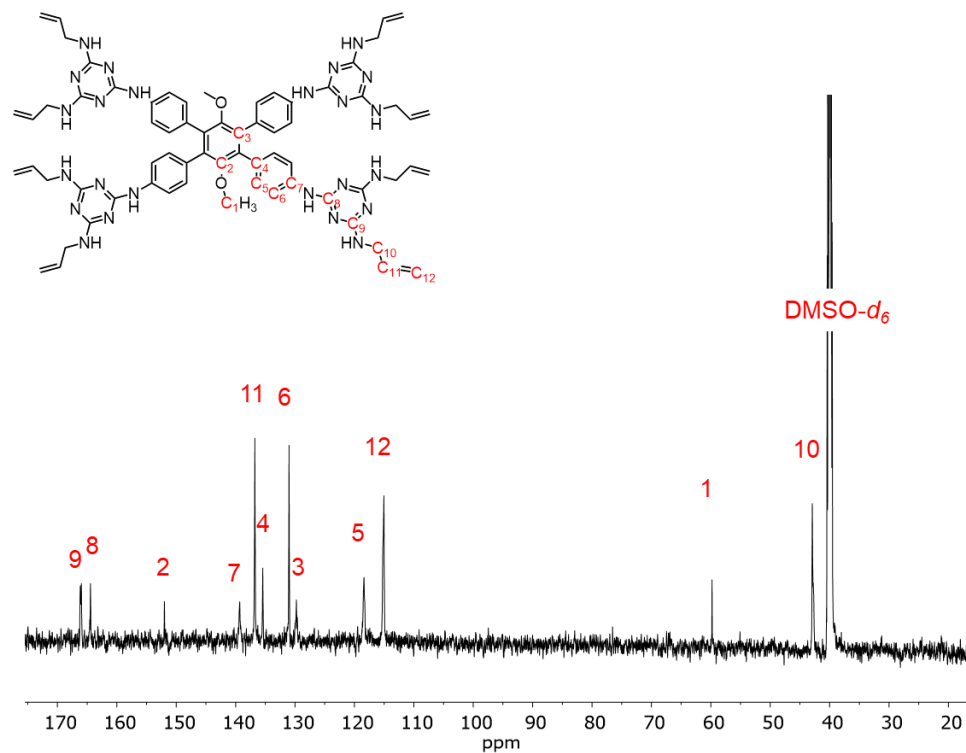
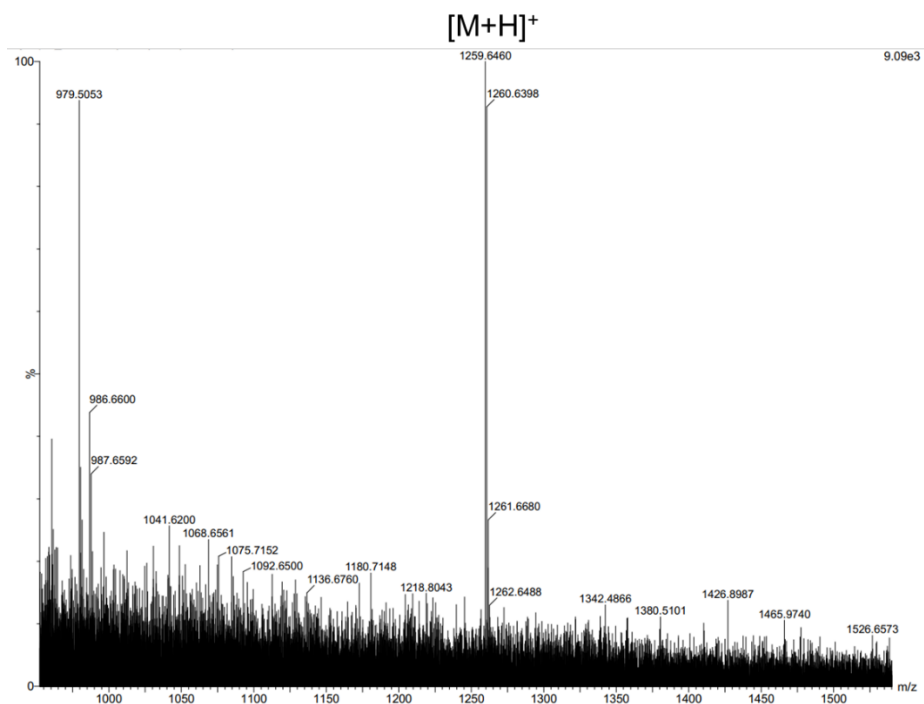


Figure S46. <sup>1</sup>H NMR spectrum of **1** in DMSO-*d*<sub>6</sub> (500 MHz) recorded at 298 K



**Figure S47.**  $^{13}\text{C}$  NMR spectrum of **1** in  $\text{DMSO-}d_6$  (150 MHz) recorded at 298 K



**Figure S48.** ESI-HRMS spectrum of **1**

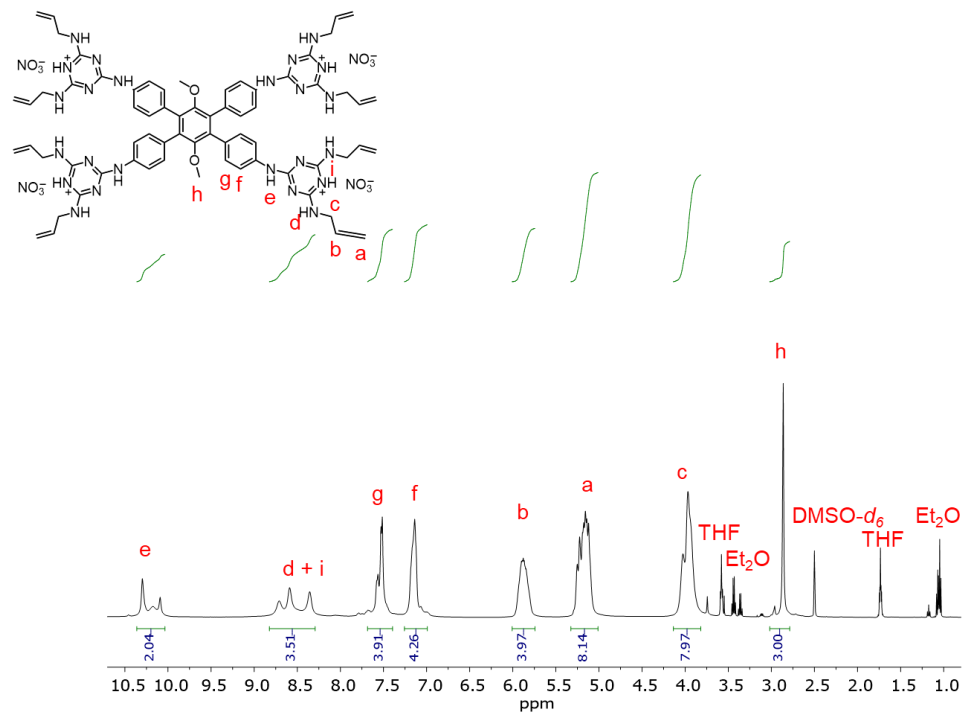


**Figure S49.**  $^1H$  NMR spectrum of  $1 \cdot 4H^+ \cdot 4NO_3^-$  crystal in  $DMSO-d_6$  (500 MHz) recorded at 298 K

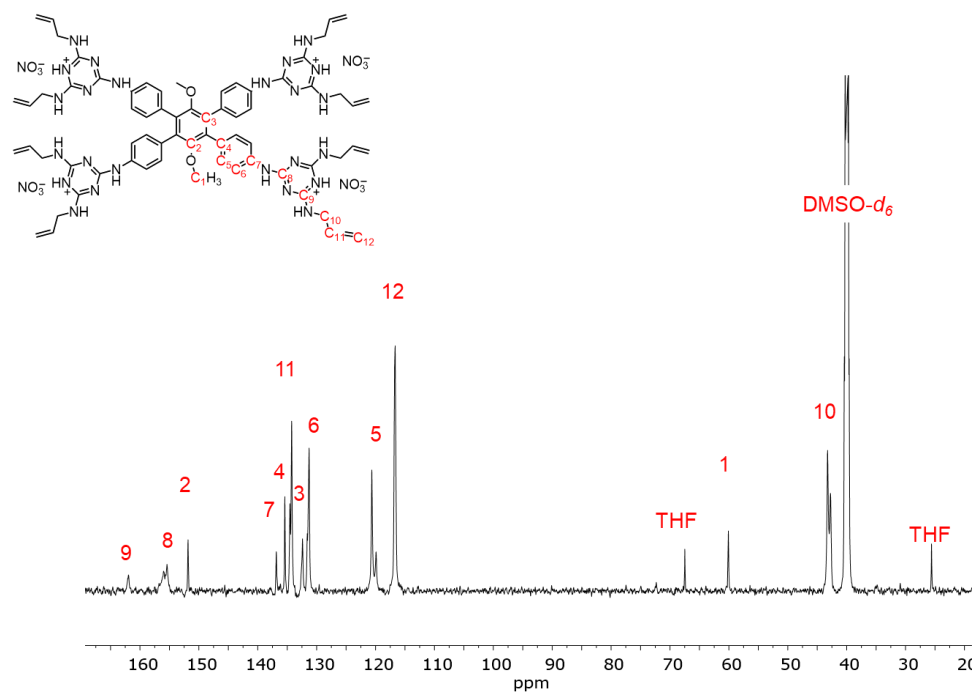


**Figure S50.**  $^{13}C$  NMR spectrum of  $1 \cdot 4H^+ \cdot 4NO_3^-$  crystal in  $DMSO-d_6$  (150 MHz) recorded at 298 K

### 3.5 References

- 222 S. Bolisetty, M. Peydayesh, R. Mezzenga, *Chem. Soc. Rev.* **2019**, *48*, 463-487.
- 223 Z. F. Wang, S. N. Zhang, Y. Chen, Z. J. Zhang, S. Q. Ma, *Chem. Soc. Rev.* **2020**, *49*, 708-735.
- 224 H. Backer, *Clin. Infect. Dis.* **2002**, *34*, 355-364.
- 225 S. Punyani, P. Narayana, H. Singh, P. Vasudevan, *J. Sci. Ind. Res. India* **2006**, *65*, 116-120.
- 226 H. Backer, J. Hollowell, *Environ. Health Persp.* **2000**, *108*, 679-684.
- 227 L. A. Shaw, SAE International, Warrendale, PA, **2008**.
- 228 World Health Organization(WHO), *Iodine as a drinking-water disinfectant* **2018**.
- 229 USEPA, *Emergency disinfection of drinking water* **2006**.
- 230 J. Steele, M. Wilson, J. Makinen, C. M. Ott, in *International Conference on Environmental Systems*, Albuquerque, NM, **2018**.
- 231 J. A. T. Pennington, *J. Am. Diet. Assoc.* **1990**, *90*, 1571-1581.
- 232 J. D. Heiner, E. A. Simmons, D. C. Hile, I. S. Wedmore, *Wild. Environ. Med.* **2011**, *22*, 329-332.
- 233 R. S. Lomande, S. A. Parab, *Asian J. Chem.* **2007**, *19*, 3299-3300.
- 234 P. Singare, R. Lokhande, *Natural Science* **2009**, *1*, 191-194.
- 235 DUPONT, *Temperature stability of anion exchange resins*, **2019**.
- 236 B. W. Maryat, in *International Conference on Environmental Systems*, Albuquerque, New Mexico, **2018**.
- 237 J. T. Hughes, D. F. Sava, T. M. Nenoff, A. Navrotsky, *J. Am. Chem. Soc.* **2013**, *135*, 16256-16259.
- 238 D. F. Sava, K. W. Chapman, M. A. Rodriguez, J. A. Greathouse, P. S. Crozier, H. Y. Zhao, P. J. Chupas, T. M. Nenoff, *Chem. Mater.* **2013**, *25*, 2591-2596.
- 239 X. R. Zhang, I. da Silva, H. G. W. Godfrey, S. K. Callear, S. A. Sapchenko, Y. Q. Cheng, I. Vitorica-Yrezabal, M. D. Frogley, G. Cinque, C. C. Tang, C. Giacobbe, C. Dejoie, S. Rudic, A. J. Ramirez-Cuesta, M. A. Denecke, S. H. Yang, M. Schroder, *J. Am. Chem. Soc.* **2017**, *139*, 16289-16296.
- 240 X. R. Zhang, J. Maddock, T. M. Nenoff, M. A. Denecke, S. H. Yang, M. Schroder, *Chem. Soc. Rev.* **2022**, *51*, 3243-3262.
- 241 A. Gogia, P. Das, S. K. Mandal, *ACS Appl. Mater. Inter.* **2020**, *12*, 46107-46118.
- 242 S. B. B. Alahakoon, S. D. D. Diwakara, C. M. M. Thompson, R. A. A. Smaldone, *Chem. Soc. Rev.* **2020**, *49*, 1344-1356.

- 243 P. Wang, Q. Xu, Z. P. Li, W. M. Jiang, Q. H. Jiang, D. L. Jiang, *Adv. Mater.* **2018**, *30*, 1801991.
- 244 C. Wang, Y. Wang, R. L. Ge, X. D. Song, X. Q. Xing, Q. K. Jiang, H. Lu, C. Hao, X. W. Guo, Y. A. Gao, D. L. Jiang, *Chem-Eur J.* **2018**, *24*, 585-589.
- 245 L. W. He, L. Chen, X. L. Dong, S. T. Zhang, M. X. Zhang, X. Dai, X. J. Liu, P. Lin, K. F. Li, C. L. Chen, T. T. Pan, F. Y. Ma, J. C. Chen, M. J. Yuan, Y. G. Zhang, L. Chen, R. H. Zhou, Y. Han, Z. F. Chai, S. Wang, *Chem* **2021**, *7*, 699-714.
- 246 F. Ren, Z. Q. Zhu, X. Qian, W. D. Liang, P. Mu, H. X. Sun, J. H. Liu, A. Li, *Chem. Commun.* **2016**, *52*, 9797-9800.
- 247 Y. H. Abdelmoaty, T. D. Tessema, F. A. Choudhury, O. M. El-Kadri, H. M. El-Kaderi, *ACS Appl. Mater. Inter.* **2018**, *10*, 16049-16058.
- 248 A. Sen, S. Sharma, S. Dutta, M. M. Shirolkar, G. K. Dam, S. Let, S. K. Ghosh, *ACS Appl. Mater. Inter.* **2021**, *13*, 34188-34196.
- 249 C. Y. Pei, T. Ben, S. X. Xu, S. L. Qiu, *J. Mater. Chem. A* **2014**, *2*, 7179-7187.
- 250 I. Hisaki, N. Ikenaka, E. Gomez, B. Cohen, N. Tohnai, A. Douhal, *Chem-Eur J.* **2017**, *23*, 11611-11619.
- 251 Z. Zhang, X. Dong, J. Yin, Z. G. Li, X. Li, D. Zhang, T. Pan, Q. Lei, X. Liu, Y. Xie, F. Shui, J. Li, M. Yi, J. Yuan, Z. You, L. Zhang, J. Chang, H. Zhang, W. Li, Q. Fang, B. Li, X. H. Bu, Y. Han, *J. Am. Chem. Soc.* **2022**, *144*, 6821-6829.
- 252 Y. Xie, T. Pan, Q. Lei, C. Chen, X. Dong, Y. Yuan, W. A. Maksoud, L. Zhao, L. Cavallo, I. Pinnau, Y. Han, *Nat. Commun.* **2022**, *13*, 2878.
- 253 R. Chen, T. L. Hu, Y. Q. Li, *React. Funct. Polym.* **2021**, *159*, 104806.
- 254 L. H. Xie, Z. Y. Zheng, Q. Y. Lin, H. Zhou, X. F. Ji, J. L. Sessler, H. Y. Wang, *Angew. Chem. Int. Edit.* **2022**, *61*, 202113724.
- 255 P. Brunet, E. Demers, T. Maris, G. D. Enright, J. D. Wuest, *Angew. Chem. Int. Edit.* **2003**, *42*, 5303-5306.
- 256 K. Hema, K. M. Sureshan, *Accounts Chem. Res.* **2019**, *52*, 3149-3163.
- 257 A. Ravi, A. Shijad, K. M. Sureshan, *Chem. Sci.* **2021**, *12*, 11652-11658.
- 258 M. Arunachalam, P. Ghosh, *Inorg. Chem.* **2010**, *49*, 943-951.
- 259 S. Mason, T. Clifford, L. Seib, K. Kuczera, K. Bowman-James, *J. Am. Chem. Soc.* **1998**, *120*, 8899-8900.
- 260 M. Arunachalam, P. Ghosh, *Chem. Commun.* **2009**, 3184-3186.
- 261 M. A. Saeed, F. R. Fronczek, M. J. Huang, M. A. Hossain, *Chem. Commun.* **2010**, *46*, 404-406.

- 262 D. A. Cullen, M. G. Gardiner, N. G. White, *Chem. Commun.* **2019**, 55, 12020-12023.
- 263 N. J. Williams, C. A. Seipp, F. M. Brethome, Y. Z. Ma, A. S. Ivanov, V. S. Bryantsev, M. K. Kidder, H. J. Martin, E. Holguin, K. A. Garrabrant, R. Custelcean, *Chem* **2019**, 5, 719-730.
- 264 K. Pandurangan, J. A. Kitchen, S. Blasco, E. M. Boyle, B. Fitzpatrick, M. Feeney, P. E. Kruger, T. Gunnlaugsson, *Angew. Chem. Int. Edit.* **2015**, 54, 4566-4570.
- 265 R. Chutia, S. K. Dey, G. Das, *Cryst. Growth Des.* **2015**, 15, 4993-5001.
- 266 E. M. Fatila, E. B. Twum, A. Sengupta, M. Pink, J. A. Karty, K. Raghavachari, A. H. Flood, *Angew. Chem. Int. Edit.* **2016**, 55, 14057-14062.
- 267 E. M. Fatila, E. B. Twum, J. A. Karty, A. H. Flood, *Chem-Eur J.* **2017**, 23, 10652-10662.
- 268 W. Zhao, A. H. Flood, N. G. White, *Chem. Soc. Rev.* **2020**, 49, 7893-7906.
- 269 M. Mantina, A. C. Chamberlin, R. Valero, C. J. Cramer, D. G. Truhlar, *J. Phys. Chem. A* **2009**, 113, 5806-5812.
- 270 R. D. Shannon, *Acta Crystallogr. A* **1976**, 32, 751-767.
- 271 R. W. Ramette, R. W. Sandford, *J. Am. Chem. Soc.* **1965**, 87, 5001.
- 272 The total iodine uptake capacity on account of the nitrate anion mass loss, will be slightly larger than the mass increase amount reported here. However, it is difficult to quantitatively measure the mass loss of nitrate anions in this process.
- 273 G. Cavallo, P. Metrangolo, R. Milani, T. Pilati, A. Priimagi, G. Resnati, G. Terraneo, *Chem. Rev.* **2016**, 116, 2478-2601.
- 274 Q. K. Liu, J. P. Ma, Y. B. Dong, *Chem. Commun.* **2011**, 47, 7185-7187.
- 275 Z. Yin, Q. X. Wang, M. H. Zeng, *J. Am. Chem. Soc.* **2012**, 134, 4857-4863.
- 276 Only less than 1% of  $I_3^-$  exists in the equilibrium.
- 277 J. L. Lambert, G. L. Hatch, B. Mosier, *Anal. Chem.* **2002**, 47, 915-916.
- 278 K. W. Robinson, *Water-quality trends in New England rivers during the 20th century*, U.S. Dept. of the Interior, U.S. Geological Survey U.S. Geological Survey, Information Services distributor, Pembroke, N.H Denver, CO, **2003**.
- 279 Y. Xie, J. Li, C. Lin, B. Gui, C. Ji, D. Yuan, J. Sun, C. Wang, *J. Am. Chem. Soc.* **2021**, 143, 7279-7284.
- 280 H. Zhang, T. Guo, Q. Li, S. Ye, ZhijianWu, *Chin. J. Inorg. Chem.* **2011**, 1, 24-28.

**Chapter 4 Hierarchical Co-assembly-enabled 3D-Printing of  
Homogeneous and Heterogeneous Covalent Organic  
Frameworks**

PREFACE for “Hierarchical Co-assembly-enabled 3D-Printing of Homogeneous and Heterogeneous Covalent Organic Frameworks” published in *Journal of the American Chemical Society*. Reproduced from The American Association for the Advancement of Science.

Zhang, M.; Li, L.; Lin, Q.; Tang, M.; Wu, Y.; Ke, C. Hierarchical-Coassembly-Enabled 3D-Printing of Homogeneous and Heterogeneous Covalent Organic Frameworks. *J. Am. Chem. Soc.* **2019**, *141*, 5154-5158. The co-first author, Mingshi Zhang, performed most of the experimental work, data analysis, and plotting. The co-first author, Longyu performed the model compound synthesis and COF simulation. Qianming Lin and Miao Tang performed the 3D printing process. The corresponding author, Professor Chenfeng Ke provided guidance on ideas and focus of the research, led the organization and planning of experiments, and significantly contributed to the writing and editing of the manuscript.



## 4.1 Introduction

Covalent organic frameworks (COFs),<sup>3,9,281-283</sup> especially imine and  $\beta$ -ketoenamine-linked COFs,<sup>284</sup> have demonstrated great promises for applications in molecular storage, separation, catalysis and energy storage due to their synthetic versatility, good chemical stability, high crystallinity, large void spaces, and accessible surface area. COFs are usually employed in the form of as-synthesized powders or 2D thin films<sup>285</sup> and membranes<sup>286</sup> to selectively adsorb and separate molecules of interest, benefiting from nano-sized pores defined by the periodically aligned molecular entities. The limited form factors of COF-based materials, however, pose challenges to expand their uses in complex 3D devices. Recently, 3D printing technology such as direct ink writing (DIW) has demonstrated promises for the fabrication of porous materials such as metal-organic frameworks (MOFs),<sup>160, 287-290</sup> yet no COF-based 3D-printed material has been reported. Establishing a method to fabricate COF-based 3D-printed monoliths will not only allow for high-rate mass transfer of substrates at the macroscale<sup>291</sup> but also enable selective adsorption and catalytic conversion of substrates with suitable sizes at the nanoscale.<sup>283</sup> Currently, the integration of these crystalline powders such as MOFs into 3D printing materials are achieved by forming MOF/polymer composites.<sup>160, 287-290</sup> However, this approach possesses several intrinsic limitations: (1) the tradeoff between the mechanical stability, which requires larger binder amount, and the high surface area, which requires lower binder amount to avoid reducing<sup>287</sup> or even blocking the nanosized pores of the fabricated monolith; (2) limited printability giving rise to the uncontrolled and uneven distribution<sup>289</sup> of the porous particles; and (3) difficulties to integrate multiple porous materials with robust interfacial binding, since individual porous material requires tailored polymer composition.

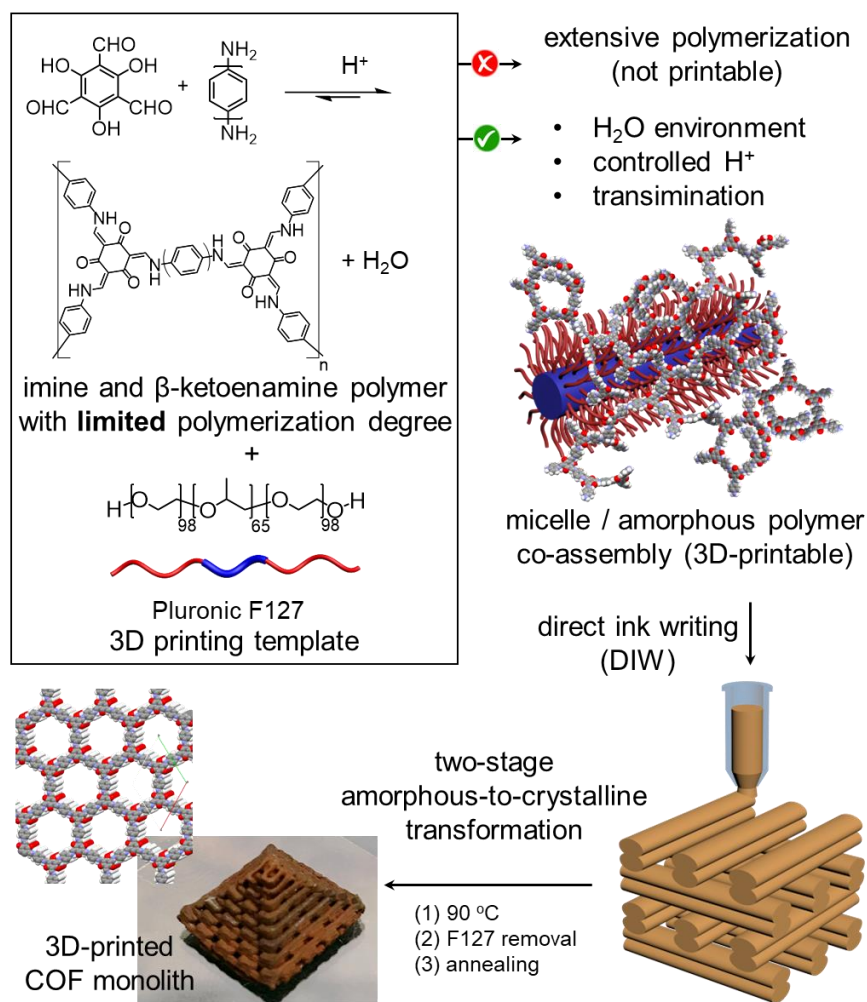


**Figure 4.1.** Design and synthesis of 3D-printed hierarchically porous imine and  $\beta$ -ketoenamine-linked COFs through a supramolecular templated co-assembly process followed by a two-stage post-printing imine network transformation.

In this communication, we present the stepwise manipulation of the imine-COFs formation process<sup>292-293</sup> to introduce COFs, for the first time, as 3D-printing materials. Through a templated hierarchical co-assembly<sup>134</sup> followed by post-printing amorphous-to-crystalline network re-organization (Figure 4.1), crystalline single- and dual-component COF monoliths have been fabricated successfully. In our design, imine and  $\beta$ -ketoenamine-based COF precursors are polymerized in an aqueous environment in the presence of a supramolecular 3D printing template Pluronic F127, affording 3D-printable hydrogels composed of imine polymer/F127 co-assemblies<sup>294</sup> (Figure 4.1). The degree of polymerization (DP) of the amorphous imine (or  $\beta$ -ketoenamine) polymer is intentionally

restrained by introducing a large excess of water, controlling the amount of acid catalyst and the introduction of a transimination step.<sup>295</sup> After 3D printing, the amorphous polymers are heated to extensively polymerize and re-organize the imine network. After the removal of F127 and solvent annealing, the 3D-printed COF-only monoliths possess homogeneous nano-to-macroscale hierarchical porous features, good structural integrity and mechanical robustness, and their measured surface areas match those of the correspondent COF powders. Furthermore, robust heterogeneous COF monoliths were obtained by 3D printing multiple hydrogels with different COF-precursors into designed 3D architectures. Benefiting from the reversible imine network formation, a molecular-level seamlessly interconnected interface is formed between two COFs, which cannot be achieved otherwise.

## 4.2 Results and Discussions

A  $\beta$ -ketoenamine COF **TpPa-1** reported<sup>65, 94</sup> by Banerjee *et al.* was chosen as the model system because of its mild synthesis conditions and high chemical stability. Solution-phase synthesized **TpPa-1** (*s-TpPa-1*) was obtained and its 2D hexagonal framework structure was confirmed by powder X-ray diffraction (PXRD) analysis. *s-TpPa-1* appear as irregular micrometer-sized particles under the scanning electron microscope (SEM, Figure S30), and its Brunauer-Emmett-Teller (BET) surface area was measured as 669 m<sup>2</sup>/g by N<sub>2</sub> sorption analysis (Figure S35). Physical blending of *s-TpPa-1* particles with F127 hydrogel affords a barely printable ink, which clogs the printer tips due to the coagulation of COF particles. The incomplete F127/*s-TpPa-1* monolith possesses no measurable surface area, and its 3D architecture quickly collapsed into powders upon F127 removal (Figure S4). In order to achieve a 3D-printable COF with homogeneity across the nano-to-macroscale, we sought to co-assemble its amorphous polymer precursor with F127 micelles (Figure S20) to form viscoelastic hydrogels for DIW. Experimentally, a THF solution (25 mL) of 1,3,5-triformylphloroglucinol (**Tp**) (0.9 g, 4.3 mmol) and an aqueous solution (6 mL) of *p*-phenylenediamine (**Pa**, 0.7 g, 6.5 mmol), *p*-toluenesulfonic acid (TsOH, 0-2.6 mmol)<sup>296</sup> and Pluronic F127 (2.0 g) were mixed together. A majority of the THF was quickly evaporated in open air and the mixture gradually turned to a red-colored opaque F127/imine-polymer hydrogel **G1** (Figure 4.2), indicating that the imine polycondensation was sufficiently restrained by the large excess of water so as to avoid precipitation. Stress-strain measurements of **G1** suggest an averaged elastic modulus of 12.0 kPa (Figure 4.3, *left*), which is sufficient to support a high-profile 3D geometry. In the step-strain study (Figure 4.3, *right*), **G1** deformed into a liquid-like material at 100% strain and immediately

recovered its elastic modulus after the shear force removal, suggesting that **G1** possesses rapid self-healing property for 3D printing. Lattice pyramids (Figure 4.2) with good structural integrity and stability were printed using **G1**. After DIW, the lattice was placed in a sealed chamber at 11 % relative humidity to gradually remove water and allow for an extensive imine polycondensation. Most of the water in the lattice was removed as indicated by the IR spectrum (Figure S17f) with 50% mass loss recorded. PXRD analysis of the freeze-dried gel (Figure S8) suggests that the periodically stacked hexagonal 2D framework had not yet been formed.

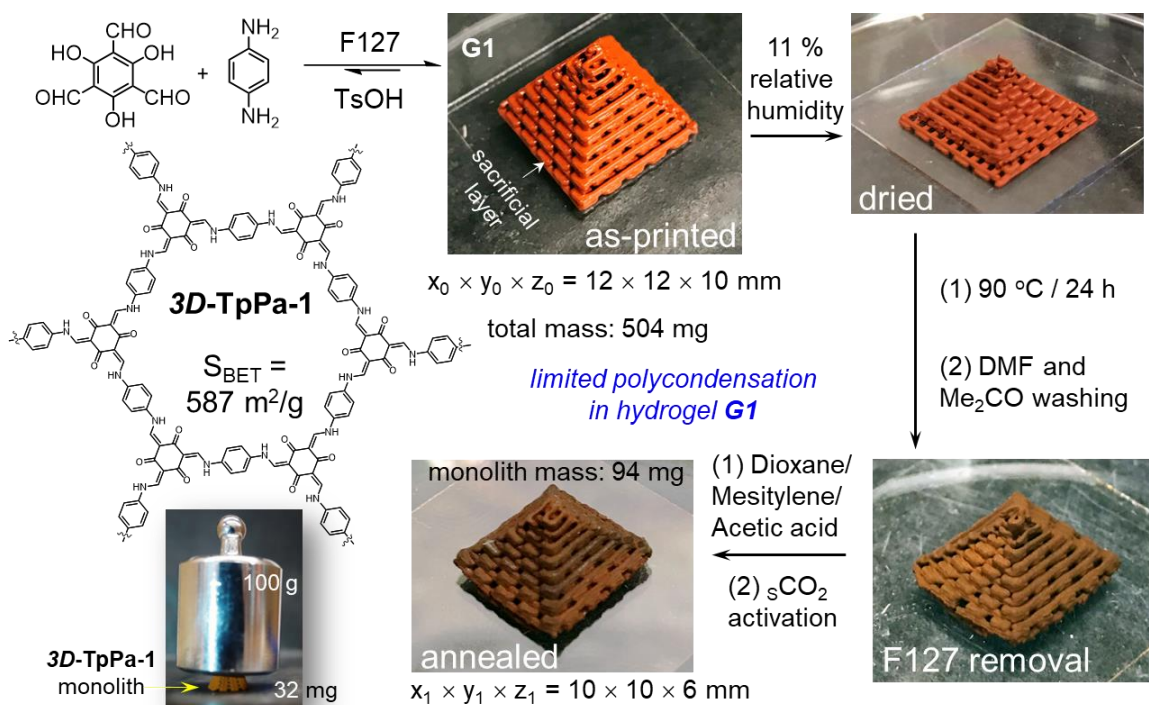


**Figure 4.2.** Synthesis of **3D-TpPa-1** through Pluronic F127 templated co-assembly followed by post-printing framework re-organization. Inset: a robust **3D-TpPa-1** cubic lattice (32 mg) loaded with a 100 g weight.

To extensively polymerize the imine network and initiate the amorphous-to-crystalline transformation, the lattice was heated to 90 °C for 24 h (Figure 4.2), followed by intensive solvent washing to remove any unreacted species as well as the F127 template. The 3D architecture of the pyramid is well maintained after washing and a ~61 % mass loss was recorded in this step. In the IR spectra (Figure 4.4a), the  $sp^3$  C-H stretching band at 2884  $\text{cm}^{-1}$  attributed to F127 disappeared after washing, suggesting a complete removal of

F127. The C=C stretching band at  $1580\text{ cm}^{-1}$  suggests an extensive imine-to- $\beta$ -ketoenamine tautomerization. PXRD profile of the monolith suggests (Figure 4.4b) the formation of a moderately crystalline **3D-TpPa-1** with diffraction peaks of  $2\theta = 4.7^\circ, 8.3^\circ, 11.1^\circ,$  and  $26.5^\circ$ . PXRD analysis of different samples obtained after F127 removal revealed that, increasing the heating time of the dried **G1** monolith from 24 h to 72 h and 120 h at  $90\text{ }^\circ\text{C}$  did not improve the monolith's crystallinity (Figure S9), nor did elevating the heating temperature to 120 or  $150\text{ }^\circ\text{C}$  (Figure S10). These results suggest that the network re-organization is hindered by the surrounding F127 matrix. However, we noticed that the amount of TsOH (0-2.6 mmol) added to the hydrogels had a significant impact on the crystallinity of the obtained **3D-TpPa-1** (Figure S11) and the stability of the 3D-printed architecture. While lower TsOH amount afforded as synthesized **3D-TpPa-1** with better crystallinity, higher TsOH amount allowed a more extensive  $\beta$ -ketoenamine polycondensation to form mechanically robust 3D architectures after solvent washing. An optimized TsOH (1.6 mmol) amount in the hydrogel was found to provide a balance in crystallinity and mechanical stability.

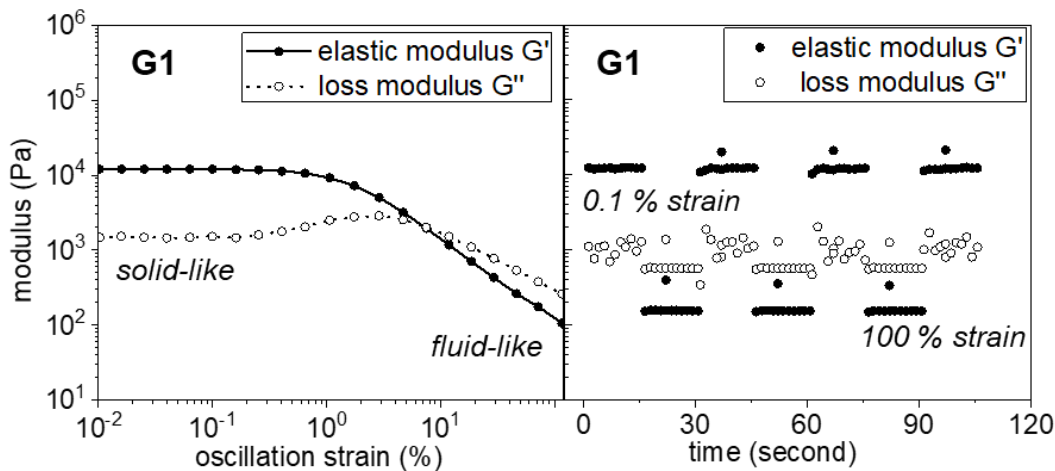


**Figure 4.3.** Stress-strain (*left*) and step-strain (*right*) rheological measurements of hydrogel **G1**.

To improve the crystallinity of the as-synthesized **3D-TpPa-1** monolith, the lattice obtained after F127 removal was annealed in a dioxane/mesitylene/acetic acid (6M) mixture at  $150\text{ }^\circ\text{C}$  for 72 h. After annealing, the crystallinity of **3D-TpPa-1** improved significantly (Figure 4.4b, green to red), and the monoliths exhibited good structural integrity and

outstanding mechanical robustness (Figure 2a, inset). Nitrogen adsorption isotherm (Figure S36) of the **3D-TpPa-1** acquired at 77 K suggests a BET surface area of 587 m<sup>2</sup>/g, which matches that of the **s-TpPa-1** we synthesized. In the SEM experiments (Figure 4.4c), interconnected nanocrystalline fibers were observed, which confirms the formation of crystalline COF throughout the monolith. Hierarchical porous features of the **3D-TpPa-1** monolith that attributed to the F127 removal were observed with pores ranging from a few nanometers to sub-micrometer throughout the dissected area of a 3D-printed lattice.

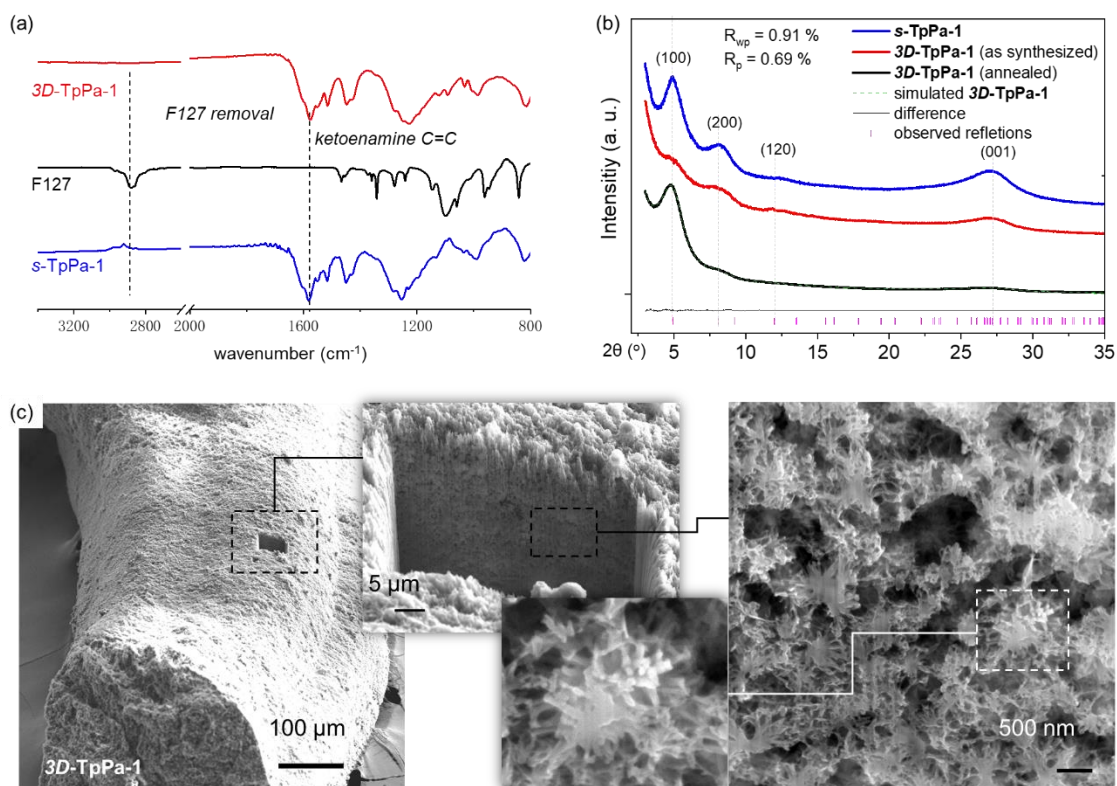


**Figure 4.4.** (a) FT-IR spectra of **s-TpPa-1**, F127, and **3D-TpPa-1**, respectively. (b) PXRD profiles of **s-TpPa-1**, as synthesized **3D-TpPa-1** after F127 removal and annealed **3D-TpPa-1**, respectively. (c) SEM images of a **3D-TpPa-1** and its focused ion beam sliced cross-section. Nano-crystalline fibers were observed in the cross-section.

Following this method, another  $\beta$ -ketoenamine COF<sup>94</sup> **TpBD-Me<sub>2</sub>** and an imine-COF<sup>297-298</sup> **TPE-COF** were successfully integrated into DIW-compatible materials (Figure 4.5a). Hydrogel **G2** formed by **Tp**, *o*-tolidine, F127 and TsOH were 3D-printed to a lattice pyramid (Figure S26). Although the hexagonal framework has not been extensively formed

after heating at 90 °C for 24 h (Figure 4.5c, green), a crystalline **3D-TpBD-Me<sub>2</sub>** monolith was obtained after solvent annealing (Figure 4.5c, red), suggesting that the  $\beta$ -ketoenamine polymer still reorganizes its network after the removal of F127 matrix. The **3D-TpBD-Me<sub>2</sub>** monolith possesses a measured BET surface area (1022 m<sup>2</sup>/g, Figure S38) similar to that of solution-phase synthesized **s-TpBD-Me<sub>2</sub>** (767 m<sup>2</sup>/g, Figure S37). In the dissected SEM sample (Figure S32), similar crystalline fibrous structures were observed with hierarchical porous features generated after F127 removal. In contrast, mixing tetrakis(4-aminophenyl)ethene, terephthalaldehyde, and F127 in the absence or presence of TsOH did not afford a homogeneous hydrogel but a non-printable yellow precipitate, which gave rise to the rapid formation of large imine polymer particles. To decrease the DP of the imine polymer, aniline was introduced to form an imine intermediate (Figure 4.5b), which subsequently reacted with tetrakis(4-aminophenyl)ethene through a transimination<sup>295</sup> polymerization in the presence of F127. A 3D-printable hydrogel **G3** was obtained and 3D-printed into lattice pyramid. Upon heating and subsequent annealing under an N<sub>2</sub> atmosphere, a crystalline monolith **3D-TPE-COF** (Figure 4.5b) with a measured BET surface area of 1373 m<sup>2</sup>/g (Figure S40) was obtained. PXRD (Figure 4.5d) and SEM analyses (Figure S33) suggest **3D-TPE-COF** possesses a periodically stacked 2D hexagonal framework at the nanoscale with hierarchical porous features.

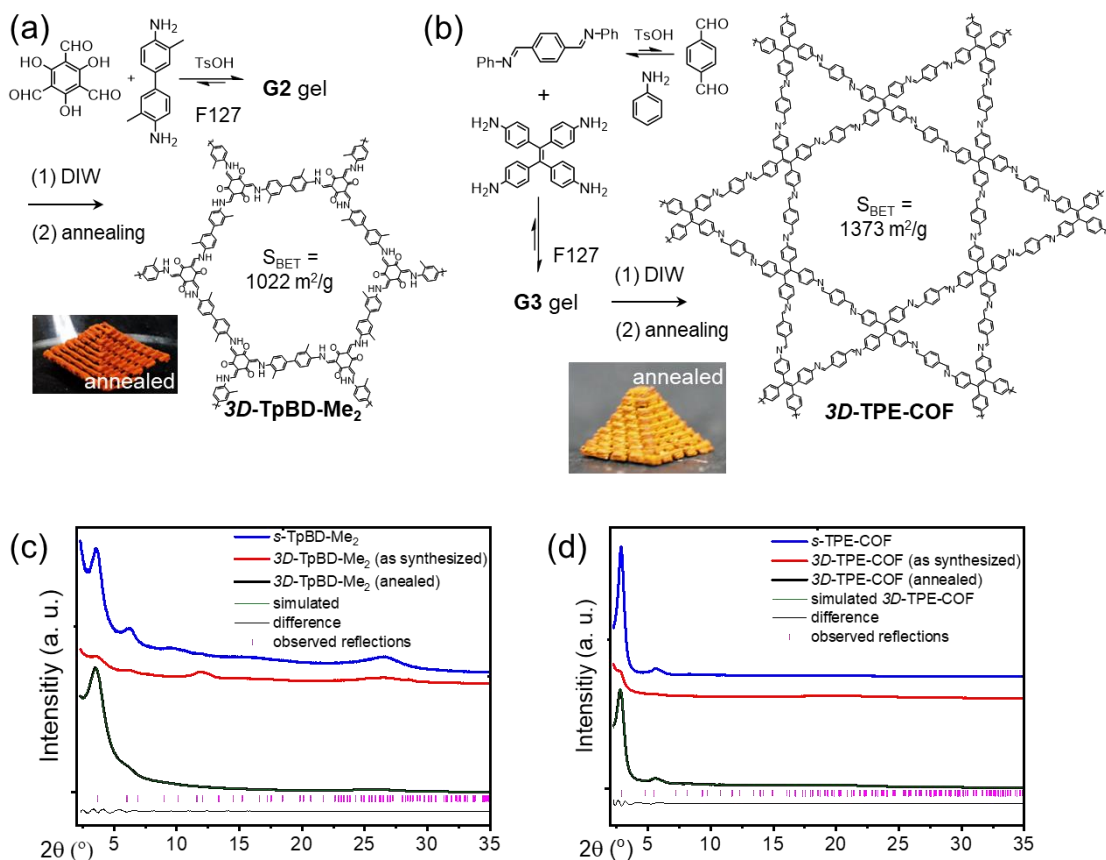


**Figure 4.5.** Synthesis of 3D-printed monoliths of **3D-TpBD-Me<sub>2</sub>** (a) and **3D-TPE-COF** (b). (c) PXRD profiles of *s*-TpBD-Me<sub>2</sub>, as synthesized and annealed **3D-TpBD-Me<sub>2</sub>**, respectively. (d) PXRD profiles of *s*-TPE-COF, as synthesized and annealed **3D-TPE-COF**, respectively.

The polymer network re-organization in these 3D-printed COF monoliths enables heterogeneous integration of different imine and  $\beta$ -ketoenamine COFs in a spatially defined 3D architecture. The cross-imation at the COF/COF interface would allow two COF materials to covalently connect to each other, therefore eliminating the binding issue in conventional fabrication methods.<sup>299</sup> Two heterogeneous lattice structures (Figure 4.6a) were 3D-printed using inks of **G1** and **G2**, and **G1** and **G3**, respectively. After the two-stage amorphous-to-crystalline transformation, mechanically robust dual-COF monolith **3D-TpPa-1/TpBD-Me<sub>2</sub>** (Figure 4.6a) with high crystallinity (Figure 4.6c) were obtained. SEM studies revealed that two COFs are seamlessly bound at the COF/COF interface (Figure 4.6b), suggesting a molecular-level connection between the two COFs. To further



demonstrate the strong interfacial binding between two COFs, the concentration of **TPE-COF** precursors in **G3** was intentionally kept significantly lower than that of **G1**. After annealing, the top layer composed of **TPE-COF** shrank more than the bottom layer composed of **TpPa-1**, forcing the heterogeneously 3D-printed monolith **3D-TpPa-1/TPE-COF** to bend into a half-round tubular structure (Figures 4.6a) at the macroscale, demonstrating the strong interfacial interaction between two COFs.

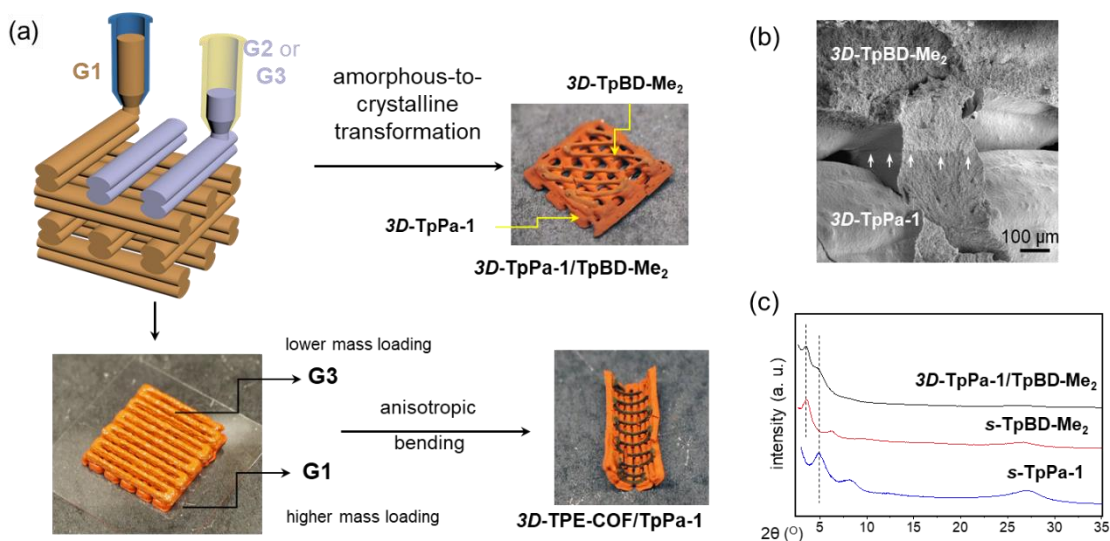


**Figure 4.6.** (a) Dual-material 3D printing of heterogeneous COF monoliths and the obtained lattice of **3D-TpPa-1/TpBD-Me<sub>2</sub>** and **3D-TpPa-1/TPE-COF**. No mechanical fracture was observed after placing 100 g weight on the **3D-TpPa-1/TpBD-Me<sub>2</sub>** monolith (221 mg). (b) SEM image of an exposed interface formed between **3D-TpPa-1** and **3D-TpBD-Me<sub>2</sub>** in the printed heterogeneous monolith. (c) PXRD profiles of *s*-**TpPa-1**, *s*-**TpBD-Me<sub>2</sub>**, and a 3D-printed heterogeneous monolith **3D-TpPa-1/TpBD-Me<sub>2</sub>**, respectively.

### 4.3 Summary

In summary, we have demonstrated a general method to integrate imine and β-ketoenamine COFs into 3D printing materials and fabricated the first set of single component and multi-component 3D-printed COF monoliths through hierarchical co-assembly enhanced direct-ink-writing, followed by two-stage post-printing network re-organization. At the nanoscale, the fabricated COF monoliths exhibit high crystallinity similar to their solution-phase synthesized COFs yet impart good mechanical robustness at the macroscale. Compared to the solution phase synthesized counterparts, these 3D-printed

monoliths possess comparable measured surface areas and hierarchical porous features, which can potentially increase the mass transport rate for molecular storage, separation and catalysis. Furthermore, dual-COF monoliths with molecular-level structural integration at the COF/COF interfaces have been successfully fabricated using two COF-precursor inks. Our approach provides a facile method to fabricate homogeneous and heterogeneous COF monoliths with high crystallinity and designed macroscale 3D architectures, which will pave the way for future applications that require sophisticated 3D architectures.

## 4.4 Appendices

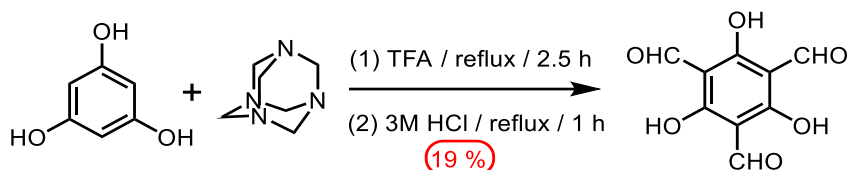
### 4.4.1 General Information

All reagents and solvents were purchased from commercial companies, including Fisher Scientific, Sigma-Aldrich, Acros Organics, Alfa Aesar, and VWR, and used without further purification, which include anhydrous phloroglucinol (99+ %), trifluoroacetic acid (99 %), anhydrous sodium sulfate (Certified ACS), aniline (99+ %), glacial acetic acid (Certified ACS), *p*-phenylenediamine (99+ %), *o*-tolidine (98 %), terephthalaldehyde (98+ %), *p*-toluenesulfonic acid monohydrate (99 %), 1,4-dioxane (Certified ACS), acetone (Certified ACS), *N,N*-dimethylformamide (Certified ACS), tetrahydrofuran (Optima™ for HPLC), methylene chloride (Stabilized/Certified ACS), hydrochloric acid (32 - 35%), absolute ethanol (200 proof), hexamethylenetetramine (ACS reagent, ≥99.0%), Pluronic® F-127 powder (BioReagent), and mesitylene (98%).

NMR spectra were recorded on either a Bruker AVIII 500 MHz spectrometer or a Bruker AVIII 600 MHz Spectrometer and referenced to residual solvent peaks. The working frequencies are 500 or 600 MHz for <sup>1</sup>H and 125 or 150 MHz for <sup>13</sup>C. Solid state <sup>13</sup>C-cross-polarization at magic-angle spinning (CPMAS) nuclear magnetic resonance measurements were performed on a Varian 400 MHz VNMRS system. Elemental analysis was performed by Intertek Pharmaceutical Services (Whitehouse, NJ). Fourier transform infrared (FT-IR) spectra were collected on a Jasco 6200. The IR spectra of the samples were collected with a universal Zn-Se ATR (attenuated total reflection) in the 600–4000 cm<sup>-1</sup> region. Powder X-ray Diffraction (PXRD) data were collected on a Rigaku MiniFlex powder X-ray diffractometer (Cu, K<sub>α1</sub>= 1.54059, K<sub>α2</sub>= 1.54439, from 2° or 3° to 35°, step size = 0.02°). UV-Vis spectra were recorded on a Shimadzu UV-1800 UV-Vis spectrophotometer. Gel permeation chromatography (GPC) was performed on a Waters Alliance GPC system using dimethyl sulfoxide (DMSO) containing 0.1% LiBr as the eluent at 50 °C. Scanning electron microscopy (SEM) data were acquired on an FEI dual beam Scios Low Vacuum SEM/FIB.

Optical microscope white-light images are recorded by an AmScope SM-1TSW2 stereomicroscope. Supercritical CO<sub>2</sub> activation was performed by a Samdri 795 Critical Point Dryer (inlet pressure ca. 1350 psi, temperature at 45 °C). The samples were activated in a porous capsule in the drying chamber and fulfilled by CO<sub>2</sub>. The CO<sub>2</sub> was kept inputting for another 10 min to purge the chamber. Next, the chamber was sealed, and the temperature was raised to 40 °C (i.e., above the CO<sub>2</sub> critical temperature) overnight to afford the activated samples. Low-pressure gas sorption measurements were performed on a Micromeritics FLEX 3.0 surface area analyzer. Samples were first activated at Samdri 795 Critical Point Dryer for 24 h and then degassed under dynamic vacuum for 24 h at 100 °C prior to each measurement. N<sub>2</sub> sorption isotherms were measured using a liquid nitrogen bath (77 K).

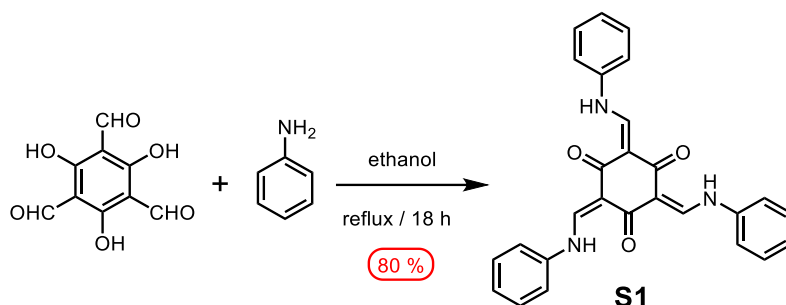
#### 4.4.2 Synthetic Methods



**Scheme S1.** Synthesis of 1,3,5-triformylphloroglucinol (TP)

**1,3,5-triformylphloroglucinol (Tp)** was synthesized according to a previously reported method.<sup>S1</sup> In an ice bath, phloroglucinol (anhydrous, 6.0 g, 47.6 mmol) and hexamethylenetetramine (15.1 g, 107.9 mmol) were added to a three-necked round bottom flask (250 mL) before trifluoroacetic acid (90 mL) was added. The reaction was degassed thoroughly by three freeze-pump-thaw cycles. Under a nitrogen atmosphere, the reaction was refluxed (oil bath temperature 100 °C) vigorously for 2.5 h. The reaction mixture gradually changed from a yellow suspension to a clear, dark red solution. A 3M HCl (150 mL) aqueous solution was added to the reaction dropwise using a constant pressure drop addition funnel. After complete addition of HCl, the reaction mixture was refluxed (oil bath temperature 100 °C) for an additional hour. The reaction mixture was then allowed to cool to room temperature, insoluble residues were removed by filtration, and the filtrate was extracted with CH<sub>2</sub>Cl<sub>2</sub> (100 mL × 5). The organic phases were combined and dried over anhydrous Na<sub>2</sub>SO<sub>4</sub>. The desired product was obtained after removing the solvent under reduced pressure, followed by recrystallization of the crude product (2.0 g) in ethanol (300

mL) at 78 °C, yielding 1.9 g of a white powder (yield = 19 %). <sup>1</sup>H NMR (500 MHz, CDCl<sub>3</sub>) δ = 10.15 (s, CHO), 14.12 (s, OH).



### Scheme S2. Synthesis of **S1**

**S1.** Compound **S1** was synthesized according to a previously reported method.<sup>S2</sup> In a 100 mL round bottom flask, **Tp** (100 mg, 0.48 mmol) and aniline (443 mg, 4.8 mmol) were dissolved in ethanol (30 mL). The reaction was refluxed overnight and then cooled to room temperature. The orange precipitate was collected by filtration, washed with cold ethanol, and dried under the reduced pressure to afford the product as a yellow solid (160 mg, 0.38 mmol, 80 % yield). <sup>1</sup>H NMR (500 MHz, CDCl<sub>3</sub>) δ = 13.0-13.4 (m, *NH*, 3H), 8.94 – 8.69 (m, *HC-N*, 3H), 7.43 (m, *Ph*, 6H), 7.32 (m, *Ph*, 6H), 7.22 (m, *Ph*, 3H).

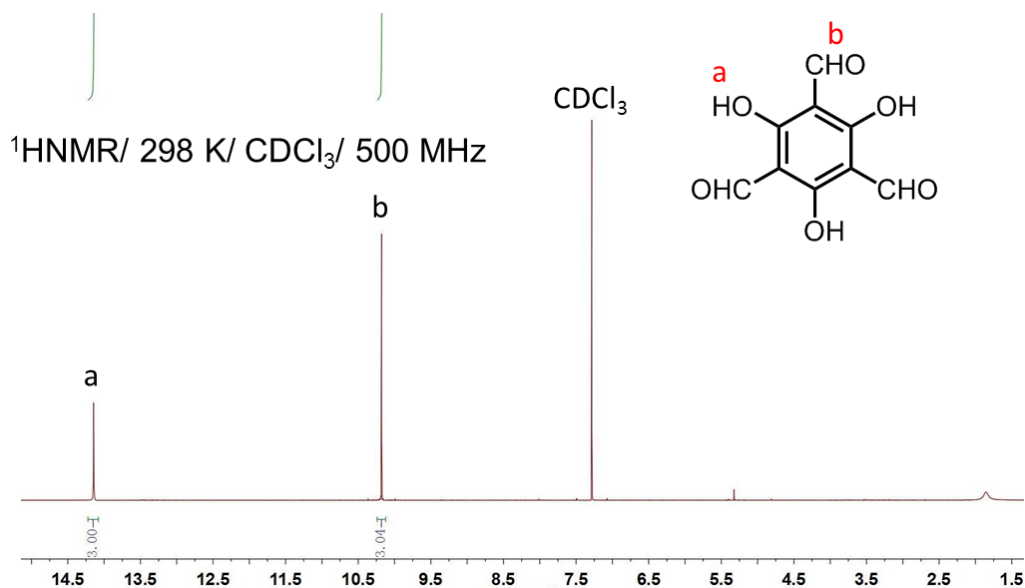


**Figure S1.** <sup>1</sup>H NMR spectrum (500 MHz, CDCl<sub>3</sub>) of **Tp** at 298 K

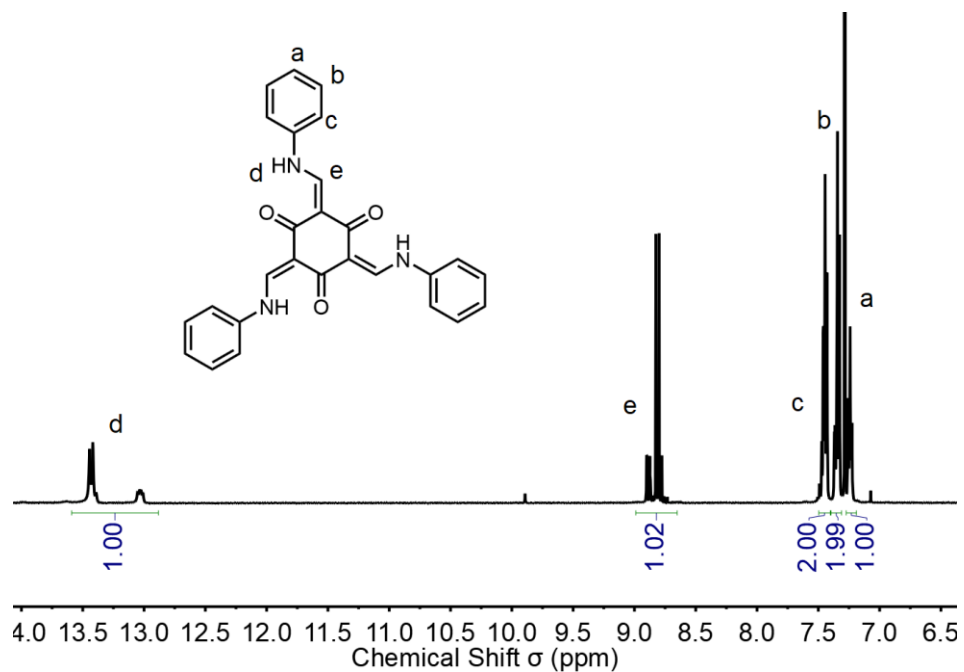
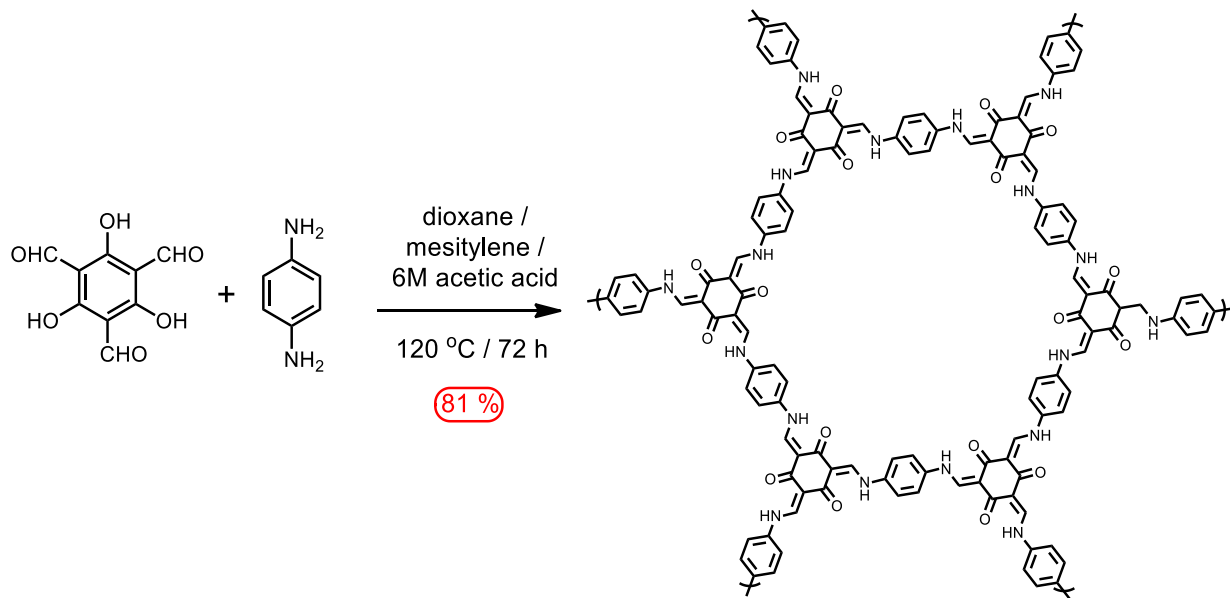
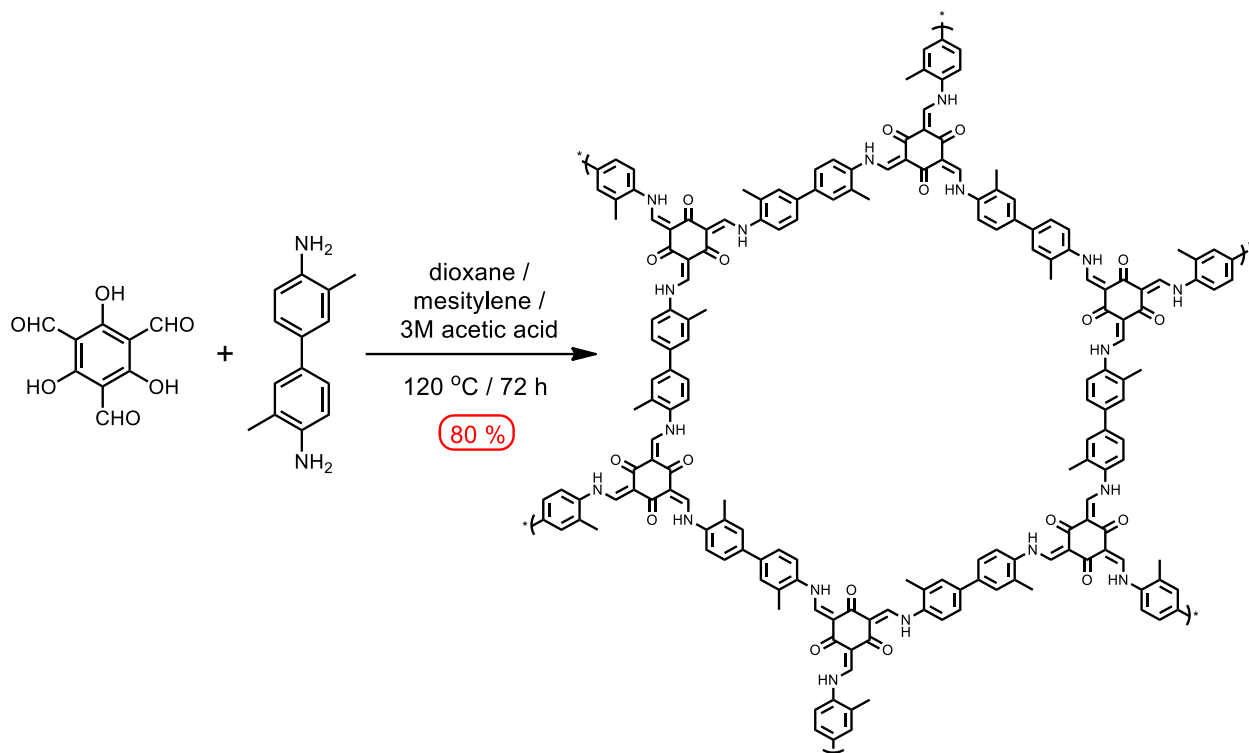


**Figure S2.** <sup>1</sup>H NMR spectrum (500 MHz, CDCl<sub>3</sub>) of **S1** at 298 K



**Scheme S3.** Synthesis of *s*-TpPa-1.

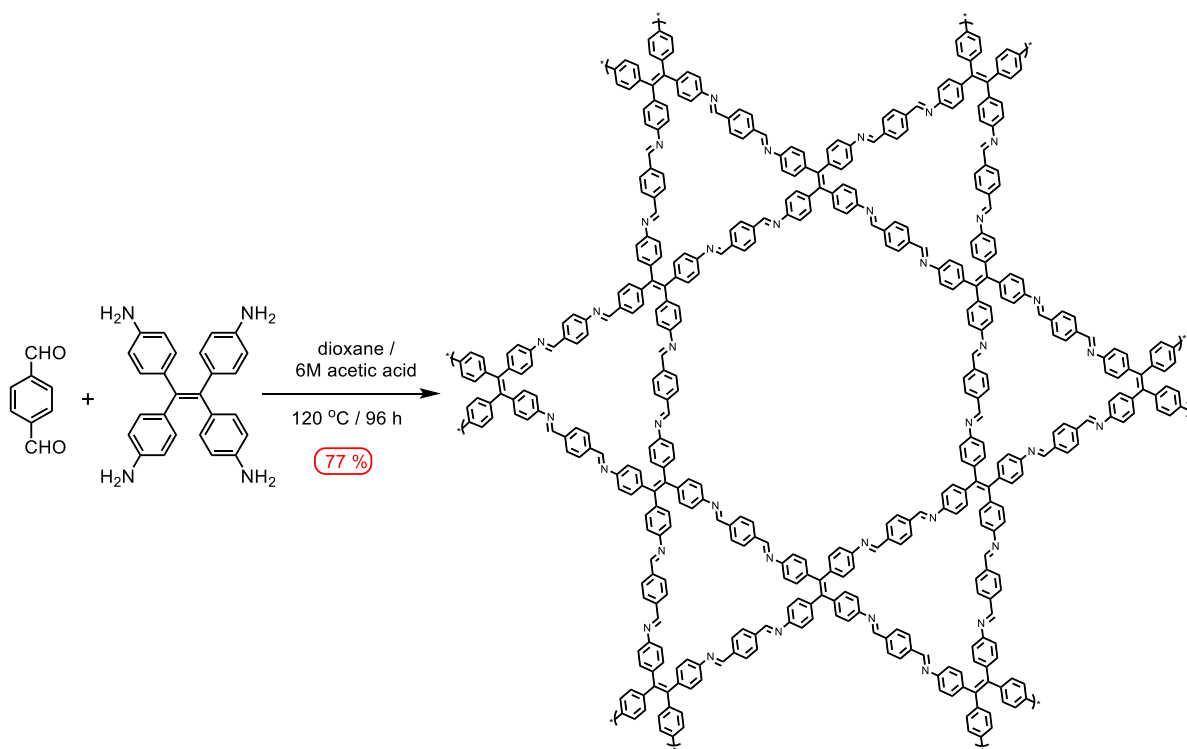
***s*-TpPa-1.** ***s*-TpPa-1** was synthesized according to a previously reported method.<sup>S1</sup> In a sealed Schlenk flask (25 mL), **Tp** (126 mg, 0.6 mmol) and paraphenylenediamine (**Pa**, 96 mg, 0.9 mmol) in a mixture of dioxane (3 mL), mesitylene (3 mL) and 6M acetic acid (1 mL) were degassed thoroughly by three freeze-pump-thaw cycles. The mixture was sonicated for 30 min at room temperature and then heated to 120 °C for 72 h. A red precipitate was generated during this period, which was collected by filtration subsequently. The collected powder was washed extensively using a large excess of DMF (3 times) and acetone (3 times). The sample was then activated using supercritical CO<sub>2</sub> and high vacuum at 180 °C for 24 h, yielding a red powder (180 mg, yield = 81%). FT-IR (powder, cm<sup>-1</sup>): 1580 (s), 1517 (m), 1451 (m), 1285(s), 1254 (s), 1127 (w), 1087 (w), 991 (m), 825 (s). Elemental analysis: C<sub>36</sub>H<sub>24</sub>N<sub>6</sub>O<sub>6</sub>·1.9H<sub>2</sub>O, calculated: C 64.5 %, H 4.2 %, N 12.5 %; found: C 65.1 %, H 3.9 %, N 11.9 %.



**Scheme S4.** Synthesis of ***s*-TpBD-Me<sub>2</sub>**.

***s*-TpBD-Me<sub>2</sub>.** ***s*-TpBD-Me<sub>2</sub>** was synthesized according to a previously reported method.<sup>S3</sup> In a sealed Schlenk flask (25 mL), **Tp** (126 mg, 0.6 mmol) and *o*-tolidine (191 mg, 0.9 mmol) in a mixture of dioxane (3 mL), mesitylene (3 mL) and 3M acetic acid (1 mL) were degassed thoroughly by three freeze-pump-thaw cycles. The mixture was

sonicated for 30 min at room temperature and then heated to 120 °C for 72 h. An orange precipitate was generated during this period, which was collected by filtration. The solid sample was washed extensively using a large excess of DMF (3 times) and acetone (3 times). The sample was activated using supercritical CO<sub>2</sub> and high vacuum at 100 °C under vacuum for 24 h, yielding an orange powder (254 mg, yield = 80 %). FT-IR (powder, cm<sup>-1</sup>): 1573 (s), 1501 (w), 1438 (m), 1273 (s), 1252 (s), 1121 (w), 996 (w), 871 (m), 804 (m). Elemental analysis: C<sub>60</sub>H<sub>48</sub>O<sub>6</sub>N<sub>6</sub>·0.3DMF·1.3H<sub>2</sub>O, calculated C 73.6 %, H 5.3 %, N 8.9 %; found: C 73.4 %, H 5.2 %, N 8.7 %.



**Scheme S5.** Synthesis of *s*-TPE-COF.

***s*-TPE-COF.** *s*-TPE-COF was synthesized based on a previously reported method.<sup>S4</sup> In a sealed Schlenk flask (25 mL), terephthalaldehyde (108 mg, 0.8 mmol) and tetrakis-(4-aminophenyl)- ethane (150 mg, 0.4 mmol) in a mixture of dioxane (6 mL) and 6M acetic acid (1 mL) were degassed thoroughly by three freeze-pump-thaw cycles. The mixture was sonicated for 30 min at room temperature and then heated to 120 °C for 96 h. An orange precipitate was generated during this period, which was collected by filtration. The solid sample was washed extensively using a large excess of DMF (3 times) and acetone (3 times). The sample was activated using supercritical CO<sub>2</sub> and high vacuum at 100 °C

under vacuum for 24 h, yielding an orange powder (199 mg, yield = 77%). **FT-IR** (powder,  $\text{cm}^{-1}$ ): 2874 (w), 1705 (m), 1619 (s), 1595 (s), 1563 (m), 1495 (s), 1409(w), 1360 (w), 1299 (m), 1197 (s), 1164 (s), 1101 (m), 1012(m), 964 (m), 881 (m), 835 (s), 783 (m). Elemental analysis:  $\text{C}_{42}\text{H}_{28}\text{N}_4 \cdot 0.4\text{DMF} \cdot 0.45\text{H}_2\text{O}$ , calculated: C 82.9 %, H 5.1 %, N, 9.8 %; found: C 82.6 %, H 4.8 %, N 9.7 %.

**3D-TpPa-1 hydrogel (G1).** Pluronic F127 (2.0 g, 0.159 mmol) was dissolved in ice-cold water (6 mL) before TsOH (0-0.5 g, 0-2.6 mmol) was added. **Pa** (0.7 g, 6.5 mmol) was added to the aqueous solution with stirring at 0 °C, forming a purple solution. In a separate reaction vessel, **Tp** (0.9 g, 4.3 mmol) was dissolved in THF (25 mL) and the solution was combined with the aqueous solution of F127/**Pa**/TsOH under vigorous stirring. The color of reaction mixture gradually changed from transparent orange to opaque red, and the temperature of the reaction was allowed to warm to room temperature. The reaction mixture was stirred in the open air to allow THF evaporation. After ca. 4 h, a red-colored opaque hydrogel was obtained (9.40 g net mass), which was subjected to rheology measurements to evaluate the hydrogel's 3D printability.

*GPC analysis.* In order to monitor the evolution of imine condensation in the hydrogel of **TpPa-1** ink, the as-prepared **G1** was freeze-dried and dissolved in DMSO. Insoluble species (ca. 35-40 % of the total mass) were removed using a syringe filter. The soluble solution was injected into the GPC, using a series of PEG of known molecular weights for comparison. As shown in Figure S3, a broad peak with a retention time of 15.6 min could be attributed to the imine polymer.

**3D-TpBD-Me<sub>2</sub> hydrogel (G2).** Pluronic F127 (2.0 g, 0.159 mmol) was dissolved in ice-cold water (6 mL) before TsOH (0.3 g, 1.6 mmol) was added. *o*-tolidine (0.96 g, 4.5 mmol) was added to the aqueous solution with stirring at 0 °C, forming a light-red solution. In a separate reaction vessel, **Tp** (0.64 g, 3.0 mmol) was dissolved in THF (20 mL) and the THF solution was combined to the aqueous solution of F127/*o*-tolidine/TsOH under vigorous stirring. The color of the mixture gradually changed from transparent orange to opaque red and the temperature of the reaction was allowed to warm to room temperature after 30 min. The reaction mixture was stirred in open air to allow THF evaporation. After ca. 4 h, an orange-colored hydrogel was obtained (10.58 g net mass), which was subjected to rheology measurements to evaluate its 3D printability.



**3D-TPE-COF hydrogel (G3).** We first attempted to prepare **3D-TPE-COF** hydrogel in a similar manner compared to those of **3D-TpPa-1** and **3D-TpBD-Me<sub>2</sub>**. Experimentally, Pluronic F127 (2.0 g, 0.159 mmol) was dissolved in ice-cold water (6 mL) before TsOH (0.15g, 0.8 mmol) was added. Tetrakis-(4-aminophenyl)-ethene (0.48g, 1.2 mmol) was added to the aqueous solution with stirring at 0 °C, forming a dark-red solution. In a separate reaction vessel, terephthalaldehyde (0.32 g, 2.4 mmol) was dissolved in THF (20 mL) and this THF solution was mixed with the aqueous solution of F127/tetrakis(4-aminophenyl)ethene/TsOH. Different from the ketoenamine-based COF hydrogels, a large amount of orange precipitate was formed immediately upon mixing, which was difficult to disperse even with vigorous stirring. After the evaporation of THF, an orange hydrogel-like substance was formed but was unsuitable for 3D printing due to severe tip clogging.

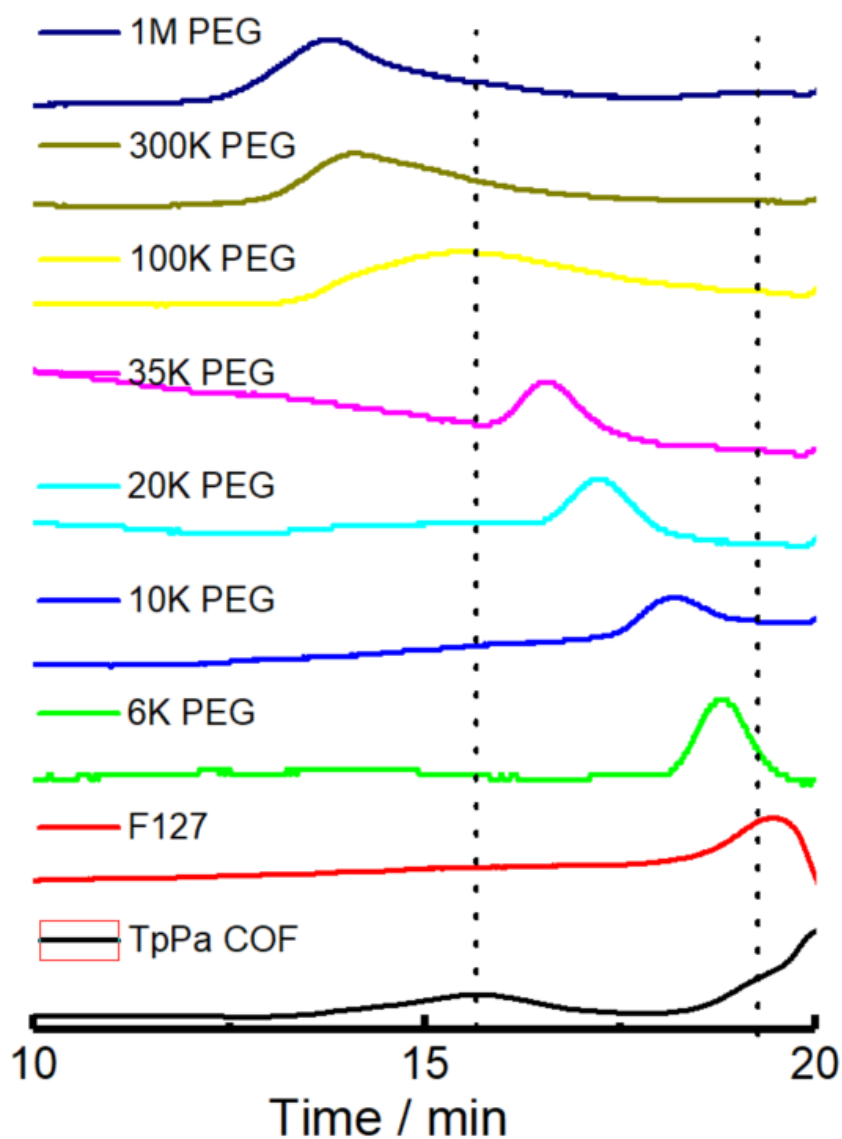


**Figure S3.** GPC profiles of PEG (6k-1M Da), F127 (red), and **TpPa-1** ink (black) measured using DMSO (containing 0.1% LiBr) as the mobile phase with a flow rate of 1.0 mL/min at 50 °C. Polymeric species (comparable to the retention time of 100k Da PEG) in **TpPa-1** ink other than F127 were recorded in the GPC profile, suggesting a limited degree of polymerization in the imine-condensation.

*Trans-imation method:* Terephthalaldehyde (0.32 g, 2.4 mmol), aniline (0.44 g, 4.8 mmol), and TsOH (0.15g, 0.8mmol) were dissolved in a mixture of 30 mL THF, 7 mL H<sub>2</sub>O and 3 mL EtOH. The clear yellow solution was stirred overnight. Pluronic F127 (2.0

g, 0.159 mmol) was dissolved in the solution once thin layer chromatography (SiO<sub>2</sub>, eluent: ethyl acetate/hexanes = 1:1, R<sub>f</sub> = 0.63) suggested that all terephthalaldehyde had been consumed. Tetrakis-(4-aminophenyl)-ethene (0.48 g, 1.2 mmol) was introduced to the solution subsequently. The reaction turned red with fine yellow particles generated. The reaction mixture was stirred vigorously in open air to allow THF and ethanol evaporation. After ca. 4 h, an orange-colored hydrogel was obtained (9.47 g net mass), which was subjected to rheology measurements.

*F127 template removal.* A 3D-printed **TpPa-1** or **TpBD-Me<sub>2</sub>** hydrogel monolith was placed in a sealed container with saturated LiCl aqueous solution (relative humidity = 11 %) for 24 h to gradually remove water from the hydrogel. After water evaporation, the monolith was transferred to an oven and heated to 90-150 °C for 24 to 72 h. The surface of the monolith darkened, which may be attributed to the oxidation of **Pa** or *o*-tolidine moieties. The monolith was then soaked in a large excess of DMF (6 × 30 mL for 24 h each) and acetone (6 × 30 mL for 24 h each) to remove the unreacted species, TsOH, and Pluronic F127 template. After the evaporation of acetone, the sample was broken into small pieces for porosity analysis or ground to powder for PXRD and FT-IR measurements. **3D-TPE-COF** monolith was placed in a sealed container with a saturated LiCl aqueous solution (relative humidity = 11 %) for 24 h to remove the water from the hydrogel. After water evaporation, the monolith was heated under N<sub>2</sub> at 90 °C for 36 h (*caution*: we noticed the porous polymer was oxidized if heated in open air). After heating, the printed monoliths were soaked in a large excess of DMF (6 × 30 mL for 24 h each) and acetone (6 × 30 mL for 24 h each) to afford **3D-TPE-COF** (F127 Removal) for PXRD and FT-IR analyses.

*Annealing.* A 3D-printed **TpPa-1** or **TpBD-Me<sub>2</sub>** monolith after F127 removal was placed in a flask with a water-chilled condenser and a mixed solvent of dioxane (3 mL), mesitylene (3 mL), and 6M acetic acid (1 mL) was added. The flask was heated to 100 °C for 48 h. Alternatively, the reaction was conducted on the same scale in a sealed container that was heated at 150 °C for 72 h. No structural deformation or cracking was observed during this period. After cooling down, the monolith was transferred to a beaker filled with DMF (30 mL, 4 h) and then acetone (30 mL, 5-6 h) to allow solvent exchange. After that, the monolith was left in open air to allow acetone evaporation. After supercritical CO<sub>2</sub> activation, the sample was sent whole for SEM, broken into small pieces for porosity analysis, or ground to powders for PXRD, FT-IR, elemental analysis, and solid-state NMR measurements.

To avoid the oxidation of imines, the heated **3D-TPE-COF** monolith was directly subjected to annealing without F127 removal. The monolith was immersed in a mixed solvent of dioxane (6 mL) and 6M acetic acid (1 mL) and heated to 100 °C under N<sub>2</sub> atmosphere for 48 h. After cooling down, the monolith was transferred to a beaker and washed with DMF (30 mL, 4 h) followed by acetone (30 mL, 6 h) for solvent exchange. After the acetone was evaporated in open air, the sample was activated using supercritical CO<sub>2</sub>. The sample was broken into small pieces for porosity analysis or ground to powders for PXRD FT-IR, elemental analysis, and solid-state NMR measurements.

**3D-TpPa-1**. IR: 1580 (s), 1517(m), 1451 (m), 1285(s), 1254 (s), 1127(w), 1087 (w), 991 (m), 825 (s). Elemental analysis: C<sub>36</sub>H<sub>24</sub>N<sub>6</sub>O<sub>6</sub>·1.95H<sub>2</sub>O, calculated: C 64.4 %, H 4.2 %, N 12.5 %; found: C 65.0 %, H 4.2 %, N 11.8 %.

**3D-TpBD-Me<sub>2</sub>**: 1573 (s), 1501 (w), 1438 (m), 1273 (s), 1252 (s), 1121 (w), 996 (w), 871 (m), 804 (m). Elemental analysis: C<sub>60</sub>H<sub>48</sub>O<sub>6</sub>N<sub>6</sub>·4H<sub>2</sub>O, calculated C 70.6 %, H 5.5 %, N 8.2 %; found: C 70.6 %, H 5.1 %, N 7.6 %.

**3D-TPE-COF**: 2874 (w), 1705 (m), 1619 (s), 1595 (s), 1563 (m), 1495 (s), 1409(w), 1360 (w), 1299 (m), 1197 (s), 1164 (s), 1101 (m), 1012(m), 964 (m), 881 (m), 835 (s), 783 (m). C<sub>42</sub>H<sub>28</sub>N<sub>4</sub>·0.75H<sub>2</sub>O, calculated: C 83.8 %, H 4.9 %, N, 9.3 %; found: C 83.6 %, H 4.9 %, N 9.5 %.

Powder-formed **s-TpPa-1** (1.0 g) was evenly dispersed in water (10 mL) with the help of ultrasonication for 1 h. The mixture was cooled to 0 °C in an ice bath before Pluronic F127 (3.5 g, 0.278 mmol) was added to the mixture. The mixture was vigorously stirred for 30 mins and then warmed to room temperature to form a blend hydrogel. The hydrogel was nearly imprintable using tips with a large inner diameter (0.8 mm) and the blend frequently clogged the tips with no complete 3D structure built. An incomplete structure was then air dried and soaked in EtOH or water to remove the F127. The structure collapsed to powder in a few minutes. Other samples were broken into small pieces for porosity analysis or ground to powders for PXRD analysis.

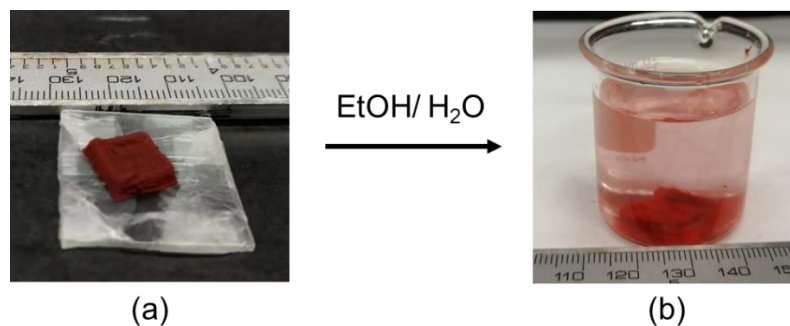


**Figure S4.** Images of (a) an air-dried *s*-TpPa-1 cube and (b) a collapsed monolith after 1 min of soaking in water.

Hydrogels **G1** and **G2** (or **G3**) were loaded into two syringe barriers and used for 3D printing. **G1** ink was printed to form a lattice structure at the bottom, and **G2** or **G3** ink was extruded on top of the lattice formed by **G1**.

[**3D-TpPa-1/TpBD-Me<sub>2</sub>**] monolith was placed in a sealed container with a saturated NaCl aqueous solution (relative humidity = 75 %) for 24 h and in saturated LiCl aqueous solution (relative humidity = 11 %) for another 24 h to even the solvent evaporation rate. The dried monolith was heated to 90 °C in an oven for 48 h. Unreacted species and F127 template were removed by soaking the monolith in a large excess of DMF (6 × 30 mL for 24 h) and acetone (6 × 30 mL for 24 h). After F127 removal, the monolith was annealed in a mixed solvent of dioxane (3 mL), mesitylene (3 mL), and 6M acetic acid (1 mL) at 100 °C for 48 h. The sample was ground to powder for PXRD measurements.

[**3D-TpPa-1/TPE-COF**] monolith was placed in a sealed container with a saturated NaCl aqueous solution (relative humidity = 75 %) for 24 h and in saturated LiCl aqueous solution (relative humidity = 11 %) for another 24 h. The dried monolith was heated to 90 °C under N<sub>2</sub> atmosphere for 48 h followed by annealing in a mixture of dioxane (6 mL) and 6M acetic acid (1 mL) under N<sub>2</sub> atmosphere at 100 °C for 48 h. The sample was ground to powder for PXRD measurements.

#### 4.4.3 Structural modeling and Powder X-ray diffraction analysis

All COF models (hexagonal 2D frameworks) were built using the Materials Studio software package, and their space groups were selected with the maximum possible

symmetry. Energy minimization was performed to optimize the geometry of the building units, employing the universal force field implemented in the Forcite module of Materials Studio. The unit cell parameters were also optimized. Pawley refinement was carried out using Reflex, a software package for crystal structure determination from PXRD pattern. The Pawley refinement was performed to optimize the lattice parameters iteratively until the  $R_p$  and  $R_{wp}$  values converged. The overlay of the observed PXRD profiles with those refined profiles shows good agreement.

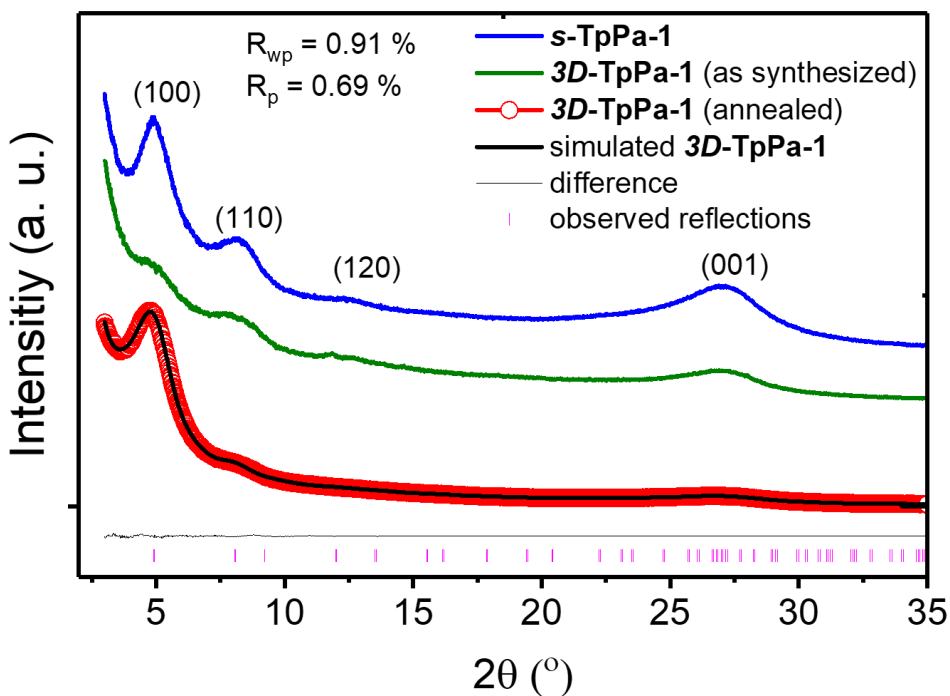


**Figure S5.** PXRD patterns and Pawley refinement of **3D-TpPa-1** (annealed) with the experimental profiles in black, Pawley-refined profiles in green, the differences between the experimental and refined PXRD patterns in black, and the observed reflections in pink. For comparison, PXRD profiles of **3D-TpPa-1** (as synthesized) in red and **s-TpPa-1** in blue were also shown in the figure.

**Table S1.** Refined unit cell parameters and atomic coordinates for **3D-TpPa-1**

<b>TpPa-1</b>			
hexagonal P-6/m, a = b = 23.1997 Å, c = 3.4248 Å			
O1	0.28081	0.53575	0.5
N2	0.40779	0.54779	0.5
C3	0.30554	0.59597	0.5
C4	0.37956	0.63946	0.5
C5	0.42377	0.61657	0.5
C6	0.45635	0.526	0.5
C7	0.43358	0.45738	0.5
C8	0.5256	0.57032	0.5
H9	0.3807	0.42194	0.5
H10	0.47574	0.6534	0.5
H11	0.54694	0.62355	0.5
H12	0.35893	0.50918	0.5

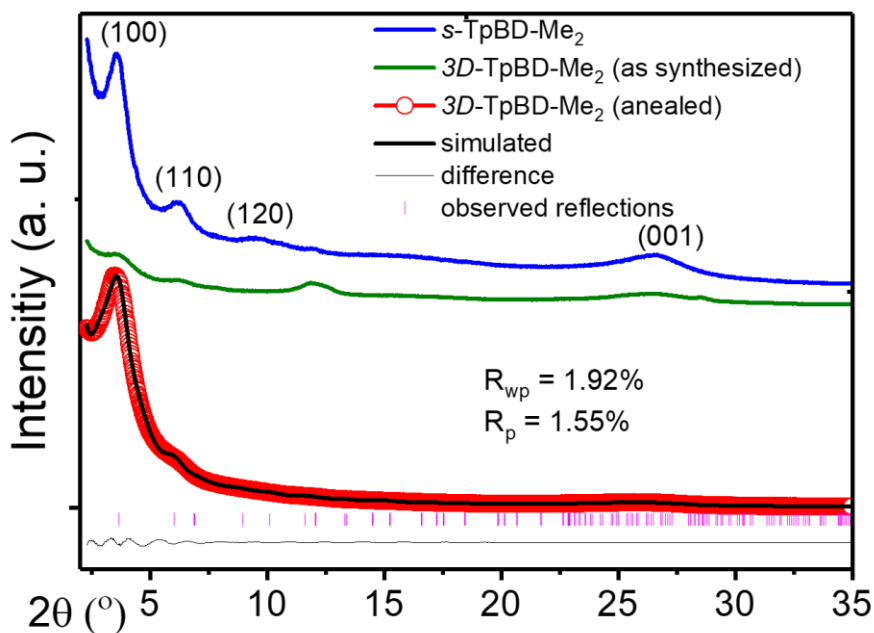


**Figure S6.** PXRD patterns and Pawley refinement of **3D-TpBD-Me<sub>2</sub>** (annealed) with the experimental profiles in black, Pawley-refined profiles in green, the differences between the experimental and refined PXRD patterns in black, and the observed reflections in pink. For comparison, PXRD profiles of **3D-TpBD-Me<sub>2</sub>** (as synthesized) in red and **s-TpBD-Me<sub>2</sub>** in blue were also shown in the figure.

**Table S2.** Refined unit cell parameters and atomic coordinates for **3D-TpBD-Me<sub>2</sub>**

<b>TpBD-Me<sub>2</sub></b>			
hexagonal P-6/m, a = b = 30.7779 Å, c = 3.8927 Å			
H1	0.34529	0.51498	0.22797
H2	0.52461	0.64155	1
H3	0.55991	0.58871	1
H4	0.41078	0.45832	1
H5	0.45825	0.65597	1



C6	0.35864	0.50405	1
H7	0.34027	0.46249	1
O8	0.28633	0.72086	0
C9	0.48897	0.5173	0
C10	0.41517	0.5293	0
C11	0.37849	0.60561	0
N12	0.43019	0.61854	0
C13	0.44725	0.58236	0
C14	0.43649	0.49805	0
C15	0.51962	0.57	0
C16	0.49917	0.60138	0
C17	0.72282	0.35898	0
C18	0.69682	0.38883	0

**Table S3.** Refined unit cell parameters and atomic coordinates for **3D-TPE-COF**

<b>TPE-COF</b>			
Hexagonal P6 $a = b = 38.9845 \text{ \AA}$ , $c = 5.6303 \text{ \AA}$			
C1	0.44397	0.48203	0.58729
C2	0.41567	0.46291	0.76649
C3	0.37909	0.46146	0.75599
C4	0.37026	0.47897	0.56374
C5	0.39853	0.49764	0.38477
C6	0.43497	0.49911	0.39627

C7	0.4803	0.44377	0.60807
C8	0.46213	0.41581	0.42601
C9	0.45971	0.37883	0.4413
C10	0.47501	0.36927	0.64108
C11	0.49213	0.39687	0.82477
C12	0.49495	0.43388	0.80764
N13	0.33319	0.47824	0.53929
C14	0.30397	0.4643	0.68942
C15	0.26778	0.46604	0.63578
C16	0.2367	0.45111	0.80094
C17	0.26386	0.48263	0.4227
N18	0.47209	0.33133	0.66797
C19	0.47294	0.30978	0.4948
C20	0.47004	0.27128	0.54398
C21	0.48443	0.25489	0.37717
C22	0.45329	0.25073	0.7564
H32	0.42199	0.44927	0.91497
H33	0.35817	0.44642	0.89742
H34	0.39215	0.51095	0.23478
H35	0.45603	0.5131	0.25506
H36	0.44993	0.42269	0.2725
H37	0.44519	0.35753	0.30019
H38	0.50356	0.38972	0.98087

H39	0.50793	0.45473	0.95101
H40	0.30563	0.45165	0.85686
H41	0.23889	0.43787	0.96517
H42	0.2873	0.49433	0.29136
H43	0.47822	0.32091	0.31416
H44	0.49768	0.27038	0.2131
H45	0.4417	0.26261	0.88755

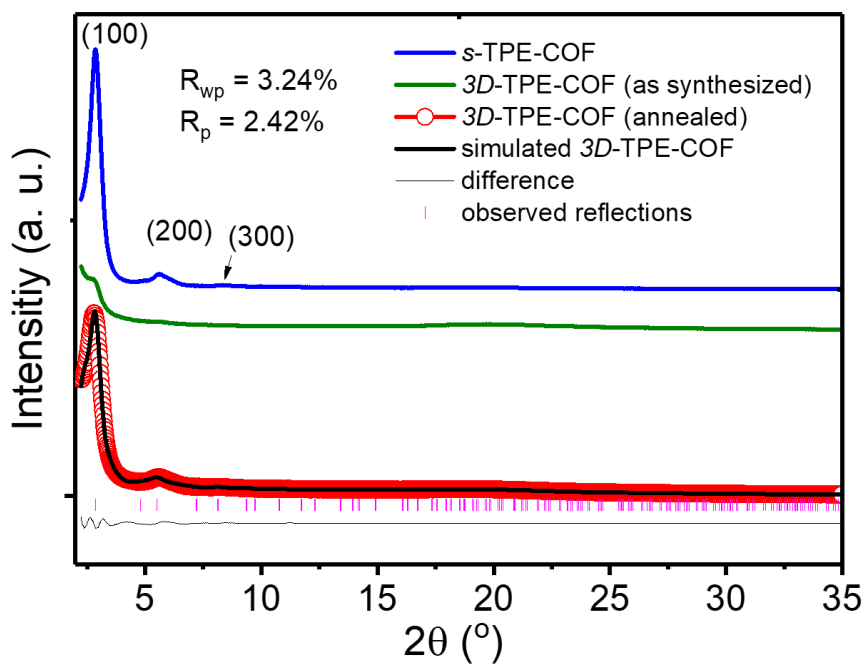


**Figure S7.** PXRD patterns and Pawley refinement of **3D-TPE-COF** (annealed) with the experimental profiles in black, Pawley-refined profiles in green, the differences between the experimental and refined PXRD patterns in black, and the observed reflections in pink. For comparison, PXRD profiles of **3D-TPE-COF** (as synthesized) in red and **s-TPE-COF** in blue were also shown in the figure.

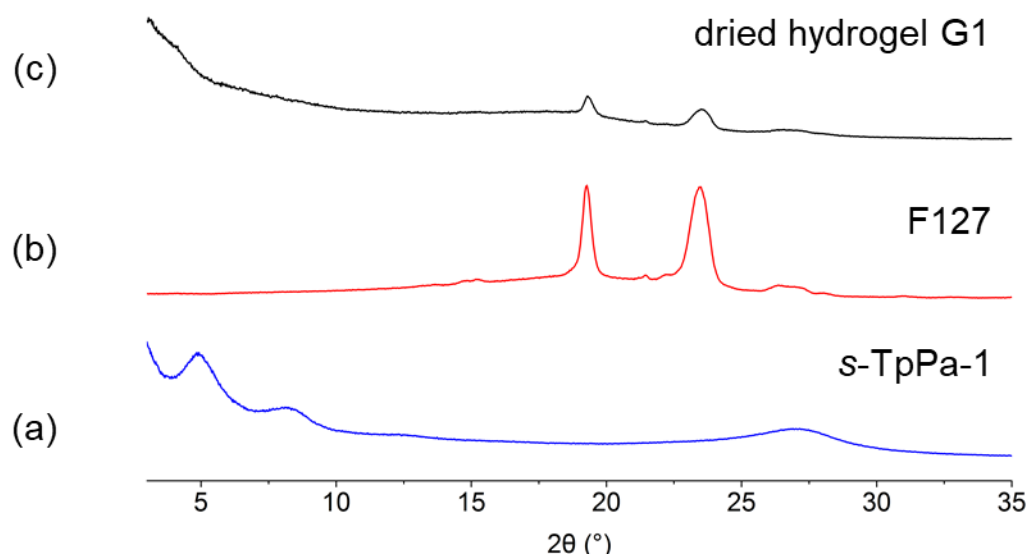


**Figure S8.** PXRD profiles of (a) *s*-TpPa-1, (b) F127 and (c) dried hydrogel G1.

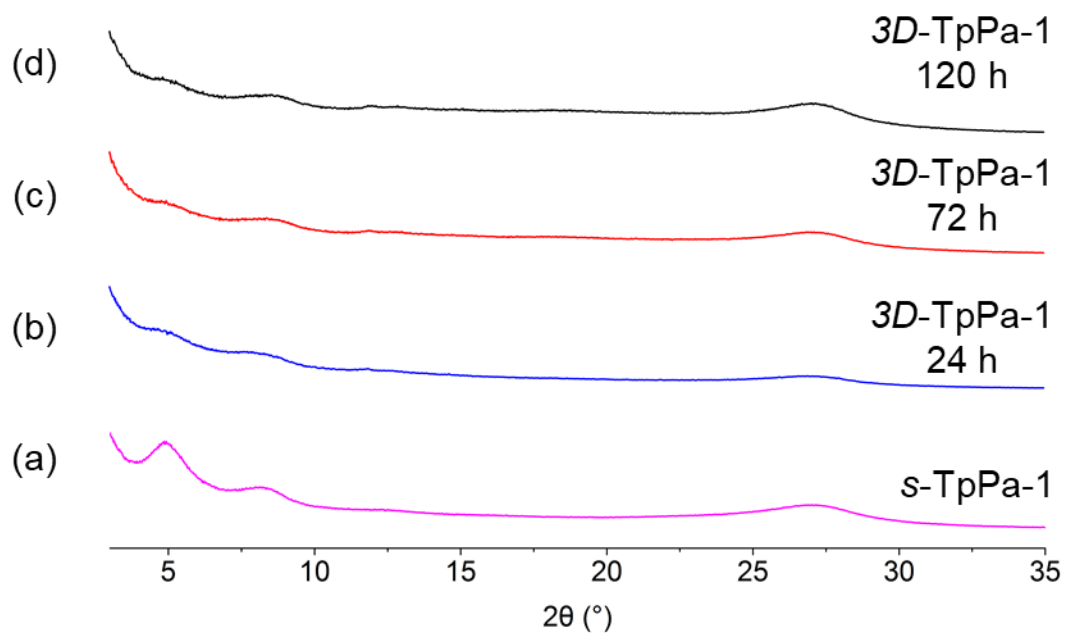


**Figure S9.** PXRD profiles of (a) *s*-TpPa-1 and (b-d) 3D-TpPa-1 samples after being heated at 90 °C for (b) 24 h, (c) 72 h, and (d) 120 h followed by F127 removal.

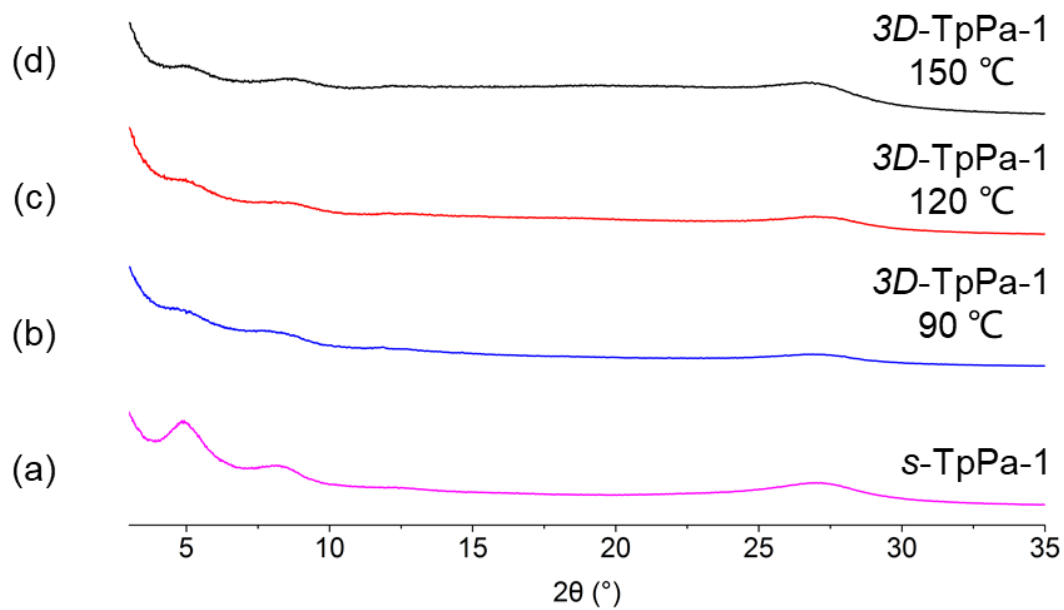


**Figure S10.** PXRD profiles of (a) *s*-TpPa-1 and (b-d) 3D-TpPa-1 samples after heating for 24h at (b) 90 °C, (c) 120 °C, and (d) 150 °C followed by F127 removal.

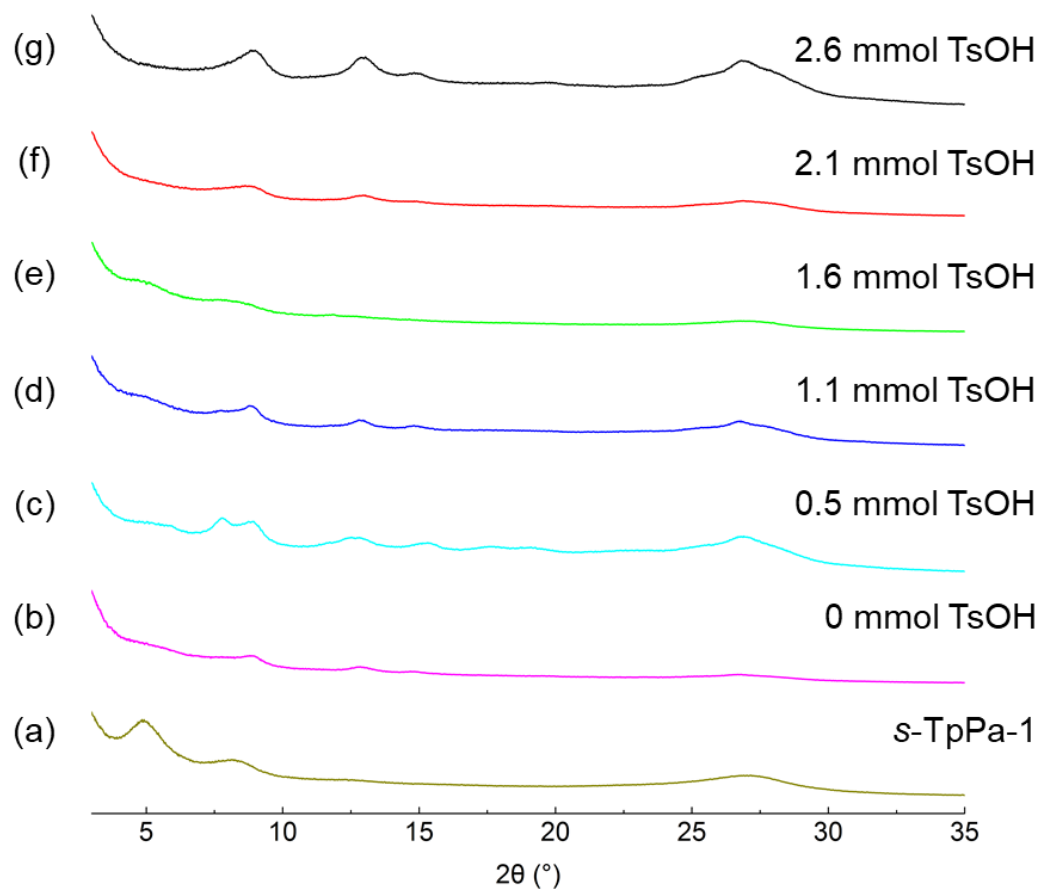


**Figure S11.** PXRD profiles of (a) *s*-TpPa-1, and (b-g) 3D-TpPa-1 samples that are synthesized in the presence of (b) 0 mmol, (c) 0.5 mmol, (d) 1.1 mmol, (e) 1.6 mmol, (f) 2.1mmol and (g) 2.6 mmol.

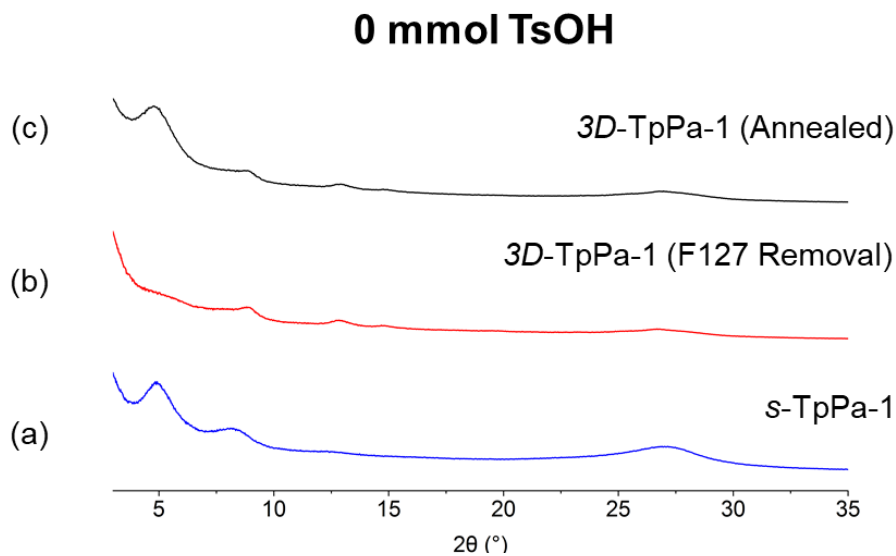


**Figure S12.** PXRD profiles of (a) *s-TpPa-1*, (b-c) as-synthesized *3D-TpPa-1* prepared in the absence of TsOH after F127 removal (b) and solvent annealing (c).

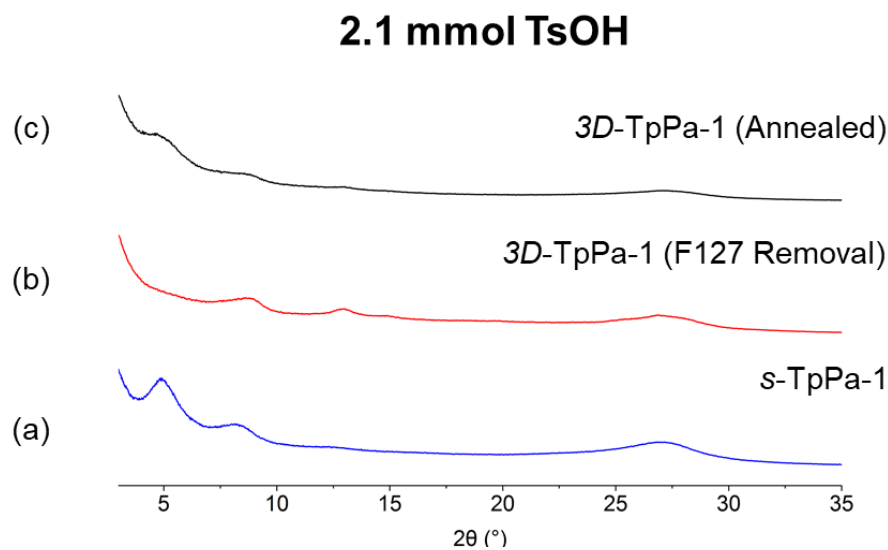


**Figure S13.** PXRD profiles of (a) *s-TpPa-1*, (b-c) as-synthesized *3D-TpPa-1* prepared in the presence of TsOH (2.1 mmol) after F127 removal (b) and solvent annealing (c).

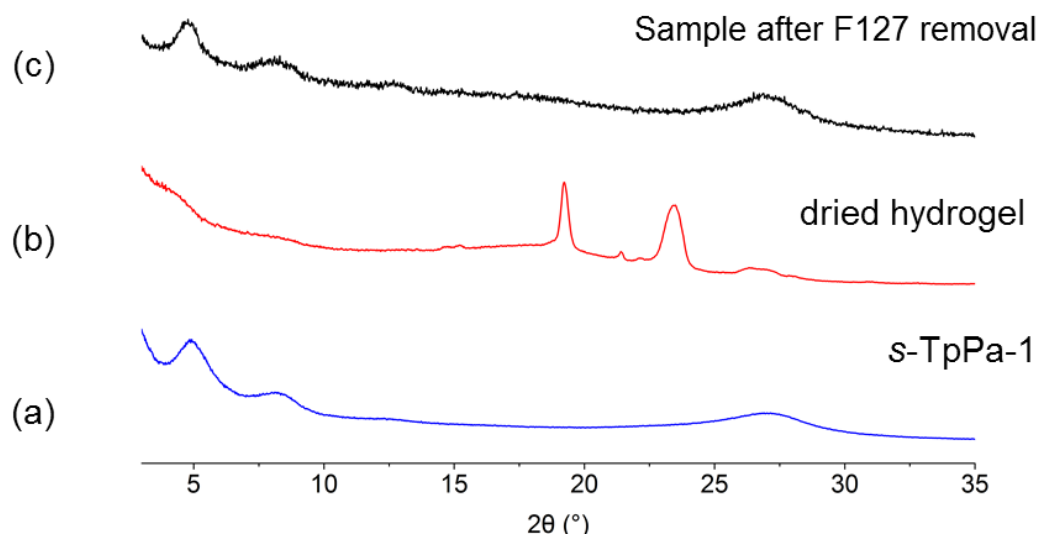


**Figure S14.** PXR profiles of (a) **s-TpPa-1**, (b) air-dried **s-TpPa-1/ F127** blend hydrogel and (c) sample after F127 removal.

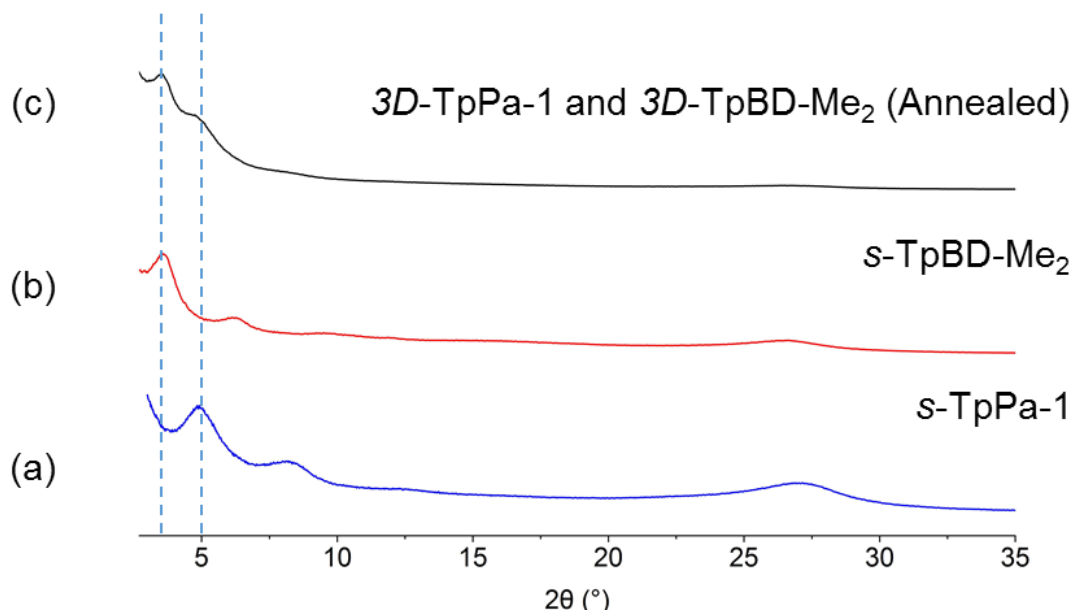


**Figure S15.** PXR profiles of (a) **s-TpPa-1**, (b) **s-TpBD-Me<sub>2</sub>**, and (c) a 3D-printed [**3D-TpPa-1/TpBD-Me<sub>2</sub>**] hetero-monolith.



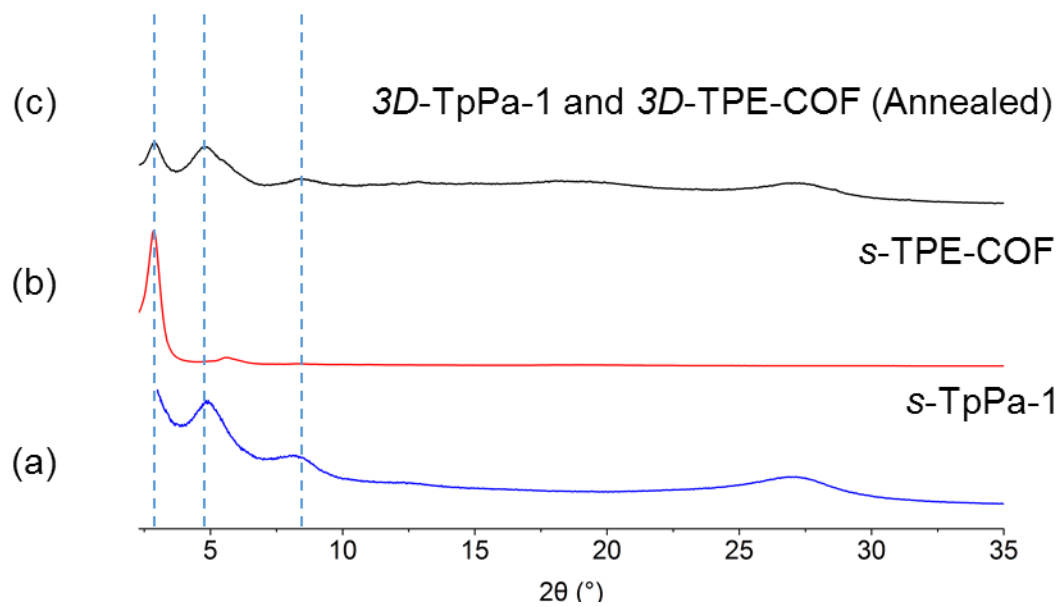


**Figure S16.** PXRD profiles of (a) *s*-TpPa-1, (b) *s*-TPE-COF, and (c) a 3D-printed hetero-COF monolith *3D*-TpPa-1/TPE-COF.

#### 4.4.4 FT-IR Spectroscopies

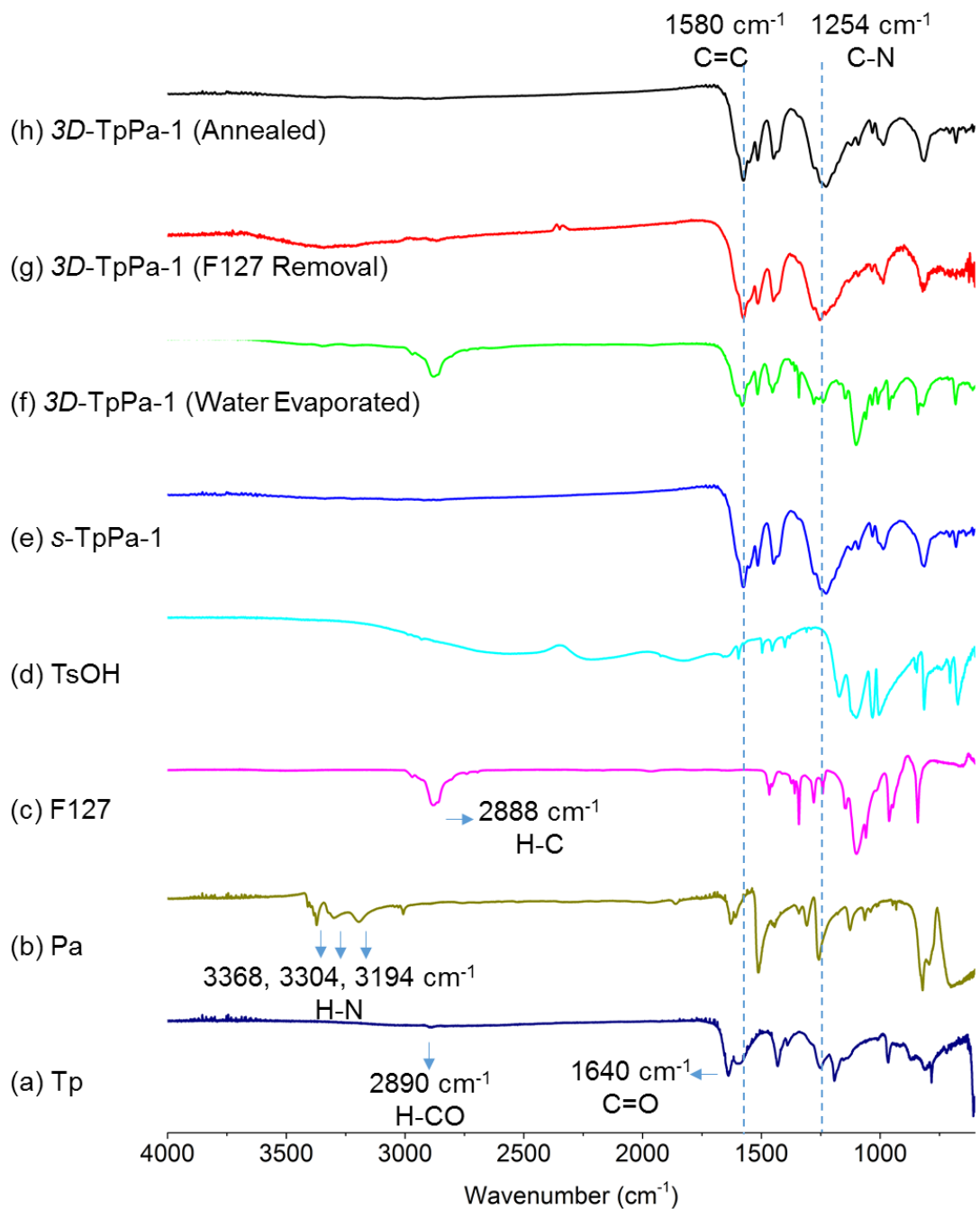


**Figure S17.** FT-IR of spectra of (a) **Tp**, (b) **Pa**, (c) F127,<sup>S5</sup> (d) TsOH, (e) **s-TpPa-1**, (f) **3D-TpPa-1** after water evaporation, (g) **3D-TpPa-1** after F127 removal and (h) **3D-TpPa-1** after solvent annealing.

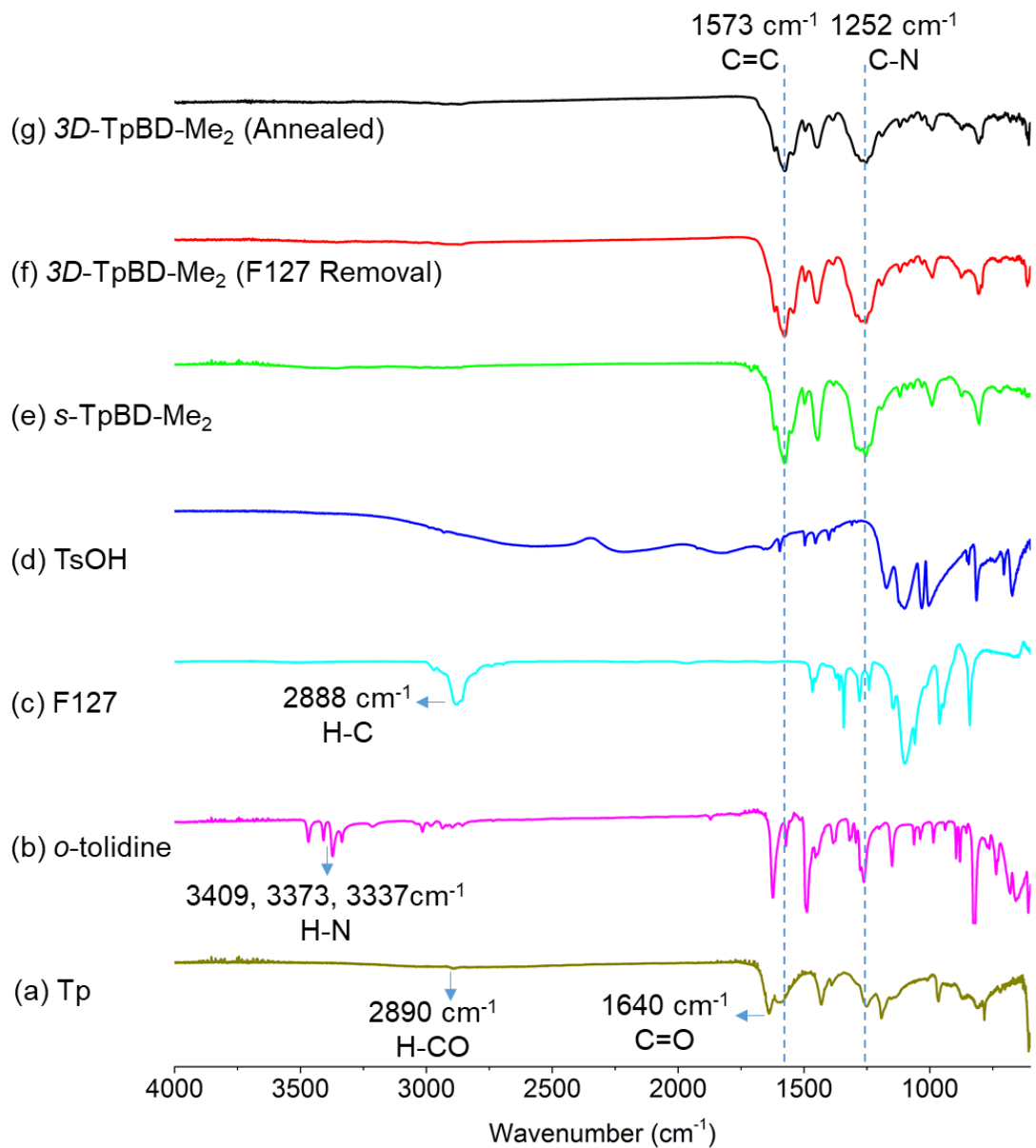


**Figure S18.** FT-IR spectra of (a) **Tp**, (b) *o*-tolidine, (c) F127, (d) TsOH, (e) *s*-**TpBD-Me<sub>2</sub>**, (f) **3D-TpBD-Me<sub>2</sub>** after F127 removal, (g) **3D-TpBD-Me<sub>2</sub>** after solvent annealing.

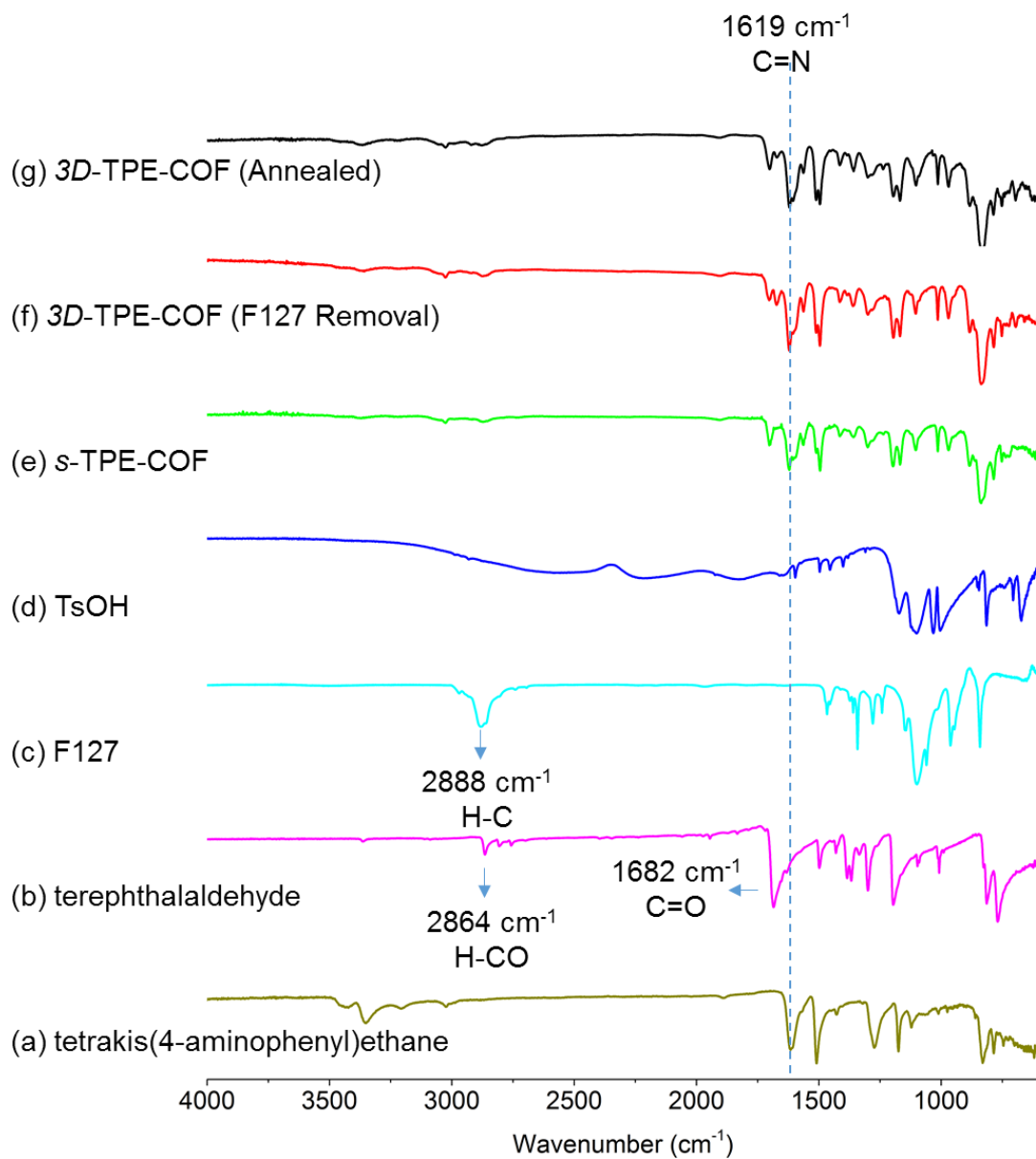


**Figure S19.** FT-IR spectra of (a) tetrakis(4-aminophenyl)ethene, (b) terephthalaldehyde, (c) F127, (d) TsOH, (e) *s*-TPE-COF, (f) *3D*-TPE-COF after F127 removal, and (g) *3D*-TPE-COF after solvent annealing.

#### 4.4.5 Rheological Studies and 3D Printing

**General information.** To evaluate the rheological properties of the prepared hydrogel for 3D printing, the elastic ( $G'$ ) and loss ( $G''$ ) moduli and self-healing behaviors were investigated. The rheological measurements were performed on a stress-controlled rheometer (TA instrument, DHR-2) with a 20-mm diameter parallel plate geometry and a measuring gap of 1 mm.

In order to measure the critical gelation temperature of Pluronic F127 hydrogels (30 w/v%) in the presence of various amount of TsOH, three samples of F127 hydrogel with 0 M, 0.6 M, and 1.0 M TsOH were prepared for temperature-dependent rheological measurements. The elastic and loss moduli of the hydrogel were monitored at an angular frequency of 1 rad/s at different temperatures. During this time-dependent measurement, the temperature was increased from 25 °C to 90 °C with a heating speed of 5 °C/min. An addition of 120 s equilibrium time was added before each test.

**Study of the F127/S1 interactions.** In order to investigate the interactions between F127 and imine/ $\beta$ -ketoenamine polymers, model compound **S1** was employed as a soluble molecular segment of the **TpPa-1** for UV-Vis studies. Experimentally, various amounts of F127 (0 wt%, 10 wt%, and 20 wt%) were added to a saturated **S1** H<sub>2</sub>O/CH<sub>3</sub>OH (v/v=1/1, 3 mL) solution for UV-Vis measurements. In the presence of F127, the shoulder peak at 465 and 335 nm was diminished as a result of F127-induced **S1** de-aggregation.

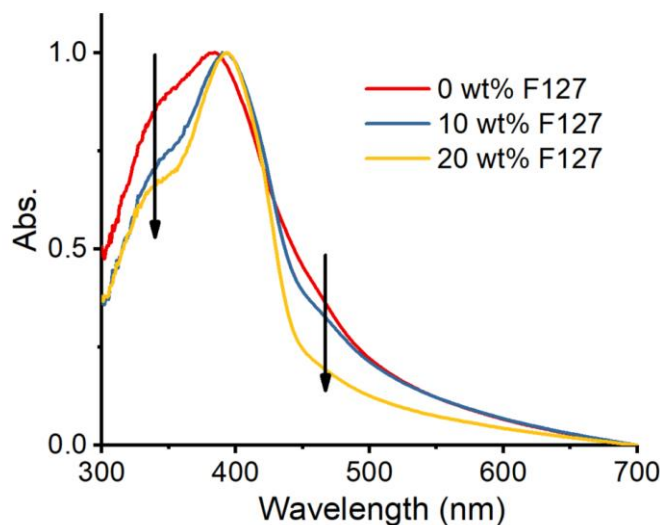


**Figure S20.** Normalized UV-Vis spectra of **S1** in H<sub>2</sub>O/CH<sub>3</sub>OH (v/v=1/1) with various amount of F127 (0 wt%, 10 wt%, and 20 wt%).

**Rheological measurements of the 3D-printable imine polymer/F127 co-assembled hydrogels.** To evaluate the 3D printability of COF precursor inks, oscillation strain sweep and dynamic step strain amplitude tests were performed at room temperature.

**Direct-ink-write 3D Printing.** 3D printing experiments were performed on an extrusion-based 3D printer (Tabletop, nScript) equipped with Nordson EFD precision smoothflower tapered tips. The freshly prepared hydrogels were loaded into Nordson EFD syringe barrels (3 mL) and installed onto the 3D printer. Three types of printing paths were generated by P-CAD software, which includes lattice cube, pyramid, and house. The printing pressure was controlled between 30 and 50 psi based on the viscosity and critical stress of different hydrogels. Printing speed was varied between 20 and 40 mm/s to allow smooth extrusion of inks from the printing nozzle.

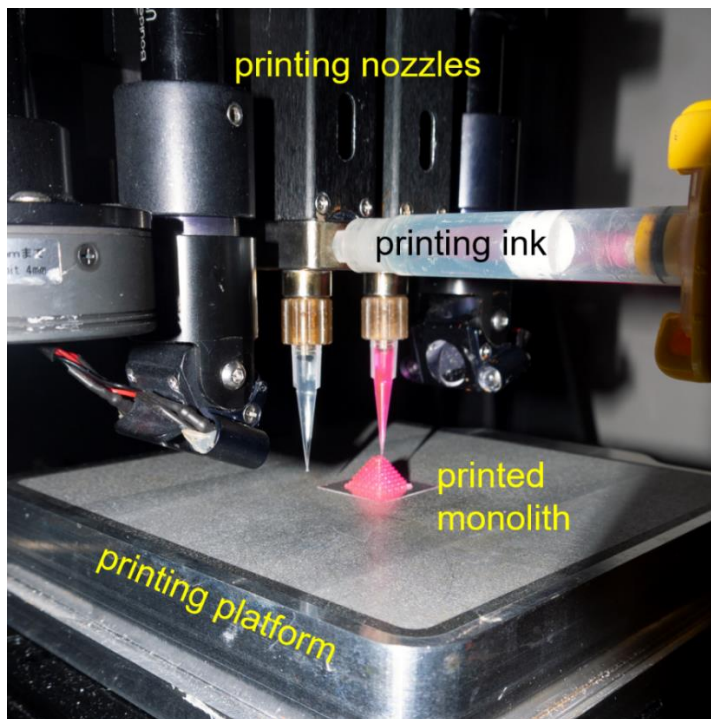


**Figure S21.** The 3D printing platform employed in this investigation.

**Single component 3D printing:** lattice pyramids ( $12.0 \times 12.0 \times 7.2$  mm) consisting of four repetitive layers were 3D printed with good structural integrity on glass slides.

**Dual-component 3D printing using: G1, G2, and G3** were loaded into separate syringe barrels and installed onto different printing heads of the 3D printer. The

heterogeneous structures were fabricated by printing the bottom section using **G1** and top section using **G2** or **G3**.

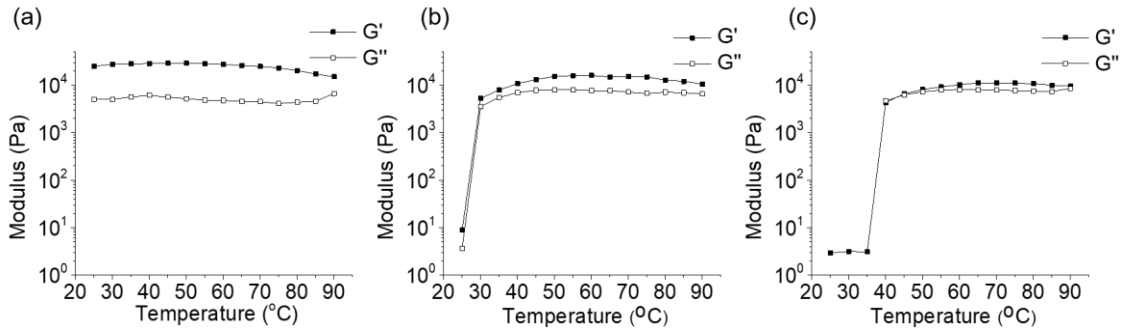


**Figure S22.** Time-dependent elastic ( $G'$ ) and loss moduli ( $G''$ ) of F127 hydrogel (30 w/v%) in the presence of TsOH at (a) 0 M, (b) 0.6 M, and (c) 1.0 M. Compared with the F127-only hydrogel, the critical gelation temperature of these hydrogels in the presence of TsOH were increased to 25 and 35 °C, respectively.

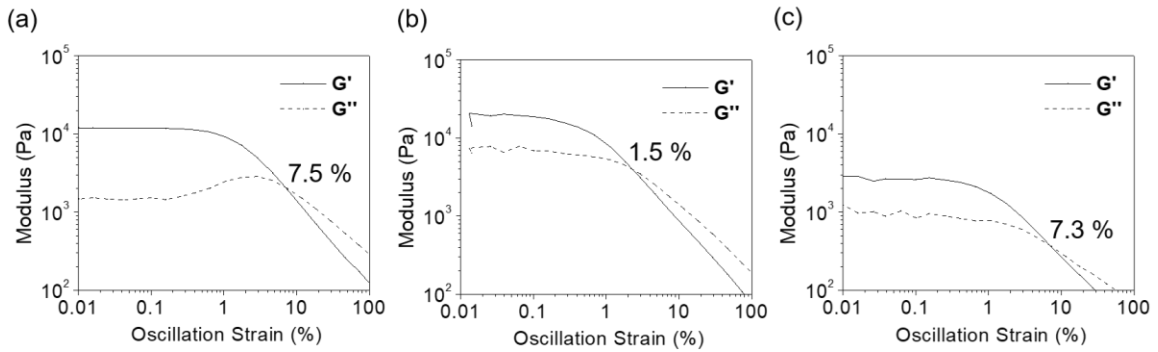


**Figure S23.** Oscillation strain sweep profiles of the prepared (a) **G1**, (b) **G2**, and (c) **G3** hydrogels, respectively. The  $G'$  and  $G''$  of the prepared inks were recorded with the oscillation strains increased from 0.01% to 100% and an angular frequency of 10 rad/s. **G1**, **G2**, and **G3** possess yield strains (where  $G' = G''$ ) of 7.5 %, 1.5 %, 7.3 %, respectively.

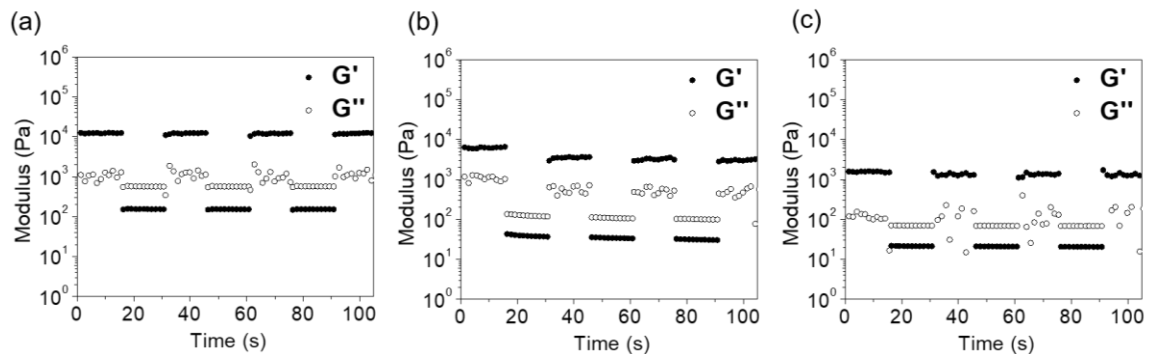


**Figure S24.** Step-strain sweep profiles of the prepared (a) **G1**, (b) **G2**, and (c) **G3** hydrogels. The  $G'$  and  $G''$  were recorded with a strain of 0.1% and 100% alternatively at an angular frequency of 10 rad/s. The period of each step is 15 s and no additional equilibrium time set in between.

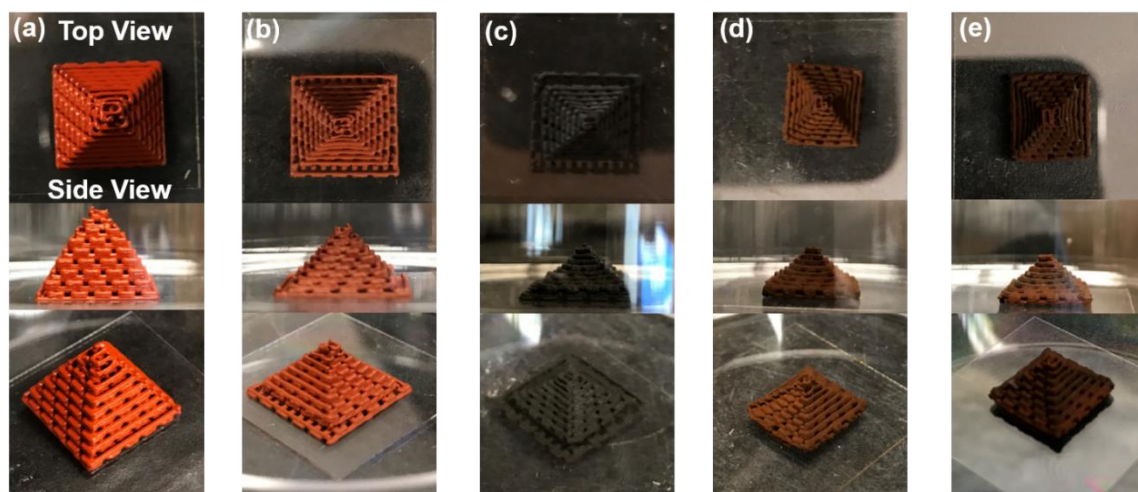


**Figure S25.** Images of a 3D-printed pyramid composed of **TpPa-1** precursors and F127 ink at different stages: (a) as-printed; (b) after drying; (c) after heating at 90 °C; (d) after F127 template removal; (e) after solvent annealing.



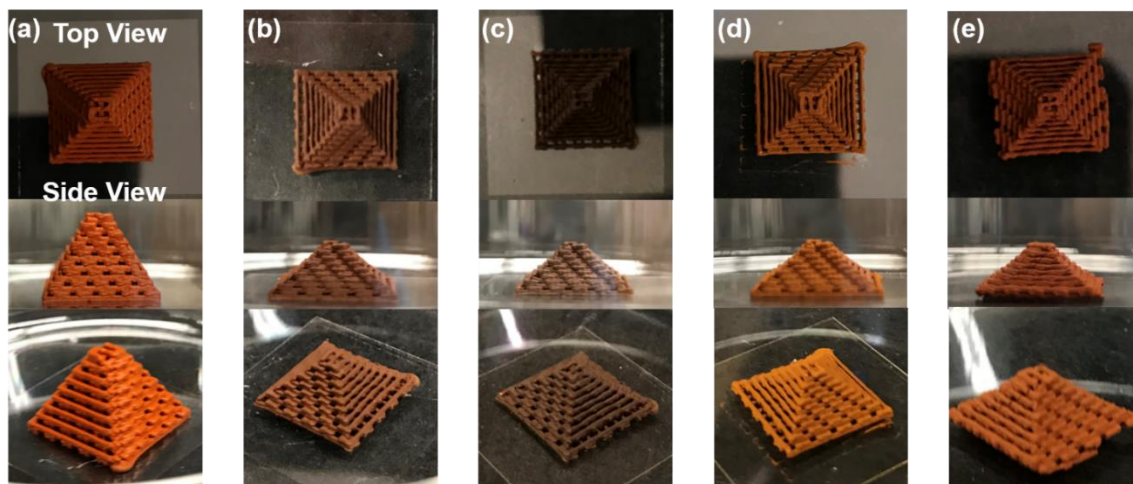


**Figure S26.** Images of a 3D-printed pyramid composed of **TpBD-Me<sub>2</sub>** precursors and F127 ink at different stages: (a) as-printed; (b) after drying; (c) after heating at 90 °C; (d) after F127 template removal; (e) after solvent annealing.

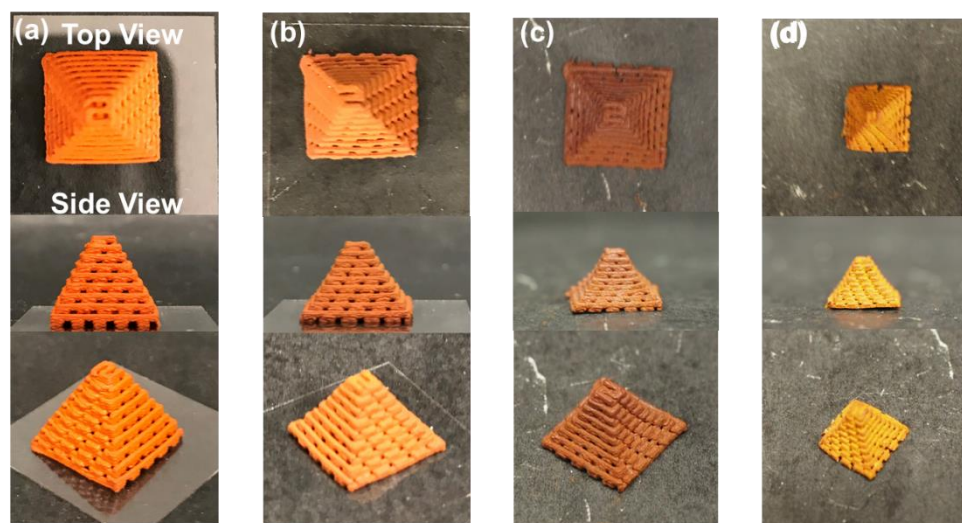


**Figure S27.** Images of a 3D-printed pyramid composed of **TPE-COF** precursors and F127 ink at different stages: (a) as-printed; (b) after drying; (c) after heating at 90 °C; (d) after solvent annealing and F127 template removal.

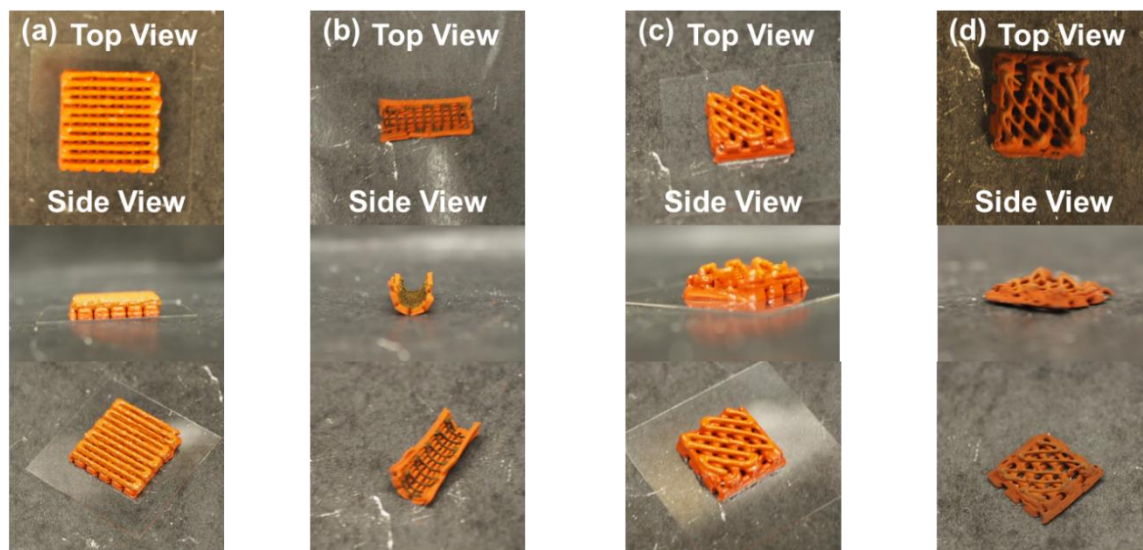


**Figure S28.** Images of 3D-printed hetero-COF monoliths. (a) An as-printed 3D-printed [3D-TpPa-1/ TPE-COF] hetero-monolith; (b) a 3D-printed [3D-TpPa-1/ TPE-COF] hetero-monolith after solvent annealing; (c) an as-printed 3D-printed [3D-TpPa-1/ TpBD-Me<sub>2</sub>] hetero-monolith; (d) a 3D-printed [3D-TpPa-1/ TpBD-Me<sub>2</sub>] hetero-monolith after solvent annealing.



**Figure S29.** Image of the solvent annealing setup for the amorphous-to-crystalline transformation.

#### 4.4.6 Morphology Analysis

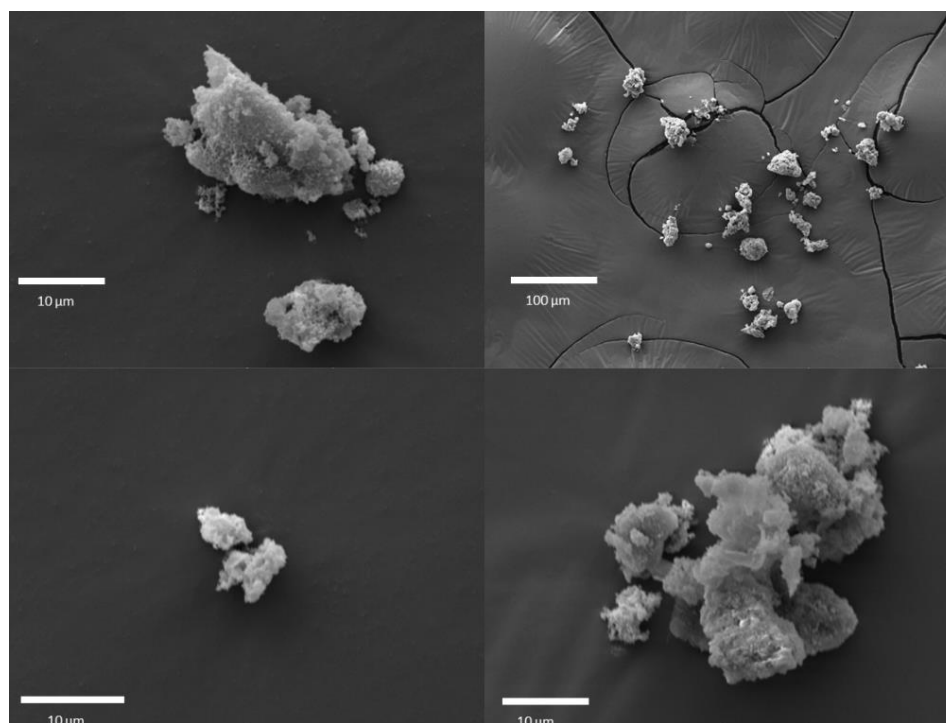


**Figure S30.** SEM images of *s*-TpPa-1 powder.

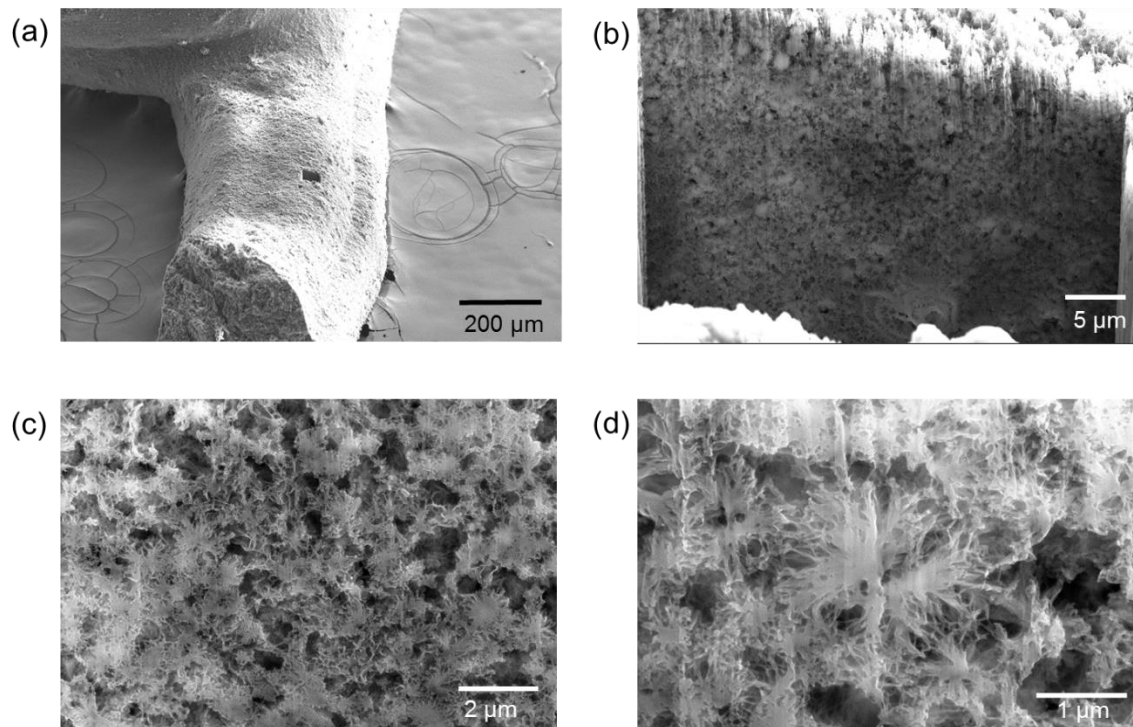


**Figure S31.** SEM images of a **3D-TpPa-1** monolith after solvent annealing. The cross-sectioned sample of the **3D-TpPa-1** monolith was prepared by  $\text{Ga}^+$  ion beam etching on an FEI dual beam Scios Low Vacuum SEM / FIB.

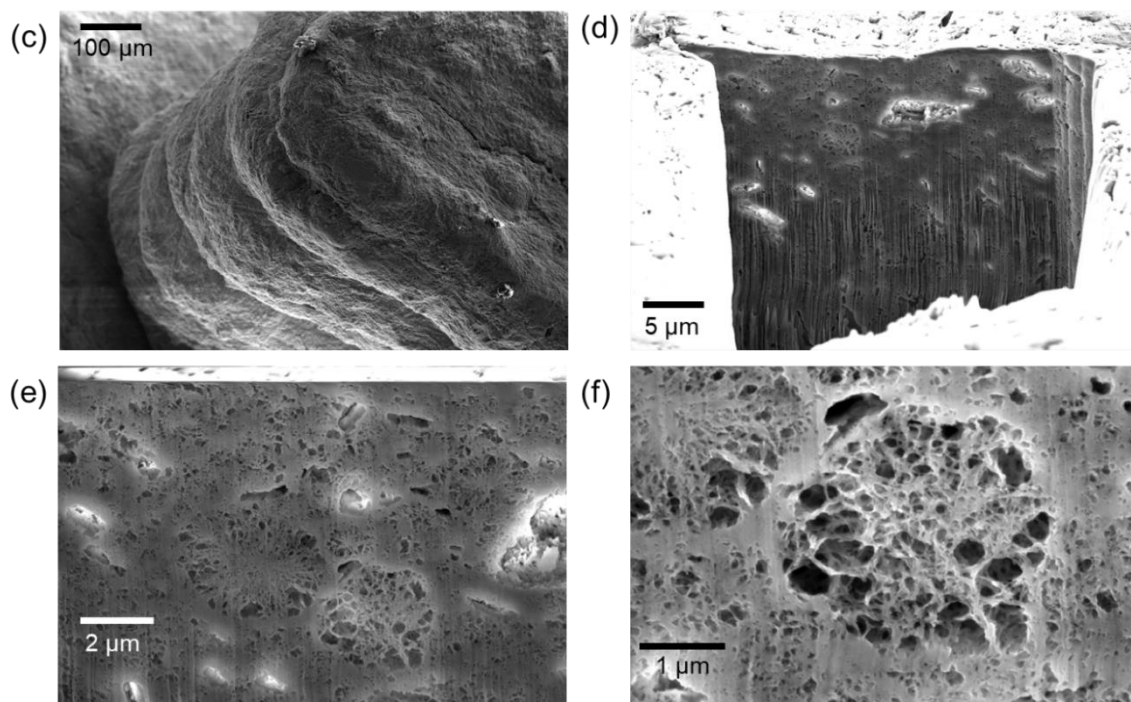


**Figure S32.** SEM images of a **3D-TpBD-Me<sub>2</sub>** monolith after solvent annealing. The **3D-TpBD-Me<sub>2</sub>** monolith was cross-sectioned by Ga<sup>+</sup> ion beam and observed with the electron beam on an FEI dual beam Scios Low Vacuum SEM/ FIB

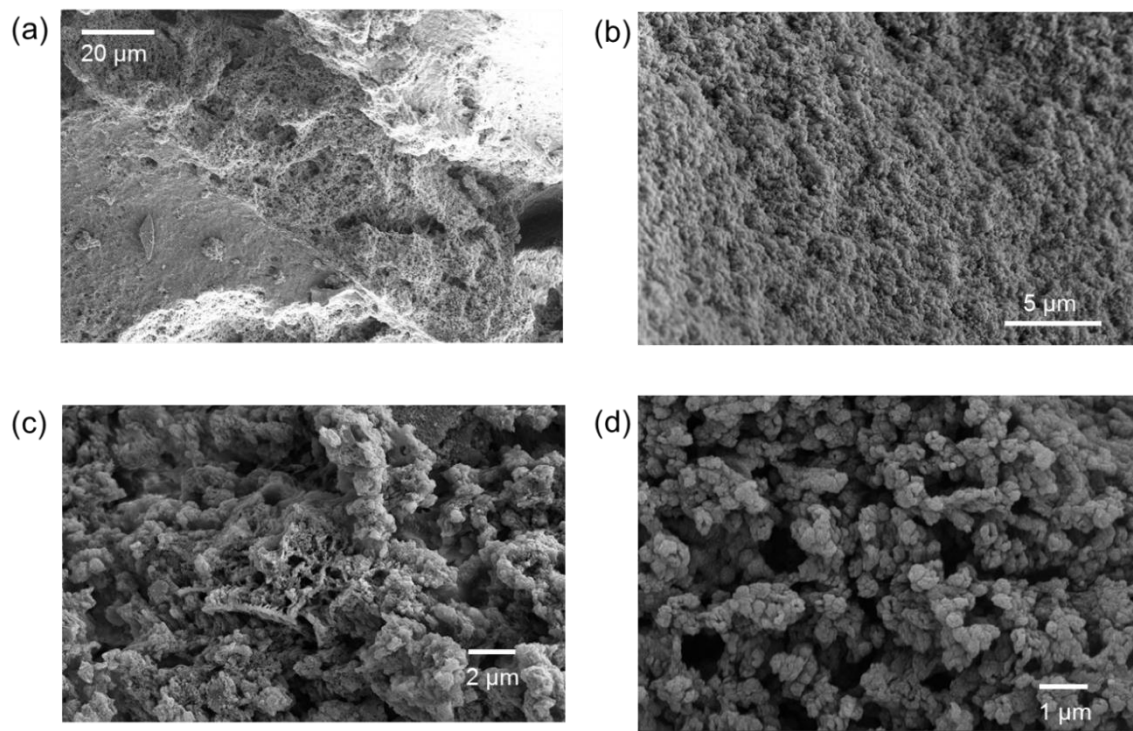


**Figure S33.** SEM images of **3D-TPE-COF** monolith after solvent annealing, which was physically broken to expose the interior structure.

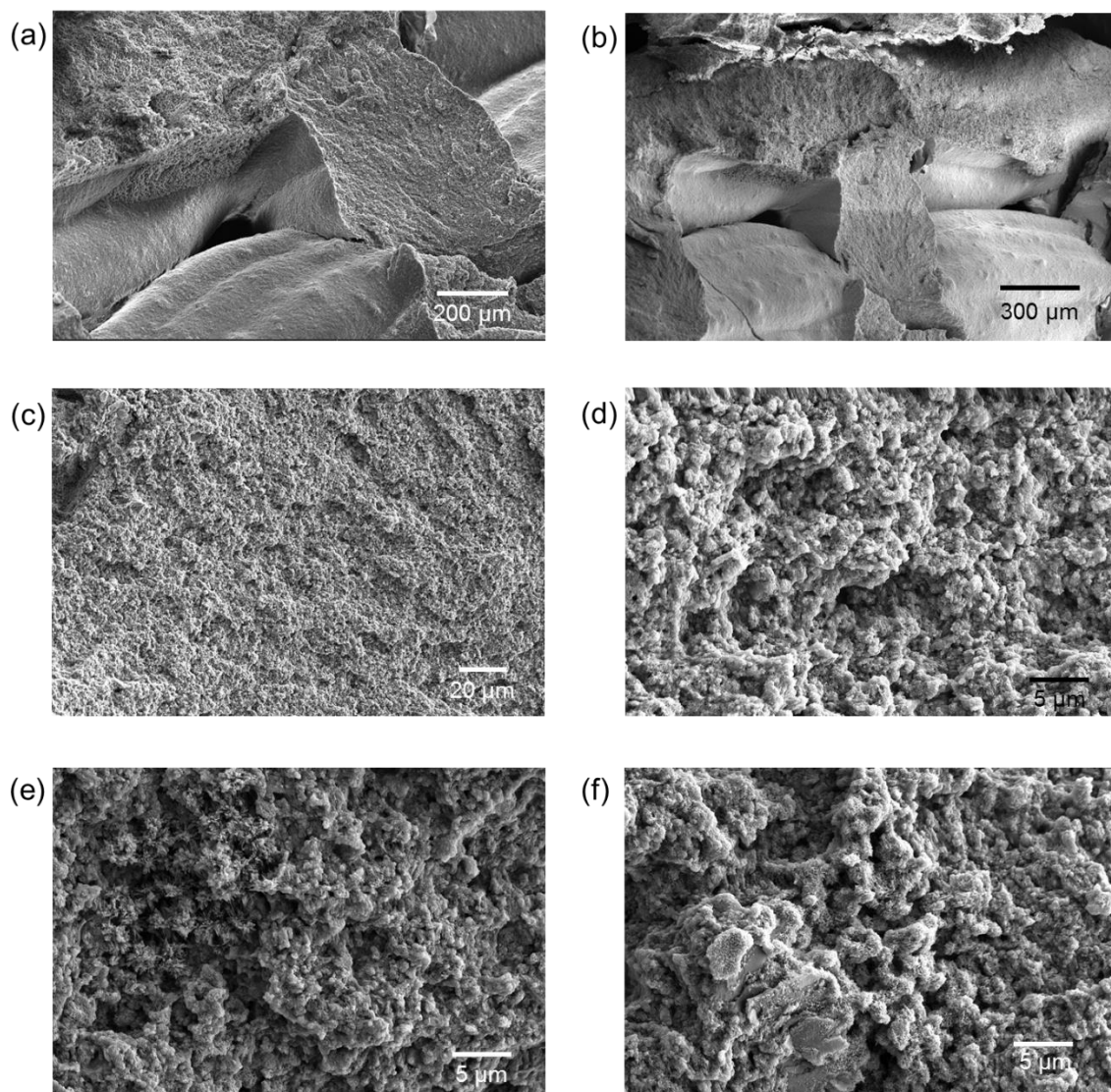


**Figure S34.** SEM images of a 3D-printed [*3D-TpPa-1*/*TpBD-Me<sub>2</sub>*] hetero-monolith, which was physically broken to expose the interface between two COFs. Images of (a-d) the interface of *3D-TpPa-1*/*TpBD-Me<sub>2</sub>*, (e) *3D-TpPa-1* section in the hetero-monolith, and (f) *3D-TpBD-Me<sub>2</sub>* section in the hetero-monolith.

#### 4.4.7 Porosity Analysis

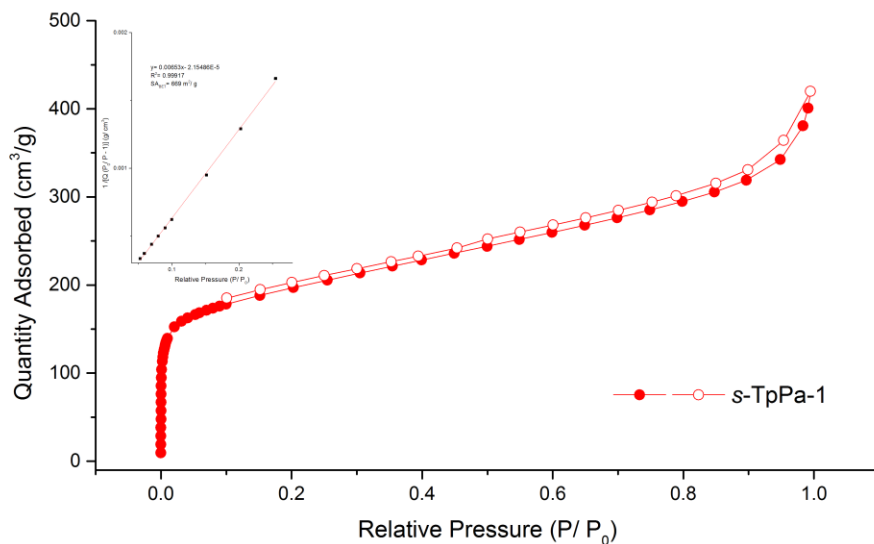


**Figure S35.**  $\text{N}_2$  sorption isotherm of **s-TpPa-1** measured at 77 K (BET surface area = 669  $\text{m}^2/\text{g}$ ).

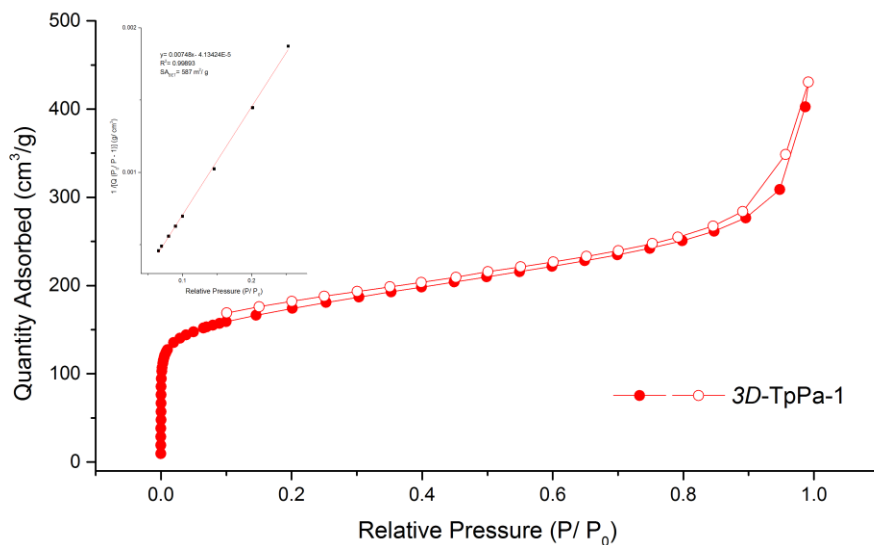


**Figure S36.**  $\text{N}_2$  sorption isotherm of **3D-TpPa-1** measured at 77 K (BET surface area = 587  $\text{m}^2/\text{g}$ ).



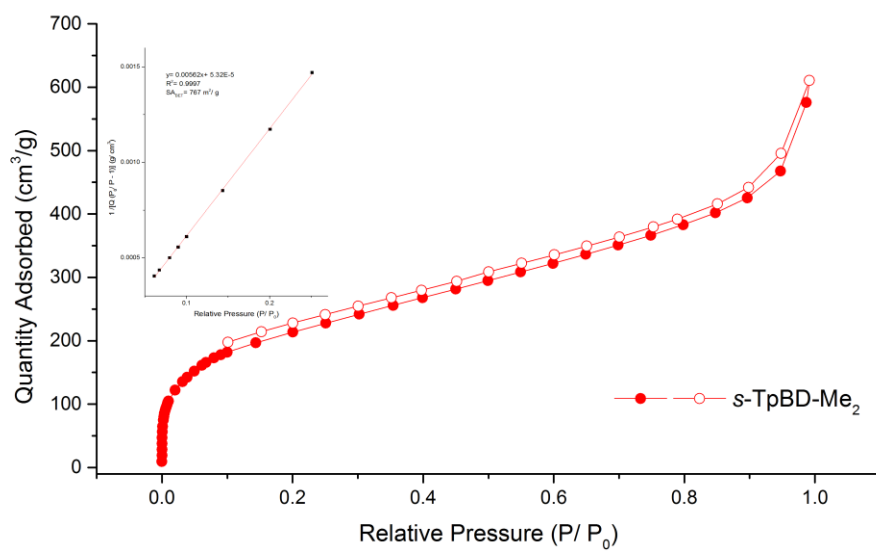


**Figure S37.** N<sub>2</sub> sorption isotherm of *s*-TpBD-Me<sub>2</sub> measured at 77 K. (BET Surface area = 767 m<sup>2</sup>/g).

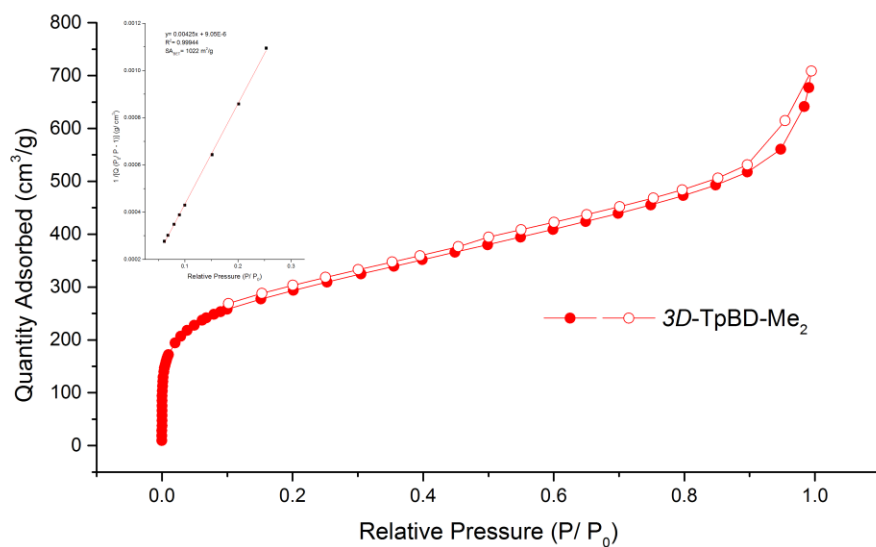


**Figure S38.** N<sub>2</sub> sorption isotherm of *3D*-TpBD-Me<sub>2</sub> measured at 77 K. (BET Surface area = 1022 m<sup>2</sup>/g).

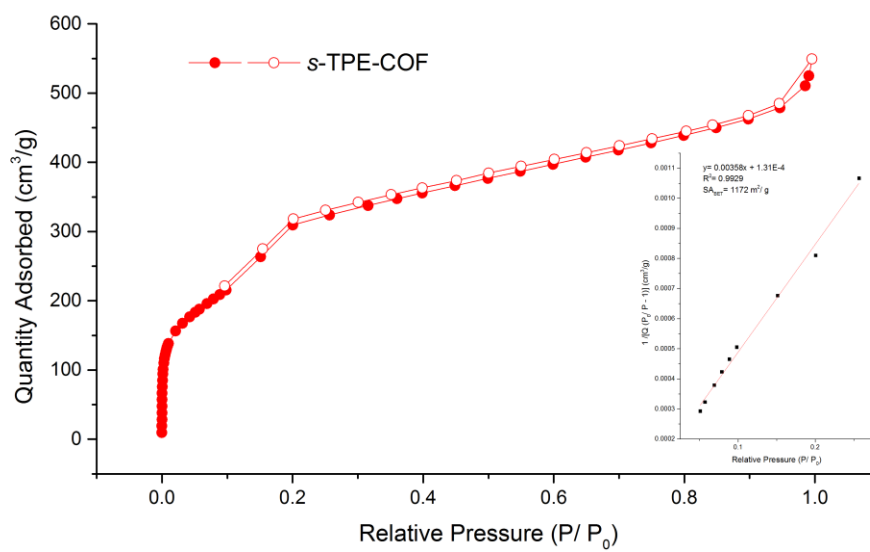


**Figure S39.**  $N_2$  sorption isotherm of *s*-TPE-COF measured at 77 K. (BET Surface area = 1172 m<sup>2</sup>/g).

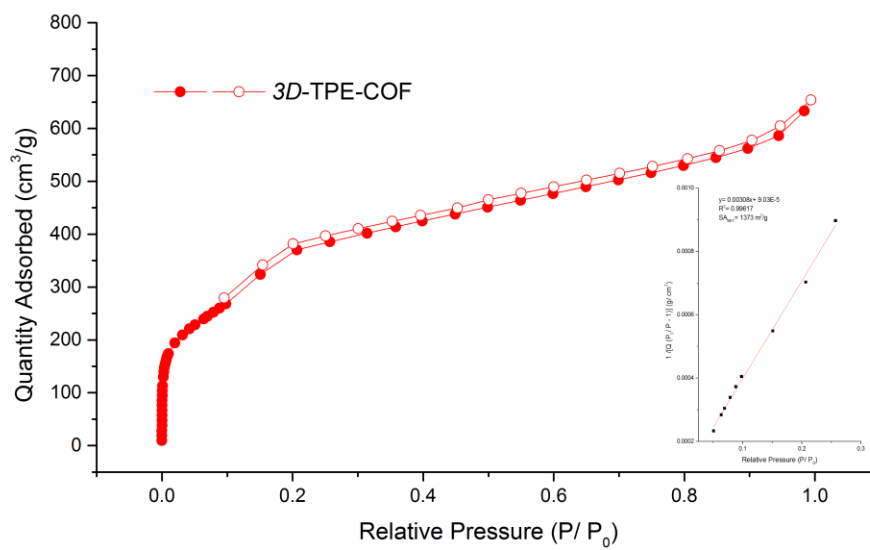


**Figure S40.**  $N_2$  sorption isotherm of 3D-TPE-COF measured at 77 K. (BET Surface area = 1373 m<sup>2</sup>/g).

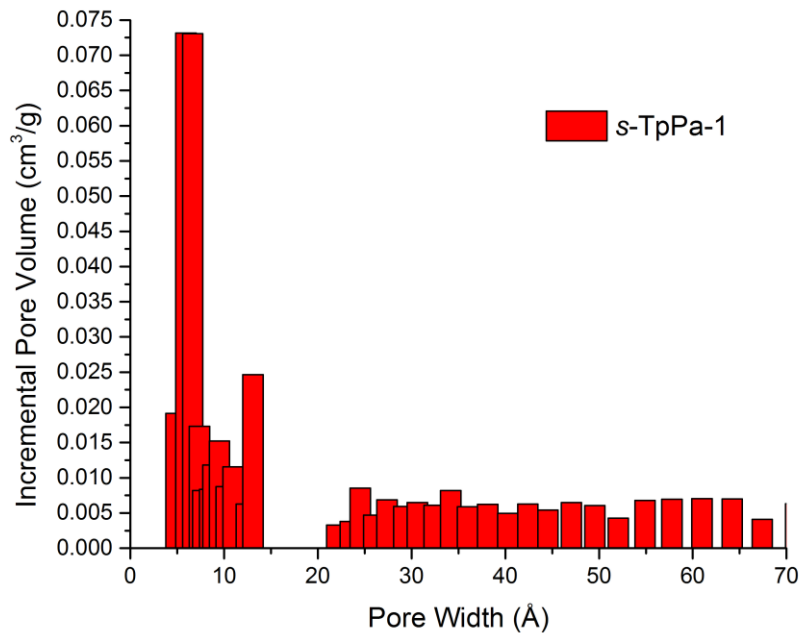


**Figure S41.** Pore size distribution of *s*-TpPa-1.

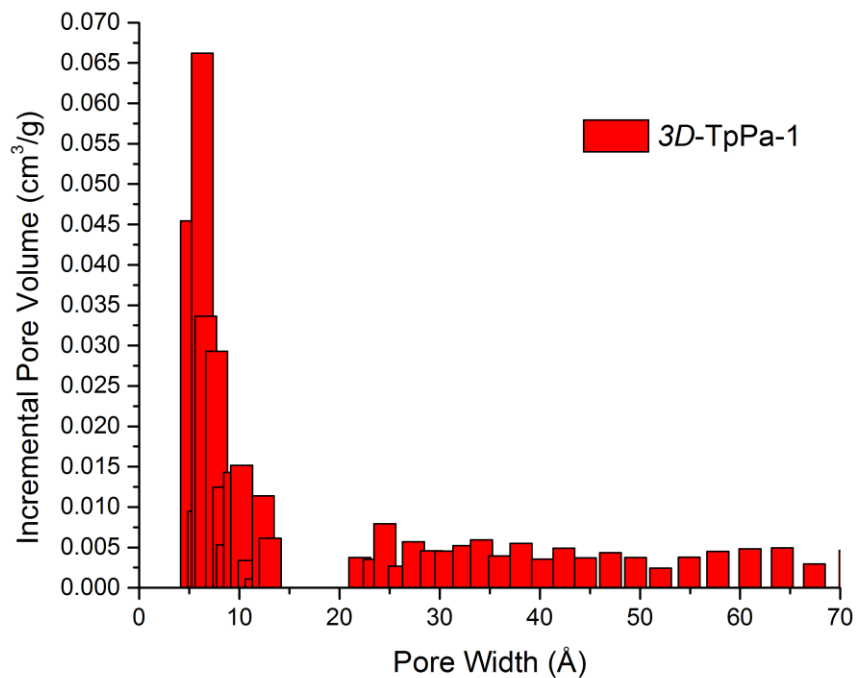


**Figure S42.** Pore size distribution of 3D-TpPa-1.

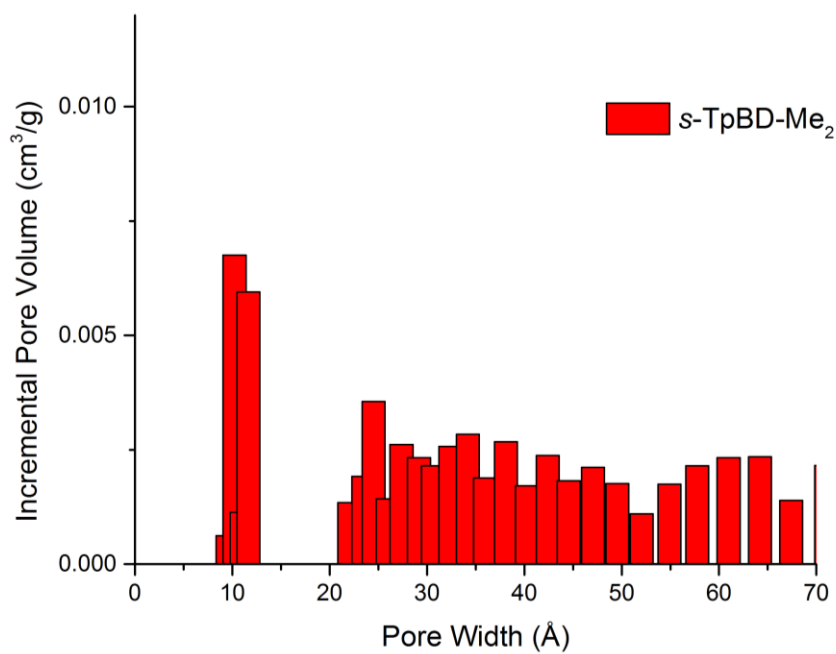


**Figure S43.** Pore size distribution of *s*-TpBD-Me<sub>2</sub>.

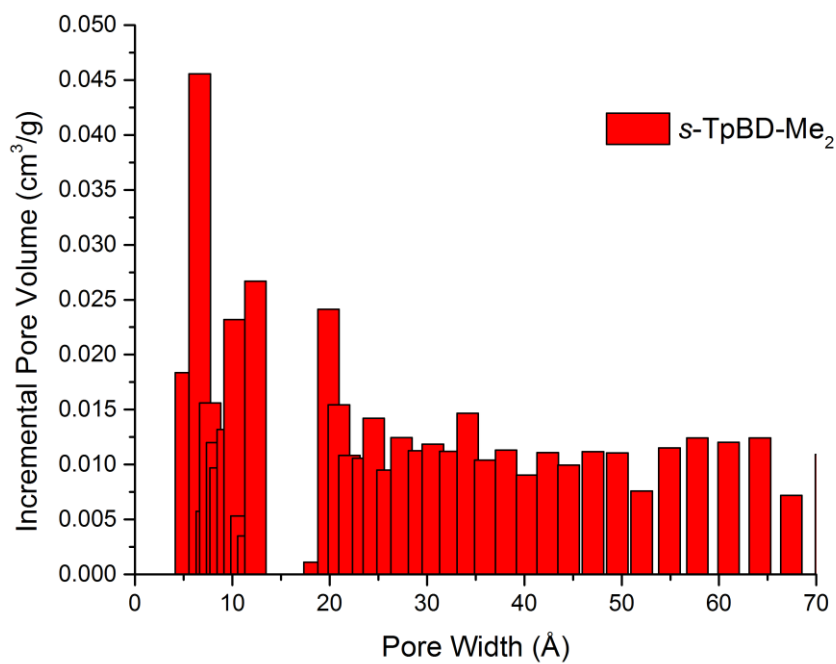


**Figure S44.** Pore size distribution of 3D-TpBD-Me<sub>2</sub> after solvent annealing.

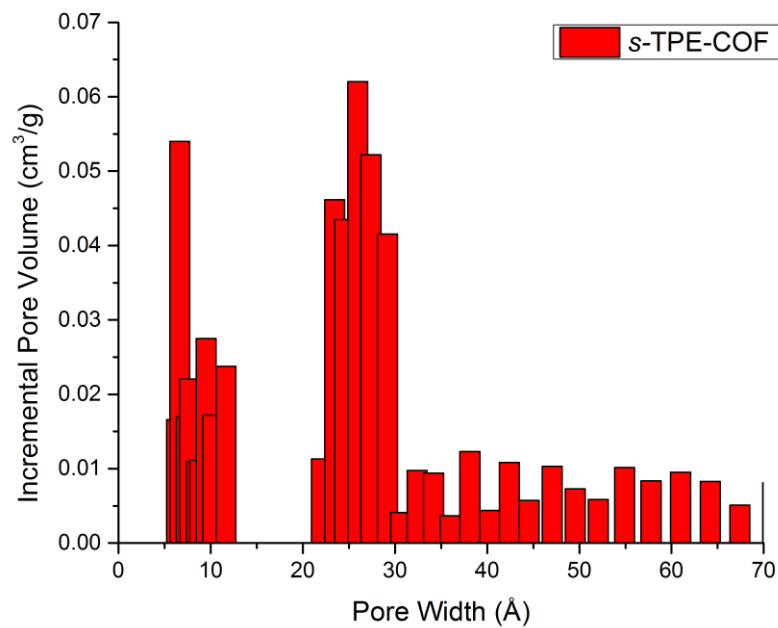


**Figure S45.** Pore size distribution of *s*-TPE-COF.

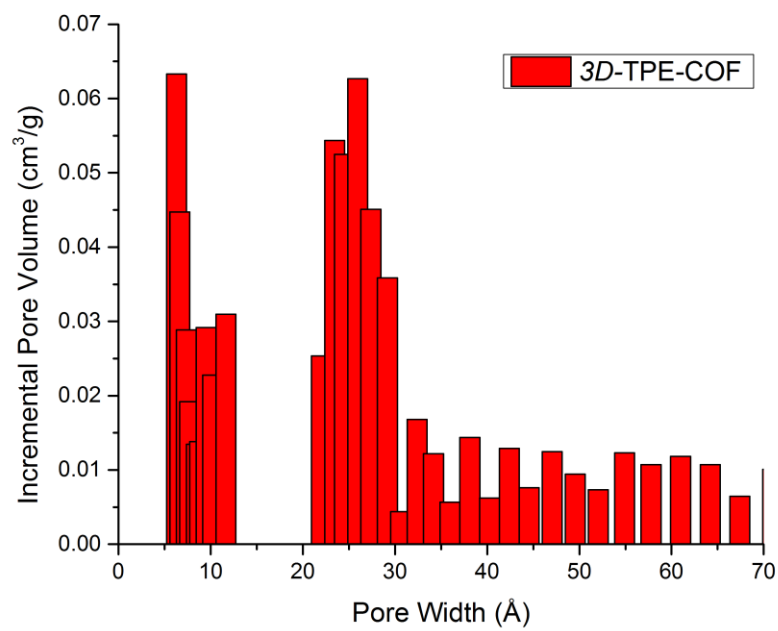


**Figure S46.** Pore size distribution of 3D-TPE-COF.

#### 4.4.8 Solid-state NMR Spectra

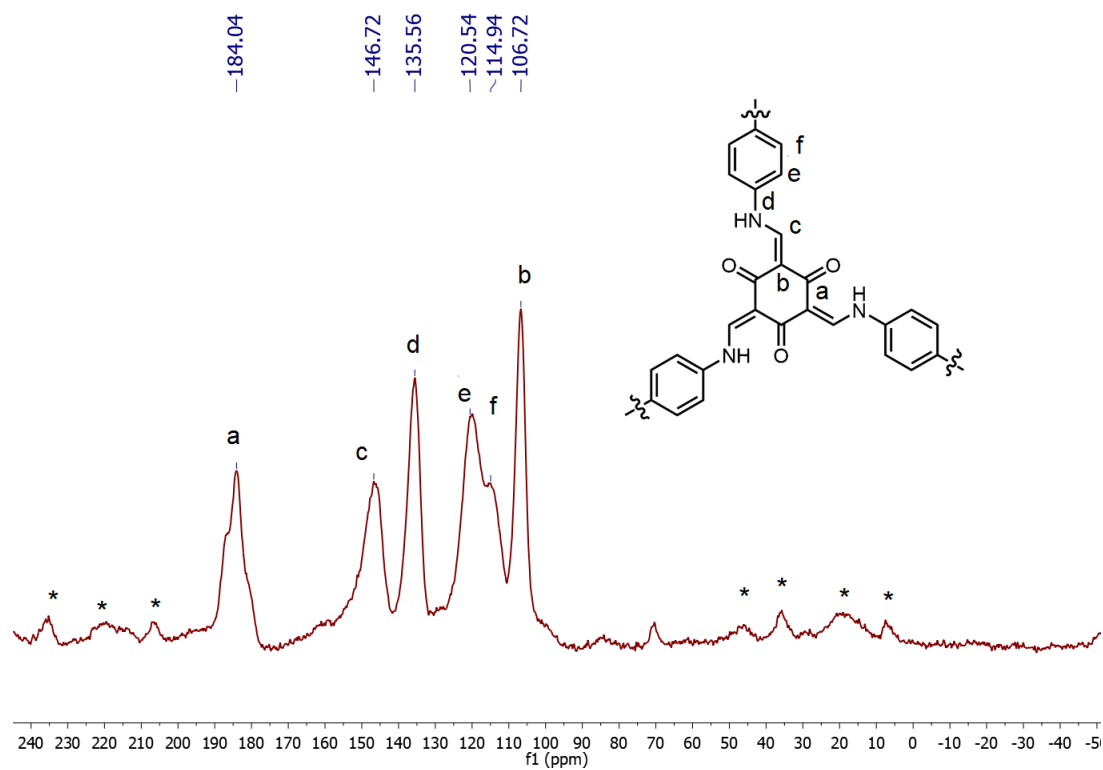


**Figure S47.** The solid-state  $^{13}\text{C}$ CPMAS NMR spectrum of **3D-TpPa-1**. The spin sidebands were marked with a \* symbol.

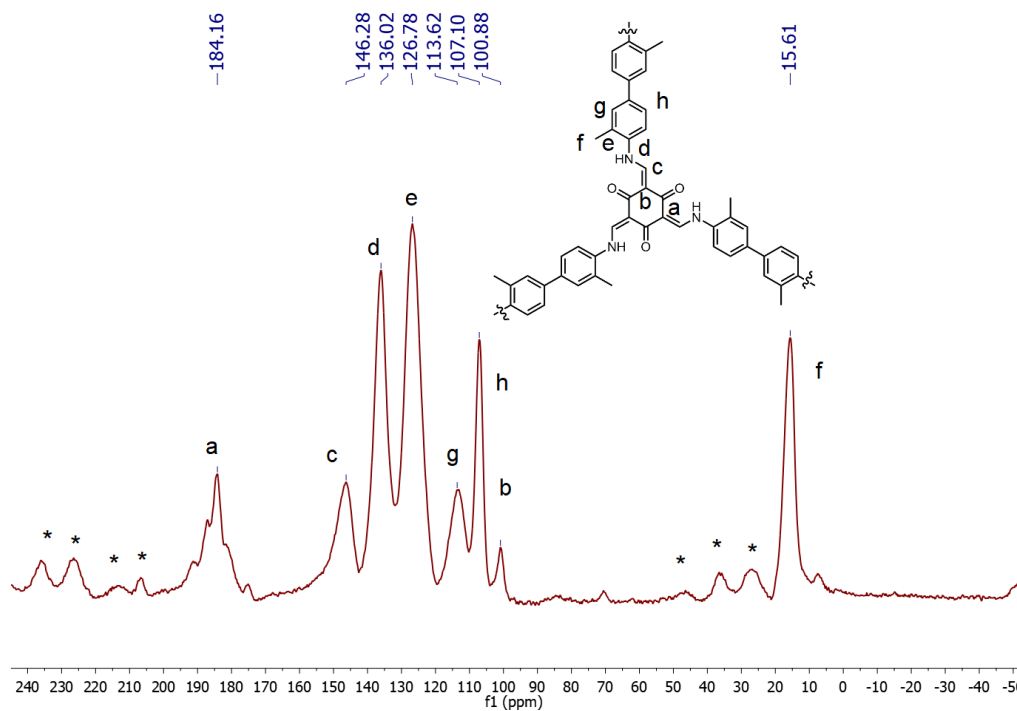


**Figure S48.** The solid-state  $^{13}\text{C}$ PMAS NMR spectrum of **3D-TpBD-Me<sub>2</sub>**. The spin sidebands were marked with a \* symbol.

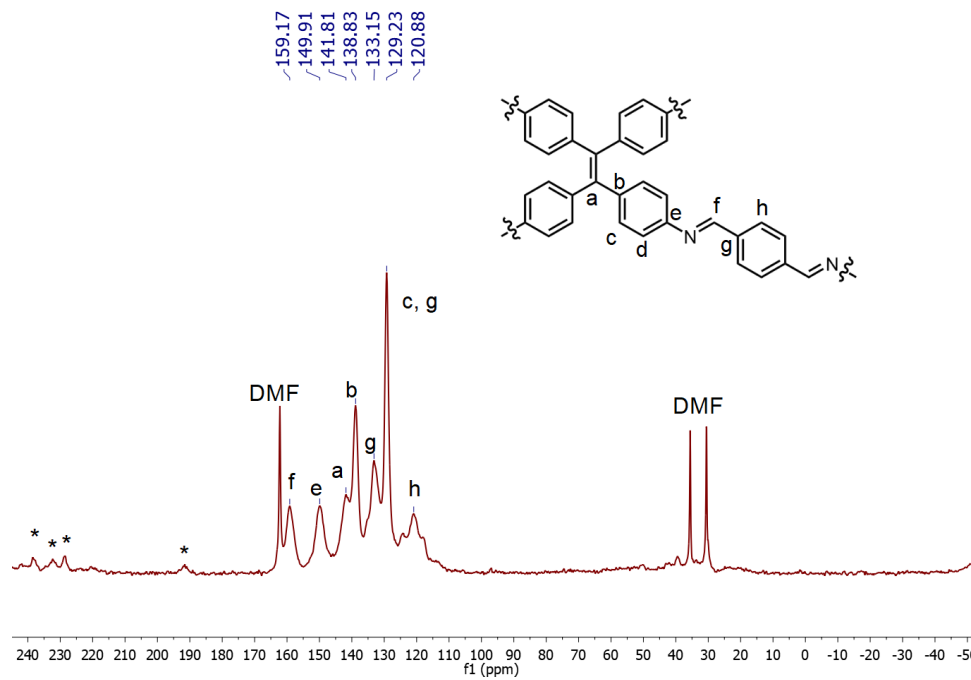


**Figure S49.** The solid-state  $^{13}\text{C}$ PMAS NMR spectrum of **3D-TPE-COF**. The spin sidebands were marked with a \* symbol.

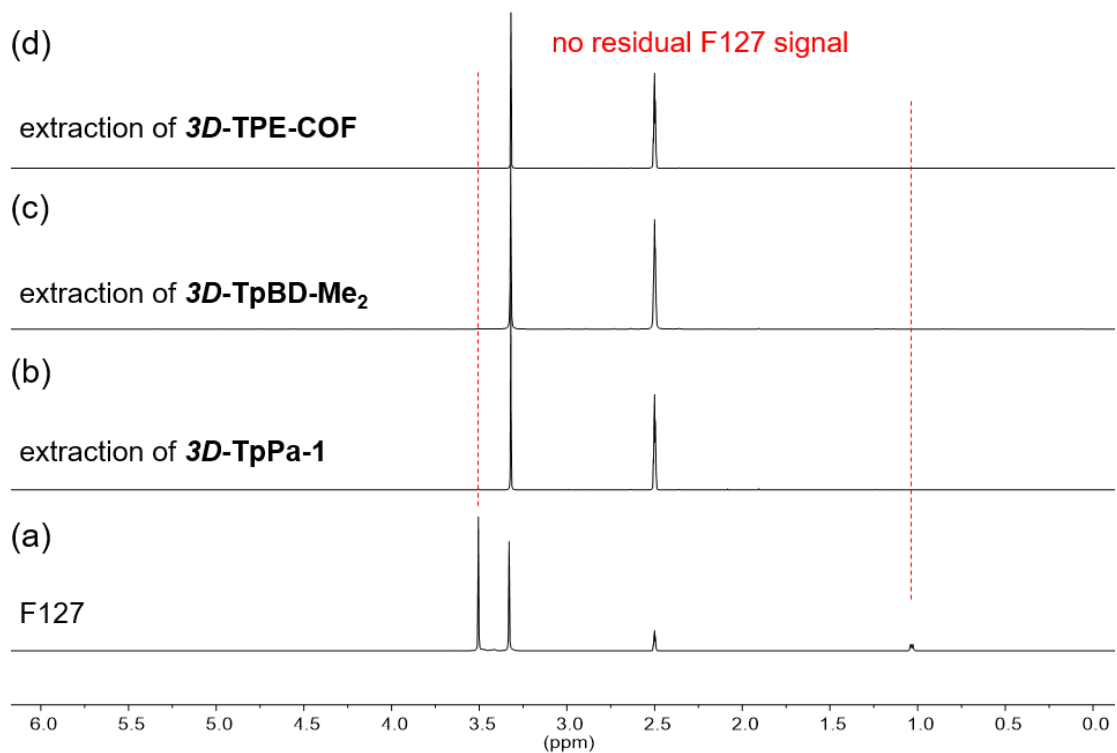


**Figure S50.**  $^1\text{H}$  NMR spectra (500 MHz, 298 K,  $\text{DMSO-}d_6$ ) of (a) F127, and (b-d) the extractions of the 3D-printed monoliths. **3D-TpPa-1**, **3D-TpBD-Me<sub>2</sub>**, and **3D-TPE-COF** were soaked in hot (80 °C)  $\text{DMSO-}d_6$  for 12 h before the  $^1\text{H}$  NMR experiment. No F127 could be extracted from the monolith, indicating a complete removal of F127.

#### 4.5 References

- 281 N. Huang, P. Wang, D. L. Jiang, *Nat. Rev. Mater.* **2016**, *1*, 16068.
- 282 R. P. Bisbey, W. R. Dichtel, *ACS Cent. Sci.* **2017**, *3*, 533-543.
- 283 Y. Song, Q. Sun, B. Aguila, S. Ma, *Adv. Sci.* **2018**, *6*, 1801410.
- 284 T. Ma, E. A. Kapustin, S. X. Yin, L. Liang, Z. Zhou, J. Niu, L. H. Li, Y. Wang, J. Su, J. Li, X. Wang, W. D. Wang, W. Wang, J. Sun, O. M. Yaghi, *Science* **2018**, *361*, 48-52.
- 285 Y. Zhao, L. Guo, F. Gandara, Y. Ma, Z. Liu, C. Zhu, H. Lyu, C. A. Trickett, E. A. Kapustin, O. Terasaki, O. M. Yaghi, *J. Am. Chem. Soc.* **2017**, *139*, 13166-13172.
- 286 H. Fan, J. Gu, H. Meng, A. Knebel, J. Caro, *Angew. Chem. Int. Edit.* **2018**, *57*, 4083-4087.
- 287 H. Thakkar, S. Eastman, Q. Al-Naddaf, A. A. Rownaghi, F. Rezaei, *ACS Appl. Mater. Inter.* **2017**, *9*, 35908-35916.



- 288 M. N. Channell, M. Sefa, J. A. Fedchak, J. Scherschligt, M. Bible, B. Natarajan, N. N. Klimov, A. E. Miller, Z. Ahmed, M. R. Hartings, *Polym. Adv. Technol.* **2018**, *29*, 867-873.
- 289 P. Pei, Z. Tian, Y. Zhu, *Microporous and Mesoporous Mater.* **2018**, *272*, 24-30.
- 290 S. Sultan, H. N. Abdelhamid, X. Zou, A. P. Mathew, *Adv. Funct. Mater.* **2019**, *29*, 1805372.
- 291 X. T. Zhou, C. J. Liu, *Adv. Funct. Mater.* **2017**, *27*, 1701134.
- 292 B. J. Smith, A. C. Overholts, N. Hwang, W. R. Dichtel, *Chem. Commun.* **2016**, *52*, 3690-3693.
- 293 J. Tan, S. Namuangruk, W. Kong, N. Kungwan, J. Guo, C. Wang, *Angew. Chem. Int. Edit.* **2016**, *55*, 13979-13984.
- 294 R. L. Truby, J. A. Lewis, *Nature* **2016**, *540*, 371-378.
- 295 E. Vitaku, W. R. Dichtel, *J. Am. Chem. Soc.* **2017**, *139*, 12911-12914.
- 296 TsOH is limited below 0.6 M to form printable viscoelastic hydrogels at room temperature, since the critical gelation temperature of Pluronic F127 increases from ca. 4 °C to 27 and 37 °C in the presence of 0, 0.6, and 1.0 M TsOH, respectively
- 297 T. Y. Zhou, S. Q. Xu, Q. Wen, Z. F. Pang, X. Zhao, *J. Am. Chem. Soc.* **2014**, *136*, 15885-15888.
- 298 L. Ascherl, T. Sick, J. T. Margraf, S. H. Lapidus, M. Calik, C. Hettstedt, K. Karaghiosoff, M. Döblinger, T. Clark, K. W. Chapman, F. Auras, T. Bein, *Nat. Chem.* **2016**, *8*, 310-316.
- 299 A. Betard, R. A. Fischer, *Chem. Rev.* **2012**, *112*, 1055-1083.

**Chapter 5 Hierarchically templated synthesis of 3D-printed crosslinked cyclodextrins for lycopene harvesting**

PREFACE for “Hierarchically templated synthesis of 3D-printed crosslinked cyclodextrins for lycopene harvesting” published in *small*. Reproduced from John Wiley & Sons, Inc.

Zhang, M.; Liu, W.; Lin, Q.; Ke, C. Hierarchically templated synthesis of 3D-printed crosslinked cyclodextrins for lycopene harvesting. *Small*. **2023**, doi: 10.1002/sml.202300323.

The results in this chapter were recently published in collaboration with several other researchers. This project was initiated by the co-first author, Dr. Wenxing Liu. However, Dr. Wenxing Liu didn't finish the project and left our group due to personal reasons. The co-first author, Minghsi Zhang further optimized the synthesis and developed the application of lycopene. Dr. Qianming Lin helped with the 3D printing of the materials. Professor Chenfeng Ke provided guidance on the idea and focus of the research, led the organization and planning of experiments, and significantly contributed to the writing and editing of the manuscript.

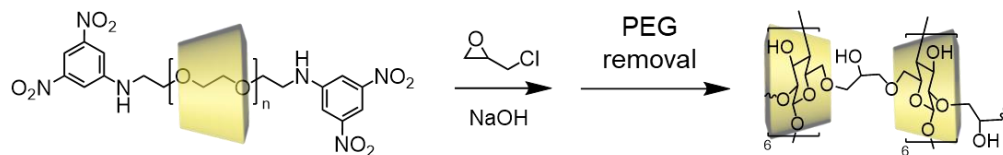
## 5.1 Introduction

Phytochemicals are plant-produced natural compounds<sup>300-302</sup> and are sustainable resources with increased demands from the pharmaceutical, cosmetic, and food industries.<sup>303-305</sup> For example, essential oils, polyphenols, and carotenoids are often costly to isolate because of their poor solubility, high volatility, rapid oxidation, and degradation.<sup>306-308</sup> Introducing macrocyclic molecules such as cyclodextrins (CDs) to form inclusion complexes with these phytochemicals in water has been demonstrated successful in improving the solubility and bioactivity of phytochemicals.<sup>309-310</sup> When CDs are crosslinked, the crosslinked polymers effectively adsorb the hydrophobic phytochemicals and protect them from degradation.<sup>311-313</sup> A variety of crosslinkages, including epichlorohydrin,<sup>314</sup> diacid chlorides,<sup>315-316</sup> fluorophenyl,<sup>317</sup> and diisocyanates,<sup>318-320</sup> have been introduced for the synthesis of crosslinked CD polymers. However, most of these crosslinked CD polymers only take advantage of the individual cavities of CDs, and they are less effective in isolating long unsaturated carotenoids such as lycopene and  $\beta$ -carotenes, which are significantly larger than the cavity of the CD. Tubular  $\alpha$ -CD polymers synthesized by Harada<sup>321</sup> and others<sup>322-326</sup> are promising for the adsorption of carotenoids, although they have only been investigated as molecular tubes for guest-complexations in solution.

To selectively harvest specific phytochemicals from the aqueous environment, employing sorbents with hierarchical porosity is highly desired. The nanometer-sized pores are critical for selective inclusion, and the macroscale voids are also crucial for fast mass transportation. To this end, fabricating CD-based macroscale architectures through 3D printing is particularly attractive<sup>327-328</sup> because the designed structure will be lightweight with a high surface area for phytochemical harvesting. However, to date, it remains synthetically challenging to introduce these tubular CD-based materials for 3D printing, such as direct ink writing (DIW),<sup>102</sup> because the existing synthetic approaches to access these nanotubular CDs conflict with the rheological requirements for DIW.

To overcome this challenge, we herein report a hierarchically templated synthesis of crosslinked CD monolith (Figure 5.1), which possesses macroscale void enabled by DIW and nanoscale  $\alpha$ -CD channels connected by diurethane linkages. Furthermore, the 3D-printed urethane- $\alpha$ -CD polymers show highly selective adsorption of lycopene from raw tomato juice, demonstrating the hierarchically designed functional 3D printing materials for efficient phytochemical harvesting.

(a) Previously reported CD-tube synthesis (Harada et al.)



(b) Previous reported 3D-printable polyrotaxanes (Ke et al.)

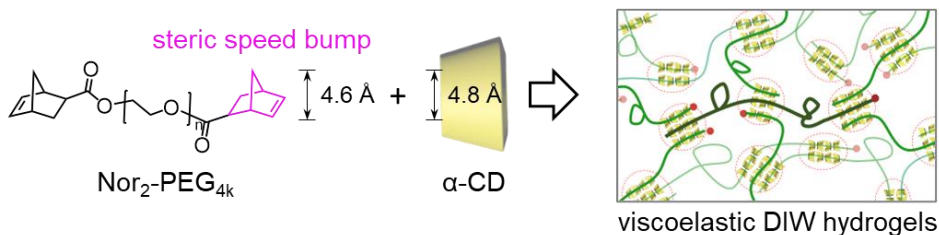


**Figure 5.1.** (a) Previous method of templated synthesis of  $\alpha$ -CD tubes. (b) Previous method of templated synthesis of 3D-printable polyrotaxanes.

## 5.2 Results and Discussions

Conventional tubular  $\alpha$ -CD polymers are synthesized through a polyrotaxane-templated method (Figure 5.1a).<sup>321</sup> First,  $\alpha$ -CD-threaded polyrotaxanes are synthesized, and the threaded  $\alpha$ -CDs are covalently linked. Next, bulky stoppers of the polyrotaxanes are removed, and the axle polymer is dethreaded to afford the tubular  $\alpha$ -CD polymer.<sup>321, 329-330</sup>

In contrast, our design features a simultaneous construction of nanotubular  $\alpha$ -CD structures and fabrication of 3D-printed architectures in one fell swoop. Specifically, 3D-printable siloxane-polypseudorotaxane is introduced as the template for the formation of nanotubular networks, and it also serves as a scaffolding template for DIW at the macroscale. Bis-triethoxysilane-based telechelic polyethylene glycols (PEG-2Si(OEt)<sub>3</sub>,  $M_n = 4, 20$  kDa) have been synthesized as axle polymers (Figure 5.2). These triethoxysilane end groups act as  $\alpha$ -CD threading speed bumps to direct a kinetic assembly of polypseudorotaxanes for 3D-printing.<sup>123, 331-332</sup> Polycondensation of the  $-\text{Si}(\text{OEt})_3$  groups in the hydrogel affords a crosslinked polyrotaxane monolith (PM), which templates the reaction between the diisocyanates and  $\alpha$ -CDs (Figure 5.2). In the next step, the PEG-siloxane network in the urethane-crosslinked PM is depolymerized and removed, affording 3D-printed monoliths comprised of urethane-crosslinked nanotubular  $\alpha$ -CDs (Figure 5.2).

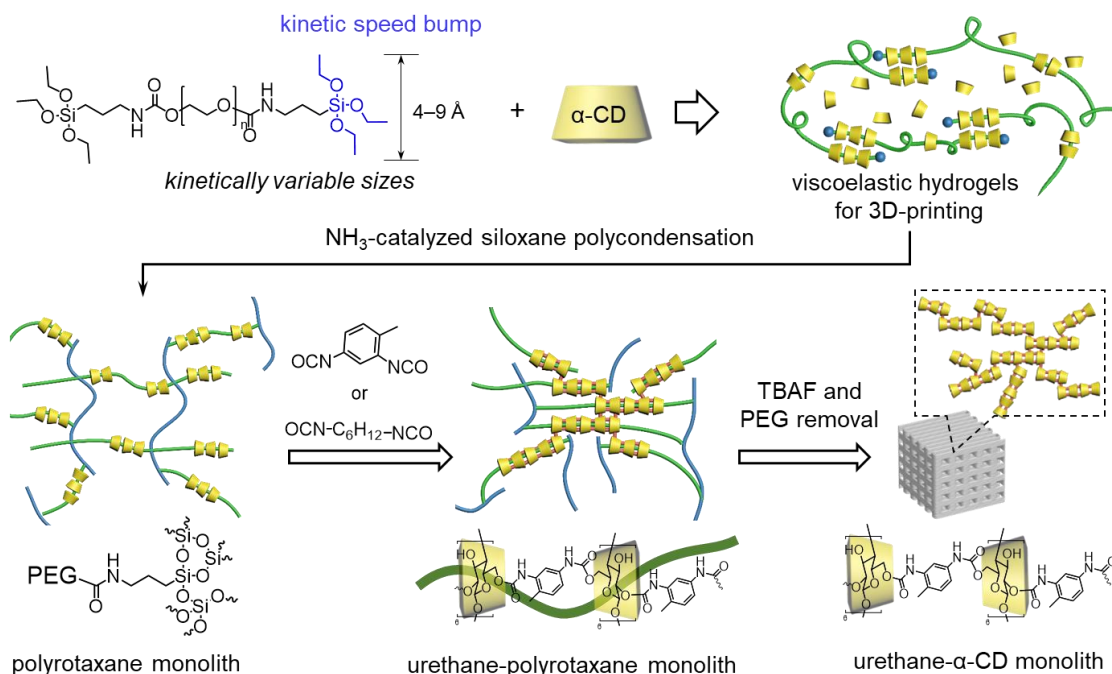


**Figure 5.2.** Templated synthesis of 3D-printed crosslinked urethane- $\alpha$ -CD monoliths. PEG-2Si(OEt)<sub>3</sub> and  $\alpha$ -CD were employed to form 3D-printable hydrogels, which were crosslinked to form polyrotaxane monolith after base-catalyzed polycondensation. After diisocyanate crosslinking of the threaded  $\alpha$ -CDs followed by PEG axles removal, 3D-printed urethane- $\alpha$ -CD monoliths were obtained.

We chose the  $-\text{Si}(\text{OEt})_3$  group as a kinetic ‘speed bump’ to regulate the rate of  $\alpha$ -CD threading to form kinetically trapped 3D-printable hydrogels. In our previous report,<sup>123</sup> we have discovered that PEGs with sterically demanding end groups such as norbornyl ( $d = 4.6 \text{ \AA}$ ) regulate the assembly of the formed polypseudorotaxanes kinetically. As a result,  $\alpha$ -CD blocks were kinetically segregated in the polypseudorotaxanes, which microcrystallized to form viscoelastic hydrogels for DIW. Since the size of the  $-\text{Si}(\text{OEt})_3$  group varies between 4–9  $\text{\AA}$ , it is expected to slow down the threading of the  $\alpha$ -CDs.

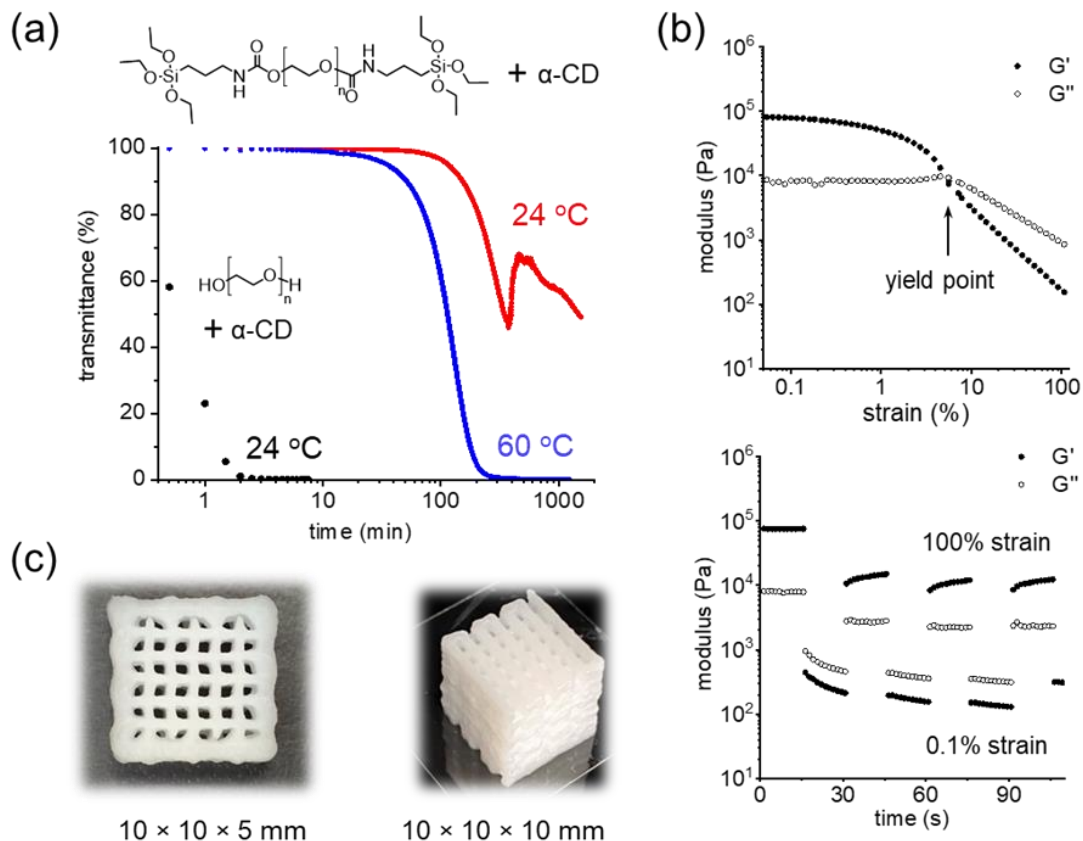


**Figure 5.3.** (a) Time-dependent transmittance (550 nm) of the polypseudorotaxanes upon mixing the PEG axle and  $\alpha$ -CD. Black dots: PEG<sub>4k</sub>-2OH (2.5 mM) and  $\alpha$ -CD (102.8 mM), red and blue dots: PEG<sub>4k</sub>-2Si(OEt)<sub>3</sub> (2.5 mM) and  $\alpha$ -CD (102.8 mM) at 24 °C and 60 °C, respectively. (b) Stress-strain and alternative step-strain rheological sweeps of a polypseudorotaxane hydrogel PRH[6, 27]. (c) Images of two 3D-printed lattices of PRH[6, 27].

When PEG-2Si(OEt)<sub>3</sub> and  $\alpha$ -CD were mixed together,  $\alpha$ -CDs were threaded onto the PEG axle, and the formed polypseudorotaxanes crystallized as precipitates. The formation and crystallization of the PEG-2Si(OEt)<sub>3</sub>/ $\alpha$ -CD polypseudorotaxanes were investigated through time-dependent UV/Vis turbidity experiments (Figure 5.3a).<sup>333-334</sup> When PEG<sub>4k</sub>-2Si(OEt)<sub>3</sub> (2.5 mM) and  $\alpha$ -CD (102.8 mM) were mixed at 24 °C, the transmittance of the reaction at 550 nm (wavelength chosen to monitor the Rayleigh diffraction of the crystallized polypseudorotaxanes)<sup>335</sup> did not change until 77 min (transmittance > 98%) and an n-shaped transmittance profile was observed afterward. The threading of  $\alpha$ -CDs and crystallization of the formed polypseudorotaxanes were accelerated at higher temperatures. At 60 °C, the transmittance started to decrease at 18 min, and reached

1% in 265 min. In comparison, the transmittance of the reaction of PEG<sub>4k</sub>-2OH (2.5 mM) and  $\alpha$ -CD (102.8 mM) rapidly decreased to 1% in 2 min. These results indicate that the formation and crystallization of the PEG-2Si(OEt)<sub>3</sub>/ $\alpha$ -CD polypseudorotaxanes are kinetically slow,<sup>123</sup> confirming that the -Si(OEt)<sub>3</sub> group is an effective kinetic ‘speed bump’ to regulate the threading of  $\alpha$ -CDs.

**Table 5.1.** Summary of the elastic moduli and PEG/CD ratios of the PRHs and PM hydrogels.

PEG <sub>4k</sub> -2Si(OEt) <sub>3</sub> (w/v %)	$\alpha$ -CD (w/v %)	feeding PEG/CD	PRHs		PMs
			elastic modulus (kPa)	found PEG/CD <sup>a</sup>	found PEG/CD <sup>b</sup>
3	10	1 : 14	3.2	1 : 16	1 : 9
6	17	1 : 11	32	1 : 12	1 : 6
<b>6</b>	<b>27</b>	<b>1 : 18</b>	<b>71</b>	<b>1 : 17</b>	<b>1 : 10.4</b>
6	33	1 : 23	34	1 : 20.5	1 : 9.5
10	56	1 : 23	31	1 : 23	1 : 10

<sup>a</sup> The found PEG/CD ratio was measured by <sup>1</sup>H NMR of the PRH. The hydrogel was centrifuged extensively to isolate the solid content, which was lyophilized for NMR analysis. <sup>b</sup> The found PEG/CD ratio was measured by <sup>1</sup>H NMR analysis of the hydrolyzed PM.

When PEG<sub>4k</sub>-2Si(OEt)<sub>3</sub> and  $\alpha$ -CD were mixed at higher concentrations, a series of viscoelastic polypseudorotaxane hydrogels (PRH, **Table 5.1**) were formed. Rheological investigations (Figures S14-S17) showed that increasing the feeding ratios of  $\alpha$ -CD to PEG<sub>4k</sub>-2Si(OEt)<sub>3</sub> enhanced the elastic moduli of the formed hydrogels. After optimizing the PEG<sub>4k</sub>-2Si(OEt)<sub>3</sub> and  $\alpha$ -CD concentrations, a polypseudorotaxane hydrogel PRH[6, 27] (6 w/v% of PEG<sub>4k</sub>-2Si(OEt)<sub>3</sub> and 27 w/v% of  $\alpha$ -CD) was found to possess good shear-thinning and self-healing properties for DIW.<sup>103</sup> PRH[6, 27] possessed an elastic moduli of  $G' = 6-8 \times 10^4$  Pa at low strains (Figure 5.3b) and a yield strain of 5% ( $G' = G''$ ). In the step-strain



sweep (Figure 5.3b), after the first strain cycle, PRH[6, 27] demonstrated excellent self-healing properties for DIW ( $G' = 1.5 \times 10^4$  Pa, Figure 5.3b). Using a DIW printer with a 400  $\mu\text{m}$  extrusion tip, woodpile lattices of  $10 \times 10 \times 5/10$  mm were 3D-printed with good structural integrity (Figure 5.3c).

The 3D-printed PRH[6, 27] lattices were placed in a sealed reaction chamber and exposed to  $\text{NH}_3$  vapor for 24 h to allow for extensive polycondensation of siloxane end groups. The crosslinked PMs were washed with an excess of DMSO and water to remove any unreacted species. The 3D-printed structures were well maintained in the dried PM ( $9.5 \times 9.5 \times 4.5$  mm, Figure 5.4a), suggesting successful crosslinking of  $\text{PEG}_{4\text{k}}\text{-2Si(OEt)}_3$  axles. In comparison, when a longer  $\text{PEG}_{20\text{k}}\text{-2Si(OEt)}_3$  was used to form polypseudorotaxane hydrogels, the 3D-printed structures were disintegrated by the solvent washing (Figures S32-S33) due to the low degree of siloxane crosslinking (Figure S34).

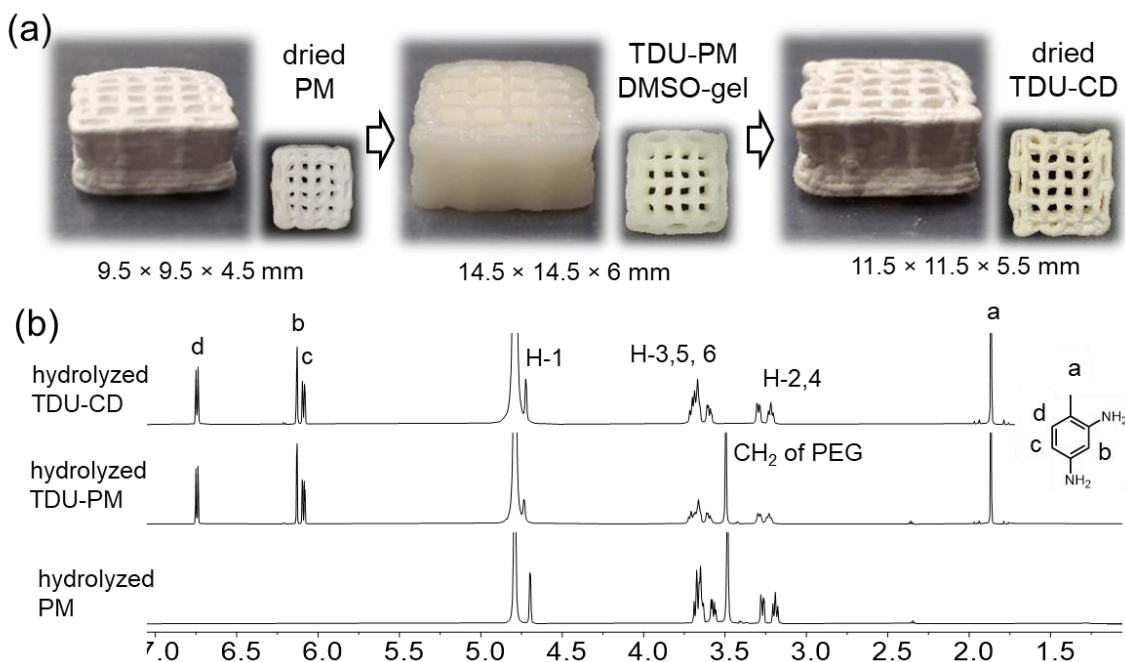


**Figure 5.4.** (a) Images (top and side views) of the 3D-printed PM, TDU-PM, and TDU-CD lattices from left to right, respectively. (b)  $^1\text{H}$  NMR (600 MHz, 298 K) of the completely hydrolyzed PM, TDU-PM, and TDU-CD in  $\text{NaOD}/\text{D}_2\text{O}$  (5%) from the bottom to the top, respectively.

The chemical composition of the PM was revealed by  $^1\text{H}$  NMR hydrolysis analysis. On average,  $10.4 \pm 0.7$   $\alpha$ -CDs per PEG were mechanically interlocked in the PM (Figure 5.4b). When a dried PM was swelled in anhydrous DMSO, its size expanded significantly

(top view:  $30 \times 30$  mm, Figure S35). The PM DMSO-gel turned transparent since the microcrystalline domains of the polyrotaxanes were disrupted in DMSO, and  $\alpha$ -CDs were freely shuttling along the PEG axles.<sup>336-337</sup> When a crosslinker 2,4-toluene diisocyanate (TDI) or hexamethylene diisocyanate (HDI), and a catalyst dibutyltin dilaurate were added to the PM DMSO-gel, its  $\alpha$ -CDs were linked via diurethane moieties. During the reaction, the neighboring  $\alpha$ -CDs on the same PEG axle should be connected easier than two  $\alpha$ -CDs from two different PEG axles in the DMSO-gel. After that, nanotubular structures were formed and further crosslinked as a network in the PM. After TDI and HDI crosslinking, a toluene-diurethane crosslinked PM (TDU-PM) and a hexamethylene-diurethane crosslinked PM (HDU) were obtained with good structural integrity (Figure 5.4a, Figures S37-38). In the TDU-PM and HDU-PM, characteristic bands of urethane linkages (C=O stretching at  $1704\text{ cm}^{-1}$  and N-H bending at  $1530\text{ cm}^{-1}$ ) were observed in the FT-IR spectra (Figures S40-S41), confirming the formation of diurethane linkages.  $^1\text{H}$  NMR digestion analysis (Figure 5.4b) showed that the PEG-to- $\alpha$ -CD ratio in the TDU-PM remained at 1:10.6, similar to its PM precursor. The TDU-to- $\alpha$ -CD ratio was measured as 9.5:1. The high TDU-to- $\alpha$ -CD ratio is required to keep the 3D-printed structure in the subsequent template removal step. Compared to the elastic modulus of 0.4 kPa for the PM hydrogel, the elastic modulus of TDU-PM hydrogel reached 54 kPa after the TDU crosslinking (Figure S19).

3D-printed lattices of TDU-PM and HDU-PM were depolymerized in the DMSO solutions of tetra-*n*-butylammonium fluoride (TBAF), which also allowed for the dethreading of PEGs. After extensive washing, off-white TDU-CD and HDU-CD monoliths were obtained. The elastic moduli of TDU-CD hydrogel reduced from 54 kPa to 16 kPa after the removal of the crosslinked PEG network (Figure S19). The dried TDU-CD monolith was measured as  $11.5 \times 11.5 \times 5.5$  mm with good shape retention after multi-step post-printing synthesis (Figure 5.4a and Figures S37-38). These TDU-CD and HDU-CD polymers are amorphous (Figures S42-S44), and the PEG axles has been completely removed shown in the  $^1\text{H}$  NMR digestion analysis (Figure 5.4b). Compared to TDU-PM, the TDU-to- $\alpha$ -CD ratio decreased slightly to 6.4:1 in TDU-CD. It is worth noting that when less TDI was used during the synthesis of TDU-PM, the obtained TDU-CD after PEG removal cracked (Figure S39). This observation supports that the formation of nanotubular  $\alpha$ -CDs is more preferred than the crosslinking of  $\alpha$ -CDs on different polyrotaxanes in the PM.

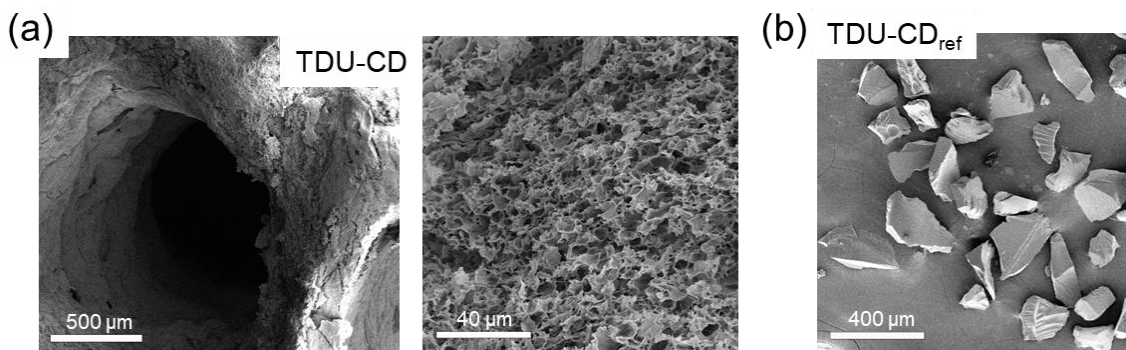


**Figure 5.5.** (a) SEM images of a TDU-CD lattice (b) SEM image of TDU-CD<sub>ref</sub>.

Since the TDU linkage is more rigid than HDU, we chose TDU-CD for more detailed investigations because the TDU-connected nanotubular structures are more suitable for the encapsulation of rigid linear phytochemicals. The freeze-dried TDU-CD lattice showed  $\sim 10\ \mu\text{m}$ -sized pores in the scanning electron microscope (SEM, Figure 5.5a) studies. To better understand the hierarchical structures of TDU-CD synthesized using the templated method, we have also synthesized a reference polymer TDU-CD<sub>ref</sub> by crosslinking  $\alpha$ -CD with TDI at a similar crosslinking density (see the Supporting Information for details). TDU-CD<sub>ref</sub> is a densely crosslinked polymer with no mesoscale features observed in SEM (Figure 5.5b).

Since the nanotubular  $\alpha$ -CDs are also densely crosslinked in TDU-CD, it is not trivial to directly observe these nanotubular structures using TEM or AFM techniques. Hence, linear PEGs of different lengths were employed as tubular- $\alpha$ -CD probes for TDU-CD and TDU-CD<sub>ref</sub>. It is well documented that each  $\alpha$ -CD includes two ethylene glycol (EG) repeating units of PEG.<sup>338-339</sup> In the presence of an excess of PEG ( $[\text{EG}]/[\alpha\text{-CD}] \geq 2$ ), TDU-CD should adsorb fewer PEGs than TDU-CD<sub>ref</sub>, because short-chain PEGs such as PEG<sub>2k</sub> and PEG<sub>4k</sub> are likely to be fully threaded into the nanotubes in TDU-CD, whereas these PEGs are more likely to be partially threaded in those randomly crosslinked  $\alpha$ -CDs in TDU-CD<sub>ref</sub>. Indeed, at different feeding ratios of PEG<sub>600</sub> to PEG<sub>100k</sub> (**Table 5.2**), the adsorbed amounts of PEGs in TDU-CD were significantly lower than those of TDU-CD<sub>ref</sub>. For example, at  $[\text{EG}]/[\alpha\text{-CD}] = 8$ , TDU-CD only adsorbed 35% and 31% of the fed PEG<sub>2k</sub> and PEG<sub>4k</sub>, respectively, compared to those of 91% and 93% for TDU-CD<sub>ref</sub>. These results provided indirect evidence for the formation of nanotubular structures in TDU-CD.

**Table 5.2.** Adsorption of PEGs of different molecular weights using TDU-CD and TDU-CD<sub>ref</sub>.

Probes	fed EG/ $\alpha$ -CD	TDU-CD		TDU-CD <sub>ref</sub>	
		adsorbed <sup>a</sup>	adsorbed	adsorbed	adsorbed
		PEG%	PEG/ $\alpha$ -CD	PEG%	PEG/ $\alpha$ -CD
PEG <sub>600</sub>	2 : 1	45%	1 : 15.1	53%	1 : 12.5
PEG <sub>2K</sub>	2 : 1	96%	1 : 23.6	100%	1 : 22.8
	8 : 1	35%	1 : 16.2	91%	1 : 6.3
	18 : 1	17%	1 : 14.8	57%	1 : 4.4
PEG <sub>4K</sub>	2 : 1	100%	1 : 45.4	100%	1 : 45.4
	8 : 1	31%	1 : 36.6	93%	1 : 12.2
	18 : 1	15%	1 : 33.6	51%	1 : 9.9
PEG <sub>20K</sub>	2 : 1	36%	1 : 630	100%	1 : 230
PEG <sub>100K</sub>	2 : 1	12%	1 : 9460	12%	1 : 9460

<sup>a</sup> the percentages of the adsorbed PEGs were measured by <sup>1</sup>H NMR analysis.

The nanotubular structures in TDU-CD allowed for selective harvesting of linear phytochemicals like lycopene from other carotenoids, including its isomers  $\alpha$ -,  $\beta$ -, and  $\gamma$ -carotenes (Figure 5.6a). Only lycopene could be threaded extensively in TDU-CD because its cross-section size is smaller than the inner diameter of  $\alpha$ -CD ( $\sim 4.7$  Å).<sup>340-341</sup> Lycopene harvesting experiments were performed by immersing 3D-printed TDU-CD monoliths in fresh tomato juice. A small amount of THF (20% v/v) was added to the tomato juice to release the hydrophobic carotenoids from the cell membranes. In THF/water, the TDU-CD hydrogel showed characteristic elastic features similar to other densely crosslinked covalent hydrogels, possessing Young's modulus of 456 kPa measured in the compression test (Figure S36). More than 13 carotenoids were extracted from the raw tomato juice using CH<sub>2</sub>Cl<sub>2</sub> (Table S4 and Figure S47), rendering the selective isolation of lycopene a challenging task. The 3D-printed TDU-CD monolith turned bright red after extensive adsorption (Figure 5.6c), which is the characteristic color of lycopene. The adsorbed

phytochemicals were completely released in acetone, and no residual lycopene was detected in the TDU-CD monolith (Figure S61). The released lycopene was subjected to high-performance liquid chromatography-mass spectrum (HPLC-MS) analysis. As shown in Figure 5.7a, a variety of carotenoids, including lycopene and its isomers  $\alpha$ -,  $\beta$ -, and  $\gamma$ -carotenes, were extracted by  $\text{CH}_2\text{Cl}_2$ , and the purity of lycopene reached ca. 82% after  $\text{CH}_2\text{Cl}_2$  extraction and silica chromatographic purification. In comparison, lycopene was selectively extracted using TDU-CD, and its purity reached 89% (Figure 5.7a). Furthermore, after extensive adsorption, the adsorption capacity of lycopene in TDU-CD was measured as 21.5 mg/g (Figure S59), whereas TDU-CD<sub>ref</sub> only adsorbed 3.2 mg/g of lycopene. The enhanced lycopene adsorption capacity of TDU-CD is attributed to the nanotubular structures formed during the templated synthesis. We also subjected the TDU-CD monolith to multi-cycle lycopene adsorption and desorption analysis (Figure S60). After five cycles of lycopene sorptions, the lycopene uptake capacity of TDU-CD monolith remained at 19.9 mg/g.

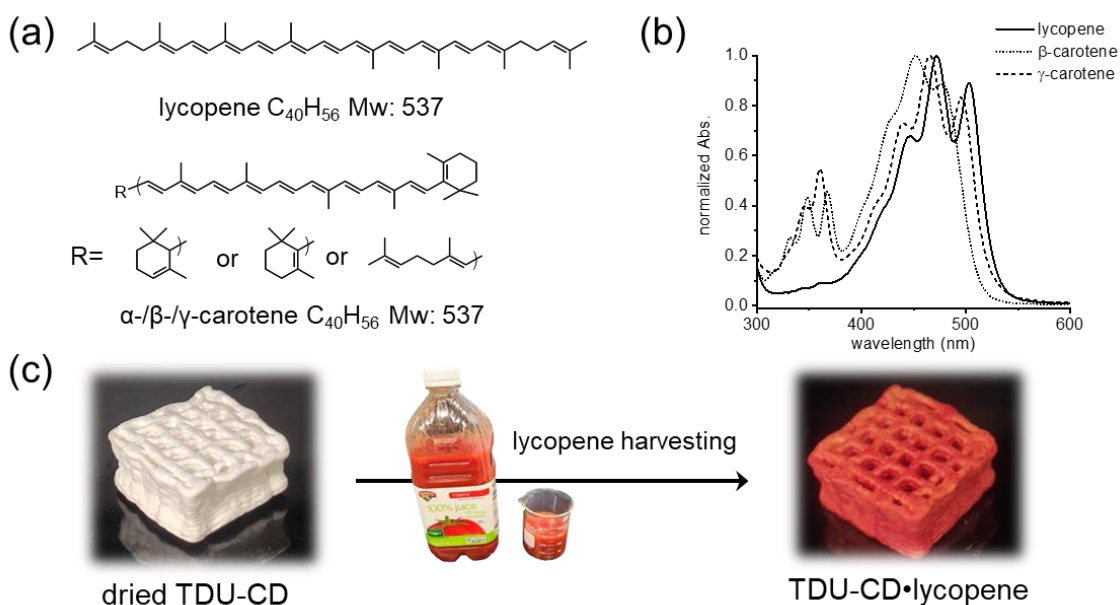


**Figure 5.6.** (a) Chemical structures of the major phytochemicals in tomato juice. (b) Normalized UV-Vis spectra of lycopene and  $\beta$ -/ $\gamma$ -carotenes in acetone. (c) Selective extraction of lycopene from tomato juice using TDU-CD.

The solvent-extracted lycopene decomposed quickly under UV-irradiation or thermal treatments because its highly conjugated alkenes are susceptible to oxidation.<sup>342-344</sup>

In contrast, lycopene adsorbed in TDU-CD is stable against photo- or thermo-degradation (Figure 5.7b). For example, lycopene degraded completely when its THF solutions were UV-irradiated for 24 h, heated to 50 °C, or refluxed temperature (66 °C), respectively. Under these conditions, more than 80% of lycopene remained undegraded in the TDU-CD•lycopene monolith (Figure 5.7b). Furthermore, the chemical stability of lycopene in TDU-CD•lycopene is better than that of TDU-CD<sub>ref</sub>•lycopene (Figure 5.7b), confirming the nanotubular structures in stabilizing lycopene in their channels. These results suggested the potential of employing 3D-printed TDU-CD as a separation and long-term storage material for photo- and thermos-sensitive phytochemicals.

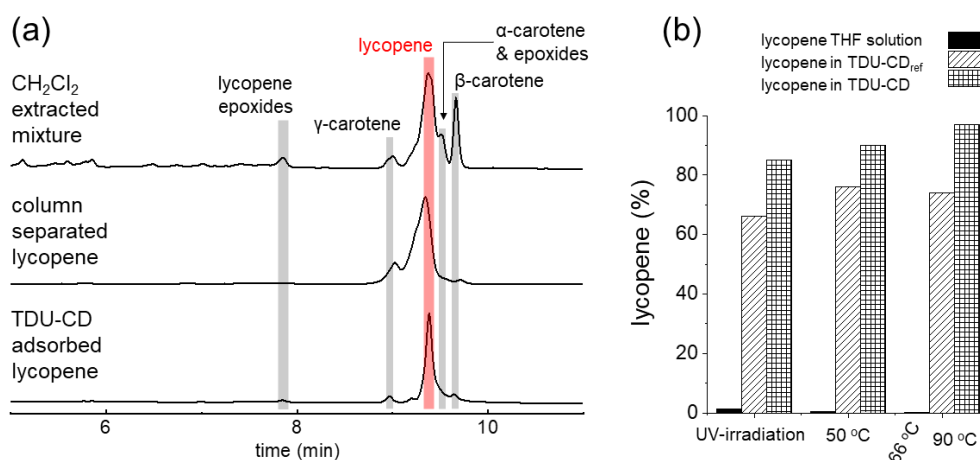


**Figure 5.7.** (a) HPLC-MS diagrams of phytochemicals extracted from tomato juice using CH<sub>2</sub>Cl<sub>2</sub> (top), purified after silica gel chromatography (middle), and adsorbed in TDU-CD. (b) Recovered lycopene after UV-irradiation and thermos-treatments, measured using the UV/Vis-spectrometer.

### 5.3 Summary

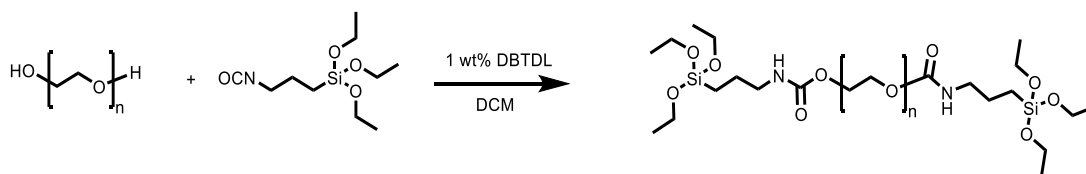
In summary, we developed a templated synthesis approach of urethane-crosslinked  $\alpha$ -CDs with nanotubular structures and 3D-printed architectures. Using tetraethoxysilane-based telechelic polyethylene glycol as the axle and  $\alpha$ -CD as the ring, kinetically trapped polypseudorotaxane hydrogels were formed and employed as the template. These hydrogels showed good viscoelastic properties for direct ink writing, and they are 3D-printed as woodpile lattices. The polypseudorotaxanes were subsequently crosslinked as polyrotaxane monoliths and further crosslinked by linking diisocyanates with the threaded  $\alpha$ -CDs as doubly crosslinked monoliths. After the depolymerization and removal of the crosslinked PEG network, diurethane-crosslinked  $\alpha$ -CD monoliths with good 3D-printed shapes and

nanotubular structures were obtained. These crosslinked  $\alpha$ -CD polymers selectively adsorbed lycopene from raw tomato juice and protected it from photo- or thermos-oxidation. The templated synthesis— using polypsedurotaxanes to template the formation of  $\alpha$ -CD tubes, as well as templating the 3D-printed architectures— presents a unique approach to develop functional 3D-printing materials with desired nanoscale features.

## 5.4 Appendices

### 5.4.1 General Information

Chemical reagents and solvents were purchased from commercial suppliers, including Fisher Scientific, Sigma Aldrich, and VWR, and were used as received. Proton nuclear magnetic resonance ( $^1\text{H}$  NMR) spectra were recorded on Bruker AVIII 500 MHz or 600 MHz spectrometers. UV-vis spectra were measured on a Shimadzu UV-1800 UV-vis spectrometer. Fourier-transform infrared (FT-IR) spectra were recorded on a Jasco 6200 spectrometer. Powder X-ray Diffraction (PXRD) data were collected on the Rigaku MiniFlex powder X-ray diffractometer. The Wide-angle X-ray scattering (WAXS) was performed with a Rigaku NANOPIX instrument with a Hypix-3000 detector. Rheological measurements were measured by a DHR-2 rheometer with a 20 mm diameter parallel plate geometry and a 1 mm measuring gap at room temperature. Optical microscope white-light images were recorded by NIKON SMZ-2T stereomicroscope. Scanning electron microscopy (SEM) images were collected on an FEI Helios 5CX dual beam scanning electron microscope. Atomic force microscopy (AFM) images were collected on an SPM SmartSPM<sup>TM</sup>-1000 microscope. The LC-MS-PDA was carried out on an Agilent LC-MS 8030 with an ESI probe.



**Scheme S1.** Synthesis of  $\text{PEG}_{4\text{k}}-2\text{Si}(\text{OEt})_3$  and  $\text{PEG}_{20\text{k}}-2\text{Si}(\text{OEt})_3$  ( $n = 90$  or  $453$ )

**Synthesis of  $\text{PEG}_{4\text{k}}-2\text{Si}(\text{OEt})_3$  and  $\text{PEG}_{20\text{k}}-2\text{Si}(\text{OEt})_3$ .**  $\text{PEG}_{4\text{k}}$  (6.0 g, 1.5 mmol) or  $\text{PEG}_{20\text{k}}$  (30.0 g, 1.5 mmol) was dissolved in  $\text{CH}_2\text{Cl}_2$  (24 mL) in a 100 mL round bottom flask. Then, 3-(triethoxysilyl)propyl isocyanate (2.37 mL, 5.0 mmol) and dibutyltin dilaurate (DBTDL, 83  $\mu\text{L}$ , 1 wt%) were added to the solution. After 24 h of stirring at room

temperature, the solvent of the reaction was removed under reduced pressure. The white residue was washed by Et<sub>2</sub>O (50 mL) to yield the PEG<sub>4k</sub>-2Si(OEt)<sub>3</sub> (6.1 g, 91%) or PEG<sub>20k</sub>-2Si(OEt)<sub>3</sub> (27.4 g, 90%).

<sup>1</sup>H NMR of PEG<sub>4k</sub>-2Si(OEt)<sub>3</sub> (600 MHz, CDCl<sub>3</sub>, ppm) δ= 4.98 (t, *J* = 5.9, 5.9 Hz, 1.3H), 4.18 (t, *J* = 4.8, 4.8 Hz, 3.9H), 3.79 (q, *J* = 7.0, 7.0, 7.0 Hz, 13.0H), 3.43 – 3.75 (s, 340.4H), 3.14 (q, *J* = 6.7, 6.7, 6.6 Hz, 4.0H), 1.56 – 1.61 (m, 4.2H), 1.20 (t, *J* = 7.0, 7.0 Hz, 17.9H), 0.64 – 0.53 (m, 4.1H). <sup>13</sup>C NMR of PEG<sub>4k</sub>-2Si(OEt)<sub>3</sub> (150 MHz, DMSO-*d*<sub>6</sub>, ppm) δ= 70.25, 69.37, 63.44, 58.15, 43.44, 23.45, 18.67, 7.64.

<sup>1</sup>H NMR of PEG<sub>20k</sub>-2Si(OEt)<sub>3</sub> (500 MHz, CDCl<sub>3</sub>, ppm) δ= 5.00 (s, 1.3H), 4.20 (t, *J* = 4.8, 4.8 Hz, 3.6H), 3.79 (m, 12.3H), 3.42 – 3.74 (s, 1818.0H), 3.14 (d, *J* = 6.7 Hz, 4.1H), 1.56 – 1.61 (m, 4.0H), 1.22 (t, *J* = 7.0 Hz, 19.2H), 0.71 – 0.53 (m, 4.2H). <sup>13</sup>C NMR of PEG<sub>20k</sub>-2Si(OEt)<sub>3</sub> (150 MHz, DMSO-*d*<sub>6</sub>, ppm) δ= 70.26, 69.38, 63.44, 58.15, 43.44, 23.45, 18.66, 7.65.

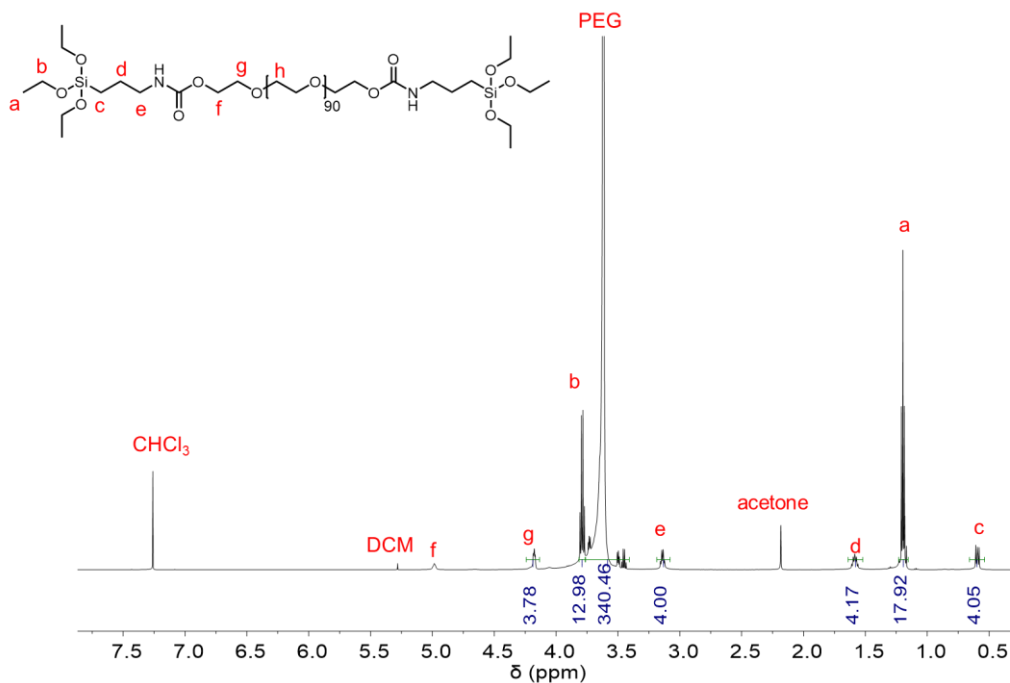


**Figure S1.** <sup>1</sup>H NMR spectrum of PEG<sub>4k</sub>-2Si(OEt)<sub>3</sub> in CDCl<sub>3</sub> (600 MHz) recorded at 298 K



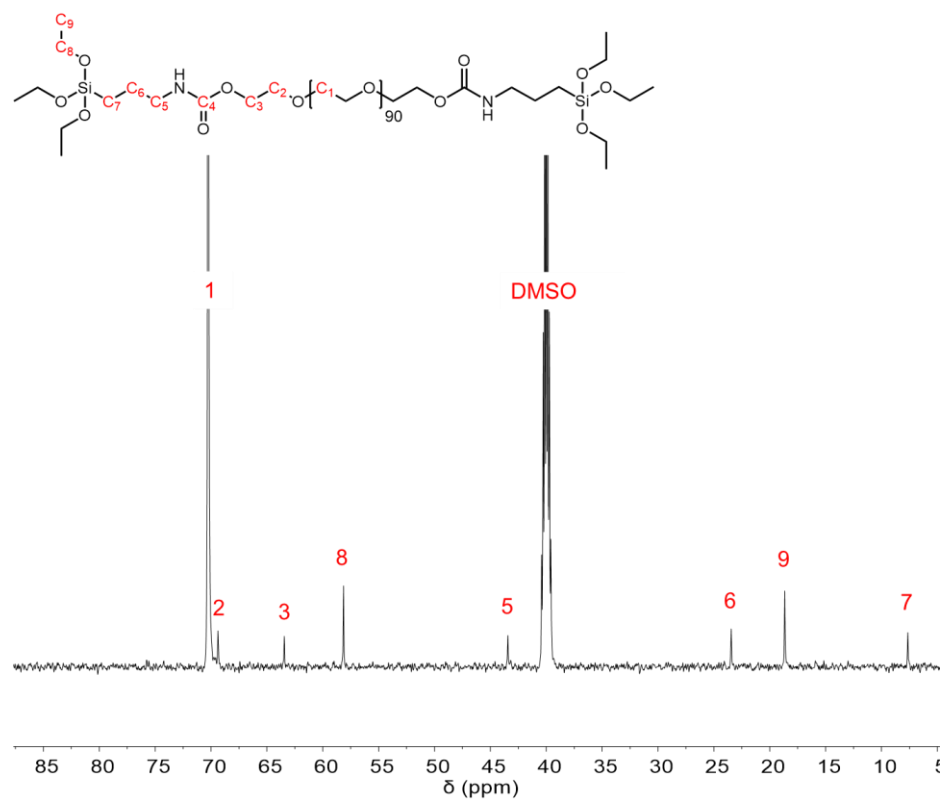


**Figure S2.** <sup>13</sup>C NMR spectrum of PEG<sub>4k</sub>-2Si(OEt)<sub>3</sub> in CDCl<sub>3</sub> (600 MHz) recorded at 298 K

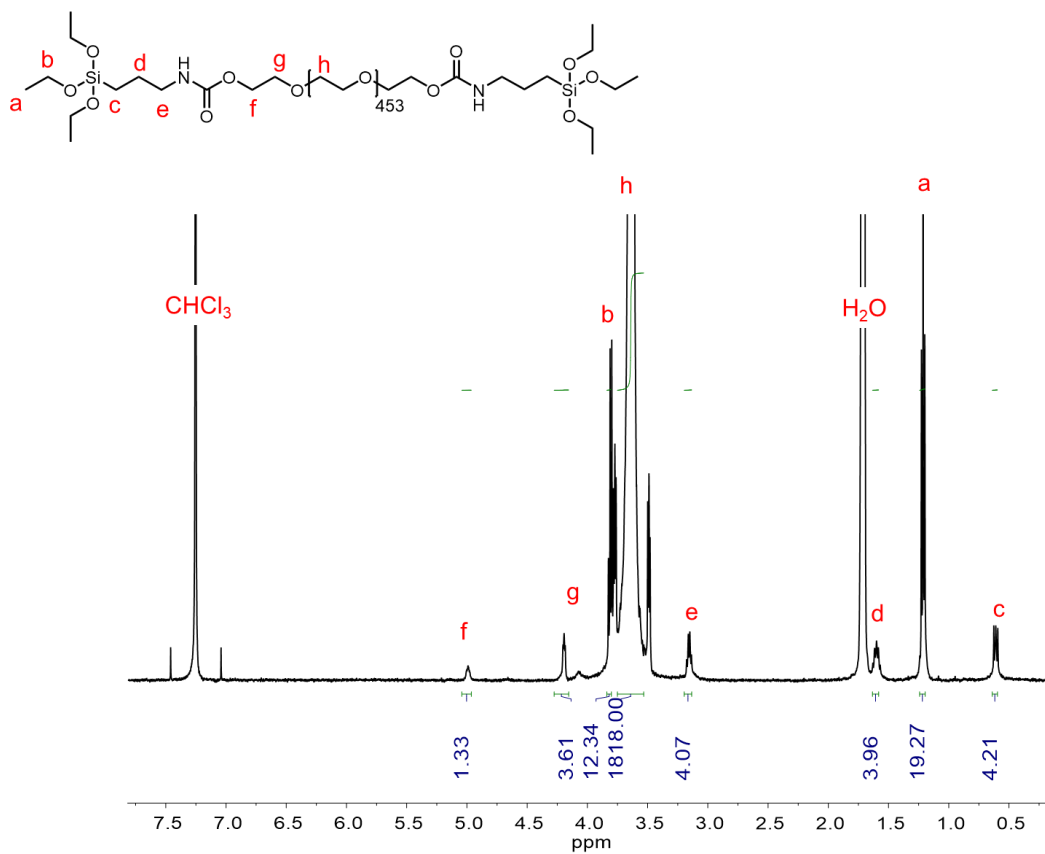


**Figure S3.** <sup>1</sup>H NMR spectrum of PEG<sub>20k</sub>-2Si(OEt)<sub>3</sub> in CDCl<sub>3</sub> (500 MHz) recorded at 298 K

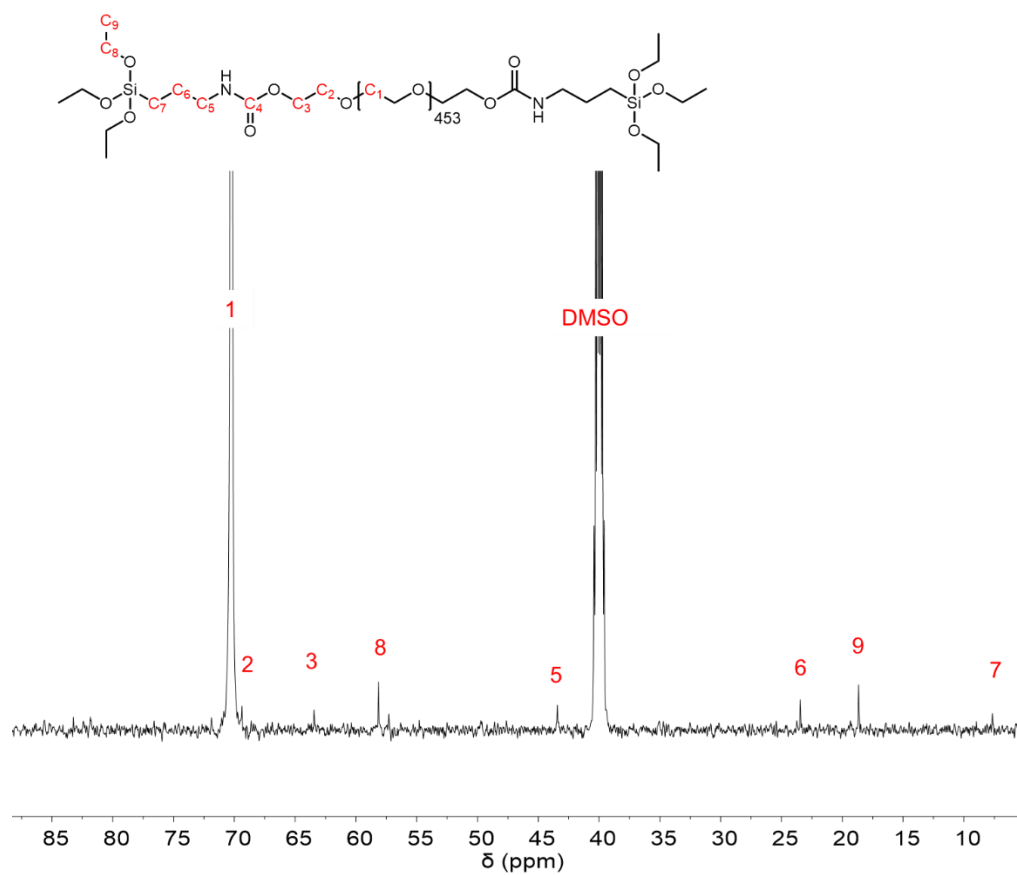
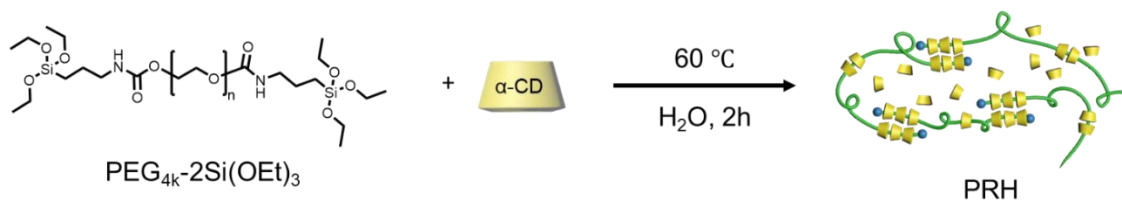


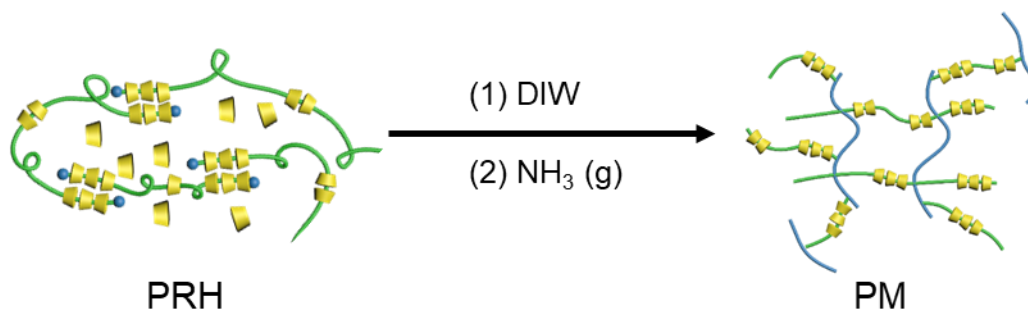
**Figure S4.**  $^{13}\text{C}$  NMR spectrum of  $\text{PEG}_{4k}\text{-2Si}(\text{OEt})_3$  in  $\text{CDCl}_3$  (600 MHz) recorded at 298 K



**Scheme S2.** Preparation of the polypseudorotaxane hydrogels

**Preparation of polypseudorotaxane hydrogels (PRHs).** A typical 3D-printable PRH was prepared by dissolving  $\alpha\text{-CD}$  (800 mg, 0.82 mmol, 27 w/v %) in water (3 mL) at 60 °C.  $\text{PEG}_{4k}\text{-2Si}(\text{OEt})_3$  (180 mg, 0.045 mmol, w/v 6 %) was added to the  $\alpha\text{-CD}$  solution, and the reaction was stirred for an additional 2 h at 60 °C. The reaction was then cooled to room temperature, and an opaque hydrogel was obtained. The hydrogel was consolidated for 12 h before the 3D printing or rheological investigations.

**Preparation of PEG<sub>20K</sub> PRHs.** A-CD (800 mg, 27 w/v %) was dissolved in DI water (3 mL) at 60 °C. Then PEG<sub>20K</sub>-2Si(OEt)<sub>3</sub> (180 mg, 6 w/v %) or PEG<sub>20K</sub>-2OH (180 mg, 6 w/v %) was added to the  $\alpha$ -CD solution, and the reaction was stirred for an additional 2 h at 60 °C. The mixture was then cooled down to room temperature to form white PEG<sub>20K</sub>-2Si(OEt)<sub>3</sub> or PEG<sub>20K</sub>-2OH PRHs. The hydrogel was consolidated for 12 h. Angular frequency sweep test, oscillation strain sweep test, steady rate sweep test, and dynamic step-strain amplitude test (Figure S20) of PEG<sub>20K</sub>-2Si(OEt)<sub>3</sub> and PEG<sub>20K</sub>-2OH PRHs were performed, respectively.



**Scheme S3.** Preparation of polyrotaxane monolith (PM).

**Preparation of polyrotaxane monoliths (PMs).** The 3D-printed PRHs was transformed into a closed chamber, and they were exposed to NH<sub>3</sub> vapor (generated from 20 mL of 2 M NH<sub>3</sub>·H<sub>2</sub>O solution) for 24 h at room temperature (24 °C). The monoliths were dried in the open air for 12 h and then lyophilized. The crosslinked monoliths were washed with an excess of DMSO (30 mL× 3) and H<sub>2</sub>O (30 mL× 3) for 24 h to remove any unreacted species. The PM hydrogels were lyophilized for digestion analysis. A PM (5 mg) was added to a 5% NaOD D<sub>2</sub>O solution at 80 °C for 6 h until no solid residual was observed. The sample was cooled down for <sup>1</sup>H NMR analysis. The experiments were repeated 3 times, and the PEG/CD ratio was measured as 1: 10.4 ± 0.7.

<sup>1</sup>H NMR (600 MHz, NaOD/D<sub>2</sub>O (5%), ppm)  $\delta$ = 4.70 (d,  $J$  = 3.1 Hz, 54.4), 3.71 – 3.62 (m, 167.8H), 3.59-3.56 (m, 59.4H), 3.48 (s, 360.0H), 3.27 (dd,  $J$  = 9.9, 3.3 Hz, 58.5 H), 3.19 (t,  $J$  = 9.2, 9.2 Hz, 60.2H).

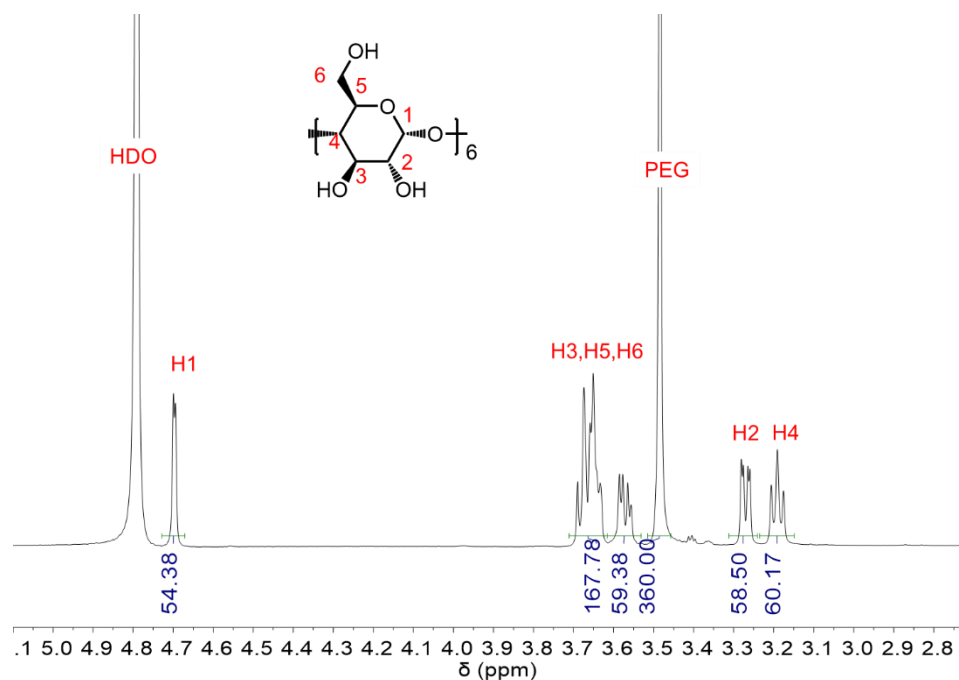
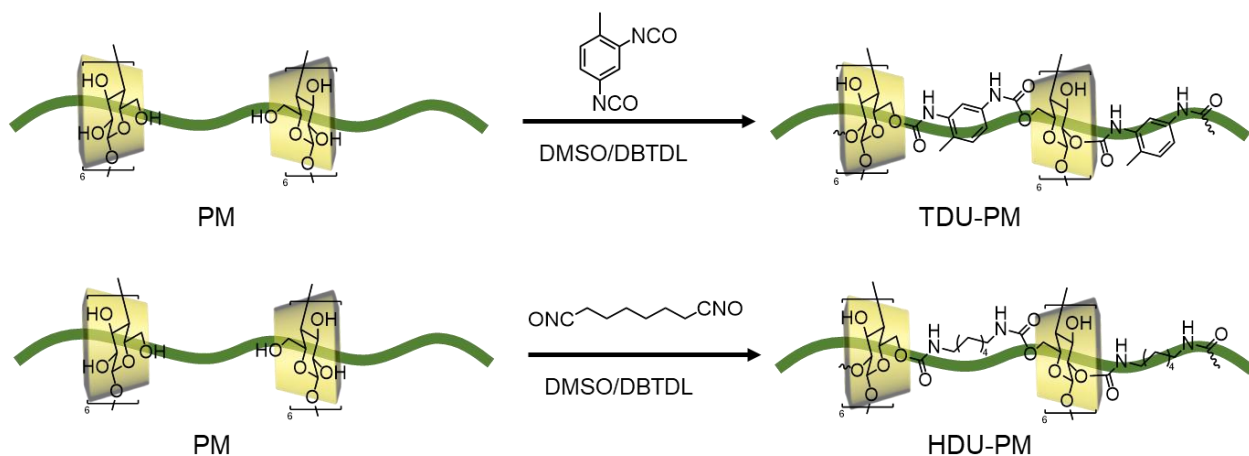


**Figure S5.** <sup>1</sup>H NMR spectrum (600 MHz) of the hydrolyzed PM in a NaOD/D<sub>2</sub>O solution (5%) recorded at 298 K.



**Scheme S4.** Templated synthesis of 3D-printed urethane-polyrotaxane monoliths.

**Preparation of TDU-PM and HDU-PM.** A dry PM (100 mg, containing 70.0 mg, 0.072 mmol  $\alpha$ -CD) was swelled in 6 mL anhydrous DMSO for 12 h. Then 2,4-toluene diisocyanate (TDI, 310  $\mu$ L, 2.16 mmol) or hexamethylene diisocyanate (HDI, 346  $\mu$ L, 2.16 mmol) was added to the reaction, followed by the addition of dibutyltin dilaurate (DBTDL,

30  $\mu\text{L}$ ). The reaction was heated at 50  $^{\circ}\text{C}$  for 24 h, and the obtained monolith was washed with an excess DMSO (30 mL  $\times$  2) and  $\text{H}_2\text{O}$  (30 mL  $\times$  2), respectively. The monolith was lyophilized to yield a white TDU-PM or HDU-PM. The CD/TDU and CD/HDU ratios were determined as 1: 9.5 and 1: 5.0, respectively, using  $^1\text{H}$  NMR digestion analysis. The PEG/CD ratios were determined as 1: 10.6 and 1: 8.0 in TDU-PM and HDU-PM.

$^1\text{H}$  NMR of TDU-PM (600 MHz, NaOD/D<sub>2</sub>O (5%), ppm)  $\delta$ = 6.72 (d,  $J$  = 7.9 Hz, 9.6H), 6.11 (s, 9.1H), 6.06 (d,  $J$  = 8.0 Hz, 9.2H), 4.71 (d,  $J$  = 3.4 Hz, 6.2H), 3.73 – 3.55 (m, 23.9H), 3.47 (s, 33.8H), 3.33 – 3.15 (m, 12.0H), 1.84 (s, 28.4H).

$^1\text{H}$  NMR of HDU-PM (600 MHz, NaOD/D<sub>2</sub>O (5%), ppm)  $\delta$ = 4.53 (d,  $J$  = 3.3 Hz, 6.6H), 3.50 – 3.37 (m, 24.0H), 3.29 (s, 45.2H), 3.14 – 2.93 (m, 12.0H), 2.66 (t,  $J$  = 6.8, 6.8 Hz, 3.4H), 2.18 (t,  $J$  = 7.2, 7.2 Hz, 16.0H), 1.07 – 1.00 (m, 19.6H), 0.92 – 0.88 (m, 19.9H).

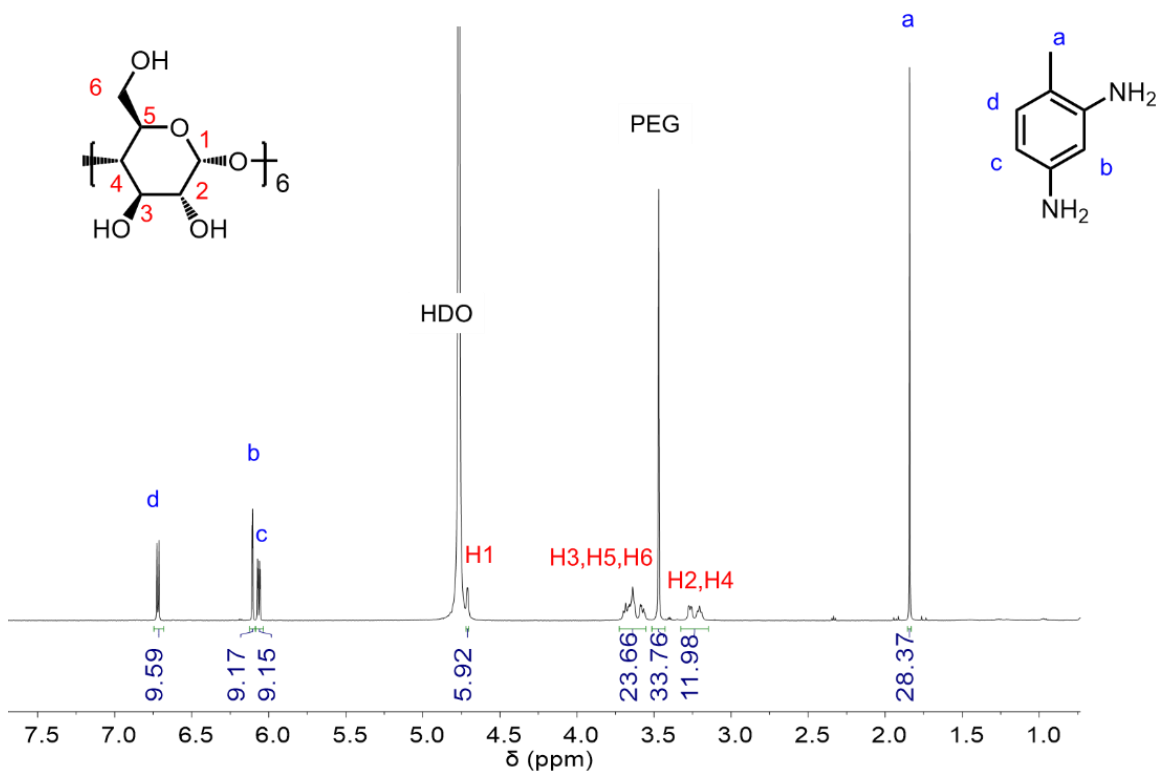


**Figure S6.**  $^1\text{H}$  NMR spectrum (600 MHz) of a hydrolyzed TDU-PM in a NaOD/D<sub>2</sub>O solution (5%) recorded at 298 K.

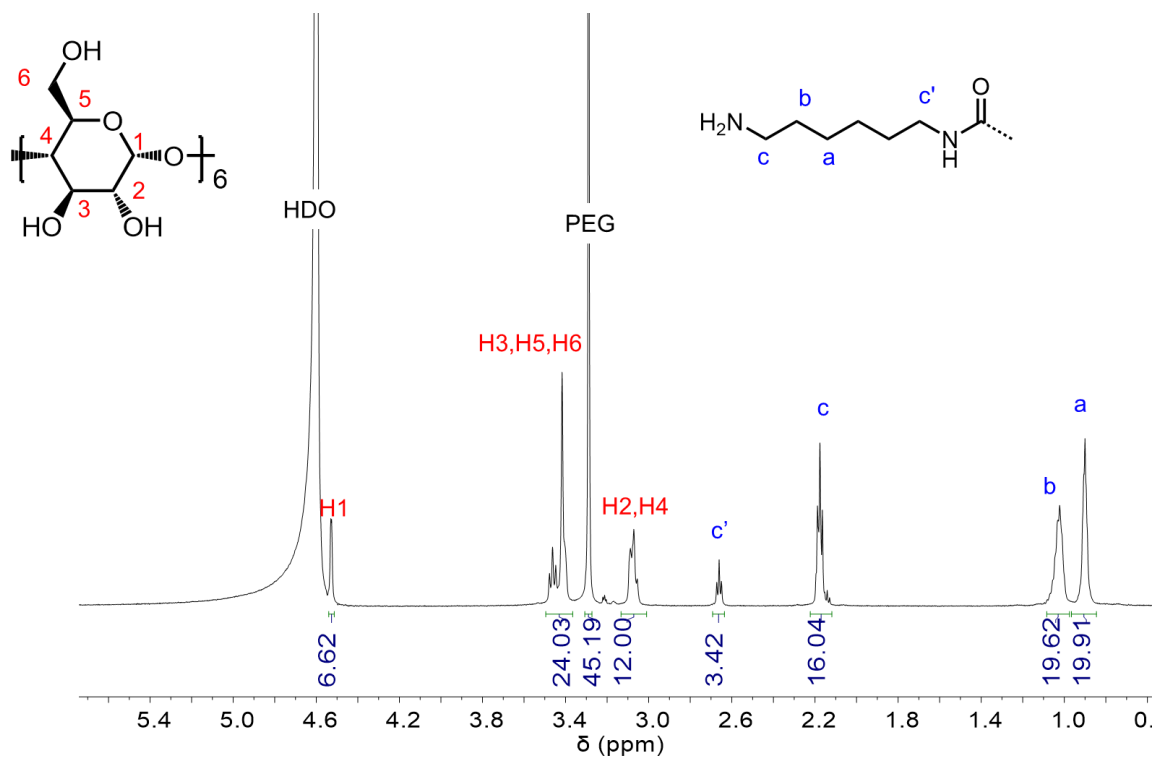
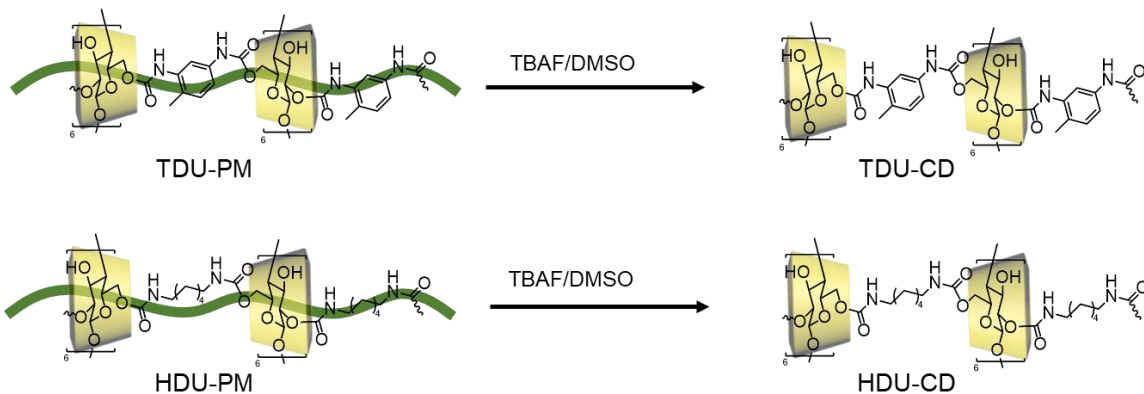


**Figure S7.**  $^1\text{H}$  NMR spectrum (600 MHz) of a hydrolyzed HDU-PM in a NaOD/D<sub>2</sub>O solution (5%) recorded at 298 K.



**Scheme S5.** Templated synthesis of 3D-printed TDU-CD and HDU-CD monoliths.

**Preparation of TDU-CD and HDU-CD.** A TDU-PM or HDU-PM was added to a TBAF DMSO solution (1 M, 6 mL) in a 20 mL vial for 48 h. Then, the monolith was washed with an excess DMSO (30 mL  $\times$  2), MeOH (30 mL  $\times$  2), and H<sub>2</sub>O (30 mL  $\times$  2), respectively. After lyophilization, a light-yellow TDU-CD (170 mg) or a white HDU-CD (145mg) was

obtained. The TDU-CD (5 mg) and HDU-CD (5 mg) were hydrolyzed in 5% NaOD/ D<sub>2</sub>O solution at 80 °C for 24 h. The CD/TDU and CD/HDU ratios were determined as 1: 6.4 ± 0.4 and 1:4.3, respectively, by <sup>1</sup>H NMR.

<sup>1</sup>H NMR of the hydrolyzed TDU-CD (600 MHz, NaOD/D<sub>2</sub>O (5%), ppm) δ= 6.72 (d, *J* = 7.9 Hz, 6.7H), 6.11 (s, 6.3H), 6.06 (d, *J* = 8.0 Hz, 6.3H), 4.70 (d, *J* = 3.2 Hz, 6.4H), 3.75 – 3.50 (m, 24.0H), 3.35 – 3.12 (m, 12.0H), 1.84 (s, 20.1H).

<sup>1</sup>H NMR of the hydrolyzed HDU-CD (600 MHz, NaOD/D<sub>2</sub>O (5%) of D<sub>2</sub>O, ppm) δ= 4.67 (d, *J* = 3.2 Hz, 6.4H), 3.76 – 3.50 (m, 24.0H), 3.30 – 3.13 (m, 12.0H), 2.81 (t, *J* = 6.8, 6.8 Hz, 3.1H), 2.35 – 2.31 (m, 14.1H), 1.24 – 1.13 (m, 17.1H), 1.08– 1.02 (m, 16.9H).

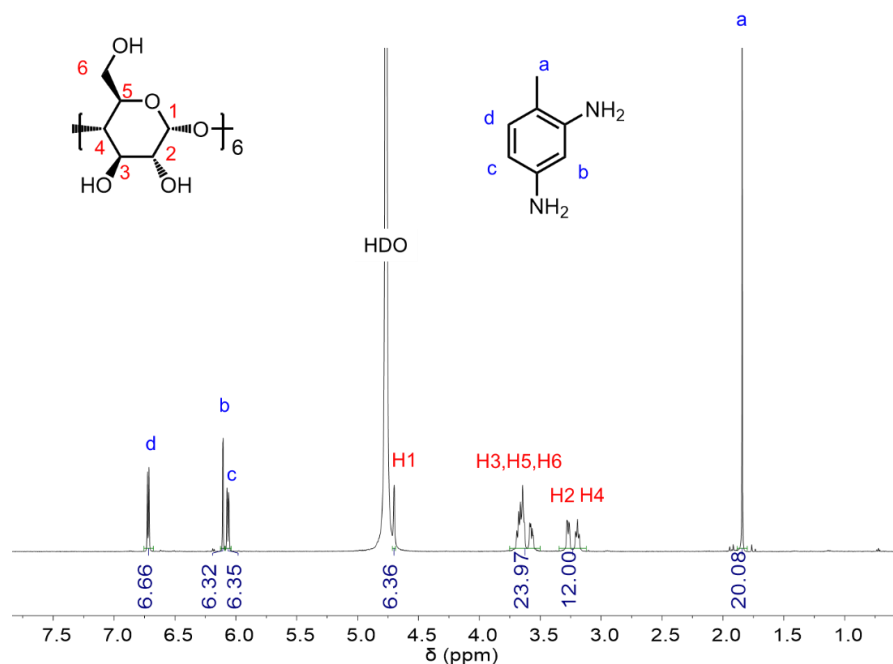


**Figure S8.** <sup>1</sup>H NMR spectrum (600 MHz) of a hydrolyzed TDU-CD in a NaOD/D<sub>2</sub>O solution (5%) recorded at 298 K.



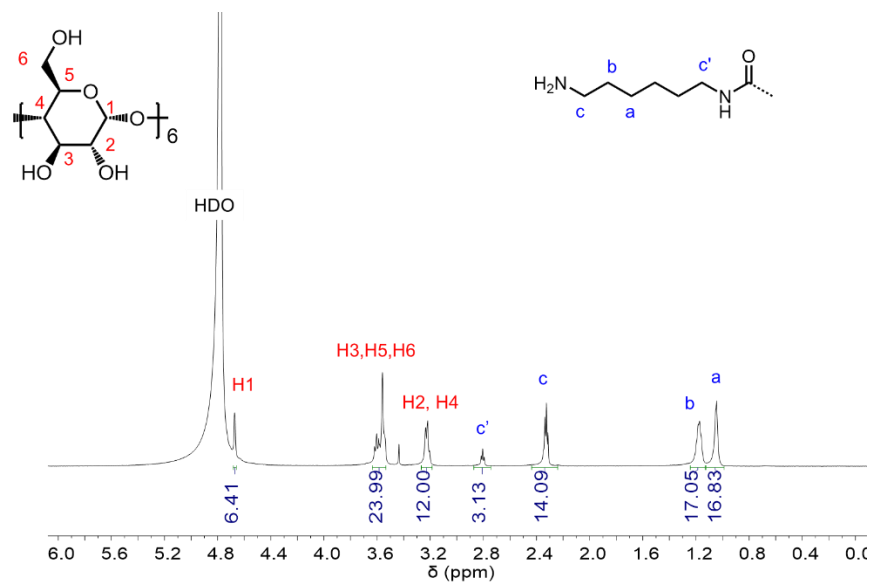
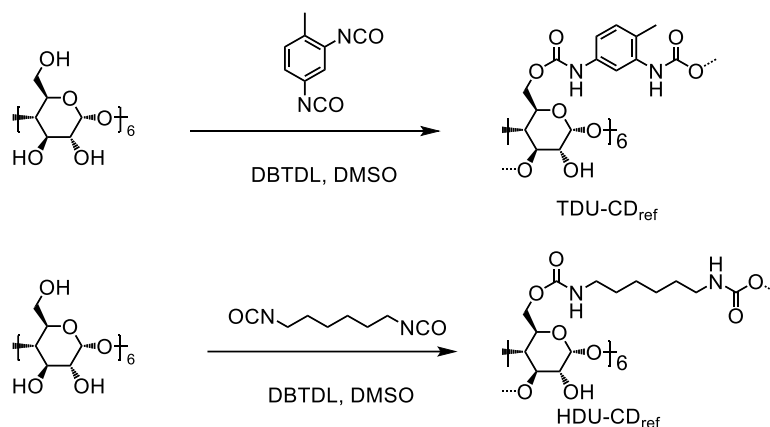


**Figure S9.** <sup>1</sup>H NMR spectrum (600 MHz) of a hydrolyzed HDU-CD tube in a NaOD/D<sub>2</sub>O solution (5%) recorded at 298 K.



**Scheme S6.** Synthesis of the crosslinked urethane- $\alpha$ -CD polymers TDU-CD<sub>ref</sub> and HDU-CD<sub>ref</sub>.

**Synthesis of the TDU-CD<sub>ref</sub> and the HDU-CD<sub>ref</sub>.** Activated  $\alpha$ -CD (1.946g, 2 mmol; pre-dried under reduced pressure at 70 °C for 2 d), TDI (14 mmol, 2.02 mL) or HDI (10 mmol, 1.60 mL) was mixed with DBTDL (15  $\mu$ L) in anhydrous DMSO in a 50 mL round bottom flask. After heating at 50 °C for 24 h, an insoluble solid was obtained, which was washed using DMSO (20 mL  $\times$  2), MeOH (20 mL  $\times$  2), and CH<sub>2</sub>Cl<sub>2</sub> (20 mL  $\times$  3). The sample was dried under the reduced pressure at 60 °C for 24 h to yield light yellow TDU-

CD (4.18 g, yield: 95%) or white HDU-CD (3.30 g, yield: 91%). The obtained TDU-CD (5 mg) and HDU-CD (5 mg) were added to a 5% NaOD/D<sub>2</sub>O solution at 80 °C for 48 h to allow for complete hydrolysis. The  $\alpha$ -CD to TDU and  $\alpha$ -CD to HDU ratios were found as 1:  $6.8 \pm 0.2$  and 1: 3.9, respectively.

<sup>1</sup>H NMR of hydrolyzed TDU-CD<sub>ref</sub> (600 MHz, NaOD (5%) of D<sub>2</sub>O, ppm):  $\delta$ = 6.68 (d, J = 7.9 Hz, 6.7H), 6.06 (s, 6.4H), 6.02 (d, J = 7.8 Hz, 6.3H), 4.65 (d, J = 3.2 Hz, 6.0H), 3.75 – 3.36 (m, 25.1H), 3.25 – 3.20 (m, 6.1H), 3.15 (m, J = 9.1, 9.1 Hz, 5.9H), 1.80 (s, 20.4H).

<sup>1</sup>H NMR of hydrolyzed HDU-CD<sub>ref</sub> (600 MHz, NaOD (5%) of D<sub>2</sub>O, ppm):  $\delta$ = 4.70 (s, 6.2 H), 3.65- 3.59 (m, 24.0 H), 3.31 – 3.20 (m, 2.5H), 2.36 – 2.31 (m, 12.7H), 1.27 – 1.15 (m, 16.1H), 1.1 – 1.06 (m, 15.7H).

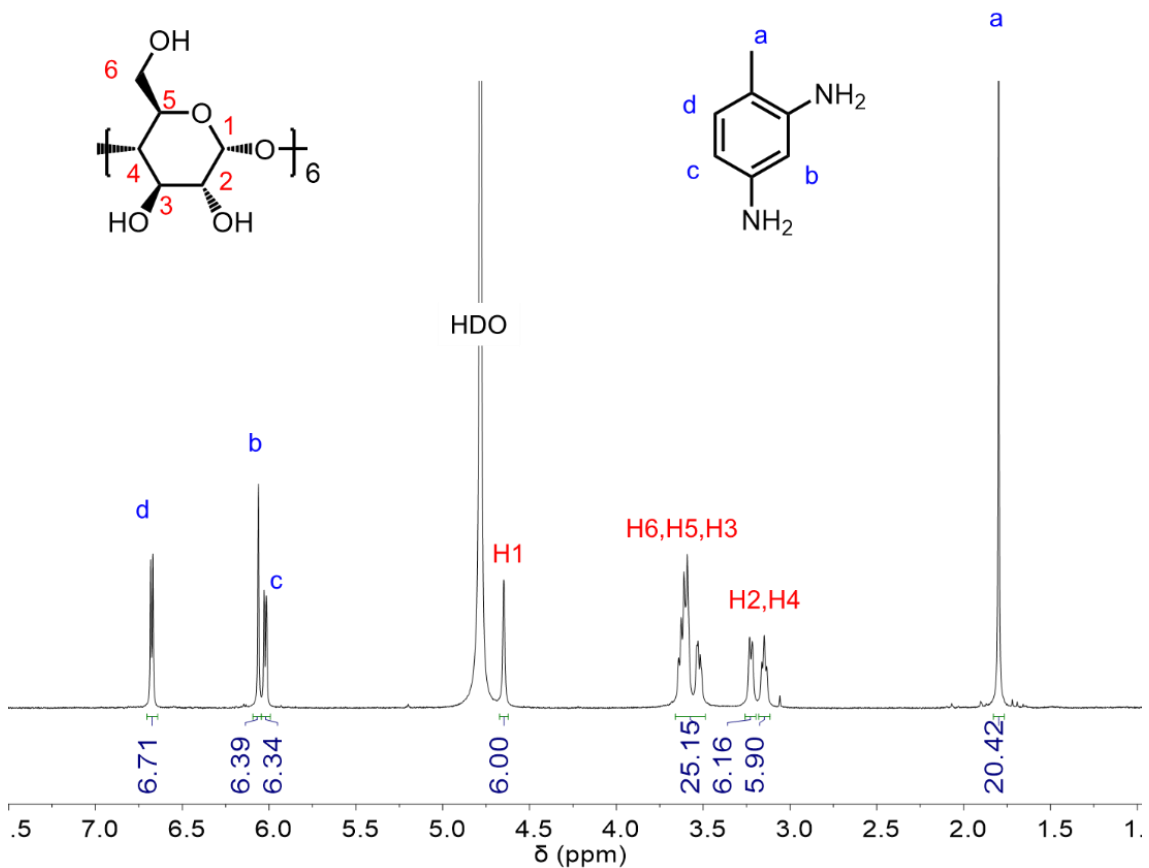


**Figure S10.** <sup>1</sup>H NMR spectrum (600 MHz) of a hydrolyzed TDU-CD<sub>ref</sub> in a NaOD/D<sub>2</sub>O solution (5%) recorded at 298 K.

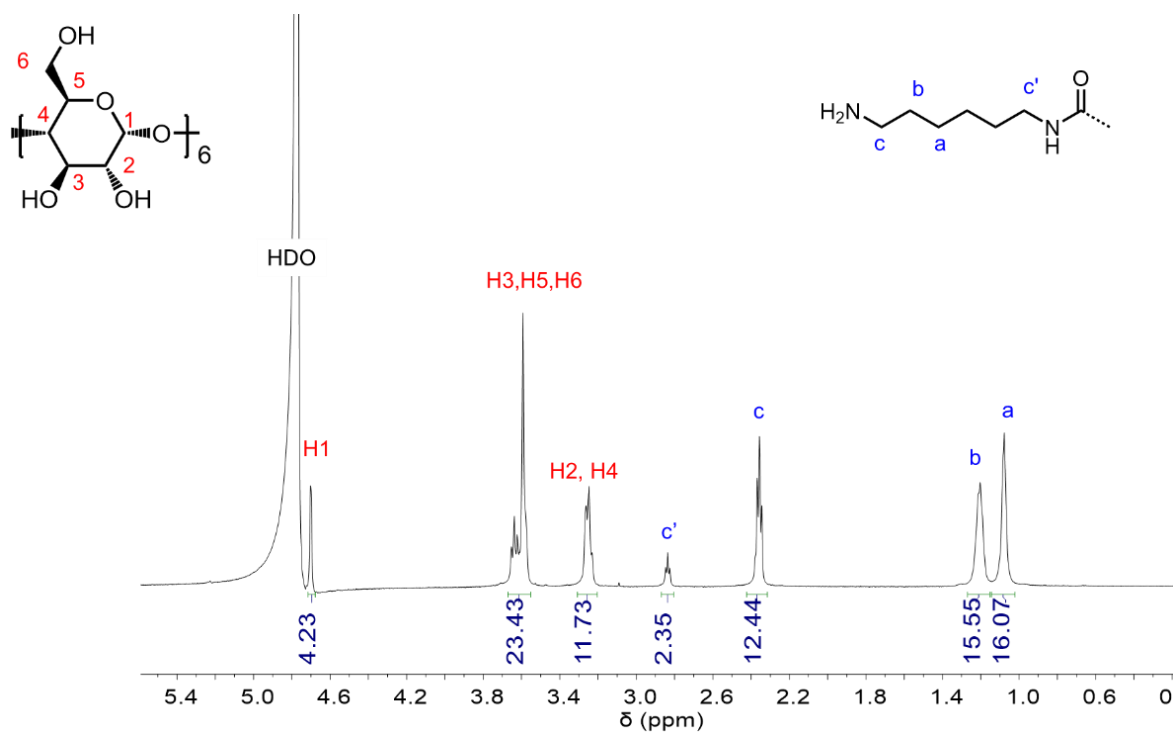


**Figure S11.**  $^1\text{H}$  NMR spectrum (600 MHz) of a hydrolyzed HDU-CD<sub>ref</sub> in a NaOD/D<sub>2</sub>O solution (5%) recorded at 298 K.

**Table S1.** Summary of the PEG-to-CD and EG-to-CD ratios of different materials

	PEG: CD <sup>a</sup>	EG: CD <sup>a</sup>	CD: diisocyanates <sup>a</sup>
<b>PM</b>	1: 10.4 ± 0.7	8.7 ± 0.6: 1	-
<b>TDU-PM</b>	1 : 10.6	8.5 : 1	1 : 9.5
<b>TDU-CD</b>	-	-	1: 6.4 ± 0.4
<b>TDU-CD<sub>ref</sub></b>	-	-	1: 6.8 ± 0.2
<b>HDU-PM</b>	1 : 8.0	11.3 : 1	1 : 5.0
<b>HDU-CD</b>	-	-	1: 4.3
<b>HDU-CD<sub>ref</sub></b>	-	-	1: 3.9

<sup>a</sup> The PEG: CD, CD: TDU, and CD: HDU ratios are measured by  $^1\text{H}$  NMR digestion experiment.

### 5.4.2 Formation of kinetically trapped 3D-printable PRHs

**Time-dependent transmittance measurement.** When  $\alpha$ -CDs are threaded onto the PEG<sub>4k</sub>-2OH or PEG<sub>4k</sub>-2Si(OEt)<sub>3</sub> axles, polypseudorotaxanes are formed, and the reaction gradually changes from transparent to opaque. A time-dependent transmission was performed by UV-Vis light scattering to study the  $\alpha$ -CDs threading kinetics. To be specific, PEG<sub>4k</sub> or PEG<sub>4k</sub>-2Si(OEt)<sub>3</sub> (15 mg or 30 mg) was dissolved in 3 mL of DI water in a quartz cuvette (optical length: 1 cm). Then  $\alpha$ -CD (150 mg or 300 mg) was added to the mixture. The transmittance was monitored at 550 nm, and the data were acquired every 30 s at 24 or 60 °C.

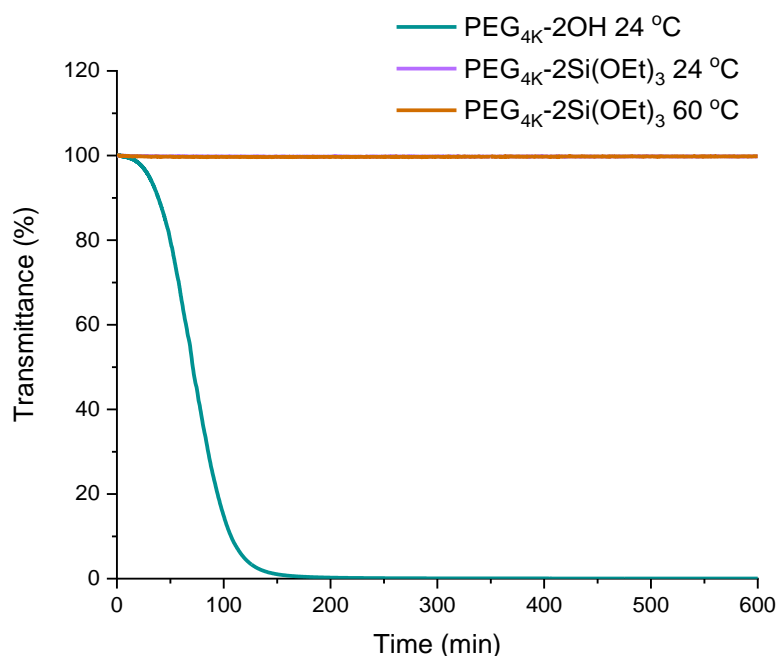


**Figure S12.** Time-dependent transmittances of the solution of  $\alpha$ -CD (51.4 mM) with PEG<sub>4k</sub>-2OH or PEG<sub>4k</sub>-2Si(OEt)<sub>3</sub> (1.3 mM) mixture at different temperatures (Cell optical path: 10 mm,  $\lambda = 550$  nm).

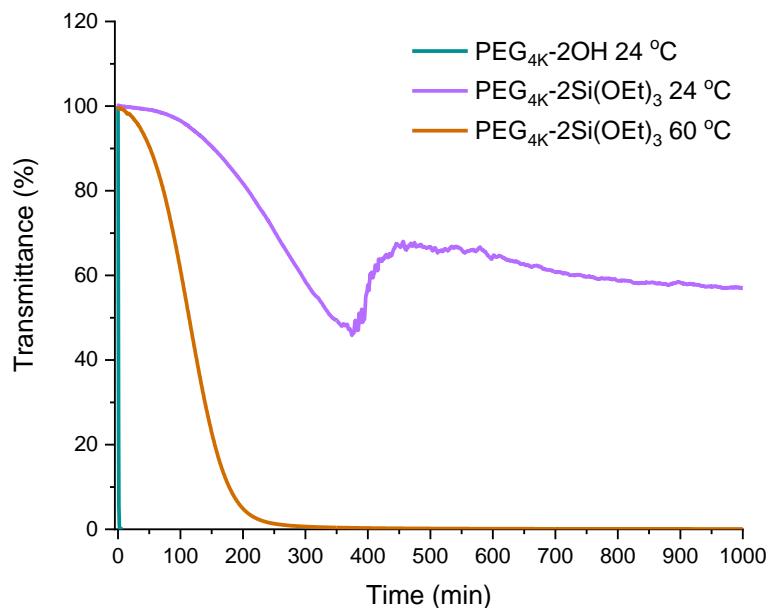


**Figure S13.** Time-dependent transmittances of the solution of  $\alpha$ -CD (102.8 mM) with PEG<sub>4k</sub> or PEG<sub>4k</sub>-2Si(OEt)<sub>3</sub> (2.5 mM) mixture at different temperatures (Cell optical path: 10 mm,  $\lambda = 550$  nm).

Rheological data is measured on a DHR-2 rheometer with a parallel plate geometry ( $D = 2.0$  cm) and a measuring gap of around 1 mm at room temperature (24 °C). Angular frequency sweep tests were performed by increasing the angular frequency from 0.1 rad/s (0.016 Hz) to 100 rad/s (15.92 Hz) at 24 °C. The oscillation strain was set as 0.1 %. Strain sweep tests were carried out by increasing the oscillation strain from 0.01% to 100%. The angular frequency was set at 1 rad/s (0.16 Hz) at 24 °C. Steady shear rate sweep tests were performed by increasing the shear rate from 1 s<sup>-1</sup> to 100 s<sup>-1</sup> at 24 °C. Dynamic step-strain amplitude tests were performed by setting the oscillation strain as 1% or 100% in each cycle at 1 rad/s. The time of strain at each step was set as 15 s.

**<sup>1</sup>H NMR analysis of PEG-to-CD ratios in PRHs.** To measure the PEG<sub>4k</sub>-2Si(OEt)<sub>3</sub> to  $\alpha$ -CD ratio in the polyrotaxane network, each PRH sample (~ 1g) was diluted by DI water (1 mL) and centrifuged at 5000 rpm for 5 min. The obtained precipitate was lyophilized (0.06 torr) for 24 h. And the found PEG<sub>4k</sub>-2Si(OEt)<sub>3</sub> to  $\alpha$ -CD ratio was measured by <sup>1</sup>H

NMR in DMSO-*d*<sub>6</sub>. The found PEG<sub>4k</sub>-2Si(OEt)<sub>3</sub> to α-CD ratios in PRHs are listed in Table S2.

**<sup>1</sup>H NMR analysis of PEG-to-CD ratios in PMs.** To study the PEG<sub>4k</sub>-2Si(OEt)<sub>3</sub> to α-CD ratio in the PM hydrogel, the polyrotaxane hydrogel was lyophilized for 24h. Then the dry PM was hydrolyzed in NaOD (5%) of D<sub>2</sub>O solution at 80 °C for 6 h for <sup>1</sup>H NMR analysis. The found PEG<sub>4k</sub>-2Si(OEt)<sub>3</sub> to α-CD ratios in PMs are summarized in Table S2.

**Table S2.** Summary of the elastic moduli and PEG-to-CD ratios of PRHs and PM hydrogels

PEG <sub>4k</sub> - 2Si(OEt) <sub>3</sub> (w/v %)	α-CD (w/v %)	feeding PEG/CD	PRHs		PM hydrogels	
			elastic modulus (kPa)	found PEG/CD <sup>a</sup>	elastic modulus (kPa)	found PEG/CD <sup>b</sup>
3	10	1 : 14	3.2	1 : 16	0.09	1 : 9
3	13	1 : 18	22	1 : 15	0.10	1 : 8
3	17	1 : 23	34	1 : 17	0.14	1 : 7
3	20	1 : 27	5.3	1 : 18	0.16	1 : 9
3	23	1 : 32	20	1 : 18	0.15	1 : 9
3	27	1 : 36	3.3	1 : 20	0.10	1 : 9
3	30	1 : 41	5.3	1 : 21	/ <sup>c</sup>	/ <sup>c</sup>
3	33	1 : 45	6.8	1 : 23	/ <sup>c</sup>	/ <sup>c</sup>
6	17	1 : 11	32	1 : 12	0.5	1 : 6
<b>6</b>	<b>27</b>	<b>1 : 18</b>	<b>71</b>	<b>1 : 17</b>	<b>0.4</b>	<b>1 : 9.5</b>

6	33	1 : 23	34	1 : 20.5	0.5	1 : 9.5
10	56	1 : 23	31	1 : 23	1.7	1 : 10

---

<sup>a</sup> The found PEG/CD ratio was measured by <sup>1</sup>H NMR of PRHs. The hydrogel was centrifuged extensively to isolate the solid content, which was lyophilized for NMR analysis. <sup>b</sup> The found PEG/CD ratio was measured by <sup>1</sup>H NMR analysis of the hydrolyzed PM. <sup>c</sup> No crosslinked PM was formed.

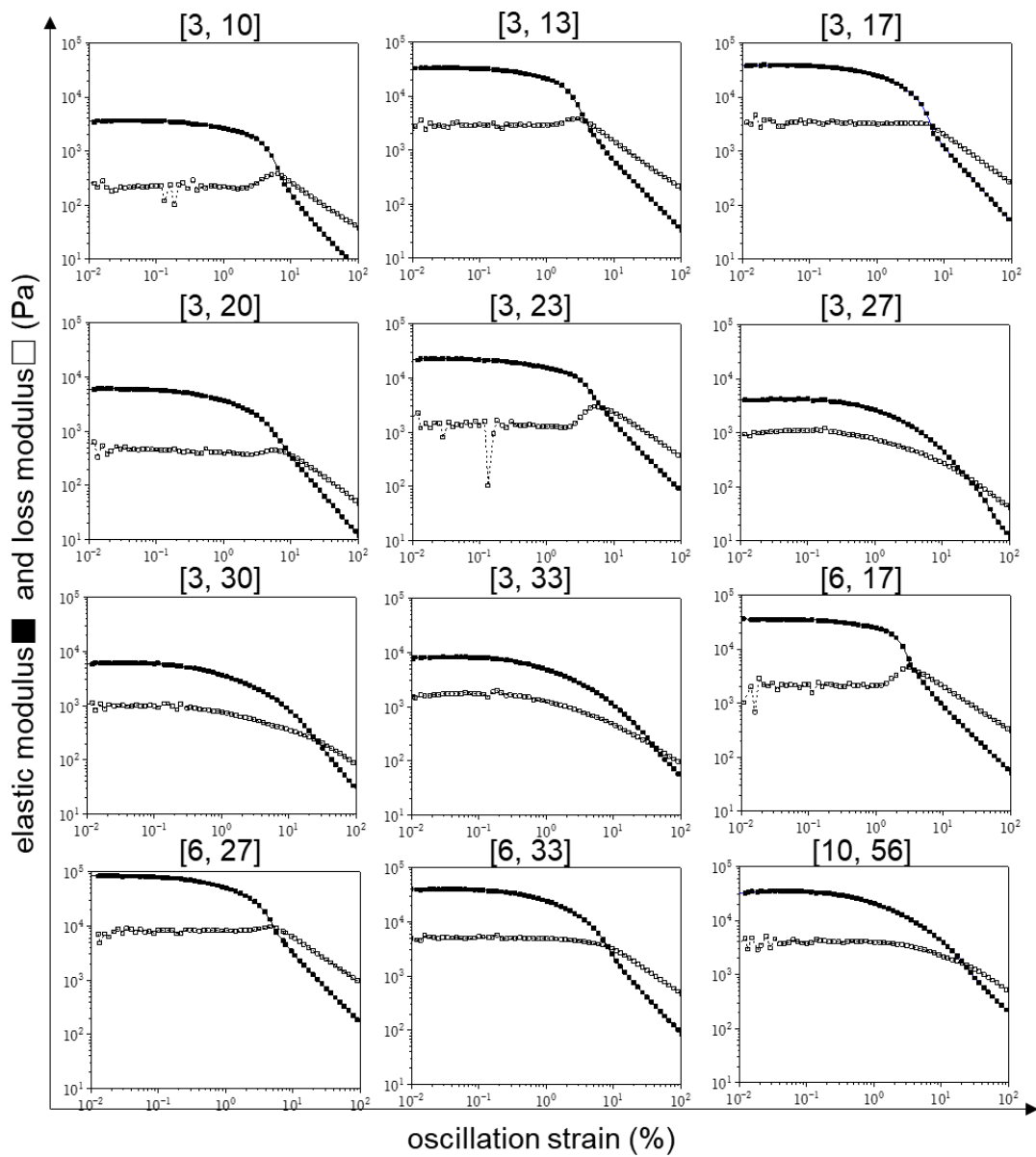


**Figure S14.** Oscillation strain sweep profiles of PRHs



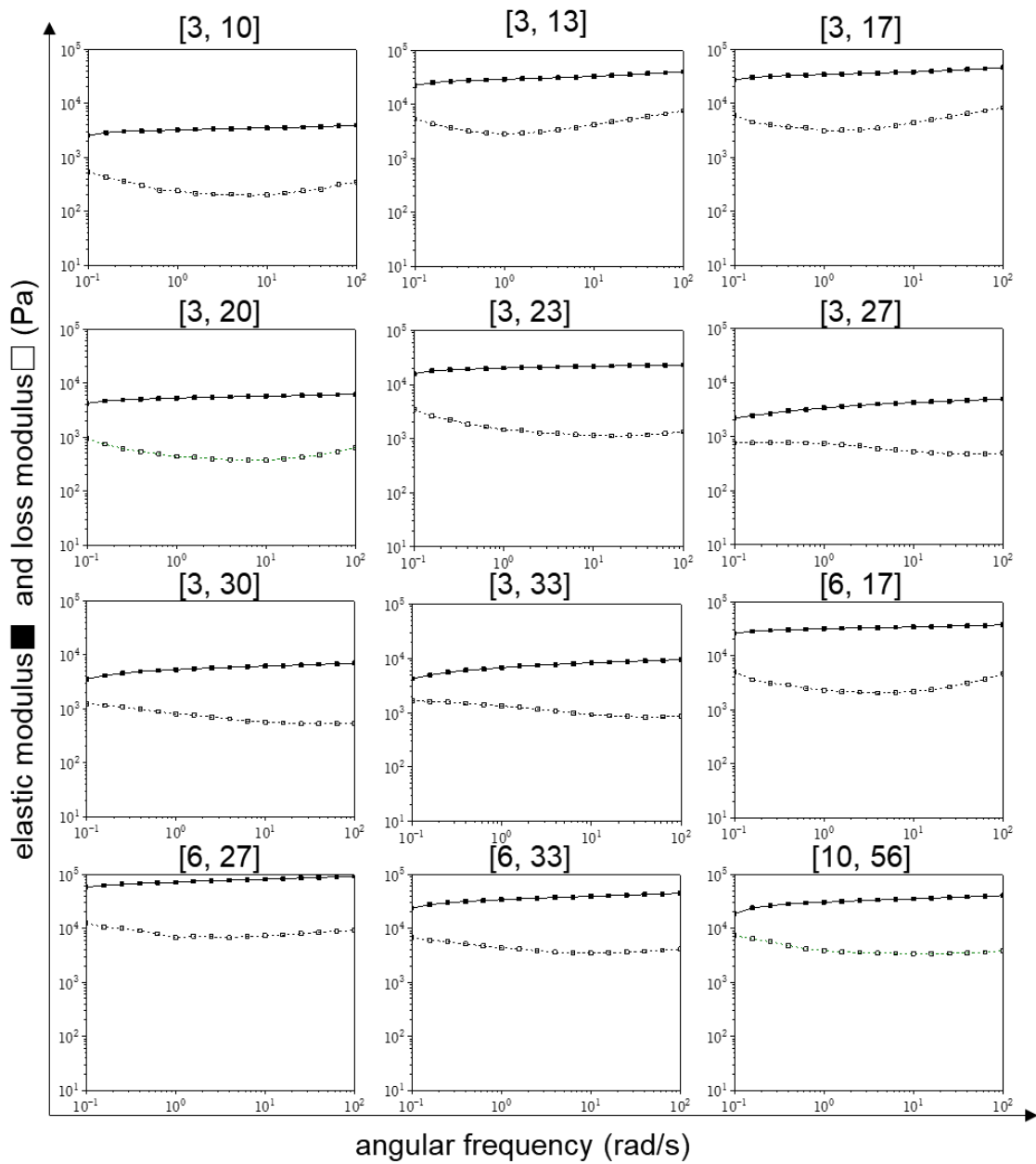


**Figure S15.** Angular frequency sweep profiles of PRHs.

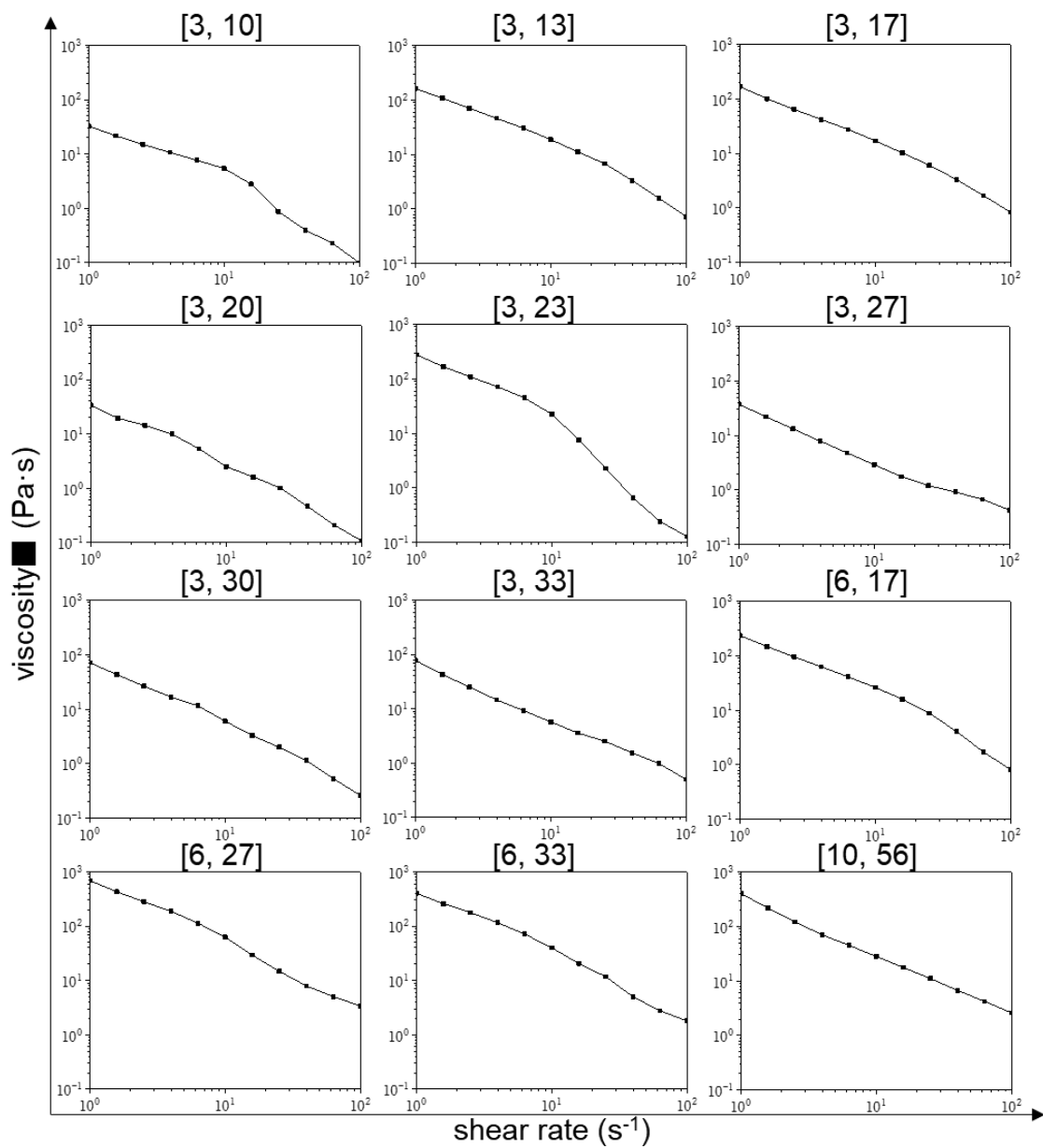


**Figure S16.** Steady shear rate sweep profiles of PRHs

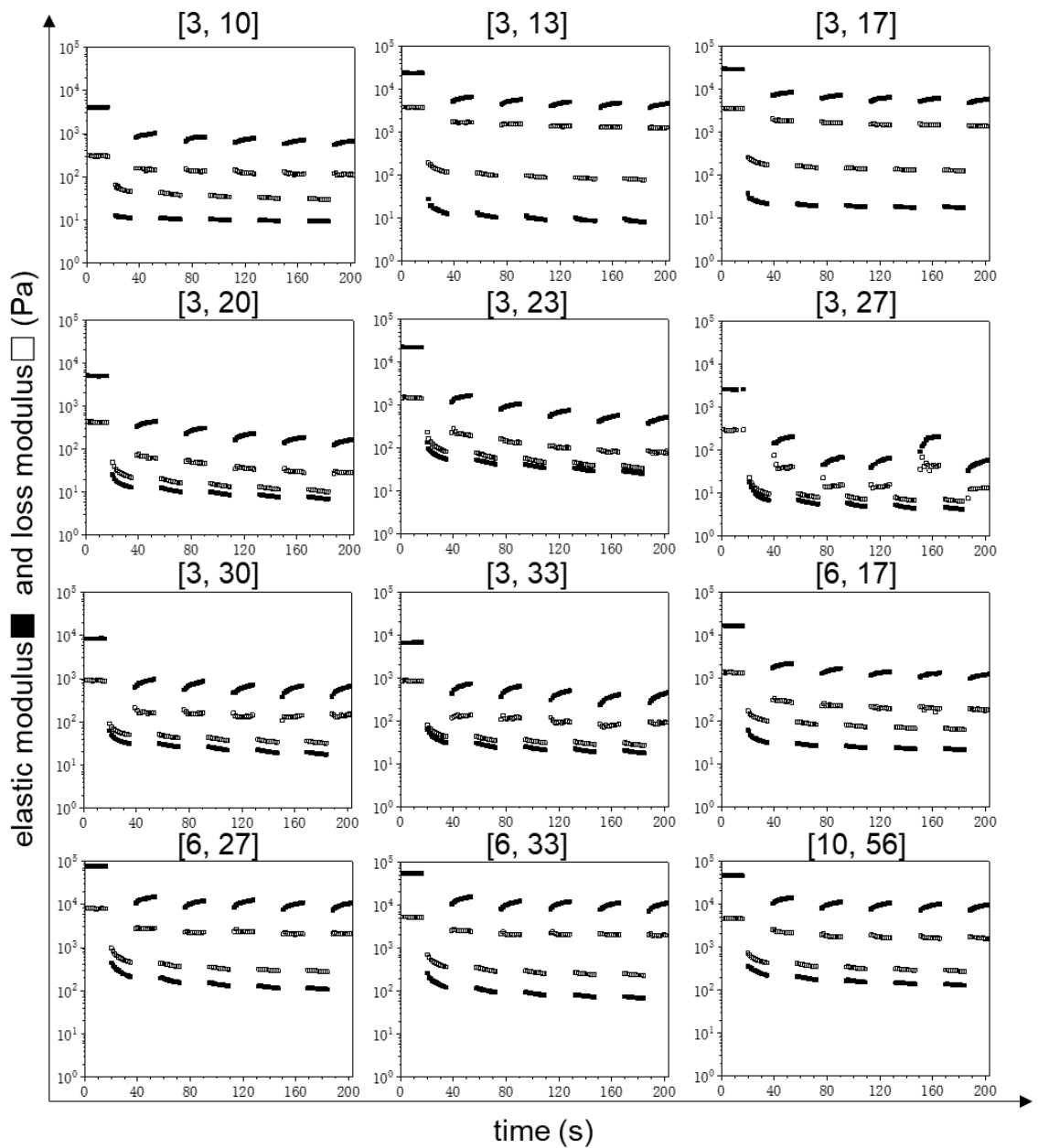


**Figure S17.** Dynamic step-strain amplitude sweeps of PRHs (the applied oscillation strain was alternated between 1% and 100% every 15 s at 1 rad/s angular frequency)

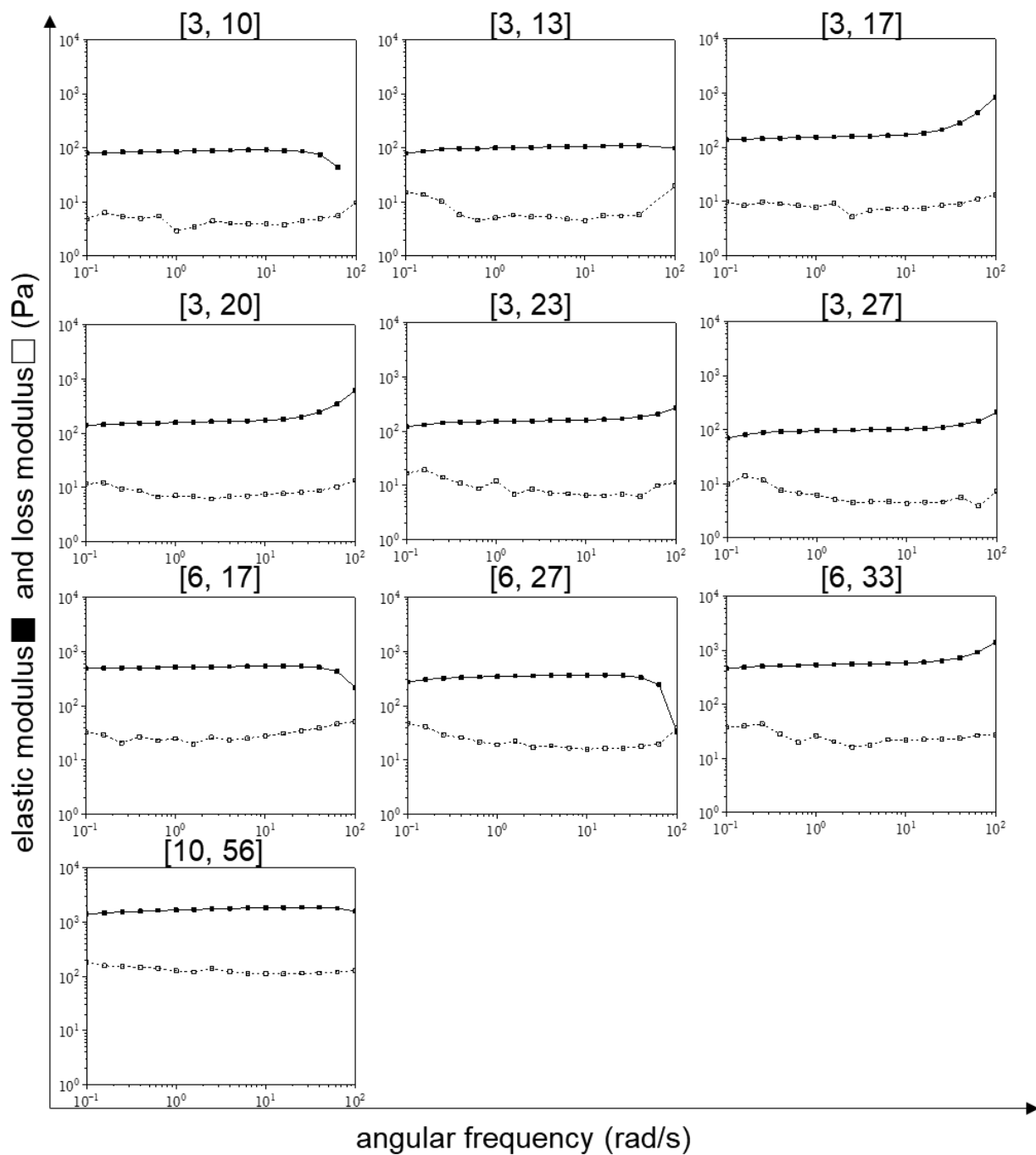


**Figure S18.** Angular frequency sweep profiles of PM hydrogel

elastic modulus  $\blacksquare$  and loss modulus  $\square$  (Pa)

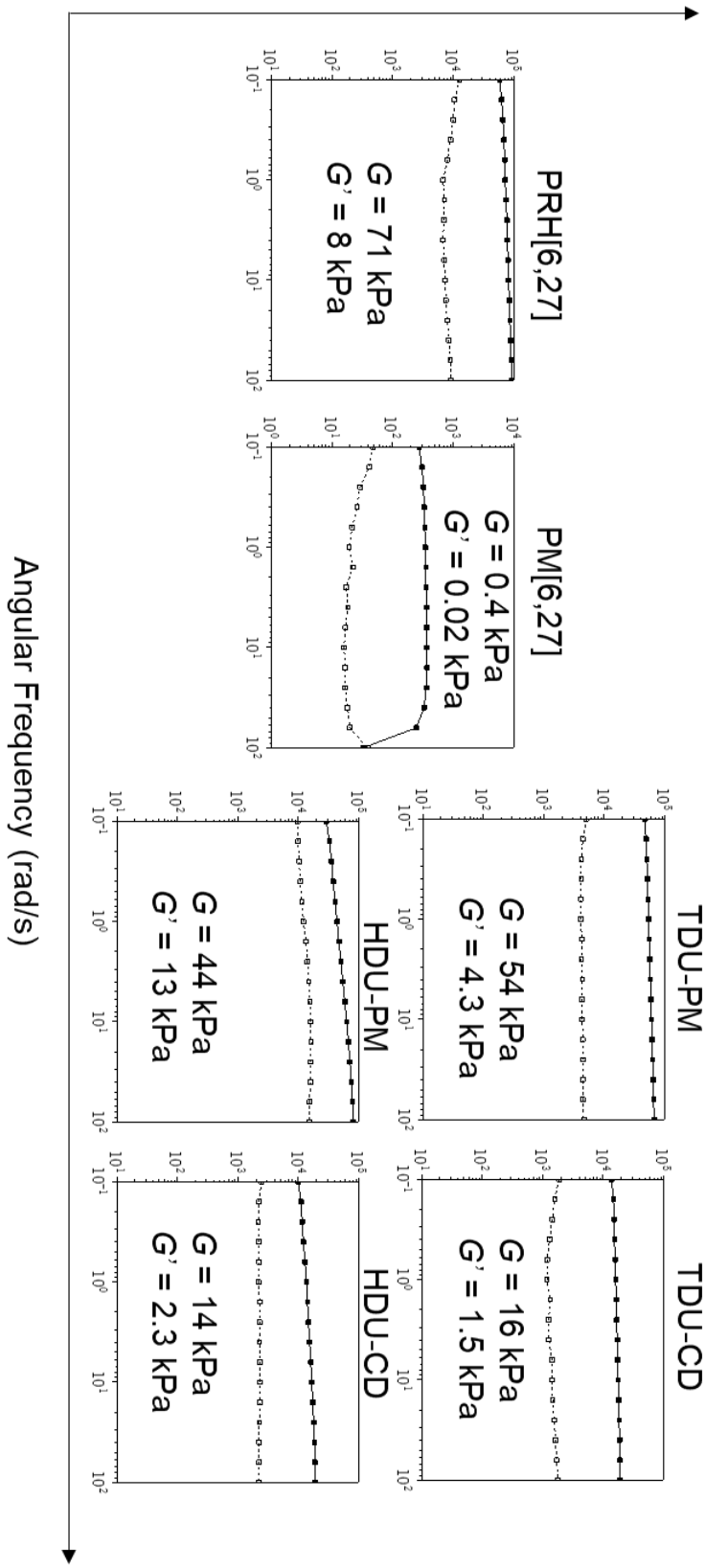


**Figure S19.** Angular frequency sweep profiles of PRH[6,27] and the hydrogel form of PM[6,27], TDU-PM, TDU-CD, HDU-PM, and HDU-CD. The hydrogels are prepared as disks with 10 mm diameter.

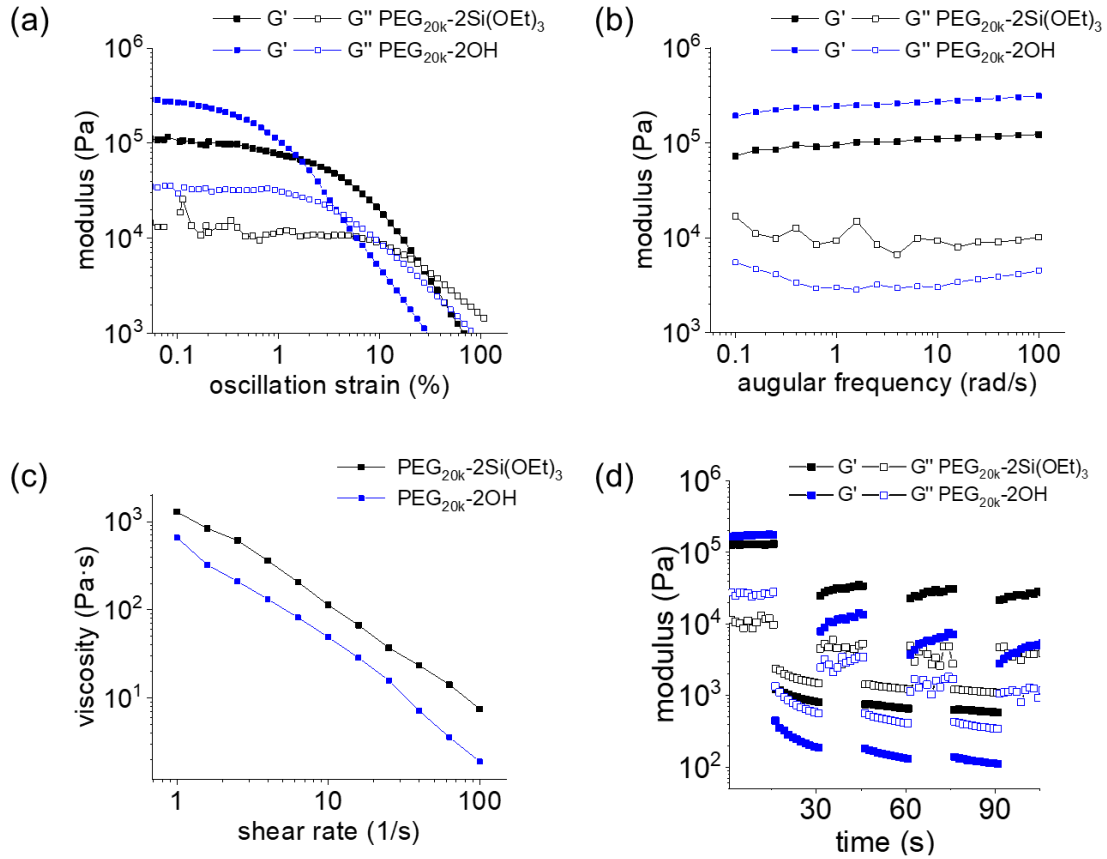


**Figure S20.** (a) Oscillation strain sweep profiles (b) Angular frequency sweep profiles (c) Steady shear rate sweep profiles and (d) Dynamic step-strain amplitude test profiles of PRH[6,27] prepared by PEG<sub>20k</sub>-OH and PEG<sub>20k</sub>-2Si(OEt)<sub>3</sub>. The applied oscillation strain was alternated between 1% and 100% every 15 s at 1 rad/s angular frequency.

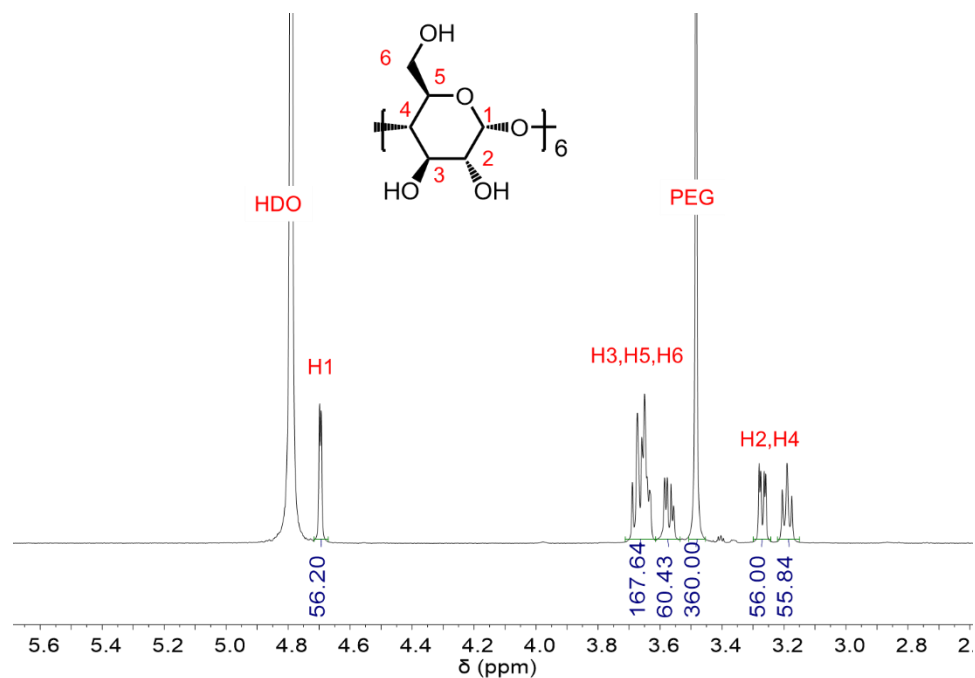


**Figure S21.**  $^1\text{H}$  NMR spectrum (600 MHz) of PM[3,10] in a NaOD/D<sub>2</sub>O solution (5%) at 298 K.

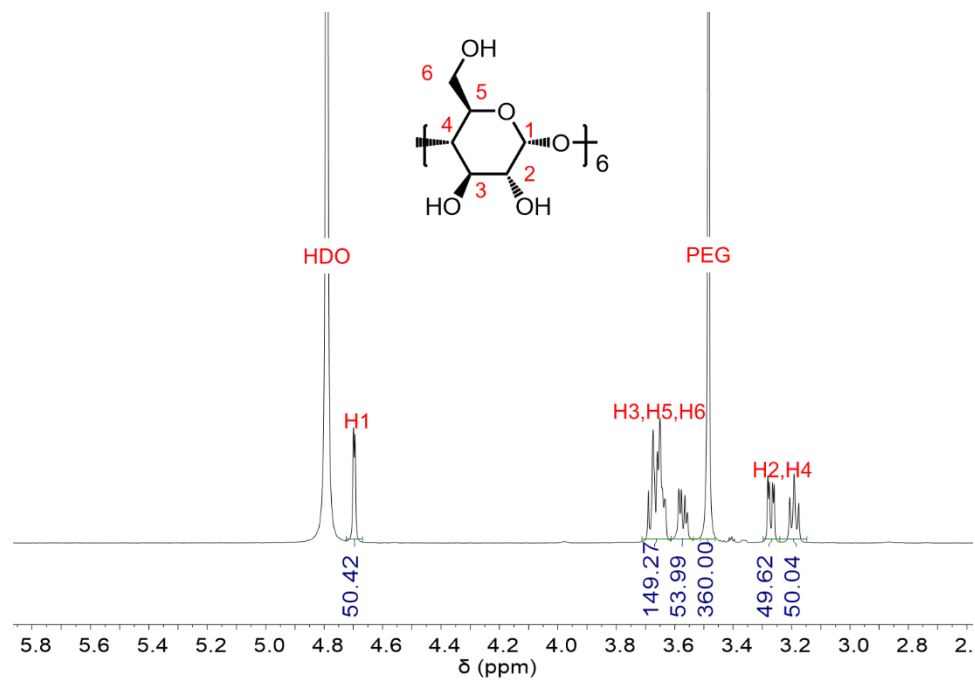


**Figure S22.**  $^1\text{H}$  NMR spectrum (600 MHz) of PM[3,13] in a NaOD/D<sub>2</sub>O solution (5%) at 298 K.

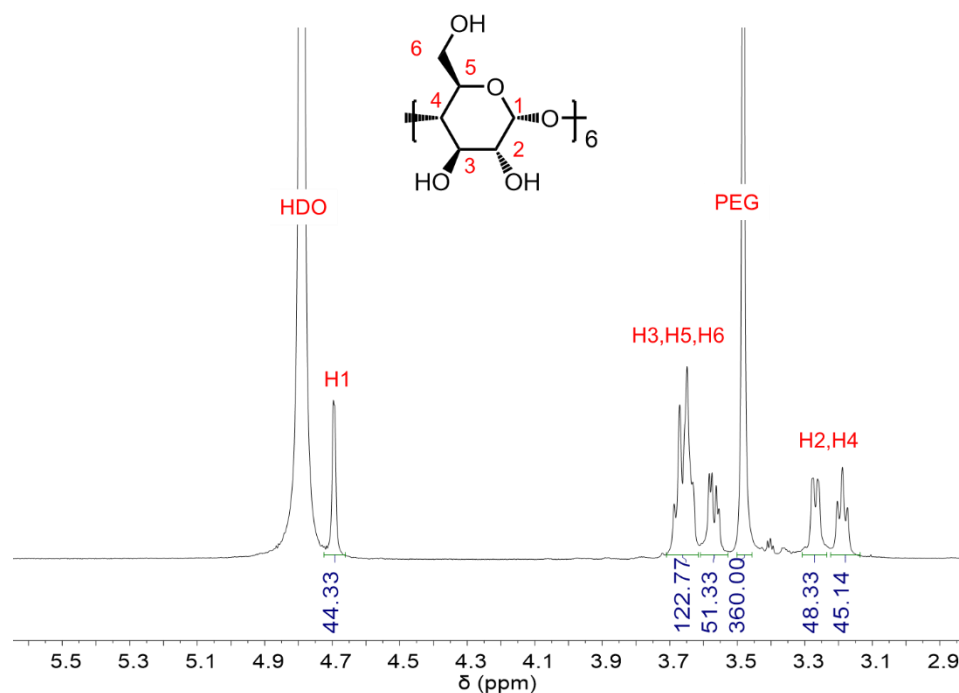


**Figure S23.**  $^1\text{H}$  NMR spectrum (600 MHz) of PM[3,17] in a NaOD/D<sub>2</sub>O solution (5%) at 298 K.

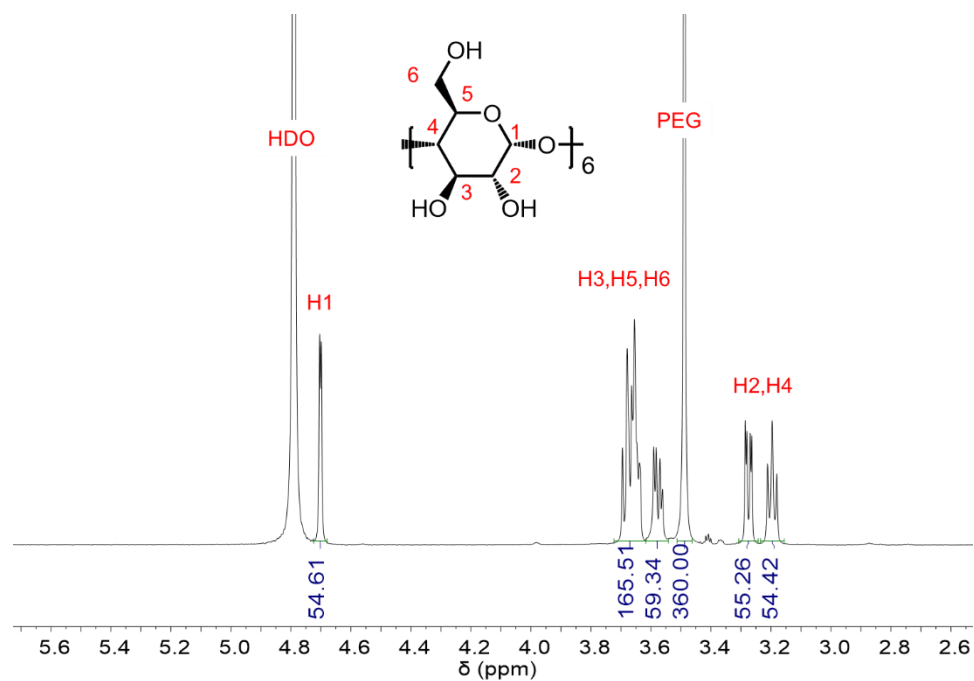


**Figure S24.**  $^1\text{H}$  NMR spectrum (600 MHz) of PM[3,20] in a NaOD/D<sub>2</sub>O solution (5%) at 298 K.



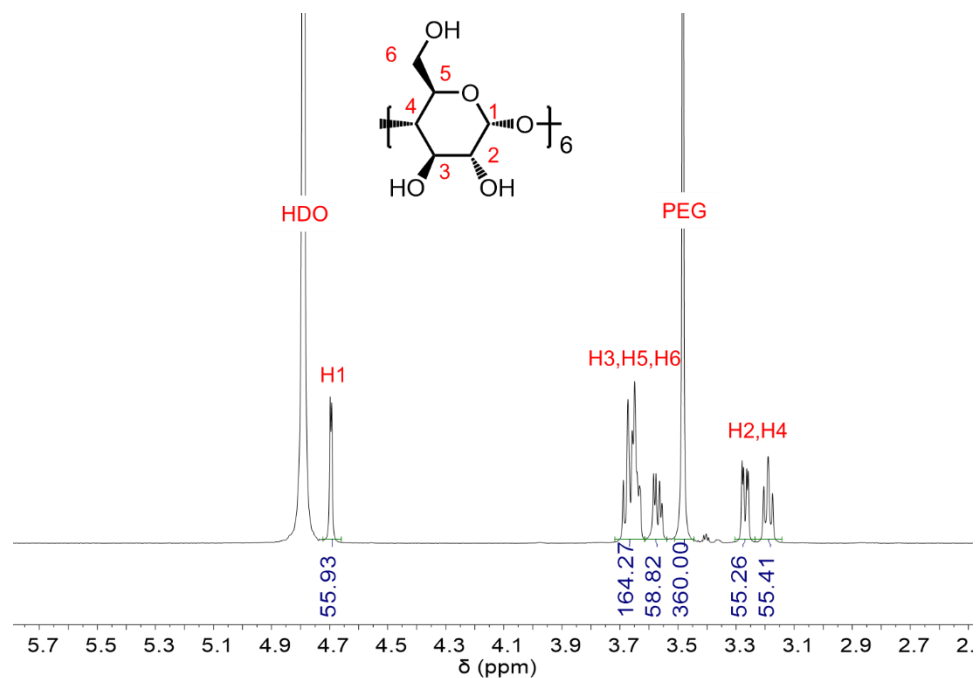


**Figure S25.**  $^1\text{H}$  NMR spectrum (600 MHz) of PM[3,23] in a NaOD/D<sub>2</sub>O solution (5%) at 298 K.

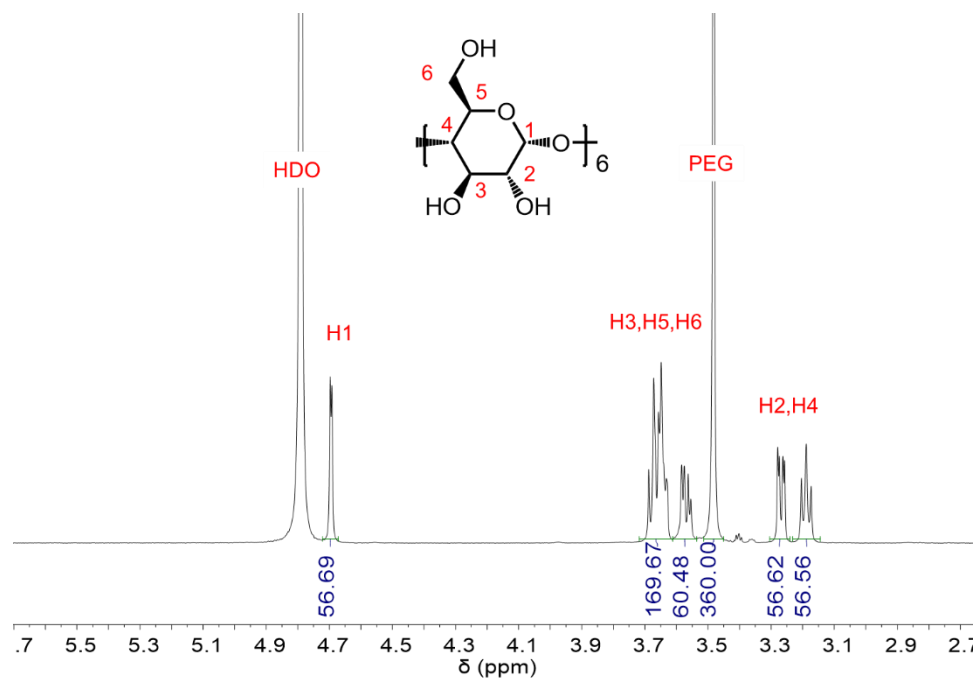


**Figure S26.**  $^1\text{H}$  NMR spectrum (600 MHz) of PM[3,27] in a NaOD/D<sub>2</sub>O solution (5%) at 298 K.

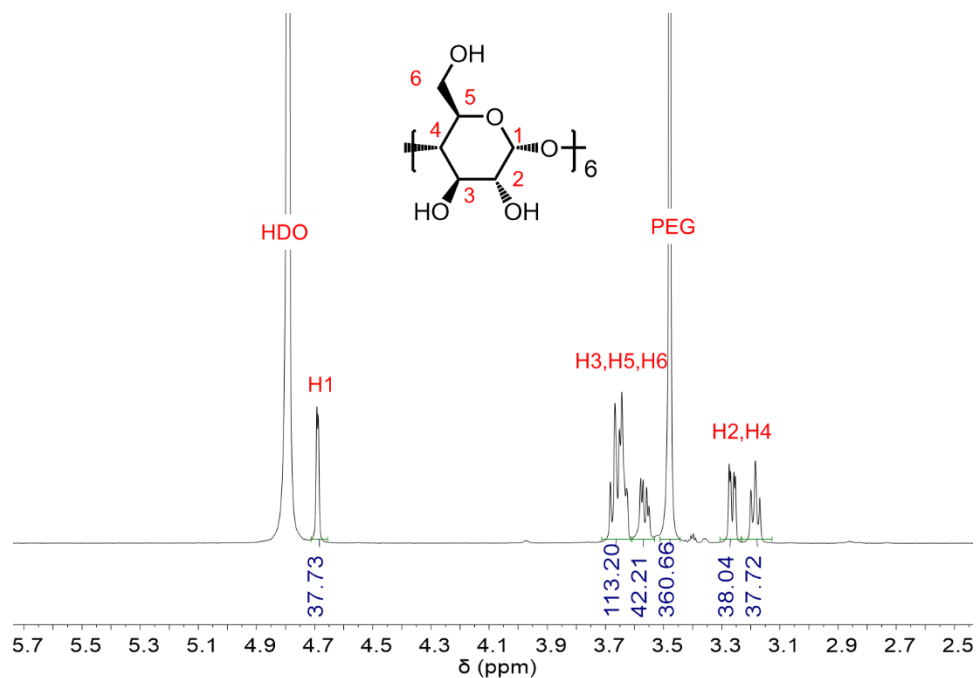


**Figure S27.** <sup>1</sup>H NMR spectrum (600 MHz) of PM[6,17] in a NaOD/D<sub>2</sub>O solution (5%) at 298 K.

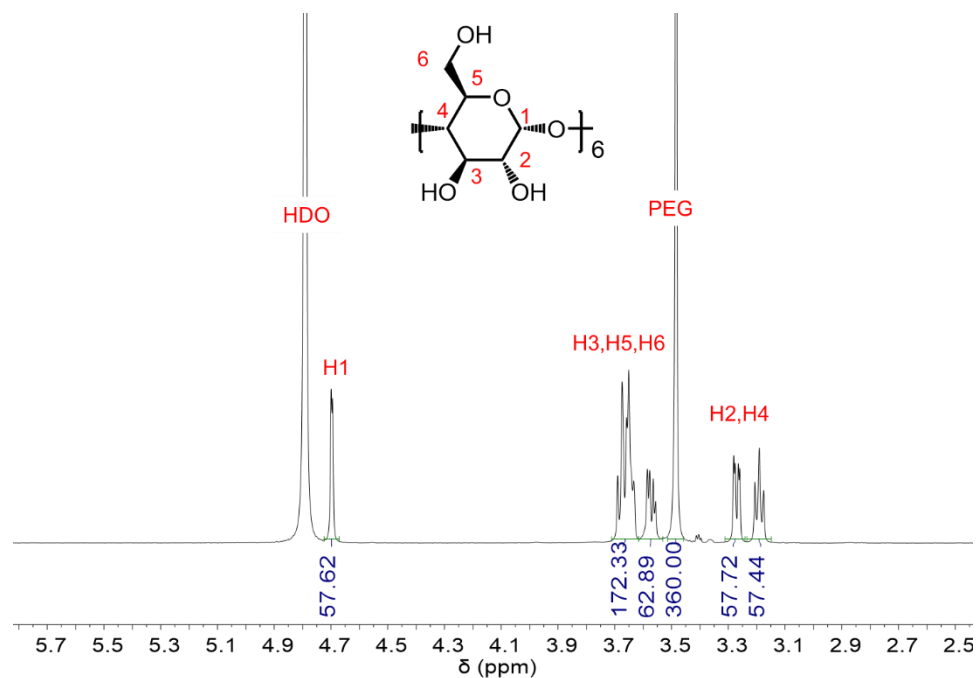


**Figure S28.** <sup>1</sup>H NMR spectrum (600 MHz) of PM[6,27] in a NaOD/D<sub>2</sub>O solution (5%) at 298 K.

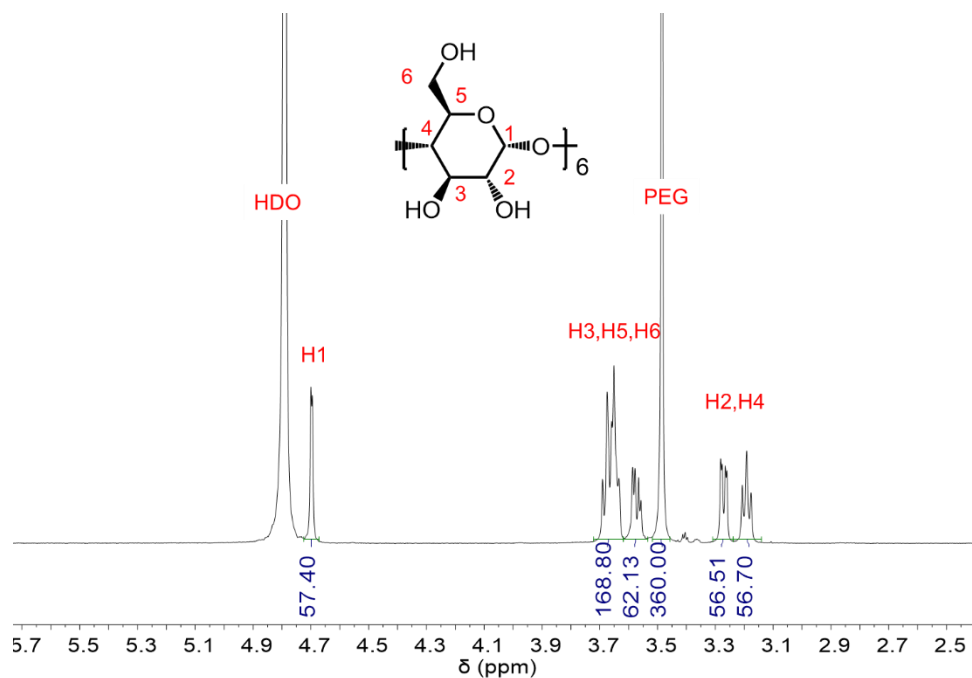


**Figure S29.**  $^1\text{H}$  NMR spectrum (600 MHz) of PM[6,33] in a NaOD/D<sub>2</sub>O solution (5%) at 298 K.

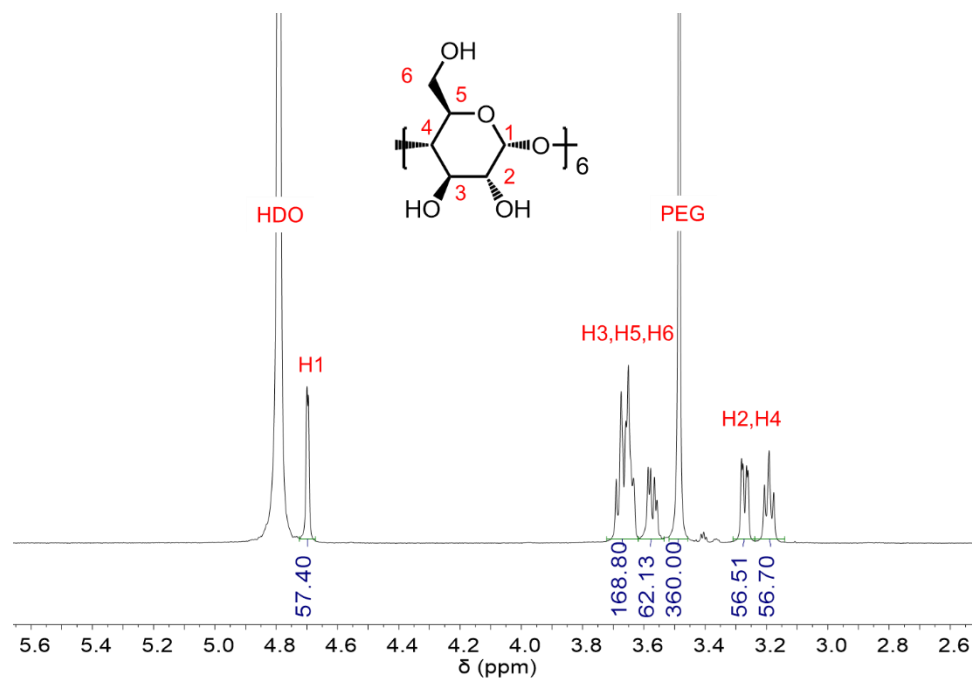


**Figure S30.**  $^1\text{H}$  NMR spectrum (600 MHz) of PM[6,54] in a NaOD/D<sub>2</sub>O solution (5%) at 298 K.

### 5.4.3 Post-printing synthesis

**3D-printing of PRHs.** A PRH[6,27] (3 mL) was loaded to a syringe barrel, centrifuged at 2,500 rpm for 2 min to remove the air bubbles, and transferred to a Nordson EFD syringe barrel for direct ink writing. Direct ink writing experiments were performed on an extrusion-based 3D printer (BioAssemblyBot, Advanced Solutions Life Sciences) equipped with Nordson EFD precision smooth flower tapered tips (i.d. = 400  $\mu$ m). Printing paths were generated by TSIM software and sliced to command the x-y-z motion of the printer.

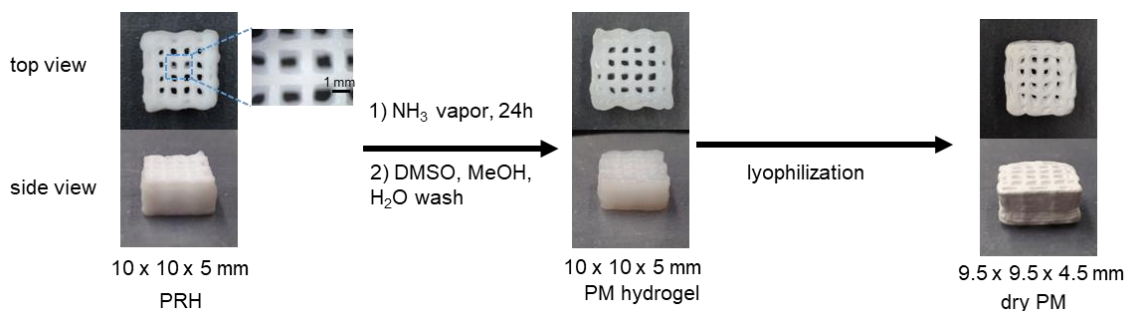


**Figure S31.** Images of 3D-printed PRH lattice and its post-printing product PM in hydrogel form and dried form, respectively.

**Crosslinking of PEG<sub>20k</sub>-2Si(OEt)<sub>3</sub> PRHs.** PRH[6,27] formed by PEG<sub>20k</sub>-2Si(OEt)<sub>3</sub> and  $\alpha$ -CD were 3D-printed to designed structures. The monoliths were kept in a closed chamber with 1, 2, or 4 M NH<sub>3</sub>·H<sub>2</sub>O (20 mL) for 24 h at room temperature for crosslinking. When the concentration of NH<sub>3</sub>·H<sub>2</sub>O increased to 7 M, the 3D-printed monoliths started to deform (Figure S32). After exposure to the NH<sub>3</sub> vapor, the monoliths were lyophilized to produce PEG<sub>20k</sub>-PM. Unlike the PEG<sub>4k</sub>-PM, the PEG<sub>20k</sub>-PM would start to deform in DMSO in 20 min and be completely dissolved in 40 mins (Figure S33).

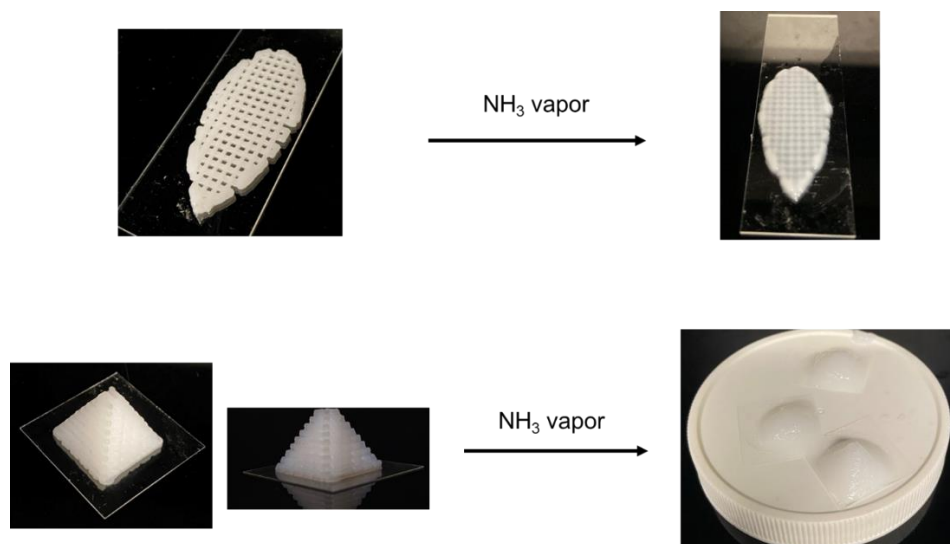


**Figure S32.** Images of 3D-printed PEG<sub>20k</sub>-PRH monoliths, and their products after exposure to NH<sub>3</sub> vapor generated by NH<sub>3</sub>·H<sub>2</sub>O (7 M).

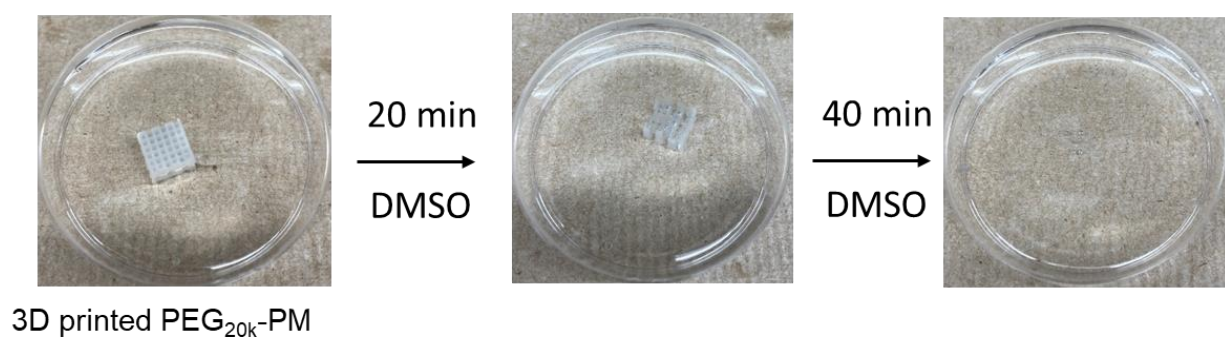


**Figure S33.** Images of 3D-printed PEG<sub>20k</sub>-PM before and after immersing in DMSO. After 40 min, the monolith was completely dissolved.

**Crosslinking of PEG<sub>20k</sub>-2Si(OEt)<sub>3</sub>.** To study the relationship between the crosslink density and the integrity of the PM, we prepared some 6 wt% and 30 wt % of PEG<sub>20k</sub>-2Si(OEt)<sub>3</sub> aqueous solution in the absence of  $\alpha$ -CD. The solutions were exposed to the NH<sub>3</sub> vapor generated by NH<sub>3</sub>·H<sub>2</sub>O (2 M) at room temperature for 24h for crosslinking.

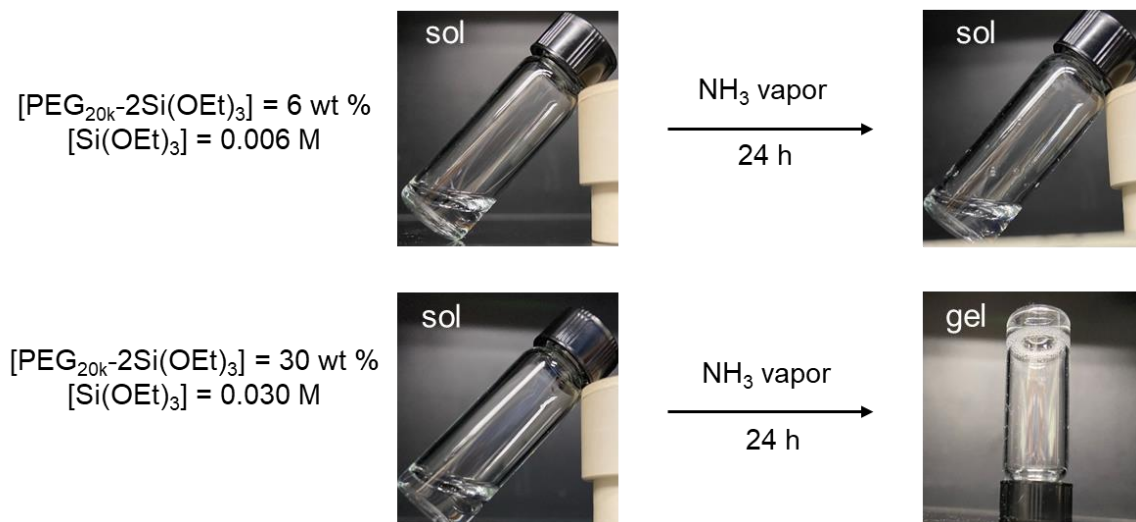


**Figure S34.** Photo images of  $\text{PEG}_{20\text{k}}\text{-}2\text{Si}(\text{OEt})_3$  (6 wt% and 30 wt%) and their product after exposure to  $\text{NH}_3$  vapor generated by 2M of  $\text{NH}_3\cdot\text{H}_2\text{O}$  solution.

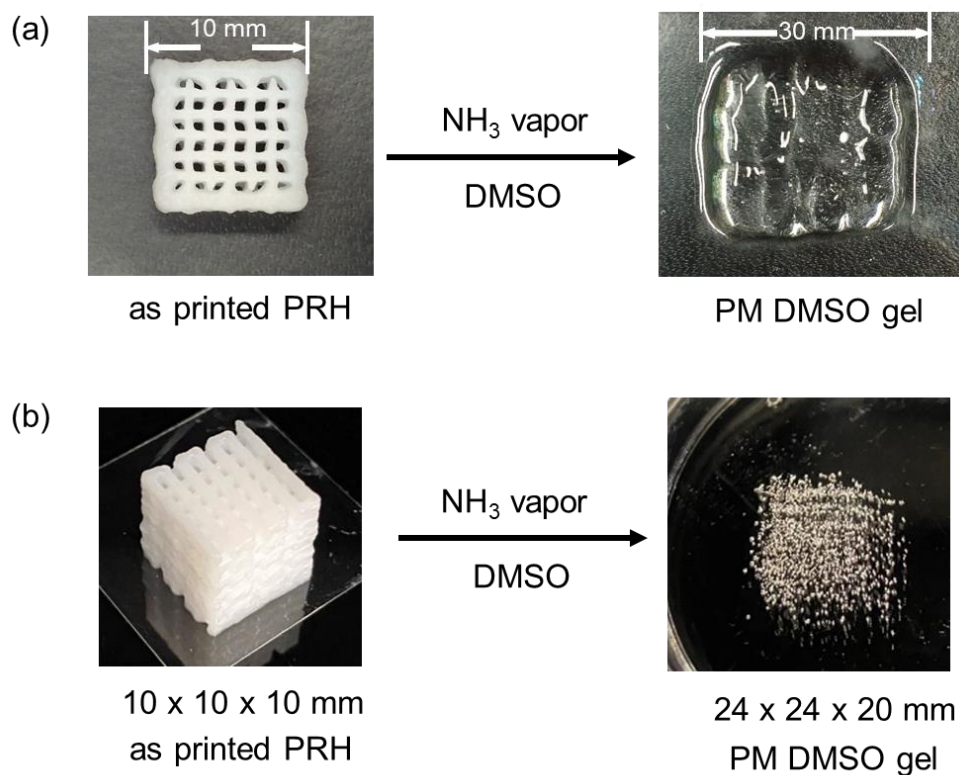


**Figure S35.** (a) Images of as printed PRH lattice and its post-printing product after exposure to  $\text{NH}_3$  vapor and washing with DMSO. (b) Images of as printed PRH lattice and its product after exposure to  $\text{NH}_3$  vapor and immersing in DMSO.

**Compressive properties of TDU-CD hydrogel.** The PRHs were added into a round mold ( $d=30$  mm). After exposure to  $\text{NH}_3$  vapor for 24 h and washing with DMSO and  $\text{H}_2\text{O}$ , the hydrogel was cut as a  $10 \times 10 \times 4$  mm solid cube. Then the solid cube was crosslinked by TDI, followed by PEG template removal using the previously described method. To mimic the lycopene adsorption condition, the modeled cube was immersed in 20 mL of THF/ $\text{H}_2\text{O}$  (1:4) solvent for 6 h. The THF/ $\text{H}_2\text{O}$  mixture was refreshed every 2 h for extensive solvent exchange. The obtained TDU-CD hydrogel was measured as an  $11.0 \times 11.0 \times 4.2$  mm cube. The compression test was performed at 0.2 mm/min at room temperature ( $24^\circ\text{C}$ ) until the monolith fractured at  $\varepsilon = 22\%$ . Young's modulus is calculated as 456 kPa at the region of  $2\% < \varepsilon < 7\%$ . The yielding stress is measured as 97 kPa (Figure S36).

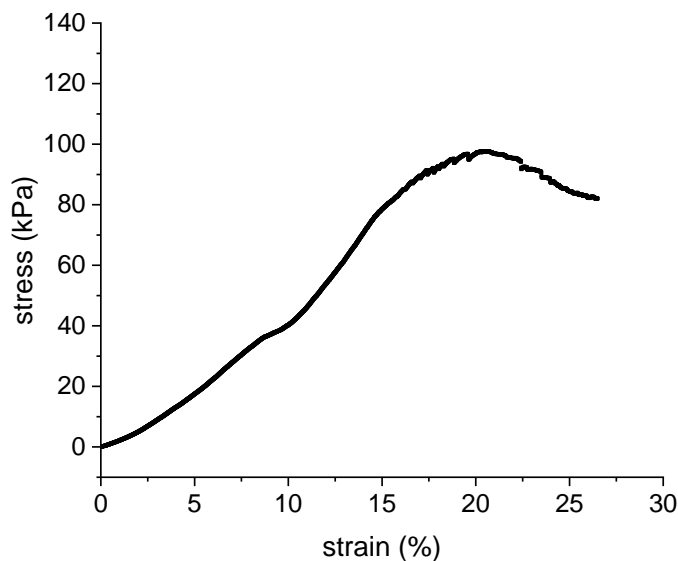


**Figure S36.** Stress-strain profile of a TDU-CD hydrogel cube ( $11 \times 11 \times 4.2$  mm) in the compression test. Strain rate: 0.2 mm/min.

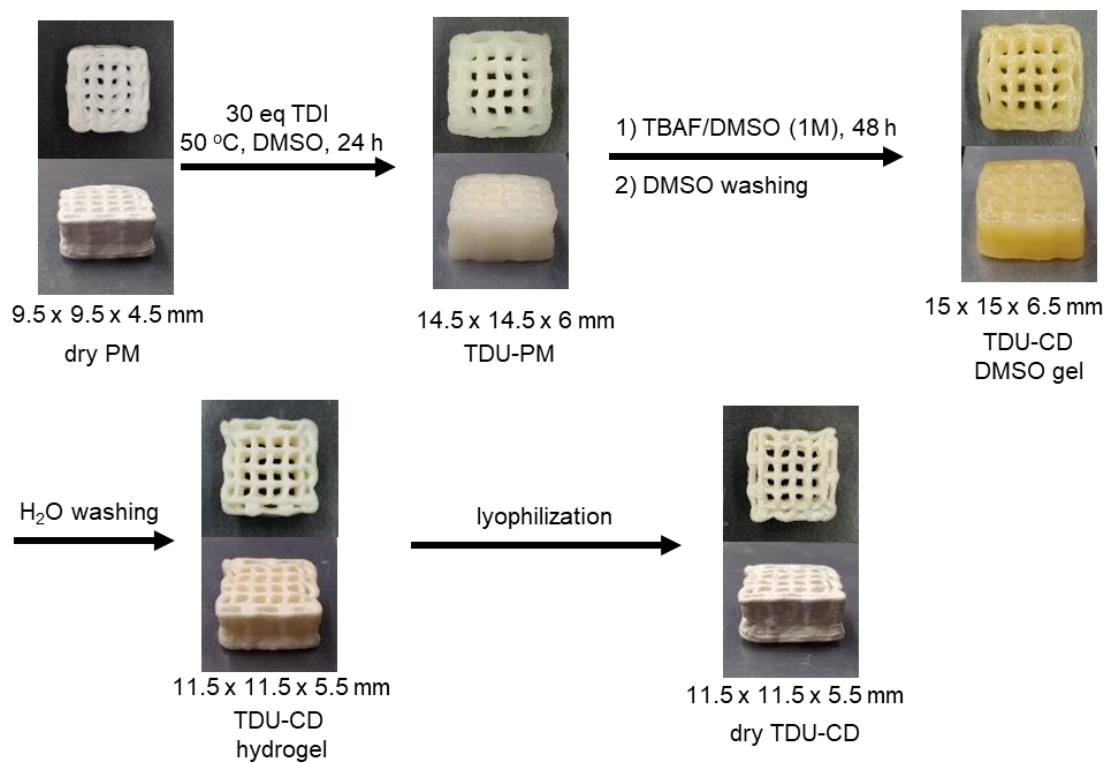


**Figure S37.** Images of 3D-printed dry PM and its post-printing products of TDU-PM DMSO gel, TDU-CD DMSO gel, TDU-CD hydrogel, and dry TDU-CD, respectively.



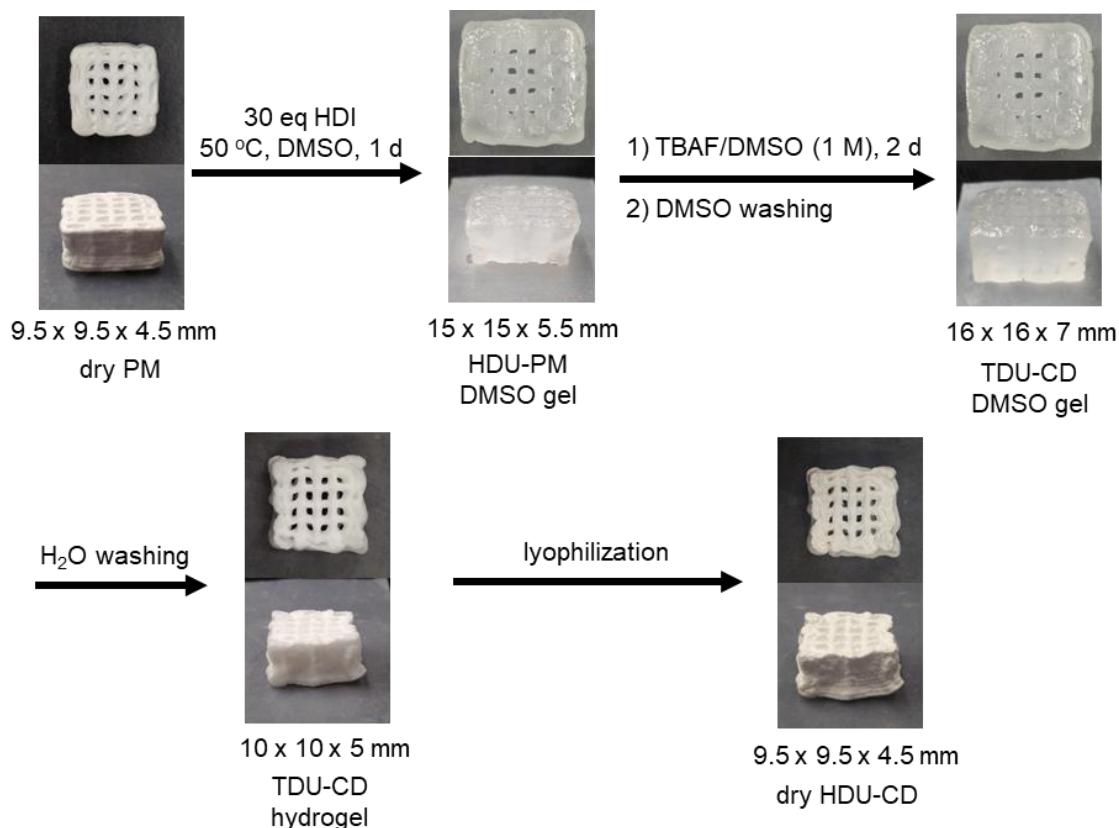


**Figure S38.** Images of 3D-printed dry PM and its post-printing products of HDU-PM DMSO gel, HDU-CD DMSO gel, HDU-CD hydrogel, and dry HDU-CD, respectively.

**Optimization of the crosslinking density of TDU in TDU-PM and TDU-CD.** A dry PM (100 mg) was swelled in 6 mL anhydrous DMSO for 12 h. Different amount of TDI (15, 20, or 30 equiv. to  $\alpha$ -CD) and dibutyltin dilaurate (DBTDL, 30  $\mu$ L) were added to the reaction. The reaction was heated at 50 °C for 24 h, and then the monoliths were washed with DMSO (30 mL  $\times$  2) and H<sub>2</sub>O (30 mL  $\times$  2). After lyophilization, the monoliths were immersed in TBAF DMSO solution (1 M) and was with DMSO and H<sub>2</sub>O. The obtained TDU-CDs with different degrees of crosslinking was hydrolyzed in NaOD/D<sub>2</sub>O solution (5%) at 80 °C for <sup>1</sup>H NMR analysis. The CD: TDU ratio was found as 1: 4.5, 1: 5.3, and 1: 6.4 when 15, 20, or 30 equiv. of TDI were added to the reaction, respectively. The TDU-CD monolith with lower DP (1: 5.3) could not maintain its integrity after DMSO washing.

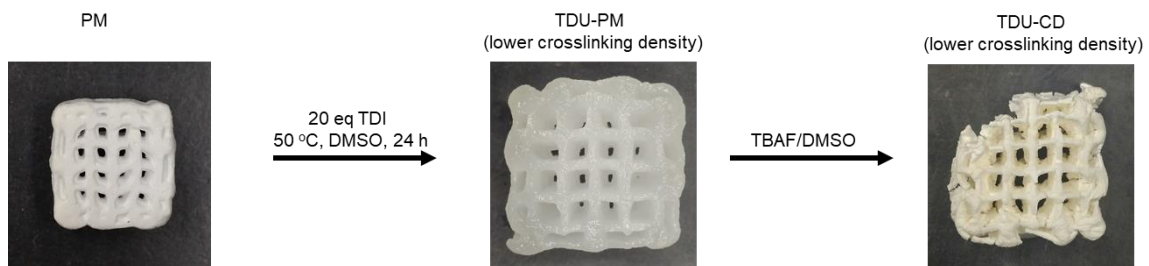


**Figure S39.** Images of 3D-printed dry PM and its post-printing products of TDU-PM (lower crosslinking density), and TDU-CD (lower crosslinking density,  $\alpha$ -CD: TDU= 1: 5.3).

#### 5.4.4 Materials characterizations

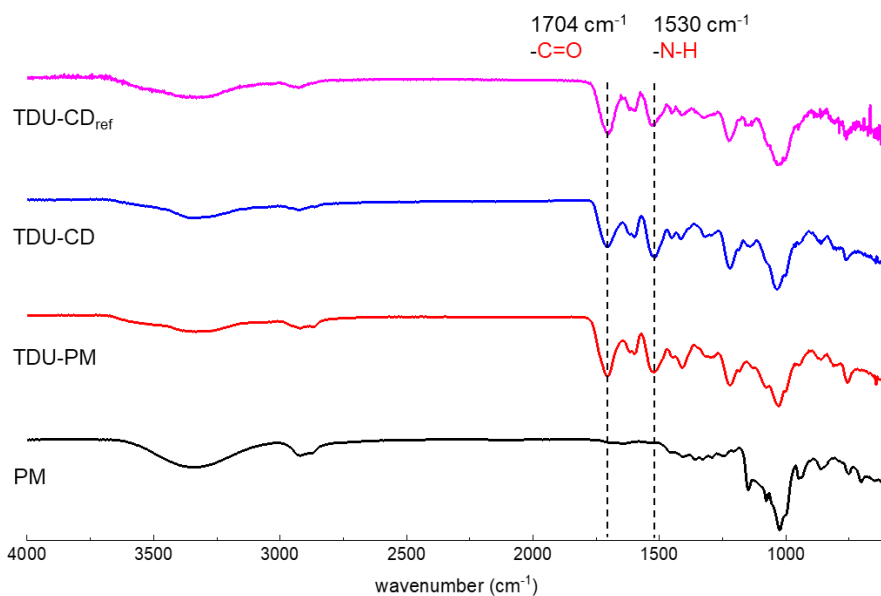


**Figure S40.** FT-IR spectra of PM, TDU-PM, TDU-CD, TDU-CD<sub>ref</sub> from bottom to top.

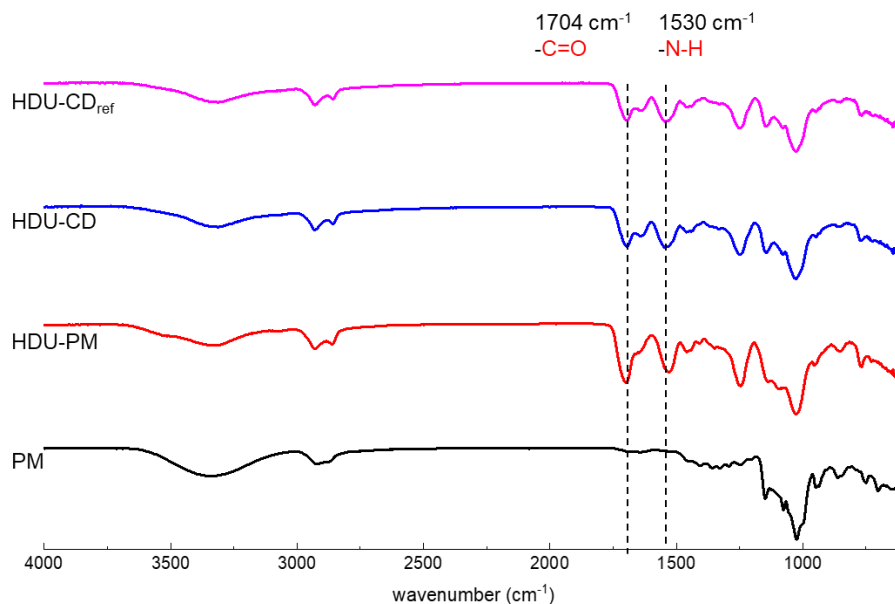


**Figure S41.** FT-IR spectra of PM, HDU-PM, HDU-CD, HDU-CD<sub>ref</sub> from bottom to top.

**PXRD and WAXS measurement.** Powder X-ray Diffraction (PXRD) experiments were carried out using a Rigaku MiniFlex powder X-ray diffractometer. The samples were grounded to fine powders before the measurement. The data were collected from 3 to 35 degrees (Figure S41-42). Wide-angle X-ray scattering (WAXS) and experiments were performed using a Rigaku NANOPIX instrument with a Hypix-3000 detector. The grounded samples or hydrogels were poured into a glass capillary for X-ray measurements (WJM-glass/Muller [borosilicate](#) capillary:  $\phi = 2.0 \times \text{length} = 80 \text{ mm}$ ) for WAXS measurements. The data was collected from 0.8 to 3.2  $\text{\AA}^{-1}$  (Figure S43).

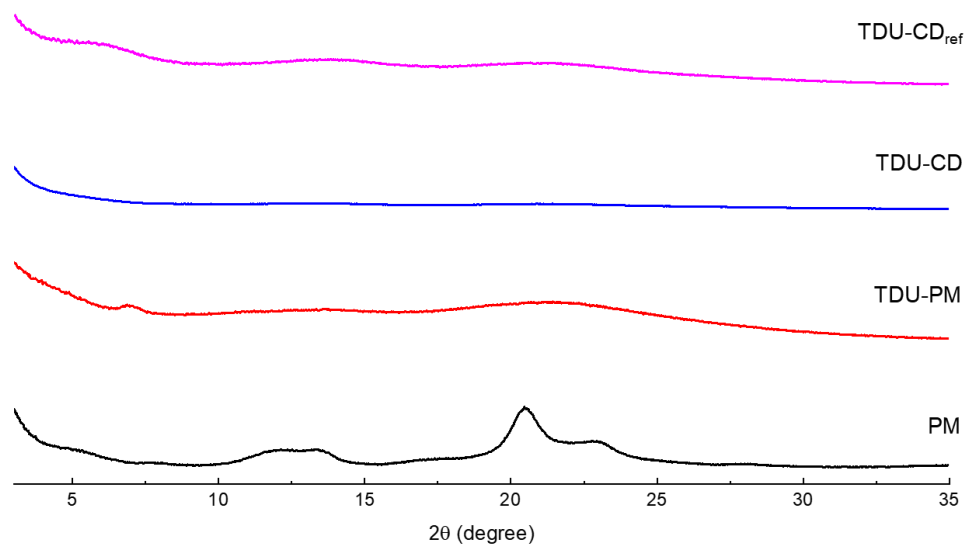


**Figure S42.** PXRD spectra of PM, TDU-PM, TDU-CD, TDU-CD<sub>ref</sub> from bottom to top.

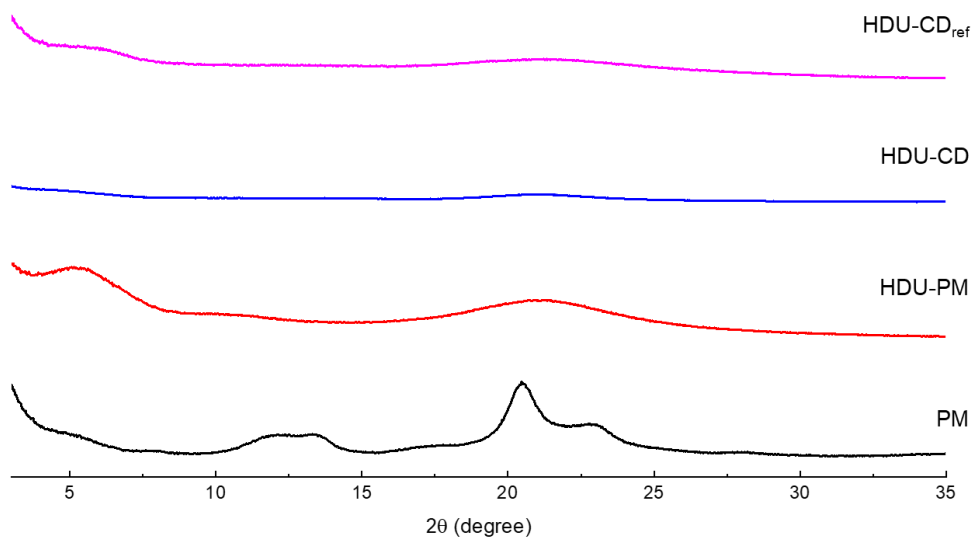


**Figure S43.** PXRD spectra of PM, HDU-PM, HDU-CD, HDU-CD<sub>ref</sub> from bottom to top.

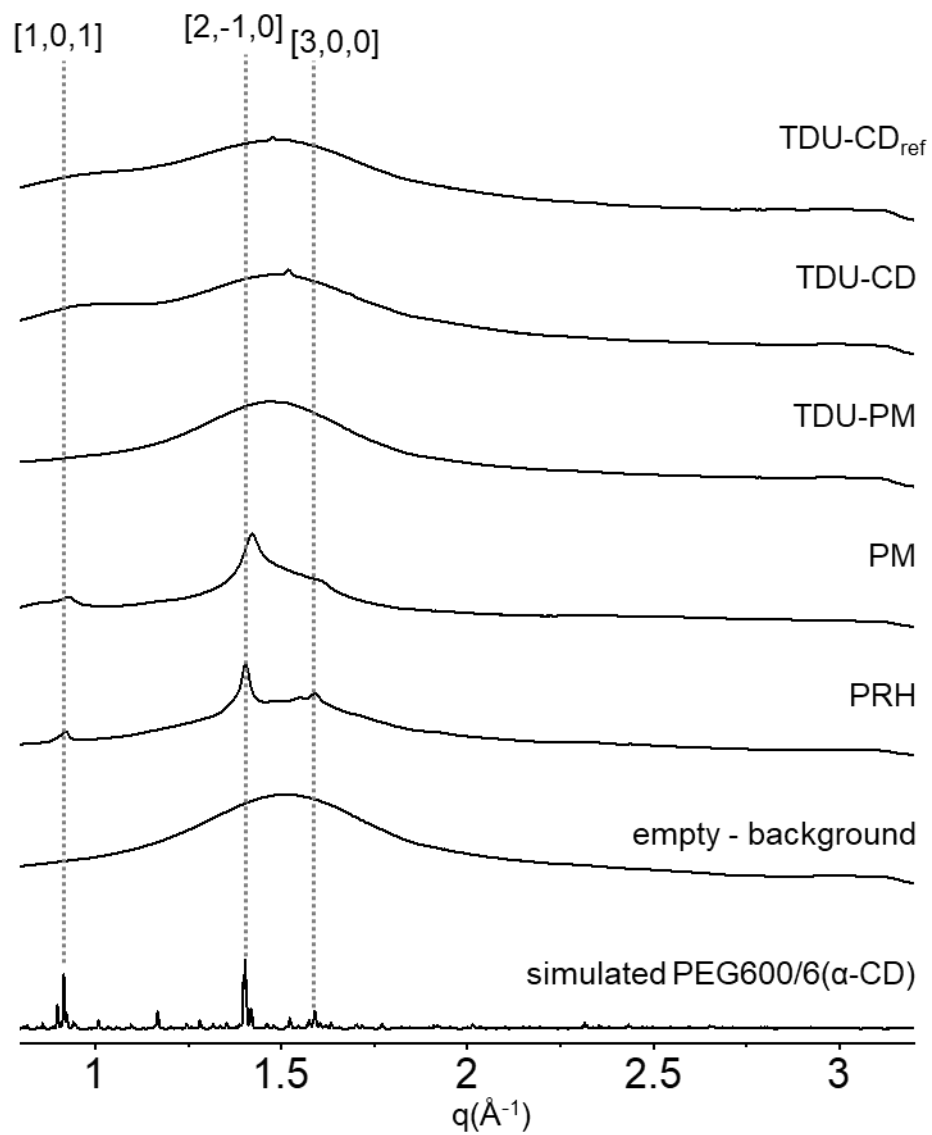


**Figure S44.** Simulated PEG600/6( $\alpha$ -CD) single crystal and experimental WAXS profiles of empty background, PRH, PM, TDU-PM, TDU-CD, and TDU-CD<sub>ref</sub> from bottom to top.

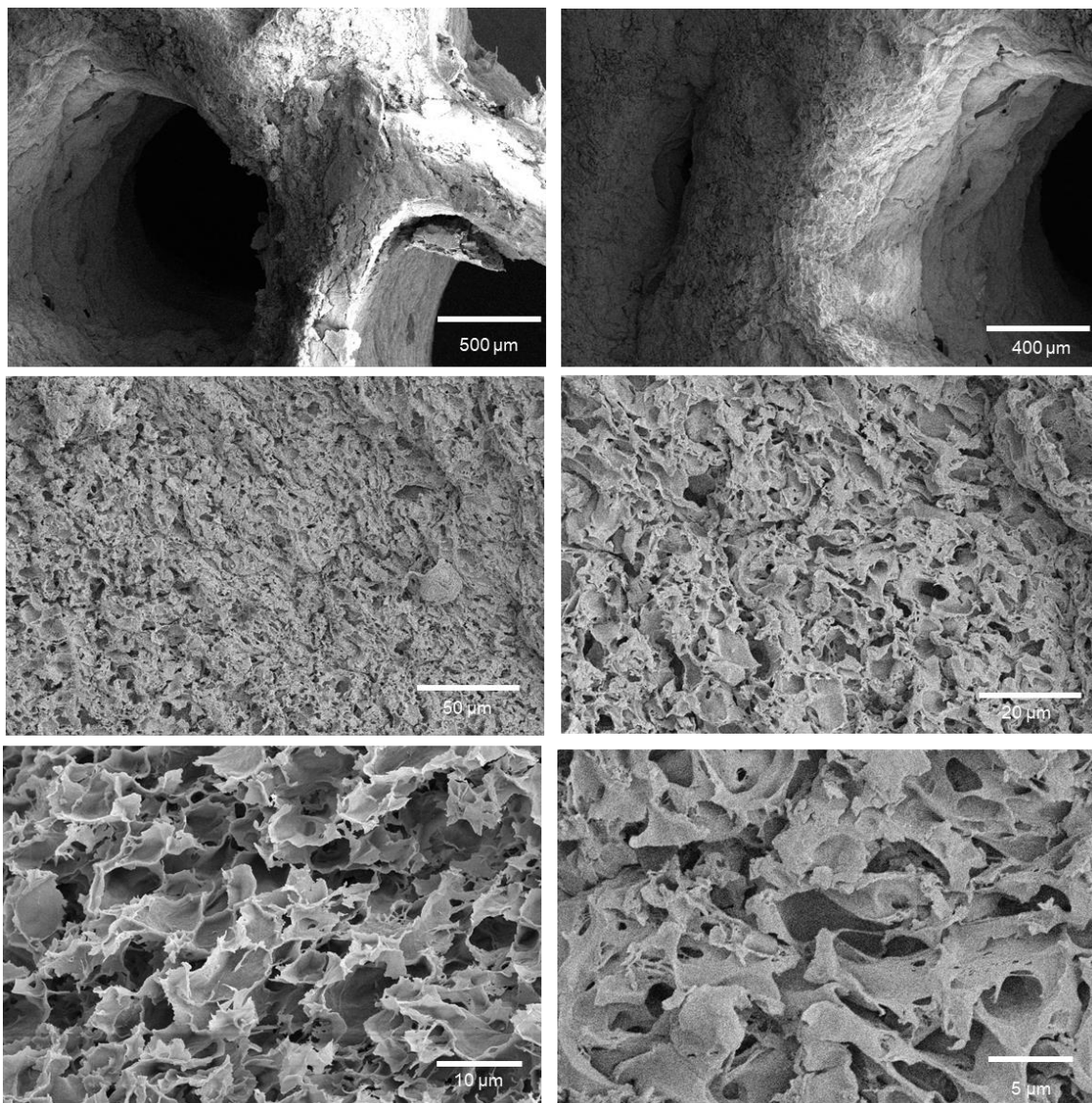


**Figure S45.** SEM images of a 3D-printed TDU-CD monolith.

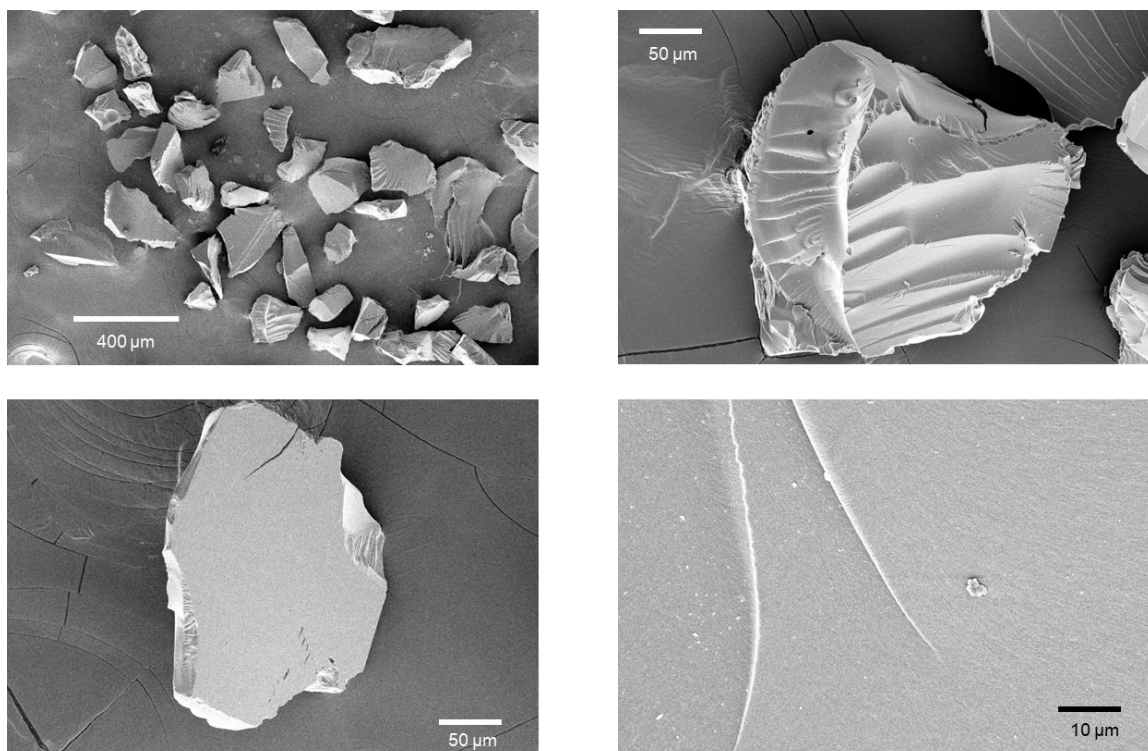


**Figure S46.** SEM images of a TDU-CD<sub>ref</sub> powdery sample.

**PEG adsorption experiment.** Dry TDU-CD<sub>ref</sub> or TDU-CD (10 mg, 0.00467 mmol of  $\alpha$ -CD) was added to D<sub>2</sub>O solution (1 mL) of PEG with different molecular weights and feeding EG/CD ratios as listed in Table S3. After shaking 5 d at 24 °C, 0.50 mL solution was taken out, followed by the addition of maleic acid as an internal standard for <sup>1</sup>H NMR analysis. In the meantime, a control sample without adding TDU-CD<sub>ref</sub> or TDU-CD was prepared for each experiment to calculate the adsorption efficiency.

**Table S3.** Adsorption of PEGs of different molecular weights using TDU-CD and TDU-CD<sub>ref</sub>.

probes	fed EG/CD	TDU-CD		TDU-CD <sub>ref</sub>	
		adsorbed <sup>a</sup> PEG %	adsorbed PEG/CD	adsorbed <sup>a</sup> PEG %	adsorbed PEG/CD
		PEG <sub>600</sub>	2 : 1	45%	1 : 15.1
PEG <sub>2K</sub>	2 : 1	96%	1 : 23.6	100%	1 : 22.8
	4 : 1	66%	1 : 17.2	99%	1 : 11.5
	8 : 1	35%	1 : 16.2	100%	1 : 5.7
	10 : 1	31%	1 : 14.6	98%	1 : 4.6
	14 : 1	22%	1 : 14.7	76%	1 : 4.3
	18 : 1	17%	1 : 14.8	66%	1 : 3.8
PEG <sub>4K</sub>	2 : 1	100%	1 : 45.4	100%	1 : 45.4
	4 : 1	52%	1 : 43.7	100%	1 : 22.8
	8 : 1	31%	1 : 36.6	100%	1 : 11.4
	10 : 1	26%	1 : 34.9	98%	1 : 9.3
	14 : 1	19%	1 : 34.1	84%	1 : 7.7
	18 : 1	15%	1 : 33.6	62%	1 : 8.1
PEG <sub>20K</sub>	2 : 1	41%	1 : 554	100%	1 : 227
PEG <sub>100K</sub>	2 : 1	12%	1 : 9458	12%	1 : 9459



PEG <sub>1M</sub>	2 : 1	21%	1 : 54051	17%	1 : 66769
-------------------	-------	-----	-----------	-----	-----------

---

<sup>a</sup> the PEGs adsorption efficiency was measured by <sup>1</sup>H NMR analysis.

#### 5.4.6 Lycopene harvesting

**Carotenoids extraction.** Fresh tomato juice (80 mL) was sonicated for 1 h and extracted using CH<sub>2</sub>Cl<sub>2</sub> (25 mL ×3). The CH<sub>2</sub>Cl<sub>2</sub> solution was dried over Na<sub>2</sub>SO<sub>4</sub>, and the solvent was removed under reduced pressure. The crude product was subjected to liquid chromatography-mass spectrometry (LC-MS) analysis (Figure S46).

**LC-MS-PDA analysis.** The LC-MS analysis of carotenoids followed a previously reported method.<sup>345</sup> The mobile phase uses a combination of two prepared solvent mixture eluents. *Eluent A*: MeOH (800 mL), deionized water (200 mL), ammonium acetate (400 mg), and formic acid (0.8 mL) were mixed and sonicated for 20 min at room temperature. *Eluent B*: Methyl tert-butyl ether (780 mL), MeOH (200 mL), water (20 mL), ammonium acetate (400 mg), and formic acid (20 μL) were mixed and sonicated for 20 min. A C18 column was preheated to 40°C before 20 μL of carotenoid in acetone solution was injected. At a flow rate of 1.2 mL/min, eluent B was linearly increased from 0 to 100% in 16 min. Then, 100% of B was held for 1 min and then returned to 0% for another 2 min. The analytes were monitored by a photodiode array (PDA) detector using the absorption at 472 nm. The mass and UV-vis data of the analytes with different retention times were used to identify the corresponding carotenoids. The relative abundance of each carotenoid was calculated by integrating its LC-PDA peak.

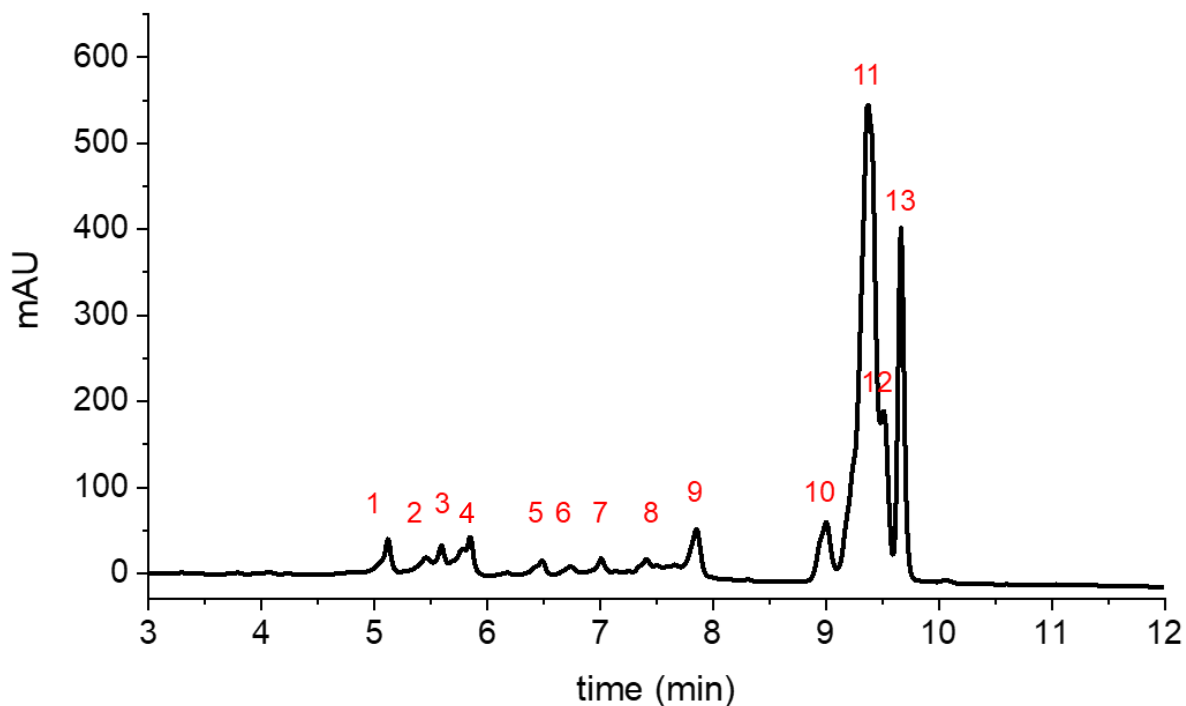
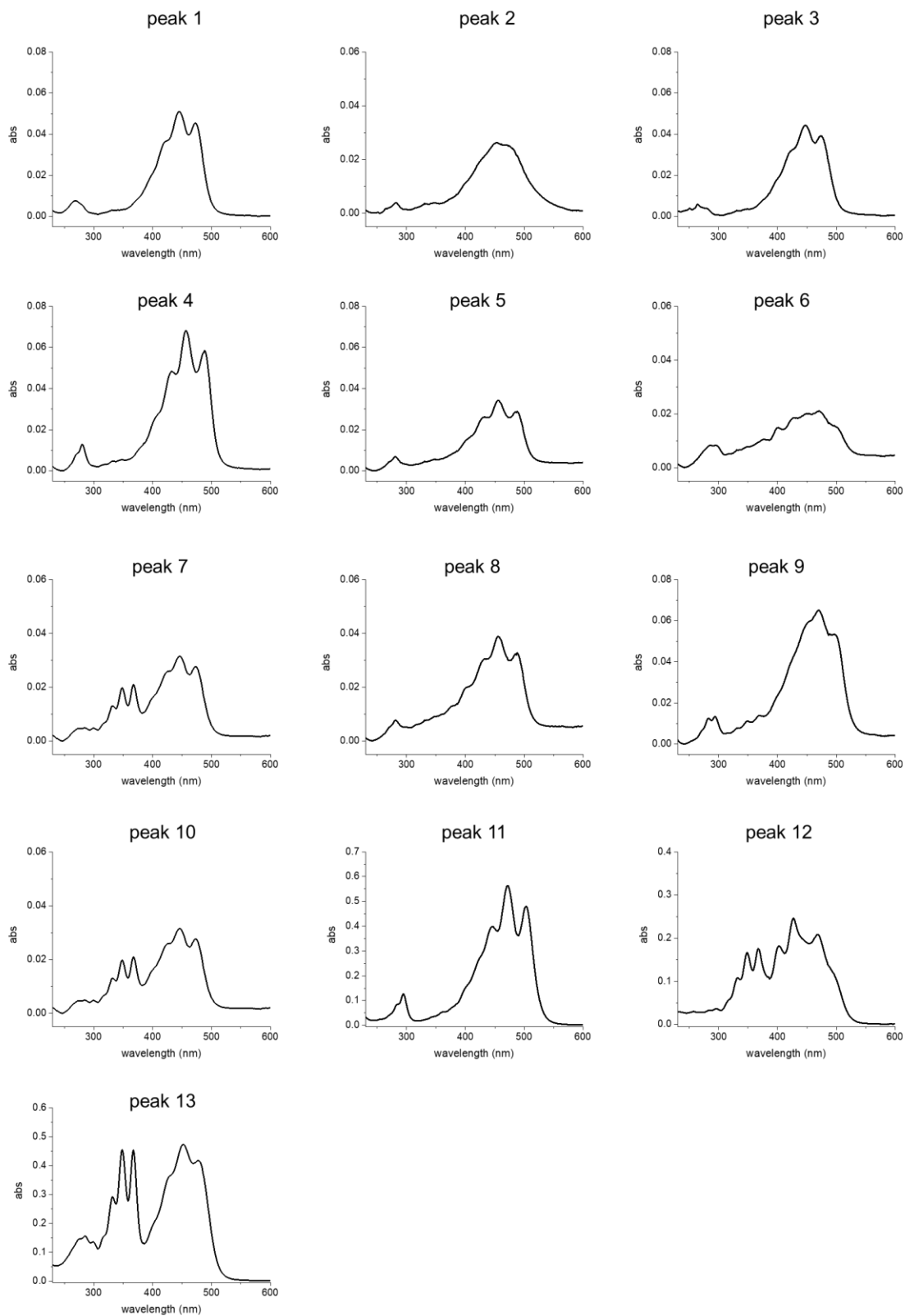


**Figure S47.** An LC-MS-PDA profile of carotenoids extracted by  $\text{CH}_2\text{Cl}_2$ . The absorptions of samples at 472 nm were monitored.

As shown in Figure S46, 13 peaks were identified in the LC-MS analysis. Among these carotenoids, analytes eluted at 5.60, 5.85, 6.73, 7.01, 7.85, 9.00, 9.37, 9.51, and 9.67 min were identified as lutein, zeaxanthin, astaxanthin, violaxanthin, lycopene epoxides,  $\gamma$ -carotene, lycopene,  $\alpha$ -carotene, b-carotene, and other side products, respectively. The integrations of  $\gamma$ -carotene, lycopene,  $\alpha$ -carotene/phytofluene/ $\beta$ -carotene epoxides mixture, b-carotene/phytofluene are calculated as 5%, 59%, 9%, and 17%, respectively. See Table S4 for details.

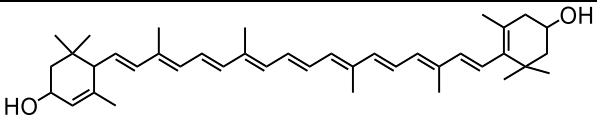
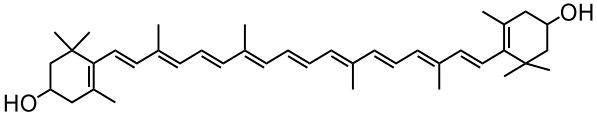
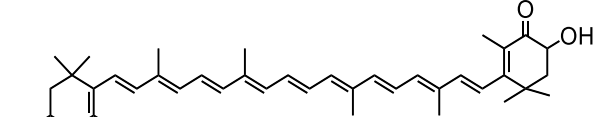
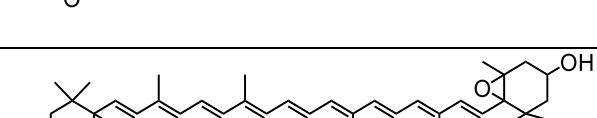
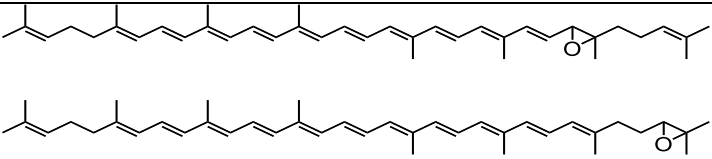
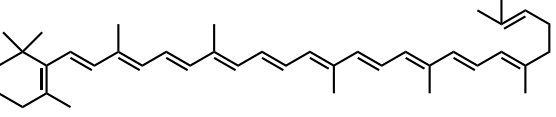
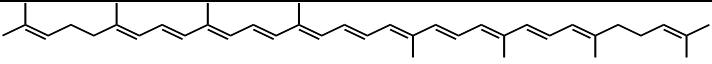
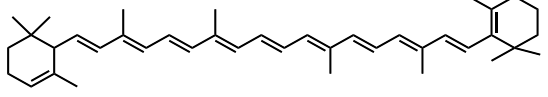
**Table S4.** Identification and chromatographic data of carotenoids extracted by CH<sub>2</sub>Cl<sub>2</sub>

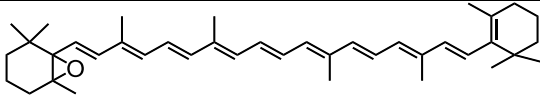
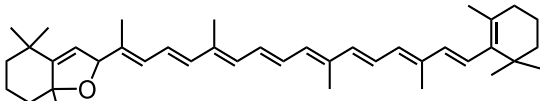
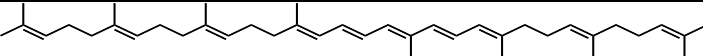
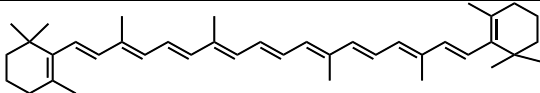
<b>peak</b>	<b>compound</b>	<b>retention time (min)</b>	<b>peak area</b>	<b>UV-vis absorption peaks (nm)</b>	<b>m/z ratios</b>
<b>1</b>	*	5.12	151849	445, 472	569, 506
<b>2</b>	*	5.46	44365	454	569
<b>3</b>	lutein	5.60	59883	447, 474	569
<b>4</b>	zeaxanthin	5.85	219878	432, 457, 488	569, 614
<b>5</b>	*	6.49	78733	432, 455, 488	571
<b>6</b>	astaxanthin	6.73	39125	450, 470	597
<b>7</b>	violaxanthin	7.01	58718	446, 474	601
<b>8</b>	*	7.41	83700	456, 488	609
<b>9</b>	lycopene epoxides	7.85	212606	470, 497	553
<b>10</b>	$\gamma$ -carotene	9.00	500541	440, 468, 496	537
<b>11</b>	lycopene	9.37	5628516	446, 472, 503	537
<b>12</b>	$\alpha$ -carotene/ phytofluene/ $\beta$ -carotene epoxides	9.51	820532	403, 427, 468 331, 348, 367	537 543 553
<b>13</b>	$\beta$ -carotene/ phytofluene	9.67	1610291	429, 452, 477 331, 348, 367	537 543



**Figure S48.** UV-Vis spectra of the separated analytes from the mixture.

**Table S5.** Chemical structures of LC-separated analytes

peak	compound	chemical structure
3	lutein	
4	zeaxanthin	
6	astaxanthin	
7	violaxanthin	
9	lycopene 5,6-epoxide  lycopene 1,2-epoxide	
10	$\gamma$ -carotene	
11	lycopene	
12	$\alpha$ -carotene	

12	$\beta$ -carotene 5,6-epoxide	
	$\beta$ -carotene 5,8-epoxide	
12	phytofluene	
13	$\beta$ -carotene	

**Silica chromatography separated lycopene.** The crude  $\text{CH}_2\text{Cl}_2$  extractant was subject to column chromatography separation ( $\text{SiO}_2$ , hexanes) to separate the desired lycopene. The isolated lycopene was characterized by LC-MS-PDA (Figure S48) and  $^1\text{H}$  NMR (Figure S50). In this sample, analytes eluted at 7.88, 9.04, 9.37, and 9.71 min are identified as zeinoxanthin (integration: 2%), g-carotene (integration: 15%), lycopene (integration area: 82%), and  $\beta$ -carotene/phytofluene/phytoene mixture (peak area: 1%), respectively.

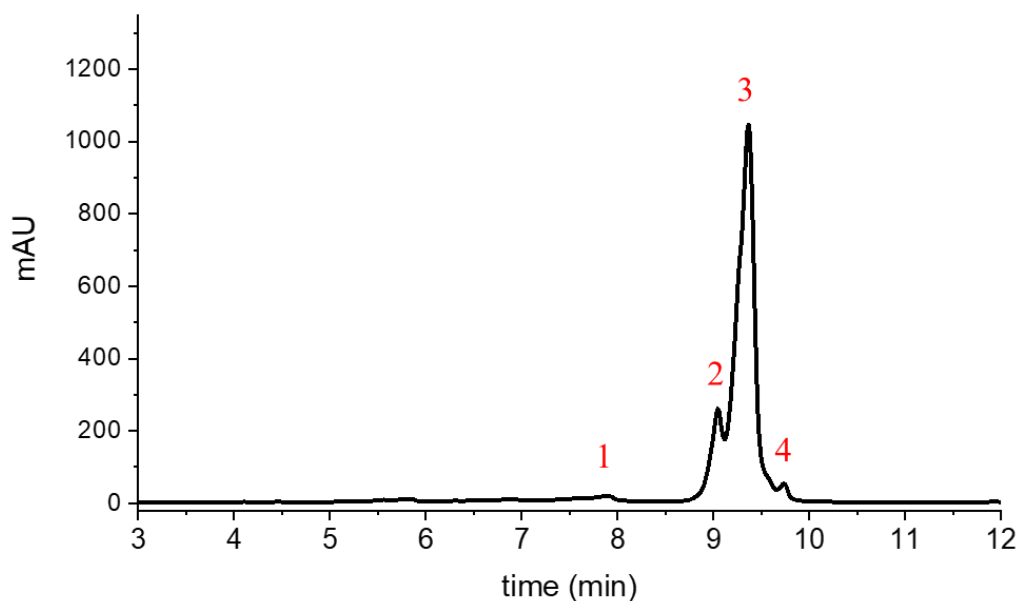


**Figure S49.** An LC-MS profile of acetone solution of silica chromatography separated lycopene. The absorptions of samples at 472 nm were monitored.

**Table S6.** Identification and chromatographic data of silica chromatography separated lycopene

<b>peak</b>	<b>compound</b>	<b>retention time (min)</b>	<b>area</b>	<b>UV-vis absorption peaks (nm)</b>	<b>m/z ratios</b>
<b>1</b>	lycopene epoxides	7.85	59753	470, 497	553
<b>2</b>	$\gamma$ -carotene	9.04	2582038	440, 468, 496	537
<b>3</b>	lycopene	9.37	13811281	447, 472, 503	537
<b>4</b>	$\beta$ -carotene/ phytofluene/ phytoene	9.71	124002	429, 452, 477 331, 348, 367 280	537 543

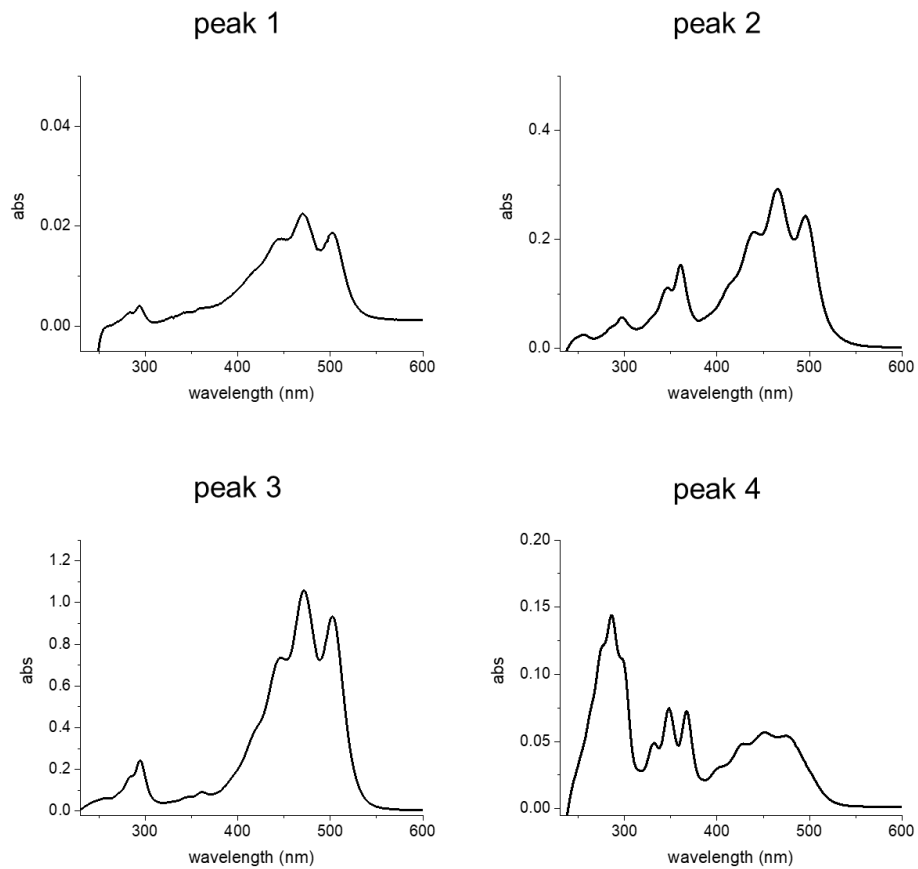


**Figure S50.** UV-Vis spectra of analytes of silica chromatography separated lycopene.



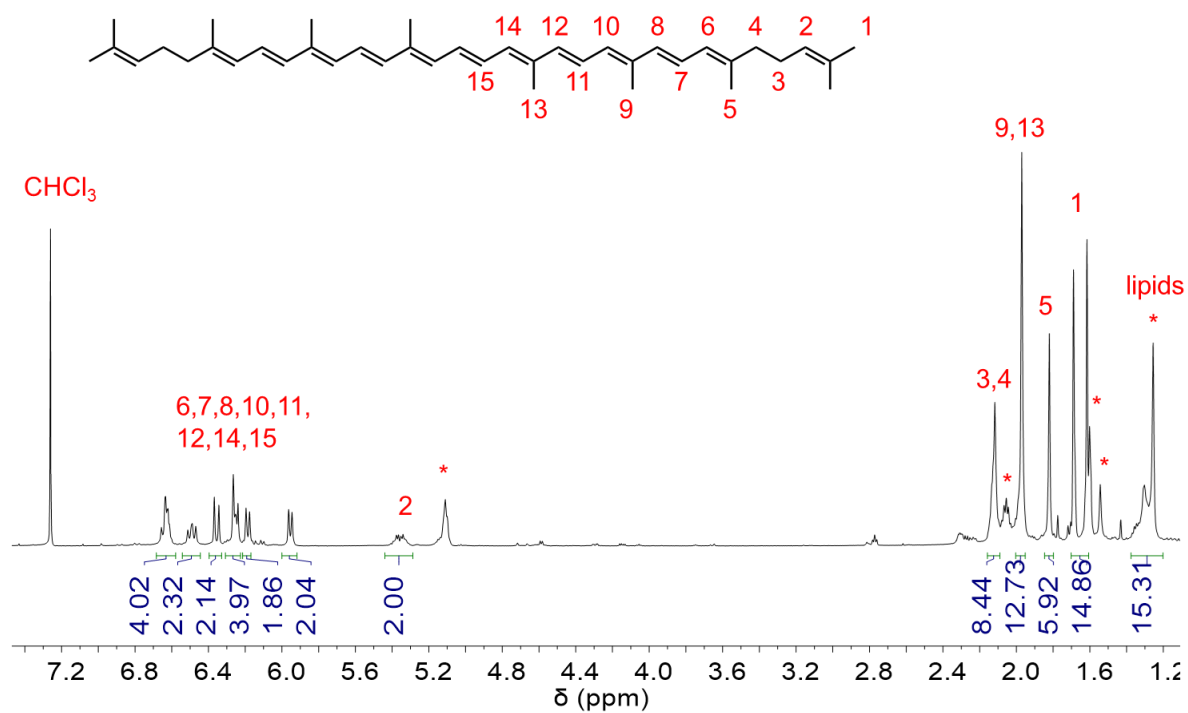


**Figure S51.**  $^1\text{H}$  NMR of (600 MHz,  $\text{DMSO-}d_6$ ) of silica chromatography separated lycopene recorded at 298 K.

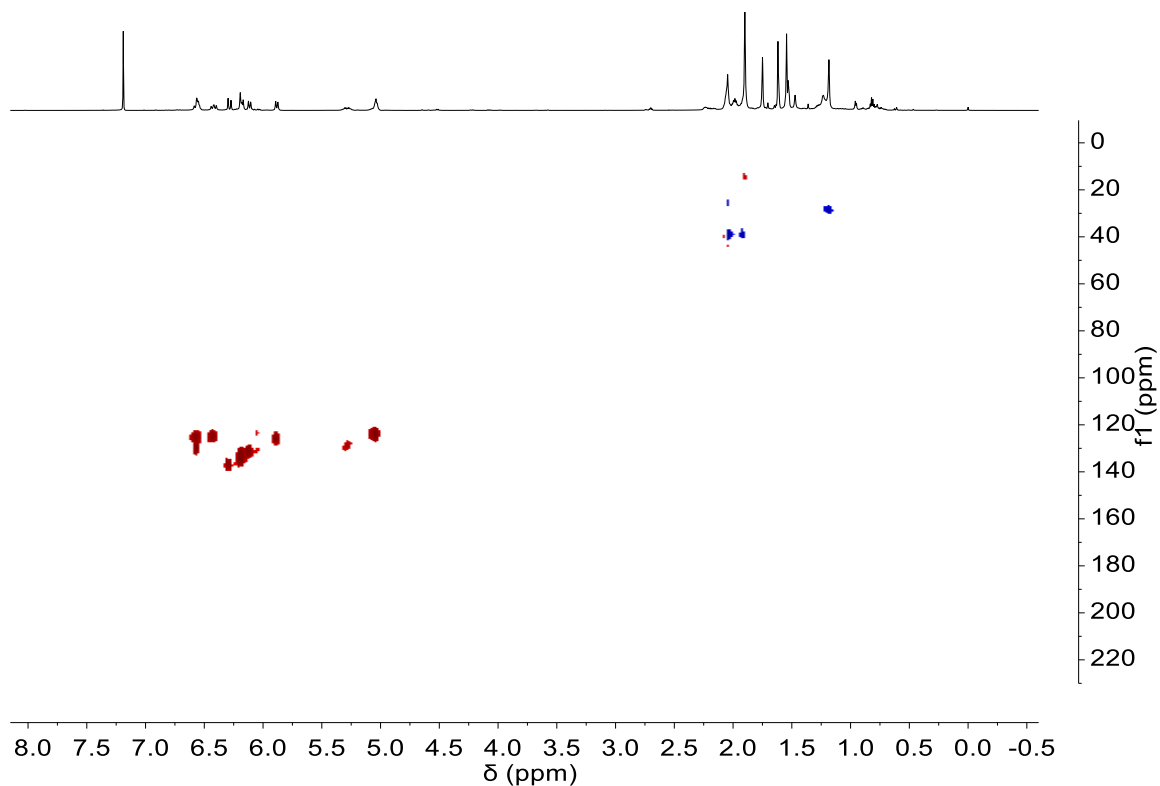


**Figure S52.**  $^1\text{H}^{13}\text{C}$  HSQC NMR spectrum (600 MHz,  $\text{DMSO-}d_6$ ) of silica chromatography separated lycopene recorded at 298 K.

**UV-vis spectra of the lycopene solution.** An 88.0  $\mu\text{M}$  silica chromatography-separated lycopene stock solution was prepared by dissolving silica chromatography separated lycopene (5.9 mg, ~80% purity, ~8.8  $\mu\text{mol}$ ) in 100 mL of acetone. Then the lycopene solution was diluted to 8.80 to 1.76  $\mu\text{M}$  for the standard curve calibration. The molar attenuation coefficient  $\epsilon$  is calculated as  $133000 \pm 4000$ ,  $180000 \pm 5000$ , and  $148000 \pm 4000 \text{ M}^{-1} \cdot \text{cm}^{-1}$  at 447 nm, 472 nm, and 502 nm, respectively.<sup>346</sup>

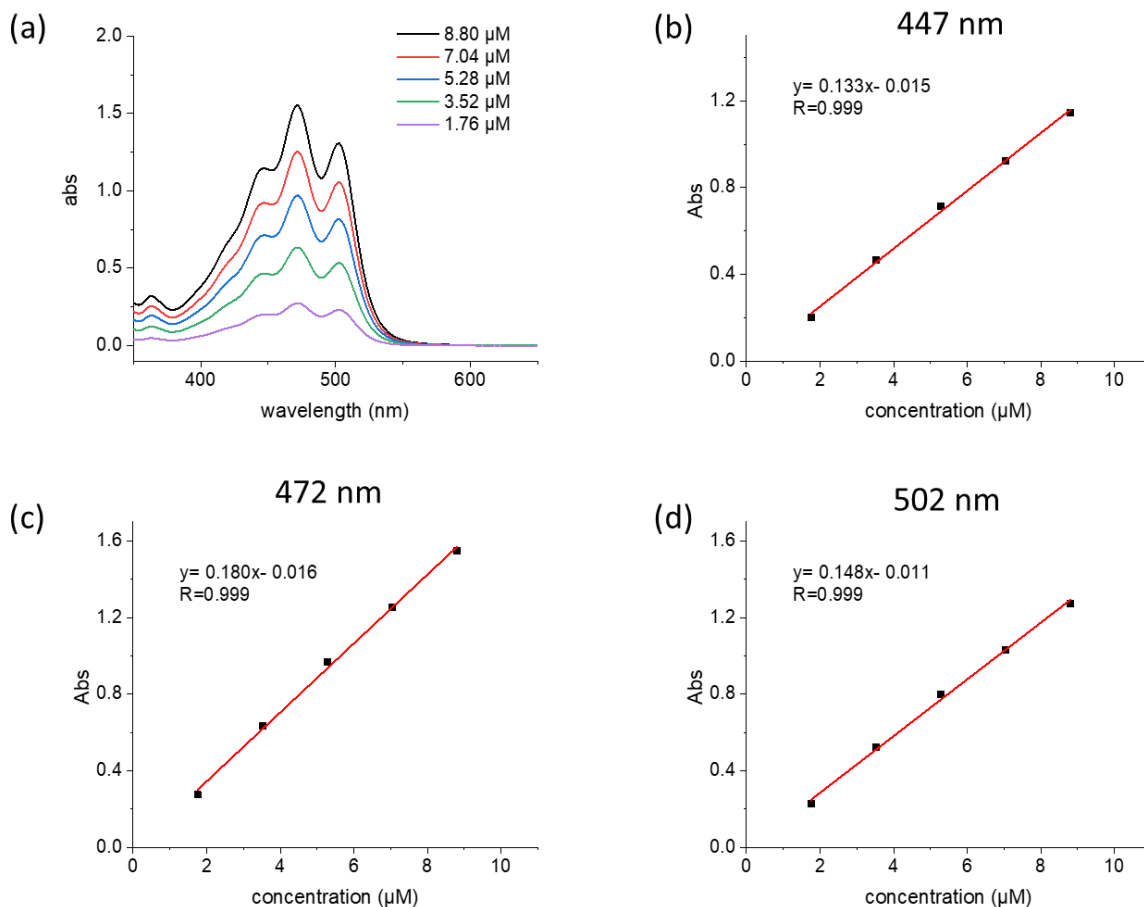


**Figure S53.** (a) UV-Vis spectra of the silica chromatography separated lycopene of acetone solution with different concentrations. And the linear fit of silica chromatography separated lycopene at (b) 447 nm, (c) 472 nm, and (d) 502 nm.

**Adsorption of lycopene using crosslinked CD polymers.** Fresh tomato juice (80 mL) was mixed with THF (20 mL) and sonicated for 1 h. A 3D-printed TDU-CD monolith or a TDU-CD<sub>ref</sub> powder (155 mg) was added to 20 mL of the tomato juice mixture and let stand. The vials are kept uncapped to allow the THF to evaporate in the open air. Every 6 h, the solution in the vials was piped out, and the new tomato juice mixture was refilled. After 48 h, the solution was pipetted out. The TDU-CD•lycopene or TDU-CD<sub>ref</sub>•lycopene was washed with water (200 mL) to remove any residue on the surface and dried under vacuum (0.06 torr) at 24 °C for 24h. The adsorbed guests in the crosslinked polymers were released by soaking the samples in acetone. The acetone solutions were subjected to LC-MS (Figures S53-54).

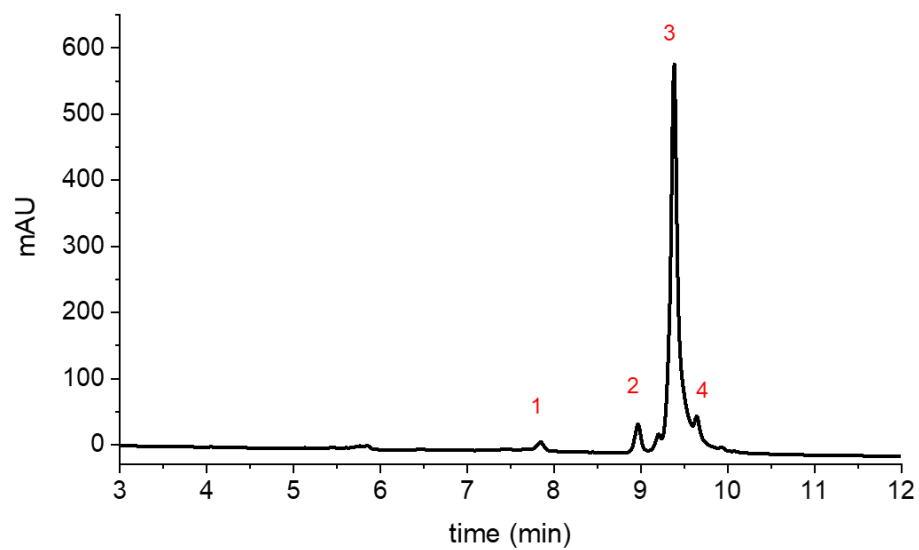


**Figure S54.** An LC-MS profile of released carotenoid solution by soaking the TDU-CD•lycopene in acetone. The absorptions of samples at 472 nm were monitored.

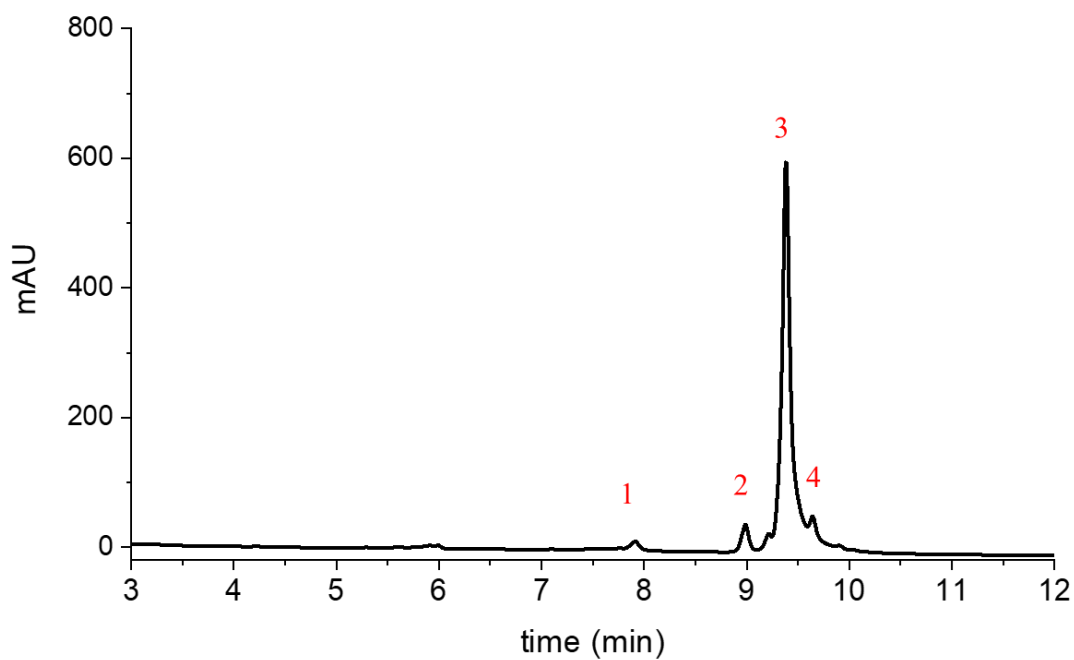


**Figure S55.** An LC-MS profile of released carotenoid solution by soaking the TDU-CD<sub>ref</sub>•lycopene in acetone. The absorptions of samples at 472 nm were monitored.

In the released carotenoids samples by soaking the TDU-CD•lycopene or TDU-CD<sub>ref</sub>•lycopene in acetone, analyses eluted around 7.85, 8.96, 9.38, and 9.64 min were identified as lycopene epoxides,  $\gamma$ -carotene, lycopene, and  $\beta$ -carotene/phytofluene mixture respectively. The integration of lycopene epoxides,  $\gamma$ -carotene, lycopene, and  $\beta$ -carotene/phytofluene mixture are calculated as 1%, 4%, 89%, and 6% in TDU-CD•lycopene and 3%, 5%, 91%, and 1% in TDU-CD<sub>ref</sub>•lycopene, respectively.

**Table S7.** Identification and chromatographic data of carotenoid in TDU-CD

<b>peak</b>	<b>compound</b>	<b>retention time (min)</b>	<b>peak area</b>	<b>UV-vis absorption peaks (nm)</b>	<b>m/z ratios</b>
<b>1</b>	lycopene epoxides	7.85	59753	470, 497	553
<b>2</b>	$\gamma$ -carotene	8.96	194010	440, 468, 496	537
<b>3</b>	lycopene	9.38	3811534	447, 472, 503	537
<b>4</b>	$\beta$ -carotene/ phytofluene	9.64	238842	429, 452, 477 331, 348, 367	537 543

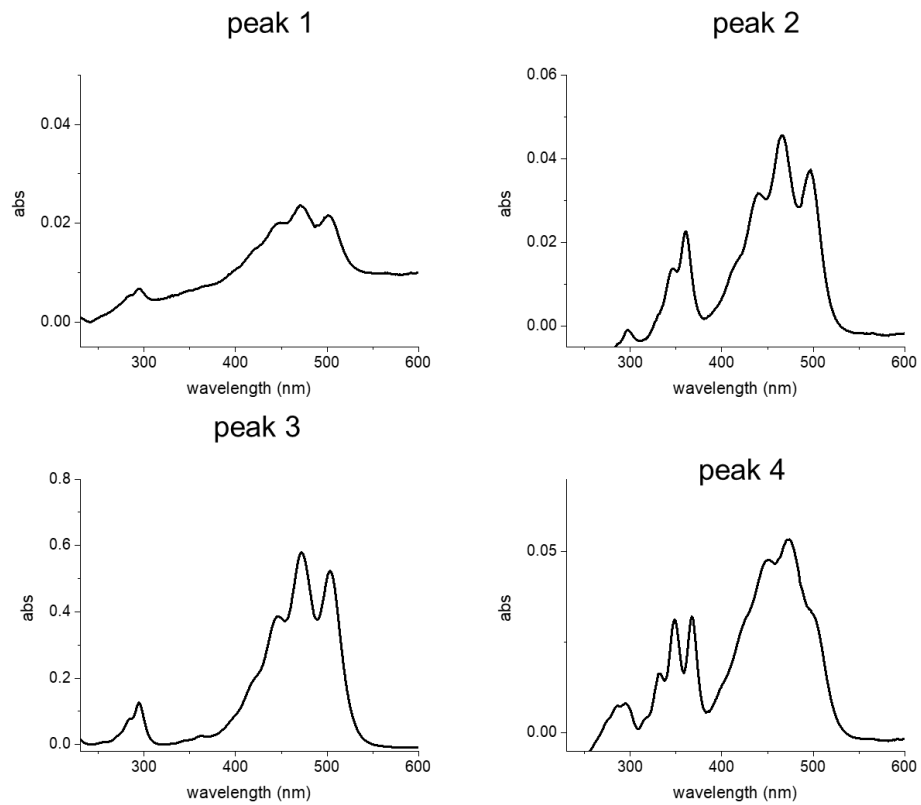


**Figure S56.** UV-Vis spectra of separated analytes TDU-CD•lycopene.

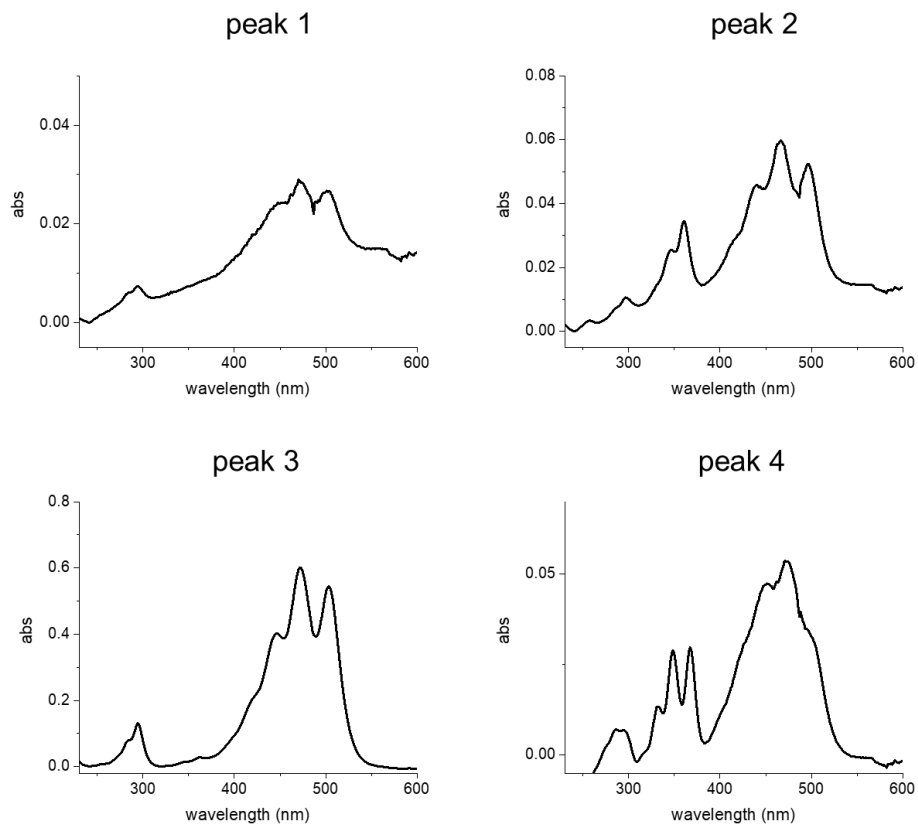


**Figure S57.** UV-Vis spectra of separated analytes in TDU-CD<sub>ref</sub>•lycopene.

**Table S8.** Identification and chromatographic data of carotenoid in TDU-CD<sub>ref</sub>

peak	compound	retention time (min)	peak area	UV-vis absorption peaks (nm)	m/z ratios
1	lycopene epoxides	7.89	132346	470, 497	553
2	$\gamma$ -carotene	8.98	233070	440, 468, 496	537
3	lycopene	9.38	4549167	447, 472, 503	537
4	$\beta$ -carotene/ phytofluene	9.63	74010	429, 452, 477 331, 348, 367	537 543





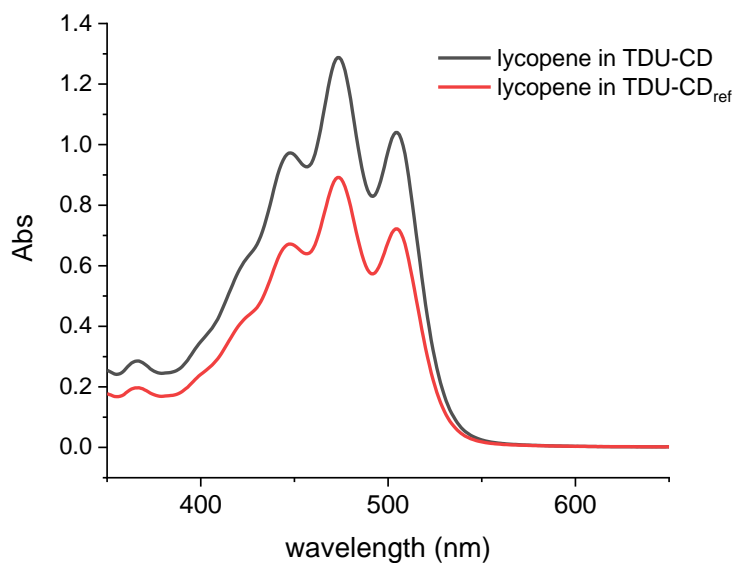


**Figure S59.** UV-vis spectra of released lycopene solution by immersing TDU-CD<sub>ref</sub>•lycopene (2.50 mg) and TDU-CD•lycopene (0.53 mg) into 3 mL of acetone.

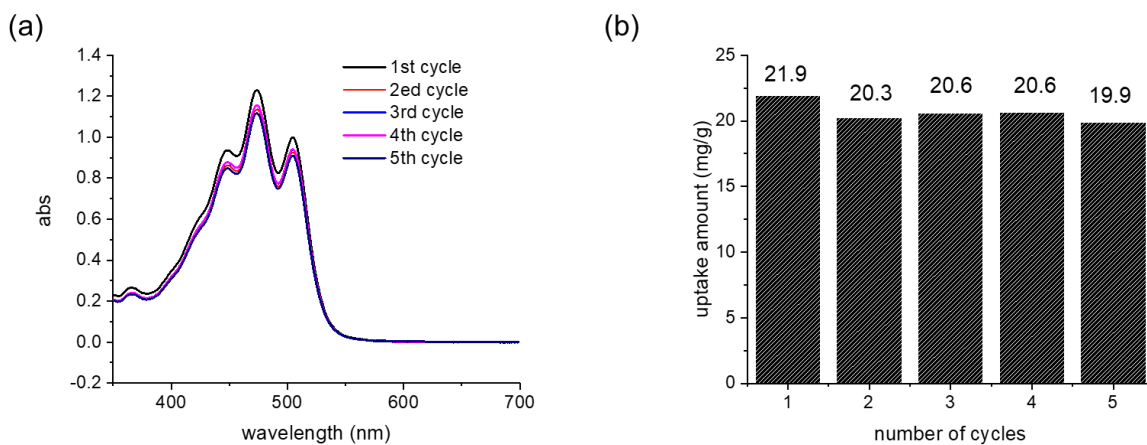


**Figure S60.** (a) UV-vis spectra of desorbed lycopene solutions by immersing TDU-CD•lycopene (0.5 mg) in 3 mL of acetone. (b) The lycopene adsorption capacity of TDU-CD in five sorption cycles.

**Desorption efficiency test.** After releasing lycopene into acetone, the recovered TDU-CD was dried in the open air for 6 h and immersed in  $\text{CDCl}_3$  or  $\text{DMSO-}d_6$  for 24 h.

The solution remains colorless, and no peaks of lycopene were shown in  $^1\text{H}$  NMR spectra (Figure S61).

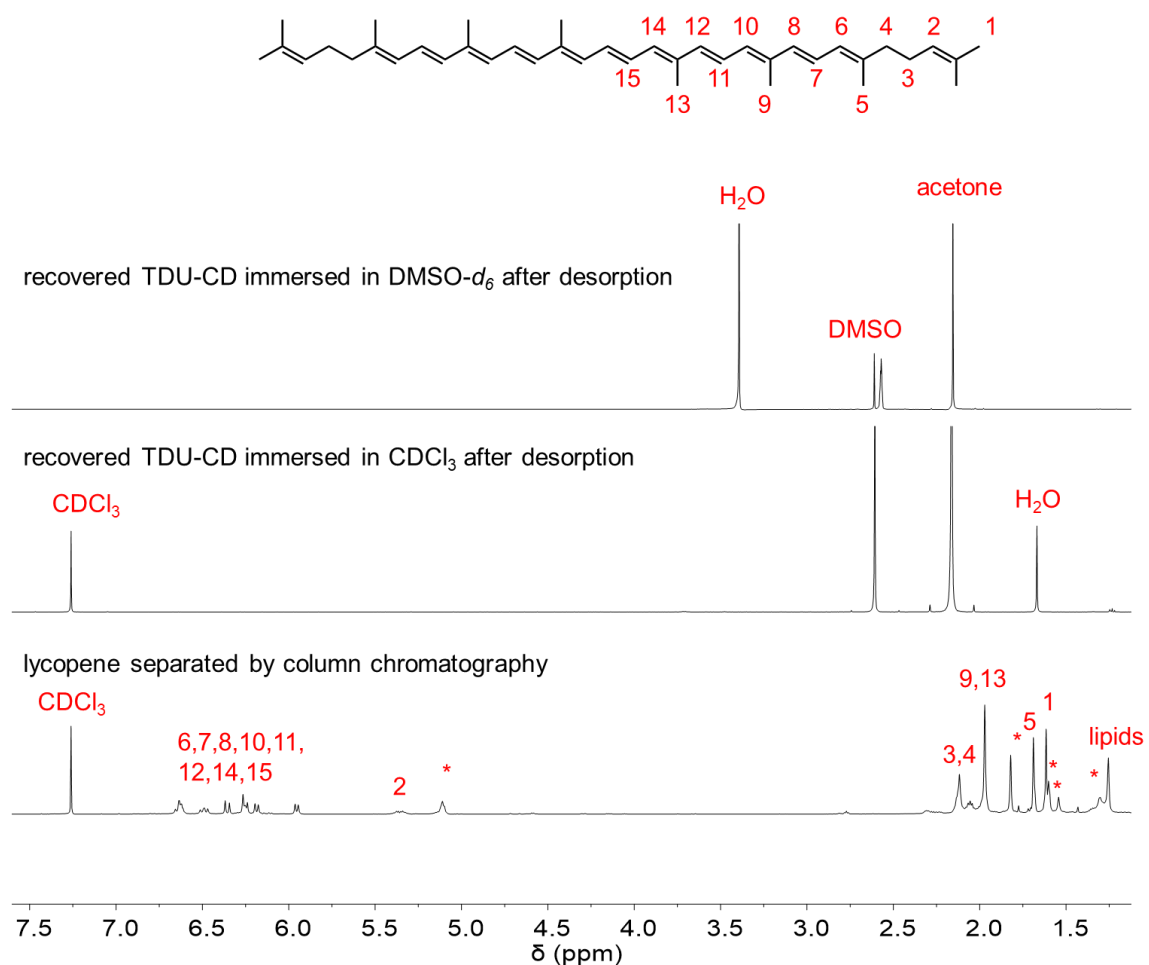


**Figure S61.**  $^1\text{H}$  NMR spectra (500 MHz, 298 K) of lycopene separated by column chromatography (bottom), recovered TDU-CD immersed in  $\text{CDCl}_3$  after desorption (middle), and recovered TDU-CD immersed in  $\text{DMSO-}d_6$  after desorption (top).

**Lycopene uptake saturation of TDU- $\text{CD}_{\text{ref}}$  study.** TDU- $\text{CD}_{\text{ref}}$  (15 mg) particles were first swelled in  $\text{DMSO}$  (2 mL) for 12 h, and then the solution was piped out. The swelled TDU- $\text{CD}_{\text{ref}}$  was immersed into the mixture of lycopene solution in  $\text{CH}_2\text{Cl}_2$  (5 mg/mL, 0.5 mL) and DI water (19.5 mL) with shanking, as the previous method described. The lycopene mixture was refreshed every 12 h. After 48 h and 120 h, around 5 mg of TDU- $\text{CD}_{\text{ref}}$ •lycopene was taken out from the vial. After washing with an excess amount of water and lyophilization, the collected TDU- $\text{CD}_{\text{ref}}$ •lycopene (2.5 mg) was immersed into acetone

(3 mL) with shaking for 12 h. The lycopene uptake amount of TDU-CD<sub>ref</sub> for 2-day adsorption and 5-day adsorption were measured as  $3.2 \pm 0.1$  and  $3.3 \pm 0.1$  mg/g, respectively, according to UV-vis spectra (Figure S62).

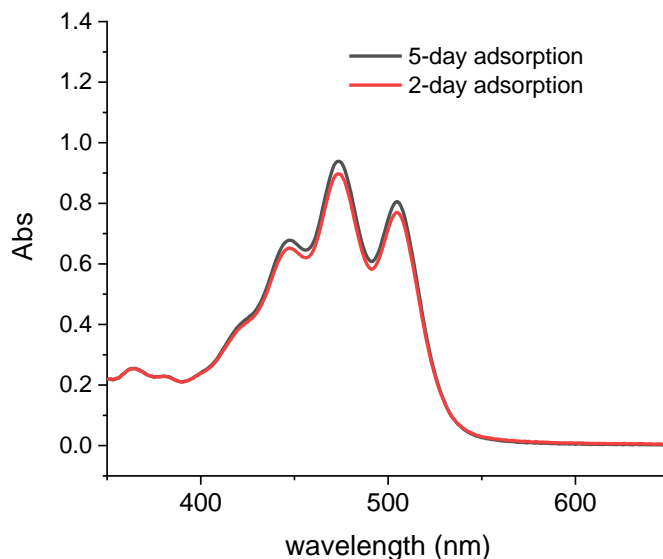


**Figure S62.** UV-vis spectra of released lycopene solution by immersing TDU-CD<sub>ref</sub>•lycopene (2.5 mg) into 3 mL of acetone after 2-day and 5-day adsorption experiments.

**Lycopene stability study.** TDU-CD•lycopene or TDU-CD<sub>ref</sub>•lycopene were heated to 50 °C for 24 h, 90 °C for 3 h, or treated with UV light for 24 h. Then lycopene was released by immersing TDU-CD•lycopene (1.0 mg) before and after heating or UV irradiation to 5 mL of acetone for 24 h with shaking. The obtained solutions were characterized by UV-vis spectroscopy (Figure S59).

In addition, to study the stability of lycopene in organic solutions, lycopene (3 mg) was dissolved in THF (300 mL). Then the 20 mL of solution was added to capped vials and heated to 50 °C, 66 °C (boiling), or treated with UV light. THF solution (3 mL) was piped out periodically for UV-vis spectra characterization (Figure S60). The lycopene content was measured using UV-vis spectroscopy by monitoring the absorption band at 504 nm. The recovered lycopene in TDU-CD•lycopene, TDU-CD<sub>ref</sub>•lycopene, and THF solution was compared in Figure S61.

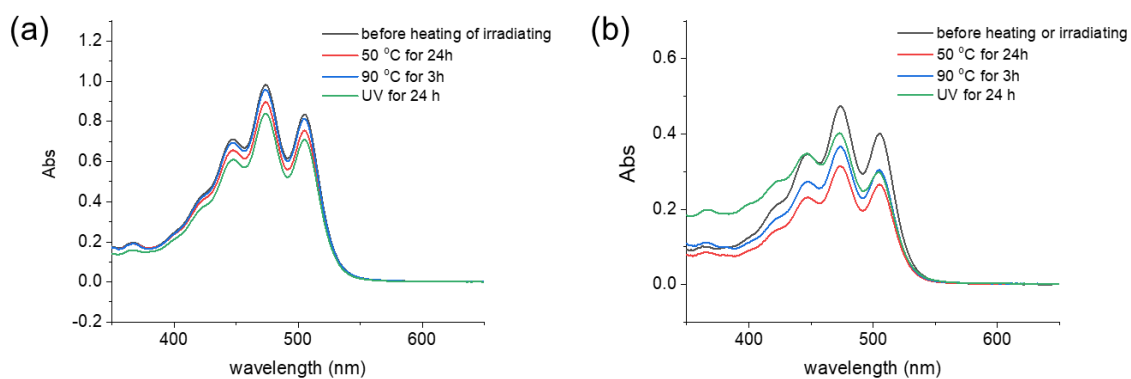


**Figure S63.** UV-Vis spectra of lycopene released from (a) TDU-CD or (b) TDU-CD<sub>ref</sub> before and after heating to 50 °C for 24 h, heating to 90 °C for 3h, and irradiating under UV light for 24 h.

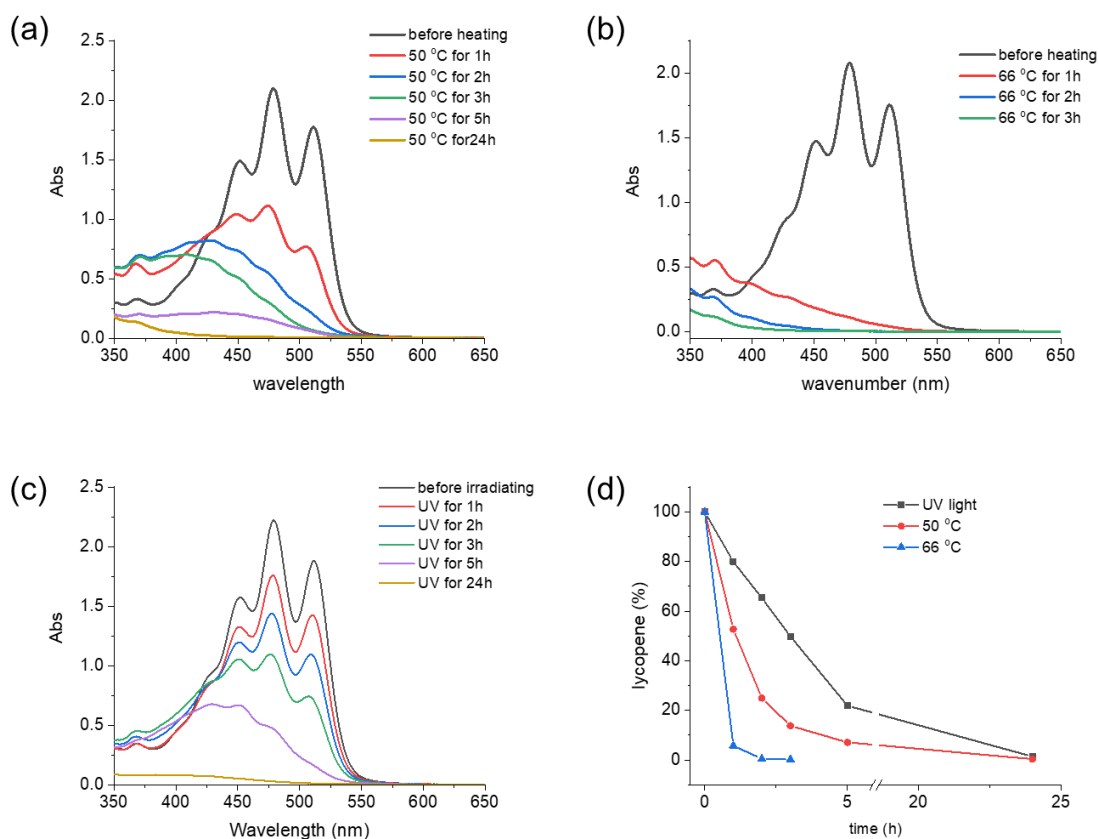


**Figure S64.** UV-Vis spectra of the lycopene solution in THF after (a) heating at 50 °C for different times, (b) heating at 66 °C for different times, (c) treating with UV for different times, (d) time-dependent recovered lycopene in THF under 50 °C, 66 °C, and UV light

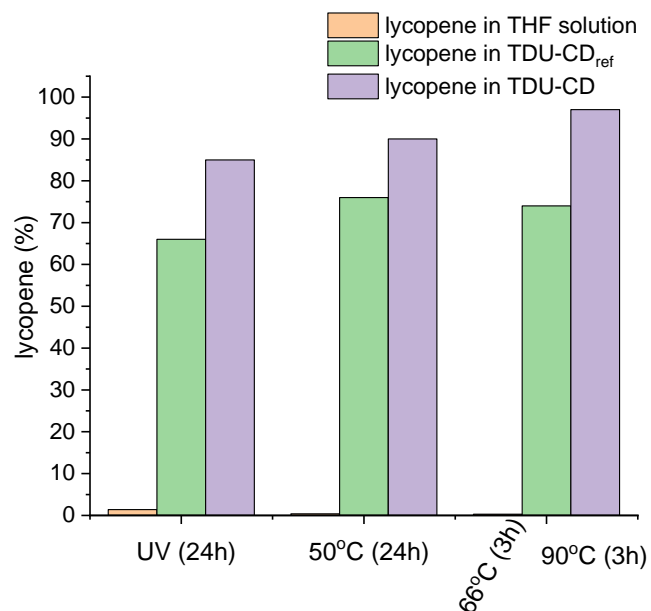


**Figure S65.** Recovered lycopene after UV-irradiation and thermos-treatments, measured using the UV-Vis spectrometer.

**TDU-CD stability study.** TDU-CD (10 mg) was heated to 90 °C or irradiated under UV light for 24h in a 20 mL open vial. Then the solid was characterized by FTIR (Figure S66) or hydrolyzed in 0.5 mL of NaOD/D<sub>2</sub>O (5%) at 70 °C and characterized by <sup>1</sup>H NMR (Figure S67).

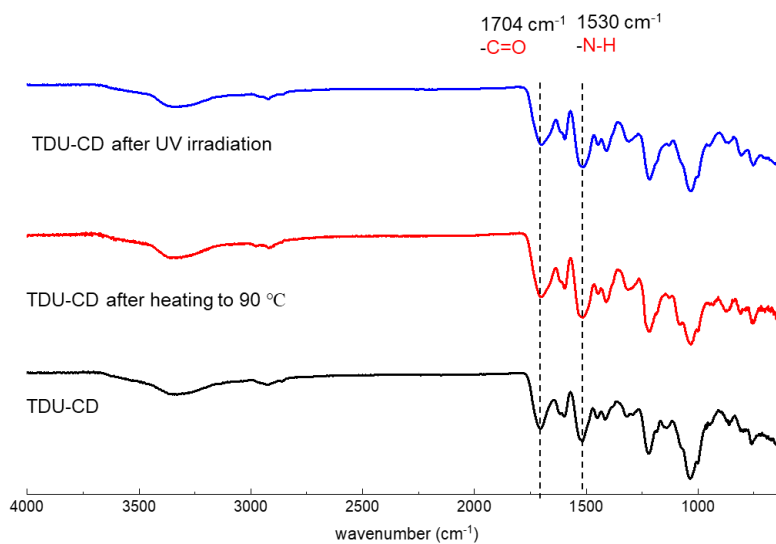


**Figure S66.** FT-IR spectra of TDU-CD, TDU-CD after heating to 90 °C for 24 h, and TDU-CD after UV irradiation for 24 h, from the bottom to the top, respectively.

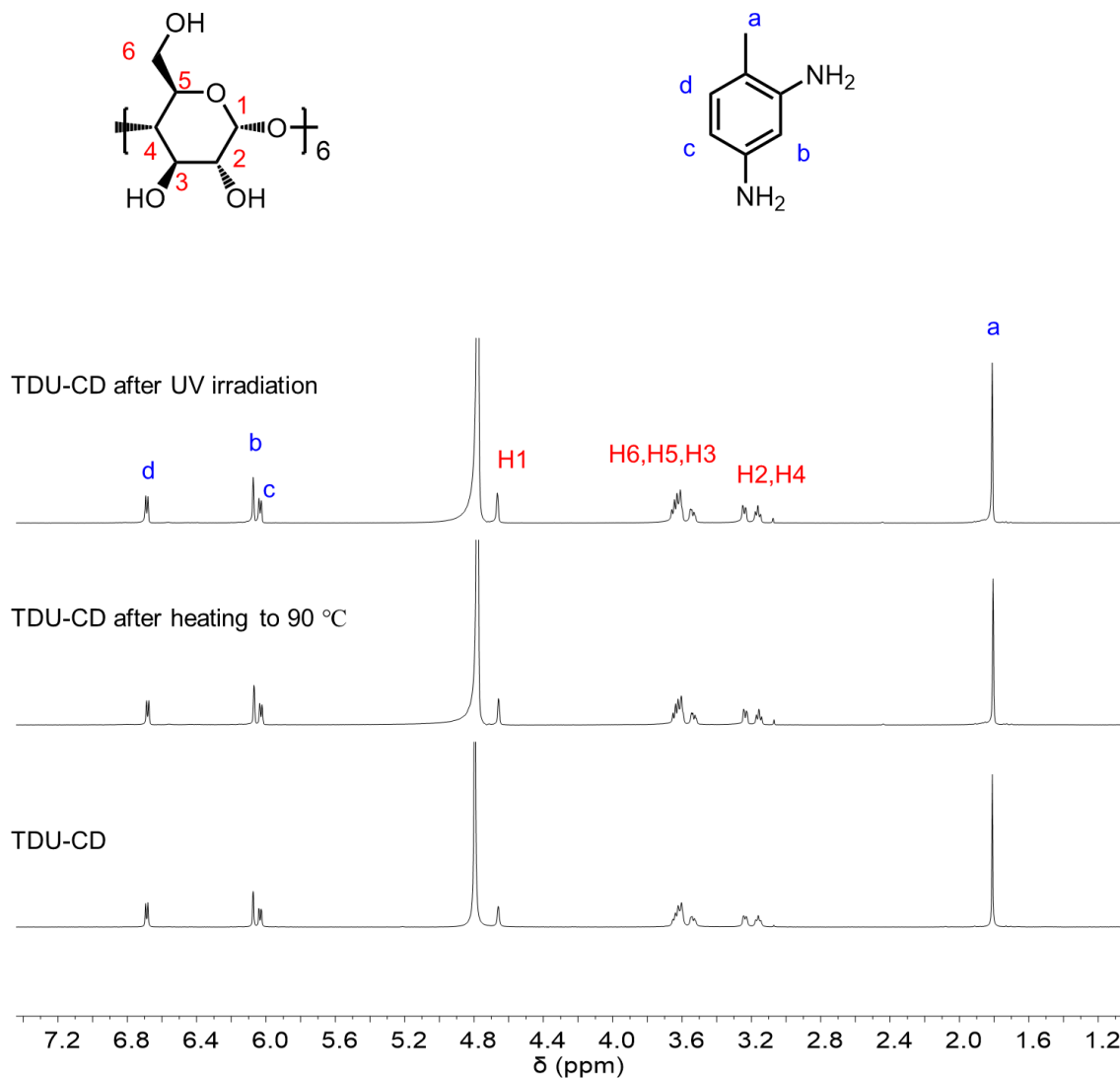


**Figure S67.**  $^1\text{H}$  NMR (600 MHz, 298 K) of the hydrolyzed TDU-CD, TDU-CD after heating at 90 °C for 24 h, and TDU-CD after UV-irradiation for 24 h in NaOD/D<sub>2</sub>O (5%), from the bottom to the top, respectively.

## 5.5 References

- 300 W. J. Craig, *J. Am. Diet Assoc.* **1997**, *97*, 199-204.
- 301 S. Rochfort, J. Panozzo, *J. Agr. Food Chem.* **2007**, *55*, 7981-7994.
- 302 A. S. Choudhari, P. C. Mandave, M. Deshpande, P. Ranjekar, O. Prakash, *Front. Pharmacol.* **2020**, *11*, 1614.
- 303 S. K. Clinton, *Nutr. Rev.* **1998**, *56*, 35-51.

- 304 Y. F. Liu, J. X. Liu, X. F. Chen, Y. W. Liu, D. L. Di, *Food Chem.* **2010**, *123*, 1027-1034.
- 305 M. Asaduzzaman, *Annu. Res. Rev. Biol.* **2022**, *37*, 87-101.
- 306 S. M. Rivera, R. Canela-Garayoa, *J. Chromatogr. A* **2012**, *1224*, 1-10.
- 307 I. Volf, I. Ignat, M. Neamtu, V. I. Popa, *Chem. Pap.* **2014**, *68*, 121-129.
- 308 M. I. Guerra-Rosas, J. Morales-Castro, L. A. Ochoa-Martinez, L. Salvia-Trujillo, O. Martin-Belloso, *Food Hydrocoll.* **2016**, *52*, 438-446.
- 309 V. Suvarna, P. Gujar, M. Murahari, *Biomed. Pharmacother.* **2017**, *88*, 1122-1144.
- 310 P. Arora, N. Dhingra, *Cyclodextrin: A Versatile Ingredient*, BoD–Books on Demand, **2018**.
- 311 W. Saenger, *Angew. Chem. Int. Edit.* **1980**, *19*, 344-362.
- 312 N. K. Dhakar, A. Matencio, F. Caldera, M. Argenziano, R. Cavalli, C. Dianzani, M. Zanetti, J. M. Lopez-Nicolas, F. Trotta, *Pharmaceutics* **2019**, *11*, 545.
- 313 V. Suvarna, B. Bore, C. Bhawar, R. Mallya, *Biomed. Pharmacother.* **2022**, *149*, 112862.
- 314 N. Morin-Crini, G. Crini, *Prog. Polym. Sci.* **2013**, *38*, 344-368.
- 315 S. Amiri, S. Amiri, *Cyclodextrins: properties and industrial applications*, John Wiley & Sons, **2017**.
- 316 Z. W. Jiang, R. J. Dong, A. M. Evans, N. Biere, M. A. Ebrahim, S. Y. Li, D. Anselmetti, W. R. Dichtel, A. G. Livingston, *Nature* **2022**, *609*, 58.
- 317 A. Alsbaiee, B. J. Smith, L. Xiao, Y. Ling, D. E. Helbling, W. R. Dichtel, *Nature* **2016**, *529*, 190-194.
- 318 F. Zha, S. G. Li, Y. Chang, *Carbohydr. Polym.* **2008**, *72*, 456-461.
- 319 J. M. Halpern, C. A. Gormley, M. A. Keech, H. A. von Recum, *J. Mater. Chem. B* **2014**, *2*, 2764-2772.
- 320 M. Arslan, R. Sanyal, A. Sanyal, *Polym. Chem.* **2020**, *11*, 615-629.
- 321 A. Harada, J. Li, M. Kamachi, *Nature* **1993**, *364*, 516-518.
- 322 T. Akai, T. Abe, T. Shimomura, K. Ito, *Jpn. J. Appl. Phys. 2* **2001**, *40*, 1327-1329.
- 323 M. Saito, T. Shimomura, Y. Okumura, K. Ito, R. Hayakawa, *J. Chem. Phys.* **2001**, *114*, 1-3.
- 324 T. Shimomura, T. Akai, T. Abe, K. Ito, *J. Chem. Phys.* **2002**, *116*, 1753-1756.
- 325 T. Ikeda, W. K. Lee, T. Ooya, N. Yui, *J. Phys. Chem. B* **2003**, *107*, 14-19.
- 326 S. Samitsu, J. Araki, T. Shimomura, K. Ito, *Macromolecules* **2008**, *41*, 5385-5392.
- 327 Q. Y. Chen, J. Y. Zhao, J. B. Ren, L. H. Rong, P. F. Cao, R. C. Advincula, *Adv. Funct. Mater.* **2019**, *29*.
- 328 X. C. Tian, K. Zhou, *Nanoscale* **2020**, *12*, 7416-7432.

- 329 T. Ikeda, T. Ooya, N. Yui, *Macromol. Rapid Comm.* **2000**, *21*, 1257-1262.
- 330 E. Ikeda, Y. Okumura, T. Shimomura, K. Ito, R. Hayakawa, *J. Chem. Phys.* **2000**, *112*, 4321-4325.
- 331 C. Y. Cheng, P. R. McGonigal, S. T. Schneebeli, H. Li, N. A. Vermeulen, C. F. Ke, J. F. Stoddart, *Nat. Nanotechnol.* **2015**, *10*, 547-553.
- 332 Y. Y. Qiu, B. Song, C. Pezzato, D. K. Shen, W. Q. Liu, L. Zhang, Y. N. Feng, Q. H. Guo, K. Cai, W. X. Y. Li, H. L. Chen, M. T. Nguyen, Y. Shi, C. Y. Cheng, R. D. Astumian, X. P. Li, J. F. Stoddart, *Science* **2020**, *368*, 1247.
- 333 I. N. Topchieva, A. E. Tonelli, I. G. Panova, E. V. Matuchina, F. A. Kalashnikov, V. I. Gerasimov, C. C. Rusa, M. Rusa, M. A. Hunt, *Langmuir* **2004**, *20*, 9036-9043.
- 334 T. Dong, Y. He, B. Zhu, K. M. Shin, Y. Inoue, *Macromolecules* **2005**, *38*, 7736-7744.
- 335 M. Ceccato, P. LoNostro, P. Baglioni, *Langmuir* **1997**, *13*, 2436-2439.
- 336 Q. Lin, X. Hou, C. Ke, *Angew. Chem. Inter. Edit.* **2017**, *56*, 4452-4457.
- 337 Q. M. Lin, L. Y. Li, M. Tang, X. S. Hou, C. F. Ke, *J. Mater. Chem. C* **2018**, *6*, 11956-11960.
- 338 A. Harada, J. Li, M. Kamachi, *Nature* **1992**, *356*, 325-327.
- 339 G. Wenz, B. H. Han, A. Muller, *Chem. Rev.* **2006**, *106*, 782-817.
- 340 J. Szejtli, *Chem. Rev.* **1998**, *98*, 1743-1753.
- 341 G. Crini, L. Aleya, *Environ. Sci. Pollut. R.* **2022**, *29*, 167-170.
- 342 F. Khachik, G. R. Beecher, M. B. Goli, W. R. Lusby, J. C. Smith, *Anal. Chem.* **1992**, *64*, 2111-2122.
- 343 J. Shi, M. Le Maguer, Y. Kakuda, A. Liptay, F. Niekamp, *Food Res. Int.* **1999**, *32*, 15-21.
- 344 R. K. Saini, A. E. D. A. Bekhit, S. Roohinejad, K. R. R. Rengasamy, Y. S. Keum, *J. Agr. Food Chem.* **2020**, *68*, 712-726.
- 345 R. E. Kopec, R. M. Schweiggert, K. M. Riedl, R. Carle, S. J. Schwartz, *Rapid Commun. Mass. Sp.* **2013**, *27*, 1393-1402.
- 346 M. Takehara, M. Nishimura, T. Kuwa, Y. Inoue, C. Kitamura, T. Kumagai, M. Honda, *J. Agr. Food Chem.* **2014**, *62*, 264-269.



## **Chapter 8 Conclusion**

In summary, this thesis has focused on the development of porous organic materials, encompassing their molecular design, host-guest interactions, and device fabrication. At the microscopic scale, the thesis provides new insights into the design of single-crystal organic materials, such as H<sub>C</sub>OFs, and showcases their host-guest interaction capabilities through obtained single-crystal data. On the macroscopic scale, the thesis achieves the device processing of porous organic materials by introducing using direct ink writing (DIW) the 3D printing techniques while retaining their crystallinity and porosity.

Chapter 1 begins with a review of the development history and classic examples of hydrogen-bonded crosslinked organic frameworks (H<sub>C</sub>OFs) and related framework materials. The methods for constructing controllable hydrogen-bonding networks using hydrogen-bonding functional groups, as well as crosslinking methods such as thiol-ene and [2+2] cycloaddition for single-crystal to single-crystal transformation, are highlighted. These methods provide effective pathways for the design and synthesis of H<sub>C</sub>OFs. By obtaining single-crystal structures through X-ray crystallography, this chapter establishes a clear connection between the H<sub>C</sub>OF structures and their unique dynamic adsorption properties. Furthermore, the chapter summarizes successful examples of 3D-printed porous materials, introduces general approaches for manufacturing printable inks, and outlines effective methods for creating pore sizes through second growth and phase separation. A comprehensive review of 3D-printing different types of porous material and their applications are presented.

Chapter 2 presents an example that investigates the framework-substrate and substrate-substrate interactions through single-crystal analysis. A series of single crystals of hydrogen-bonded organic framework complexed with various guests, including aniline, o-toluidine, m-toluidine, p-toluidine, toluene, and N-vinyl-2-pyrrolidone, were obtained. Structural analysis of the single crystals reveals the formation of cyclic tetramers within HOF-1 due to strong HOF-1-guest hydrogen bonding and N-H· $\pi$  interactions. Weak C-H· $\pi$  or C-H·O interactions between guests further stabilize these cyclic tetramers. The strong framework-substrate interactions enable the absorption of aniline and N-vinyl-2-pyrrolidone in the same cavity of HOF-1, with residual acid within HOF-1 catalyzing alkylation reactions within the cavity. This example contributes to a deeper understanding of host-guest and guest-guest interactions in crystals and their impact on chemical reactions within the pores.

Chapter 3 reports a novel ion-type H<sub>c</sub>OF applied for the simultaneous removal of iodine molecules and I<sup>-</sup> ions at high temperatures. H<sub>c</sub>OF-7, formed through eutectic formation of protonated organic monomers and nitrate dimer, exhibits a porous hydrogen-bonded network and covalent crosslinking through thiol-ene reactions. It not only achieves stability at high temperatures due to covalent crosslinking but also effectively removes iodine and iodide from water through its halogen-bonding groups and anion exchange. H<sub>c</sub>OF-7 demonstrates outstanding total residual iodine removal ability at low concentrations of iodine and iodide, with total residual iodine concentrations as low as 0.22 ppm measured after the intake of a 5 ppm iodine/iodide solution. Additionally, its supramolecular design exhibits strong selectivity. The filled H<sub>c</sub>OF-7 column shows significant breakthrough volumes (18.3 to 20.0 L g<sup>-1</sup>) in dynamic adsorption experiments at different temperatures (23-90 °C). This content inspires researchers to construct novel covalently linked porous single-crystal materials and utilize rational host-guest supramolecular interactions for applications such as water treatment.

Chapter 4 presents a novel and versatile method for integrating covalent organic frameworks (COFs) with imine or  $\beta$ -ketoenamine linkages into 3D-printed materials. The printable glue with appropriate shear thinning and rapid self-healing properties is achieved through the co-assembly of 3D printing template Pluronic F127 and imine polymers in an aqueous environment. After removing F127, a transition from amorphous to crystalline state is achieved through annealing, resulting in the 3D printed synthesis of three different adhesive-free imine-based COFs. The obtained materials exhibit high crystallinity, high surface area hierarchical pores, good structural integrity, and strong mechanical stability. Furthermore, this research demonstrates the integration of different COFs into a single device through molecular-level interconnections. This study inspires researchers on how to process COFs into binder-free 3D devices, through hierarchical self-assembly and template synthesis.

Chapter 5 reports a template synthesis method for 3D printable nanotubular polymeric materials crosslinked with amino-methylated  $\alpha$ -cyclodextrin ( $\alpha$ -CD). Ink with good rheological properties suitable for direct ink writing (DIW) is prepared by the precisely controlled self-assembly of tetraethoxysilane-based telechelic polyethylene glycol and  $\alpha$ -cyclodextrin polypseudorotaxane. After 3D printing into the desired macroscopic shapes, the obtained polypseudorotaxane is crosslinked through multiple steps, and the PEG axis is removed, resulting in hollow nanotubular structures and mesopores. The resulting 3D-

printed amorphous porous organic polymer selectively adsorbs lycopene from tomato juice, protecting it from light or heat degradation. This work emphasizes the combination of bottom-up molecular assembly and synthesis with top-down 3D architectural manufacturing, highlighting the layered template synthesis method for developing functional 3D printable materials.

Overall, this thesis demonstrates the methods and mechanisms for the development of single-crystalline porous organic materials and their integration into devices. The author aims to contribute as a bridge between molecular structure design, molecular self-assembly, micro-meso pore engineering, and macroscopic structure from a bottom-up approach. It is envisioned that through the integration of knowledge from different fields such as crystal engineering, reticular chemistry, polymer chemistry, 3D printing, and mechanics, significant contributions can be made towards the manufacturing of scalable, high-performance organic porous materials that are designed, tailorable, and suitable for large-scale industrial device applications.